

**EUROPEAN  
MECHANICS  
SOCIETY**

# **Euromech Colloquium 509**

## **Vehicle Aerodynamics**

External Aerodynamics of Railway Vehicles, Trucks, Buses and Cars

## **Proceedings**

(final version)

24. & 25.3.2009 at

Hermann-Föttinger-Institute,

TU Berlin

(Chair of Fluid Mechanics, Prof. Dr.-Ing. C. O. Paschereit)

Chairman: Dr.-Ing. Martin Schober, Bombardier Transportation  
Co-Chairmen: Professor Lennart Löfdahl, Chalmers University &  
Dr.-Ing. C. Navid Nayeri, TU Berlin



# Contents

<b>Unsteady RANS simulations of flows around a simplified car body</b> <i>Thomas Ceyrowsky, Christoph Brücker, Rüdiger Schwarze</i>	5
<b>Wind tunnel tests on heavy road vehicles: cross wind induced loads</b> <i>Federico Cheli, Roberto Corradi, Edoardo Sabbioni, Gisella Tomasini</i>	15
<b>Train shape optimisation to improve cross-wind behaviour</b> <i>Federico Cheli, Francesco Ripamonti, Daniele Rocchi, Gisella Tomasini</i>	27
<b>Unsteady aerodynamic crosswind stability of a high-speed train subjected to gusts of various rates</b> <i>Ben Diedrichs</i>	40
<b>Qualitative investigation of the main flow features over a TGV</b> <i>Thomas Duriez, Jean-Luc Aider, Elisa Masson, Jose E. Wesfreid</i>	52
<b>Investigations of aerodynamic correction methods applied to a slotted wall wind tunnel</b> <i>Matthias P. Eng, Tim E. Walker</i>	58
<b>CFD validation project on a vehicle-scale model under the constraint of an open jet wind tunnel</b> <i>Oliver Fischer, Timo Kuthada, Nils Widdecke, Jochen Wiedemann</i>	70
<b>Comparison of experimental and numerical results for a reference CAF train exposed to cross winds</b> <i>Javier García, Jorge Muñoz, Antonio Crespo, Aitor Berasarte</i>	82
<b>Experimental investigation on a detailed european tractor-trailer configuration</b> <i>Johannes Haff, Mattias Jönsson, Hugues Richard, Sigfried Loose</i>	93
<b>Shape optimization in train aerodynamics</b> <i>Astrid H. Herbst, Johannes Mauss, Jan Heiland, Alexander Orellano</i>	105
<b>Wind tunnel experiments of a high speed train exposed to cross wind on ground and bridge configurations</b> <i>Lars Hoefener, Daniel Romann, Christian Navid Nayeri, Thorsten Tielkes, Christian Oliver Paschereit</i>	117

<b>Important gaps in the science of car aerodynamics</b> <i>Wolf-Heinrich Hucho</i>	130
<b>PIV investigation of the flow field underneath a generic high-speed train configuration</b> <i>Mattias Jönsson, Johannes Haff, Hugues Richard, Sigfried Loose, Alexander Orellano</i>	139
<b>Shape optimization of a bus for crosswind stability</b> <i>Siniša Krajnović, Haukur Elvar Hafsteinsson, Eysteinn Helgason, Branislav Basara</i>	151
<b>Flow field around and in a Saab 9-3 convertible</b> <i>Jesper Marklund, Håkan Danielsson, Lennart L"ofdahl</i>	163
<b>CFD analysis of the underfloor aerodynamics of a complete TGV high speed train set at full scale</b> <i>Elisa Masson, Eliane Allain, Nicolas Paradot</i>	177
<b>Detached Eddy Simulation and validation on the aerodynamic train model</b> <i>Thomas W. Muld, Gunilla Efraimsson, Dan S. Henningson, Astrid H. Herbst, Alexander Orellano</i>	193
<b>Single- and multi-objective aerodynamic optimization of a simplified vehicle test body using evolutionary algorithms and artificial neural networks</b> <i>Christoph Niedermeier, Norbert Grün, Thomas Indinger</i>	207
<b>Aerodynamic simulation of a car overtaking a lorry using embedded mesh technology</b> <i>Sven Perzon, Johan Stangvik, Per Österdahl, Lasse Christoffersen</i>	219
<b>Comparison of wind tunnel tests results on the ATM train</b> <i>Daniele Rocchi, Martin Schober, Federico Cheli, Alexander Orellano, Gisella Tomasini</i>	229
<b>Reference wind tunnel measurements on aerodynamic coefficients of ICE 3 end car</b> <i>Nina Rüd, Sigfried Loose, Thomas Kowalski, Arnd Rüter, Martin Schober, Marc Stiepel</i>	239
<b>Cross wind safety: operation of railway freight vehicles under strong gusts</b> <i>Nina Rüd, Thorsten Tielkes</i>	251
<b>Railway ballast flying phenomenon: from numerical computations toward risk assessment</b> <i>Gilles Saussine, Elisa Masson, Jacques Thomas-Jean, Nicolas Paradot, Eliane Allain, Frédéric Josse</i>	258
<b>Dynamics of flow in wake behind Ahmed body</b> <i>Václav Uruba</i>	270

<b>A practical scientific approach for aerodynamic truck design</b>	282
<i>Gandert van Raemdonck, Michel van Tooren</i>	
<b>abstract: Flow control over simplified 3D bluff-bodies and road vehicles</b>	293
<i>Jean-Luc Aider, J. J. Lasserre, J. F. Beaudoin, V. Herbert, Jose E. Wesfreid</i>	
<b>abstract: The effect of unsteady crosswind forces on train dynamic behaviour</b>	294
<i>Chris Baker</i>	
<b>abstract: Further development and application of the SaOB actuator array for manipulation of large vehicle aerodynamics</b>	295
<i>Isaac Dayan, Ilan Fono, Avi Seifert</i>	
<b>abstract: Determination of aerodynamic coefficients of the TGV Duplex in wind tunnel for flat ground configurations</b>	296
<i>Rémi Grégoire, Nicolas Paradot, Jean-Paul Bouchet</i>	
<b>abstract: Comparison of the flow field and aerodynamic performance of different regional trains exposed to cross winds by means of CFD and wind tunnel experiments</b>	297
<i>Henning Kroll, Martin Schober, Christian Navid Nayeri, Christian Oliver Paschereit</i>	
<b>abstract: Towing tank experiments for heavy vehicle aerodynamics</b>	298
<i>Christian Navid Nayeri, Jakob Marquard, Andreas Fischer, Christian Oliver Paschereit</i>	
<b>abstract: Aerodynamic analysis of high-speed trains by CFD simulations based on Lattice Boltzmann and Finite Volume Method</b>	299
<i>Yiwei Wang, Yiran An</i>	
<b>List of participants</b>	300



## UNSTEADY RANS SIMULATIONS OF FLOWS AROUND A SIMPLIFIED CAR BODY

Thomas Ceyrowsky\*, Christoph Brücker<sup>†</sup> and Rüdiger Schwarze<sup>†</sup>

\*MAN Turbo AG  
Calculation / R&D Compressors (PC1), Steinbrinkstr. 1, 46145 Oberhausen, Germany  
e-mail: thomas.cejrowsky@man.eu

<sup>†</sup>Institute of Mechanics and Fluid Dynamics,  
TU Bergakademie Freiberg, Lampadiusstr. 4, 09596 Freiberg, Germany  
e-mails: christoph.bruecker@imfd.tu-freiberg.de,  
ruediger.schwarze@imfd.tu-freiberg.de

**Keywords:** Ahmed body, Aerodynamics, URANS simulation, Crow instability

**Abstract:** *Computational fluid dynamics (CFD) is a popular tool in the design and optimization process of vehicles. Reliable numerical models of the vehicle aerodynamics should resolve basic features of the flow around the vehicle under investigation without any fitting procedure. On the other hand, the simulations should be economical, i. e. long computing times and high memory requirements should be avoided. In our contribution, numerical simulations of the flows around the Ahmed reference car body based on the unsteady Reynolds-averaged Navier-Stokes (URANS) equations are presented. The Ahmed body is a simplified car used in automotive industry to investigate the influence of the flow structure e. g. on the drag. The flow around the Ahmed body exhibits basic features, which are also characteristic for other bluff body vehicles, namely trucks, buses or trains: There exist large coherent vortex structures and elongated separated flow regions downstream of the Ahmed body. The vortices, the detached flows, and the boundary layers at the body contours interact strongly, these interactions are of fundamental importance for aerodynamical parameters of the car. In our study, Ahmed bodies with different rear geometries (slant angles  $\varphi$  of  $25^\circ$  and  $35^\circ$ ) are investigated. The findings from the numerical simulations are in agreement with corresponding experiments. Based on the numerical data, we give an explanation of the basic mechanisms of the unsteady flow behavior.*

## 1 INTRODUCTION

Computational fluid dynamics (CFD) is a tool of rising popularity in the design and optimization process of vehicles. Methods are available which allow an automatic shape optimization in a virtual wind tunnel[1]. As a major requirement, the employed numerical models of the vehicle aerodynamics should resolve basic features of the flow around the vehicle under investigation without any fitting procedure. On the other hand, the simulations should be economical, i. e. long computing times and high memory requirements should be avoided.

In our contribution, numerical simulations of the flows around the Ahmed reference car body [2] are presented. The Ahmed reference body is a simplified car model which is employed in the automotive industry in order to investigate the influence of the flow structure e. g. on the drag of the vehicle. Good aerodynamic design of a vehicle requires a good understanding of the flow phenomena and the relationships between the aerodynamic parameters and the shape of the vehicle.

The flow around the Ahmed body exhibits basic features, which are also characteristic for other bluff body vehicles, namely trucks, buses or trains: There exist large coherent vortex structures and elongated separated flow regions downstream of the Ahmed body, which give the main contributions to the drag [2, 3]. The location at which the flow separates determines the size of the separation zone, and consequently the drag force. Clearly, a precise simulation of the wake flow and of the separation process is essential for the accuracy of drag predictions. The vortices, the detached flows, and the boundary layers at the body contours interact strongly. These interactions are of fundamental importance for the aerodynamical parameters of the vehicle.

The Ahmed body has the dimensions length  $l = 1044 \text{ mm}$ , height  $h = 288 \text{ mm}$  and width  $w = 389 \text{ mm}$ , Fig. 1. The length of the slant part is  $l_S = 222 \text{ mm}$ , whatever the angle  $\varphi$ . The distance between the ground and the bottom surface of the Ahmed body is  $b = 50 \text{ mm}$ . In the experiments of Lienhart et al. [3], the incoming flow velocity is  $U^{in} = 40 \text{ m/s}$ . The kinematic viscosity of air is  $\nu = 1.5 \times 10^{-5} \text{ m}^2/\text{s}$ . The Reynolds number is  $Re = Ul/\nu = 2.784 \times 10^6$ . In the experiments, a critical rear body slant angle  $\varphi_c = 30^\circ$  is found at which the drag is maximum. Far below this value, the wake is nearly steady and quasi two-dimensional (minor changes in streamwise direction). Then, the flow evolves to a complex three-dimensional very dissipative structure, when the angle is increased. At the critical angle, the flow structure changes drastically: for higher slant angles, the wake becomes again quasi two-dimensional. Two different rear slant angles ( $\varphi_1 = 25^\circ$  and  $\varphi_2 = 35^\circ$ ) are considered in the numerical simulations, which correspond to a high-drag configuration with strongly three-dimensional wake ( $\varphi_1$ ) and a low-drag configuration with quasi two-dimensional wake ( $\varphi_2$ ).

The flow around the Ahmed body has been already used as a test case for turbulence modeling under steady-state conditions [4, 5]. In our study, the flow around the Ahmed body is investigated in numerical simulations based on the unsteady Reynolds-averaged Navier-Stokes (URANS) equations. The boundary conditions of the simulations fit to the constant parameters in the experiments of Lienhart et al. [3]. Different turbulence models and numerical schemes have been tested in order to find out the best settings for the simulations. Finally, benefits and short-comings of the URANS approach in comparison to LES are discussed. Therefore, our numerical data (drag coefficients, velocity profiles and Strouhal numbers) are compared to the experimental [3] and recent numerical results from large eddy (LES) [6, 7] and lattice Boltzmann simulations (LBM) [8] in order to judge the accuracy of our model. We also compare our numerical efforts (computing times and memory requirements) with the data of the other



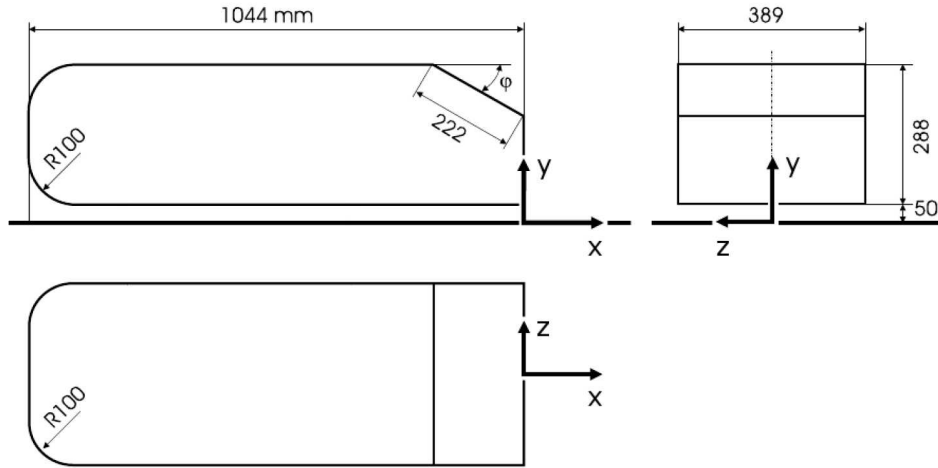


Figure 1: Ahmed reference body: geometry and dimensions.

investigations in order to judge the efficiency of the URANS approach as well.

## 2 NUMERICAL MODEL

### 2.1 Model equations

A numerical solution of the fundamental flow equations demands a direct numerical simulation, in order to obtain all velocity and pressure scales of the turbulent flow field. This would be a very time and memory consuming task. Alternatively, the fundamental equations can be phase-averaged in order to separate larger resolved from smaller unresolved velocity and pressure scales. Therefore, the numerical model of the transient mean flow around the Ahmed body is based on the unsteady Reynolds-averaged Navier-Stokes (URANS) equations

$$\frac{\partial \langle u_i \rangle}{\partial x_i} = 0 \quad (1)$$

$$\frac{\partial \langle u_i \rangle}{\partial t} + \frac{\partial}{\partial x_j} (\langle u_j \rangle \langle u_i \rangle) = -\frac{1}{\rho} \frac{\partial \langle p \rangle}{\partial x_i} + \nu \frac{\partial^2 \langle u_i \rangle}{\partial x_k^2} + \frac{\partial \tau_{ij}}{\partial x_j} \quad (2)$$

Here,  $u_i$  is the velocity,  $p$  is the pressure and  $\tau_{ij}$  are the Reynolds stresses. The material parameters of air are density  $\rho = 1.2 \text{ kg/m}^3$  and kinematic viscosity  $\nu = 1.5 \times 10^{-5} \text{ m}^2/\text{s}$ . The brackets  $\langle \dots \rangle$  indicate phase-averaged quantities.

### 2.2 Turbulence model

The unknown Reynolds stresses  $\tau_{ij}$  are provided by a turbulence model. Three different models have been employed in the simulations, the Realizable  $k$ - $\epsilon$  model (RKE) [9], the SST  $k$ - $\omega$  model (SST) [10] and the Reynolds stress model (RSM) of Launder et al. [11]. Additionally, wall functions are employed in order to describe the mean velocity and the turbulence quantities in the near-wall regions.

### 2.3 Grid and boundary conditions

The computational domain of the virtual wind tunnel has the global dimensions length  $L = 8364 \text{ mm}$ , height  $H = 1400 \text{ mm}$  and width  $W = 1870 \text{ mm}$ . The inlet boundary is located

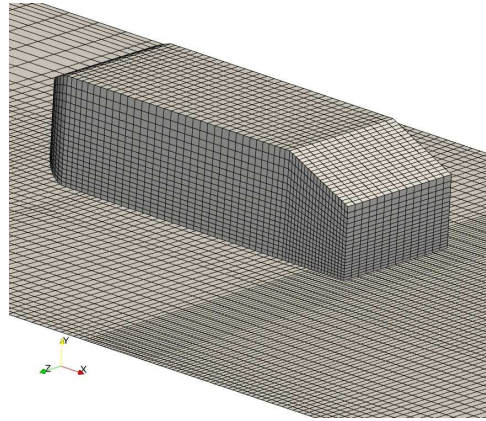


Figure 2: Computational grid around the Ahmed body.

2100 mm  $\simeq 2l$  upstream of the front, the outlet is located 5220 mm =  $5l$  downstream of the end of the Ahmed body. The center of the coordinate system is placed in the middle of the inlet bottom line. The lock-structured grid contains  $5.1 \times 10^5$  cells and employs 67 blocks. The stilts of the experiment by Lienhart et al. [3] are neglected in the numerical simulations, see figure 2. Local grid refinement has been applied in some core flow regions (stagnation region in front of the Ahmed body, wake flow region past the Ahmed body) where larger gradients of the flow quantities are expected.

At the inlet, constant values for the velocity  $\underline{U}^{in} = (40 \text{ m/s}, 0, 0)$  and the turbulence quantities  $k^{in} = 0.24 \text{ m}^2/\text{s}^2$ ,  $\epsilon = 2.4 \text{ m}^2/\text{s}^3$  are given. In the simulations with the RSM, the Reynolds stresses  $\tau_{ij}^{in}$  are estimated from  $k^{in}$ . At the outlet, a constant pressure  $p = 10^5 \text{ Pa}$  is prescribed. Finally, the no-slip condition is applied at the top, the bottom and the side walls of the channel.

## 2.4 Numerics

The model equations are solved with the open-source CFD-package OpenFOAM, which is based on a finite-volume formulation. All flow variables are stored at the geometric center of the hexahedral shaped cells. Different numerical schemes have been tested in the simulations. Convective fluxes are obtained with first order upwind interpolation, linear interpolation or a total variation diminishing (TVD) interpolation scheme, respectively. Diffusive fluxes are obtained from the central differencing scheme. Momentum and pressure equations are solved in a segregated fashion according to the SIMPLE coupling algorithm. Finally temporal integration is performed due to the implicit Euler scheme.

All simulations have been performed with a time-step width  $\Delta t = 5 \times 10^{-5} \text{ s}$  for a physical flow  $\tau_{phys} = 1 \text{ s}$ . However, only the period  $\tau_{phys} = 0.4 \text{ s} \dots 1 \text{ s}$  is considered in the evaluation of the flow data.

## 3 RESULTS

### 3.1 Overall flow structure

The performance of the turbulence models and numerical methods has been determined in a preliminary investigation. The outcome of the tests is that the best choice for the numerical simulations is the RKE turbulence model and the TVD scheme for the determination of convective fluxes. All results which are discussed below have been produced with these settings.

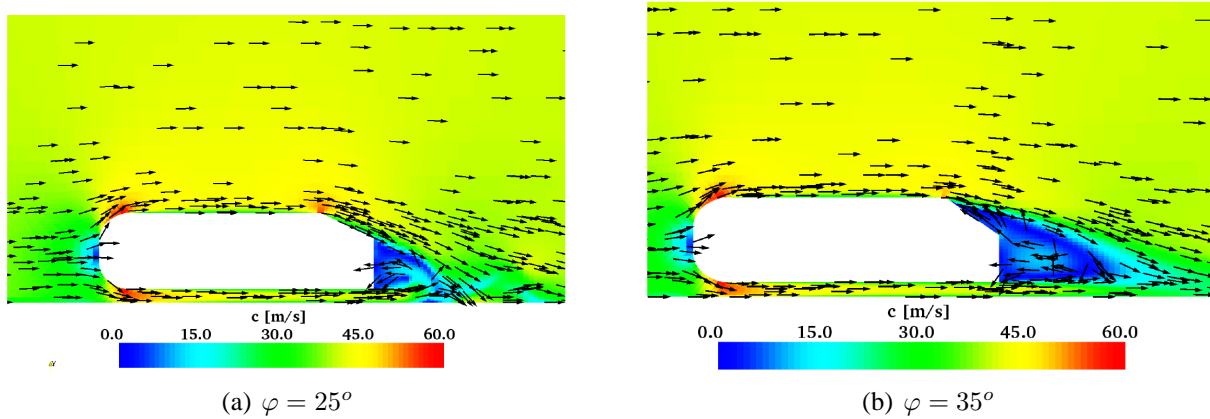


Figure 3: Flow velocity around the Ahmed reference body, symmetry plane at  $z = 0$  mm.

The numerical simulations resolve well known features of the flow around the Ahmed body, fig. 3. The incoming flow is decelerated and deflected by the front of the Ahmed body. Boundary layers develop on top, at the bottom and at the side faces of the body. The main difference between the two configurations is the structure of the separation region: In case of  $\varphi_1 = 25^\circ$ , the flow follows the slant and separates at the rearward slant onset, whereas in case of  $\varphi_2 = 35^\circ$ , the flow is already fully separated over the slant. Erroneously, no closed separation bubble is found on the slant in case of  $\varphi_1 = 25^\circ$ , although this feature was clearly observed in the experiments. These findings are in agreement with prior comparisons between experimental and numerical data [4, 5].

In both configurations, our numerical results of the incoming flow at the front part of the Ahmed body are in good agreement with the experimental data of Lienhart et al. [3]. Therefore this part of the flow around the Ahmed body is not discussed.

### 3.2 High-drag configuration

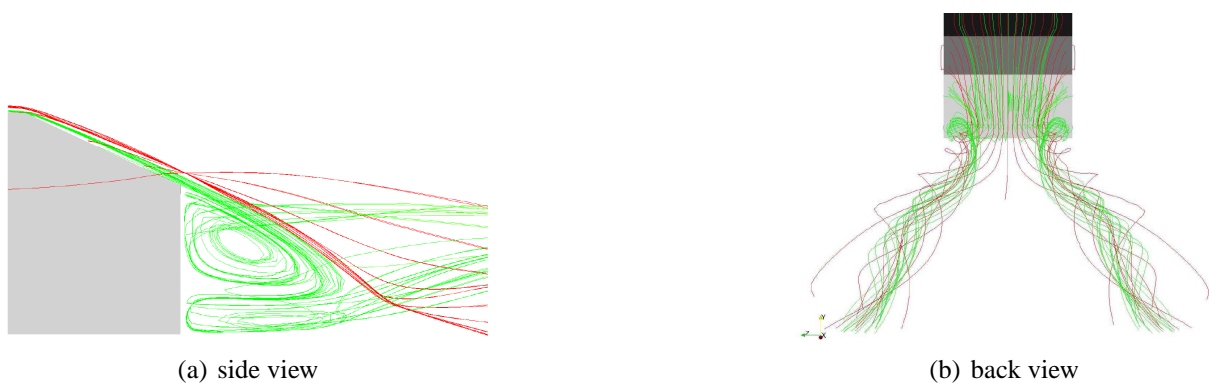


Figure 4: High-drag configuration: visualization of the flow field.

For slant angle  $\varphi_1 = 25^\circ$ , the flow structure over the slant and in the wake is shown in fig. 4. As mention above, the flow follows the slant and separates at the rearward slant onset, fig. 4a. Strong side vortices are found in the flow, which interact over the slant and the near-body wake region, fig. 4b.

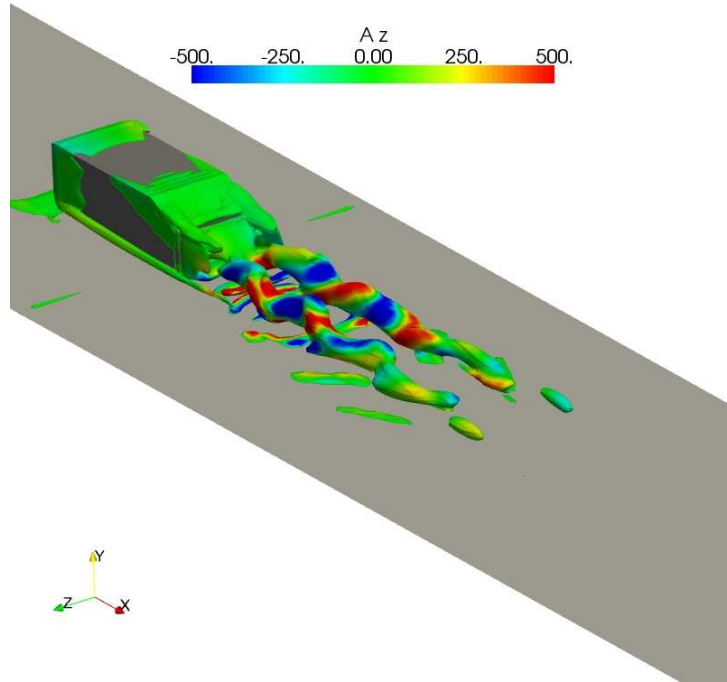


Figure 5: High-drag configuration: instantaneous wake flow.

The URANS simulation for the slant angle  $\varphi_1 = 25^\circ$  do not run in steady state. This observation is in contradiction with the URANS simulation of Guilmineau [14], which have reached steady-state conditions. In our simulation, the flow field exhibits a long-term oscillating behavior, especially in the wake flow region of the Ahmed body. Noticeable temporal velocities changes are observed in the wake flow, fig. 5. Here, the  $Q$ -criterion is used in order to visualize the side vortices in the wake. Isosurface  $Q = 2500 \text{ s}^{-2}$  are colored with the local lateral acceleration  $A_z = \frac{\partial \langle u_z \rangle}{\partial t}$  in  $\text{m/s}^{-2}$ . It is evident, that the lateral acceleration coincides with a strong deformation of the side vortices.

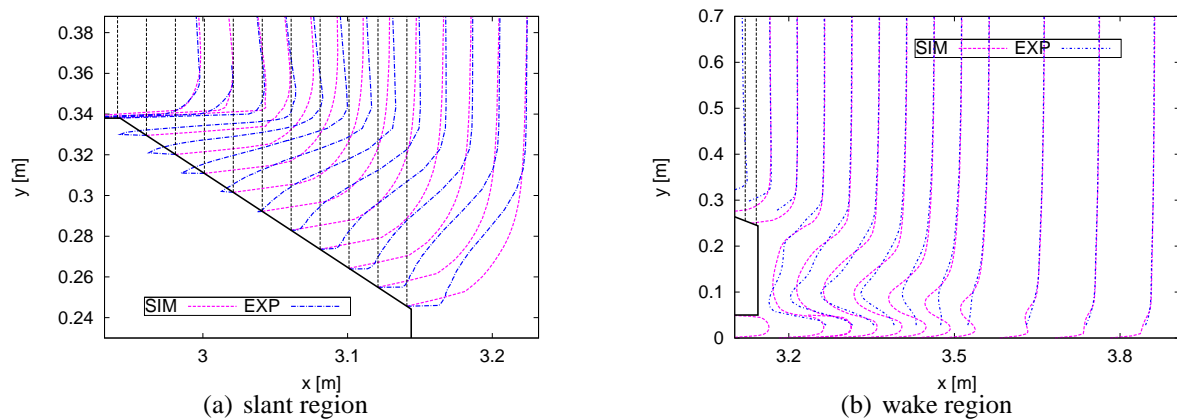


Figure 6: High-drag configuration: velocity profiles.

The unsteady behavior of the wake flow has been already discussed in the literature, see e.

g. [6, 7]. Two different types of instability, the small-scale Kelvin-Helmholtz or the large-scale Crow instability [12, 13] could be responsible for this behavior. We assume, that the Crow instability is induced when the side vortices interact on the slant.

As expected, the long-term time-averaged velocity profiles from the numerical simulation are not in agreement with the experimental results, see fig. 6. The difference is mainly due to the fact, that the closed separation bubble on the slant is not resolved in the simulation. Therefore, the prediction of the slant flow region is very poor, fig. 6a, whereas in the wake region, the agreement between simulation and experiment is satisfactory, fig. 6b. Here, LES [6, 7] and LBM [8] give a much better prediction of the mean velocity profiles on the slant and in the wake.

### 3.3 Low-drag configuration

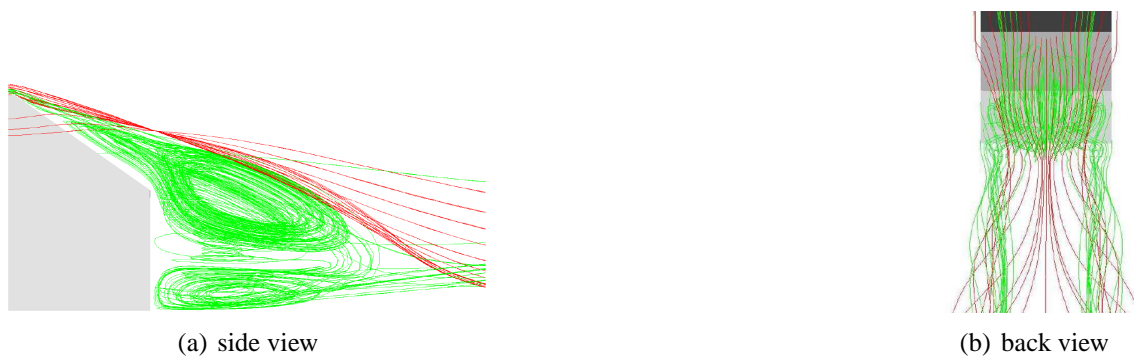


Figure 7: Low-drag configuration: visualization of the flow field.

For slant angle  $\varphi_2 = 35^\circ$ , the flow structure over the slant and in the wake is shown in fig. 7. As discussed above, the flow is fully separated over the slant, fig. 7a. Here, much weaker side vortices are found in the flow, which do not interact over the slant, fig. 7b.

The URANS simulation for  $\varphi_2 = 35^\circ$  converge to steady state conditions, temporal velocities changes are not observed in the wake flow. The weak side vortices, which are again visualized by the  $Q$ -criterion. The isosurface  $Q = 2500 \text{ s}^{-2}$  is not accelerated laterally,  $A_z \simeq 0 \text{ m/s}^2$  on the hole isosurface, fig. 8.

Not surprisingly, the agreement between the velocity profiles from the experiment and the simulation is satisfactory for the slant and good for the wake region, fig. 9. For this configuration, LBM [8] gives a similar prediction of the mean velocity profiles on the slant and in the wake, whereas LES data is not available for this case.

### 3.4 Flow parameters and numerical efforts

Table 1 compares drag coefficients  $C_D$  and Strouhal numbers  $St = U^{in} f_{osc}/h$ , which have been found in experimental and recent numerical investigations. The oscillation frequency is determined by the inspection of the Fourier spectrum of the flow variables in a specific point of the front or wake region, respectively. Obviously, the prediction of these characteristic parameters is similar in the simulations with LES, LBM and URANS for  $\varphi_1 = 25^\circ$ . The uncertainty of  $St$  seems to be due to the fact, that different signals have been analyzed by means of Fourier transformation. For case  $\varphi_2 = 35^\circ$ , LBM gives a decrease for  $C_D$ , which is in agreement with

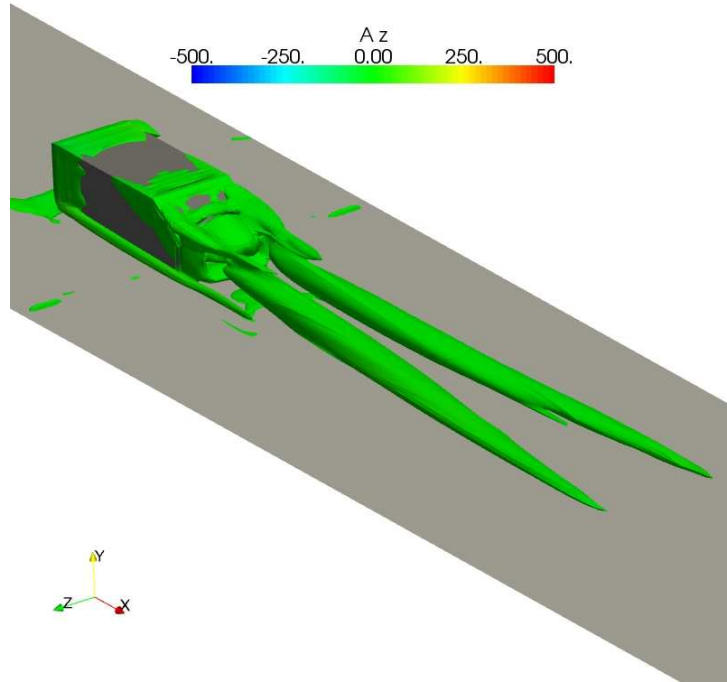


Figure 8: Low-drag configuration: instantaneous wake flow.

the measurements. Here the URANS simulation overestimates  $C_D$  noticeably. However, because the mean flow field does not exhibit any long-term fluctuation, a simulation based on the steady Reynolds-averaged Navier-Stokes equations seems to be the better choice, see e. g. Craft et al. [15].

Finally, the numerical efforts for the different approaches, namely LES, LBM and URANS are compared in table 2. The computation times  $\tau_{comp}$  (in CPUh), which are given in [8] and [7], are related to the calculated physical flow time  $\tau_{phys}$  (in s). Therefore  $\tau^{1s} = \tau_{comp}/\tau_{phys}$  is the computing time for one second of real (physical) flow time.

It is evident, that the URANS simulation has the lowest value for  $\tau^{1s}$ , although it is not performed on a high performance computer. URANS simulations can run on a workstation or

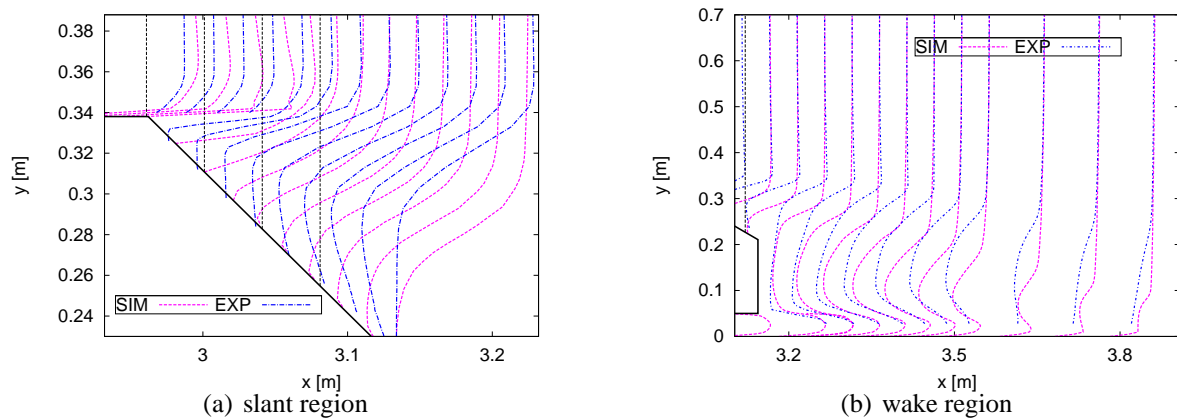


Figure 9: Low-drag configuration: velocity profiles.

author	study	$\varphi_1 = 25^\circ$		$\varphi_2 = 35^\circ$
		$C_D$	$St$	$C_D$
Lienhart et al. [3]	EXP	0.285	-	0.26
Fares [8]	LBM	0.28	-	0.20
Minguez et al. [7]	LES	>0.3	0.15 (front) 0.42 (wake)	-
Krajnovic, Davidson [6]	LES	0.292	0.15, 0.26 (front + wake)	-
present	URANS	0.285	0.50 (wake)	0.287

Table 1: Drag coefficients and Strouhal numbers.

author	study	mesh points	$\tau^{1s}$ CPUh/s	memory GByte	system
Fares [8]	LBM	$18 \times 10^6$	220	-	32 2.8 GHz CPU
Minguez et al. [7]	LES	$21 \times 10^6$	172	18	NEC SX8
present	URANS	$5 \times 10^5$	48	1	4 2.2 GHz CPU

Table 2: Numerical efforts for LES, LBM and URANS.

a PC, because the numerical grids are typically much coarser and time step sizes much larger than in corresponding LES or LBM simulations.

#### 4 CONCLUSIONS

Numerical simulations based on the unsteady Reynolds-averaged Navier Stokes (URANS) equations have been performed for the generic Ahmed body with slant angles  $25^\circ$  and  $35^\circ$ . The simulations resolve most of the basic flow features correctly, characteristic vortex structures and separated flow regions are found. In case of a slant angle of  $25^\circ$ , the flow field in the simulations exhibits a long-term oscillating behavior. Contrary, in case of a slant angle of  $35^\circ$ , the flow field in the simulations remains nearly constant without a significant unsteady behavior. These numerical findings are again in agreement with corresponding experimental observations.

For the slant angle  $25^\circ$ , the mean velocity profiles in the critical region on the slant are not correctly resolved with the URANS approach. Here, other approaches like large eddy simulations or lattice Boltzmann simulations give significant better results. For the slant angle  $35^\circ$ , the URANS simulation gives good results for the flow.

The URANS simulations give for both cases reasonable values for drag coefficients and the Strouhal number of the long-term flow oscillations in case of the slant angle  $25^\circ$ . Here, the performance of large eddy simulations or lattice Boltzmann simulations is not much better. However, the decrease in the drag coefficient between the case  $25^\circ$  and  $35^\circ$  is not found in the URANS simulations. Finally, the numerical efforts for the URANS simulations are much lower than the efforts for large eddy simulations or lattice Boltzmann simulations.

Therefore we suggest that URANS models should be applied in early-stage optimization simulations, whereas large-eddy or lattice Boltzmann simulations should be employed in late-stage final tuning simulations.

## REFERENCES

- [1] F. Muyl, L. Dumas, V. Herbert. *Hybrid Method for Aerodynamic Shape Optimization in Automotive Industry*. Computers and Fluids, **33**, 849-858, 2004.
- [2] S.R. Ahmed, G. Ramm. *Some Salient Features of the Time-Averaged Ground Vehicle Wake*. SAE Technical Paper, 1984.
- [3] H. Lienhart, C. Stoots, S. Becker. *Flow and Turbulence Structures in the Wake of a Simplified Car Model*. Stuttgart, Germany, 2000.
- [4] S. Jakirlic, R. Jester-Zurker, C. Tropea. *9th Joint ERCOFTAC/IAHR/QNET-CFD Workshop on Refined Turbulence*. Darmstadt, Germany, 2001.
- [5] R. Manceau, J. P. Bonnet: *10th Joint ERCOFTAC/IAHR/QNET-CFD Workshop on Refined Turbulence Modelling*. Poitiers, France, 2002.
- [6] S. Krajnovic, L. Davidson. *Flow Around a Simplified Car, Part 1: Large Eddy Simulation*. Journal of Fluids Engineering, **127**, 907-918, 2005.
- [7] M. Minguez, R. Pasquetti, E. Serre. *High-Order Large-Eddy Simulation of Flow Over the "Ahmed body" Car Model*. Physics of Fluids, **20**, 095101, 2008.
- [8] E. Fares: *Unsteady Flow Simulation of the Ahmed Reference Body Using a Lattice Boltzmann Approach*. Computers and Fluids, **35**, 940-950, 2006.
- [9] T.-H. Shih, W. W. Liou, A. Shabbir, Z. Yang, J. Zhu. *A New  $k-\epsilon$  Eddy Viscosity Model for High Reynolds Number Turbulent Flows*. Computers and Fluids, **24**, 227-238 1995.
- [10] F. R. Menter. *Two-Equation Eddy-Viscosity Turbulence Models for Engineering Applications*. AIAA Journal, **32**, 269-289, 1994.
- [11] B. E. Launder, G. C. Reece, W. Rodi. *Progress in the Development of a Reynolds-Stress Turbulence Closure*. Journal of Fluid Mechanics, **68**, 537-566, 1975.
- [12] S. C. Crow. *Stability Theory for a Pair of Trailing Vortices*. AIAA Journal, **8**, 2172-2179, 1970.
- [13] P. G. Saffman. *Vortex Dynamics*. Cambridge University Press, New York, 1992.
- [14] E. Guilmineau. *Computational Study of Flow Around a Simplified Car Body*. Journal of Wind Engineering and Industrial Aerodynamics, **96**, 1207-1217, 2008.
- [15] T. J. Craft, S. E. Gant, H. Iacovides, B. E. Launder, C. M. E. Robinson. *Computational Study of Flow Around the Ahmed Car Body (Case 9.4)*. Proceedings of the Ninth ERCOFTAC/IAHR Workshop on Refined Turbulence on Modelling, Darmstadt, Germany, October 4-5, 2001.



## WIND TUNNEL TESTS ON HEAVY ROAD VEHICLES: CROSS WIND INDUCED LOADS

F. Cheli<sup>1</sup>, R. Corradi<sup>1</sup>, E. Sabbioni<sup>1</sup> and G. Tomasini<sup>1</sup>

<sup>1</sup> Department of Mechanical Engineering, Politecnico di Milano  
Via La Masa 1, 20156 Milano, Italy  
e-mail: [federico.cheli@polimi.it](mailto:federico.cheli@polimi.it)  
[roberto.corradi@polimi.it](mailto:roberto.corradi@polimi.it)  
[edoardo.sabbioni@polimi.it](mailto:edoardo.sabbioni@polimi.it)  
[gisella.tomasini@polimi.it](mailto:gisella.tomasini@polimi.it)

**Keywords:** vehicle aerodynamic coefficients, vehicle admittance function, wind tunnel experimental tests, cross wind, road heavy vehicles.

**Abstract.** *The sensitivity of road heavy vehicles aerodynamic coefficients to different testing parameters (scenario, vehicle type, turbulence intensity) is experimentally investigated in this paper through wind tunnel experiments. Tests have been carried out in the Politecnico di Milano wind tunnel using 1:10 scale vehicle models. Force and moment mean aerodynamic coefficients have been analyzed for different vehicle types (VAN, trailer, tanker), scenarios (flat ground, embankment, viaduct), expositions (upwind, downwind), turbulence conditions (low turbulence and atmospheric boundary layer simulation) and varying yaw angles. Force and moment aerodynamic coefficient have been measured by means of a six-components dynamometric balance, while the flow pattern around the vehicle has been assessed through pressure taps on the vehicle surface.*

## 1 INTRODUCTION

Due to the serious consequences on road/rail transportation safety, the interest for the study of wind induced rollover of road and rail vehicles has grown up. In fact trains, high sided lorries, trucks, tankers etc. are particular at risk of rollover when running on exposed sites such as embankments, viaducts or long span bridges ([1],[4]). Over the years, several studies ([2],[3]) and EU projects have been focused on the prediction of these accident. For what railways is concerned, a task of the BRITE-EURAM TRANSAERO project (1994-1998) has been devoted to the study of cross wind effects on rail vehicles ([6]). Moreover within the DeuFrako and the Aerodynamic in Open Air (AOA) projects a risk analysis associated to cross wind on trains has been performed. For what road vehicles is concerned, during the EU project WEATHER involving among the others Birmingham University, Nottingham University and Politecnico di Milano, different techniques (full scale and wind tunnel experiments and CFD) for evaluating mean aerodynamic coefficients of a VAN have been applied and compared ([8]) in order to develop an alarm system for advising the driver of potentially critical situations due to cross wind. However all the proposed approaches for assessing the rollover risk associated with cross wind are based on the knowledge of the vehicle mean aerodynamic coefficients.

In this paper, the sensitivity of different road heavy vehicles mean aerodynamic coefficients to some testing parameters (scenario, vehicle type, turbulence intensity) has been investigated in order to highlight which among these parameters are the most significant from the rollover point of view. In particular, wind tunnel tests have been carried out on 1:10 scale models of different heavy vehicles (truck, lorry with trailer and tanker) considering three infrastructure scenarios (flat ground, viaduct and embankment), both with and without boundary layer simulation. Mean aerodynamic coefficients have been measured through a six components industrial dynamometric balance, while the flow pattern around the vehicle has been reconstructed by means of a series of pressure taps on the vehicle surface.

## 2 EXPERIMENTL SET-UP

In Figure 1 the three 1:10 scale vehicle models used during wind tunnel test are shown. The first is a VAN (high-sided lorry, see Figure 1 on the left) 8m long, 2.5m wide and 3.5m high in full scale. The tanker (Figure 1 centre) and the truck (composed by a tractor and a semitrailer, Figure 1 on the right) are 14m long, 2.7m wide and 3.65m high in full scale.



Figure 1: Scale vehicle models: VAN (left), tanker (centre), truck (right).

In order to investigate the influence of the boundary conditions on the vehicle aerodynamic coefficients, different infrastructure scenarios have been considered (flat ground, single and double viaduct and embankment). The flat ground scenario consists in the vehicle running on a flat terrain and represents the international reference wind tunnel testing condition.

Viaduct and embankment scenarios have been built according to the geometrical data provided by Autostrade Italiane (Italian Highways) and relative to the most common typologies present in Italy. Figure 2 shows the double viaduct scale model (1:10) and its corresponding section. The viaduct is 10m high (full scale). This means that the streamwise velocity profile is uniform at road level when low turbulence conditions are considered (Figure 10 – a). In Figure 3 the embankment and its section are represented.

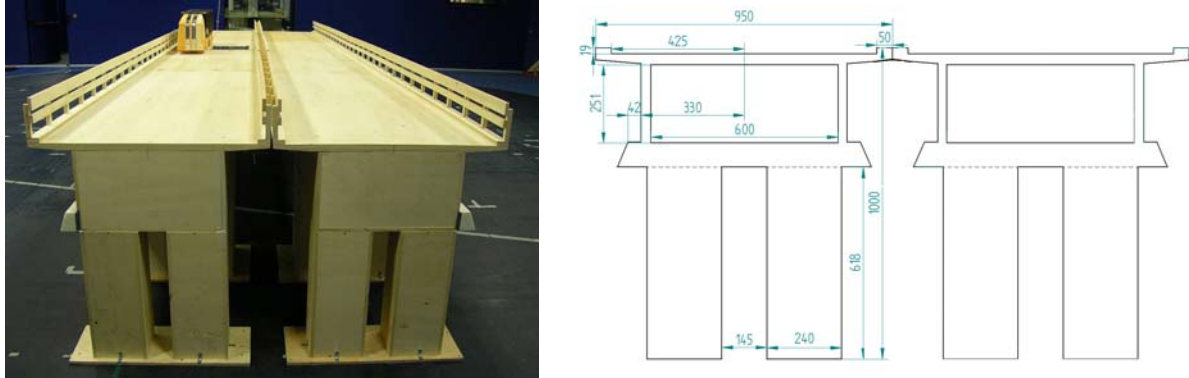


Figure 2: Viaduct: scale model and section (measures in millimeters).

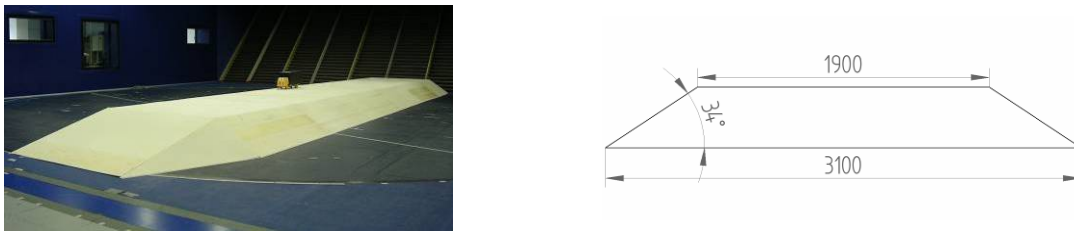


Figure 3: Embankment: scale model and section (measures in millimeters).

## 2.1 Force, speed and pressure measurements

Aim of wind tunnel tests is to assess the aerodynamic loads acting on a vehicle and due to cross wind. It is to point out that rigid models have been used during the tests, this meaning that the geometrical characteristics of tested vehicles are reproduced, but not their inertial, stiffness and damping properties. Thus the dynamic interaction between the vehicle and the wind cannot be experimentally evaluated. The aerodynamic loads acting on the vehicle have been measured through a six components industrial dynamometric balance positioned under the vehicle model and connected to its wheels. Figure 4 shows the measurement set up. As it can be seen, the connection bars between the vehicle wheels and the balance are shielded from the wind. During the tests carried out in flat ground configuration, the balance is placed under the wind tunnel ground level, while it is hidden respectively into the viaduct and the embankment during the other experiments. At the purposes of obtaining the aerodynamic coefficients, the wind speed was measured through Pitot tubes. In particular, during all the tests, a Pitot tube at 0.6m in model scale has been used to measure the mean wind speed (Figure 5). Moreover, in order to allow the comparison between aerodynamic coefficients assessed in low and high turbulence conditions, during the tests on flat ground, the mean wind speed has been measured also by a Pitot tube set at VAN centre of gravity (cog) height  $h_G$  (full-scale equivalent of 2.7m).

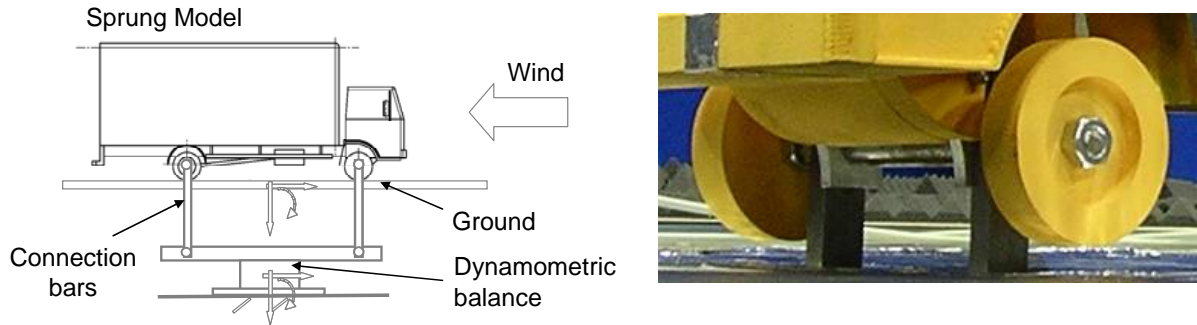


Figure 4: Linkage between the vehicle and the dynamometric balance.

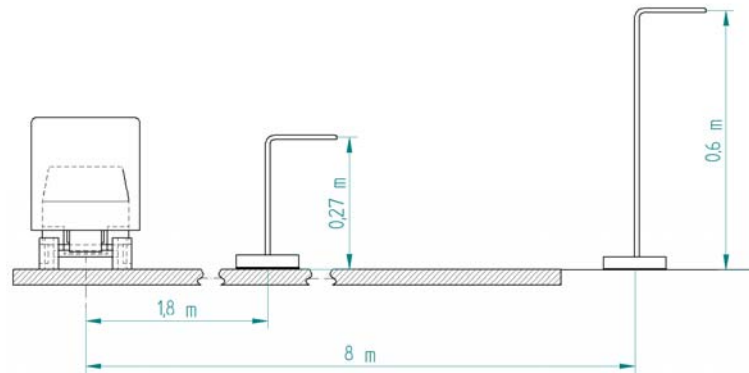


Figure 5: Wind speed measurements: Pitot tubes placement for flat ground scenario.

Together with the force measurements, in order to investigate the flow pattern around the vehicle, the vehicle models have been instrumented with pressure taps. In Figure 6 the map of the pressure taps on the VAN and the trailer is shown: 32 tap have been placed on the VAN and 64 on the trailer.

## 2.2 Turbulence conditions simulated during wind tunnel tests

As known, the characteristics of the turbulent wind depend on the terrain type. In order to evaluate the influence of the boundary layer on the aerodynamic loads acting on the vehicle, tests have been carried out with (mean turbulence) and without boundary layer simulation (low turbulence).

Low turbulence flow has been obtained in the standard wind tunnel operating conditions. It is characterised by a uniform vertical profile of the mean wind velocity. Figure 10(a) shows the streamwise normalised velocity profile at the height ( $z_{ref}=0.6$  m). As it is possible to see, the boundary layer develops for few centimetres over the floor and when the gradient is blown over, the mean value of the wind velocity remains constant. In this flow conditions, fluctuations of the wind velocity are very limited: they result superimposed to the mean velocity value as uncorrelated noise. This leads to a small turbulence intensity and short integral length scales (see Table 1).

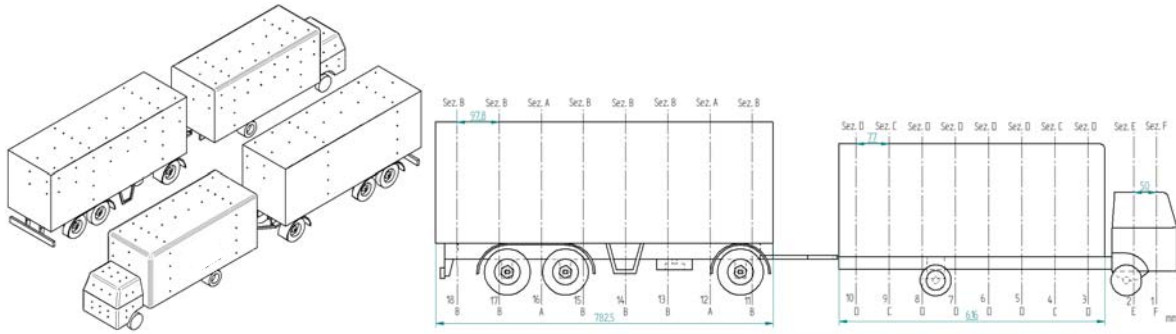


Figure 6: Pressure taps map.

During boundary layer simulations, turbulence conditions have been achieved by positioning in the wind tunnel, before the test section, an array of nine turbulence-producing spires (Figure 7 and Figure 8) and roughness elements at ground level (Figure 9). The spires present triangular profile and they allow to reproduce the velocity gradient effectively approximating an atmospheric boundary layer.

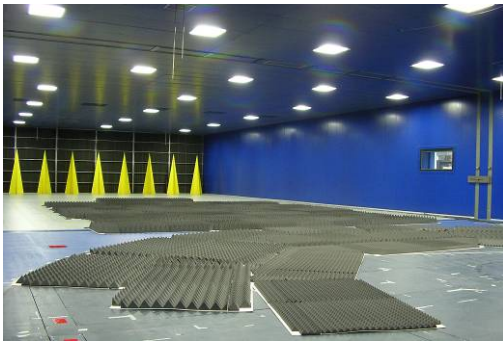


Figure 8: Wind tunnel set up for boundary layer simulations.

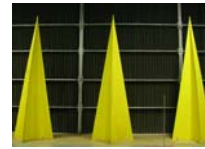


Figure 7: Turbulence-producing spires.



Figure 9: Roughness elements.

The vertical profile of the streamwise velocity  $U(z)$  normalised with respect of the wind speed measured at the reference height  $z_{ref}=0.6m$  ( in model scale) is shown in Figure 10 for the two simulated turbulence conditions.

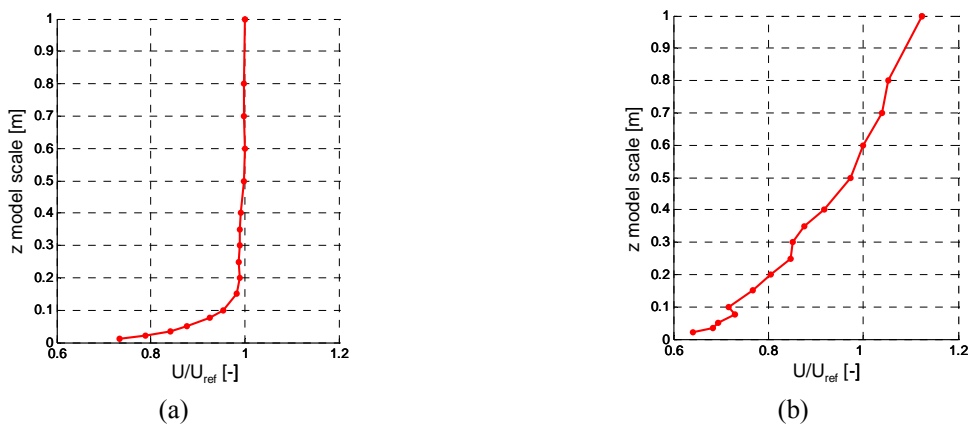


Figure 10: Normalised streamwise vertical velocity profile ( $z_{ref}=0.6m$ , model scale): low turbulence (a) and mean turbulence (b).

Table 1 summarizes the main statistical properties associated with the two turbulence conditions reproduced into the wind tunnel, i. e. the turbulence intensity along the wind direction  $I_u$  and the integral length scales along  $x$  and  $y$  measured at the reference height  $z_{\text{ref}}=0.6\text{m}$ .

	$I_u$ (%)	$^xL_u$ (m)	$^yL_u$ (m)
Low turbulence	2	0.10	0.033
Mean turbulence	20	1.185	0.3292

Table 1: Wind characteristics in low and mean turbulence conditions measured at the reference height  $z_{\text{ref}}=0.6\text{m}$  (model scale).

Finally, Figure 11 shows the comparison between the normalized PSD measured in the wind tunnel in mean turbulence conditions and the interpolation of the real wind PSD provided by Von Karman as a function of the reduced frequency. A good agreement can be noticed, meaning that the frequency content of the wind simulated in the wind tunnel is equivalent to the natural wind, also at low reduced frequencies  $f^xL_u/\bar{U}$ .

### 3 MEAN AERODYNAMIC COEFFICIENTS

#### 3.1 Mean pressure coefficients

In order to study the flow pattern around the vehicle surface, the pressure distribution around the vehicle surface has been analyzed. For the purposes of the current work the mean pressure coefficient ( $C_p$ ) is defined as:

$$C_p = \frac{P_i - P}{0.5\rho\bar{U}^2} \quad (1)$$

where  $P_i$  is the pressure at tap  $i$ ,  $P$  is the ambient (reference) pressure,  $\rho$  is the density of air and  $\bar{U}$  is the mean streamwise velocity at 0.6m above the ground (model scale).

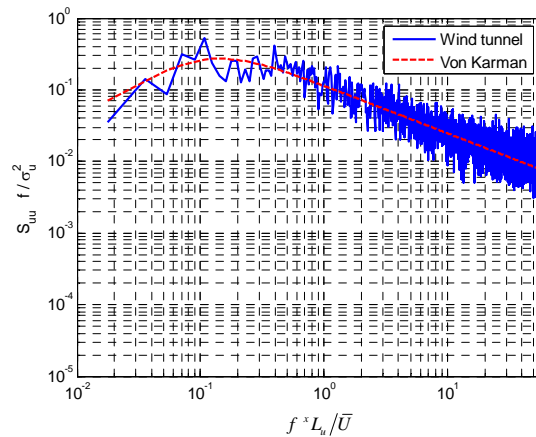


Figure 11: Normalised streamwise vertical velocity PSD at 0.6m above the ground (model scale).

As an example of the obtained results, Figure 12 and Figure 13 respectively show the pressure coefficients data around the cabin (section 1, Figure 6) and the body (section 4, Figure 6) of the VAN for a large variety of yaw angles. Flat ground and low turbulence conditions are considered. Mean pressure coefficients  $C_p$  are assumed positive when the arrows are directed from outside to inside the vehicle.

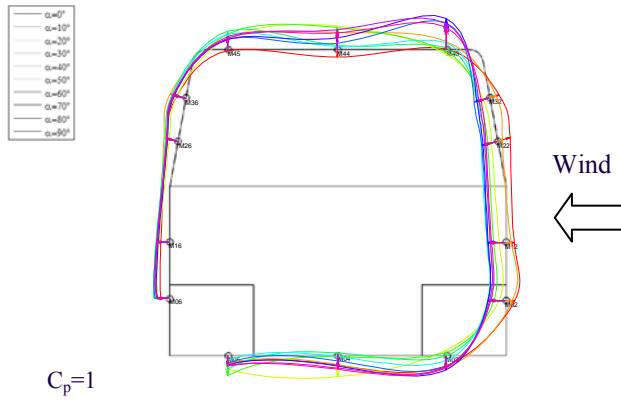


Figure 12: VAN, low turbulence, flat ground, section 1 (see Figure 6): pressure coefficient  $C_p$  at different yaw angles.

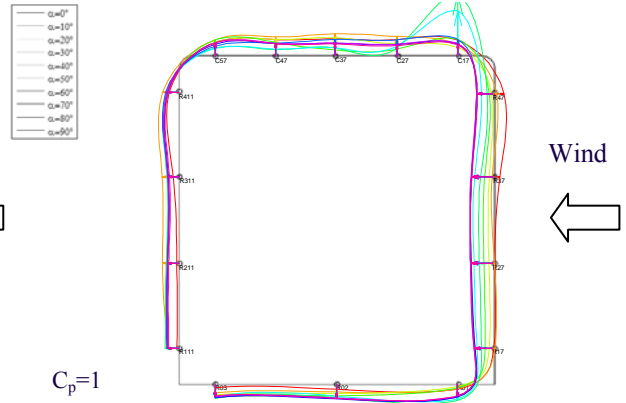


Figure 13: VAN, low turbulence, flat ground, section 4 (see Figure 6): pressure coefficient  $C_p$  at different yaw angles.

A uniform distribution can be seen on the leeward surface of the VAN cabin. On the windward surface, pressure is negative till the yaw angle is lower than  $20^\circ$ , then becomes positive. In correspondence of the top corner, a negative pressure peak can be observed for yaw angles higher than  $60^\circ$  (Figure 12). Similar considerations can be made for the pressure distribution around VAN body (Figure 13). The main difference is that the negative pressure peak in correspondence of the top corner is present for yaw angles comprised within  $40^\circ$  and  $60^\circ$ . This difference is due to the shape of the top corners of the VAN, which is smooth, and of the VAN body, which is sharp.

### 3.2 Mean force coefficients

The mean aerodynamic force coefficients are defined, as a function of the yaw angles (Figure 14), as:

$$C_{Fi} = \frac{\bar{F}_i}{1/2\rho\bar{U}^2 A} \quad C_{Mi} = \frac{\bar{M}_i}{1/2\rho\bar{U}^2 Ah} \quad (i=x,y,z) \quad (4)$$

where  $\bar{F}_i$  are the mean values of the force components while  $\bar{M}_i$  are the mean values of the corresponding moments, evaluated with respect to the origin of the reference system of Figure 14. The parameter  $A$  represents the vehicle lateral surface (XZ plane, Figure 14),  $h$  is the vehicle height and  $\bar{U}$  is the mean streamwise velocity at 0.6m above the ground (model scale).

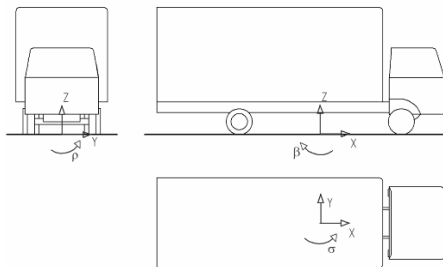


Figure 14: Reference system for the aerodynamic forces measurement.

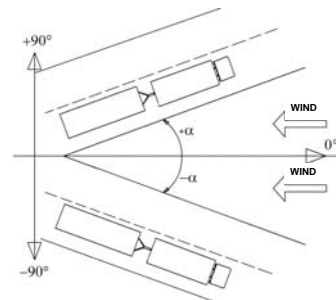


Figure 15: Yaw angle  $\alpha$ .

Figure 16 and Figure 17 show two of the main aerodynamic coefficients for the cross wind problem that are the vertical force and the rolling moment coefficients as a function of the yaw angle. Such coefficients are measured on the VAN 1:10 scale model (see Figure 1) on flat ground in conditions of low turbulence flow that represent the reference configuration. The rolling moment coefficient shows two different behaviours as a function of the yaw angle: increasing with a linear trend up to about  $55^\circ$  and then a value almost constant up to  $90^\circ$  where it reaches the value of 1.1. As already observed for rail vehicles ([7]), these two behaviours correspond to different wind-vehicle interaction: from low to high yaw angles, the vehicle modifies its behaviour from slender to bluff body. The rolling moment is mainly due to the distribution of the pressure along the vertical axis: from the data analysis, it has been found that the equivalent quote where the side force is applied is constant over the yaw angle. As a consequence, the trend of the lateral force coefficient is equivalent to that of the rolling moment.

Figure 16 shows that the vertical force coefficient is positive (up directed) at almost all yaw angles and this means that the vertical force is a lift force.

Figure 18 and Figure 19 show respectively vertical force and rolling moment coefficients measured on VAN vehicle with flat ground configuration in terms of comparison between smooth flow and turbulent flow (Table 1). It is possible to note that, while the rolling moment coefficient does not show significant differences between the two configurations, the vertical force coefficient is very sensitive to the turbulence flow conditions. In particular, the greatest differences on the lift force are highlighted at high yaw angles, where the vehicle behaves as bluff body. In fact, the different turbulence levels influence the flow especially in correspondence of the zone where the flow is detaching, that is in correspondence of the vehicle upwind edge. Over the critical angle ( $\alpha=55^\circ$  for this vehicle), varying the turbulence level, the wake behind the detach point is modified and, as a consequence, this leads to a modification of the pressure field especially in the upper part of the vehicle with the corresponding variation of the vertical coefficient.

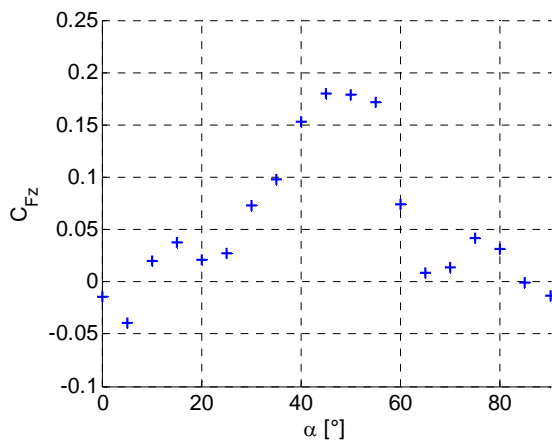


Figure 16: VAN, flat ground, low turbulence: vertical force coefficient  $C_{Fz}$ .

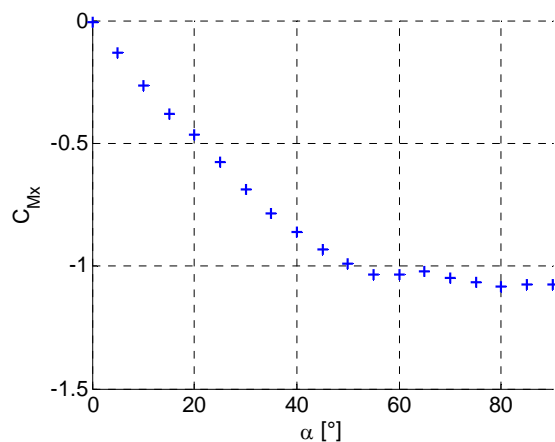


Figure 17: VAN, flat ground, low turbulence: rolling moment coefficient  $C_{Mx}$ .



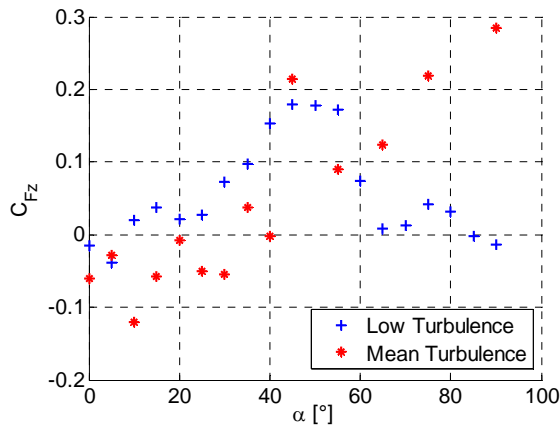


Figure 18: VAN, flat ground, vertical force coefficient  $C_{Fz}$ : low turbulence vs mean turbulence.

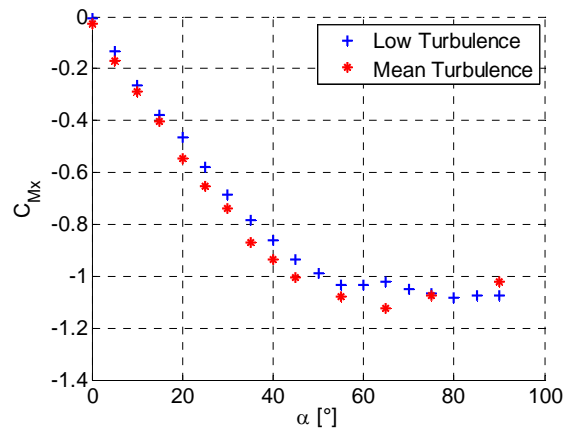


Figure 19: VAN, flat ground, rolling moment coefficient  $C_{Mx}$ : low turbulence vs mean turbulence.

All the tests have been performed with different wind speeds: 8 m/s and 12 m/s for the low turbulence conditions and 5m/s and 8m/s for mean turbulent flow. These tests have allowed to verify the Reynolds number independence of the coefficients in a range from about  $1 \cdot 10^5$  to  $2 \cdot 10^5$ . Table 2 shows the Reynolds number corresponding to the tested wind speeds where, as typical dimension, the wide of each vehicle has been assumed that is  $D=0.25m$  for the VAN,  $D=0.2m$  for the tanker and  $D=0.25m$  for the truck.

VEHICLE	VAN		TANKER		TRUCK	
Wind speed	8 (m/s)	12 (m/s)	8 (m/s)	12 (m/s)	8 (m/s)	12 (m/s)
Reynolds number	$1.34 \cdot 10^5$	$2 \cdot 10^5$	$1.06 \cdot 10^5$	$1.6 \cdot 10^5$	$1.3 \cdot 10^5$	$1.98 \cdot 10^5$

Table 2: Wind speed and corresponding Reynolds numbers tested in wind tunnel for VAN, tanker and truck.

Figure 20 and Figure 21, that represent the vertical force and the rolling moment aerodynamic coefficients measured with the VAN in the reference conditions (flat ground, low turbulence), show that both the coefficients do not highlight significant differences for the two considered Reynolds number at all yaw angles.

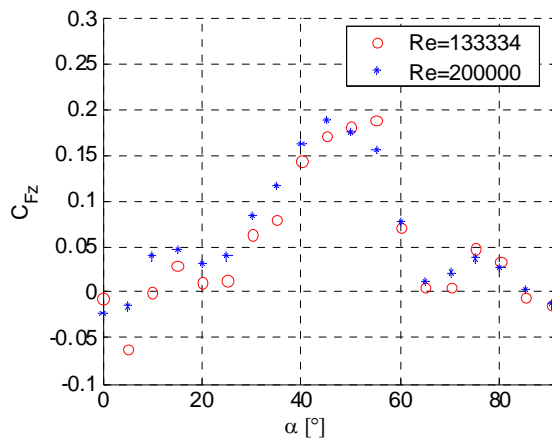


Figure 20: VAN, flat ground, vertical force coefficient  $C_{Fz}$ : different Reynolds numbers.

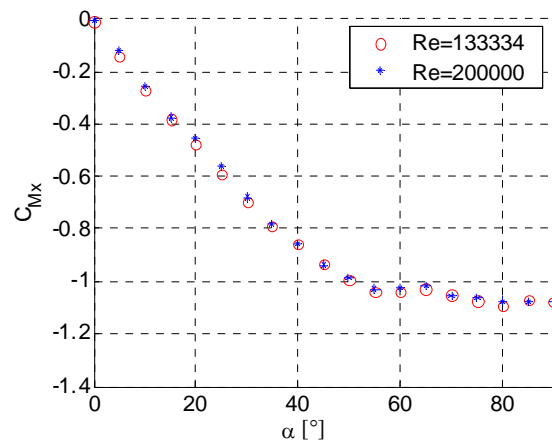


Figure 21: VAN, flat ground, rolling moment coefficient  $C_{Mx}$ : different Reynolds numbers.

The comparison between the three tested vehicles is shown in Figure 22 and in Figure 23 for the two main considered aerodynamic coefficients. We can note that the rolling moment coefficients measured on the tanker is lower, since very low yaw angles, than that of VAN and truck, characterized by similar lateral geometries (Figure 1). Differences between VAN and truck arise only at high angles ( $>40^\circ$ ), where the vehicle behaves as bluff body. The three different geometries in fact lead to a variation in the position of the flow detach point with a consequent modification in the flow structure behind the vehicles. On the otherwise, significant differences are observed in the vertical force coefficient, between VAN and truck, especially at low yaw angles (Figure 22).

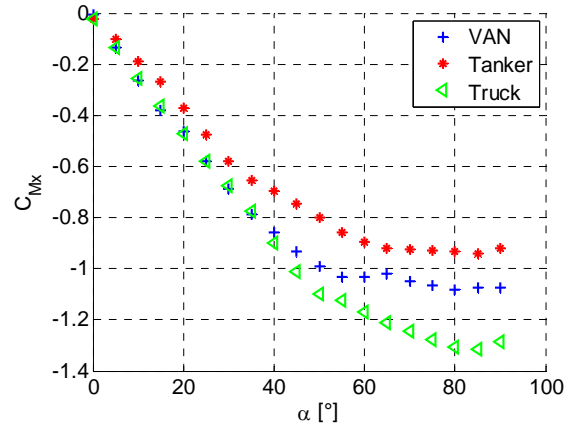
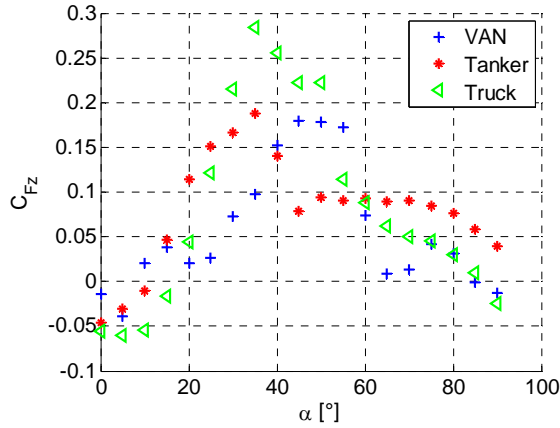


Figure 22: Flat ground, vertical force coefficient  $C_{Fz}$ : comparison between VAN, tanker and truck.

Figure 23: Flat ground, vertical force coefficient  $C_{Mx}$ : comparison between VAN, tanker and truck.

In the following, the effects on the aerodynamic coefficients associated to the scenario where the vehicle is running will be shown. In particular, a comparison between the VAN coefficients measured with flat ground, single viaduct, double viaduct and embankment is shown in Figure 24 and Figure 25, respectively for the vertical component and for the rolling moment.

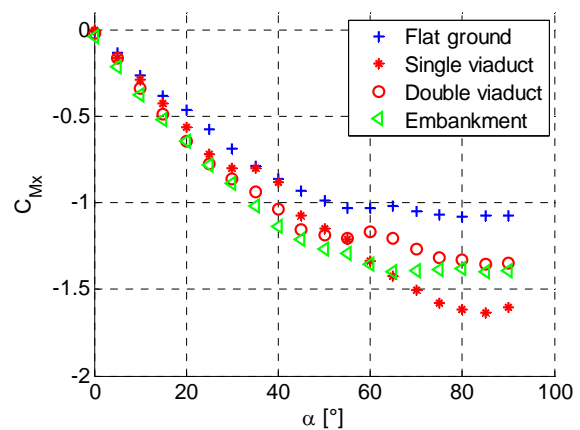
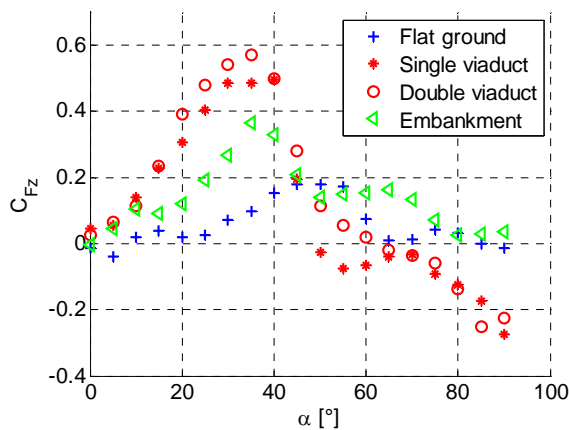


Figure 24: VAN, low turbulence, upwind, vertical force coefficient  $C_{Fz}$ : comparison between different scenarios.

Figure 25: VAN, low turbulence, upwind, rolling moment coefficient  $C_{Mx}$ : comparison between different scenarios.

From Figure 24 it is possible to observe that while the vertical forces measured with flat ground and with embankment are upward directed for all yaw angles, the corresponding com-

ponents measured with viaduct, both single and double, get from positive to negative in correspondence of the yaw angle  $\alpha=50^\circ$  that means that the vertical force get from upward to downward directed. Increasing the yaw angle, this scenario modify more and more the flow direction in the YZ plane and so the detach point is shifted up to generate a negative lift force. The rolling moment coefficient shows a similar trend for all the considered scenarios but differences arise in the absolute values, especially for high yaw angles. The most critical scenarios are the embankment, for angles up to  $60^\circ$ , and the single viaduct, for angles higher. With the embankment configuration, in fact, the flow is accelerated in correspondence of the ramp and this induces an overpressure on the upwind surface of the vehicle that increases the overall force in lateral direction and, as a consequence, the rolling moment.

Finally, Figure 26 and Figure 27 show the effect of the wind direction with respect to the vehicle position (upwind and downwind configuration) as an example, for the embankment scenario. Also in this case, the vertical force coefficient shows, in the two configurations, two different trends as a function of the yaw angle.

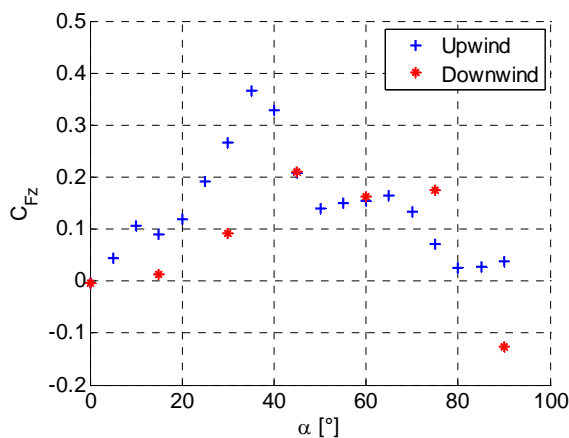


Figure 26: VAN, low turbulence, embankment, vertical force coefficient  $C_{Fz}$ : comparison between upwind and downwind.

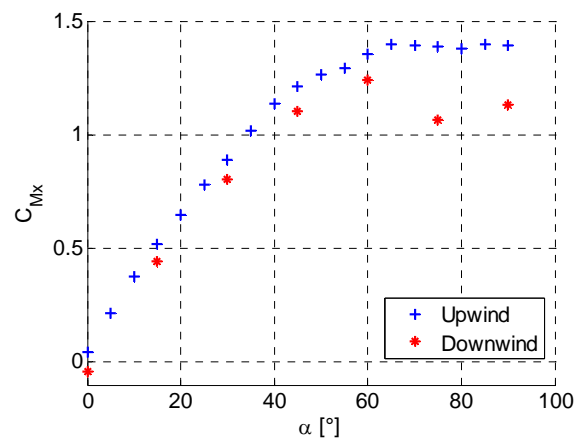


Figure 27: VAN, low turbulence, embankment, rolling moment coefficient  $C_{Mx}$ : comparison between upwind and downwind.

When the vehicle is upwind, this coefficient increases up to about 0.4 and then decreases up to about 0; on the contrary, in downwind conditions, the coefficient reached its maximum value (lower than one measured upwind) at  $\alpha=45^\circ$  and then it remains almost constant excepted for the angle  $\alpha=90^\circ$ , where a negative value has been registered. In terms of rolling moment coefficient, from Figure 27, it is possible to observe that the main differences arise over the critical angle, at high yaw angles. In this range of angles, in fact, the upwind vehicle is directly subjected to the wind action while, when the vehicle is downwind, the wind is partially slowed down.

#### 4 CONCLUSIONS

Through a large experimental campaign carried out in wind tunnel on different scale vehicle models, a sensitivity analysis of the aerodynamic coefficients to the test conditions and configurations has been carried out.

At low yaw angles, it has been shown that variations in the Reynolds number (up to  $2 \cdot 10^5$ ) and in the turbulence conditions (turbulence intensity  $I_u=2\%$  and  $I_u=20\%$ ) do not lead to significant modifications in the two main aerodynamic coefficients, that are the vertical force and the rolling moment coefficients. On the other hand, both these components have highlighted a strong sensitivity to both the scenario (flat ground, single and double viaduct and

embankment) and the vehicle's position on the scenario itself (upwind and downwind condition).

All the data obtained from this experimental campaign have been used also to set up a numerical-experimental methodology, based on the aerodynamic admittance function, for the evaluation of the safety of a road heavy vehicle subjected to cross wind ([5]).

## 5 ACKNOWLEDGMENTS

The work described in this paper has been founded within the EU project WEATHER. and the National PRIN Project titled "Improvement of safety, comfort and handling of the heavy vehicles".

## REFERENCES

- [1] C.J. Baker, S. Reynolds, *Wind induced accidents of road vehicles*. *Accid. Anal. Prev.*, **246**, 559-575, 1992.
- [2] C.J. Baker, *Ground vehicles in high cross winds-Part I: steady aerodynamic forces*. *Journal of Fluids and Structures*, **5**, 69-90, 1991.
- [3] C.J. Baker, *Ground vehicles in high cross winds-Part II: unsteady aerodynamic forces*. *Journal of Fluids and Structures*, **5**, 91-111, 1991.
- [4] C.J. Baker, S.A. Coleman, High sided vehicles in cross wind. *Proc. 6<sup>th</sup> US Wind Engineering Conference*, Houston, TX, USA, 1999.
- [5] F. Cheli, P. Belforte, S. Melzi, E. Sabbioni, G. Tomasini, *A numerical-experimental approach for evaluating cross wind aerodynamic effects on heavy vehicles*. *Journal of Vehicle System Dynamics Supplement*, **44**, 791-804, 2006.
- [6] F. Cheli, R. Corradi, G. Diana, G. Tomasini, *A Numerical-Experimental Approach to Evaluate the Aerodynamic Effects on Rail Vehicle Dynamics*. *Journal of Vehicle System Dynamics Supplement*, **41**, 707-716, 2003.
- [7] M. Boccione, F. Cheli, R. Corradi, S. Muggiasca, G. Tomasini, *Crosswind action on rail vehicles: wind tunnel experimental analyses*, *Journal of Wind Engineering and Industrial Aerodynamics*, **96**, 584-610, 2008
- [8] M. Sterling, A. Quinn, C. J. Baker, D. M. Hargreaves, F. Cheli, E. Sabbioni, G. Tomasini, D. Delaunay, H. Morvan, *A comparison of different methods to evaluate the wind induced forces on a high sided lorry*. Paper submitted to the *Journal of Wind Engineering and Industrial Aerodynamics*.

## TRAIN SHAPE OPTIMISATION TO IMPROVE CROSS-WIND BEHAVIOUR

Federico Cheli<sup>\*</sup>, Francesco Ripamonti<sup>\*</sup>, Daniele Rocchi<sup>\*</sup>, Gisella Tomasini<sup>\*</sup>

<sup>\*</sup>Mechanical Engineering Department  
Politecnico di Milano, Via La Masa 1, 20156 Milano, Italy  
[federico.cheli@polimi.it](mailto:federico.cheli@polimi.it), [francesco.ripamonti@polimi.it](mailto:francesco.ripamonti@polimi.it), [daniele.rocchi@polimi.it](mailto:daniele.rocchi@polimi.it),  
[gisella.tomasini@polimi.it](mailto:gisella.tomasini@polimi.it),

**Keywords:** Railway vehicle design, Aerodynamics, Wind tunnel tests, CFD.

**Abstract.** *The aerodynamic loads, due to transversal wind, can have significant effects on the running safety of railway vehicles since they can modify the running stability of the vehicle with an increasing risk of overturning. The cross wind effects become particularly critical in combination with high running speed, with sudden variations of aerodynamic loads, for instance at an exit from a tunnel, and with cant deficiency, in curve. Moreover, nowadays cross wind effects on railway vehicles are a present problem due to the necessity of defining interoperability standards on this specific topic (TSI). In particular, at the design stage of a new railway vehicle, an aerodynamic study, able to verify the vehicle stability to cross wind action, becomes necessary. This work presents an aerodynamic analysis of cross wind effect on the new AnsaldoBreda EMUV250 train. Two approaches have been used: wind tunnel tests and Computational Fluid Dynamic (CFD) analysis. While the experimental study allows to have a higher confidence in the absolute values of the measured forces, the numerical calculations allow to obtain a more detailed information (pressure field and velocity map of the whole flow,...), very useful to understand the flow field around the vehicle and, as a consequence, to identify the more effective aerodynamic parameters. The aerodynamic coefficients of the first vehicle of the EMUV250 train original version have been measured by wind tunnel tests performed at different angles of wind exposure. Then the CFD analyses have been carried out in order to evaluate the parameters that mostly affect the aerodynamic force. The numerical results have been validated by the experimentally measured aerodynamic coefficients. As a result of the numerical study carried out on the original version of the EMUV250 model, two new vehicle geometries, with improved aerodynamic characteristics in terms of overturning risk, have been designed and tested in the wind tunnel. Starting from these results, through a numerical-experimental methodology, developed during these last years at Mechanical Engineering Department of Politecnico di Milano, the cross wind aerodynamic behaviour of the train can be analyzed in terms of Characteristic Wind Curves, that represent the limit wind speeds leading the railway vehicle to overcome safety limit conditions.*

## 1 INTRODUCTION

The aerodynamic loads, due to transversal wind, can have significant effects on the running safety of railway vehicles since they can modify the running stability of the vehicle with an increasing risk of overturning. The cross wind effects become particularly critical in combination with high running speed, with sudden variations of aerodynamic loads, for instance at an exit from a tunnel, and with cant deficiency, in curve [1].

Moreover, nowadays cross wind effects on railway vehicles are a living matter due to the necessity of defining interoperability standards on this specific topic (TSI, [2]). In particular, in the design stage of a new railway vehicle, an aerodynamic study, able to verify the vehicle stability to cross wind action becomes necessary.

This work presents an aerodynamic analysis of cross wind effect on the new EMUV250 train. Two approaches have been used: wind tunnel tests [3], [4], [5] and CFD Computational Fluid Dynamic analysis [6]. While the experimental study allows to have an higher confidence in the absolute values of the measured forces, the numerical calculations allow to obtain a more detailed information (pressure field and velocity map of the whole flow,...), very useful to understand the flow field around the vehicle and, as a consequence, to identify the more effective aerodynamic parameters [6].

In the first step, the aerodynamic coefficients of the first vehicle of the EMUV250 train original version have been measured by wind tunnel tests performed at different angles of wind exposure. In the second step, CFD analyses have been carried out in order to evaluate the parameters that mostly affect the aerodynamic force. The numerical results have been validated by the experimentally measured aerodynamic coefficients. As a result of the numerical study carried out on the original version of the EMUV250 model, a new vehicle geometry, with better aerodynamic characteristics in terms of overturning risk, has been designed and tested in the wind tunnel.

In this work only the static aerodynamic coefficients have been analysed. In a next paper, starting from these data, by the numerical-experimental methodology developed, during these last years, at Mechanical Engineering Department of Politecnico di Milano, the cross wind aerodynamic behaviour of the train will be analyzed in terms of Critical Wind Curves, that represent the limit wind speeds that lead the railway vehicle to safety limit conditions [2], [3], [7].

## 2 EXPERIMENTAL WIND TUNNEL TESTS

In order to experimentally evaluate the effect of modifications applied to the train shape, the mean aerodynamic coefficients have been measured through tests carried out on 1:10 scale model of the first vehicle of the EMUV250 in the Politecnico di Milano wind tunnel.

In particular, in the first phase, the coefficients, with a very large range of Reynolds numbers, have been measured on the original version of the train in order to validate the CFD analysis. In the second phase, the model of the last release of the train, designed on the basis of the results obtained by the CFD analysis, has been tested in the wind tunnel and the new coefficients have been measured.

Tests have been carried out on the flat ground scenario: this configuration corresponds to the condition of train running on a flat terrain (without ballast and rail) and it represents the reference configuration in the TSI Standard [2]. In particular, in the wind tunnel, the flat ground has been realized through a rectangular plate set at an height of  $h=300\text{mm}$  in order to have an incoming wind speed profile as uniform as possible. As represented in Figure 1, for the tests carried out in the High Speed Section (HSS), at different Reynolds numbers, the plate has been connected to an open parallelepiped steel structure (flat 1); for the tests at low

Reynolds number, performed in the boundary layer test section, the table is positioned at the same height by means of a series of columns but without the steel structure (flat 2). The main difference between the two scenarios is the thickness of the flat:  $s=50\text{mm}$  for the flat 2 and  $s=10\text{mm}$  for the flat 1.

Figure 2 represents the vertical wind speed profile measured over the table: it is possible to observe that, over the flat ground, the boundary layer thickness is equal to about 50mm. In all the performed wind tunnel tests on first vehicle, a down-stream body has been placed next to model (Figure 1) to reproduce the correct boundary conditions.

All the aerodynamic coefficients have been measured in conditions of smooth flow consisting in the standard wind tunnel operating conditions (the turbulent intensity  $I_u=0.2\%$ ).

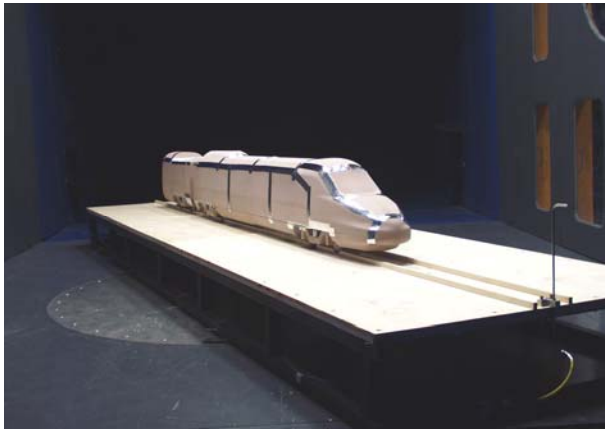


Figure 1: Experimental wind tunnel tests, High Speed Section: EMUV250 train on flat 1 scenario.

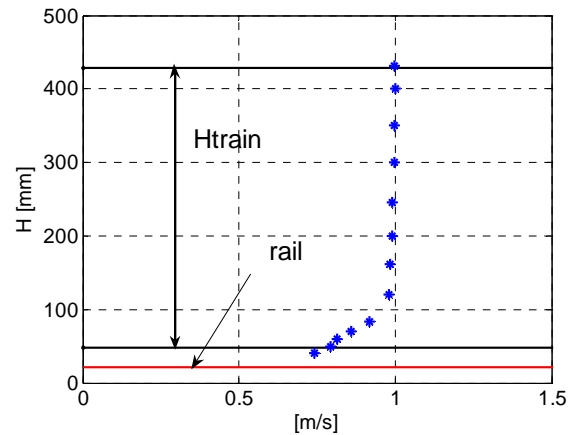


Figure 2: Experimental wind tunnel tests: vertical profile of the wind speed in the flat ground configuration normalized at  $z_{ref}=400\text{mm}$ .

The experimental set up is composed by both an external 6-components industrial dynamometric balance ([5]) for the measurement of the aerodynamic loads and a pitot tube, placed at the reference height ( $z_{ref}=0.4\text{ m}$ ), to measure the field wind speed.

As represented in Figure 3, the model is suspended to the dynamometric balance through four beam elements connected in correspondence of the internal wheelsets. The bogies and the wheelsets, geometrically similar to the corresponding real elements, are rigidly connected to the carbody.

Figure 4 shows the reference frame adopted to the definition of the aerodynamic forces: the reference system is connected to the carbody and its origin coincides with the carbody centre, at the track level. The aerodynamic forces measured in the static tests allowed to define the static aerodynamic coefficients as a function of the angle of attack  $\alpha$ . The non-dimensional coefficients are defined as follows:

$$C_{Fi} = \frac{F_i}{\frac{1}{2}\rho\bar{V}^2 A} ; \quad C_{Mi} = \frac{M_i}{\frac{1}{2}\rho\bar{V}^2 AH} \quad i = x, y, z \quad (1)$$

where  $F_i$  and  $M_i$  are the aerodynamic loads components in the train local reference system (Figure 4), evaluated in correspondence of the rail height, at the track midpoint;  $A$  is the lateral carbody surface (in the XZ plane, Figure 3),  $\rho$  is the air density,  $H$  is the vehicle's height,  $\bar{V}^2$  is the mean square value.

In the following, for privacy reasons, the experimental and numerical coefficients will be presented as the ratio between the coefficient itself and the value of the reference coefficient at  $90^\circ$ .

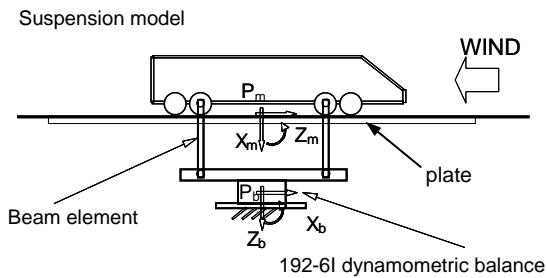


Figure 3: Experimental wind tunnel tests: scheme of the connection between dynamometric balance and vehicle model.

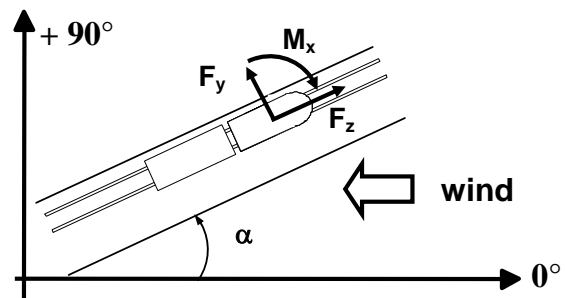


Figure 4: Experimental wind tunnel tests: reference system adopted for the aerodynamic forces and for the angles of attack.

## 2.1 Experimental results on the original version

According to the quasi-steady theory [9], the aerodynamic force is evaluated by the following expression:

$$F_i = \frac{1}{2} \rho A \bar{C}_i V_{rel}^2 \quad (2)$$

where  $\bar{C}_i$  is the mean aerodynamic coefficient and  $V_{rel}$  is the relative wind-train speed. In order to optimize the train aerodynamics with respect to the overturning risk, it is necessary to reduce the aerodynamic force, especially the rolling moment (that is dependent from the lateral force) and the vertical force: considered that the air density and the maximum train speed are fixed, this means to reduce both the exposed surface  $A$  and the aerodynamic coefficient  $\bar{C}_i$ .

Wind tunnel tests have been performed on original version of the first vehicle of the EMUV250 train on flat 1, in smooth flow conditions, both in High Speed Section (HSS) and in Boundary Layer Speed Section (BLSS). The tests in the HSS (4mX4m wide) have been carried out for Reynolds numbers from  $9.33 \cdot 10^4$  to  $1.1 \cdot 10^6$ , over the range of angles of attack  $0^\circ$ - $30^\circ$ , due to the dimensions of this test section that does not allowed higher yaw angles. On the contrary, the tests in the BLSS have been carried out for only one Reynolds number but over the complete range of angles of attack  $0^\circ$ - $90^\circ$ .

Figure 5 shows the vertical and lateral force coefficients experimentally measured in the two different test sections, for different Reynolds numbers. It is possible to observe that, over the range of yaw angles  $0^\circ$ - $30^\circ$ , the lateral force coefficients show a trend independent from the Reynolds number; on the other hand, the vertical force coefficients show that, for yaw angles of  $25^\circ$ - $30^\circ$ , higher Reynolds number lead an increasing on the modulus of the coefficient.

The tests performed in the BLSS show that the measured coefficients are in agreement with the corresponding values measured in the HSS, in the range  $0^\circ$ - $30^\circ$ . Both the coefficients linearly increase up to a critical angle that, for the considered configuration, is equal to about  $40^\circ$  where they reach a pick value. Over the critical angle, they show an oscillation around an almost constant value.



In the following, these last series of experimental data have been adopted as reference for the comparison with the CFD analysis.

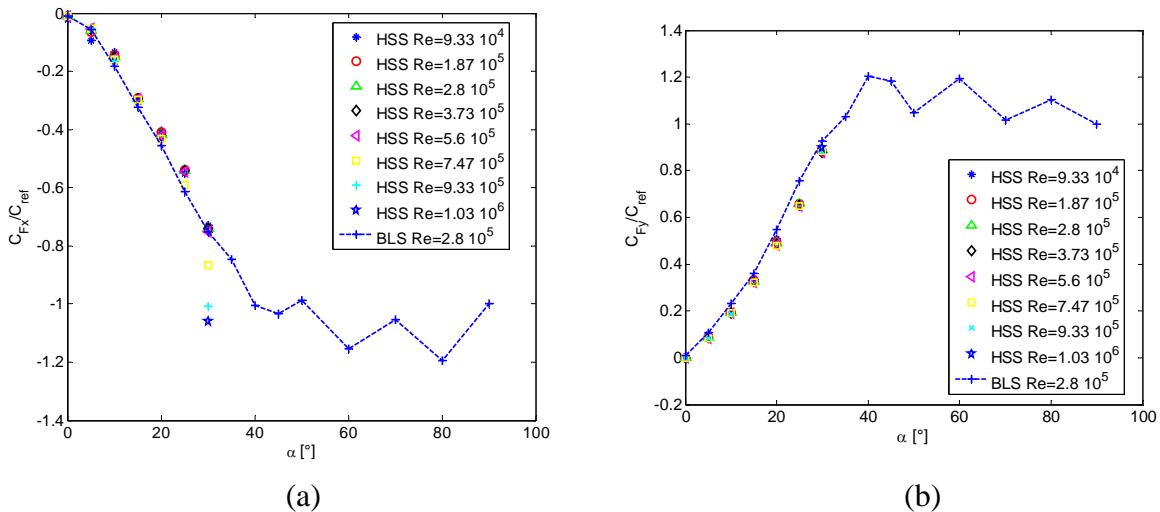


Figure 5: Reynolds number effect on the  $C_{Fx}$  (a) and  $C_{Fy}$  (b) coefficients: High Speed Section tests (points) and Boundary Layer Section tests (broken line).

### 3 CFD NUMERICAL ANALYSIS

For high speed trains, the typical range of angles of attack, experienced in the operating conditions, is bounded in  $0-30^\circ$ , due to the low value of the ratio between the absolute wind speed and the train speed. In order to reduce the risk of overturning due to the cross wind, it is necessary to decrease the aerodynamic coefficients (especially the ones related to rolling moment and lateral and vertical force) in the range of angles of attack  $0-30^\circ$ .

CFD analyses have been performed to deeply investigate the flow field in order to optimize the train aerodynamics in terms of response to the transversal wind. In fact, numerical studies allow to collect more information with respect to the experimental tests on both the static pressures on the vehicle surfaces and the velocity field around it.

The investigation of the flow field around the AnsaldoBreda EMUV250 High speed train model at different wind exposures was performed by means of 3D CFD analyses. The considered geometry represents the 1:10 scale model in order to simulate the same Reynolds number conditions of the wind tunnel tests. The quality of the simulation results has been assessed by a comparison between experimental and numerical results in terms of global forces and the analysis of the flow structure was used to define the geometry modification during the aerodynamic optimization stage. All the CFD analyses have been performed using the commercial code FLUENT<sup>®</sup> [8].

#### 3.1 3D CFD model

CFD analyses have been performed at the same wind speed considered during the experimental campaign equal to  $10$  m/s corresponding to a Reynolds number equal to  $1.87 \cdot 10^5$ , (referred to the train model height). The low turbulence intensity ( $I_u=2\%$ ) characterizing the wind tunnel flow (in common wind tunnel practice, it is considered laminar), together with the consideration of low levels of self-induced turbulence (at very low angles of exposure the flow is expected to be mainly attached to the train walls) allow to perform preliminary analyses resolving the Navier-Stokes equation without any turbulence model. A full direct numerical simulation is not feasible at the considered large Reynolds number because of the amount of

computational effort required. Therefore it has been decided to perform an analysis of the problem consisting in solving the Navier-Stokes equations on a coarser mesh (with respect to the DNS requirements) tolerating that the results will be affected by the approximation of the lack of the contribution of all the small turbulence scale filtered out by the grid spatial dimension. In particular, close to the wall, where the smallest turbulence scales are present, the adoption of a grid with larger dimensions will result in overestimating the slope of the velocity profile and consequently the shear stresses [9].

Simulations were performed considering the flow as incompressible and using a segregated solver. A first and a second order upwind method were chosen for the Navier Stokes equations while the velocity-pressure coupling has been performed with a SIMPLEC scheme.

The geometry of the solid model consists in the locomotive and  $1/3$  of the first trailer coach, positioned on a “flat ground” scenario. In Figure 6-a the CAD 3D model is reported.

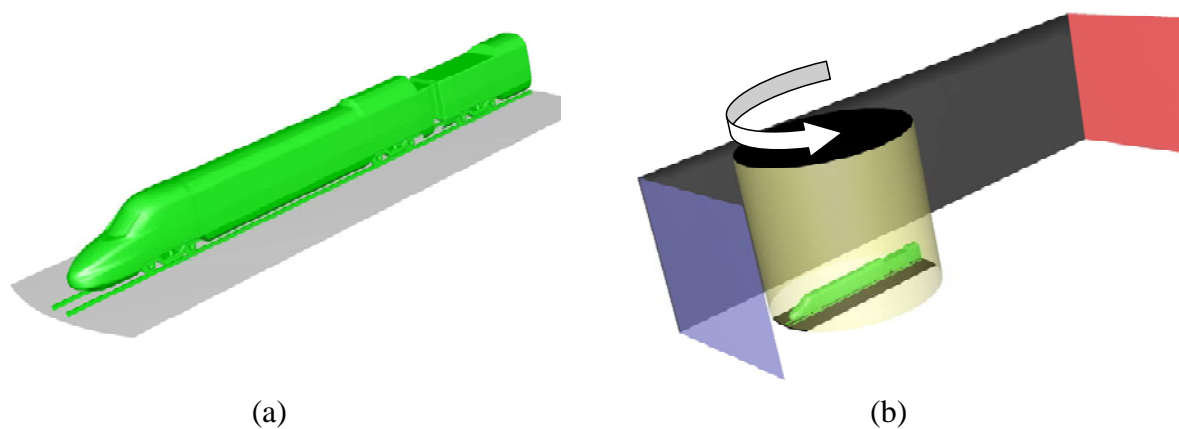


Figure 6: CFD numerical analysis; the EMUV250 (original design) 3D CAD model (a) and the computational domain (b).

In order to perform analysis at different yaw angles, the computational domain is divided in two parts: a cylindrical “core” containing the model geometry and a prismatic “exterior” representing the far field. A relative rotation between the two parts allows to reconstruct the computational grid at different wind exposures without remeshing operation in order to perform the different simulations and to compare results on the same mesh (Figure 6-b).

In this work the hexahedral cell meshing technique is adopted [8], with a finer spatial resolution near the train surface (the minimum cell dimension is set to  $5\text{ mm}$  on the train surface) in order to correctly reproduce the geometrical details and to better approximate the more severe gradients of this zone. A coarser spatial resolution is kept in the exterior region where the flow is less perturbed. The computational grid distribution is specifically designed to study attached flows conditions where no large wake structures are expected and its adoption is correct only at low angles of exposure. The total cells number is about 4.2 million. The simulations have been performed on a cluster Xeon – Exadron (32 bit, using 3 bi-processor nodes, Intel Xeon 3.06 GHz) of CILEA (computer centre of the Milan universities).

The velocity inlet boundary condition is applied on the front plane at about  $1.5\text{ m}$  from the vehicle (Figure 6-b). A uniform velocity profile is adopted in order to compare the results with the experimental ones where the floor boundary layer was cut off by the flat ground. On the rear plane ( $8\text{ m}$  from the model in order to allow a correct evolution of the velocity field) the pressure outlet condition is set to a gauge value equal to  $0$ . For the other four planes, confining the flow and reproducing the wind tunnel geometry, the rigid wall condition is considered.

The air has been considered in standard conditions:  $P=101325 Pa$ ,  $T=288.15 K$ ,  $\rho=1.225 kg/m^3$ ,  $\mu=1.7894 \cdot 10^{-5} kg/(m/s)$ .

### 3.2 3D CFD results

3D simulations were performed at the same yaw angles, that have been experimentally investigated, in the range from  $0^\circ$  to  $30^\circ$ . In fact, as it will be better explained later, the linear trend followed by the aerodynamic coefficients in this range of yaw angles is due to a flow pattern that is mainly attached or directed along the train walls. The departure from this linear trend traces the demarking threshold between a fully separated flow, as happens around bluff bodies, and an attached flow with possible separation bubble typical of aerodynamic profiles at low angles of attack. The CFD numerical investigation is therefore limited at exposures less than  $30^\circ$  where the adopted mesh and solution strategy are appropriate.

The results of the numerical simulations are compared to the experimental ones in terms of aerodynamic coefficients (normalized with respect the same experimental coefficient at  $90^\circ$ ) in Figure 7 following the formulation and sign convention reported respectively in (1) and Figure 4.

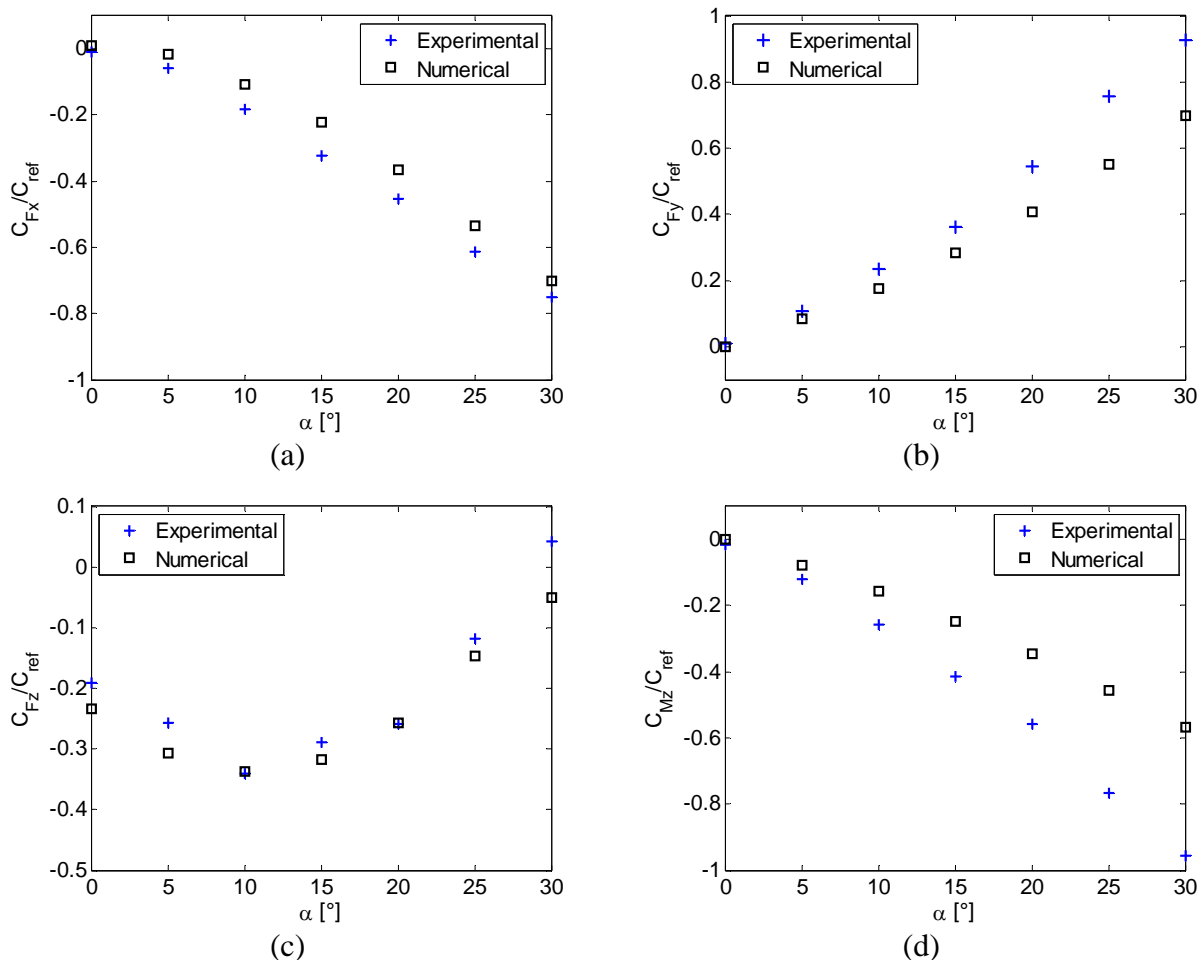


Figure 7: EMUV250 first vehicle (original design); the experimental-numerical comparison on the  $C_{Fx}$  (a),  $C_{Fy}$  (b),  $C_{Fz}$  (c) and  $C_{Mz}$  (d) coefficient.

A good agreement is shown between numerical and experimental data in terms of both slope and absolute value validating the adopted numerical approach. The agreement is very satisfactory for the  $C_{Fz}$  coefficient at all the different angles of exposure, while for the other

coefficients a trend appears, moving towards the largest angles, increasing the discrepancy between the experimental and numerical data, in terms of absolute values. Anyway it is important to remark that the experimental flat ground thickness affects the aerodynamic forces and, as a consequence, the numerical-experimental comparison.

An interpretation of the coefficient trends is proposed by the analysis of the flow structure by means of the CFD results visualization. The analysis of the pathlines shows that, while at  $0^\circ$  the flow is directed along the train lateral walls, approaching large angles of exposure, a separation zone appears. The flow in the separation zone is characterized by three dimensional structures mainly produced by the wind interaction with the train nose.

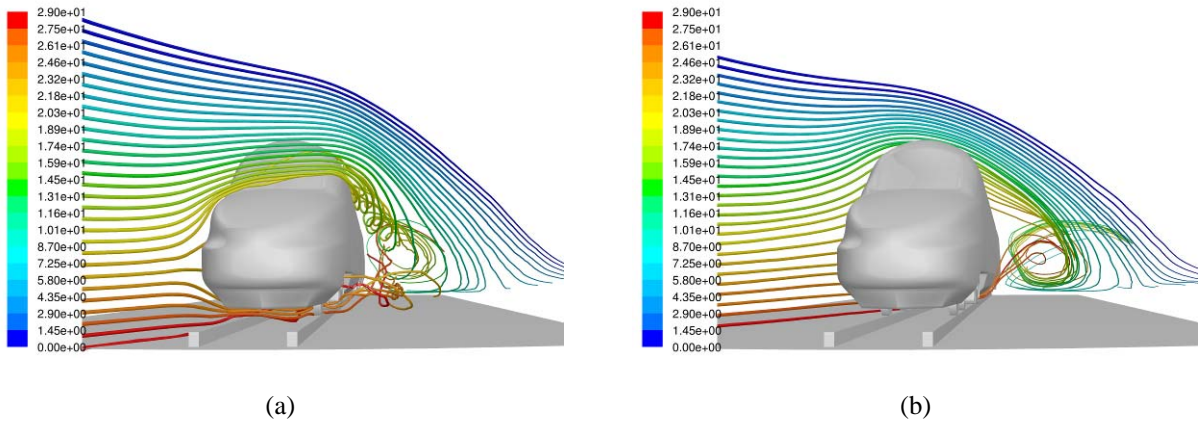


Figure 8: EMUV250 first vehicle (original design) CFD numerical analysis; path lines at  $25^\circ$  crossing the train nose (a) and the train body (b).

Increasing the angle of exposure a larger and larger part of the flow cross the vehicle raising the upwind flank and passing over the train roof. The train roof curvature drive the flow in the upper part, behaving as an airfoil, till to reach separation condition in the downwind flank. The flow that is detached from the roof in the downwind part mixes together with the flow that, blowing over the train nose, is deflected along the train axis giving rise to a complex three dimensional vortex structure as well described by the Figure 8. The air that passes through the under carbody region, with a larger and larger flow increasing the angle of exposure, is upwards sucked by the over mentioned three dimensional vortex (Figure 8-b). The downwind flank is therefore characterized by a large flow separation zone where the fluxes coming axially from the train nose, downward from the roof and upward from the under carbody region mixes together.

The main differences that can be noticed between experimental and numerical coefficients at the largest angles of exposure, may therefore be explained by the consideration that the laminar model is not well suitable to reproduce complex separated flows. The not correct reproduction of the behavior and of the dimension of the separation zone introduces an approximation in the numerical prediction that becomes larger, the larger is the importance of such flow pattern with respect to the global flow field.

Hereafter a simple analysis of the aerodynamic force and moment acting on the train is reported. In Table 1 is presented, for each exposure angle, the contribution of the shear stresses and the contribution of the normal pressure in the definition of the global drag forces in order to define the importance of the two terms. The contribution of the shear stresses on the other force components is negligible and it is not here included. The numerical simulation outlined that the 20% of the drag force is due to shear stresses for angles of exposure less than  $20^\circ$ . The overestimation of the  $C_{Fz}$  coefficient by the performed CFD simulations may be attri-

buted to an overestimation of the shear stresses due to a wrong velocity gradient normal to the wall in absence of a wall treatment model.

Yaw Angle	Shear stresses contribution on the global force $F_z$	Pressure contribution on the global force $F_z$
0°	23.6%	76.4%
5°	20.4%	79.6%
10°	20.9%	79.1%
15°	24.1%	75.9%
20°	32.3%	67.7%
25°	73.3%	26.7%

Table 1: EMUV250 first vehicle (original design) CFD numerical analysis; shear stresses and pressure contributions to the  $F_z$  drag force.

The larger contribution of the shear stresses, for angles of exposure greater than 20°, confirms the modification in the flow structure and the larger discrepancy between numerical and experimental results highlights the deficiency of the numerical model to reproduce similar flow fields.

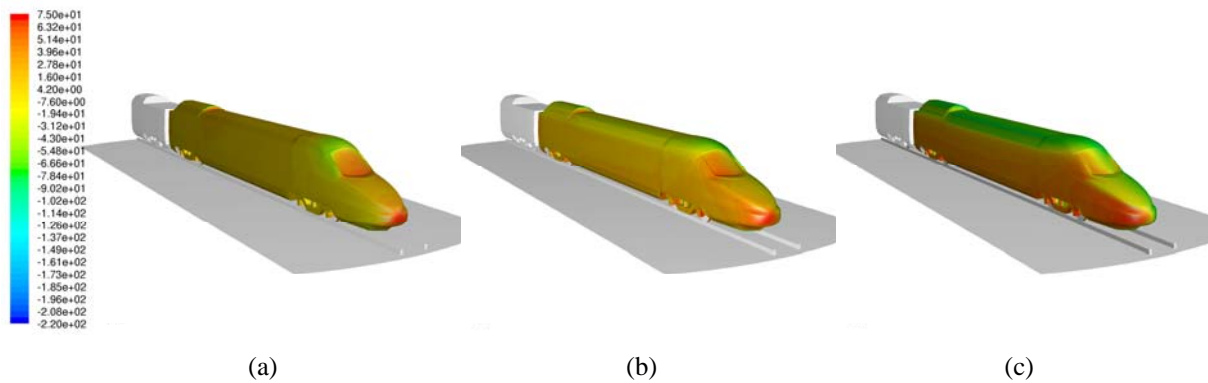


Figure 9: EMUV250 first vehicle (original design) CFD numerical analysis; static pressure distribution on the train walls at 0° (a), 15° (b) and 30° (c).

In Figure 9 the color map of the static pressure distribution on the train surface are reported at 0°, 15° and 30° angle of exposure. It is clearly visible the position of the stagnation point moving towards the upwind flank at high angles of exposure. The pressure distribution is bounded to the velocity distribution around the train profile and in particular is evident the large suction zone on the roof at high angles of exposure when large flows cross the train upper part.

An investigation on the contribution that the different train zones give on the global  $F_x$  and  $F_y$  forces is proposed by dividing the vehicle in 4 parts by means of a vertical and horizontal planes. The vertical plane splits the geometry in two symmetric half called “upwind” and “downwind” while the horizontal plane cuts the vehicle at a height equal to the connection between the front window and the train hood in two parts called, in the following, “up” and “down”. Figure 10 reports the contributions of the integral of the normal pressure and of the shear stresses, performed on each surface, projected along the vertical and lateral direction at each angle of exposure. This analysis allows to detect which are the surfaces governing the aerodynamic phenomena.

As far as concerns the  $C_{F_x}$  coefficient it is visible how the lifting behavior of the force is mainly due to the contribution of the upper part of the train, while the lower part accounts on-

ly for a small positive quantity. The contribution trends of the “upwind-up” part and of the “downwind-up” one are similar outlining that the flow is attached along the whole roof. A limited discrepancy between the two values appears only at high angles of exposure where smaller values for the downwind surface suggest the existence of the separation point at a certain position on the rear part of the roof curvature. The contribution due to the suction, which is induced by the roof curvature driving the flow in the upper part, increases its strength with the increase of the transversal flow (high angles of exposure) as visible in the static pressure distribution reported in Figure 9. In the lower part of the train the acceleration of the flow produces a negative force contribution of small entity. The comparison between the sum of the contribution of upper parts and the sum of the contributions of the lower parts is reported in Figure 11-a together with the global experimental coefficient.

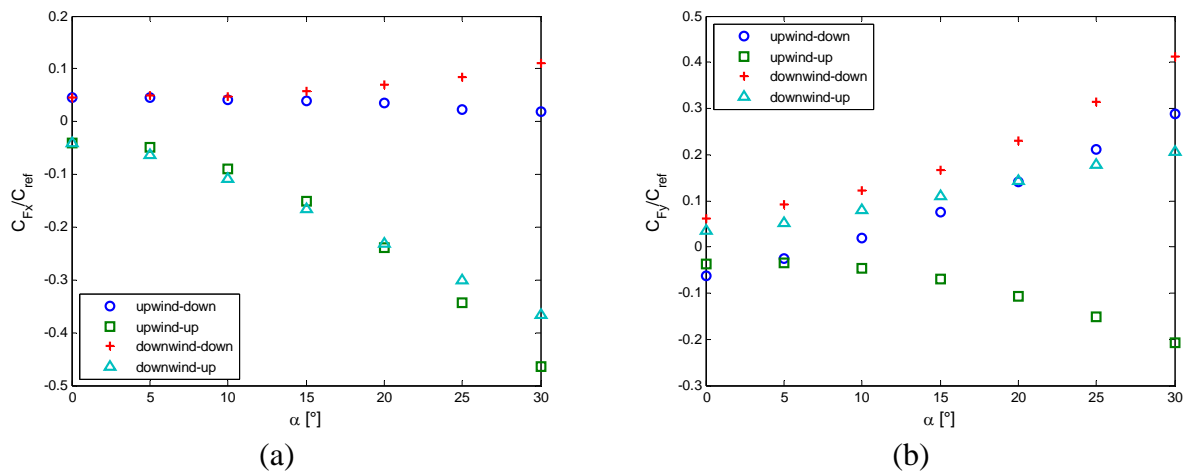


Figure 10: EMUV250 first vehicle (original design) CFD numerical analysis; contribution of each part of the train to  $C_{Fx}$  (a) and  $C_{Fy}$  (b).

Analyzing the  $C_{Fy}$  coefficient, it is visible how the contribution of each part of the train acts in the direction to increase the lateral force apart from the “upwind-up” one: the suction present in that region acts, in fact, against the wind direction. This effect is counterbalanced by the contribution of the “downwind-up” part where a suction similar to the previous one acts along wind. The result is clearly shown in Figure 11-b where the sum of the up/down parts are compared with the experimental global result.

From the analysis of Figure 11-b is evident how the global trend of the lateral force is mainly produced by the train lower part behavior while the upper part one is negligible.

The three dimensional vortex generated by the interaction between the flow detached from the vehicle nose and the flow arriving from the train roof originate a narrow wake sucking the flow passing under the carbody (Figure 8-b) with a strong suction on the downwind flank. This suction sums up to the pressure on the lower part of the upwind flank (Figure 9) to determine the global lateral force coefficient  $C_{Fy}$ .

The coefficient trend is in good agreement with the experimental one denoting that the global flow is well reproduced by the CFD results even with a very simple laminar approach. A better reproduction in quantitative terms is expected adopting a finer mesh grid or a turbulence model able to better simulate the flow behavior in the separation zone.

From all the considerations deduced from the CFD analysis, an attempt to improve the aerodynamic performances of the train was carried on by modifying the train roof geometry being the modification of the under carbody region more difficult due to the presence of many

auxiliary systems and more restrictive geometry requirements. The new geometry was obtained reducing the roof curvature with the aim:

- to reduce the wind speed in the upper part and, as a consequence, the lift force;
- to reduce the interaction between the flow coming from the train roof and the flow coming from the train nose.

The new solution was experimentally tested in the wind tunnel defining the aerodynamic coefficients that will be compared with those related to the original geometry.

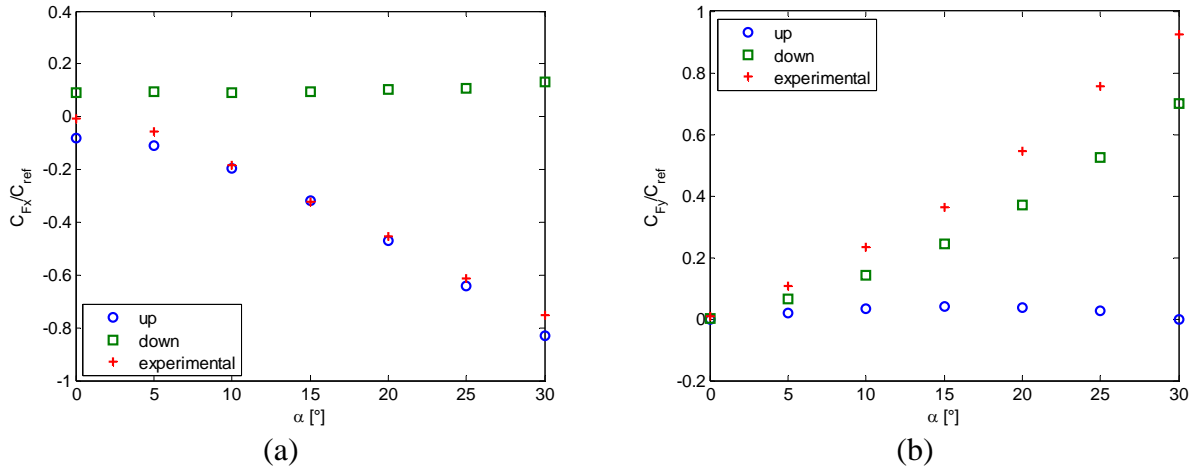


Figure 11: EMUV250 first vehicle (original design) experimental-numerical comparison; upper part contribution versus lower part to  $C_{Fx}$  (a) and  $C_{Fy}$  (b).

#### 4 OPTIMISATION OF THE TRAIN AERODYNAMICS: EXPERIMENTAL RESULTS

Relying on all the considerations deduced from the CFD analysis, an attempt to improve the aerodynamic performances of the train was carried out. The carbody regions, that mainly influence the train aerodynamic behaviour, are the under carbody, the roof and the nose. As previously explained, each region influences a specific coefficient rather than another, even if it has been pointed out that the resulting force depends on a complex flow, mix of the effects of all the regions. Anyway, since the under carbody modifications are not achievable due to the presence of many auxiliary systems and more restrictive geometry requirements, only a change of the roof and the nose geometry has been taken into account.

A new roof geometry was obtained reducing the roof curvature. Two main modifications have been carried out:

- the higher element on the roof at the end of coach has been reduced;
- the roof curvature in a transversal section is lowered and the maximum height of the train with respect to rail has been slightly reduced.

The roof geometry modifications should be more visible at higher exposure angles, where a larger flow crosses the transversal train profile.

A second modification of the train geometry concerned the nose. As previously stated, it plays a very important role in the generation of the 3D complex flow around the train. In order to investigate its effect, a new nose version part has been defined by modifying the hood and the front window inclination (Figure 13).

Therefore a final version of the first vehicle model of the EMUV250 train (in the following called “new model”) has been designed and produced with also few modifications on the roof geometry to accomplish not only the technical requirements related to the overturning risk but

also all the different requests related to safety standards (especially crash test) and space constraints. Figure 12 and Figure 13 show respectively the original and the new CAD model.

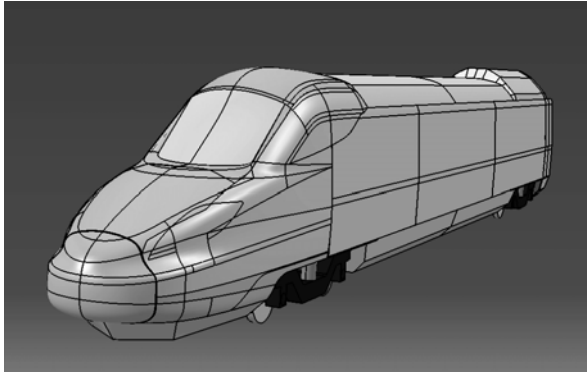


Figure 12: Solid model of the EMUV250 train first vehicle in the *original* version.

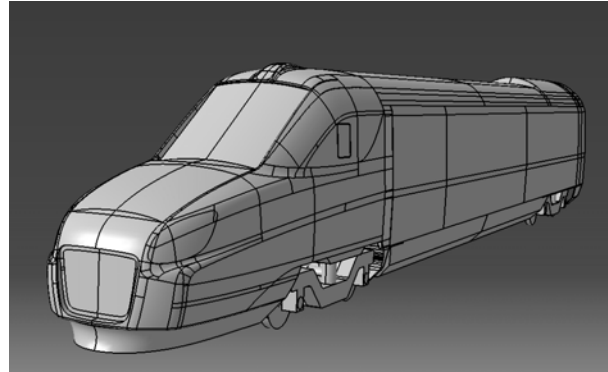


Figure 13: Solid model of the EMUV250 train first vehicle in the *new* version.

The aerodynamic coefficients respectively of vertical and lateral force measured on the new model are reported in Figure 14, as a function of the angle of exposure, and compared to the corresponding coefficients on the original model. In particular, from Figure 14-a it is possible to see that the vertical force coefficient  $C_{Fx}$  measured on the new model shows a significant reduction with respect to the previous version at all the angles of exposure (about 25% in the range 0-30°). Concerning the rolling moment, Figure 14-b shows that the  $C_{Fy}$  is lower than the corresponding aerodynamic coefficients measured on the original version.

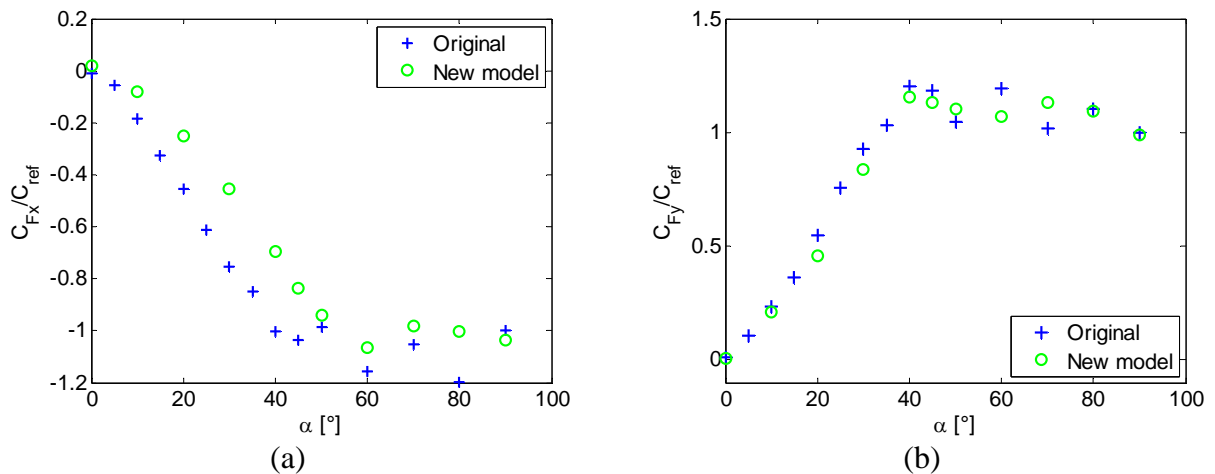


Figure 14: EMUV250 first vehicle experimental wind tunnel tests; flat ground, smooth flow: comparison between vertical force coefficient  $C_{Fx}$  (a) and lateral force coefficient  $C_{Fy}$  (b) measured on the *original* model and on the *new model*.

## 5 CONCLUSIONS

An aerodynamic analysis has been performed on the EMUV250 first vehicle with the goal to define and to improve the train safety under cross wind condition. In the paper a combined use of wind tunnel investigation and numerical CFD study has been adopted to find a more efficient train geometry in terms of aerodynamic behavior. A simple laminar 3D solution succeeded in reproducing the main flow patterns allowing for an interpretation of the experimental results.



An analysis of the influence of the different parts of the train geometry on the definition of the aerodynamic forces has been presented starting from the CFD results. A new version of the EMUV250 train first vehicle has been experimentally investigated in wind tunnel: the new model, characterized by significant modifications especially on the nose and the roof geometry.

## ACKNOWLEDGEMENTS

The research has been developed with the financial support of AnsaldoBreda S.p.A., which also provided the physical train models for the wind tunnel experimental tests.

## REFERENCES

- [1] Schulte-Werning, B. The TRANSAERO Project – Joint European Railway Re-search on Transient Aerodynamics, *Notes on Numerical Fluid Mechanics* **79**, 11-24, 2002. Springer-Verlag Berlin.
- [2] *Technical Specification for Interoperability*, HS RST TSI.
- [3] Baker, C.J. The wind tunnel determination of crosswind forces and moments on a high speed train, *Notes on Numerical Fluid Mechanics* **79**, 46-60, 2002. Springer-Verlag Berlin.
- [4] Suzuki, M., Tanemoto, K., Maeda, T. Aerodynamic characteristics of train / vehicles under cross winds, *Journal of Wind Engineering and Industrial Aerodynamics*, **91**, 209-218, 2003.
- [5] M. Boccione, F. Cheli, R. Corradi, S. Muggiasca, G. Tomasini, Crosswind action on rail vehicles: wind tunnel experimental analyses, *Journal of Wind Engineering and Industrial Aerodynamics*, **96**, pp. 584-610, 2008
- [6] Khier, W., Breuer, M., Durst, F. Numerical computation of the 3 D turbulent flow around high speed trains under side wind conditions, *Notes on Numerical Fluid Mechanics* **79**, 75-86, 2002. Springer-Verlag Berlin.
- [7] R. Cooper, Atmospheric turbulence with respect to moving ground vehicles, *Journal of Wind Engineering and Industrial Aerodynamics*, **17**, 215-238, 1984.
- [8] Fluent® user's guide
- [9] E.Simiu & R.Scanlan, Wind Effects On Structures, *Wiley-Interscience Publication*, New York, 1986.

# UNSTEADY AERODYNAMIC CROSSWIND STABILITY OF A HIGH-SPEED TRAIN SUBJECTED TO GUSTS OF VARIOUS RATES

**Ben Diedrichs**

KTH Aeronautical and Vehicle Engineering, Div. of Rail Vehicles  
SE-10044 Stockholm, Sweden  
Bombardier Transportation, Department of Aero- and Thermodynamics  
SE-72173 Västerås, Sweden

**Keywords:** Railway vehicle aerodynamics, crosswind stability, train overturning, CFD

**Abstract.** *This paper presents unsteady aerodynamic results of crosswind stability obtained numerically for the class 808 leading control unit of Deutsche Bahn AG's high-speed train Inter-City Express 2. The effects of two linearly increasing gusts are explored by means of Detached Eddy Simulation (DES), where the yaw angle of the flow goes from a basic wind of  $8.1943^\circ$  to a maximum wind of  $23.3644^\circ$ . The rise times of the gusts correspond to 1.3073 and 2.6146 vehicle lengths (0.5 and 1 sec at the train speed of 250 km/h), which are chosen with respect to the potential excitation of the natural car body frequencies regarding the vehicle dynamics. In total, one DES and three Delayed-DES (D-DES) are carried out with the commercial code STAR-CD, using three background turbulence models,  $k-\epsilon$ ,  $k-\omega$  SST and Spalart-Allmaras, on two meshes adapted for high- and low-Reynolds number wall modeling about the vehicle surfaces. The results show a satisfactory level of coherence, where results are indirectly (using Ref. [1]) verified against wind tunnel data and Reynolds Averaged Navier Stokes (RANS) results of the basic and maximum wind. Admittedly, the results of the D-DES using the  $k-\omega$  SST turbulence model are questionable in that the turbulence prediction on the lee-ward side seems deficit. However, the level of the principal loads agrees well with the other DES and RANS.*

*It is demonstrated that the drag force, the pitch moment and in particular the yaw moment overshoot significantly (depending on the gust properties) compared to the steady results, which may have implications on the vehicle stability. Assessing the unsteady effects of numerous gusts on various vehicles may seem prohibitively expensive from a computational point of view. To overcome the bottle neck of the indeed compute intensive DES, a Quasi Transient Gust Modelling technique is invented and tested somewhat satisfactorily using the linear gusts. The aerodynamic effects of exiting a tunnel and the gust used in European TSI [2] are subsequently explored with this technique. The results of particularly the TSI gust are very instructive, as it shows significant unsteadiness of the kind that is not taken into account in the current standard.*

## 1 INTRODUCTION

The understanding of crosswind stability for rolling stock has matured considerably in the railway community during the last two decades. This is partly owing to the work with the European legislations on Technical Specifications for Interoperability (TSI) [2], which has triggered several research projects, some referred to in, for example, Diedrichs 2008 [1]. Further, the ecological aspects for a sustainable development will continue to put crosswind

stability of vehicles into the focus, as reduction of energy consumption hinges on the ability to reduce the stabilizing vehicle weight.

Unfortunately, the properties of real wind are rarely constant. However, steady modeling of crosswind stability for rail vehicles has been standardized and subjected to some convenient assumptions to avoid some of the cumbersome complexity. In this perspective, the motivation for this work is to explore the unsteady effects of the principal aerodynamic loads using DES for the class 808 leading control unit of Deutsche Bahn AG's high-speed train ICE 2, when immersed into simple gusts. The study is different from that by Krajnović 2008 [3] who used three cars and a comparatively complex gust based on the work by Ryan and Dominy [4]. The current numerical work uses the wind tunnel model geometry of the ICE 2 train, cf. Orellano and Schober 2006 [5] and Diedrichs 2008 [1], running on a ballast and rail track bed according the European standard prEN 14067-6 [9]. Here, linearly increasing gusts are used, where the response should be easy to study.

Further, the paper discusses a swift modeling technique, referred to as Quasi Transient Gust Modeling (QTGM), which is used to exemplify the effects of exiting a tunnel into various levels of crosswind. QTGM is also applied to the wind model prescribed in the European TSI [2], where the results reveal some significant unsteadiness that potentially may affect some of the natural car body frequencies.

## 2 DEFINITIONS

$U_t$ ,  $U_w$ , and  $U_R$  denote train, wind and resultant wind speed, where  $U_w$  is acting perpendicular to the track, why  $U_R^2 = U_t^2 + U_w^2$ . The principal aerodynamic loads in terms of forces ( $C_{Drag}$ ,  $C_{Side}$  and  $C_{Lift}$ ) and moments ( $C_{Roll}$ ,  $C_{Pitch}$  and  $C_{Yaw}$ ) with respect to the directions of ( $x$ ,  $y$ ,  $z$ ) are defined according to EN 14067-1 [6]. The origin of the coordinate system is located mid the bogies, at the centerline of the vehicle and at top of rail.  $x$ ,  $y$  and  $z$  point in the directions of the train, perpendicular to the train side and vertically towards the ground respectively, see Fig. 1. The geometrical scaling of the aerodynamic loads are based on  $l=3$  m and  $A=10$  m<sup>2</sup>, at full scale dimensions (FSD). All lengths are given in FSD in what follows. Further, loads and static pressure ( $C_p$ ) are scaled with the dynamic head pressure based on  $U_R$ .

$C_{R-LR} = C_{Roll} - C_{Lift} \cdot b_0/l$  is a key parameter that denotes the roll over moment about the lee-rail. The distance  $2 \cdot b_0 = 1.5$  m defines the nominal lateral distance between the contact points of a wheel-set for standard gauge track of 1435 mm. In absence of all the other loads, it can be used to predict vehicle overturning in two-dimensional sense.

## 3 VEHICLE MODEL AND COMPUTATIONAL DOMAIN

The train model consists of the leading test- and a simplified end-car, shown in Fig. 1a, which reflects a typical wind tunnel set up to encourage subsequent experimental verifications. The geometry is similar to a previous study by the same author (Ref. [1]) which purpose was to compare steady results of relatively high yaw angles with wind tunnel data. To this end, the previous model was mounted on pillars that were also used in the calculations. Here, the pillars are removed and the train is running on ballast and rail track bed detailed in Ref. [7], see Fig. 1. Two simplified rails are used, which are 150 mm high, 50 mm wide and separated 1435 mm. This gives a ground clearance between the rails and underbelly of the vehicle of 271 mm. Further, to avoid mechanical contact in the experiment, a gap is introduced between the cars of 5 cm. The height  $h_t$ , width  $w_t$  and length  $l_t$  of the test unit are 3.856, 3.020 and 26.56 m, where the car body length is measured from the nose to centre of the inter-car gap of the test car. The total length of the trackbed including the 30° slopings at the leading edge is  $12.5 \times h_t$ , where the total length of the two cars is  $9.2 \times h_t$ , see Fig. 1b.

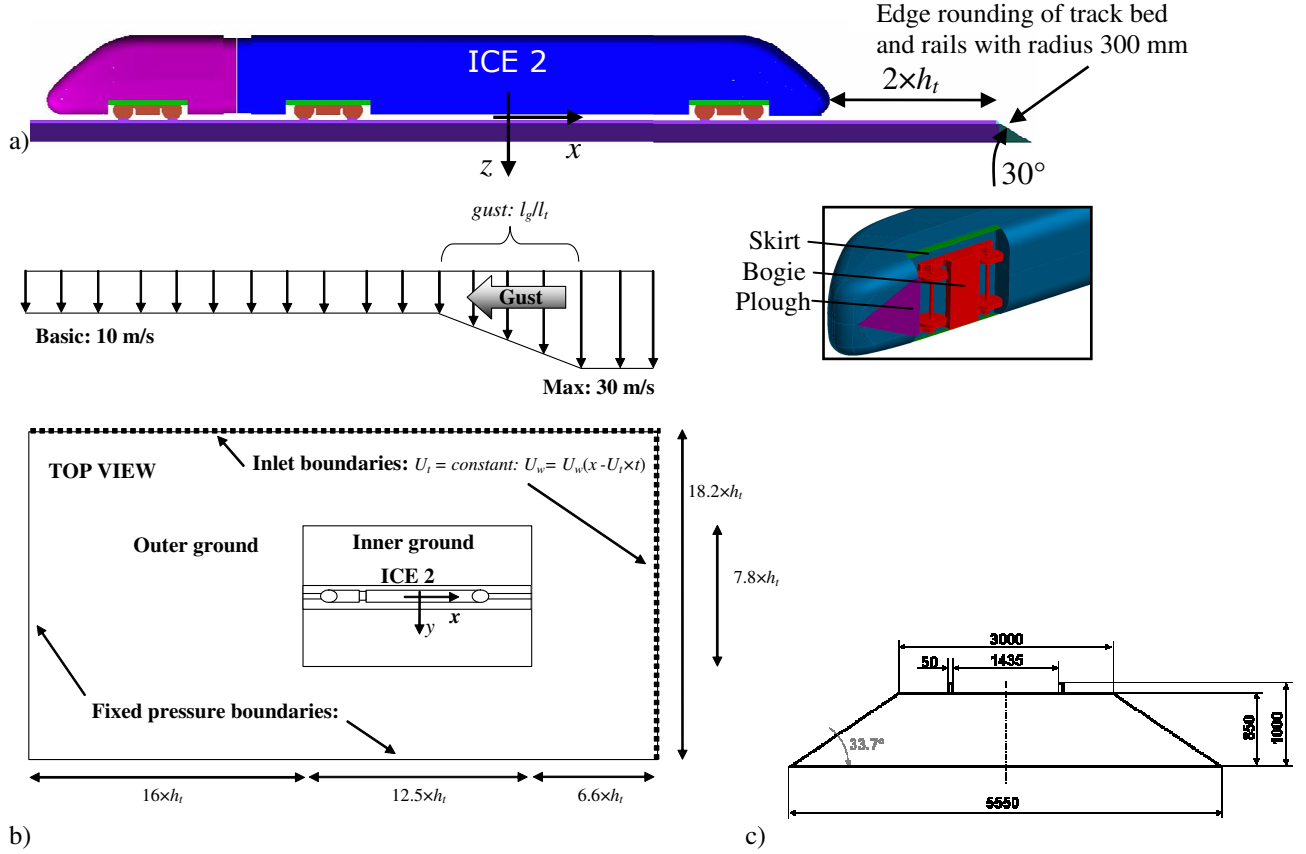


Figure 1: Vehicle model of the ICE 2 train that features a plough, bogies partly covered with bogie skirts, inter-car gap. a) ICE 2 model. b) Computational domain. c) Ballast and rail track bed geometry.

#### 4 COMPUTATIONAL DOMAIN AND BOUNDARY CONDITIONS

The computational domain, depicted in Fig. 1b, is a square box with height  $7.8 \times h_t$ , where the boundary conditions are as follows:

- Low turbulence block profile inlet condition for  $U_R$ , which corresponds to Reynolds numbers (Re) of  $1.5 \times 10^6$  and  $1.0 \times 10^6$  for the high- and low-Re wall modelling, respectively. Re is based on the reference length  $l=3$  m, and on a modified dynamic molecular viscosity. Wind speed and turbulence are applied to the north and east boundaries of Fig. 1b, which are functions of time ( $t$ ) and longitudinal component ( $x$ );
- south and west boundaries, see Fig. 1b, are outlets based on fixed pressure;
- ceiling and outer ground use symmetry boundary and slip conditions, respectively;
- no-slip wall boundaries are used for the surfaces of the train.

#### 5 NUMERICAL AND TURBULENCE MODELLING

The results of the present RANS, DES and Delayed-DES (D-DES) are obtained with the commercial software package STAR-CD versions 4.04 and 4.06 from CD-Adapco. The domain decomposition scheme offers a 2<sup>nd</sup> order discretization accuracy of the advective fluxes of the momentum equations, which are discretized using MARS (Monotone Advection Reconstruction Scheme, 2<sup>nd</sup> order accurate TVD scheme. A compression factor of 1 is used in the unsteady calculations, which minimizes dissipation and maximizes the sharpness resolution of gradients).

## RANS

Hi-Re turbulence closure is treated with the quadratic nonlinear eddy-viscosity model (NLEVMM) of Shih et al. 1993 [8]. The NLEVMM provides inequality of normal stresses, can predict some effects of streamline curvature via a different response to rotational and irrotational strains and henceforth also obey basic realizability constraints (to ensure positive normal stresses). Low-Re turbulence closure is introduced via the  $k-\omega$  SST model (Shear Stress Transport) of Menter 1993 [9], which blends automatically between the Wilcox  $k-\omega$  [10] and the Jones and Launder 1972 [11] standard  $k-\varepsilon$  turbulence models in the inner and outer part of the boundary layer, respectively. In the low- and hi-Re meshes the first cells adjacent to the walls of the train are adjusted to meet the requirements of  $y^+ < 2$  and  $30 < y^+ < 150$ .

## DES and D-DES

Hi-Re turbulence closure is obtained with the  $k-\varepsilon$  eddy-viscosity model, which was used by Rolén et al. 2004 [12] in a similar application for the Aerodynamic Train Model. Low-Re turbulence closure is achieved with the  $k-\omega$  SST model of Ref. [9] and the Spalart–Allmaras model [13]. The analogue Smagorinsky constants of the DES are 0.65, 0.61 and 0.65, respectively. The Hi-Re calculation used a three level implicit (quadratic backward implicit) time scheme in conjunction with SIMPLE. However, the Low-Re calculations used the PISO scheme and a time discretisation that offers a formal accuracy lying between first and second order. Mean CFL numbers, where time step is adjusted when applying the gusts, are typically 0.27 and 0.24 for the HRM and LRM (short for High-Re and Low-Re Meshes, described next).

## 6 COMPUTATIONAL MESHES AND CALCULATED CASES

Two computational meshes referred to as HRM and LRM based on polyhedral cells (P) are generated with the automatic mesh tool of CCM+ v3.02 – v3.06 from CD-Adapco, described in Table 1. Mind, that the current polyhedral meshes require approximately half the number of cells to obtain the same number of cells faces compared to a hexahedral mesh.

Mesh	Cells $\times 10^6$	Vertices $\times 10^6$	Turbulence model	Yaw angles [Deg]	Gust $l_g/l_t$	STAR-CD version
HRM	5.0	21.3	RANS: Quadratic $k-\varepsilon$	8.1943, 23.3644	-	4.04
			DES: $k-\varepsilon$	8.1943 – 23.3644	1.3073, 2.6146	
LRM	6.3	23.5	RANS: $k-\omega$ SST	0, 8.1943, 13, 18, 23.3644, 30, 35, 40	-	4.06
			RANS: S-A	8.1943		
			D-DES: $k-\omega$ SST	8.1943 – 23.3644	1.3073	
			D-DES: S-A*		1.3073, 2.6146	

Table 1: Results database. \*) Includes rise and decay of gust (see Figs. 7e,f).

The HRM is generated with 7 prismatic cell layers of constant thickness adjacent to walls. The LRM mesh is generated with 12 and 5 prismatic cell layers around the walls of the cars and moving ground, respectively, where the corresponding growth rates are 1.3 and 1.1. The total heights of the prismatic cells of the stationary and moving walls are 0.91% and 3.1% of  $h_t$  for both meshes. For practical reasons, Re is limited to  $10^6$  for the LRM to fulfil  $y^+ < 2$  about wall surfaces. Figure 2, provides snapshots of the HRM mesh and some of the refinements.

Gusts are here based on a basic and maximum wind of yaw angles  $8.1943^\circ$  and  $23.3644^\circ$ , respectively. For a train speed of 250 km/h, which is the dividing line for Class 1 trains according to the European TSI [2], the above yaw angles correspond to crosswind of 10 m/s and 30 m/s. The latter is a plausible wind speed in the context of overturning (recall, for example, TSI prescribes 29.5 m/s at 250 km/h with a lateral track plane acceleration of 0.5

$\text{m/s}^2$ ). Further, the gusts of  $l_g/l_t$ , see Table 1 and Fig. 1b, of 1.3073 and 2.6146 give rise times of 0.5 and 1.0 sec at  $U_t = 250 \text{ km/h}$ . The rise times are chosen with respect to the response of the natural frequencies of the vehicle, cf. Diedrichs et al. 2007 [14]. Lippert [15] demonstrated for a high-speed rolling stock that gusts with rise times longer than 1.0 sec would typically give less significant transient response of the vehicle dynamics.

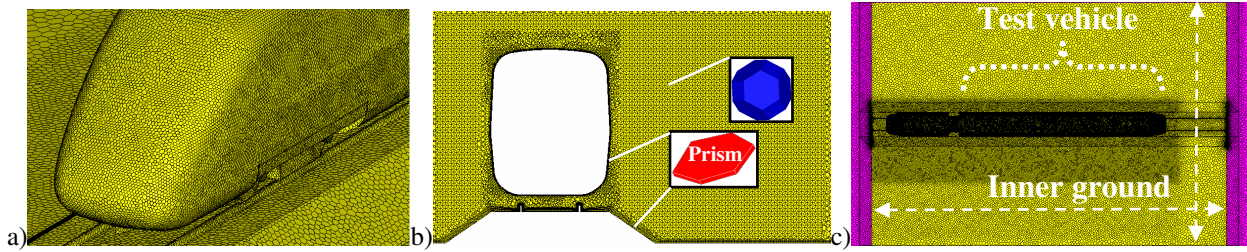


Figure 2: Polyhedral mesh: a) Front-end of test vehicle. b) Cross section mid the vehicle. c) Top view.

## 7 STEADY STATE RESULTS

The main objective here is the recordings of the aerodynamic loads of the ICE 2 leading car as a function of time, when the vehicle becomes immersed into the linear gusts. Unfortunately, testing of such simple gusts in a wind tunnel is quite challenging. Therefore, in the present work, RANS serve the purpose of validating data prior to and after the gusts have passed the vehicle. Recall that RANS for crosswind stability in conjunction with polyhedral meshes for the present vehicle compared well with wind tunnel experiments (Ref. [1]). Moreover, a second objective of the current paper is to demonstrate a technique to model arbitrary gusts using steady results, preferably obtained via RANS.

### Flow fields

Figure 3 shows the flow fields of the RANS and DES. The illustrations depict surface streamlines colored with static pressure ( $C_p$ ),  $C_p$  contours at 15 m from the nose and iso-surfaces of the flow where  $C_p = -0.9$ . The iso and contour plots of  $C_p$  illustrates the intensity of the suction pressure particularly about the lee-ward side of the nose and of the lee-vortex. The HRM:DES: $k-\varepsilon$  gives the most intense suction pressure (Fig. 3c) and vigorous turbulence on the lee-ward side (Fig. 3g). In this context, the deficiency of the peak suction pressure of the lee-vortex predicted with RANS, compared to the experiment, was brought to the attention in the study of Ref. [1]. The strength of the lee-vortex is usually an indicator of the suitability of the numerical scheme. Here, the HRM:DES: $k-\varepsilon$  is subjected to less diffusion effects but it should be debated whether the flow field representation is more accurate. It is further observed that the LRM:RANS: $k-\omega$  SST and LRM:D-DES: $k-\omega$  SST yield the weakest suction pressure of the lee-vortex (Figs. 3b,d) and the most dampened turbulence (Fig. 3h) respectively. The implications of a stronger lee-vortex is larger overturning loads, where the latter is sensitive to changes in the flow field adjacent to the upper lee-ward corner of the vehicle, discussed further in connection to Fig. 8.

$C_p$  around the vehicle body is shown in Fig. 4 for both the basic ( $\beta = 8.1943^\circ$ ) and maximum ( $\beta = 23.3644^\circ$ ) wind cases, at 2.5, 7 and 15 m from the nose. High and low values of  $C_p$  are illustrated with deformations of the body contour normal to the surface being either inward or outward, respectively. According to Fig. 8, differences around the UL part of the cross-section should be emphasized. The LRM:RANS&D-DES: $k-\omega$  SST calculations ( $\beta = 23.3644^\circ$ ) predict a minor vortex at the lee-ward side at  $z \sim -3 \text{ m}$ , which agrees with the LRM:RANS: $k-\omega$  SST of Ref. [1]. At  $\beta = 8.1943^\circ$  all results are close, why in Fig. 4, only the results of LRM:RANS:S-A are displayed.

Animations of  $C_p$  (not shown here) of the current gusts reveal that the largest fluctuations occur near the ground, and that the suction pressure around the top wind ward corner and lee-vortex is remarkably stable. The transition from the basic to the maximum wind is a smooth process without over shootings or history effects (confirmed by Krajnović [3]). Instantaneous data of  $C_p$ , during the event of the gust, agree remarkably well with  $C_p$  data of the intermediate yaw angles of the RANS results. All this taken together may motivate modeling of the principal loads imposed by other gusts in accordance to what is described in section 9.

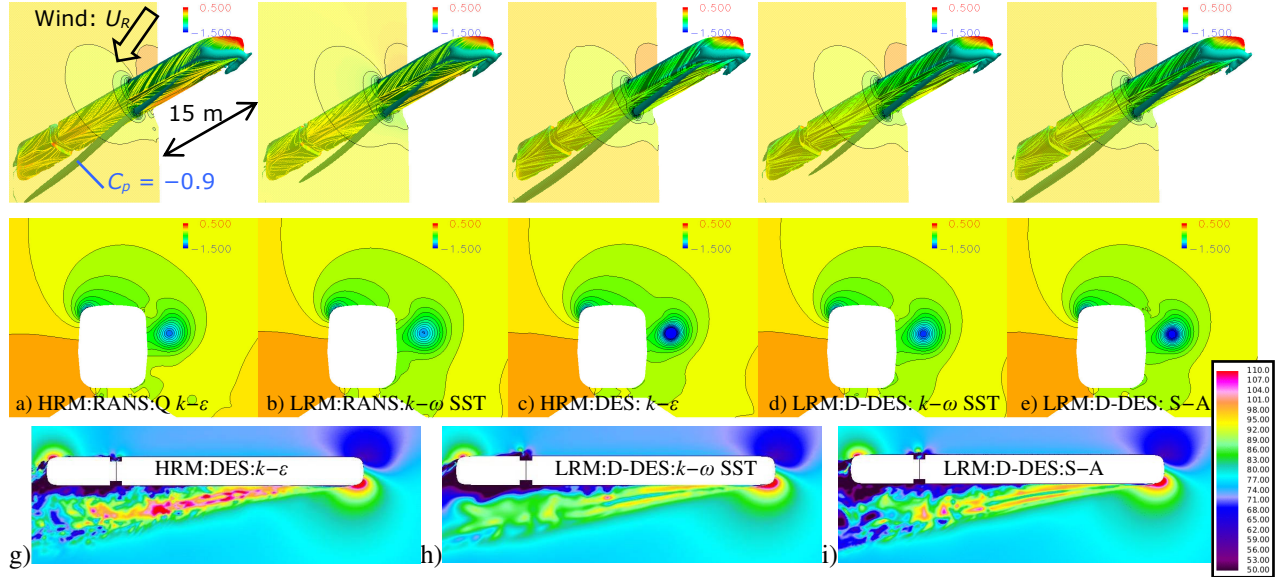


Figure 3: Flow fields of  $\beta=23.3644^\circ$ . a) HRM:RANS:  $Q k-\epsilon$ , b) LRM:RANS: $k-\omega$  SST, c) HRM:DES: $k-\epsilon$ , d) LRM: D-DES: $k-\omega$  SST, e) LRM:D-DES:S-A. g-i) Instantaneous velocity magnitude;  $z/h_f=-0.7261$  and  $U_t=69.4444$  m/s.

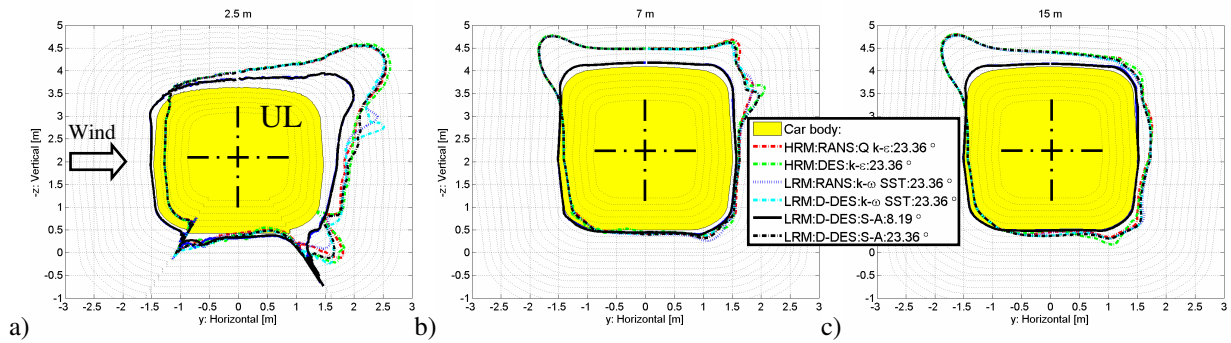


Figure 4:  $C_p$  around the car body (normalized with  $U_R$  based on  $\beta = 23.3644^\circ$ ) at a) 2.5 m, b) 7 m and c) 15 m from the nose.

### Aerodynamic loads

Figure 5a,b compare the aerodynamic loads of the RANS and the time averaged DES regarding the basic ( $\beta = 8.1943^\circ$ ) and maximum ( $\beta = 23.3644^\circ$ ) winds. By comparison to the HRM:RANS:  $Q k-\epsilon$ , the HRM:DES: $k-\epsilon$ , LRM:RANS: $k-\omega$  SST, LRM:D-DES: $k-\omega$  SST and LRM:D-DES:S-A give differences of the important lee-rail moment of the basic wind of 6.0, 0.2, 4.1 and 4.1%, respectively. For the maximum wind the corresponding differences are 6.4, 1, 3.1 and 3.6%. Thus, all our DES essentially predicts the similar results, which is confidence-inspiring. In particular, the lift force is predicted somewhat consistently. Lift is typically challenging to render accurately for the current application, cf. Ref. [1], as it is very sensitive to the flow split underneath and above the vehicle. Notice that for the current vehicle and track bed (as opposed to the flat ground), the lift force is comparable to the side force and is therefore contributing much more to the overturning ( $C_{R-LR}$ ). The experimental wind tunnel results of the

flat ground scenario, cf. Ref. [1], are also included. It reveals that the flat ground situation reduces the important overturning load with as much as 35% and 28% for the two yaw angle cases. Notice the disproportionate reduction of the lift force. The augmentation of the loads caused by the ballast and rail track bed agrees well with the observations for the ICE 3 train, Ref. [16], and also by numerous studies at Bombardier Transportation of other rail vehicles.

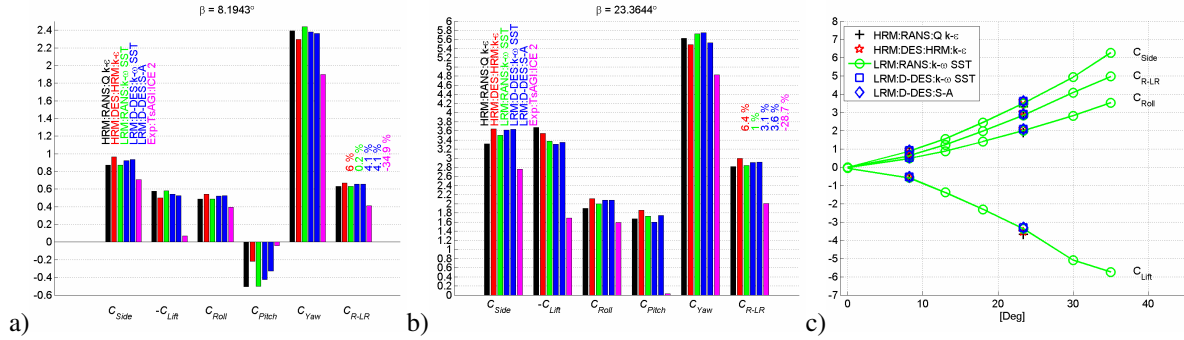


Figure 5: Aerodynamic loads. a) Basic wind of  $\beta = 8.1943^\circ$ . b) Maximum wind of  $\beta = 23.3644^\circ$ . c) All yaw angles.

## 8 UNSTEADY RESULTS

### Aerodynamic loads

$x' = 0$  defines the beginning of the augmentation of the aerodynamic loads, as the gust impinges the vehicle. If the gust is infinitely steep the full strength of the impact, in terms of the overturning moment, will occur after one vehicle length, i.e.  $x'/l_t = 1$  (apart from the time it takes for the flow to build up laterally, discussed below). It is instructive to exemplify this extreme situation. This is carried out with the LRM:RANS: $k-\omega$  SST data of the basic ( $\beta = 8.1943^\circ$ ) and maximum ( $\beta = 23.3644^\circ$ ) wind. The principal loads of the basic wind are continuously replaced by that of the maximum wind along the vehicle, illustrated in Fig. 6. Results are shown in Fig. 7a. The results of the aerodynamic drag, pitch and yaw moments show significant unsteady characteristics, which for leading cars in general are amplified due to the disproportionate loads about the front-end. The results emphasize that the potential overshoot of the yaw moment, for the current  $\beta$  range, is approximately 1.3. The peak occurs when the vehicle is immersed half way into the gust, i.e.  $x'_{peak}/l_t = 0.5$ .



Figure 6: Situation of infinitely steep gust.

The DES of the gusts of  $l_g/l_t = 1.3073$  and  $2.6146$  have longer  $x'_{peak}/l_t$ , as shown in Figs. 7b-f. As  $l_g/l_t$  increases  $x'_{peak}/l_t$  approaches unity and the overshooting will ebb away. At this point the transition event can be based on the steady results of Fig. 5c, where the loads would pass through the discrete yaw angles of our RANS database of  $8.1943^\circ$ ,  $13^\circ$ ,  $18^\circ$  and  $23.3644^\circ$ . Albeit the unsteady characteristics of the principal loads that is demonstrated here, the latter approach is practised in the TSI [2], further discussed in section 9.

The ratio of peak yaw moment of the two gusts obtained with HRM:DES: $k-\epsilon$  and HRM:RANS:Q  $k-\epsilon$  compared to the infinitely steep gust are 91% ( $1.17/1.28$ ) and 86% ( $1.10/1.28$ ). The corresponding data for the steeper gust calculated with LRM:D-DES: $k-\omega$  SST, LRM:D-DES:S-A and LRM:RANS: $k-\omega$  SST is 87%.



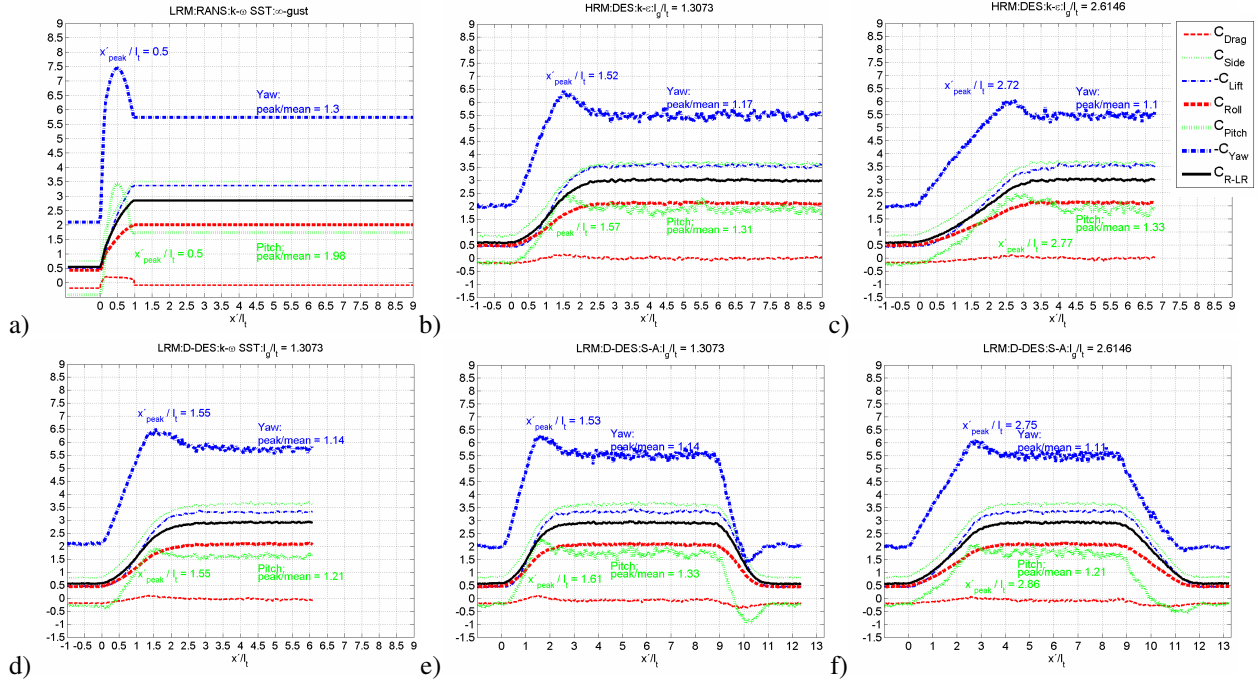


Figure 7: Loads as a function of distance that are normalized with  $U_R$  based on  $\beta = 23.3644^\circ$ . a) Infinitely steep gust based on LRM:RANS:k- $\omega$  SST. b) HRM:DES:k- $\epsilon$ :  $l_g/l_t = 1.3073$ . c) HRM:DES:k- $\epsilon$ :  $l_g/l_t = 2.6146$ . d) LRM:D-DES:k- $\omega$  SST:  $l_g/l_t = 1.3073$ . e) LRM:D-DES:S-A:  $l_g/l_t = 1.3073$ . f) LRM:D-DES:S-A:  $l_g/l_t = 1.3073$ .

### Load distribution around the car body

In Fig. 8 the car body is split into four parts, where the loads are evaluated using the unsteady recordings. It is shown that the largest side force is at the upper lee-ward (UL) and lower lee-ward (LL) parts. On the upper wind-ward (UW) part the side force is pointing towards the crosswind as a result of the accelerating flow that produces a strong suction pressure about the top corner of the roof, cf. Fig. 3.

As far the lee-rail moment is concerned the UL part contributes with the largest fraction. Here the lift and side forces contribute in the same sense, whereas on the UW and LL they counteract each other. Consequently, the lee-rail moment may be more forgiving to erroneous predictions in the flow field around the UW part as opposed to the UL part, despite the quite large loads.

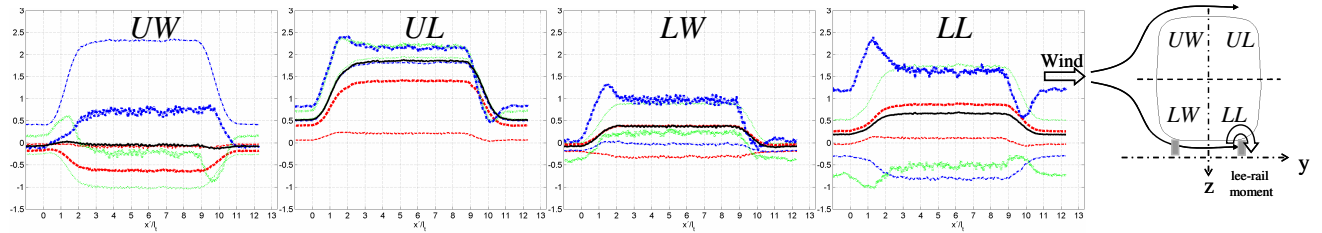


Figure 8: Loads of the car body split into four parts as a function of the distance  $x'$ . LRM:D-DES:S-A.  $l_g/l_t = 1.3073$ . Notation of loads is similar to Fig. 7.

## 9 QUASI TRANSIENT GUST MODELLING

A new and swift technique to model the effects of arbitrary gusts in a quasi unsteady fashion is proposed, referred to as Quasi Transient Gust Modelling (QTGM). It is an extension of the concept introduced in connection to Fig. 6. The justification of the approach is based around the previous discussions, where history effects of the unsteady loads may be neglected, the unsteady surface pressure throughout the gust and the loads of the basic and maximum winds compare well with RANS (see section 7).

The modelling divides the test vehicle into a sufficient number of longitudinal elements  $\Delta x$ , shown in Fig. 9. Here, 110 equidistant elements are used tentatively for the test vehicle, where each element represents less than 1% of the vehicle length. The modelling consists of a single assumption, namely: for each element steady data (e.g. from RANS) may be applied, where the choice of data at any given position along the vehicle and at any given time is based on the local crosswind conditions of  $\beta$ . Since steady data are typically recorded for a few  $\beta$  (see Fig. 5c), intermediate data are readily obtained by interpolating results for each  $\Delta x$  in question at each time step. Here, the procedure is demonstrated by using the LRM:RANS: $k-\omega$  SST database (see Table 1 and Fig. 5c). The unsteadiness of the results is introduced by advecting the gust profile  $U_w = U_w(x - U_t \times t)$  in time with  $\Delta t \sim \Delta x / U_t$  similar to that described in Fig. 6. Further, the principal integral loads are based on the sum of all elements  $\Delta x$ , where results of intermediate yaw angles are obtained by interpolating data of the RANS database for each  $\Delta t$ . Results of the effects of the passing gust is then obtained almost instantly by comparison to the DES that typically requires weeks of processing on a multi core main frame.

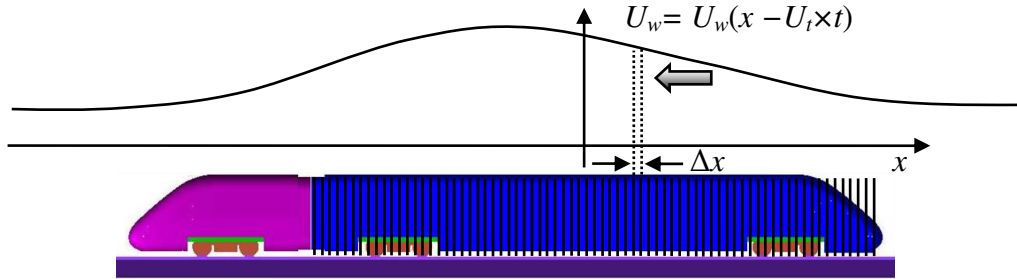


Figure 9: Quasi Transient Gust Modelling based on steady results.

### Linear gusts

Results of QTGM are first explored for the linear gusts, where  $l_g/l_t = 1.3073$  and  $2.6146$ , using data of LRM:RANS: $k-\omega$  SST. Results are shown in Fig. 10 and should be compared to those of Figs. 7b-f. QTGM gives a similar unsteadiness of the drag force, pitch and yaw moments as the DES. In particular, the ratios of peak to mean yaw moments are 1.18 (1.17; 1.14; 1.14) and 1.07 (1.1) for the respective gusts. The numbers in the brackets correspond to the DES of (HRM: $k-\varepsilon$ ; LRM: $k-\omega$  SST, LRM:S-A) and (HRM: $k-\varepsilon$ ) for the two gusts.

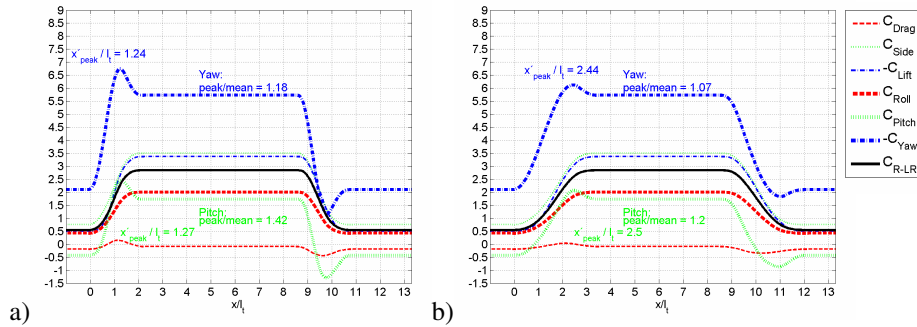


Figure 10: QTGM of the linear gusts of  $l_g/l_t =$  a) 1.3073 and b) 2.6146.

The corresponding values of QTGM of  $x'_{peak}/l_t$  are shorter than those of the DES. For the steeper gust,  $x'_{peak}/l_t$  for the yaw moments are (1.52–1.55, 1.24) which corresponds to the results of the (DES, QTGM). The longer gust exhibits the corresponding values (2.72–2.75, 2.44). Thus, the difference in peak location seem to have a systematic discrepancy of  $\Delta x'_{peak}/l_t \sim 0.3$ , which is 22 and 11% of the respective gusts ( $l_g/l_t$ ). Part of that difference is attributed the time it takes for the flow to establish across the vehicle in the lateral direction. This is not accounted for in the steady results, but should motivate a correction factor. There is also a small

uncertainty as to when the gust starts to affect the vehicle. Further, the onset of the advecting flow of the DES at the relatively large discrete boundary faces as opposed to a smoothly changing face, advection and diffusion tend to smooth the velocity profile before it impinges the vehicle. QTGM are not prone to such distortions. Figure 11 plots the local yaw angle of the flow, ( $\beta^* = \tan^{-1}(v/u)$ , where  $u$  and  $v$  are the lateral and longitudinal velocity components), across the whole domain at  $y = 0$ , at three different heights and at three instants where: a) Front of the gust reaches the nose of the vehicle ( $x'/l_t = 0$ ), b) front of the gust reaches the rear of the vehicle and c) rear of the gust reaches the end of the vehicle. From Figure 11 it can be discerned that the local yaw angle is larger than that of a linear profile, which is caused by the accelerating flow ( $v$ -component) that rises over the top of the vehicle model. More importantly, the onset and finish of the profile is well contained within the gust ( $l_g/l_t$ ). This justifies the comparison of QTGM with DES, prerequisite a proper correction in time is applied. The former method may then provide good qualitative assessments of the principal loads also for other gusts.

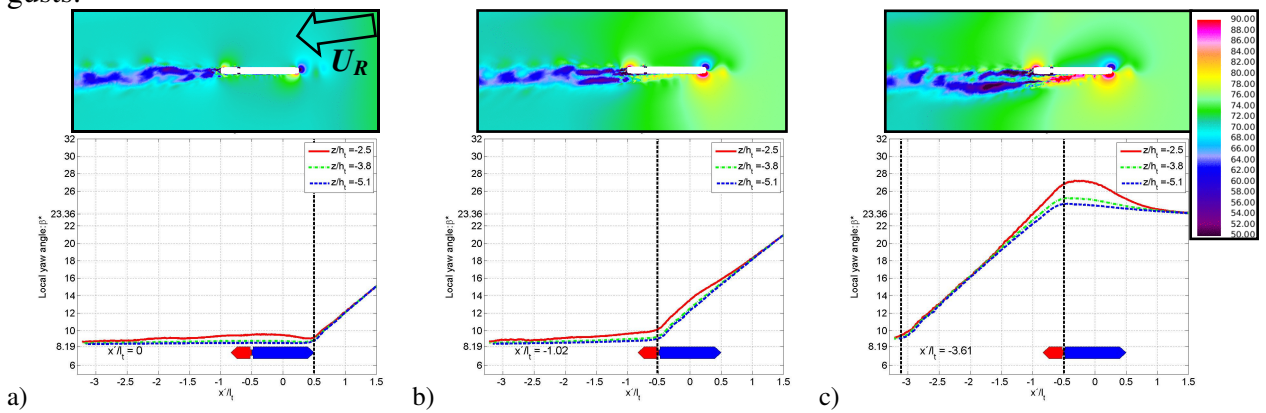


Figure 11: Local yaw angle of the flow at  $y = 0$  for the results of HRM:DES: $k-\epsilon$ . Colors represent the velocity magnitude of the flow field (at  $z/h_t = -0.5187$ ) where  $U_t = 69.4444$  m/s (250 km/h).

### Tunnel exit

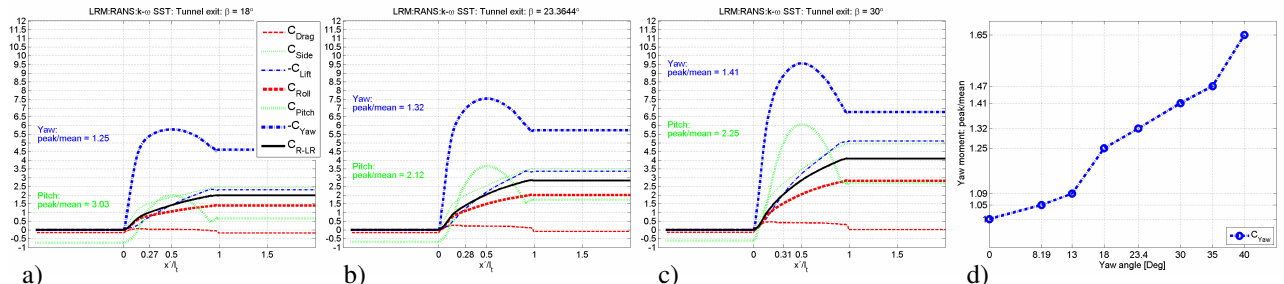


Figure 12: QTGM of tunnel exit. The second number on the  $x'$  axis signifies where 50% of the lee-rail overturning moment is achieved.

Exiting a tunnel into crosswind would conceivably give the fastest aerodynamic response, shown in Fig. 12. The basic loads are obtained at  $\beta = 0$ , which is valid in open air or approximately in a large enough tunnel. The disproportionate loads around the front-end of the vehicle gives a rather steep increase of the crucial side force and roll moments. 50% of the lee-rail overturning moment is obtained within  $x'/l_t \sim [0.18, 0.22, 0.27, 0.28, 0.31, 0.31, 0.35]$  for the yaw angles used in Fig. 12d. Thus, the smaller the yaw angle, the steeper the relative initial growth of the overturning loads. Further, Fig. 12d shows that the ratio of peak to mean of the yaw moment increases steadily with the yaw angle, where for the highest wind speed applied here, the ratio is 65% larger than the steady result of the maximum wind.

## TSI Gust

Finally, the effects of the gust prescribed in the European TSI [2] are evaluated with QTGM for the leading car of the ICE 2 train (without time correction). As mentioned earlier, the intention of the TSI methodology is to apply the gust with uniform crosswind speed along the vehicle at any given time. Albeit, here the gust is frozen and propagates relative to the vehicle according to Fig. 9. This gives a non-uniform crosswind distribution that may be perceived as the more correct situation. The train speed  $U_t$  is again 250 km/h and the maximum gust wind speed, perpendicular to the train side, is 30 m/s. These are the only dependent variables needed to describe the exponential rise and decay of the TSI gust, where all other data are provided by the standard. Fig. 13a shows the local yaw angle  $\beta^*$  of the gust profile, where its' length is comparable to the vehicle. Hence, the natural car body frequencies are likely excited, cf. Lippert [15]. Fig. 13b shows the QTGM assessment of the impact. Again, the disproportionate effect of the nose, discussed in connection to Fig. 12, gives a steeper rise of the important loads compared to the decay. In the current example, the peak to mean of  $C_{R-LR}$  is 1.64, where the ratio of maximum to mean crosswind speed is 1.6946 (prescribed in the TSI). The corresponding ratio for the yaw moment is as high as 1.78. Notice also that the decay of the propagating gust causes  $C_{Drag}$ ,  $C_{Yaw}$  and  $C_{Pitch}$  to momentarily fall below the steady values at the end of the descend. Such an effect is not captured with a uniformly changing profile, which may affect the vehicle stability further.

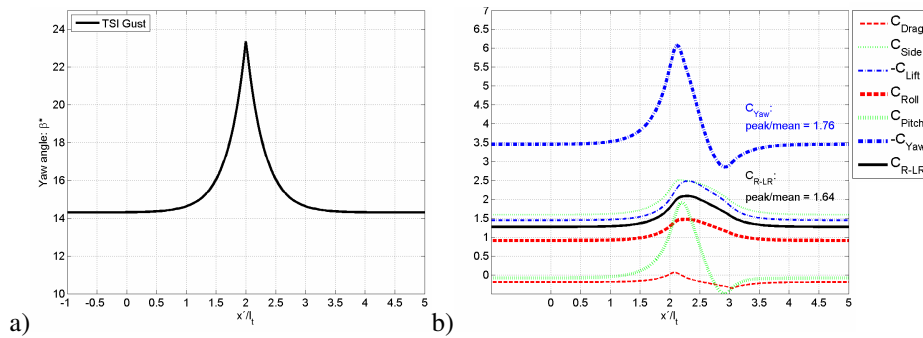


Figure 13: a) TSI Gust. b) QTGM of TSI gust.

## 10 CONCLUSIONS

Transient aerodynamic loads have been calculated on a typical wind tunnel model of a high speed train (leading car of ICE 2) running on a ballast and rail track bed. The unsteady flow calculations (DES) are confined to linearly changing crosswind speed, which is a simple starting point for such studies. Also the selected gusts have been chosen with respect to the natural car body frequencies, where the rise time of the gusts corresponds to 0.5 s and 1.0 s at the train speed of 250 km/h.

Two fine polyhedral meshes, (for hi- and low-Re wall modelling) were used for the RANS and DES, where results showed a satisfactory level of coherence.

During the event of the gust, the surface pressure about the car body did not reveal any noticeable history effects. Rather the transition from basic to maximum wind occurred smoothly, where instantaneous data of surface pressure agreed remarkably well with the intermediate RANS data. The unsteadiness in the loads is introduced by local flow changes along the vehicle, which caused a significant overshooting of particularly the yaw moment.

The current findings have motivated a new technique to swiftly model the evolution of aerodynamic loads of arbitrary gusts. The modelling is tentatively based on steady results (suggestively RANS, but steady results via DES is also possible) which would give a fair representation of the loads for the range of yaw angles caused by the gust. Admittedly, a length wise correction (stretching in time) of the loads is needed to compensate for the lateral

initiation of the flow, which needs further attention in future work. Future studies need to demonstrate the applicability for other vehicles and also address the situation of higher yaw angles.

The results are currently exploited in an ongoing study, at the VINNOVA Centre of Excellence for ECO<sup>2</sup> Vehicle Design at the Royal Institute of Technology (KTH) in Stockholm, to explore the rail vehicle implications of gusts strong enough to cause overturning.

## ACKNOWLEDGEMENT

This study is carried out as an integral part of the Vinnova Centre of Excellence for ECO<sup>2</sup> Vehicle Design at the Royal Institute of Technology (KTH) in Stockholm.

## REFERENCES

- [1] Diedrichs, B. 2008. Aerodynamic calculations of crosswind stability of a high-speed train using control volumes of arbitrary polyhedral shape. BBAA VI International Colloquium on: Bluff Bodies Aerodynamics & Applications. Milano, Italy, July, 20-24 2008
- [2] Directive 96/48/EC. 2006. Interoperability of the trans-European high speed rail system.
- [3] Krajnović, S. 2008. Numerical Simulation of the Flow Around an ICE2 Train Under the Influence of a Wind Gust. INTERNATIONAL CONFERENCE ON RAILWAY ENGINEERING 2008 (IET ICRE2008), Challenges for Railway Transportation in Information Age, 25-28 March, 2008, Hong Kong, China.
- [4] Ryan, A. and Dominy, R. G. 2000. Wake survey behind a passenger car subjected to a transient cross-wind gust. SAE 2000-01-0874.
- [5] Orellano, A. and Schober, M. 2006. Aerodynamic Performance of a Typical High-Speed Train. WSEAS TRANSACTIONS on FLUID MECHANICS, Issue 5, Volume 1, ISSN 1790-5087, <http://www.wseas.org>.
- [6] EN 14067-1. 2003. Railway Applications – Aerodynamics – Part 1: Symbols and units. European standard.
- [7] prEN 14067-6. 2007. Railway Applications – Aerodynamics – Part 6: Requirements and test procedures for cross wind assessment. European standard.
- [8] Shih, T-H., Zhu, J. and Lumley, J. L. 1993. A realizable Reynolds Stress Algebraic Equation Model. 9<sup>th</sup> Symposium on Turbulence Shear Flows. Kyoto, Japan, August 10-18, 1993.
- [9] Menter, F. R. 1993. Zonal two equation  $k-\omega$  turbulence models for aerodynamic flows. Proc, 24<sup>th</sup> Fluid Dynamics Conf., Orlando, Florida, USA, 6-9 July, Paper No. AIAA 93-2906.
- [10] Wilcox, DC. 1993. Turbulence Modeling for CFD. DWC Industries Inc., 5354 Palm Drive, La Canada, California 91011, USA.
- [11] Jones, W. and Launder, B. 1972. The prediction of laminarization with a two-equation model of turbulence. Int. J. Heat Mass Transfer. Vol. 15, pp. 301–314.
- [12] Rolén, C., Rung, T. and Wu, D. 2004. Computational modelling of cross-wind stability of high speed trains. European Congress on Computational Methods in Applied Sciences and Engineering. ECCOMAS. P. Neittaanmäki, T. Rossi, S. Korotov, E. Oñate, J. Périaux, and D. Knörzer (eds.) Jyväskylä, 24–28 July.
- [13] Spalart, P. R. and Allmaras, S. R. 1992. A one-equation turbulence model for aerodynamic flows. AIAA-92-0439.
- [14] Diedrichs, B., Berg, M., Stichel, S. and Krajnović, S. 2007. Vehicle dynamics of a high-speed passenger car due to aerodynamics inside tunnels. Proc. Instn Mech. Engrs, Part F: J. Rail and Rapid Transit, 221 (F4), 527–546.
- [15] Lippert, S. 1999. On side wind stability of trains. Master Thesis, Royal Institute of Technology (KTH) Stockholm, Sweden TRITA – FKT Report 1999:38, ISSN 1103-470X. ISRN KTH/FKT/EX--99/38—SE.
- [16] Schober, M., Weise, M., Orellano, A., Deeg, P. and Wetzel, W. 2008. WIND TUNNEL INVESTIGATION OF AN ICE 3 ENDCAR ON THREE STANDARD GROUND SCENARIOS. BBAA VI International Colloquium on Bluff Bodies Aerodynamics & Applications Milano, Italy, July, 20-24 2008.

## QUALITATIVE INVESTIGATION OF THE MAIN FLOW FEATURES OVER A TGV

Thomas Duriez<sup>\*†</sup>, Jean-Luc Aider<sup>\*</sup>, Elisa Masson<sup>†</sup> and Jose E. Wesfreid<sup>\*</sup>

<sup>\*</sup>Laboratoire Physique et Mécanique des Milieux Hétérogènes (PMMH)  
CNRS UMR 7636; ESPCI; Paris6; Paris7  
ESPCI, 10, rue Vauquelin, 75231 Paris cedex 05, France  
e-mail: [aider@pmmh.espci.fr](mailto:aider@pmmh.espci.fr)

<sup>†</sup>Unité Physique du Système Ferroviaire  
SNCF - Direction de l'Innovation et de la Recherche, 45 rue de Londres, 75379 Paris Cedex 08, France  
e-mail: [elisa.masson@sncf.fr](mailto:elisa.masson@sncf.fr),

**Keywords:** High-Speed Trains, Visualisations, PIV

**Abstract:** *In this paper, we present the results of a preliminary investigation of the flow features encountered over a TGV. As a matter of fact, it is the first step in a more detailed analysis which is necessary in the perspective of future flow control experiments. The experimental investigation has been carried out in a low-speed hydrodynamic channel with a small-scale model. The consequence is that the Reynolds number based on the length  $L$  of the model is relatively low ( $Re_L = 1.26 \cdot 10^5$ ) compared to the full-scale aerodynamic Reynolds number ( $Re_L = 10^9$ ) so that the results can only be used as qualitative tools to illustrate the main features encountered in the flow over a TGV. Particle Image Velocimetry (PIV) and Laser Induced Fluorescence (LIF) visualizations were carried out in most of the critical regions over a TGV: the front nose, the pantograph cavity, the spacings between the coaches and the rear part of the model.*

*Clearly some common features can be found with the flow over a road vehicle. For instance, both LIF and PIV show the strong vortex shedding, the large recirculation bubble and the large counter-rotating vortices created over the rear part of the model, very similar to a Ahmed body with a  $25^\circ$  rear slant. The flow over the flat panels of the coaches constituting the TVG is also more complex than expected because of the perturbations induced by the pantograph cavities and the deep cavity between the coaches. Finally, a synthesis is proposed pointing out the most critical areas in a perspective of flow control for drag reduction.*

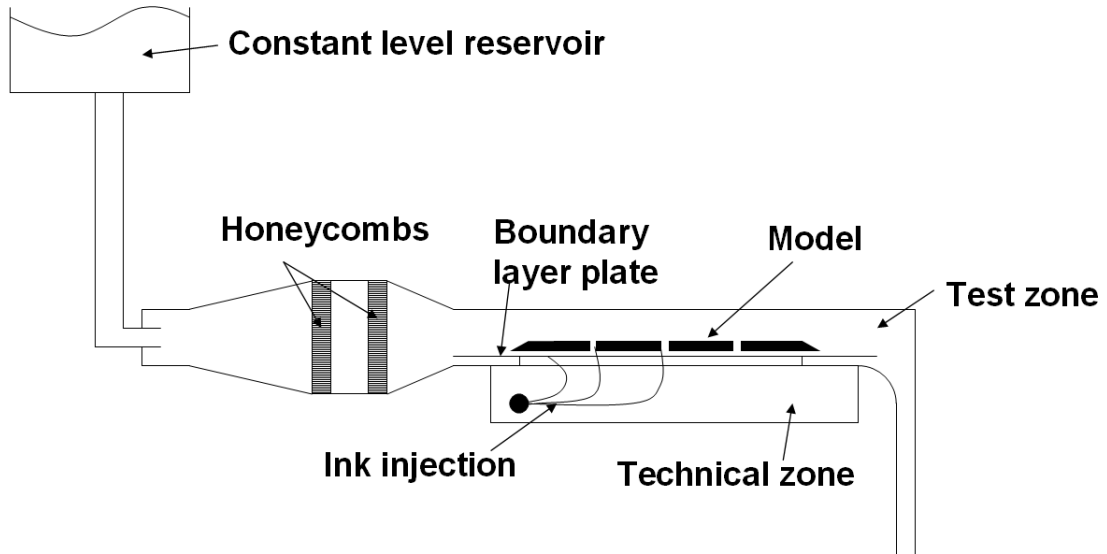


FIGURE 1: Scheme of the hydrodynamic tunnel with the model placed in the test section.

## 1 INTRODUCTION

The flow around a high speed train is a challenge to the fluid mechanics community. While the use of experimental techniques on an operating vehicle only gives partial information on the flow, both reduced-model and numerical based investigations are confronted with the problems of the high Reynolds and Mach numbers. A full length and fully detailed numerical simulation of the unsteady flow at a Reynolds number around  $10^8$  stays out of reach or at a prohibitive cost. The reduced model studies seems to have found a good compromise with a few coaches at 1 : 7 scale ratio in a wind tunnel at  $40m.s^{-1}$  [5]. Nevertheless the cost of the studies in a wind tunnel large enough to allow this kind of model with the ability to simulate the moving ground and the boundary layer is still heavy. In this study we present qualitative results obtained on a 1 : 127 small-scale model in a hydrodynamic channel. The Reynolds number reached based on the model length  $L$  is  $Re_L = 1.26 \cdot 10^5$ .

## 2 EXPERIMENTAL SET-UP

### 2.1 THE HYDRODYNAMIC TUNNEL

The experiments have been carried in the PMMH low-speed hydrodynamic tunnel. The flow inside the hydrodynamic tunnel used (Fig. 1) is gravity driven thanks to a reservoir whose water level is kept constant. The height between the reservoir and the point of return to ambient pressure is three meters. The tunnel can be used either in open flow for ink visualisation or closed flow for PIV measurements. A steady laminar incoming flow is obtained through the combinaison of a slow diverging section followed by two honeycombs and a short converging section. The test area is a rectangular section of  $150 \times 100mm^2$  over a length of  $800mm$ . Note that the channel is fully plexyglas which allows optical access from all side, especially in the axis of flow from downstream. Below the test zone is a submerged area used to install the dye injection lines other equipment. The speed of the flow in the configuration used is  $15cm.s^{-1}$ .

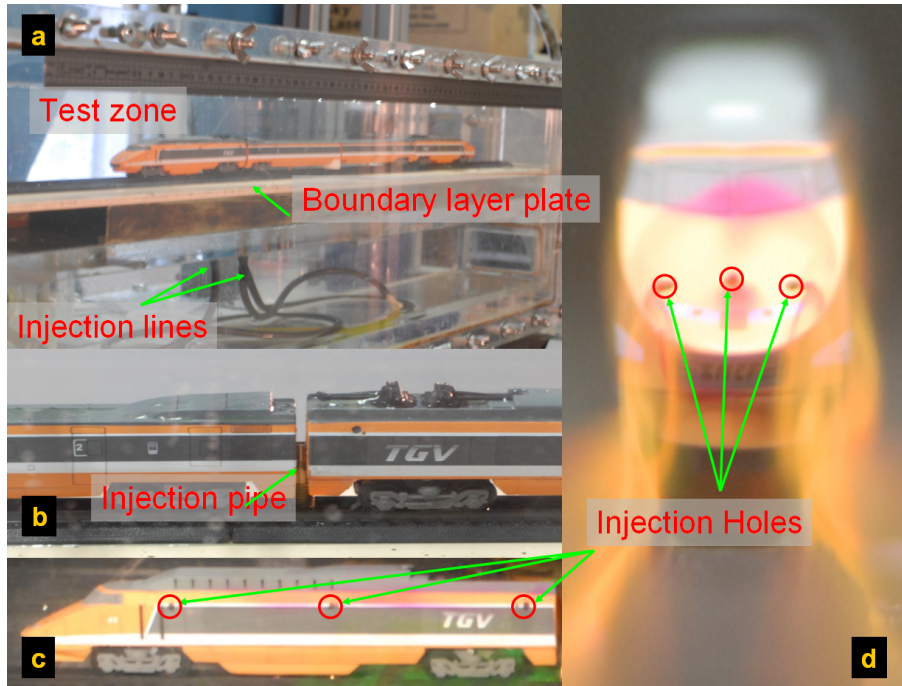


FIGURE 2: Photographs of the model. Injection lines come from the technical zone through the separation and boundary layer plates (a). Two injectors are placed in the intercoach spaces (b). Holes of  $0.5\text{mm}$  diameter are placed along the sides of the engine coach (c) and on the face (d)

## 2.2 THE SMALL-SCALE MODEL

The model is a toy in  $1 : 127$  scale made up of two nose or tail coaches and two middle coaches of a TGV-PSE (see Fig. 2). The model has a total length of  $L = 630\text{mm}$  for a height of  $h = 31\text{mm}$  and a width of  $l = 23\text{mm}$ . The intercoach space are  $2\text{mm}$  long. The model is positioned on rails which themselves are set on a plate for  $900\text{mm}$  long plate. This boundary layer plate is a flat plate at both ends bevelled and placed at a  $20\text{mm}$  to cut the previous boundary layer of the channel with a thickness around ten millimeters. Thus, a new boundary layer is at the leading edge of the boundary layer plate which results in a boundary layer thickness as low as possible. An engine coach was hollowed, equipped with a mouthpiece for the admission of dye and holes of  $0.5\text{mm}$  have been placed on the hull. Thus it is possible to fill the coach with dye have the near wall area of the train seeded. In addition the intercoach spaces are equipped with dye injectors. It is possible to reverse the model in order to have either the front or rear coach equipped with wall injection of dye. The Reynolds number for a velocity of  $U^\infty = 15\text{cm}\cdot\text{s}^{-1}$  and a total length of  $L = 630\text{mm}$  is  $1.26 \cdot 10^5$ . The pantographs could only be kept in lowered position.

## 2.3 LIF AND PIV EQUIPPEMENT

The visualisation have been obtained through Laser Induced Fluorescence. The fluorescent dyes used are the rhodamine-B or fluorescein. The volume visualisations are obtained either with ambient light or a UV punctual source. The plane visualisations are achieved with plane laser sheets issued from argon or YaG continuous lasers. Image acquisition is achieved with a numeric reflex camera or a numeric camcorder. Two PIV set-ups are available. The first one is made of a  $2 \times 15\text{mJ}$  pulsed laser and a double framed camera with a  $1600 \times 1200$  resolution



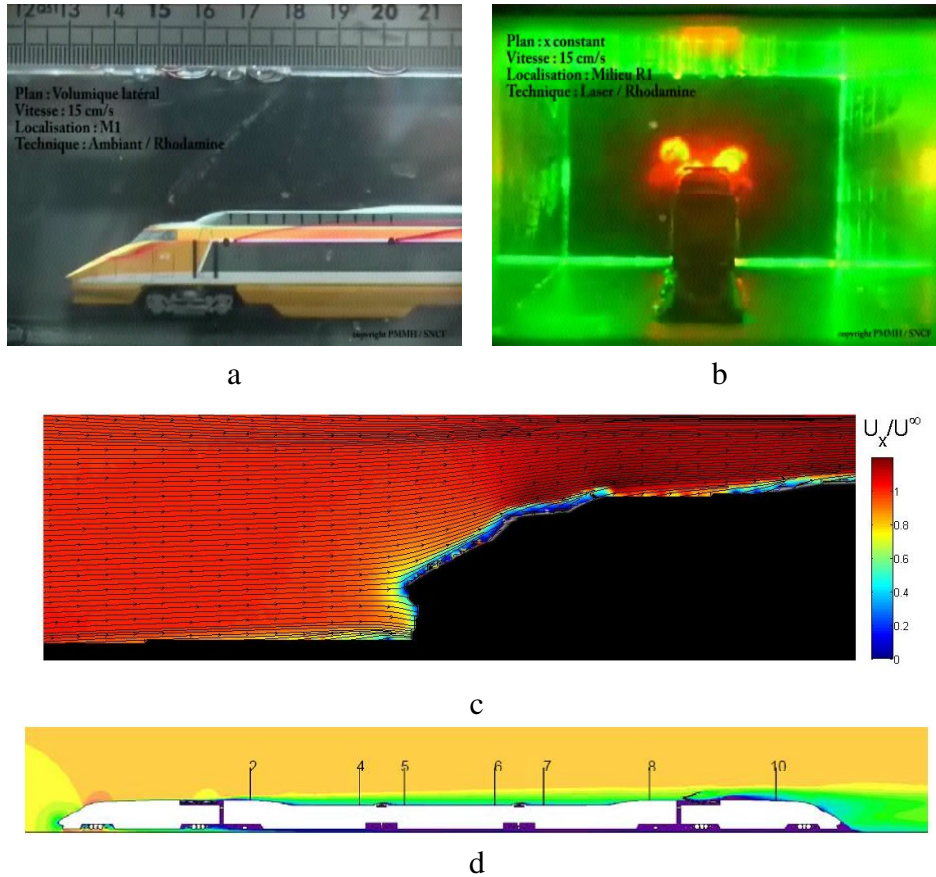


FIGURE 3: Photographs of the flow around the front coach of the model. The swirl of the dye lines shows the existence of pillar vortices on the nose coach edges (a). The cross section plane at the end of the first coach shows the existence of longitudinal vortices on the roof (b),(c) (d)

and can achieve a  $15Hz$  acquisition rate. The second one is a homemade time resolved PIV system made of a  $2W$  YAG continuous laser and a high-speed Phantom Camera which allows an acquisition rate up to  $1KHz$ . Both these configurations allow the measurement of the two velocities component in the plane defined by the laser sheet and the object focus plane of the camera.

### 3 FLOW VISUALISATIONS AND PIV

This configuration is quite far away from the canons of the reduced model high-speed train tests [5]. In particular there is a  $10^3$  factor on the Reynolds number, the flow can be considered as incompressible, the incoming boundary layer is hardly simulated and the wall is not moving. Despite these facts we managed to identify some of the known salient features of the flow around a high-speed train.

#### 3.1 Front coach and longitudinal structures

On the visualisations is observed that the dye wraps around the side edges of the front engine coach (Fig. 3a) and show vortical structures that raise to the roof. Downstream we find their traces in the laser cross section (Fig. 3b). As the position of the laser cross section is moved further downstream the flow has to deal with pantograph cavities and intercoach spaces and more streamwise vortical structures are present with a strong unsteady behaviour. The mean

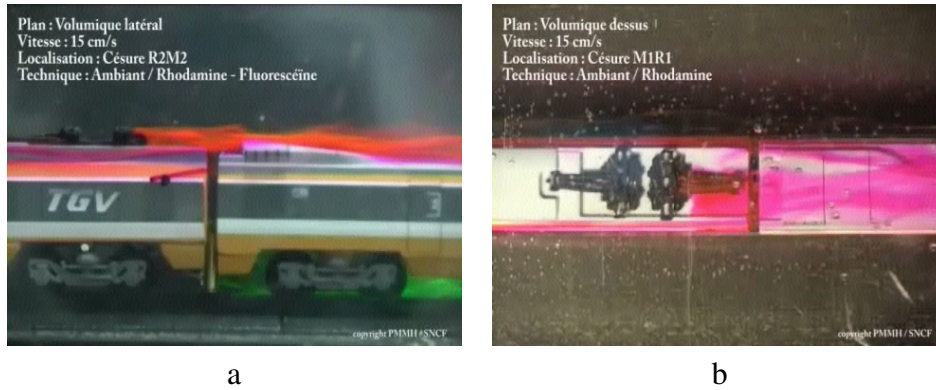


FIGURE 4: Photographs of the flow around the front pantograph cavity of the model. We can observe that the dye enters the intercoach spacing and fills the cavity where a recirculation occurs.

velocity field in the symmetry plane of the front coach (Fig. 3c) shows a deceleration of the flow at the nose and an acceleration at the beginning of the roof. Numerical simulations with RANS modelisation of the turbulence[4] shows the same qualitative behavior (Fig. 3d).

### 3.2 Pantograph cavity

As it was not possible to raise the pantograph on the model, the flow downstream the rear coach is very different from the case of a high-speed TGV. However, the visualisations showed in Fig. 4 allow to see the reverse flow that occurs in these cavities. We can also observe the separation experienced by the flow on the roof downstream the cavity.

### 3.3 Wake

At the exception of the recirculation bubble that is attached to the wall, all the structures expected in the wake of a high speed train are shown in Fig. 5. We can clearly observe the instable shear layer due to boundary layer separation at the roof end on Fig. 5a and c. Due to the absence of reproduction of the moving ground the recirculation bubble observed on the Fig. 5c is attached to the ground while it should be attached to the train. Fig.5b shows the existence of quasi-longitudinal vortices detached from the rear coach as has been observed in operating tests or numerical simulations[2]. We can notice that these kind of structures are the same that the one obtained in the wake of an Ahmed body[1]. The time resolved PIV measurement shown at Fig. 5d shows the alterne vortex shedding due to the separation of the boundary layers on the side of the end coach as has already been reported on smoke visualisations [3]. The vortex shedding exhibits a Strouhal number of 0.2 like in the case of the bidimensional cylinder.

## 4 CONCLUSIONS

While being far away from the ideal conditions to perform accurate measurements on high speed trains we show that the flow around a small-scale model with a moderate Reynolds number has already experienced enough transitions to have the essential features of the flow around a high-speed train. At the exception of the near wall flow we reproduce the qualitative behavior of the flow. While it is impossible to obtain quantitative results in agreement with measures on operating material it is predictable that a study driven on this kind of model should give the correct sensibility of the real flow. The methodology possesses the advantages of being much cheaper than a 1 : 7, full-scale experiment and numerical simulations depending on the accu-

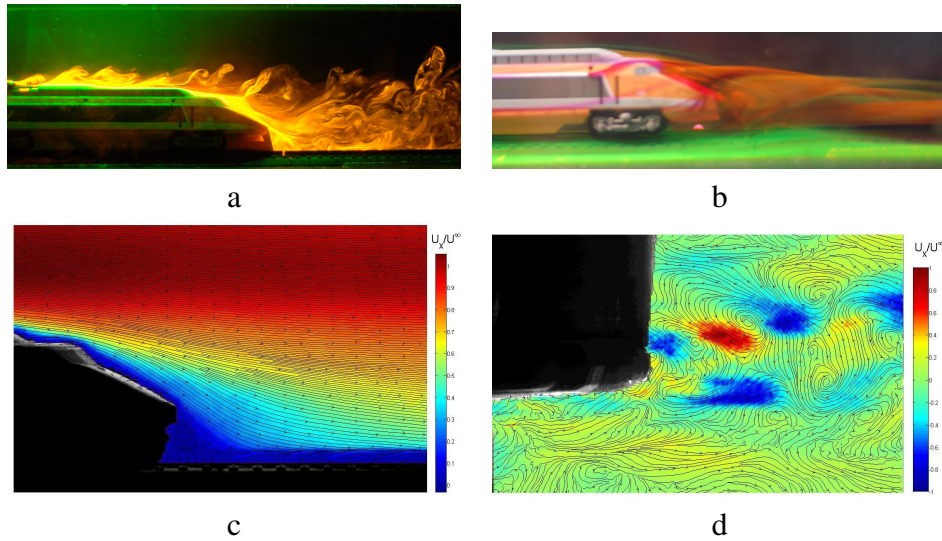


FIGURE 5: Lif visualisation in the symmetry plane of the rear coach (a). Volume visualisation of the wake (b). PIV measurement of the mean velocity modulus in the symmetry plane of the wake (c). Time resolved PIV obtained velocity amplitude cartography in a plane parallel to the ground at the altitude of the nose with the mean flow subtracted (d).

racy. Moreover it is well adapted to parametric studies and full flow investigation in a reduced time, actually the results presented have been obtained in two days. In the scope of flow control these preliminary results bring the confirmation that the flow behavior and sensibility can be qualitatively predicted from this kind of methodology. The parametric testing of different flow control strategy can be greatly helped and fastened by reducing the number of strategies to test before wind tunnel, numerical or full scale tests, leading to more solution efficiently tested at a reduced cost.

## RÉFÉRENCES

- [1] S. R. Ahmed. Influence of base slant on the wake structure and drag of road vehicles. *J. Fluids Eng.*, **105** :429–434, 1983.
- [2] Adrian Gaylard. A comparison of a conventionnal rans and a lattice gas dynamics simulation - A case study in high speed rail aerodynamics. In *Proc. IMech Symposium*, 1998.
- [3] Y. Kohama, T. Koshikawa, and Okude. Wake characteristics of a high speed train in relation to coach oscillations. In *Proc. of Vehicle aerodynamics*, The Royal Aeronautical society, Loughborough Univ. Of Tech., UK, 1994.
- [4] N. Paradot. *Étude numérique et expérimentale de la résistance à l'avancement d'un train à grande vitesse*. PhD thesis, Université de Poitiers, 2001.
- [5] J. A. Schetz. Aerodynamics of high-speed trains. *Annu. Rev. Fluid Mech.*, **33** :371–414, 2001.

## INVESTIGATION OF AERODYNAMIC CORRECTION METHODS APPLIED TO A SLOTTED WALL WIND TUNNEL.

Matthias P. Eng\*, Tim E. Walker<sup>†</sup>

\*TU-Berlin/Volvo Car Corporation  
Dept. 91760/PVT3, SE-405 31 Göteborg, Sweden  
e-mail: [eng.matthias@googlemail.com](mailto:eng.matthias@googlemail.com), [meng4@volvocars.com](mailto:meng4@volvocars.com)

<sup>†</sup>Volvo Car Corporation  
Dept. 9176/PVT3, SE-405 31 Göteborg, Sweden  
e-mails: [twalke18@volvocars.com](mailto:twalke18@volvocars.com)

**Keywords:** Correction method, Slotted wall wind tunnel, Horizontal buoyancy, Empty test section gradient.

**Abstract.** *The principle development tool employed by automotive aerodynamicists is the full-scale wind tunnel. At the Volvo Car Corporation, the full-scale wind tunnel (PVT) is of the slotted wall type, and has recently been upgraded with a new five belt moving ground simulation system. However, the measured drag forces in the Volvo wind tunnel have always been, and remain, significantly above the average of other European wind tunnels, and have not been corrected. The objective of this project was to analyze how different correction methods for drag and lift force measurements can be applied in PVT and how they can be optimized. Therefore different aerodynamic effects due to the restricted boundaries in a wind tunnel had to be observed.*

*Two effects were in the main focus. The solid and wake blockage, which causes a dynamic pressure difference, and the horizontal buoyancy, which directly imposes a force onto the model. While the model affected change in dynamic pressure already is quite well explored, the horizontal buoyancy needed further investigation. To be able to separate between wind tunnel induced and model induced buoyancy measurements a detailed analysis of the pressure distribution in the empty test section had to be carried out in PVT. In this context the influence of how the boundary layer suction affects the pressure distribution was also studied.*

*As the basis for all calculations a combination of two data sets were used. One part was the EADE correlation study from 1999, the other part was a comparison of different competitor car tests carried out in PVT and other wind tunnels since the upgrade in 2006. These cars represented a large variance of vehicle shapes and sizes. The resulting correction method shows that a good correlation with other wind tunnels can be achieved using simple vehicle parameters.*

## 1 INTRODUCTION

The Volvo full scale wind tunnel (known as PVT) was opened in 1986 and has a slotted wall test section. In order to improve the airflow simulation around and underneath the car, as well as to include the effect of rotating wheels a 5-belt ground simulation system was installed in 2007.

The presence of boundaries at the test section, whether in the form of solid walls, porous walls, or a free jet shear layer, can cause different experimental results as if the boundaries of the moving fluid would be infinitely far away, modeling real world conditions. Interferences between collector and nozzle or airflow and walls can produce a pressure gradient with which the model will interact during the measurement. A correction factor is therefore required for the measured values to more closely mirror reality. It is still necessary to know, that even the best correction only can produce good values when the tunnel already produces a good flow simulation. At the Volvo wind tunnel despite the large test section and the slotted walls higher drag values were measured than in competitor wind tunnels. With the upgrade of the ground simulation system the circumstance of high drag values remained.

In this context the aerodynamic department of the Volvo Car Corporation decided to introduce a correction to their full scale wind tunnel and it is the task of this project to show different correction methods, apply a correction to measured values and compare and evaluate different measured and corrected values. When the tunnel was originally built, the methods for obtaining a correction method for slotted walls was not fully available or understood.

## 2 FUNDAMENTALS

Since the first usage of wind tunnels for engineering development the problem of a constrained air flow is known. Considerable research has been undertaken to better model the wind tunnel effects and to obtain better techniques to improve the measurement and comparability between tunnels.

### 2.1 The Volvo full scale automotive wind tunnel - PVT

The Volvo wind tunnel consists of a slotted wall design. In this construction the test section boundaries are made by walls with slots in flow direction, behind those slots is a plenum, which can be freely ventilated by the airflow through the slots. The plenum is closed against the environment, so that the mass flow through the tunnel always remains the same. The empty tunnel behaves like a closed wall tunnel, because no air will flow through the slots. When there is a large model in the wind tunnel, the airflow has the possibility to escape from the test section through the slots and re-enter behind the model again, so the test section is prevented from large blockage. But now it is known that the flow in slotted wall test sections is much more complicated than previously assumed. The interaction between plenum and test section is highly dependent on the slot opening ratio and is still not fully understood. Even when the flow can ventilate through the slots, the blockage in slotted wall wind tunnel is not negligible.

The wind tunnel at the Volvo Car Corporation was designed to test full scale passenger cars and half scale trucks in 1986 for aerodynamic and thermodynamic purposes; therefore in addition to the turn table a dynamometer was also installed; located downstream in the test section. The slotted test section walls have an open area ratio of 30%; each wall and the ceiling have longitudinal slats. The test section has a height of 4.1m, a width of 6.6m and has in total a length of 15m, with a cross sectional area of 27m<sup>2</sup>. The test section turn table has a ra-

diameter of 3.3m. The main fan has a power of 5MW and can generate wind speeds of up to 250km/h.

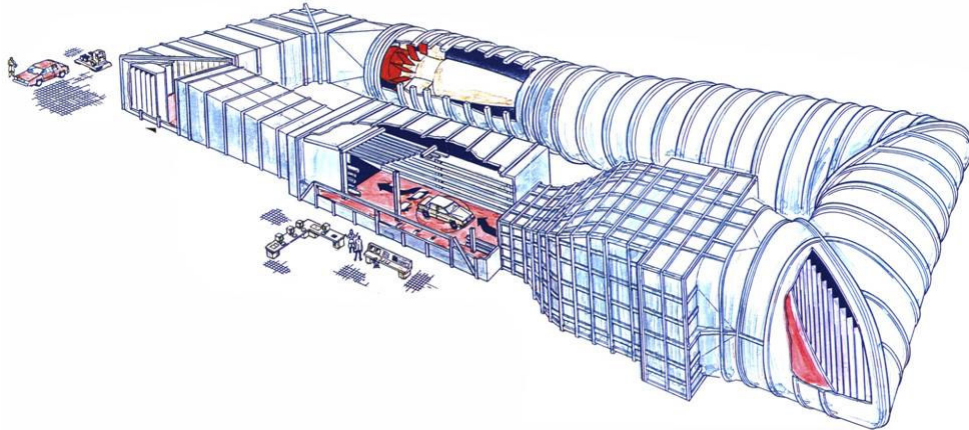


Figure 1: Volvo wind tunnel PVT.

In order to guarantee an adequate flow simulation for road vehicles the boundary layer needs to be minimized. The Volvo wind tunnel achieves this through a combination of different boundary layer treatment systems. The first step is a scoop directly after the nozzle, which eliminates the boundary layer. In front of and partly around the turn table a distributed suction system is installed into the test section floor. A second distributed suction system is installed on the turn table in the front part of the model. In conjunction to the improved suction system, a road simulation system was installed into the wind tunnel during recent upgrades. The road simulation is a 5-Belt system and consists of a 1m wide and 5.3m long centre belt and four small belts for each wheel (Wheel drive units – WDU).

## 2.2 Constraint test section flow

In contrast to the streamline shapes, automotive bodies are characterized by a small slenderness ratio, a large separation region at the bluff rear end and a high drag value resulting in a large wake. Bluff bodies can be followed by large separation bubbles and with returning flow and a significant larger wake.

A car is not 100% a bluff body; for modern cars, the flow stays attached over major parts of the model surface and usually only separates far behind at the trailing edge of the car. But even if the size of the separation bubble is significantly smaller than the model volume, the flow displacement and the resulting blockage by the near and the far wake of a car in a constraint flow is not negligible. Typical car models are described as quasi-streamlined bodies with the flow separation behind the maximum cross sectional area.

The purpose of wind tunnels is to simulate an air flow. The air flow has to be very stable, constant and repeatable. The wind tunnel flow should also imitate the flow conditions obtained in reality. For closed wall test sections it has been known for some time that the flow displacement causes blockage in the test section. The air flow goes around the model, but still has to stay in between the test section walls. Flows in real world conditions have the capacity to travel around the object with no limitation placed on its expansion; this is not the case for the wind tunnel. This blockage effect becomes greater as the model to test section ratio be-

comes larger. It needs to be noted that the solid body blockage is not the only influence on the measured drag; numerous literatures (e.g. Ref. [1], Ref. [4]) highlight the effects of various factors such as jet expansion, nozzle blockage, collector blockage, the wake blockage and gradient effects. Some of them are investigated for open-jet wind tunnels Ref. [1], and others are typical closed wall phenomena.

There is currently no widely accepted correction method for slotted wall wind tunnels and it is still discussed as something between a closed and an open-jet wind tunnel. It is currently not possible to fully describe the flow through the slots with the objective of a tunnel correction.

### 2.3 Correction theory

The classical correction based on potential flow theory using mirror images to represent wind tunnel boundaries was first derived by LOCK. Further contributions were published for example by GLAUERT Ref. [3] and many others. The need for boundary corrections arises because the flow over the model in a stream of finite extent is different from the flow over the same model in a stream of infinite extent. The fundamental cause that blockage occurs is often said to be a simple change in the free stream velocity,

$$U_{corr} = U_{\infty} + \Delta u \quad (1)$$

Where  $U_{\infty}$  is the velocity in the empty tunnel,  $U_{corr}$  is the velocity corrected for blockage and  $\Delta u$  is the change in axial velocity due to blockage. The total effect acting on the model is a sum of different interferences, which can be expressed by different perturbation velocities  $\varepsilon$ .

$$\sum \varepsilon = \frac{\Delta u}{U_{\infty}} \quad (2)$$

$$U_{corr} = U_{\infty} (1 + \sum \varepsilon) \quad (3)$$

Eq. (3) given in form for the dynamic pressure:

$$\frac{q_{corr}}{q} = (1 + \sum \varepsilon)^2 \quad (4)$$

The correction of the dynamic pressure is only one part of the complete correction formula. The other factors which influence the measured values are directly on the model acting forces, such as pressure gradients. These so called horizontal buoyancy forces have to be treated differently and are introduced into the correction procedure before any dynamic pressure corrections are applied Ref. [1]. The entire correction formula can be written as

$$C_{Dcorr} = \frac{(C_{Dmeas} + \Delta C_{DHB})}{q_{corr}/q} \quad (5)$$

This, from MERCKER suggested, correction theory is be the starting point for the development and application of a correction formula for the Volvo wind tunnel.

### 3 TUNNEL INTERFERENCE EFFECTS

Mercker further suggests a theoretical concept of how to correct slotted wall test sections without the need of an exact knowledge of the flow through the slots.

**Conventional thinking:** A slotted wall wind tunnel has a hybrid test section behaving partly as a closed wall wind tunnel (confined flow) and partly as an open-jet (expanded flow). Slot opening tunes the results to those measured on the road (transition from confined to expanded flow).

**Different way of thinking:** The slotted wall wind tunnel behaves like a closed wall wind tunnel. But when the slots are opened a positive pressure gradient is generated in the test section, which pushes the model forward and decreases drag (example: ETB tested in ETW).

Quotation by MERCKER.

According to this theory, the correction for the dynamic pressure is the same as the correction for closed wall test sections Ref. [4] and the horizontal buoyancy term is described by a combination of empty tunnel gradient effect and model induced buoyancy force.

$$\frac{q_{corr}}{q} = (1 + \varepsilon_s + \varepsilon_w)^2 \quad (6)$$

$$\Delta C_{DHB} = \Delta C_{DHB \text{ empty tunnel}} + \Delta C_{DHB \text{ model}} \quad (7)$$

#### 3.1 $\varepsilon_s$ – solid body displacement

The solid body blockage effect describes the change in flow velocity around the car due to the blockage in the test section. While airflow in reality has the possibility to expand, the flow is constrained by the tunnel walls and causes a higher dynamic pressure than in an unconstrained flow; this causes higher forces on the car.

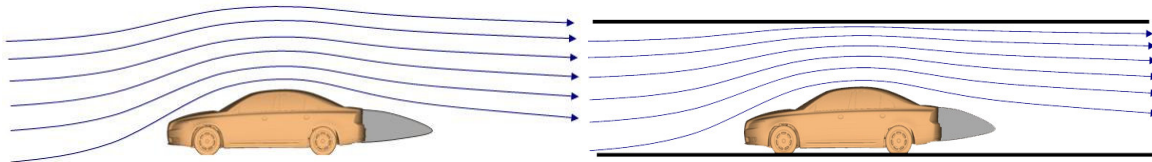


Figure 2: Airflow around a car in free stream and in closed wall test section

The correction for this effect is given in Ref. [2] and was derived with the help of the potential flow theory.

$$\varepsilon_s = \tau \sqrt{\frac{V}{L}} \left( \frac{A}{C} \right)^{3/2} \quad (8)$$

The tunnel shape factor  $\tau$  is explained by THOMPSON.

$$\tau_{closed} = 0.406 \cdot \left( \frac{B}{H} + \frac{H}{B} \right) \quad (9)$$

$$\underline{\underline{\tau = 0.8315}}$$



### 3.2 $\varepsilon_w$ – effect of wake blockage

The other interference effect in closed and slotted wall test sections is the wake blockage. The presence of a model even when it is a streamlined body causes a wake in the far flow field. The wake is a region of smaller velocity behind the model due to shear flow. In order to keep the volume flux constant, the flow velocity around the wake is faster than without model. This is similar to the blockage effect and causes higher drag forces.

The wake theory is quite complex so most correction formulas are based on empirical data. The MERCKER developed wake correction term seems to be quite simple, and uses a personally developed empirical wake blockage constant  $\eta = 0.41$ .

$$\varepsilon_w = \frac{A}{C} \cdot \left( \frac{C_{Dmeas}}{4} + \eta \right) \quad (10)$$

With the use of these perturbation velocities it is possible to correct the wind tunnel for its changed dynamic pressure. The so called Q-correction is only dependent on simple geometry data of the tunnel and the model to test.

## 4 HORIZONTAL BUOYANCY

The horizontal buoyancy is an especially important factor in determining the correction formula for the slotted wall wind tunnel. One part of the buoyancy effect is the model independent tunnel induced horizontal buoyancy, which is caused by the empty test section pressure gradient. The other part is according to MERCKERS assumption Eq. (6) the so called model induced horizontal buoyancy, which is caused by an interference between the model and the tunnel slots.

### 4.1 Tunnel induced horizontal buoyancy

The tunnel induced horizontal buoyancy is caused by the pressure gradient in the empty test section. In order to determine this, on the model acting force, the pressure distribution in the test section has to be measured. It is needed to get  $C_p$  distribution in the centerline of the test section in the height of the stagnation streamline on most cars of approximately  $z=600\text{mm}$ . The values for the pressure distribution of the wind tunnel before the upgrade are known and can't be repeated. The pressure distribution in the actual, post upgrade wind tunnel were also measured; however, further analysis raised doubts regarding the reliability of these values. The reason for this is, that the measurements were performed with the traverse, which causes an own blockage in the wind tunnel and influences the measurements. So the tests were repeated with a new probe holder.

The measurements are performed under two different ground simulation settings and for three different speeds. For the standard case the complete ground simulation was turned on; this included the boundary layer suction, the moving ground, the wheel drive units, the tangential blowing and the scoop. The second configuration was made with the same settings as before but with only the boundary layer suction devices turned off. The probe was mounted manually into every measurement position which is in the centerline ( $y=0\text{mm}$ ) of the empty test section and went from the scoop at  $-5500\text{mm}$  to the collector at  $9500\text{mm}$  (The tunnel coordinate system was centered on the turn table.). In steps of  $100\text{mm}$  to  $500\text{mm}$  the probe was

moved through the test section measurements were taken in every positions with wind speeds of at 80km/h, 140km/h and 200km/h.

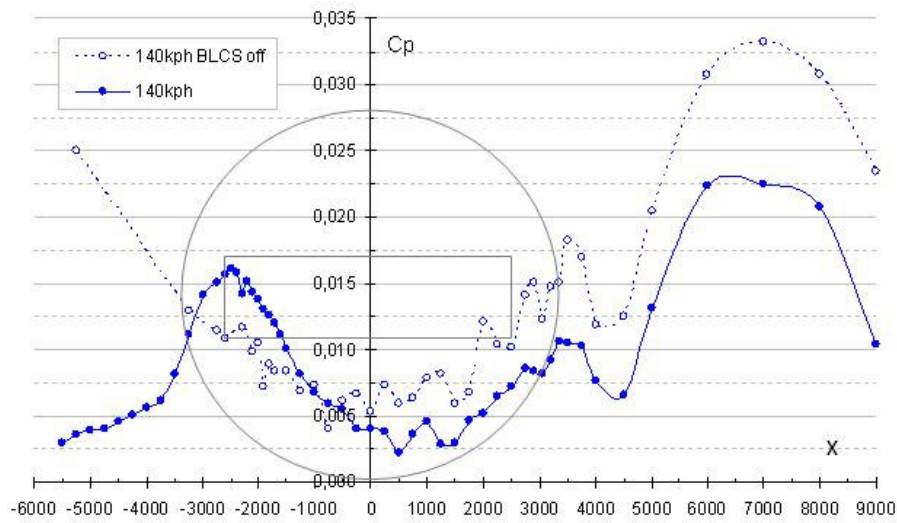


Figure 3:  $C_p$  distribution in the test section with and without boundary layer suction.

The tunnel induced buoyancy force is caused by a pressure difference between the front of the car and the rear. Because the tunnel pressure gradient is superimposed onto the car, the car is noticing a horizontal force which does not have any connection to the real drag on the car. To determine this force it is needed to determine the pressure at the position of the front bumper of the car and at the position of the wake closure point. The difference in  $C_p$  directly describes the caused difference in  $C_D$ . To approximate the wake closure point, MERCKER suggests a simple linear formula which describes the wake length dependent on the model slenderness.

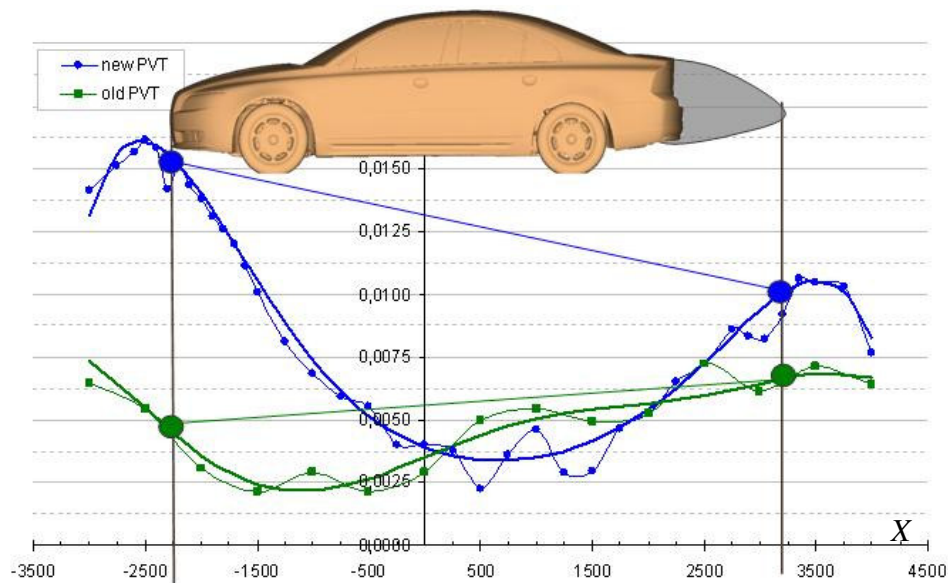


Figure 4:  $C_p$  distribution on the turn table of the old and new PVT.

Figure 3 shows the  $C_p$  distribution in the tunnel before and after its upgrade. Additionally, a typical car is positioned in the chart and the  $C_p$  at the front bumper and the wake closure point are marked. The tunnel buoyancy effect can be calculated by just taking the differences by using a polynomial trendline.

$$\Delta C_{DHB \text{ empty tunnel}} = C_{p_{\text{wake closure}}} - C_{p_{\text{front bumper}}} \quad (11)$$

#### 4.2 Model induced horizontal buoyancy

The last part of the correction method to be explained is the model induced horizontal buoyancy. Because there does not exist an analytical way to determine the model induced buoyancy MERCKER suggested to use reverse engineering. The idea is that for a model where the correct drag value is known, it is possible with Eq.(6) to calculate the horizontal buoyancy.

$$\Delta C_{DHB \text{ model}} = C_{D_{\text{corr}}} \cdot \frac{q_{\text{corr}}}{q} - C_{D_{\text{meas}}} - \Delta C_{DHB \text{ empty tunnel}} \quad (12)$$

If this would be done for a certain number of cars it should be possible to find the relationship between the model geometry and the horizontal buoyancy. Mercker suggested to use the EADE'99 data with his corrected values for the open-jet wind tunnels Ref.[8]. Because of problems with this test data and because the wind tunnel was not yet upgraded 1999 it was tried during this project to use another dataset. Test data from 15 cars of different manufacturers tested in the Volvo wind tunnel as well as in other tunnels or even in coast down tests are the background for further calculations.

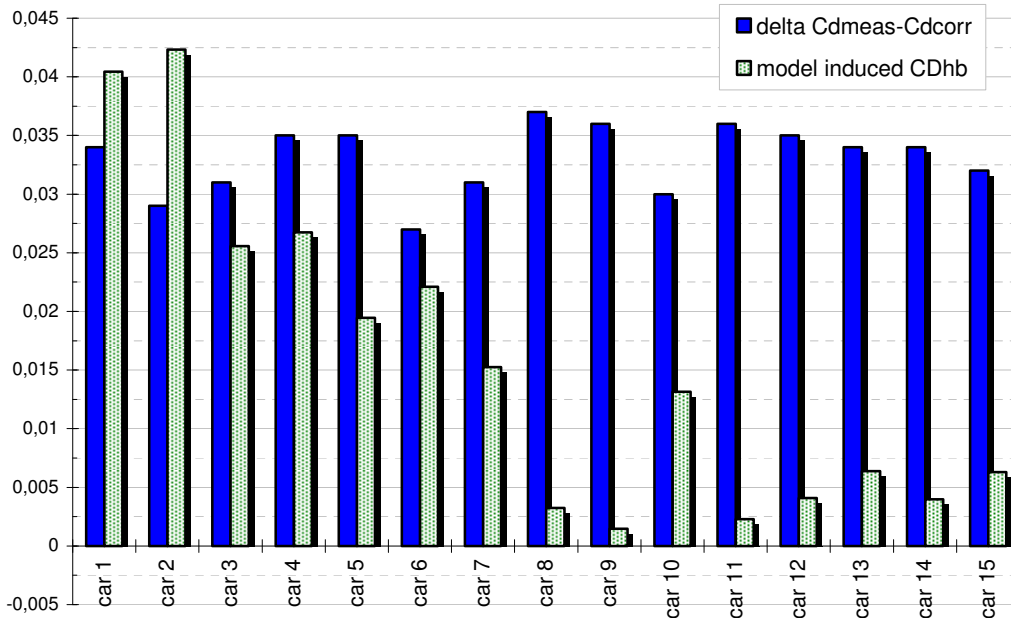


Figure 5: Calculated model induced horizontal buoyancy and delta value of 15 car dataset.

In Fig.6 the calculated delta between measured and correct value and the model induced buoyancy for the 15 cars are given. The models are from a large variance in shape, size and

drag, and are sorted by frontal area so that car1 is the largest and car 15 the smallest car in the dataset. The chart does not show any relationship between car size and difference between correct and measured drag, while the model induced horizontal buoyancy shows the tendency to become smaller, the smaller the model is. To describe this relationship sufficiently, an adequate factor had to be found. MERCKER suggests that the model induced horizontal buoyancy is dependent on many parameters and that a non dimensional factor has to be developed from them.

- $V$  – model volume
- $A$  – model frontal area
- $L$  – model length
- $C$  – tunnel cross section
- $m$  – model shape
- $n$  – tunnel shape

Table 1: Parameter of model and tunnel geometry.

Starting from this, a factor has to be developed which describes the bulkiness of the model. Because the tunnel remains the same for every test, these parameters can be ignored and because the tunnel cross section would be in the denominator while the tunnel shape factor (i.e. the open area ratio) is non dimensional, the resulting factor has the dimension of an area.

$$S_{GB} = \frac{A}{L} \cdot \sqrt{\frac{V}{\sqrt{A}}} (C_{D,meas})^3 \quad (13)$$

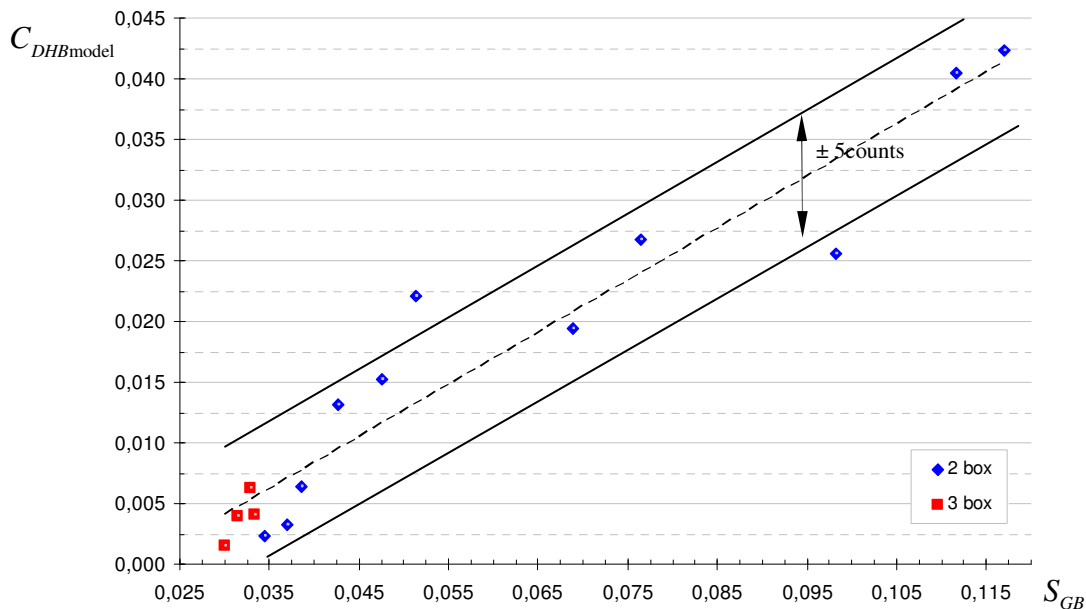


Figure 6: General blockage area  $S_{GB}$  vs. model induced horizontal buoyancy.

The so called general blockage area  $S_{GB}$  plotted vs. the model induced horizontal buoyancy shows a good linear relationship. With this equation it is possible to forecast the horizontal buoyancy for every other model in the Volvo wind tunnel. This is the last step needed in the application of a correction for the Volvo wind tunnel.

## 5 APPLICATION OF THE CORRECTION METHOD

To evaluate the correction method, reliable data are needed. Ideally the correction method should be validated using new data with different vehicles measured in different tunnels. This data is however not yet available. Therefore it is only possible to show how the correction method affects the 1999 EADE data. This is shown in Fig. (7). Since the tunnel dimensions after the upgrade are identical to those of the original tunnel the only value which makes the difference is the tunnel induced buoyancy. To correct the drag values from the old PVT, the same correction formula is used. To determine the tunnel induced buoyancy the pressure distribution before the upgrade Fig.(3) had to be utilized.

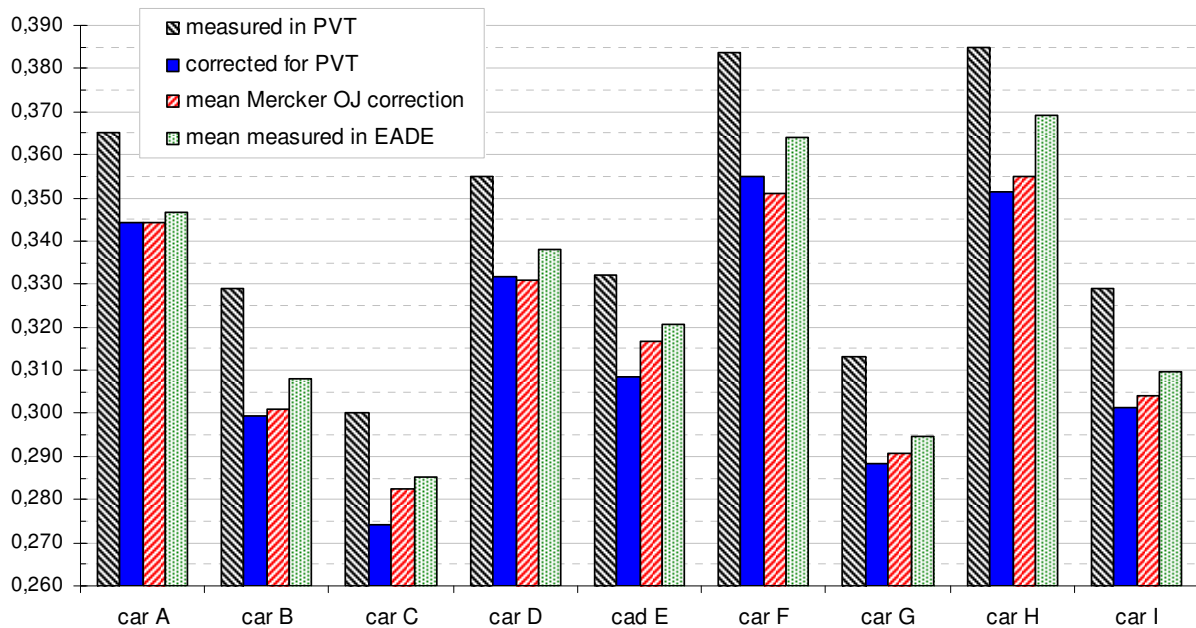


Figure 7: Application of the PVT correction on EADE'99 data.

In Fig.(8) are the measures values from PVT and the values after the new correction plotted. To evaluate the correction, the mean of all measured values from the EADE'99 tunnels are plotted, as well as the average of the by MERCKER corrected open-jet (OJ) tunnel values Ref. [8].

## 6 CONCLUSION

The application of the correction method to the EADE'99 data Fig.(8) showed that the corrected drag values agree very well with the values the from MERCKER corrected open-jet data. The corrected values from the Volvo wind tunnel are on average 2 counts lower than the corrected open-jet values. The good accordance of the corrected drag values with average corrected and the mean measured values shows that the correction method is working reliably and will be the basis for the correction method used in the Volvo wind tunnel.

## TABEL OF ABBREVIATIONS

$PVT$	-full scale wind tunnel of the Volvo car corporation
$EADE$	-European Aerodynamic Data Exchange
$WDU$	-Wheel drive units (part of the road simulation system)
$U_{\infty}$	-Velocity in the empty tunnel
$U_{corr}$	-Velocity corrected for blockage
$\Delta u$	-change in axial velocity due to blockage
$\varepsilon$	-perturbation velocity due to different interference effects
$q$	-dynamic pressure in the test section
$q_{corr}$	-dynamic pressure in the test section corrected for blockage
$C_D$	-drag coefficient
$\Delta C_{DHB}$	-drag difference due to horizontal buoyancy
$C_{Dmeas}$	-measured drag coefficient in the wind tunnel
$\Delta C_{DHBempty\ tunnel}$	-horizontal buoyancy due to the empty tunnel pressure gradient
$\Delta C_{DHBmodel}$	-horizontal buoyancy due to model induced pressure gradient
$C_{Dcorr}$	-corrected drag coefficient
$\varepsilon_S$	-perturbation velocity due to solid body blockage
$\varepsilon_W$	-perturbation velocity due to wake blockage
$\tau$	-Tunnel shape factor
$V$	-model volume
$A$	-model frontal area
$L$	-model length
$C$	-test section cross section $C = 27m^2$
$B$	-test section width $B = 6.6m$
$H$	-double of the test section height $H = 8.2m$
$\eta$	-empirical wake blockage constant $\eta = 0.41$
$C_P$	-pressure coefficient
$m$	-arbitrary model shape factor
$n$	-arbitrary tunnel shape factor
$S_{GB}$	-general blockage area
$OJ$	-Open-jet wind tunnel

## ACKNOWLEDGEMENTS

I would like to thank the following people for their support throughout the project:

My supervisor and the co-author Tim Walker for his help and guidance in all aspects of this project. Edzard Mercker who visited us in Gothenburg to give advice about a correction for the Volvo wind tunnel and who supported us in the rest of this project. And last, but certainly not least, I would like to thank my manager at VCC, Alexander Broniewicz, for giving me the opportunity to work within the Volvo aerodynamics team.

## REFERENCES

- [1] E. Mercker; G. Wickern; J. Wiedemann. Contemplation of Nozzle Blockage in open-jet Wind-Tunnels in View of Different 'Q' Determination Techniques. *SAE Technical Paper* 970136, 1997
- [2] G. Wickern. On the Application of Classical Wind Tunnel Corrections for Automotive Bodies. *SAE Technical Paper* 2001-01-0633, 2001.
- [3] H. Glauert. Wind Tunnel Interference on Wings, Bodies and Airscrews. *A.R.C., R&M no.1566*, 1933.
- [4] E. Mercker. Closed Test Section Wind Tunnel Blockage Corrections for Road Vehicles, *SAE Technical Paper* SP-1176, 1996.
- [5] E.L. Maskell. A Theory of the Blockage Effects on Bluff Bodies and Stalled Wings in a closed Wind Tunnel. *R&M no.3400*, Nov 1963.
- [6] E. Mercker. On the Correction of Open and Slotted Wall Wind Tunnels. ECARA / EADE Meeting at Volvo, Gothenburg, Nov. 2006.
- [7] J. Wiedemann; O. Fischer; P. Jiabin. Further Investigations on Gradient Effects. *SAE Technical Paper* 2004-01-0670, 2004.
- [8] E. Mercker; J. Wiedemann. On the Correction of Interference effects in Open-jet Wind Tunnels. *SAE Technical Paper* 960671. 1996.

## CFD VALIDATION PROJECT ON A VEHICLE SCALE MODEL UNDER THE CONSTRAINT OF AN OPEN JET WIND TUNNEL

Oliver Fischer <sup>\*</sup>, Timo Kuthada <sup>†</sup>, Nils Widdecke and Jochen Wiedemann

<sup>\*</sup> IVK/FKFS

Universität Stuttgart, Pfaffenwaldring 12, 70569 Stuttgart, Germany  
e-mail: Oliver.Fischer@fkfs.de,

<sup>†</sup> IVK/FKFS

Universität Stuttgart, Pfaffenwaldring 12, 70569 Stuttgart, Germany  
e-mail: Timo.Kuthada@fkfs.de

**Keywords:** Vehicle, Aerodynamics, CFD, Wind tunnel interference effects, open jet

**Abstract.** *CFD application is increasing in automotive industrial application and is more and more integrated in the aerodynamic design process of new vehicles. This process is still distinguished by parallel development with wind tunnel experiments and CFD simulation results, which demands comparable results to be generated by both development tools.*

*Wind tunnel interference effects are not simulated in most industrial CFD applications. The comparison with experimental results normally shows differences due to wind tunnel effects and ground simulation effects. Therefore a deeper understanding of these effects and methods is necessary to fully reproduce experimental values with CFD.*

*This paper focuses on the correct simulation of interference effects and gives an overview on the validation efforts with a scale model inside an open jet wind tunnel. These studies include experimental data from the real wind tunnel as well as CFD simulation results with and without wind tunnel effects.*

*Results of flow field data and integral values of different wind tunnel configurations are shown. These wind tunnel configurations feature different pressure distributions resulting in different forces and pressures. The effect of the static pressure distribution on drag and lift is simulated correctly. Furthermore, a comparison with blockage free simulation results demonstrates the influence of the open jet wind tunnel on the flow.*



## 1 INTRODUCTION

The parallel aerodynamic development of vehicles using CFD and wind tunnel tests requires a good comparability between results generated with both methods. As standard CFD simulations neglect the influence of wind tunnel interference effects, the comparability of the interference-free CFD results and experimental values cannot be perfect.

Furthermore, it is possible to investigate blockage effects with CFD by changing the wind tunnel test section to get a deeper insight into individual interference effects and to validate different aspects of correction methods. To be able to use CFD to investigate these effects, it has to be ensured that all effects will be captured correctly in a simulation of the whole wind tunnel test section with a vehicle model present.

The purpose of this validation study is to develop a detailed model of a wind tunnel to be able to compare CFD and experimental results, in order to understand the significance of various details of the test environment, and to gain a better understanding of wind tunnel interference effects.

This paper describes an approach to investigate open jet interference effects using CFD. It features a detailed simulation of the IVK model scale wind tunnel (MWK) with a detailed scale model present in the test section.

All simulations were performed with EXA PowerFLOW<sup>TM</sup>. The inherently transient nature of the underlying Lattice-Boltzmann Algorithm makes it capable of capturing most turbulence effects in the highly turbulent shear layer surrounding the open-jet wind tunnel test section. The shear layer development directly affects the static pressure distribution along the test section which has a strong influence on the measured forces. Therefore, this is important for a correct simulation of interference effects.

## 2 OPEN-JET INTERFERENCE EFFECTS

Open-jet interference effects denote several effects which modify the flow around an object inside a wind tunnel test section compared to ideal free flow conditions. Thereby they affect the measured forces acting on the object. These effects are due to the different boundary conditions inside a test section, such as the proximity of the nozzle and the highly turbulent shear layer between jet and static air in the plenum chamber. They have been investigated for decades, especially to develop and improve analytic correction methods which can be applied in daily wind tunnel work. These correction methods are aimed to increase the comparability of measurement results obtained in different wind tunnels. The influence of open-jet interference effects on open-jet wind tunnel measurements has been described in detail in the literature [1-14]. Detailed information on these effects can be found in these cited publications.

## 3 NUMERICAL SCHEME

Aerodynamic CFD simulations at IVK/FKFS are carried out with EXA PowerFLOW<sup>TM</sup> based on the Lattice-Boltzmann method [15]. PowerFLOW<sup>TM</sup> is well known and widely applied in the automotive industry. One of its advantages is the automatic discretization of the simulated fluid volume, which reduces the overall setup time. There is a wide variety of validation reports available [e.g. 16, 17].

For high Reynolds numbers, the boundary layer is simulated by a wall-model. Due to the transient nature of PowerFLOW<sup>TM</sup>, it uses a Very-Large-Eddy-Turbulence-Model to calculate the effects of the generated turbulence. This means, that only the larger eddies are calculated directly and the energy dissipation of turbulence scales smaller than lattice size is realized by

solving the two transport equations for  $k$  and  $\varepsilon$  and including a “swirl-viscosity” into the Lattice-Boltzmann algorithm [18]. The lattice in PowerFLOW<sup>TM</sup> is composed of voxels, which are three-dimensional cubic cells. The lattice also includes surfels, which are surface elements that occur where the surface of a body intersects the fluid.

PowerFLOW<sup>TM</sup> was chosen because it is a transient solver. Therefore it is capable to capture all turbulence effects in the highly turbulent shear layer. The shear layer development directly affects the static pressure distribution along the test section and therefore is important for a correct simulation of interference effects.

#### 4 EXPERIMENTAL SETUP

All measurements for this project were carried out in the IVK model scale wind tunnel (MWK) of Stuttgart University which is an open-jet Göttingen-type wind tunnel with single return duct. The tunnel is equipped with a five belt rolling road system including several systems for boundary layer control like suction and tangential blowing [19]. However the simulation of the effects of such installations is not part of the current study. Therefore all experiments and simulations are done without any ground simulation.

The standard static pressure distribution of MWK is nearly constant over the whole test section length which is not typical for an automotive wind tunnel. Therefore horizontal buoyancy effects are very small in the MWK in its standard configuration, which will be referred to as configuration 1. Several methods to change the static pressure distribution in the test section of the MWK can be used to investigate horizontal buoyancy effects. One such method was used for the so-called configuration 2 and configuration 3. Configuration 2 and 3 represent static pressure distributions which are more typical for an automotive wind tunnel. The results from all three configurations are discussed in this paper.

The vehicle model used in this study is a detailed 1/4th scale notchback model with side mirrors and a detailed underbody design but no underhood flow (closed grille).

The flow field itself was investigated with a fast response multi hole pressure probe to gain understanding of flow velocities and angles. Several measuring planes were placed around the model and in the near wake. The grid of all measuring planes was 10-by-10 mm. Due to the fast response characteristics of the pressure probe the so called “Flying Probe” technique has been used to determine the velocity components of the flow field [20]. Due to the limited acceptance cone of the probe, the recirculation flow inside the near field wake could not be captured. Therefore the near field wake area is blanked (checkered area) in the plots (Fig. 4-7).

#### 5 COMPUTATIONAL PROCEDURE

Four different setups with the 1/4th scale vehicle model were studied. The first one is the model in a typical CFD setup. That is, the boundaries are far enough to have little influence on the model while the floor boundary condition is set to provide development of the boundary layer to match the thickness measured in the experiment. This setup is referred to as the PowerFLOW<sup>TM</sup> Digital Wind Tunnel (DWT).

The second case is the vehicle model inside the IVK model scale wind tunnel (MWK) in its configuration 1. The third and fourth cases are the vehicle model inside the IVK model scale wind tunnel (MWK) in its configuration 2 and 3. These will be referred to as DIVK config. 1, DIVK config. 2 and DIVK config. 3 respectively. More details on the validation and description of the DIVK simulation can be found in [21].

A detailed CAD model of the vehicle was used for both setups. The entire volume was discretized by using cubic volumetric cells (voxels) and different levels of variable resolution (VR). The finest cells have a size of 0.75 mm. The VR schemes around the vehicle are the same for both cases. Static floor and static wheels setups were used in all cases.

Table 1 summarizes the number of cells and the physical simulated time required to obtain a stabilized flow field on a 80 CPUs Linux cluster. The physical time gets lower with each case due to the used possibility of the so-called “seeding” process, where the simulated flow field of a prior simulation can be used to initialize (or seed) a subsequent simulation.

	Voxels	Physical time
DIVK (1)	51 millions	1.45 s
DIVK (2)	55 millions	1.07 s
DIVK (3)	55 millions	0.8 s
DWT	41 millions	0.49 s

Table 1: Number of cells, physical simulated time and the CPU time

## 6 VALIDATION

A detailed wind tunnel model was generated to match the IVK model scale wind tunnel (MWK) in Stuttgart (Fig. 1). It was used for DIVK to ensure that all interference effects will be simulated correctly. The wind tunnel model includes a plenum chamber with test section, collector, diffuser and traversing system. The nozzle contraction, return duct and turning vanes are not part of the model, which was used for the results shown in this paper.

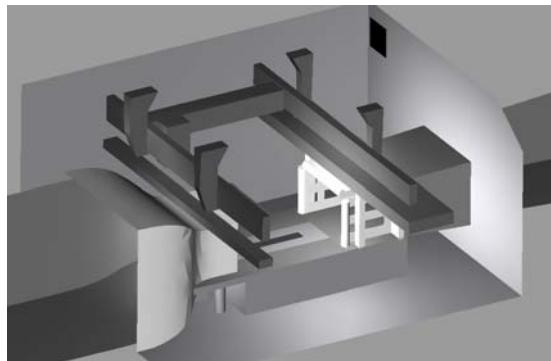


Figure 1: Digital model of IVK model scale wind tunnel (DIVK)

All dimensions of the virtual wind tunnel correspond to the test section dimensions of the real tunnel. The computational domain size of the simulation is limited by the virtual wind tunnel model. Both nozzle and diffuser ducts were extended in flow direction to prevent any influence on flow inlet and outlet.

MWK uses delta-wings as turbulence generators to prevent the tunnel from buffeting. They are attached to the inner nozzle walls at the nozzle exit plane. Detailed digital reproductions of these wings in DIVK enable the correct simulation of the shear layer development along the test section which is important for the reproduction of the static pressure distribution.

The computational mesh of the simulation is refined for shear layer and boundary layer regions to resolve the flow accurately. The wind velocity was set to 50 m/s. Turbulence inten-

sity and turbulence length scale were set to 0.003 and 1.5 mm respectively corresponding to the experimental setup.

## 6.1 TESTSECTION FLOOR BOUNDARY LAYER

The correct reproduction of the boundary layer in the simulation is very important for both drag and lift. Comparative aerodynamic force measurements of production cars with and without boundary layer control have shown that the influence of boundary layer variations is even stronger on lift forces than on drag forces [19].

The MWK is equipped with a 5-belt system for road simulation which was not in operation. But for the correct simulation of the boundary layer development along the test section, the roughness of the inactive centerbelt had to be taken into account [22] by defining an area with higher roughness compared to standard wall conditions on the steel test section floor surrounding the centerbelt.

Several numerical investigations were carried out to match the boundary layer development along the test section with the measured profiles. The simulated boundary layer profiles in the empty test section match the measured profiles in the vehicle's vicinity ( $625\text{mm} > x > -625\text{mm}$ ) as can be seen in Fig. 2. Therefore the agreement between measured and simulated boundary layer development can be considered excellent.

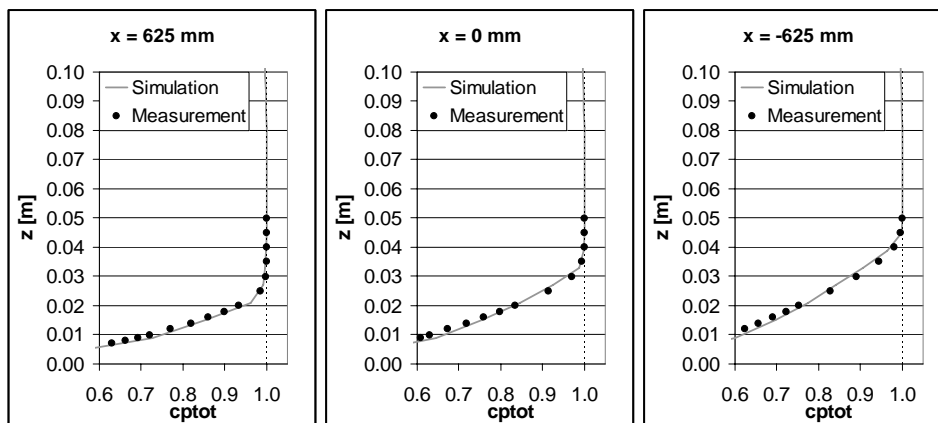


Figure 2: Comparison of boundary layer in test section simulation and measurement (configuration 1)

An influence on boundary layer development could not be observed when the modified static pressure distribution of configuration 2 and 3 was used in experiment or simulation. Therefore only the result of configuration 1 is shown here.

## 6.2 STATIC PRESSURE DISTRIBUTION

Furthermore, the comparison shows a good agreement of the basic flow structure of the shear layer in experimental and numerical results. The simulated static pressure distributions for configuration 1, 2 and 3 are in good agreement with the experimental data as can be seen in Fig. 3.

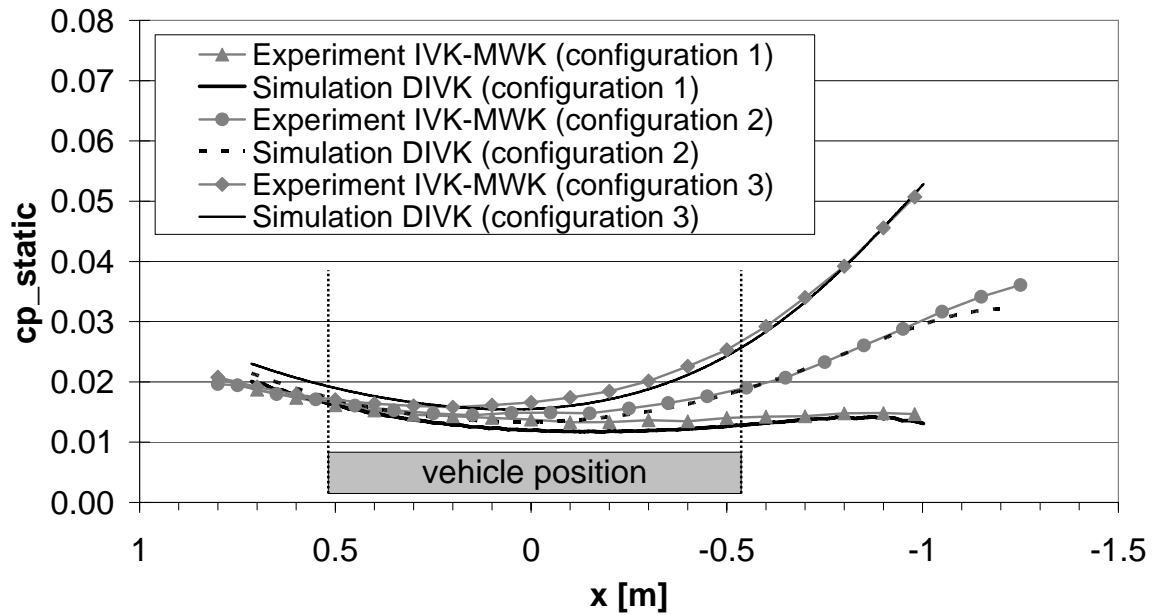


Figure 3: Static pressure distribution in the empty test section (configuration 1, 2 and 3)

## 7 COMPARISON

In this section, results from experiment and simulation in the digital model of MWK (DIVK) and the Digital Wind Tunnel (DWT) are compared and discussed.

Table 2 shows a comparison of the drag and lift values for the seven cases. As shown in the table, the difference in drag between the experiment and DIVK for configuration 1 is only 2 counts. For configurations 2 and 3, the experimental drag is reduced as a result of the wind tunnel pressure distribution. The DIVK results for configurations 2 and 3 exactly reproduce the drag reduction. The differences are 1 count for both configurations. DWT should be comparable to configuration 1 because of the nearly flat static pressure distribution but it produces a difference of 11 counts, probably due to other blockage effects.

	CD	CL	CLF	CLR	DELTA CD (DIVK-EXP)	DELTA CD (DWT-EXP)
Exp (1)	0.291	0.150	0.051	0.099	-0.002	-0.011
DIVK (1)	0.289	0.171	0.057	0.114		
Exp (2)	0.281	0.151	0.050	0.101	0.001	-0.001
DIVK (2)	0.282	0.174	0.057	0.117		
Exp (3)	0.269	0.154	0.048	0.106	0.001	0.011
DIVK (3)	0.271	0.176	0.055	0.122		
DWT	0.280	0.162	0.051	0.112		

Table 2: Drag and Lift values for the Experiment, DIVK and DWT. Deltas denote the difference between simulation and experimental values.

Although the lift is overestimated in all simulation cases (especially the rear lift), the effect of the changed pressure distribution is perfectly reproduced, which can be concluded from Table 3. Table 3 shows so-called Delta-Deltas between simulation and experiment. Delta-Deltas denote the difference of the effect of a changed pressure distribution between simulation and experiment. The effect of the static pressure distribution on drag and lift is simulated correctly because all Delta-Deltas are very close to zero.

	$\Delta\Delta CD$	$\Delta\Delta CL$	$\Delta\Delta CLF$	$\Delta\Delta CLR$
[DIVK (1) -DIVK (2)] - [Exp (1) - Exp (2)]	-0.002	-0.002	-0.001	-0.001
[DIVK (1) -DIVK (3)] - [Exp (1) - Exp (3)]	-0.004	-0.001	-0.001	-0.001

Table 3: Delta-Deltas of Drag and Lift between simulation and experimental results

Fig. 4 and 5 show a comparison of the static pressure for the three experiments (config. 1, 2 and 3) and the six PowerFLOW<sup>TM</sup> runs (DIVK and DWT, config. 1, 2 and 3) in the X=750 mm plane. The simulation data was extracted at exactly the same measurement points as the experimental data.

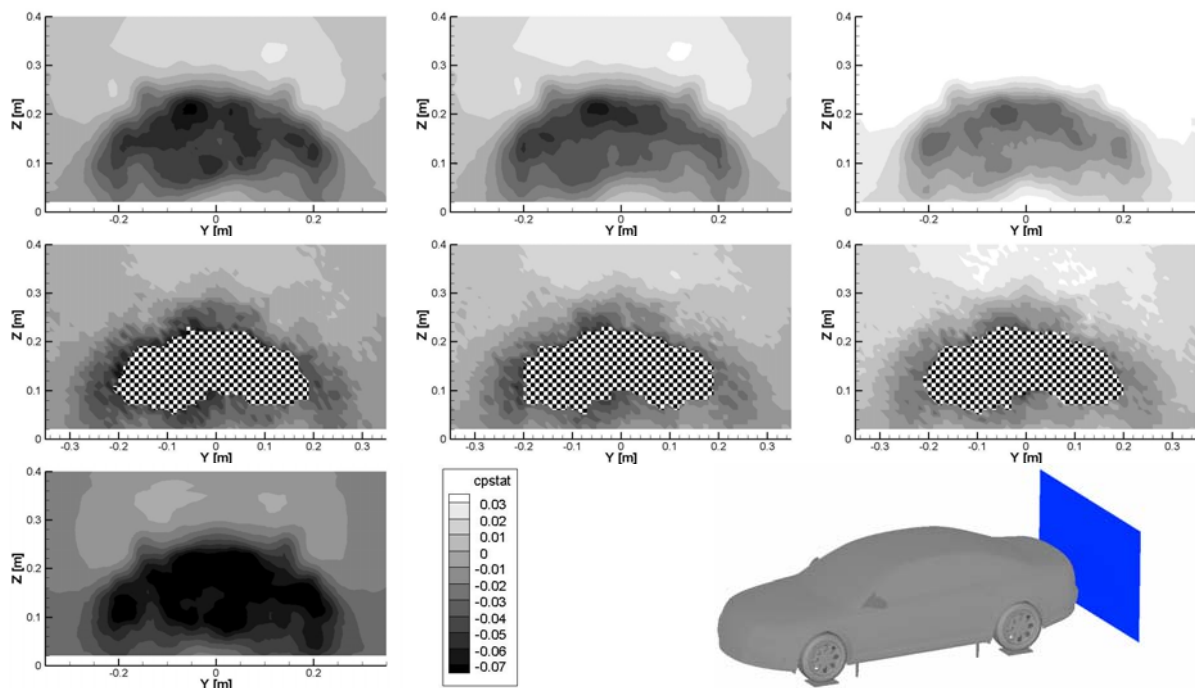


Figure 4:  $C_p$ -static at X=750 mm plane (near field wake): Wind Tunnel Model DIVK (config. 1, 2, 3) (top row from left to right); experiment (config. 1, 2, 3) (no measurements in checkered area) (2<sup>nd</sup> row from left to right); Digital Wind Tunnel DWT, legend, physical plane location (bottom row)

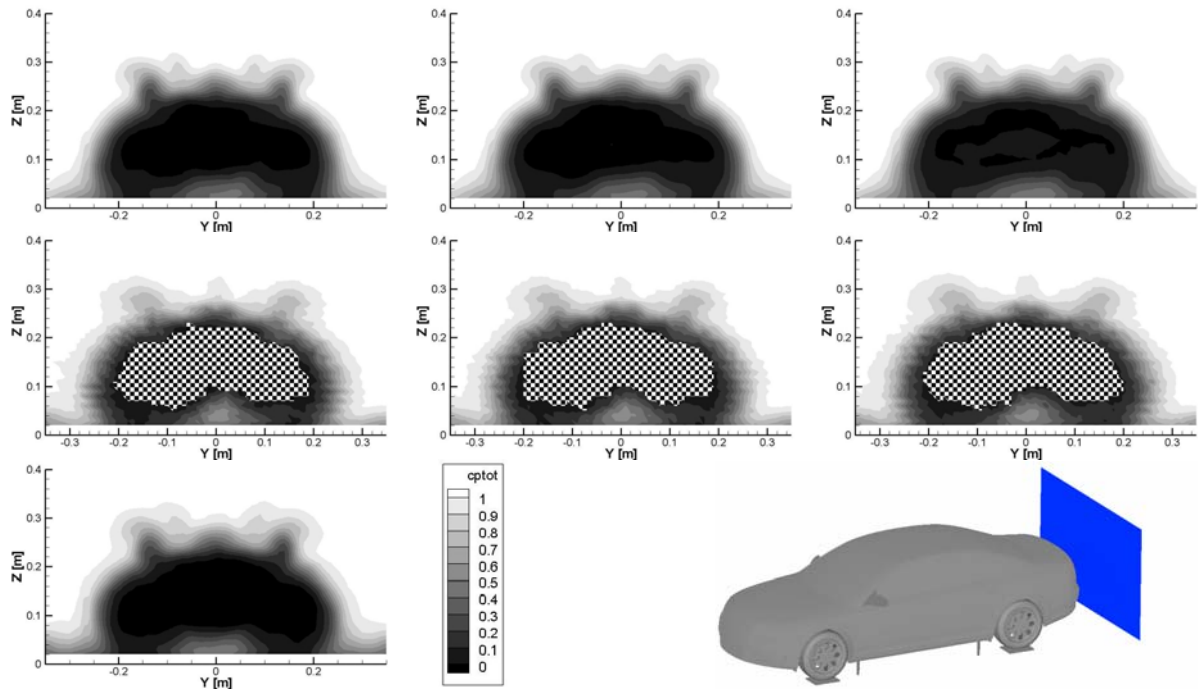


Figure 5:  $C_p$ -total at  $X=750$  mm plane (near field wake): Wind Tunnel Model DIVK (config. 1, 2, 3) (top row from left to right); experiment (config. 1, 2, 3) (no measurements in checkered area) (2<sup>nd</sup> row from left to right); Digital Wind Tunnel DWT, legend, physical plane location (bottom row)

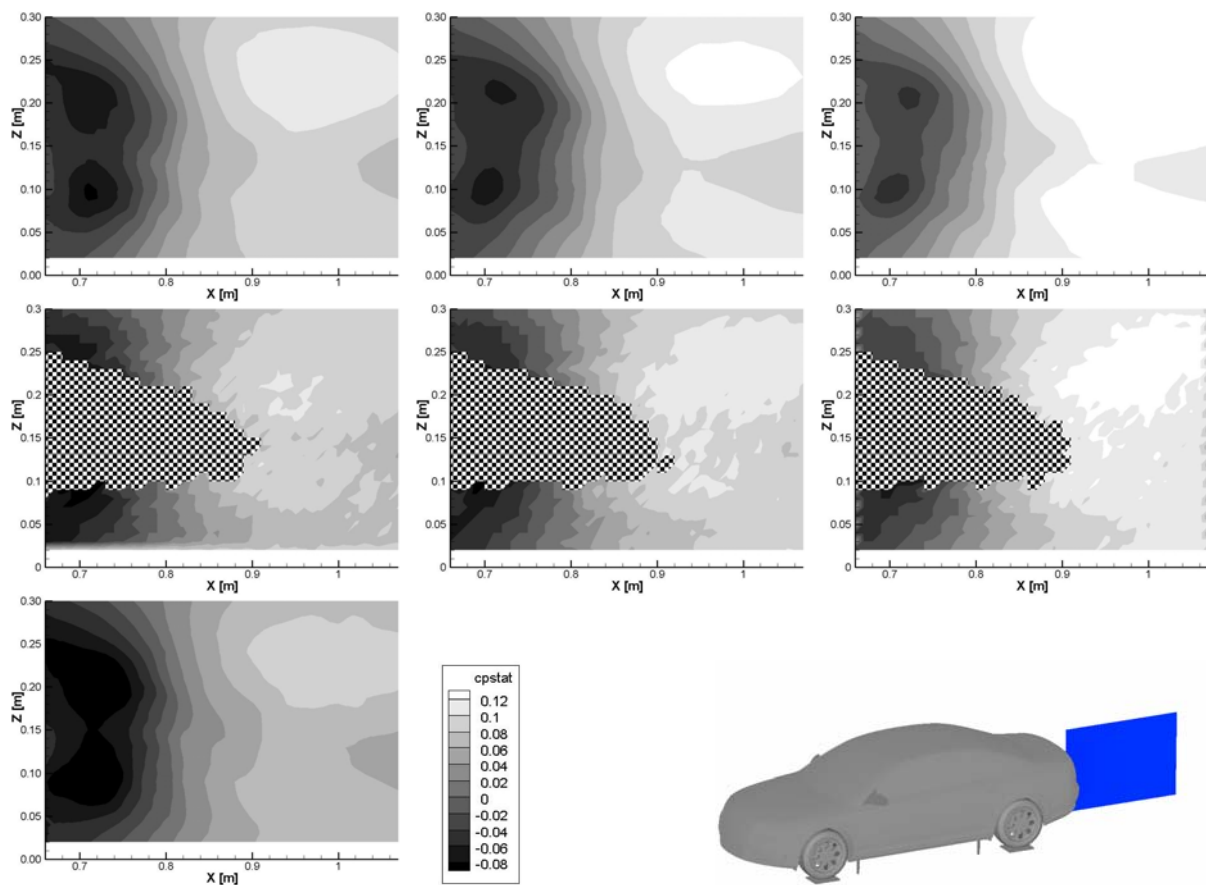


Figure 6:  $C_p$ -static at  $Y=0$  mm plane (near field wake): Wind Tunnel Model DIVK (config. 1, 2, 3) (top row from left to right); experiment (config. 1, 2, 3) (no measurements in checkered area) (2<sup>nd</sup> row from left to right); Digital Wind Tunnel DWT, legend, physical plane location (bottom row)

The comparison shows a good agreement of the basic flow structure of experimental and DIVK results with small discrepancies in detail, especially concerning small vortices in the simulation resulting from the a-pillar vortex (visible in Fig. 4 and 5). The static pressure level seems to be higher in configuration 2 and 3 (both simulation and experiment) which is due to the rise of the static pressure distributions (see Fig. 3). The figures show that the static pressure variation around the vehicle simulated with DIVK is more comparable to the experiment than the DWT static pressure results.

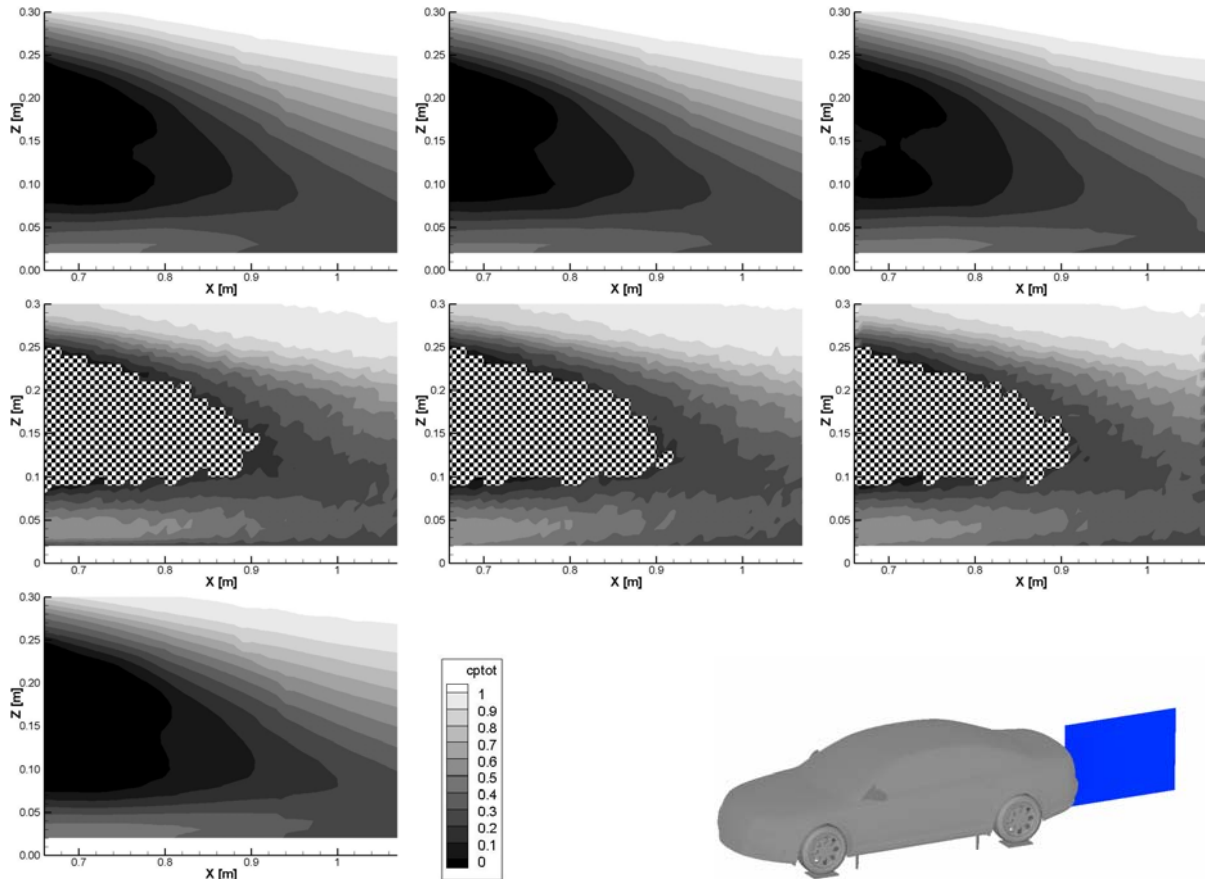


Figure 7:  $C_p$ -total at  $Y=0$  mm plane (near field wake): Wind Tunnel Model DIVK (config. 1, 2, 3) (top row from left to right); experiment (config. 1, 2, 3) (no measurements in checkered area) (2<sup>nd</sup> row from left to right); Digital Wind Tunnel DWT, legend, physical plane location (bottom row)

Fig. 6 and 7 show the static and total pressure respectively in the  $Y=0$  mm plane for the different experimental and simulation setups. The low and high static pressure regions are captured by both the DWT and DIVK. The influence of the static pressure distribution is visible in configuration cases 2 and 3 while the effect seems to be slightly stronger in simulation compared to experiment. The increasing pressure close to the vehicle base is caused by the changing wind tunnel pressure distribution and this directly influences vehicle drag (see Table 2). The good agreement between experiment and simulation of the total pressure in near field wake can be observed in Fig.7. The separation angles at upper and lower edge are well reproduced. Slight differences in underbody flow velocity are visible which could be one reason for the differences in lift.



## 8 CONCLUSIONS

In this investigation the IVK model wind tunnel (MWK) together with and without a detailed notchback model has been simulated with EXA PowerFLOW™.

The results of the simulations with a detailed notchback model show, that the simulation including open-jet wind tunnel interference effects (DIVK) are closer to experimental data obtained in MWK than simulation data obtained without consideration of wind tunnel interference effects. The influence of wind tunnel interference effects on the flow structure becomes evident by comparing simulated and measured drag and lift values. The effect of the static pressure distribution on drag and lift is simulated correctly.

Although, this approach is not practical for a vehicle development process yet because of the high computational effort necessary for the simulation of all open-jet interference effects, it can be concluded that it is possible to simulate wind tunnel interference effects in CFD and that such an approach delivers a valuable contribution to improve the agreement between experiment and simulation.

## ACKNOWLEDGEMENTS

This research was funded by EXA Corporation as part of the Center for Digital Vehicle Development. The authors would like to thank Richa Mann, Brad Duncan and Steve Remondi for their support. The authors would like to thank David Schroeck for his support during the multi hole pressure probe measurements.

## ABBREVIATIONS

CFD:	Computational Fluid Dynamics
IVK:	Institut für Verbrennungsmotoren und Kraftfahrwesen, Universität Stuttgart
FKFS:	Forschungsinstitut für Kraftfahrwesen und Fahrzeugmotoren Stuttgart
MWK:	IVK model scale wind tunnel
DIVK (n):	Digital model of MWK in configuration n (static pressure distribution)
EXP (n):	Measurements in MWK in configuration n (static pressure distribution)
EXA:	EXA Corporation
DWT:	standard digital wind tunnel provided by EXA without wind tunnel interference effects (box)
LBM:	Lattice-Boltzmann Method

## REFERENCES

- [1] Mercker, E. and Wiedemann, J.: On the Correction of Interference Effects in Open Jet Wind Tunnels. *SAE Technical Paper*, **960671**, Detroit, 1996.
- [2] Mercker, E., Wickern, G., Wiedemann, J.: Contemplation of Nozzle Blockage in Open Jet Wind-Tunnels in View of Different 'Q' Determination Techniques, *SAE Technical Paper*, **970136**, Detroit, 1997.
- [3] Wickern, G.: On the Application of Classical Wind Tunnel Corrections for Automotive Bodies, *SAE Technical Paper*, **2001-01-0633**, Detroit, 2001.

- [4] Wickern, G.: Gradient Effects on Drag due to Boundary-Layer Suction in Automotive Wind Tunnels, *SAE Technical Paper*, **2003-01-0655**, Detroit, 2003.
- [5] Wiedemann, J., Fischer, O., Pang J.: Further Investigations on Gradient Effects, *SAE Technical Paper*, **2004-01-0670**, Detroit, 2004.
- [6] Wickern, G., Schwartekopp, B.: Correction of Nozzle Gradient Effects in Open Jet Wind Tunnels, *SAE Technical Paper*, **2004-01-0669**, Detroit, 2004.
- [7] Mercker, E., Cooper, K.R., Fischer, O., Wiedemann, J.: The influence of a Horizontal Pressure Distribution on Aerodynamic Drag in Open and Closed Wind Tunnels, *SAE Technical Paper*, **2005-01-0867**, Detroit, 2005.
- [8] Mercker, E., Cooper, K.R.: A Two-Measurement Correction for the Effects of a Pressure Gradient on Automotive, Open-Jet, Wind Tunnel Measurements, *SAE Technical Paper*, **2006-01-0568**, Detroit, 2006.
- [9] Wetzel, W.: *Übertragbarkeit aerodynamischer Beiwerte von Windkanalversuchen im Modellmaßstab auf reale Fahrzeuggeometrien (Validity of aerodynamic coefficients determined from wind tunnel tests in model scale for real full scale vehicle geometries)*, PhD Thesis, University of Karlsruhe, 2001.
- [10] Perzon, S.: On Blockage Effects in Wind Tunnels – A CFD Study, *SAE Technical Paper*, **2001-01-0705**, Detroit, 2001.
- [11] Yang, Z., Schenkel, M., Fadler, G.J.: Corrections of the Pressure Gradient Effects on Vehicle Aerodynamic Drag, *SAE Technical Paper*, **2003-01-0935**, Detroit, 2003.
- [12] Yang, Z., Schenkel, M.: Assessment of Closed-Wall Wind Tunnel Blockage Using CFD, *SAE Technical Paper*, **2004-01-0672**, Detroit, 2004.
- [13] Yang, Z., Nastov, A., Schenkel, M.: Further Assessment of Closed-Wall Wind Tunnel Blockage Using CFD, *SAE Technical Paper*, **2005-01-0868**, Detroit, 2005.
- [14] Ewald, B. (ed.): *Wind Tunnel Wall Corrections*, AGARDograph 336, 1998.
- [15] Lietz, R., Mallick, S., Kandasamy, S. and Chen, H.: Exterior Airflow Simulations Using a Lattice Boltzmann Approach, *SAE Technical Paper*, **2002-01-0596**, Detroit, 2002.
- [16] Bartelheimer, W.: Berechnung der Fahrzeugumströmung bei BMW: Validierung und Einsatz von EXA PowerFLOW, Tagung "Fahrzeug-Aerodynamik", Haus der Technik, München, 2001.
- [17] Parpais, S., Farce, J., Bailly, O., Genty, H.: A Comparison of Experimental Investigations and Numerical Simulations around Two-box form Models, MIRA, 4th Int. Conference of Vehicle Aerodynamics, Warwick, 2002
- [18] Mallick, S., Remondi, S., Chen, H. and Pervaiz, M.: Developing CFD through Validation of Turbulence Models, MIRA, 3th Int. Conference of Vehicle Aerodynamics, Warwick, 2000
- [19] Wiedemann, J. and Potthoff, J.: The New 5-Belt Road Simulation System of the IVK Wind Tunnels, *SAE Technical Paper*, **2003-01-0429**, Detroit, 2003.
- [20] Schröck, D.: Implementierung eines Programms zur Durchführung und Auswertung von Strömungsfeldmessungen im IVK-Modellwindkanal, Diploma Thesis, Institut für Verbrennungsmotoren und Kraftfahrwesen, Universität Stuttgart, 2005

- [21] Fischer, O., Kuthada, T., Widdecke, N. and Wiedemann, J.: CFD Investigations of Wind Tunnel Interference Effects. *SAE Technical Paper*, **2007-01-1045**, Detroit, 2007.
- [22] Kuthada, T., Schröck, D., Potthoff, J. and Wiedemann, J.: The Effect of Center Belt Roughness on Vehicle Aerodynamics. *SAE Technical Paper*, **2009-01-0776**, Detroit, 2009.

## COMPARISON OF EXPERIMENTAL AND NUMERICAL RESULTS FOR A REFERENCE CAF TRAIN EXPOSED TO CROSS WINDS

Javier García\*, Jorge Muñoz\*, Antonio Crespo\* and Aitor Berasarte†

\*Dpto. Ingeniería Energetica y Fluidomecanica. Grupo de Investigación de Mecánica de Fluidos Aplicada a la Ingeniería Industrial. Universidad Politécnica de Madrid. C/ Jose Gutierrez Abascal, 2. 28006 Madrid (Spain)  
e-mail: javier.garciag@upm.es,

† CAF (Construcciones y Auxiliar de Ferrocarriles, S.A.). J. M. Iturrioz, 26. 20200 Beasain (Spain)  
e-mail: aberasarte@caf.net

**Keywords:** High speed train, aerodynamics, cross winds, CFD, experiments

**Abstract.** *This work presents the comparison of results obtained numerically and experimentally for a reference high speed train of CAF exposed to cross winds. Two different scenarios are studied: first, a flat ground scenario and second, the configuration of ballast and rails proposed by the current TSI HS RST and the prEN 14067-6:2007. The purpose is to study the behavior of the train against cross winds and to investigate the accuracy that typical steady state CFD-RANS methods produce by comparison with experimental results.*

*The experimental data are obtained in a wind tunnel with a 1:15 scaled model. Yaw angles between 0° and 70°, in steps of 5° are considered. Besides, in the case of ballast and rail configuration, both windward and leeward cases are included. The model consists of a first car and a dummy end-car. The results for a Reynolds number equal to  $7.6 \times 10^5$  are presented.*

*A sensitivity analysis of the results to the RANS models and discretization scheme is presented. It is found that the best agreement with the experiments corresponds to the  $k-\epsilon$  realizable and third order discretization scheme. Numerical simulations have been carried out with the Fluent commercial code.*

*In general, the numerical results show a good agreement with the experiments, although some discrepancies appear mainly for the higher yaw angles. Therefore, for the yaw angles of practical interest, the CFD analysis turns out to be a useful tool for predicting the aerodynamic response of the train. These results can be used to obtain the stability range of the train.*

## 1 INTRODUCTION

This work presents the comparison of results obtained numerically and experimentally for a reference high speed train of CAF exposed to cross winds. Two different scenarios are studied: first, a flat ground scenario and second, the configuration of ballast and rails proposed by the current TSI HS RST (Ref. [1]) and the prEN 14067-6:2007 (Ref. [2]). The purpose is to study the behavior of the train against cross winds and to investigate the accuracy that typical steady state CFD-RANS methods produce by comparison with experimental results.

The numerical simulations have been carried out with the FLUENT commercial code. Different two equations turbulent closure methods have been checked, and it is found that the best agreement with the experimental results corresponds to the  $k-\varepsilon$  realizable model. All the results presented in this paper have been obtained with this model.

The geometrical configuration studied numerically, see Fig. (1), is the one corresponding to the experiments performed in the S10 wind tunnel of the Institut Aérotechnique (IAT) in Saint-Cyr l'École (France). The objective is to compare the numerical and experimental results in order to validate the numerical procedure. The train model consists of the leading test unit followed by a simplified dummy end-car to provide a more realistic flow around the test unit. The model and the dimensions of the computational domain are shown in Fig. (1). The model scale is 1:15. The experiments were carried out for three different velocities; however the numerical simulations correspond to the intermediate velocity of 40 m/s.

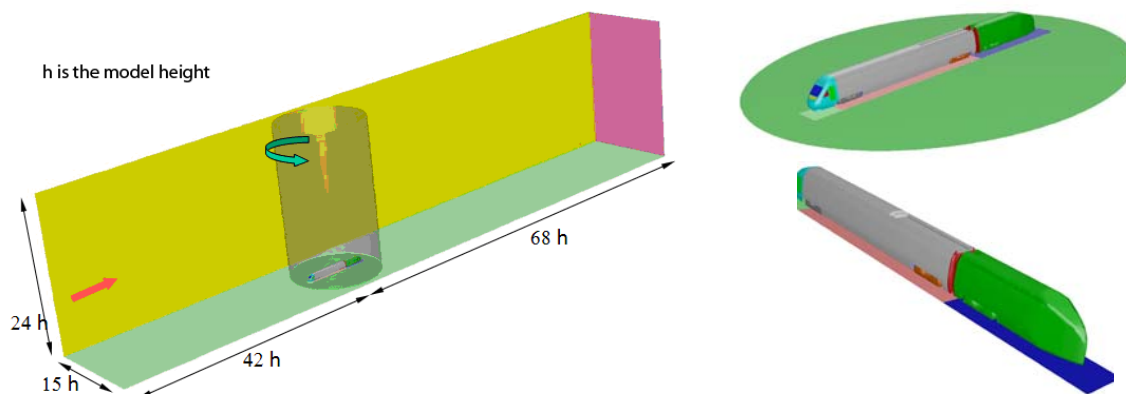


Figure 1. Computational domain dimensions and details of the geometry used in the numerical simulations.

The experiments were made both for flat ground, Fig. (2a), and for ballast and rail configurations, Fig. (2b), as proposed by the current TSI HS RST and the prEN 14067-6:2007.

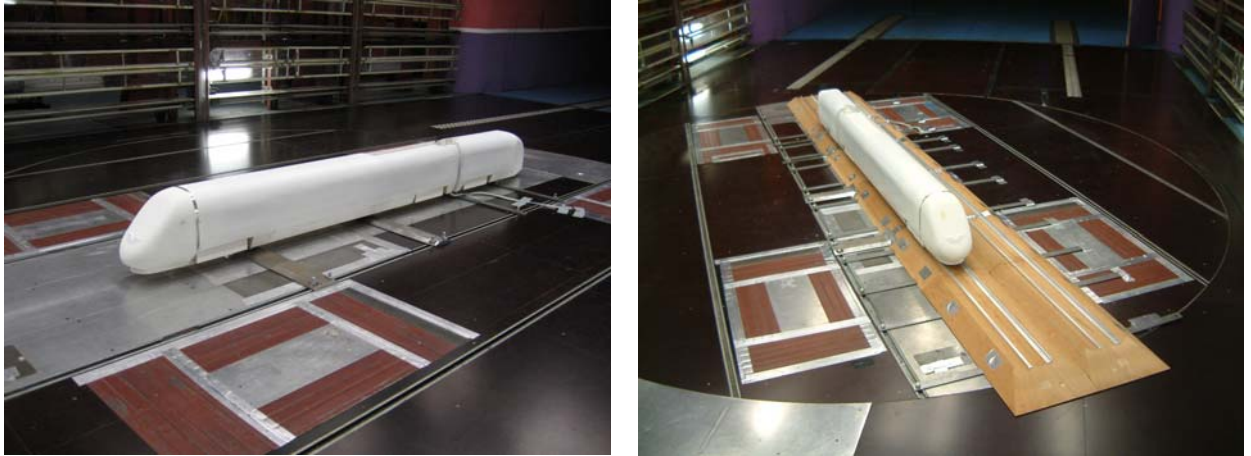


Figure 2. a) Model used for flat terrain, b) Model for ballast and rail configuration.

In the following section the numerical model, boundary conditions and meshes used in the calculations are presented. In the next section, the numerical results obtained are discussed, and a comparison with the experimental results is also included. Finally, some conclusions derived from this work are commented.

## 2 NUMERICAL MODEL

The numerical simulations were performed with the FLUENT commercial code, assuming that the compressibility effects are negligible, using steady RANS models and the SIMPLE method for solving the coupling between pressure and velocity. Two different turbulence closure methods were checked: the  $k-\epsilon$  standard model and  $k-\epsilon$  realizable model. Also a sensitivity study of the influence of the discretization order was performed. The studied convective discretization schemes were first and second order upwind and a third order MUSCL (*Monotone Upstream-centered Schemes for Conservation Laws*) scheme. By comparison with the experiments for two yaw angles ( $15^\circ$  and  $30^\circ$ ) the best results were found to be those corresponding to the  $k-\epsilon$  realizable model with a third order scheme, Fig. (3).

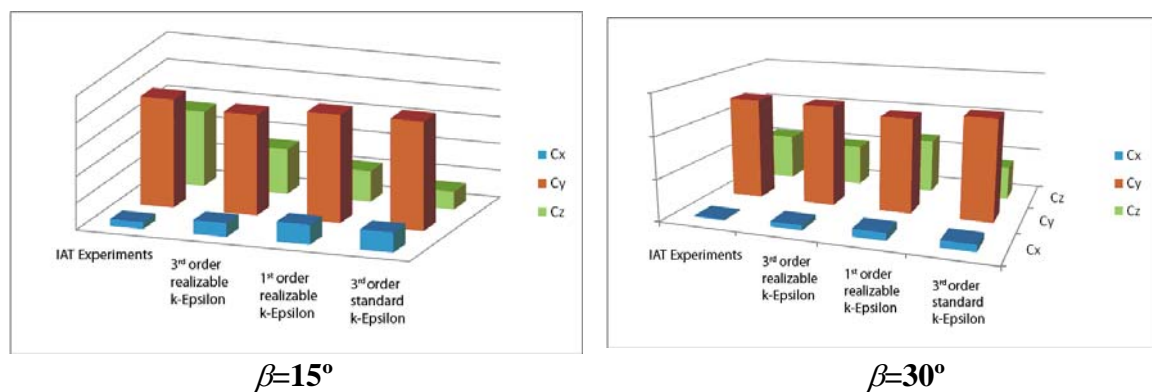


Figure 3. Comparison of the numerical and experimental results for yaw angles equal to  $15^\circ$  and  $30^\circ$ .

The coordinate system and the definitions of the moments and yaw angle are shown in Fig. (4). The force and moment coefficients are non-dimensionalized with a reference length  $l=3\text{m}$  and a reference surface  $A=10\text{m}^2$ , scaled conveniently.

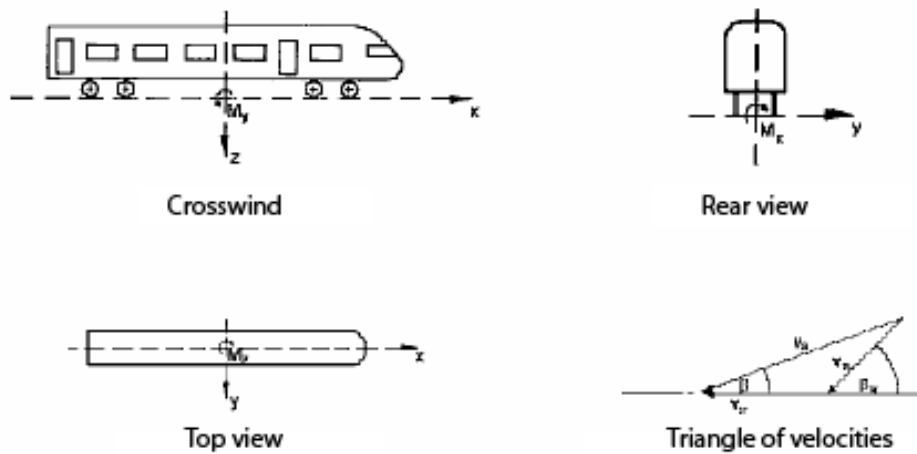


Figure 4. Coordinate system and definition of the moments and the yaw angle  $\beta$ .

The boundary conditions used in the calculations are as follows:

- In the inlet, a uniform velocity equal to 40m/s was assumed, which corresponds to  $Re=7.6 \times 10^5$  based on the train height. Inlet values of  $k=0.24\text{m}^2/\text{s}^2$  and  $\varepsilon=0.004\text{m}^2/\text{s}^3$  were imposed, corresponding to the turbulence of the inlet flow in the wind tunnel, 1%, and the hydraulic diameter  $D_h=4.91\text{m}$ . However, the results do not seem to be very sensitive to these values.
- No-slip standard logarithmic law-of-the-wall boundaries were used for the surfaces of the train, ballast and rail, and ground.
- At the outlet, upper and side boundaries, corresponding boundary conditions were supposed to be located far enough, so that zero gradients for all variables were fixed.

A multiblock mesh was used in order to be able to introduce minor geometrical or mesh modifications without having to mesh the whole model again. A hexahedral mesh was used except in local regions (bogies) where, due to the geometrical complexity, tetrahedral cells were employed, Fig. (5). Near the walls, the grid was refined to obtain a unit wall distance for the first grid point  $y^+=yu^*/\nu < 100$ , where  $u^*$  is the friction velocity and  $\nu$  the kinematic viscosity,  $1.4 \times 10^{-5}\text{m}^2/\text{s}$ . Taking into account the computational resources available, the number of cells was limited to  $5 \times 10^6$  for the cases corresponding to flat ground and slightly higher for the ballast and rail scenarios.



Figure 5. Details of the mesh used in the simulations.

### 3 RESULTS

#### 3.1 Flat ground scenario

In the following the results obtained for a flat terrain are presented. Pressure and velocity distributions are included and besides a comparison between the numerical and experimental force and moment coefficients is shown.

Fig. (6) gives the pressure distribution for the first car for both the windward and leeward sides. As it was expected, the pressure increases with the yaw angle for the windward side and decreases for the leeward side. This is partly due to the flow separation behind the train. The same tendency can be seen in Fig. (7), corresponding to the pressure distribution in a cross section between bogies.

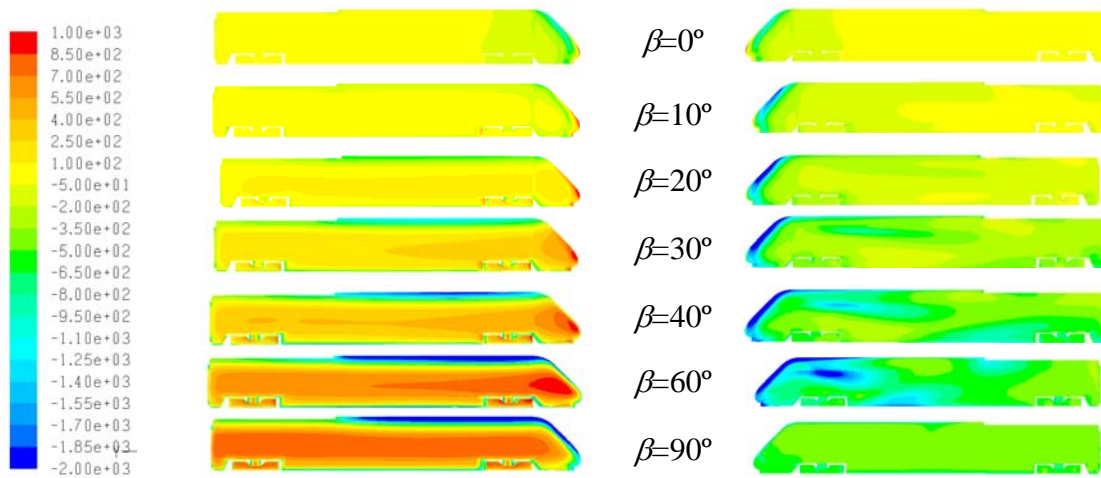


Figure 6. Pressure distribution for the windward (left) and leeward (right) sides.

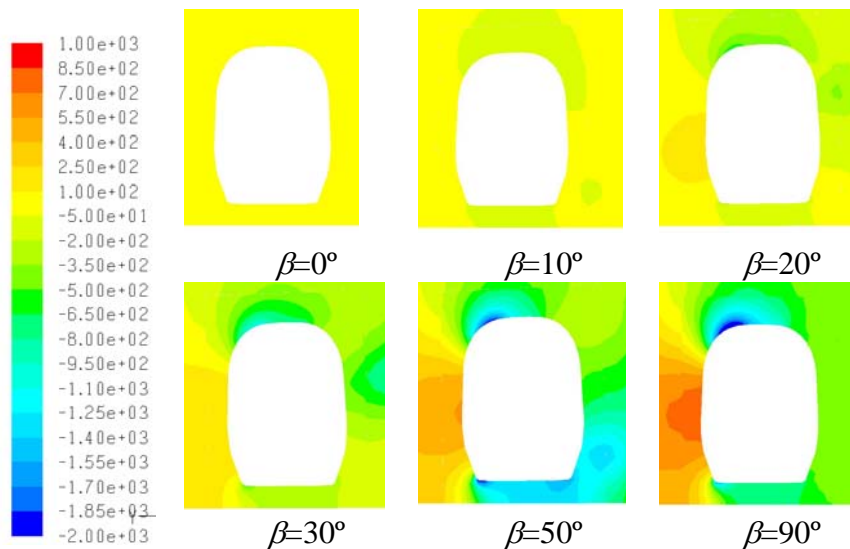


Figura 7. Pressure distribution in a cross section between bogies.

The flow separation can be observed in Fig. (8), where the pathlines of the fluid particles emitted from the nose are presented. For yaw angles lower than  $30^\circ$  the pathlines are close to the leeward side for a significant distance. However, the windward side has visible pathlines only for yaw angles lower than  $15^\circ$ .



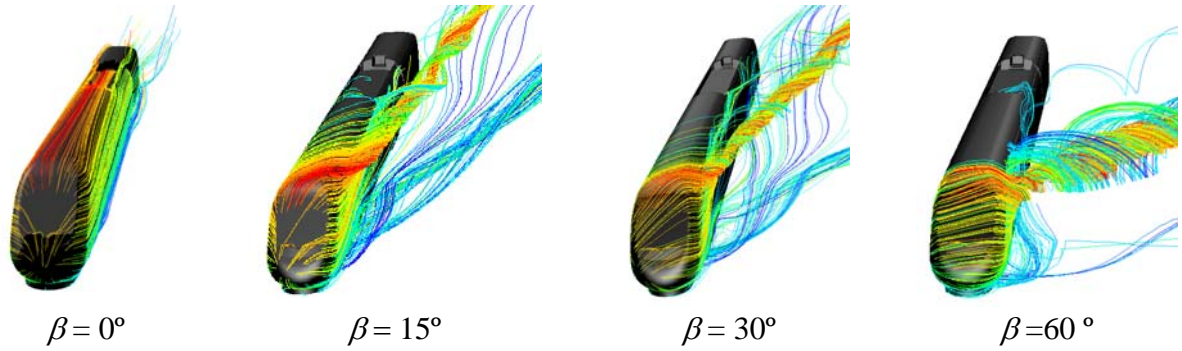


Figure 8. Pathlines for different yaw angles.

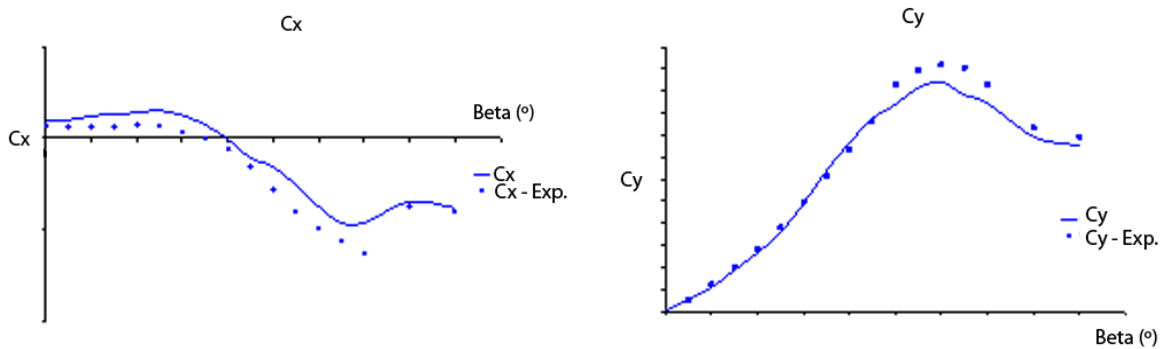
The force and moment coefficients are defined as usual:

$$C_i = \frac{F_i}{\frac{1}{2} \rho V_\infty^2 A} \quad (1)$$

$$C_{mi} = \frac{M_i}{\frac{1}{2} \rho V_\infty^2 AL} \quad (2)$$

being  $i=x, y$  and  $z$  in each case and  $F_i$  and  $M_i$  the force and moment components respectively,  $\rho=1.226\text{kg/m}^3$ , and, as it was mentioned before,  $V_\infty=40\text{m/s}$ . The surface and length values used to normalize the forces and moments were:  $A=10/15^2\text{m}^2$  and  $L=3/15\text{m}$ , where 15 is the scale factor. The coordinate system is shown in Fig. (4).

In Fig. (9), the force and moment coefficients obtained numerically are presented as a function of the yaw angle, and compared to the experimental values, represented by a single and dotted line, respectively. The drag coefficient increases with the yaw angle up to an angle equal to  $25^\circ$ , and then decreases and becomes negative for yaw angles slightly lower than  $40^\circ$  ( $35^\circ$  in the experiments). This indicates that the wind gives a positive propulsive force for yaw angles higher than  $40^\circ$ . In general, the agreement between numerical and experimental results is quite good, except for the lift coefficient  $C_z$ , and the pitching moment  $C_{my}$ . A possible explanation for this discrepancy could be that the bars used to fix the model produce flow disturbances in the undercar region. This effect was not considered in the simulation and therefore the vertical force and the pitching moment are different to the experimental values. Similar results were obtained by Matschke, Ref. [3].



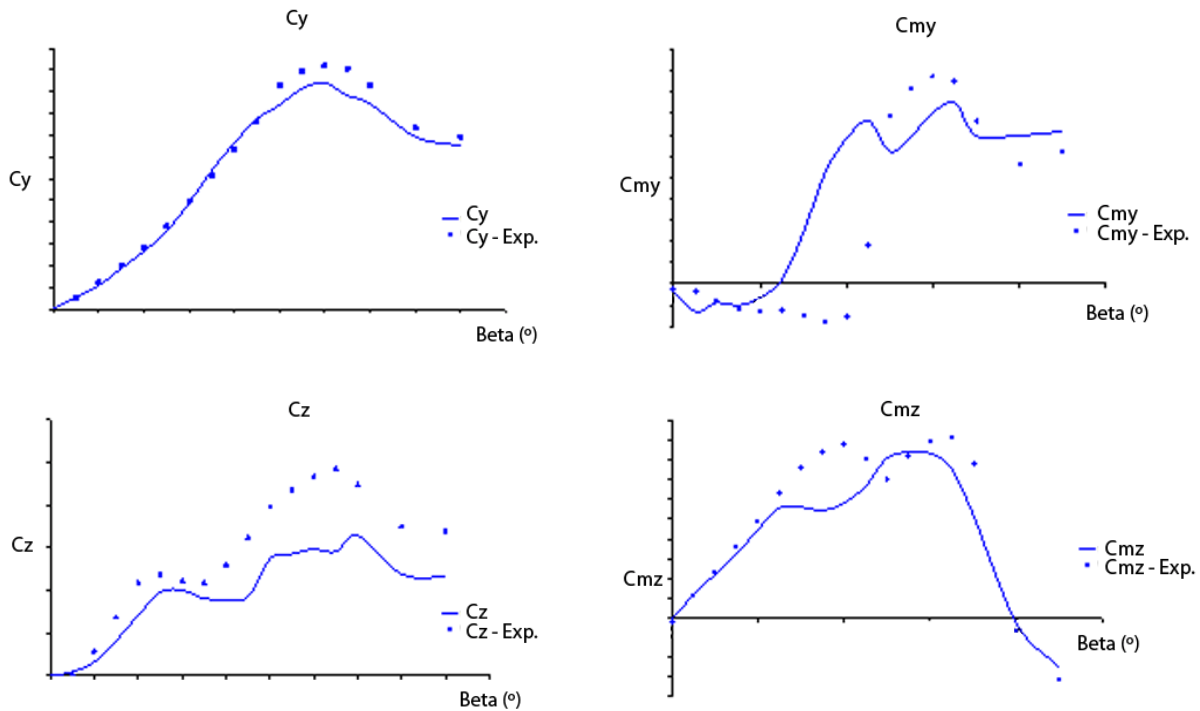


Figure 9. Comparison of the numerical and experimental force and moment coefficients.

### 3.2 Ballast and rail configuration

In the following, the results obtained for a ballast and rail scenario are presented. Pressure and velocity distributions are included and besides, a comparison for the numerical and experimental force and moment coefficients is shown.

Fig. (10) and (11) give the pressure distribution for the first car, for both the windward and leeward sides. Fig. (10) corresponds to the case where the train is on the windward track and Fig. (11) to the case where the train is on the leeward track. As it was expected, the pressure increases with the yaw angle for the windward side and decreases for the leeward side. This is partly due to the flow separation behind the train. The same tendency can be seen in Fig. (7), corresponding to the pressure distribution in a cross section between bogies.

Comparing the pressure distributions for the windward side corresponding to a flat ground and a ballast and rail configuration, it can be seen that for this latter configuration, maximum pressure values are shifted down when the train is located on the windward track. This is consistent with the fact that the incident wind has a vertical component due to the ballast. This tendency does not appear when the train is located on the leeward track. In this case, the differences with the flat ground configuration are negligible.

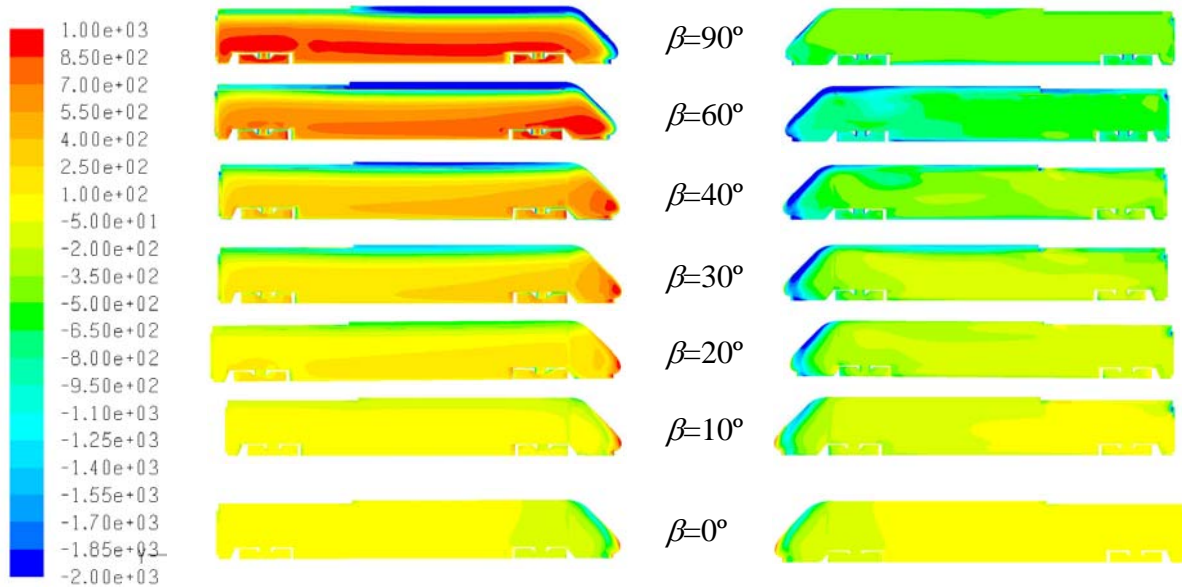


Figure 10. Pressure distribution for the windward (left) and leeward (right) sides. Train is located on the windward track.

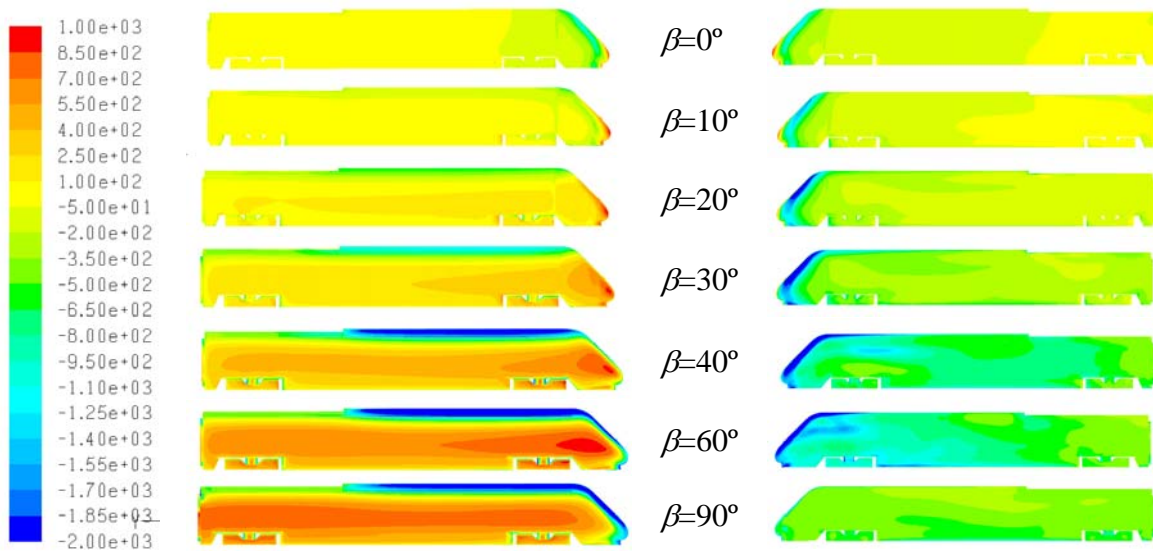


Figure 11. Pressure distribution for the windward (left) and leeward (right) sides. Train is located on the leeward track.

Fig. (12) and (13) show the pressure distribution in a cross section between bogies. It seems that the extreme values, for both positive and negative values, are greater when the train is located on the windward rail. These figures suggest that the flow separation increases with the yaw angle. This can be easily seen in Fig. (14), where the pathlines are represented. The behaviour is similar to the flat ground case, although the ballast produces more flow recirculation.

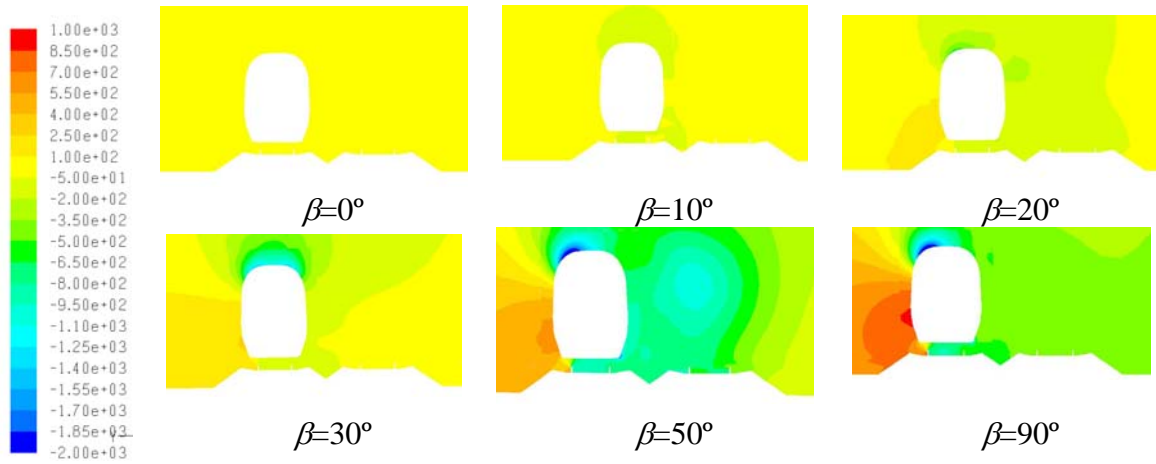


Figure 12. Pressure distribution in a cross section between bogies. Train is located on windward track.

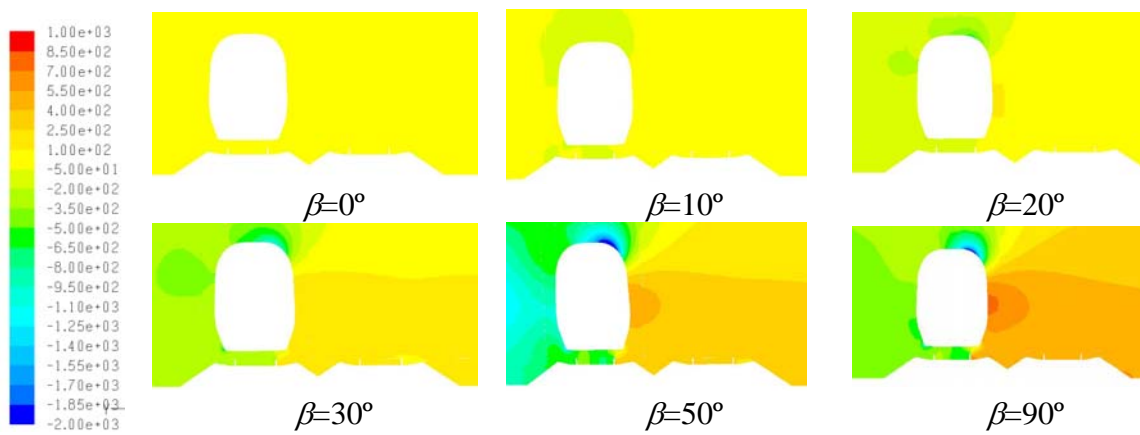


Figure 13. Pressure distribution in a cross section between bogies. Train located on leeward track.

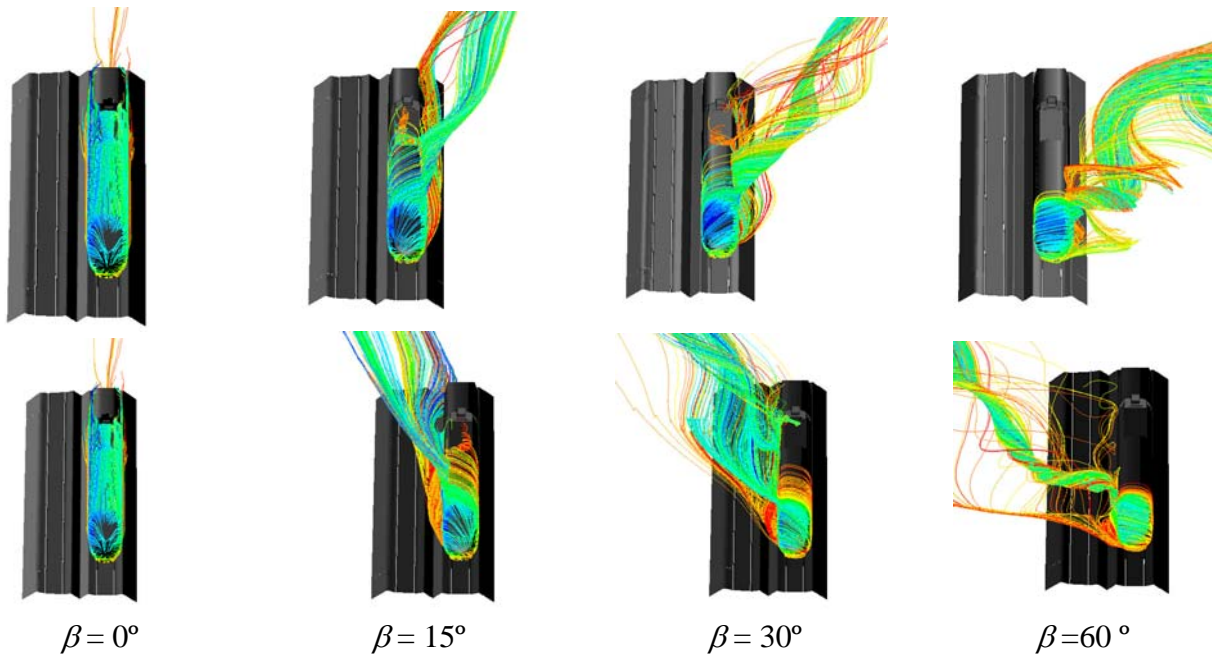


Figure 14. Pathlines for different yaw angles. Upper figures correspond to train located on leeward track and lower figures to the windward case.

In Fig. (15), the force and moment coefficients obtained numerically are presented as a function of the yaw angle. The experimental values are also included for comparison. The negative values of the yaw angle correspond to the case where the train is located on the windward track, and positive values to the case where the model is on the leeward track. For the drag coefficient the behavior is similar to the flat ground case, although more discrepancies are found with the experiments. This may be due to the presence of more recirculations caused by the ballast. For the side force, the agreement is quite good between experiments and numerical results. For the lift force, the values obtained in the range between  $-60^\circ$  and  $60^\circ$  are very close to the experimental ones; outside this range, where the flow separation is more important, discrepancies appear. The same tendency was found for the flat ground configuration.

Regarding the moment coefficients, in general, the agreement between experimental and numerical values is quite good for the range between  $-60^\circ$  and  $90^\circ$ ; outside this range, the differences are greater.

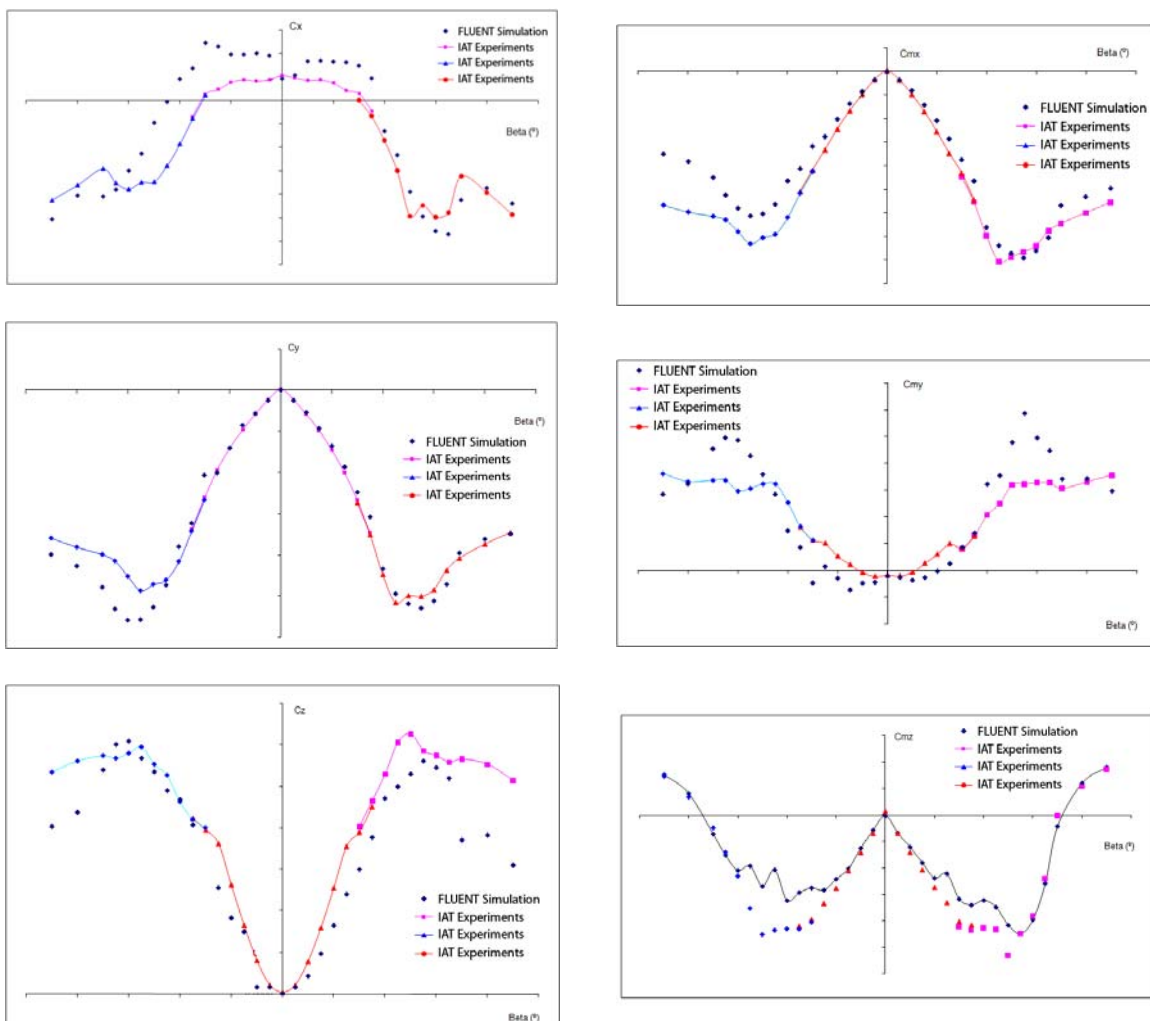


Figure 15. Comparison of the numerical and experimental force and moment coefficients. Ballast and rail configuration.

## 4 CONCLUSIONS

The current work has addressed the numerical assessment of the aerodynamic characterisation of a high-speed train in different crosswind scenarios: on a flat ground and on a ballast and rail configuration (for yaw angles between  $0^\circ$  and  $90^\circ$ , and  $-90^\circ$  and  $90^\circ$ , respectively). The numerical results have been compared with experiments in order to validate the numerical procedure. A sensitivity study of the results to the turbulence closure method and order of discretization of the convective scheme has been made. It is found that the best results are obtained with the  $k-\varepsilon$  realizable model. In general, the agreement between numerical and experimental results is quite good. More discrepancies are found for the higher yaw angles, where the flow separation is more important. In summary, for the yaw angles of practical interest, the CFD analysis turns out to be a useful tool for predicting the aerodynamic response of the train. These results can be used to obtain the stability range of the train.

## 5 ACKNOWLEDGEMENTS

This work was carried out within the AVI-2015 project (Ref. [4]), co-founded by the CDTI through the CENIT program.

## 6 REFERENCES

1. TSI HS RST 2008. "Technical specification for interoperability relating to the 'rolling stock' sub-system of the trans-European high-speed rail system". Official Journal of the European Union. 21 February 2008.
2. DRAFT prEN 14067-6:2007. "Railway Applications - Aerodynamics - Part 6: Requirements and test procedures for cross wind assessment". CEN March 2007.
3. Matschke, G. 2000. *Computational Simulation of Aerodynamic Forces and Side Wind Behaviour of Railway Vehicles*. European Congress on Computational Methods in Applied Sciences and Engineering, ECCOMAS 2000.
4. <http://www.avi2015.com/>

## EXPERIMENTAL INVESTIGATION ON A DETAILED EUROPEAN TRACTOR-TRAILER CONFIGURATION

**Johannes Haff, Mattias Jönsson, Hugues Richard, and Sigfried Loose**

German Aerospace Center (DLR)  
Institute of Aerodynamics and Flow Technology, Bunsenstr. 10, 37073 Göttingen, Germany  
e-mail: Johannes.Haff@dlr.de, Mattias.Joensson@dlr.de,  
Hugues.Richard@dlr.de, Sigfried.Loose@dlr.de

**Keywords:** experimental research, truck configuration, PIV

**Abstract.** *This paper summarizes first results of experiments with a detailed truck model performed at the beginning of this year. Objective of these tests was to show the model behavior in experimental conditions and to gain first impressions about the flow field characteristics of a detailed tractor-trailer configuration.*

*The experiments were performed in the open test section wind tunnel of DLR Göttingen and in the cryogenic wind tunnel of DNW Cologne. They included flow visualizations with particle image velocimetry and force measurements.*

*In addition to these results, a new test set-up in a water towing tank will be described in which the investigation of new drag reducing devices is planned for the near future.*

## 1 INTRODUCTION

The transport sector of heavy vehicles will continue to become larger in the next years with the result of dramatically increasing total costs for fuel consumption. Therefore a research program at DLR was started to contribute to the reduction of aerodynamic drag and fuel costs in future.

The results presented in this paper give an overview of the current status of the investigations with a detailed tractor-trailer configuration. The measurements were performed in the beginning of 2009 and are divided into two different parts: Flow visualization methods applied in an open test section wind tunnel in Göttingen and force measurements performed in the cryogenic wind tunnel in Cologne

At first the investigations in the conventional open test section wind tunnel of DLR Göttingen are described. The tests were mainly used to investigate the model behavior in the test section. Furthermore the tunnel is suitable for optical measurement techniques due to the easy access to the open test section. The measurements with PIV delivered first results about the flow field around the truck model. The experiments were conducted at a maximum Reynolds number of 630,000.

The second part of this study summarizes the results of measurements in the cryogenic wind tunnel of DNW in Cologne. The tests included force measurements with an external balance. The advantage of this tunnel is a high maximum Reynolds number and the large test section which avoid blockage effects. The tests described in the following were performed at ambient conditions. A maximum Reynolds number of 1,000,000 was achieved.

The last chapter of this paper describes a new test set-up which will be used for future investigations of new drag reducing devices. These investigations will be performed in a water towing tank with installed intermediate floor. Preliminary results of a first test will also be described.



## 2 TRUCK TEST MODEL

The test program described in this paper was performed with a 1/15<sup>th</sup> scale truck model which corresponds to a typical European tractor-trailer design with a two-axis tractor and a three-axis trailer chassis (see Fig. (1)). The tractor cab geometry (Scania R Topline) and the axis parts were produced by WEDICO Truck & Construction Models GmbH. The remaining truck dimensioning was developed in accordance with the rules of the European Community [3]. The objective was to create a realistic model of a full scale truck. Additional parts like mirrors, sun shield and mud flaps were available in full detail. It has to be considered that the model is not equipped with an engine cooling system. Pressure holes are installed on the side, roof and back of the cab surface. The main dimensions of the model are given in Fig. (1). Also shown is the orientation of the coordinate system. The origin is located in the middle of the gap between tractor and trailer in x-direction and in the symmetry plane of the model in y-direction with  $z = 0$  defined on the ground.

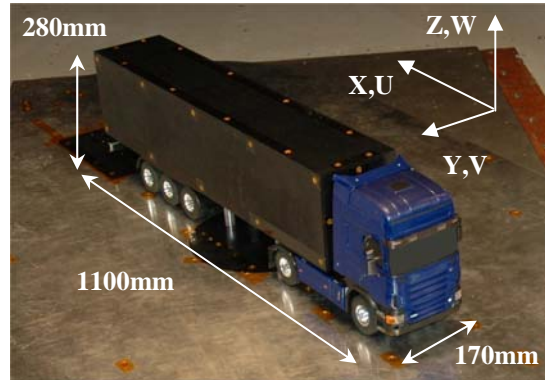


Figure 1: 1/15<sup>th</sup> scale truck model.

## 3 FLOW VISUALIZATION IN THE 1M-TUNNEL (1MG)

### 3.1 Test Configuration (1MG)

The investigations started with tests in the conventional open test section wind tunnel of the DLR Göttingen which has a squared test section of 1.0m x 0.7m and 1.4m length. The tunnel is driven by a 88kW motor and reaches a maximum flow velocity of 65m/s. The model was fixed on a ground board with the wheels attached to it. The board itself has a rounded leading edge and was installed 85mm above the tunnel ground floor plane. The test set-up is described in Fig. (2). The blockage of the model in the test section was 7.2%, [4]. The experiments in this facility were mainly used to investigate the model behavior under test conditions and to get a better understanding of the overall truck aerodynamic. The maximum achievable tunnel velocity with the model build in was 55m/s ( $M = 0.16$ ) which corresponds to a Reynolds number of 630,000 based on the model width.

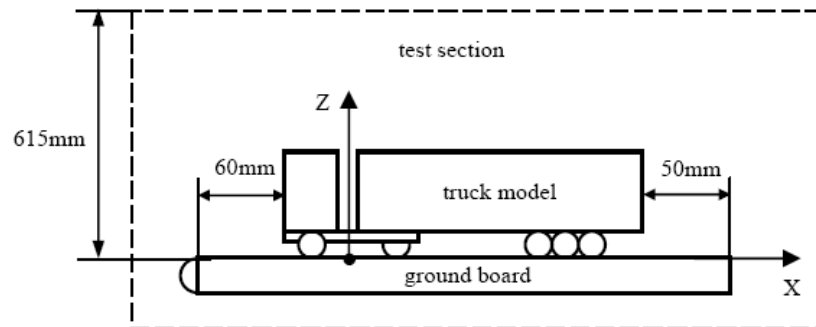


Figure 2: Test configuration in 1MG.

### 3.2 PIV set-up

For the measurement of the instantaneous flow field around the truck model, a two-component PIV system was used. The light sheet with a thickness of approximately 2-4mm was produced by a Q-switched dual oscillator Nd:YAG laser. A PCO Sensicam QE CCD camera with a resolution of 1376 x 1040 pixels and a dynamic range of 12 bit was used. The camera was equipped with a 50mm focal lens. Droplets of DEHS (Di-Ethyl-Hexyl-Sebacat) with a mean diameter of 1 $\mu$ m were used as tracer particles.

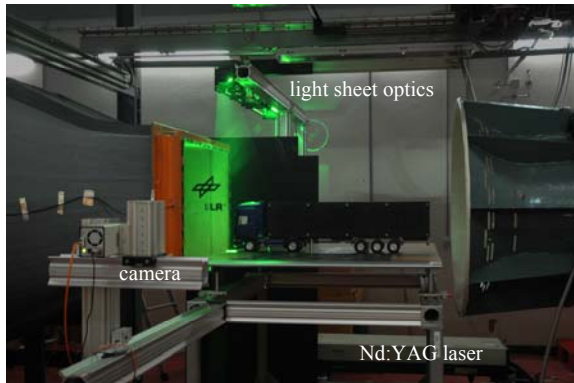


Figure 3: PIV set-up in 1m-tunnel.

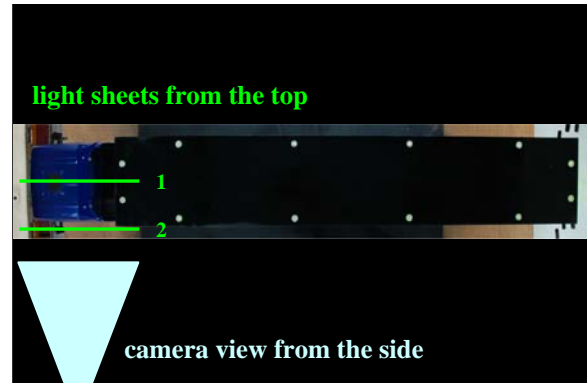


Figure 4: Camera and light sheet position.

The evaluation of the PIV images was done using the PIVview software. The multi-grid interrogation algorithm was used for cross-correlation of the particle images in conjunction with double-correlation. For the calculation of the average velocity field 320 instantaneous velocity fields were taken into account. Further information about the PIV technique can be found in [1, 2].

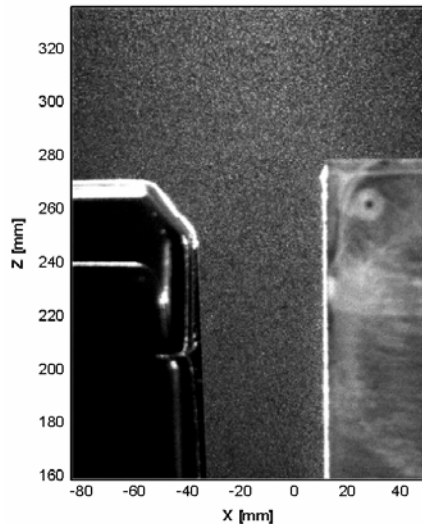


Figure 5: Particle image.

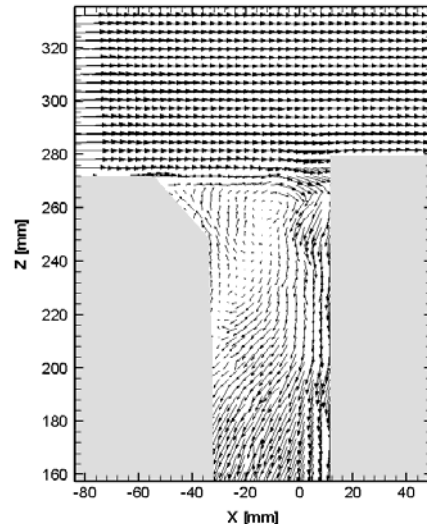


Figure 6: Calculated vector field.

For PIV, the test configuration as described in Section 3.1 was used. All PIV measurements described in the following were made at a yaw angle of 0°. The investigations can be divided into three different parts: The field of view covers 1) the whole truck length 2) the gap area 3) the mirror region.

All investigations were carried out with the light sheet installed vertical to the ground board in driving direction. The camera was viewing from the side as shown in Fig. (3) and Fig. (4). For the first two cases the light sheet was positioned at the symmetry line of the model (green line 1 in Fig. (4)). To visualize the flow field along the full truck length the light sheet optics and the camera system had to be shifted seven times.

The visualization of the flow field behind the mirror was realized with the light sheet positioned to the middle of the mirror width (green line 2 in Fig. (4)). Due to reflections coming from the sharp edges of the surface the left cab side was taped. This will be explained more detailed in the presentation of the test results.

An example of the evaluation of PIV is given in Fig. (5) and Fig. (6). Fig. (5) shows a particle image for the visualization of the gap region with roof and side extenders not installed. The calculated velocity vector field is given in Fig. (6). It has to be considered that only half of the vectors were shown for a more clear presentation of the vector field.

### 3.3 Test results (1MG)

The investigation started with the visualization of the flow field along the symmetry plane of the truck model with camera view direction from the side. All results described in the following were made at zero yawing angle and at a Reynolds number of 630,000.

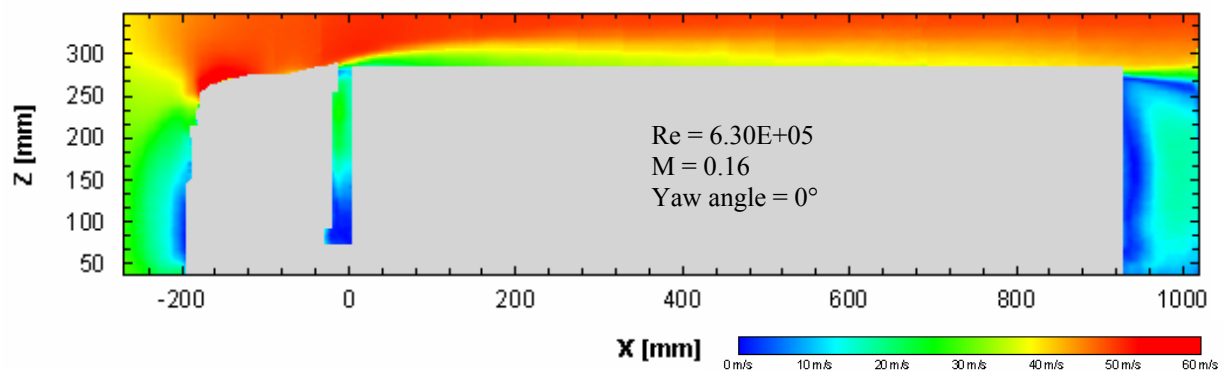


Figure 7: Mean velocity contour plot of the truck model with mounted roof and side extenders.

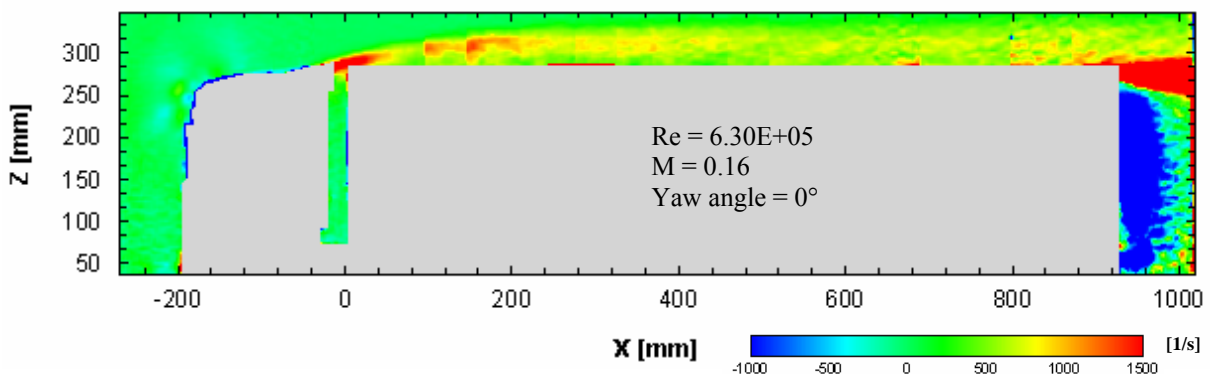


Figure 8: Mean y-vorticity contour plot of the truck model with mounted roof and side extenders.

The flow field was subdivided into seven measuring planes of the same size. The results of all planes were assembled to get the data of the whole flow field in one plot as shown in Fig. (7) and Fig. (8). The slow velocity regions in the stagnation area of the tractor front, in the gap

region between tractor and trailer and in the wake can be identified. The flow stagnated at the tractor front and is accelerated strongly along the roof (see Fig. (9)). Reduced velocities can be seen in the gap region due to the effect of the extenders. The wake shows vortices separating from the trailer roof and behind the trailer base. Both vortex fields are counterrotating. Due to the small distance between the trailer end and the end of the test section the access to the wake was limited. Therefore the results can not be presented in detail.

The flow in the area of the gap shows a significant influence of the roof extender which shields the gap region but results in a high deflection of the free stream flow. Fig. (8) shows turbulent structures separating from the trailing edge of the roof extender. The vortex structures still exist up to the trailer end. This effect is due to the imperfect adjustment of the roof extender and can also be seen in Fig. (10), the visualization with smoke. A continuous laser was used to generate a light sheet at the symmetry line of the truck. With a smoke lance installed at the center position inside the wind tunnel nozzle smoke was blown directly to the model front. The result of the smoke visualization of the gap flow without extenders is completely different.

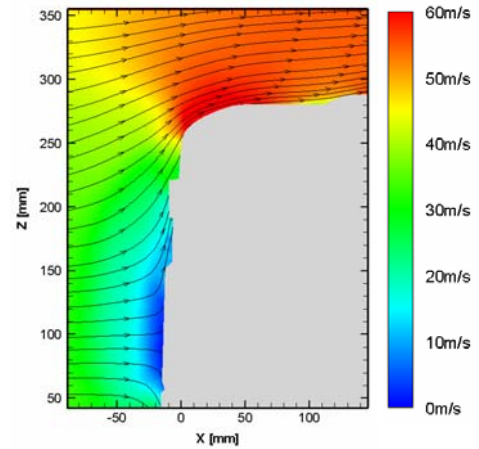


Figure 9: Mean velocity field of the truck front.



Figure 10: Smoke visualization with and with no installed roof and side extenders.

The air flows parallel to the trailer roof whereas no deflection can be detected. The installation of tractor extenders is typical for modern trucks. The drag reducing potential of these devices was also discussed in [6].

In the following the results of the gap flow visualization with PIV are shown for two configurations: 1) The configuration with installed extenders and a gap width of 27mm 2) the configuration without extenders and a gap width of 48mm. The results are given in Fig. (11) and Fig. (12). Velocities of up to only half of the values of the free stream flow are achieved in the upper gap region when the cab is equipped with extenders. The velocities in the bottom gap area are close to zero. Without installed extenders the flow is stagnated from the trailer front and diverted downwards into the gap. In some regions of the gap the flow achieves velocities equal to the free stream velocity. The stream traces in the left images of Fig. (11) and Fig. (12) can not be seen as streamlines but they indicate the different flow structures. So the vortex behind the trailing edge of the cab is visible (Fig. (12)). The right images show a zoomed view with a vector field describing the velocity components. For a better presentation only half of the vectors are shown there.

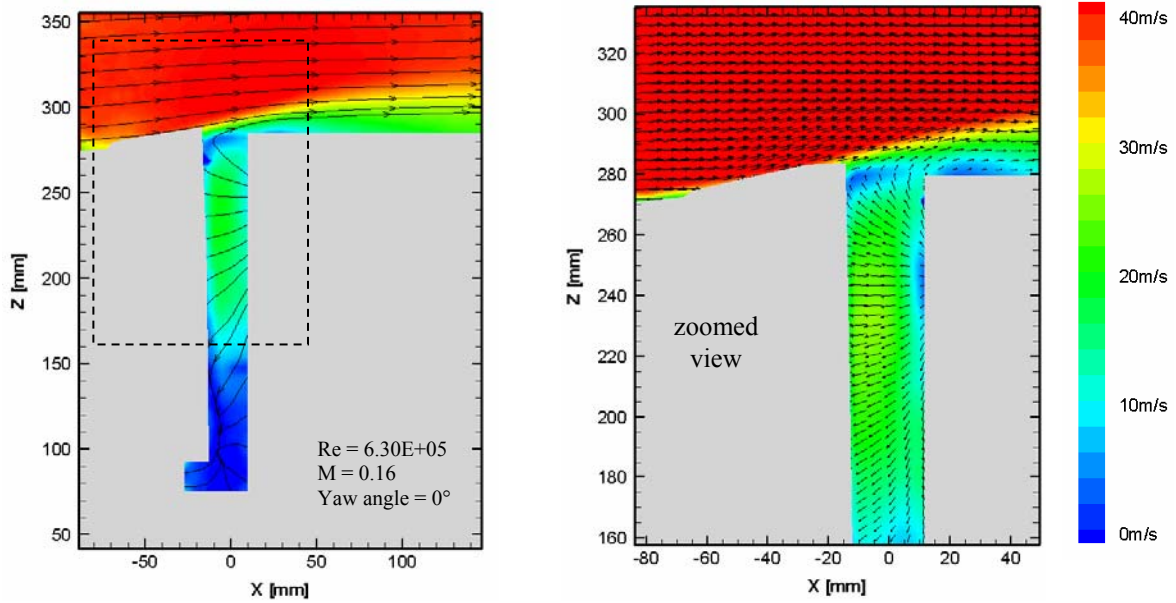


Figure 11: Mean velocity field in the gap region with mounted roof and side extenders.

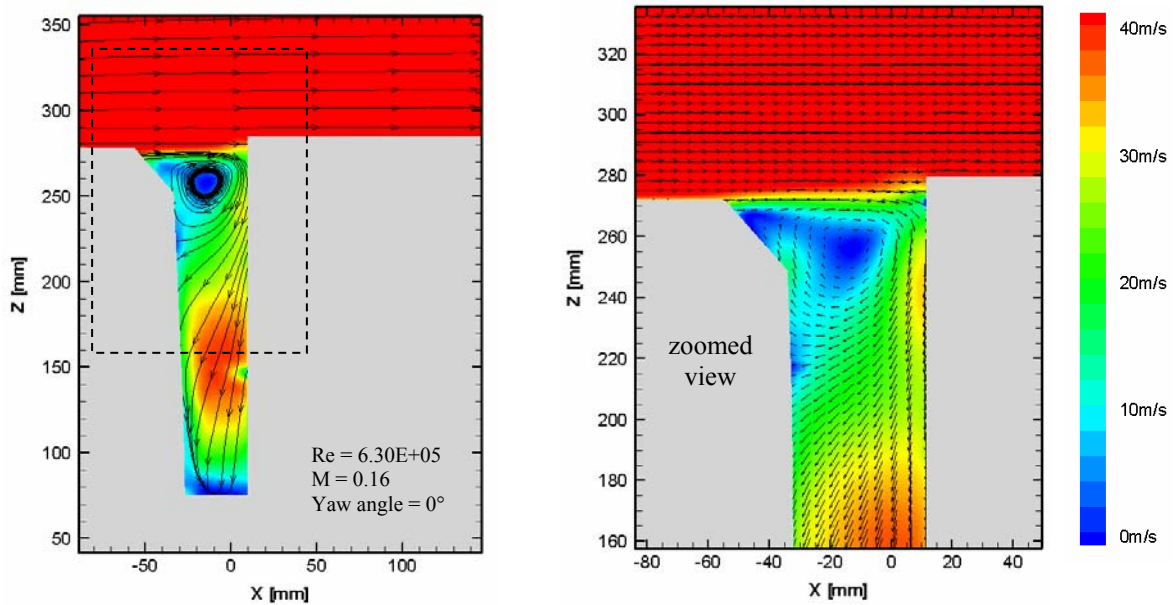


Figure 12: Mean velocity field in the gap region without roof and side extenders.

The following results show the flow field behind the driver side mirror and were made with roof and side extenders installed. Tape was attached to the cab side to minimize laser sheet reflection. The particle image in Fig. (13) shows the remaining reflections caused by the sun shield and the mirror. In Fig. (14) these areas are left blank. The results show a deflection of the flow up- and downwards the mirror face. The mirror acts as stagnation area with a wake behind. Inside the wake two counterrotating vortices are generated (see also Fig. (15)).

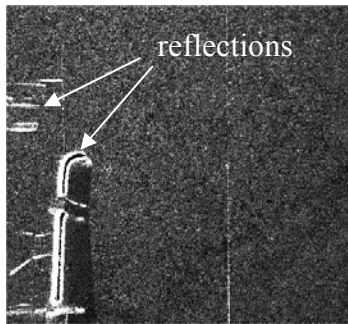


Figure 13: Particle image.

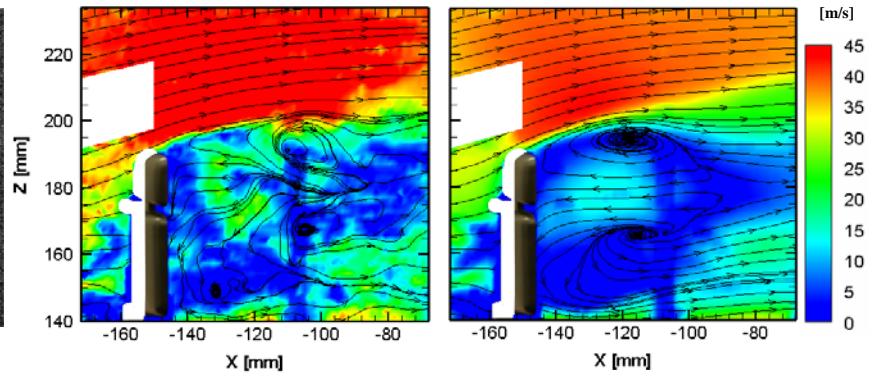


Figure 14: Mean velocity of the instantaneous magnitude field (left) and the average (right) of the flow field behind the mirror.

Both vortices are located in the upper half of the wake. The strength of the upper vortex is much higher. A more detailed discussion of the aerodynamic effect of a side mirror can be found in [5].

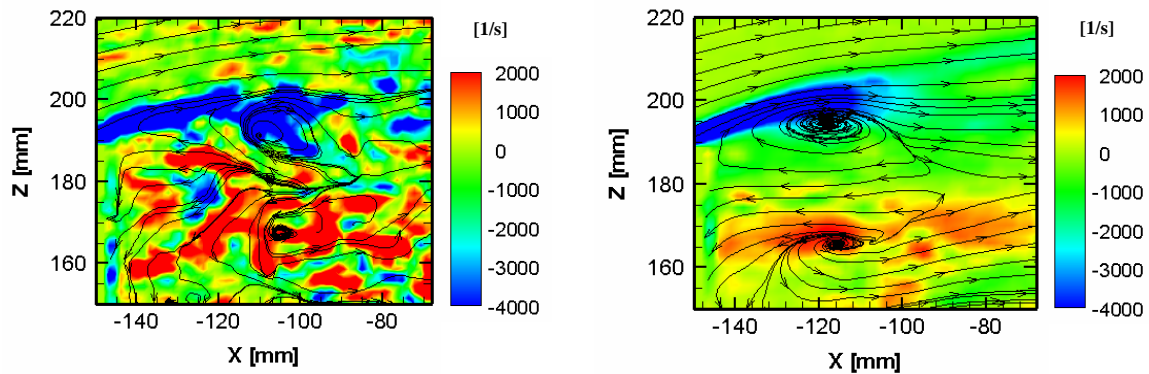


Figure 15: Instantaneous y-vorticity field (left) and averaged y-vorticity field (right) of the mirror wake.

## 4 FORCE MEASUREMENTS IN THE CRYOGENIC WIND TUNNEL

### 4.1 Test configuration (KKK)

In the cryogenic wind tunnel of DNW in Cologne force measurements were conducted at Reynolds numbers up to 1,000,000. The 2.4m x 2.4m closed wall test section with a length of 5.4m allows a maximum mach number of 0.325 at 300K. The tunnel temperature can be reduced up to 100K. In the present case the measurements were performed at ambient temperature only. The maximum mach number at  $Re = 1,000,000$  was  $M = 0.25$  (at 293.15K) with a low blockage of 0.84% at zero yawing angle, [4]. The description of the test set-up is given in Fig. (18). The installed model in KKK can be seen in Fig. (17) and was only tested with installed extenders. For the measurement of the forces and moments a conventional external balance was used.



Figure 17: Truck model in KKK.

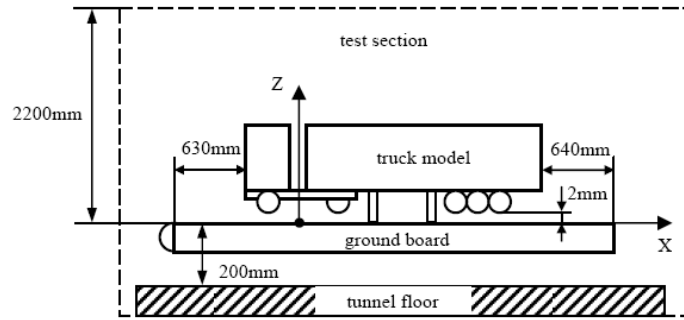


Figure 18: Test configuration in KKK.

#### 4.2 Test results (KKK)

A Reynolds number dependency was investigated at two different yawing angles ( $0^\circ$ ,  $-10^\circ$ ) at ambient temperature between  $Re = 400,000$  and  $Re = 1,000,000$ . An investigation starting from lower Reynolds numbers could not be performed because the tunnel can not run constant below a mach number of 0.1. A Reynolds number effect could be detected for the lift and pitching moment coefficient (see Fig. (19) and (20)). The analysis of the results showed a low fluctuation of these coefficients in the range of  $Re = 400,000$  and  $Re = 500,000$ . The effect disappear at Reynolds numbers higher than 500,000. For the remaining coefficients, no Reynolds number effects were detected.

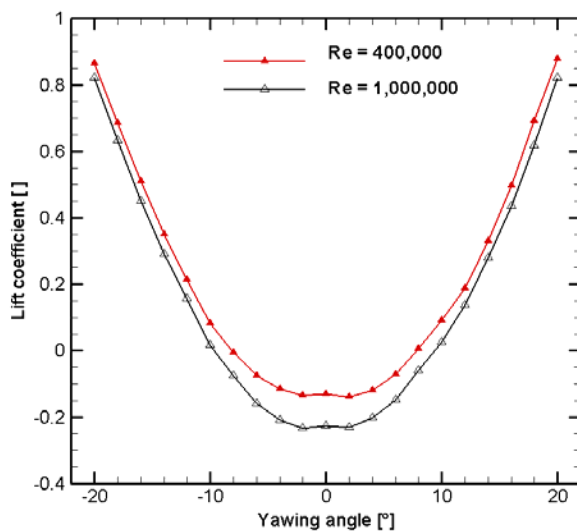


Figure 19: Lift coefficient.

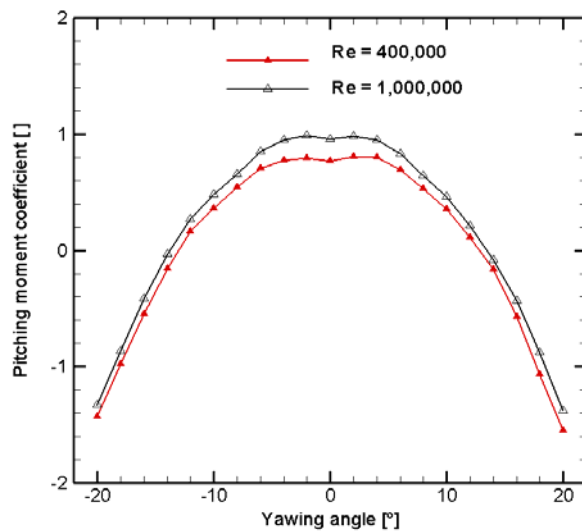


Figure 20: Pitching moment coefficient.

The drag and side force coefficient show a symmetric flow behavior of the model at different yawing angles (Fig. (21) and Fig. (22)). The reproducibility of the results was tested and can be confirmed. No hysteresis effects were detected.

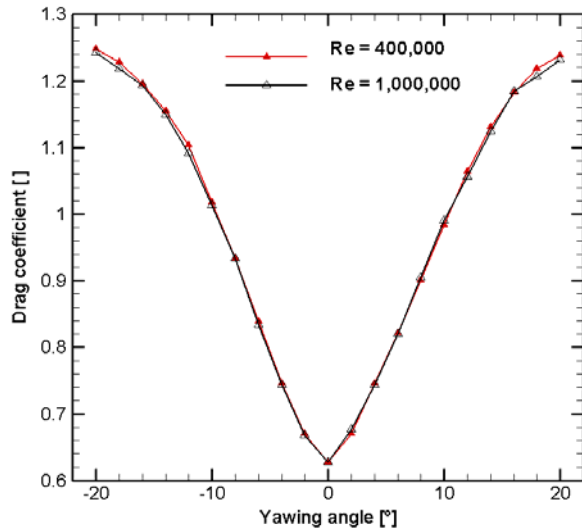


Figure 21: Drag coefficient.

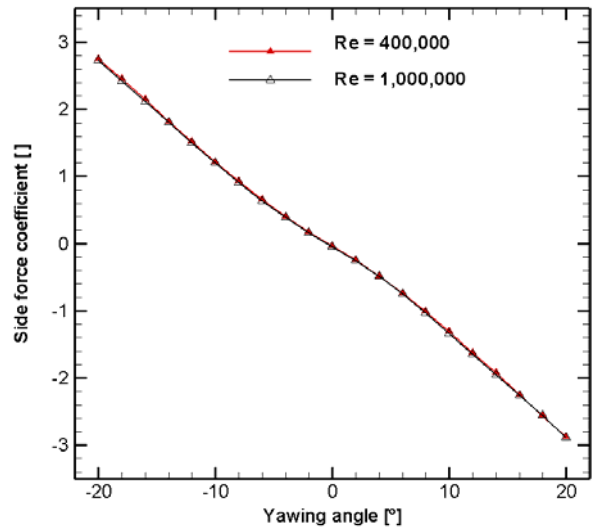


Figure 22: Side force coefficient.

## 5 PRELIMINARY TEST IN THE WATER TOWING TANK

The goal of this study is the reduction of the aerodynamic drag of a tractor-trailer configuration. Therefore a detailed truck model is used. To enable a realistic investigation of a ground vehicle the simulation of the underbody flow is necessary. Therefore, a new test set-up was planned in the water towing tank of DLR Göttingen (WSG).

The test facility with a test section of 1.1m x 1.1m has a length of 18m. The 7kW direct current motor allows an infinitely variable control of the test rig velocity up to 5m/s. At this maximum velocity and a water temperature of 293K a Reynolds number of 736,000 (based on the model width of the truck model) can be achieved.



Figure 23: Installed truck model in WSG.

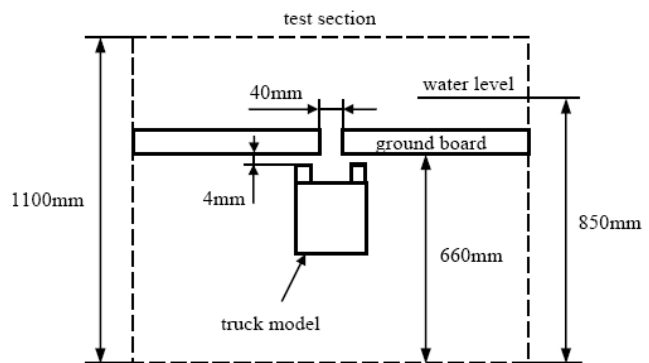


Figure 24: Sketch of the test set-up.

At first the flow field of the truck model, especially the wake field, shall be investigated. It was assumed that no disturbing effects may be produced from the clamping of the model. Therefore, the model was fixed in overhead position with the fixture attached to the underbody as shown in Fig. 23. An intermediate floor was used to enable the simulation of the ground flow. The floor is subdivided in two parts by a gap. All geometric parameters of the ground (width of the gap, height of the active test section, etc.) can be adjusted individually. The ground has a length of 6m and is spanned over the full tunnel width.



Force measurements were performed with the model installed as depicted in Fig. (23) and Fig. (24). At a rig velocity of 3m/s and a water temperature of 288K a Reynolds number of 450,000 has been achieved. A blockage of 6.14% can be stated for  $\psi = 0^\circ$ , [4].

The forces and moments were measured with an external 6-component piezo balance from Kistler. During each test run the data were sampled at a rate of 1kHz. The average of the measured signals was calculated for a defined region of the intermediate floor where the average velocity signal was nearly constant. The average of 30 runs provided a drag coefficient of  $C_D = 0.643$ . The results of the force measurement in KKK at zero yawing angle and at the same Reynolds number provided a drag coefficient of  $C_D = 0.622$ . It was not expected that the values are so close together. First of all, the experiments in the water towing tank are different to the measurements in KKK because the ground floor effect is considered. Secondly the installed floor moved slightly due to the pressure field of the model.

## 6 CONCLUSIONS AND OUTLOOK

The experiments gave a first impression about the flow behavior of the truck model. These results allow the further development of the truck model and the test set-ups. Furthermore the test sections which will be used for future investigations of drag reducing devices were presented. This describes the available options for the realization of this research program.

In this context it has to be noted that the 1M-Tunnel is not really suitable for investigations with a 1/15<sup>th</sup> scale truck model due to the high blockage of more than 5% and the short test section length. But the facility will be used for preliminary testing of drag reducing devices and their efficiency.

Detailed investigations will be performed in the water towing tank. For further testing the intermediate floor will be improved to avoid motion due to the pressure field of the truck model and the test section will be increased to reduce blockage. For this the distance between tunnel ground and intermediate floor can be increased. Furthermore it is planned to enable rolling wheels during the test runs.

In addition to the investigations of the main flow field of a truck the underbody flow shall also be investigated in future. The potential of the underbody region for drag reduction should be very high. For these investigations a second floor is available without gap. The model can be fixed at the roof to avoid the disturbance of the underbody flow.

## REFERENCES

- [1] J. Westerweel. *Fundamentals of digital particle image velocimetry*. Laboratory for Aero & Hydrodynamics - Delft University of Technology, Delft, Netherlands, 1997
- [2] M. Raffel, C.E. Willert, J. Kompenhans. *Particle Image Velocimetry – A practical Guide*, Springer, 1997
- [3] Official Journal of the European Communities. Council Directive 96/53/EG, 1996
- [4] Society of Automotive Engineers. *SAE Wind Tunnel Test Procedure for Truck and Buses*, SAE J1252 (1981)
- [5] Truck Manufacturers Association. *Test, Evaluation, and Demonstration of Practical Devices/Systems to Reduce Aerodynamic Drag of Tractor/Semitrailer Combination Unit Trucks*. Final Report, 2007
- [6] B.L. Storms, J.C. Ross. *Detailed Experimental Results of Drag-Reduction Concepts on a Generic Tractor-Trailer*. Annual Progress Report for Heavy Vehicle System Optimization Program, U.S. Department of Energy, 30-48, 2006

## SHAPE OPTIMIZATION IN TRAIN AERODYNAMICS

Astrid H. Herbst\*, Johannes Mauss<sup>†</sup>, Jan Heiland<sup>†</sup> and Alexander Orellano<sup>†</sup>

\* Bombardier Transportation, Department of Aero- and Thermodynamics,

SE-72173 Västerås, Sweden

e-mail: astrid.herbst@se.transport.bombardier.com,

<sup>†</sup> Bombardier Transportation, Department of Aero- and Thermodynamics,

D- 16761 Hennigsdorf, Germany

e-mails: johannes.mauss@de.transport.bombardier.com,

jan.heiland@de.transport.bombardier.com,

alexander.orellano@de.transport.bombardier.com

**Keywords:** Aerodynamics, Shape optimization

**Abstract.** *The importance to lower the aerodynamic resistance of rail vehicles to reduce the energy consumption is increasing with rising energy prices and the vital necessity to reduce the CO<sub>2</sub> production to slow down the climate change. This study shows the method which is being utilised within Bombardier for the development of a new generation of regional and high-speed trains to increase the aerodynamic performance related to head-pressure pulse, drag and cross-wind stability.*

## 1 INTRODUCTION

The final design of a train is an optimization balancing various requirements. These can originate from specific customer requests which in their turn are formulated to meet the requirement of the transport market in a specific region. Further, legal specifications e.g. ensuring the health of passengers and staff or ensuring the interoperability between different countries must be obeyed.

Designing the outer shape of a train has major impact on the aerodynamic performance of the vehicle. Traditionally, a way of exploring the set of design modifications with regard to their aerodynamic performance has been to check them experimentally in the wind tunnel. Here the iterative development of further designs is based on theory and engineering skills. However, this approach is rather costly and time consuming. Further, in many cases due to the large number of possible designs it is unlikely that the truly optimal design in the sense of Pareto can be found without assistance of automatic tools. Implementing the approach of automated optimization in train aerodynamics Bombardier Transportation pursues the target of overcoming several disadvantages of the common design process. On the one hand side the conventional iteration between designing and evaluating the model is speeded up and directed by an optimization algorithm; on the other hand the aim is not to fulfil all given constraints and requirements but to deliver the optimal solution. The increasing performance and price drop of today's computers facilitate the use of modern CAE based optimization tools for determining the optimal parameters for the external shape of trains.

Automated shape optimization requires a parameterized model, which is manipulated by altering the design variables until the optimal set of geometry defining parameters are found. Therefore the model is evaluated in a CFD simulation and the generated data together with the current parameter setting enable the optimization algorithm to calculate an improved parameter set for the next iteration.

In order to fully exploit the possibilities of this approach

- a fully automatic loop including the generation of candidate shapes based on a parameterized geometry
- the preparation and generation of a computational mesh and
- the evaluation of the design

is required.

One challenge is to organize all tasks in a manner so that they can be integrated into one optimization loop without requiring manual input. Up to the present stage, the process of preparing a simulation included a lot of manual manipulation starting with the preparation of the model for CFD applications in CATIAV5, the mesh generation process and the simulation including pre- and post-processing.

Furthermore the whole complexity of designing a train is to be considered in the loop of optimization including ergonomic requirements for integrating the drivers cab, crash structure concept and integration, ergonomic constraints on the visibility of signals at the track taking into account sitting and/or standing drivers, bogie movements and Industrial Design aspects.

The parameterized model should be capable to reproduce all important features like different fronts, spoilers, pantographs, bogie cut out and cross sections, while a-priori integrating most of the requirements mentioned above. Additional constraints like the maximal extensions of the shape are met during the optimization by restricting the parameters respectively.

With this approach, a mathematical optimization algorithm such as the Simplex algorithm, gradient-based methods or genetic algorithms can be utilized for the optimization of the shape design. This requires the optimization problem to be defined with an objective function which includes the costs of the design that one wants to minimize using design variables. The conditions which have to be satisfied are introduced as constraints. The goal is to identify the best design under given conditions. However, it has to be kept in mind that the term “best” is relative and depends on the parameterization and an even better solution may exist.

## 2 PROCESS INTEGRATION AND OPTIMIZATION ALGORITHM

### 2.1 Process integration

A typical setup for an optimization process focusing on an aerodynamic problem includes the creation and configuration of the parameterized geometry, the generation of the mesh for calculation, the calculation and computation of the relevant variables and the computation of an optimized parameter setting using an optimization algorithm (see Figure 1). Note that all components have to be set up so they can be integrated into one process flow automatically without manual manipulation. It has to be kept in mind that the stability with which the different components perform has significant impact on the outcome of the optimization as the major part of the designs have to be evaluated in the correct way in order for the optimization algorithm to converge towards the true minimum. A distinct feature of any flow design process is that it is computationally costly and particularly time consuming if the number of degrees of freedom is high. Therefore a reliable and efficient tool is needed in order to determine which design under the current conditions is suited best.

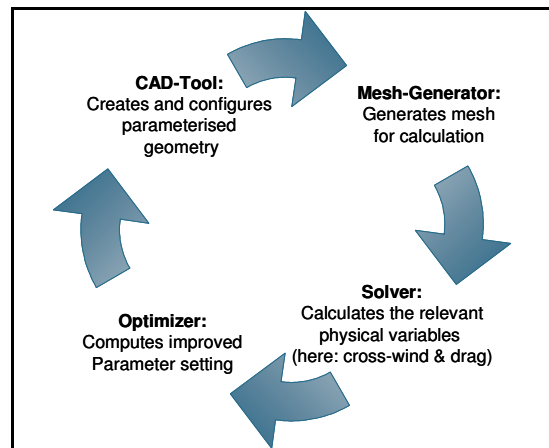


Figure 1: Optimization process flow

The heart of the optimization is the tool ModeFrontier by ESTECO. The optimizer used is ModeFrontier 4.0.2 which provides a variety of different algorithms for direct optimization and for design of environment (DOE) applications as well as means for evaluating and post processing the generated data. In addition it manages the whole file system generated during the optimization, which is very useful for handing over data from one tool to another as well as for error tracing.

The implementation was deduced from a general approach for shape optimization on the base of a parameterized model. All design variables and their ranges are initially defined within ModeFrontier and only the current setting is then applied to the CATIA V5 CAD-model through a direct interface. The resulting CAD model is transferred via a SSH connection to a workstation or cluster, where batch scripts call the respective tools to prepare the mesh for the evaluation in the software tools e.g. START by Principia and Prosurf, ProAM and CCM+ by CD Adapco. After the evaluation the outputs are transferred back to ModeFrontier, which evaluates the final target function in Matlab and assigns the values to internal output variables. This information together with the current parameter setting is fed back to the optimizer, which generates, by means of the collected data, a new improved parameter setting for the following iteration.

## 2.2 Optimization algorithms

The optimization algorithms provided in ModeFrontier have been implemented by the company ESTECO which is distributing the software. The two optimizers chosen are the Simplex algorithm, following the approach by Nelder & Mead [2] and the genetic algorithm MOGA-II [3]. The version available for the simplex in ModeFrontier has been updated in order to be applicable also for discrete variables and constraints. In the following the description of the algorithm according to the documentation in ModeFrontier is given.

A simplex is a polyhedron containing  $n+1$  point in an  $n$ -dimensional space. The SIMPLEX is initialized by  $n+1$  initial designs. The scheduler follows an algorithm for moving the initial points along with their function values, closer to the optimal point of the objective until the scheduler either exceeds its maximum number of iterations or converges. The movement of the simplex is given by three operations: "Reflection", "Expansion" and "Contraction". In the reflection movement, the vertex corresponding to the worst value of the objective function is reflected to the opposite face to obtain a new value. When the reflection movement gives a new minimum, it can generally be expected to decrease the function value further by moving along in the same direction with the simplex. When the reflection movement gives a new point that is worse than all the other vertices except the worst, the simplex is contracted by exchanging the new point with the worst point. SIMPLEX is a sequential algorithm for single objective optimization and cannot be parallelized.

Suited for multiobjective optimization is a genetic algorithm is based on principles derived for the explanation of genetic processes in nature such as selection, mutation and cross-over and applies them formulating an algorithm for optimization problems. The optimization algorithm used was the generic algorithm MOGA-2, which computes new designs generation by generation. Each member of a new generation is derived from its direct ancestors by randomly mutating and crossing over their genomes, in terms of their defining design variables. In the case that the successor is not worse regarding all objective functions replaces its parent, the natural procedure of selection.

## 3 SINGLE-OBJECTIVE OPTIMIZATION WITH REGARD TO HEAD-PRESSURE PULSE

### 3.1 Objective

As a pilot project for this approach, an optimization of the shape with respect to one single objective function has been performed. The objective function is evaluated with respect to head pressure pulse. A train's front passing by generates an increase in pressure in front of it

and a decrease in pressure at the sides of the nose. Therefore due to the changing pressure levels, pressure loads e.g. on the surrounding infrastructure of the track will be generated. The allowed pressure changes are restricted by the Technical Specification for Interoperability (TSI) and can also be subject to further restrictions due to specific requirements of the operator.

The optimization with regard to head pressure pulse has been carried out in the project “Front shape and slipstream for wide body trains at higher speeds” within the framework of Gröna tåget. The goal is to generate a design which has a good performance both with respect to slipstream and with respect to head pressure pulse since the front for most modern trains may well operate as the rear as well. The objective is to give input to front design including shape constraints. This includes the front design considerations such as space envelope, crash structure, ergonomic constraints such as the visibility of signals at the track and the space available for the passenger compartment. These geometrical constraints have been implemented partly as simple bounds of the parameters and partly as constraints in the current approach.

The doubledecker train has been chosen as the first geometry to develop and test this approach. This geometry is particularly suited as reference data from traditional ways to improve the design with regard to head pressure pulse is available. Further, it is a challenging test case with regard to fulfil the requirements posed by TSI.

The objective function to be minimized during the optimization loop is the amplitude of the head pressure pulse. Figure 2 illustrates schematically how the pressure distribution in front of a train usually varies as a function  $x$ -axes. The measurement positions are specified in TSI. The pressure is measured at 2.5 m distance from centre track at seven heights: 1.5 m, 1.8 m, 2.1 m, 2.4 m, 2.7 m, 3.0 m and 3.3 m. The objective function is the maximum of head pressure pulse amplitude  $\max \Delta c_p$  measured at the 7 measurement positions:

$$\max \Delta c_p = \max_{y_i} \Delta c_p, y_i \in \{1.5, 1.8, 2.1, 2.4, 2.7, 3.0, 3.3\}m \quad (1)$$

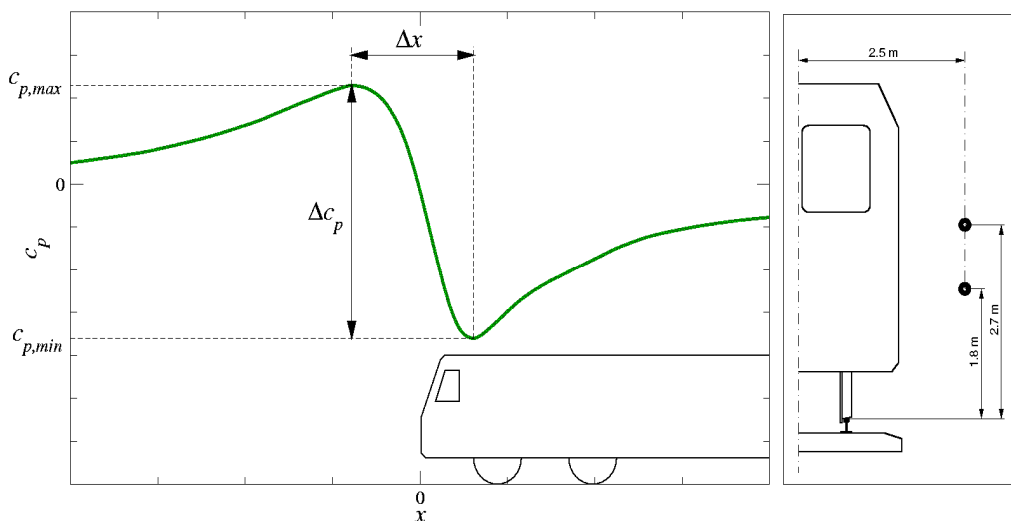


Figure 2: Head pressure pulse amplitude and average pressure gradient and position of measurement locations parallel to the rail

### 3.2 Parametric and computational model

The parameterization has high impact on the outcome of the optimization. An optimization is only capable to identify the best design with respect to the parameterization. Therefore, it is important that the parameterization captures all relevant features with regard to the optimization problem. However, the number of parameters should be as small as possible to keep the computational effort in affordable limits.

Modifications of the external shape pertain to the shape of the front up to the first bogie keeping the cross sectional area at the connection to the first car constant. The parameterization has been carried out in CATIA defining several design variables which control the shape defining splines.

The challenge for shape optimization involving aerodynamic computations is to resolve the structures which are significant in order to capture the trends. In order to develop an efficient method, two optimization loops have been implemented. One evaluates the objective function based on the solution for the inviscid flow at low computational cost using surface preparation in PROSURF, generation of surface mesh using PROAM. The inviscid flow calculation is carried out using the panel solver START by the company Principia. For higher accuracy the second loop evaluating the objective function based on a RANS calculation at the cost of moderate computational effort has been created using the polyhedral mesher in STAR-CCM+ and the RANS computation in STAR-CCM+.

The parametric models were generated in CATIA, one for the use in the loop with the panel method START and one for the loop with STARCCM+. Both models are controlled using exactly the same parameters. The model for the use with the inviscid solver START contains less details as flow separation cannot be predicted well with such a method. Therefore the bogie cutouts have been closed, the bumpers have been excluded and the cutout for the coupler has been closed. Apart from that, both models are the same (see Figure 3).

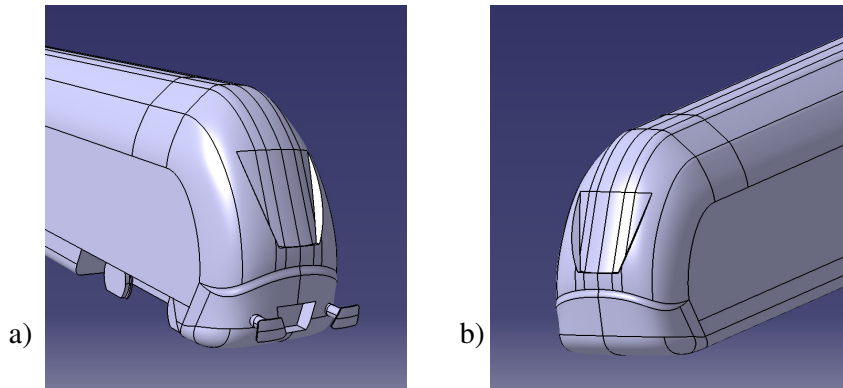
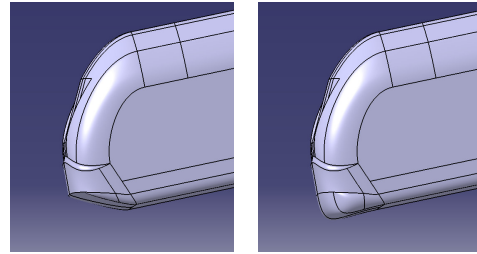


Figure 3: Parametric model for the use with (a) starccm+ and (b) START.

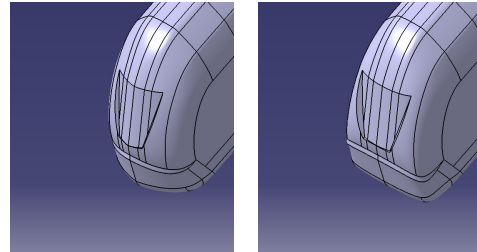
Initially, 10 parameters were subject to the optimization. To illustrate the effect of the different parameters, Figure 4 shows the change of two parameters at a time from their lower bounds to their upper bounds. The bounds of the parameter ranges, that mainly should ensure both wide design variety and the compliance with the constraints, were set in respect to maximal feasibility and stability in CATIA. However, in order to enlarge the search space the boundaries were relaxed during the optimization process.



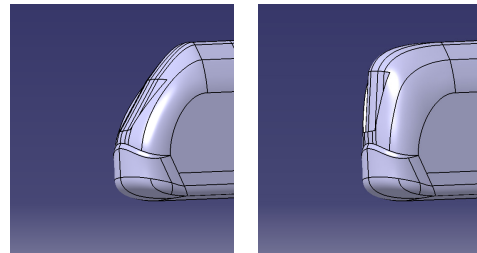
**tg\_down\_tip**  
**tg\_down\_vagon**



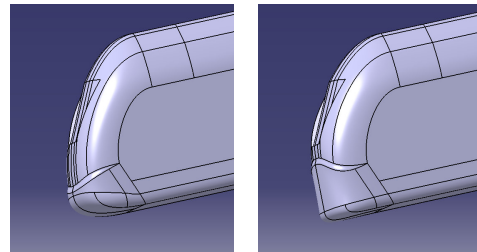
**lat\_tg\_center**  
**lat\_tg\_side**



**tg\_up\_tip**  
**tg\_up\_vagon**



**nose\_v**  
**front\_v**



**flex\_v**  
**flex\_h**

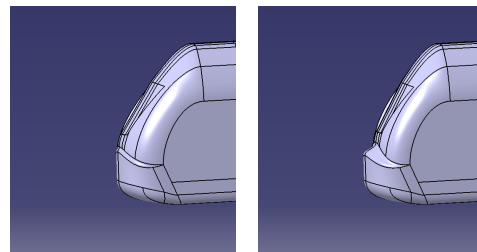


Figure 4 Illustration of influence of the ten controlling parameters. Two parameters have been varied between the picture in the left column and the corresponding picture in the right column.

For the computation in both START and STAR-CCM+, a grid resolution study has been carried out. Here the goal in terms of the optimization procedure is to identify a suitable resolution which preserves the aerodynamic performance trends with the minimum number of grid points necessary in order to reduce the computational power required. As a series of computations is carried out, some attention has to be paid to this. For the prospective design candidates computations with higher resolution have been carried out.

For the optimization loop using STAR-CCM+ version 3.02.003, polyhedral meshing methodology with prism layers to increase the resolution close to the walls has been applied. In order to model the turbulence, a k-epsilon turbulence model in a high-Reynolds number formulation has been used. The model has been chosen due to the higher robustness compared to e.g. a hybrid formulation for the wall model. The advective terms in the governing equations as well as the corresponding parts in the equations for the turbulence modeling are approximated using second order upwind-differences. A half plane of a one car model with a symmetry boundary condition has been computed in order to reduce the computational effort. Since the track bed has significant impact for the correct computation of the head pressure pulse [1], the track bed according to TSI has been included.

For the optimization both the simplex algorithm and genetic algorithms have been used.

### 3.3 Results

In order to check the improvement gained through the optimization procedure, the best design resulting from the optimization procedure is compared to the double decker train with head shape A5 (see Figure 5 for comparison of the shapes). This front design was the best result from a previous optimization campaign, which was based on an iterative process involving both numerical tools and measurement results from the wind tunnel. This optimization was not based on a mathematical algorithm but on engineering skills and physical understanding.

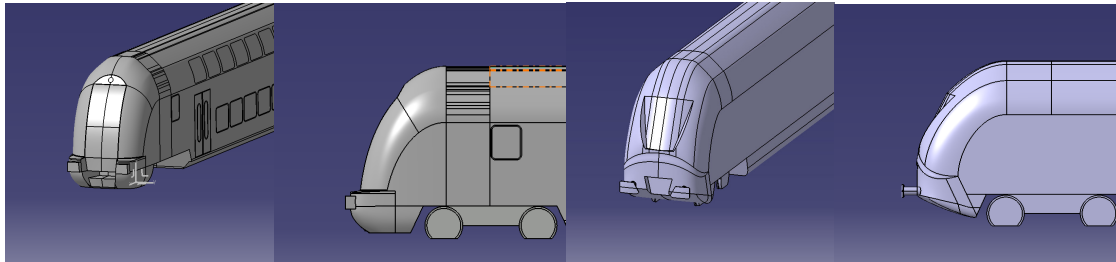


Figure 5: Best new design from optimization procedure (right hand side) compared in shape to the best previous design (left hand side, head shape from manual optimization). The improvement for the new design is 3,8%.

Both designs have been meshed and computed in ccm+ with the same computational domain, boundary conditions, resolution and setup. The resolution was a fine resolution with a polyhedral mesh consisting of 900000 cells. Both designs basically fulfil the same constraints. However some have been updated since the last campaign when A5 was developed. The train direction indicator is now wider due to customer request which puts on a further constraint. The improvement of the new design resulting of the optimization process presented is 3,8 %, with  $\Delta C_p=0,2922$  at the critical height of 2,1 m for the head shape A5 and  $\Delta C_p=0,2811$  at the critical height of 1,8 m (TSI) for the new design.

## 4 AEROEFFICIENT MULTIOBJECTIVE OPTIMIZATION FOR VERY HIGH SPEED TRAINS

### 4.1 Objective function for energy consumption reduction and cross-wind stability

The overall goal of the aerodynamic optimization for very high speed trains is to design a train which is as efficient as possible (*AeroEfficient*). In particular the objectives for the work presented here are the reduction of aerodynamic drag and the increase of stability with respect to cross-wind. Reduction of aerodynamic drag saves energy demand of trains and reduces costs. Limiting drag and maximizing stability also increase acceleration, which reduces traveling time.

The energy necessary to run a train at high speed is predominantly dependent on the aerodynamic resistance. The reduction of the aerodynamic drag running the train at 300km/h has therefore been chosen as goal function for the optimizer.

The coefficient for the aerodynamic drag has been calculated in a RANS simulation in STAR CCM+ based on the following formula:

$$c_d = \frac{F_x}{0.5 \cdot \rho \cdot V^2 \cdot A} \quad (2)$$

Here  $F_x$  is the force in driving direction,  $\rho$  is the air density,  $V$  denotes the driving speed and  $A$  represents the reference area which is standardized to be  $10m^2$  within the train aerodynamics community [1].

Maximising the load on the most critical bogie related to derailment has been chosen to be the goal for increasing the cross-wind stability.

The behaviour of a train under cross-wind is a function of the angle of attack of the accumulated cross wind and air stream. Since it is too expensive to compute the so called characteristic wind curve in full, only one but characteristic point of the curve was taken.

The respective aerodynamic coefficients, computed in a RANS simulation in STAR CCM+, are passed over to a quasi static multi body simulation tool called "P1" which models the train with two bogies, two wheel sets and the car body. This system features in total twelve degrees of freedom and is able to capture the displacements between the car body and the bogies (secondary suspension) and between the bogies and the wheel sets (primary suspension). Due to the displacements in the suspension the restoring moment is reduced and cross-wind stability decreases. The model incorporates the most relevant characteristics of cross-wind stability and is used during concept phase within the Bombardier process. The common criteria for judging the cross-wind stability is wheel unloading. The higher the wheel load under cross wind condition the more cross-wind stable is the vehicle.

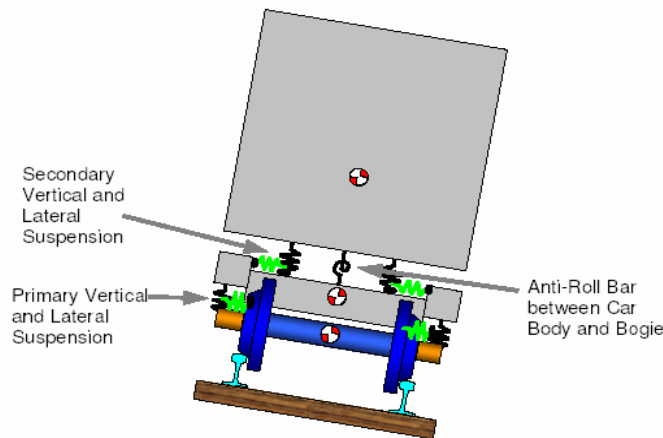


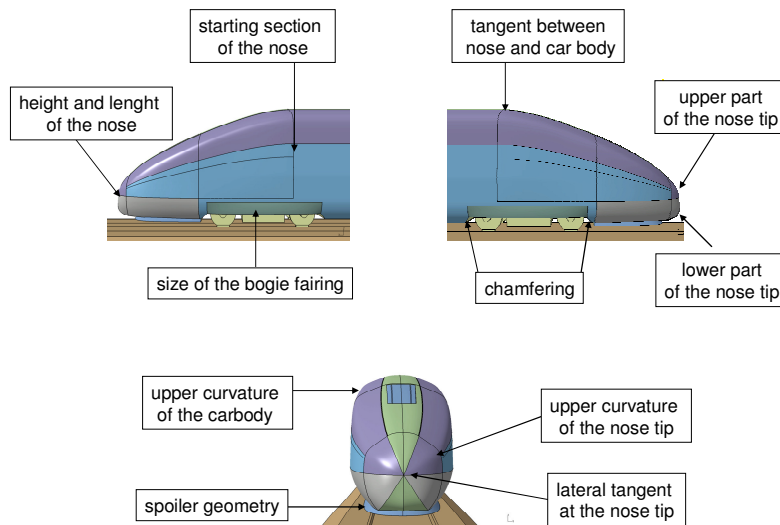
Figure 6: Quasi-static multi body simulation method used for the determination of the cross-wind stability which served as goal function

The approach is quasi static, i.e. transient phenomena are not accounted for. The results nevertheless agree well with transient multi-body simulations (MBS). A MBS is time dependant and also captures track irregularities and is used for ride comfort analyses.

#### 4.2 Parametric model

Generating the parametric CAD model and defining the range of the parameters is one of the most sensitive parts in the process of optimization. The goal is to generate a model that gives most degree of freedom to the optimizer, keeps all the necessary constraints by minimizing the amount of parameters at the same time.

The focus of this optimization was on the shape of the head/tail of the train but the bogie cut outs and the curvature of the car body are parameterized as well.



As mentioned at the beginning it is necessary to design the head and the tail equally. Since the optimal shapes of head and tail investigated separately are different it is a very challenging task to find a compromise that works well in both cases.

To enable the optimizer to find such a solution several geometrical features of the head/tail (see picture above) were parameterized. Changing those features enables to generate a huge variety of different shapes of completely different aerodynamic quality defining a powerful basis for the optimization.

In the bogie region a parametric bogie cut out was implemented that could be varied in length and by applying a variable chamfering at its boundary. The chamfering interacts with the variable fairing that covers the not chamfered part of the cut outs.

### **4.3 Results**

Before setting up the multi-objective optimization both objectives were investigated and optimized separately both to estimate the potential and to check possible correlations. Comparing the best designs, coming from the drag and from the crosswind optimization confirmed that both objectives are not correlated. Good performance in drag does not mean a good crosswind behavior, and vice versa.

Therefore a multiobjective optimization was to be run. That means in first terms a doubling of computational costs for every iteration and a significant rise of the amount of iterations, mainly due to the facts, that the dimension of the response spaces is incremented and that straight forward algorithms like all gradient based and the SIMPLEX aren't applicable. Furthermore a multiobjective optimization does not come up with a unique solution but with a set of Pareto optimal solutions. Optimality for a design in the sense of the Pareto means that it is not dominated by a design performing better in all objectives of the optimization.

The optimization was stopped after 173 iterations of the MOGA-II algorithm, which delivered 5 Pareto-optimal designs. In total the multiobjective optimization took about 8477 CPU hours on a cluster of 1.4 GHz processors. The chose of the final best design had to be done in the post processing, taking into account the relative importance of the two objectives drag and cross wind stability. Furthermore for efficiency reasons the optimization was carried out on a relative coarse mesh, so further investigations on the reliability of the achieved results are necessary.

## **5 CONCLUSIONS**

The work presented shows that the process for aerodynamic optimization has been established. All constraints on a realistic train have been taken into account. Pilot projects on a single objective optimization of the outer shape with regard to head pressure pulse as well as an aero-efficient optimization with regard to both drag and cross-wind have been carried out. The process enables close cooperation within the departments of BT on the design of the outer shape. This way, significant aerodynamic features are incorporated in the whole process of planning and production.

## ACKNOWLEDGEMENTS

The optimization with regard to head pressure pulse has been carried out in the project “Front shape and slipstream for wide body trains at higher speeds” within the framework of Gröna tåget.

## REFERENCES

- [1] A. Stiebritz. *Aerodynamic certification measurements of high-speed trains of head pressure pulse*, Diploma Thesis Work, University of Berlin and Bombardier, 2008.
- [2] J. A. Nelder and R. Mead. *Computer Journal* 7, 308, 1965.
- [3] S. Poles. *MOGAI: An improved multi-objective genetic algorithm*, Technical report, ESTECO, 2003.
- [4] W.L. Davis. *General Electric Review*, 1926.
- [5] T. Schill. *Rechnerbasierte Fahrwiderstandsprognose von Schienenfahrzeugen*, Student thesis, TU Berlin and Bombardier, 2004.
- [6] J.L. Peters: *Windkanaluntersuchungen zum Widerstandsverbesserungspotential von konstruktiv abgesicherten Drehgestellschürzen und Dachgeräteverkleidungen am ICE*, Technical report, Krauss Maffei Verkehrstechnik, 1996.
- [7] J.L. Peters: *Aerodynamics of very high-speed trains and maglev vehicles: State of the art and future potential*. *Int. J. of vehicle design*. Special Publication SP3, 308–341.
- [8] European Norm, EN 14067-4 Railway Applications. Aerodynamics. Requirements and test procedures for aerodynamics in open track, 2005.

## WIND TUNNEL EXPERIMENTS OF A HIGH SPEED TRAIN EXPOSED TO CROSS WIND ON GROUND AND BRIDGE CONFIGURATIONS

Lars Hoefener\*, Daniel Romann<sup>†</sup>, Christian Navid Nayeri<sup>†</sup>, Thorsten Tielkes\*, and Christian Oliver Paschereit<sup>†</sup>

\*Systemverbund, DB Systemtechnik, Department of Aerodynamics and HVAC  
Deutsche Bahn AG, Völckerstraße 5, 80939 München, Germany  
e-mails: lars.hoefener@deutschebahn.com,  
thorsten.tielkes@deutschebahn.com

<sup>†</sup>Department of Fluid Mechanics of Hermann-Föttinger-Institut  
Technische Universität Berlin, Müller-Breslau-Str. 8, 10623 Berlin, Germany  
e-mails: christian.nayeri@tu-berlin.de, oliver.paschereit@tu-berlin.de

**Keywords:** Cross wind, Bridge, Embankment, Sweep-independence principle, Over speeding

**Abstract:** *The paper presents results of a wind tunnel test campaign of a high speed train carried out at the GroWiKa wind tunnel of the TU-Berlin. The main goal of the study was to gain certain details of a high speed train's flow field imposed to strong cross winds. In order to assess the influence of the infrastructure on the developing flow field, the investigations were performed with a scaled ICE3 model (1:15),  $Re=3.34 \cdot 10^5$  and three different local infrastructure features. Besides the true flat ground (FG according to TSI HS RST and DB Ril807) configuration, the standard single track with ballast and rail one (STBR according to prEN 14067-6:2009) and a typical DB standard bridge deck configuration were studied for two wind scenarios, i.e. a pure cross wind (yaw=90°) and a yaw angle of 30° which is more relevant to fast running high speed trains. However, the post processing of the measurement data obtained for oblique inflow is in progress and the present paper has to be focused on the orthogonal case, thus. A comparison of the results should provide a more detailed picture of local differences in the resulting flow field induced by different track types.*

*Of major interest are improvements in the understanding of reasons for deviations of the aerodynamic properties of vehicles placed on such structures. The studies will help to gain further insight into the details of the flow development around the train and may be used for validation purposes.*

*The measurements were performed mainly by means of a two component LDV probe allowing the simultaneous determination of stream wise and wall normal velocity components with a high spatial resolution. Moreover, the application of the hardware-coincident mode allowed an accurate derivation of the second order moments. By measurement of velocity cuts at different span wise and stream wise positions the determination of flow features upstream of the train position, on top of the infrastructure as well as in their wake were possible. What is more, some details of the underbelly flow field were measured.*

## 1 INTRODUCTION

For more than four decades high speed trains have been in operation, but since the nineties of the last century the high speed railway traffic has seen a rapid growth in many parts of the world. Due to economic reasons the today's vehicle are light-weight built and the maximum train speed has been increased exceeding 300 km/h. Thus, the sensitivity of the vehicle to cross winds has become a safety issue for the operation of trains and is regulated by national standards in UK [1] and Germany [2]. Moreover, it was introduced into European regulation by means of the TSI [3] and prEN 14067-6:2009 [4].

The overall flow field acting on a train running at normal operation speed under cross wind conditions results from an interference of the train-induced slipstream flow field with the wind gust. Strictly spoken the motion of this longitudinal aligned slipstream is coupled with the train movement and is superimposed by the perpendicular orientated wind gust. Usually the aerodynamic properties of a train in terms of lift, side force and rolling moments are determined in a static wind tunnel test [5] as a first step to assess the cross wind risk. The effective inflow which acts on a train is modelled as a superposition of both components and the model is skewed according to the inflow.

For the bridge and embankment configuration, such a static wind tunnel experiment suffers the fundamental problem of an improper representation of the real flow situation. Under full-scale track side conditions, the train-generated slipstream flow field of a high speed train ( $v_{tr} \approx 100$  m/s) bestrides the resulting flow field as the wind gust does usually not exceed a speed  $v_w \approx 35$  m/s. During static wind tunnel tests this situation is simulated by a uniform inflow inclined to the model. Yet this simplification causes a number of shortcomings. For example, the flow separation setting in on the leeward side of the train model is not a realistic representation of the full-scale conditions [6] any more and the so called sweep-independence principle is not valid for the critical low yaw angles any longer [7]. What is more, an adaptability of the Baker hypothesis [8] is questionable for such a configuration. Recent studies performed in the context of the AOA project [9] pointed out a lack of knowledge about the resulting flow field around a high speed train passing a bridge. Wind tunnel measurements [10, 11] showed a speed up of the flow field in the absence of a train. However, it is still unclear how the bridge flow modifies the aerodynamic coefficients of a vehicle on top of the bridge deck. This issue is closely connected to the physically incorrect treatment of the relative movement of the train in relation to the bridge in a static wind tunnel test. In the past, wind tunnel experiments were often performed on embankment models with a limited lateral extension. Schober et al. [6] performed visualisations of the leeward side of the embankment with tufts and confirmed the occurrence of flow circulation around the leading edge of a 3d embankment model which has a significant impact on the flow field. Thus, it is strongly recommended to extend the infrastructure element to both wind tunnel walls or to apply end plates on both sides to ensure an accurate inflow condition for lower yaw angles. Yet, this will increase the blockage ratio and may introduce additional interferences of the wall boundary layer.

The fundamental problem can be tackled in a wind tunnel by applying a moving-model rig [12], but such tests are expensive and complex. A promising approach to overcome the above mentioned shortcomings is a usage of CFD methods to study the flow field taking into consideration a relative motion of the train and the infrastructure subjected to a wind gust. Such elaborate numerical simulations are not state of the art yet and require a diligent validation of experimental data, thus. Diedrichs et al. [13] studied a two-track embankment configuration applying an accurate CFD which was validated by wind tunnel measurements. Their conclusions



highlight the fundamental importance of a suitable numerical simulation set-up and the usage of comprehensive validation data to obtain accurate results of the CFD. So far, wind tunnel experiments are often solely dedicated to derive integral aerodynamic vehicle properties. This paper provides data of wind tunnel measurements for a validation of advanced CFD methods based on flow quantities which would allow a simulation of the flow field under consideration of more realistic ground conditions.

## 2 Experimental set-up

The wind tunnel measurements were carried out at the large wind tunnel (GroWiKa) facility of the Department of Fluid Mechanics of Hermann-Föttinger-Institut of Technische Universität Berlin. The closed loop wind tunnel has a 10 m long test section with a constant cross section  $w_{t_m} \times h_m \approx 2 \text{ m} \times \sqrt{2} \text{ m}$ . The nozzle has a contraction ratio of 6.25 resulting in a free stream turbulence level of less than 1%. The wind tunnel fan with an electric power of 500 kW allows maximum wind speeds of more than 40 m/s. For the present investigations a wind tunnel model at a scale of 1 : 15 was available so that at the typical flow speed of  $u_{ref} = 25 \text{ m/s}$  used in the experiments  $Re \approx 3.4 \cdot 10^5$  was achieved ( $\zeta = 20^\circ\text{C}$ ,  $\nu = 14.6 \cdot 10^{-6} \text{ m}^2/\text{s}$ , reference length  $l_{ref}^{1/15} \cdot 3 \text{ m}$ ). Due to the large model scale and the closed test section, blockage effects are high and become more important particularly at larger yaw angles. The blockage ratio  $h_b/h_m$  of the end car on flat ground and of the bridge model alone are as high as 14% and 19.5%, respectively. Since the most critical configuration results in an accumulated geometric blockage of up to  $1/3$ , the requirements of prEN 14067-6:2009 [4] could not be met.

The velocity distribution in the flow field is mainly studied by means of a two component ( $\lambda_{green} = 514.5 \text{ nm}$ ,  $\lambda_{blue} = 488 \text{ nm}$ ) Laser Doppler Velocimetry (LDV) system from Dantec Dynamics (BSA F60). The backward scattering system with a power of 250 mW is equipped with a bragg cell allowing to determine regions of backward flow. It is mounted on a precise 3D traversing unit and permits the simultaneous determination of two orthogonal velocity components with a high spatial resolution. The usage of the coincident measurement mode allows the accurate derivation of the second order moments as well. By changing the position and the orientation of the LVD-probe, measurements of the upstream flow (initial condition), of the flow on top of the infrastructure and of the train model and of the flow in the wake region could be carried out. This allows not only to determine the surrounding flow field but also the underbelly flow for selected cuts. In order to access various span wise positions with different distances to the transparent wind tunnel walls different focal lengths were applied. An aerosol generator was placed in the combustion chamber spraying DEHS particle to provide a sufficient seeding for the laser measurements.

In addition, a Prandtl probe was used to determine the free stream velocity and the ambient conditions were continuously monitored. Finally, a hot wire probe was used to validate the inflow condition for a limited number of runs.

Fig. 1 shows the test section with the train and bridge models for both yaw angles. For the vehicle investigations an ICE 3 model (scale 1:15, see Fig. 2) was used with some simplifications in the bogies and underbelly cavities region. A wake body and an upstream extension of the infrastructure features ensured a sufficient upstream and wake flow representation for all considered yaw angles. The train model was placed at a vertical ground distance  $235 \text{ mm}/15$  of the wheels.

Three different configurations were studied: besides the flat ground (FG) and single track with ballast and rails (STBR) also a typical German railway bridge. In the ground configurations the model was placed on an elevated splitter plate to ensure a nearly block-shape boundary layer

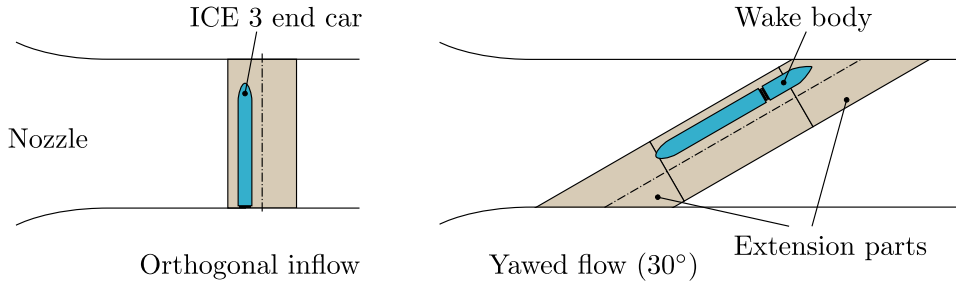


Figure 1: Train and bridge models in the test sections



Figure 2: ICE 3 model on an elevated splitter plate in the test section of the GroWiKa

profile. The cross section of a typical German railway bridge consists of a trapezoid-shaped cantilever with a constant geometry in span wise direction. Fig. 3 sketches the geometry of the top panel and the used model dimension.

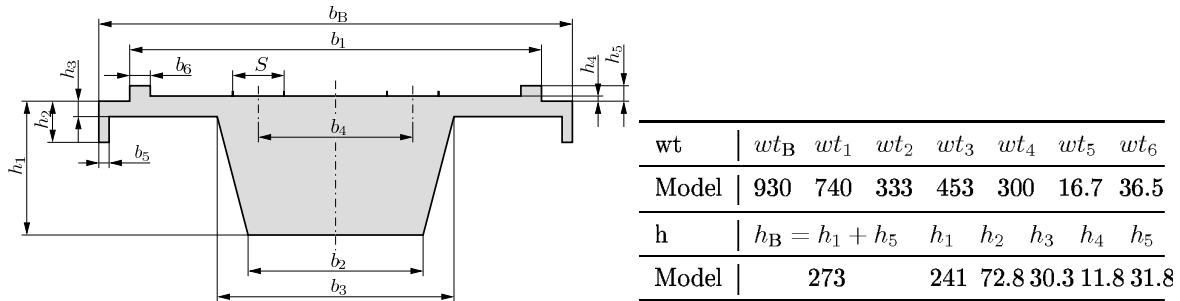


Figure 3: Cross section of the bridge model, widths  $wt$  and heights  $h$  (mm) of the bridge model

### 3 Results

In this section the results of measurements obtained for the different ground configurations FG, STBR as well as the bridge deck are presented and discussed.

#### 3.1 Configurations with flat ground and ballast & rail

As mentioned above for the two ground configurations the train was placed on a splitter plate at a distance of  $\Delta z/l_{ref} = 1.68$  downstream from the leading edge. The coordinate system and other details of the configuration for the pure cross wind case (yaw angle  $90^\circ$ ) are shown in Fig. 4 and Fig. 5.

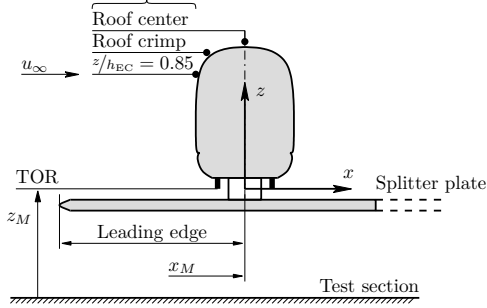


Figure 4: ICE 3 model on FG configuration

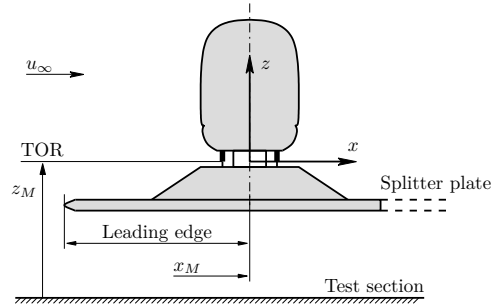


Figure 5: ICE 3 model on STBR configuration

In general, the velocity profiles are similar in the outer region for  $z/l_{ref} > 2.5$  as can be seen in Fig. 6. One obvious difference, however, is that in the FG case higher velocities are achieved in the lower part of the train near the ground. There, the air passes through the gap between the underbelly and the ground and forms a jet on the lee ward side. Another difference is that the flow on the roof apparently separates later due to higher velocities. In combination with the jet flow in the underbelly, in the centre this flow field most probably leads to the development of a pair of two counter-rotating vortices parallel to the train in the wake region of the FG configuration.

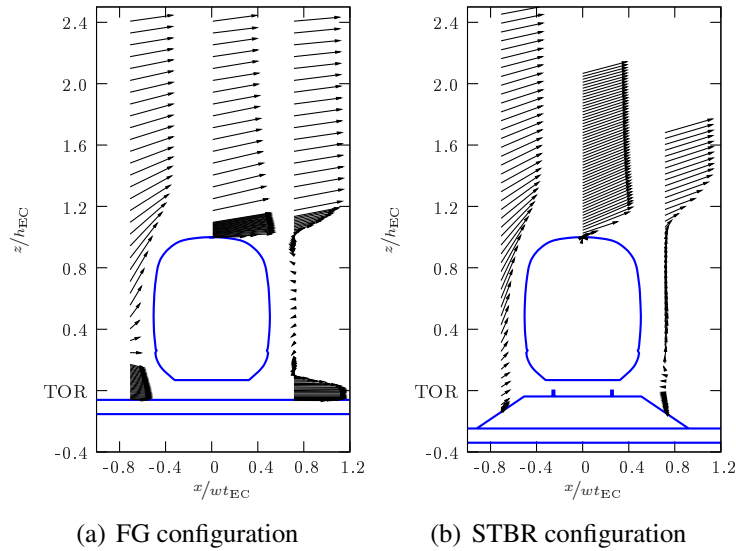


Figure 6: Velocity vectors composed from  $\bar{u}$  and  $\bar{w}$ , centre region  $y/l_{EC} = 0.52$  of the endcar

The flow is deflected upwards further upstream of the vehicle side wall for the STBR. Therefore, the separation is shifted to the wind ward side but the maximum horizontal velocities on the roof centreline are somewhat smaller than in the FG case. Moreover, the upwards directed lee ward flow suggests a large separation vortex in the wake region.

For the nose region both mean velocity vector plots (Fig. 7 a-b) support the presence of a complex 3d circulation flow around the train. At this position the separation occurs further downstream effecting the free flow in the outer region only marginally. An interesting flow feature of the STBR-case is the following: The vectors exhibit a downward orientation on the lee ward side of the nose (at  $x/wt_{EC} = 0.7$ ) in Fig. 7 b, while at the centre region it has an upward flow direction in Fig. 6 b. These observations lead to the assumption that a stationary

vortex with an axis normal to the lee ward wall of the train exists. This was also confirmed by visualizations with china clay which indicated the existence of this vortex.

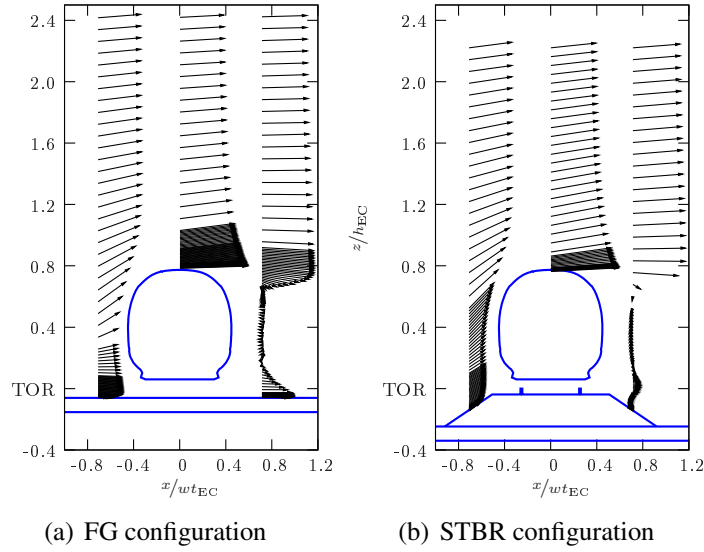


Figure 7: Velocity vectors composed from  $\bar{u}$  and  $\bar{w}$ , nose region of the endcar ( $y/l_{EC} = 0.9$ )

Vertical profiles of the mean axial velocity component and of the RMS-values on the centreline of the vehicle ( $y/w_{tEC} = 0.52$ ) are shown in Fig. 8 a-b for the FG and in Fig. 8 c-d for the STBR configuration, respectively. Both configurations exhibit nearly the same free stream velocity of about  $1.2u_{ref}$ . However, the maximum of the mean profiles at the roof centreline ( $x/w_{tEC} = 0$ ) ranges up to  $1.6u_{ref}$  for the FG, thus exceeding the STBR case in Fig. 8 c by 15%.

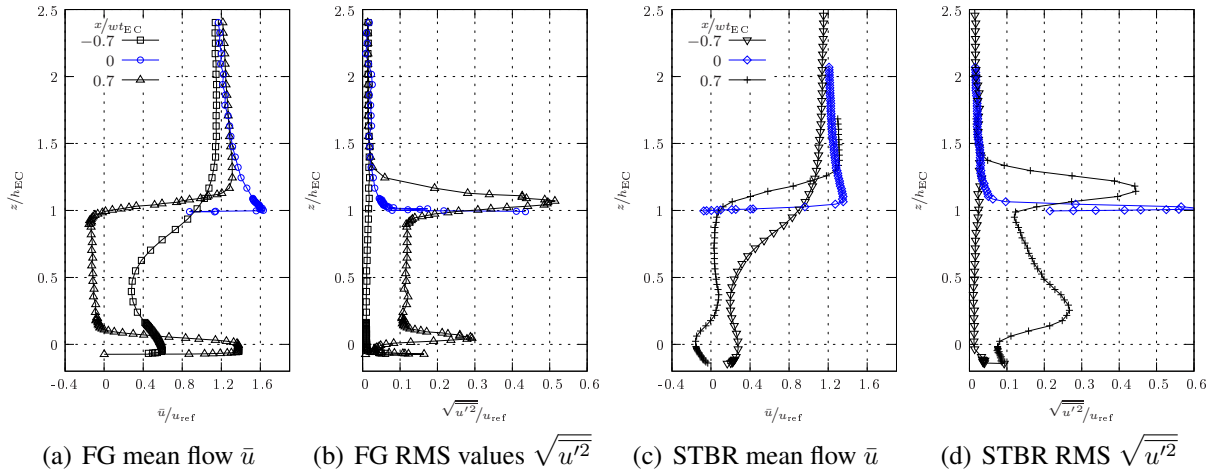


Figure 8: Profiles of axial velocity component, at mid span of the train ( $y/w_{tEC} = 0.52$ )

At this position the flow separation apparently sets in further upstream for the STBR configuration due to the stronger upward deflection of the flow on the wind ward edge of the ballast bed leading to a reduced flow speed up in the roof area. In the vicinity of the separation zone a shear layer develops characterised by a local peak of the RMS-values. The maximum values of the fluctuations correspond to the large velocity gradients due to the inflection point of the mean velocity profile. The highest RMS-values at the centreline position are attained in the

STBR case. However, due to limitations in the optical access for the LDV, points with even higher values might have been missed in the vicinity of the vehicle roof in the FG case. Thus it is not entirely clear whether higher RMS values occur for  $z/h_{EC} = 1$  as the ones shown.

Another distinct jet of high momentum fluid develops in the underbelly region further upstream of the car ( $x/wt_{EC} = -0.7$ ) for the FG only. Yet the maximum fluctuations ( $\sqrt{u'^2}/u_{ref} \leq 0.3$ ) remain lower than these in the upper shear layer ( $z/h_{EC} \approx 1.1$ ) even in the wake region. As indicated by Fig. 8 b, increased RMS-values are obtained on the lee ward side around  $z/h_{EC} = 0.1$  which corresponds to the zero crossing of the mean velocity profile. In contrast the shielding effect of the rails and the early flow deflection upstream of the wind ward side of the vehicle obviate the evolution of such a jet for the STBR case.

### 3.2 Configuration with bridge

For the investigation of the bridge flow, a Cartesian coordinate system according to Fig. 9 is used. The x- and z-coordinates were non-dimensionalized with the width and height of the bridge,  $w_{tB}$  and  $h_B$  respectively. The origin is placed in the downstream x-direction at the

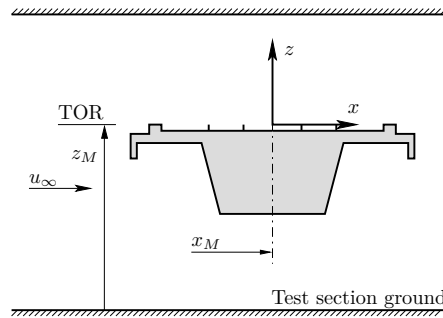
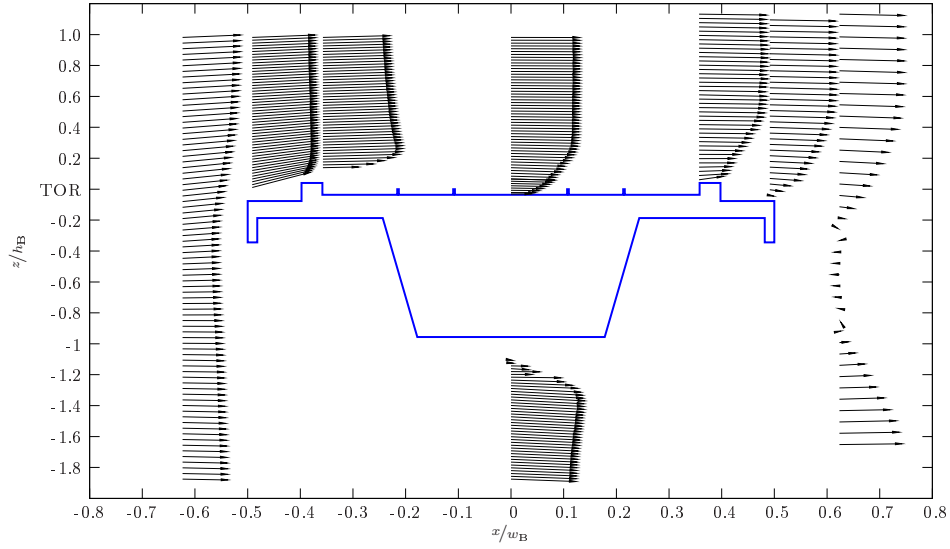


Figure 9: Coordinate system of bridge measurements

centreline of the bridge, the span wise y-coordinate starts at the test section side wall while the z-axis begins at the TOR. In order to minimize the circulation around the bridge deck, the bridge model was placed in the wind tunnel test section such that the distance between the deck and the test section ceiling was the same as between the lower surface of the bridge and the test section floor. All profiles are obtained at the lateral position  $y/l_{EC} = 0.12$  in the region of the rearmost boogie of the end car.

In Fig. 10 the resulting mean flow vectors are plotted for different locations of the bridge composed from the  $\bar{u}$  and  $\bar{w}$  velocity. The first profile upstream of the bridge at  $x/wt_{EC} = 0.62$  shows an asymmetric shape relative to the bridge deck thus indicating an unequal flow rate passing above and below the bridge. Obviously the flow separation at the lower leading edge of the bridge deck leads to an additional flow deflection and blockage resulting in an unwanted circulation. Moreover, local separations occur on the steps caused by the wind ward and lee ward cable troughs and a massive separation evolves in the wake region downstream of the bridge.

The vertical profiles shown in Fig. 11 highlight the asymmetry of the velocity profiles further upstream of the bridge at  $x/wt_{EC} = 0.62$ . The strong velocity gradient occurring underneath the bridge leads to a local maximum of RMS in the centre of the bridge at  $x/wt_{EC} = 0$ . Further downstream, a large separation zone is clearly visible at  $x/wt_{EC} = 0.62$ . Both regions of high shear are characterized by elevated levels of the fluctuations, but the interaction of both separations


 Figure 10: Flow vectors composed of  $\bar{u}$  and  $\bar{w}$ , bridge without train

on the lower side causes higher RMS in the lower part of the strong wake region downstream of the bridge deck.

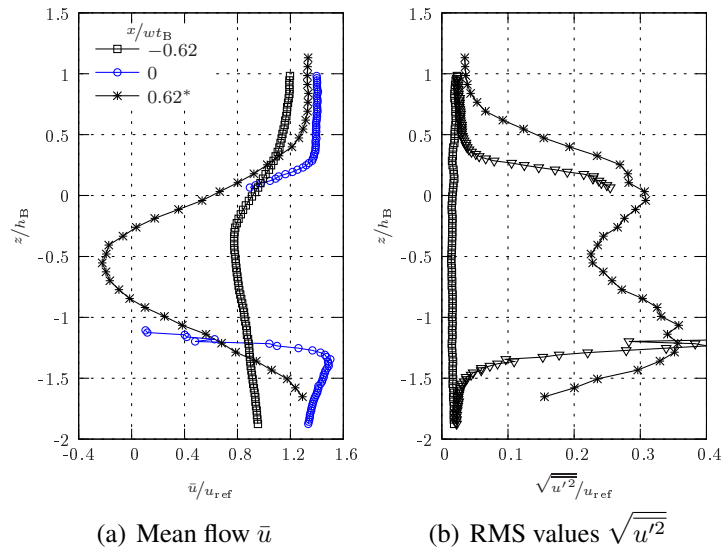


Figure 11: Profiles of axial velocity component, full bridge cut, without train

A detailed view of the flow on the upper side of the bridge is given in Fig. 12. This region is of major importance as far as the flow field developing on a high speed train traveling over a bridge is concerned. The distortion of the velocity profile is evident downstream of the local separation at  $x/w_B = -0.36$ . At this position the LDV measurements did not reach as close to the bridge as at other positions. A pronounced maximum in the mean value forms there at  $z/h_B \approx 0.22$  and would most probably lead to highly increased side forces for a train in this region. Further downstream, the flow relaxes leading to a decrease of maximum of the mean flow as well as of the RMS values. While the magnitude of the fluctuations decreases significantly, the shear layer grows in vertical direction only slightly.

Furthermore, in Fig. 13 a comparison with results obtained by the DLR Göttingen in the

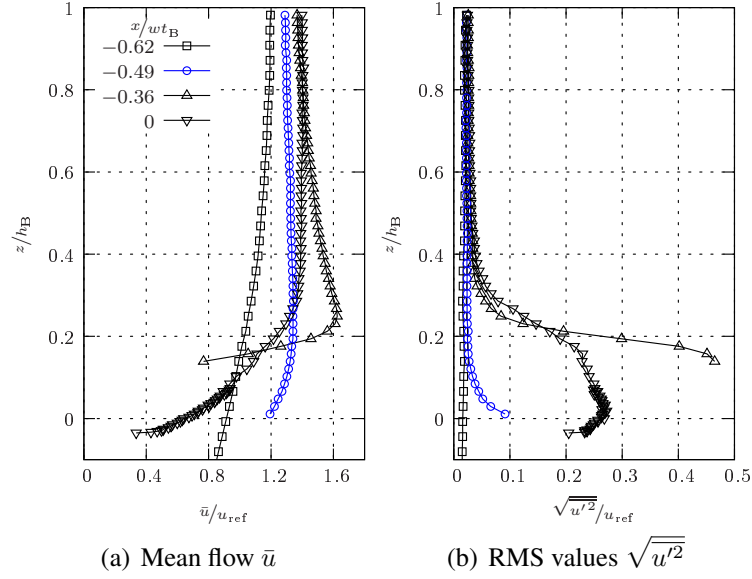


Figure 12: Profiles of axial velocity component, on top of the bridge without train

DNW-NWB large wind tunnel in Brunswick [10] on a similar bridge model at a scale 1:25 is shown. The DLR-measurements were done with a lower scale model and in an open test section, thus the blockage is much lower (about 5%). The Reynolds number based on the reference

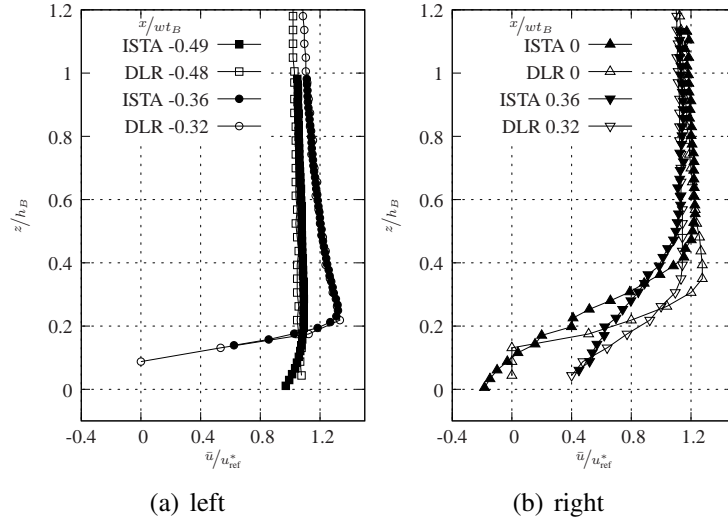


Figure 13: Profiles of the axial velocity component, comparison of present measurements and results of [10]

length  $l_{ref} = 3$  m for the DLR investigation ( $Re \approx 4.5 \cdot 10^5$ ) was almost 33% higher than for the present study ( $Re \approx 3.4 \cdot 10^5$ ). The DLR results were carried with a 10-hole probe. This lower blockage ratio leads to a significantly lower flow over speed in comparison to the present study. In order to allow for a more realistic comparison, an ad-hoc correction of the inflow velocity was applied for both series by means of a corrected  $u_{ref}^*$  considering the individual ratio of the geometric blockage for both configurations.

The wind ward profiles for Fig. 13 left ( $x/wt_B < 0$ ) agree well with this correction and indicate an effective flow over speeding factor for the wind ward track as high as  $u/u_{ref}^* \approx 1.3$ . Please notice, that the DLR measurements for the centreline position is for some reason truncated

and does not determine the backward flow present for  $z/h_B < 1.3$ . Significant differences in the blockage ratio and even more the clear differences in the behaviour of the open test section used for DLR tests cause fundamental deviations of the massively separated flow field in the wake region which surely cannot be accounted for by simple velocity corrections. Moreover, the slightly higher relative model height of both campaigns  $h_B/wt_B$  adds an additional bias to the results. Therefore, the results do not agree on the lee ward side of the bridge any more.

In the following, results obtained for the configuration with an ICE 3 train model resting on the wind ward side of the bridge are presented. Most profiles are gained at the lateral position of the rearmost boogie ( $y/l_{EC} = 0.12$ ) to allow comparisons. Whereas the profiles at  $x/wt_B = 0.36$  and  $0.62$  are measured at  $y/l_{EC} = 0.5$  instead.

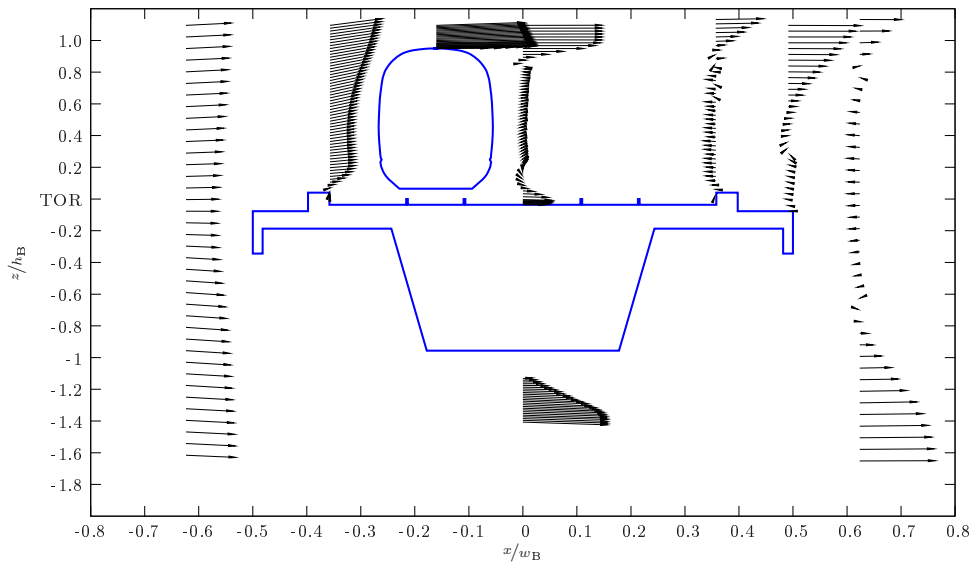


Figure 14: Flow vectors composed of  $\bar{u}$  und  $\bar{w}$ , bridge with train

The vector plot presented in Fig. 14 shows an overview of the flow field. The inflow vectors ( $x/wt_B = -0.62$ ) demonstrate the strong deflection and acceleration of the flow on the wind ward half of the bridge. At the bridge centreline the outer flow is almost parallel to the axial wind tunnel direction, while the vectors at the lee ward side of the train indicate a downwards oriented flow as part of a large wake region. This behaviour is somewhat similar to the results observed in the nose region of the STBR configuration as discussed when considering Fig. 6 b and Fig. 7 b. The good symmetry of the wind ward profile shown in Fig. 15 supports clearly the reduced circulation in comparison to Fig. 11. Again, the flow at the bottom side of the bridge velocities is more accelerated reaching up to  $1.8u_{ref}$ .

A comparison of the axial velocity profiles on top of the bridge is given in Fig. 16. First of all, the two most up stream profiles ( $x/wt_B = -0.62$  and  $-0.49$ ) employ an almost constant gradient. However, the bluff bridge body causes a local separation at  $x/wt_B = -0.49$ . In this high shear region the high local velocity gradients lead to increased fluctuations in Fig. 16 b. At the lee ward edge of the forward facing step ( $x/wt_B = -0.36$ ) a rather large region of local back flow develops, while the general shape of the profile is comparable to the wind ward side of the train for both ground configurations (see Fig. 8,  $x/wt_{EC} = -0.7$ ). The wide spreading shear layer leads to increased fluctuations for  $z/h_{EC} < 0.29$ . Overall the highest flow velocities exceeding twice  $u_{ref}$  are reached at the roof centreline of the vehicle, further down stream not more than  $(1.7u_{ref})$  are registered at the top side of the bridge. In addition, the profile at the bridge centreline



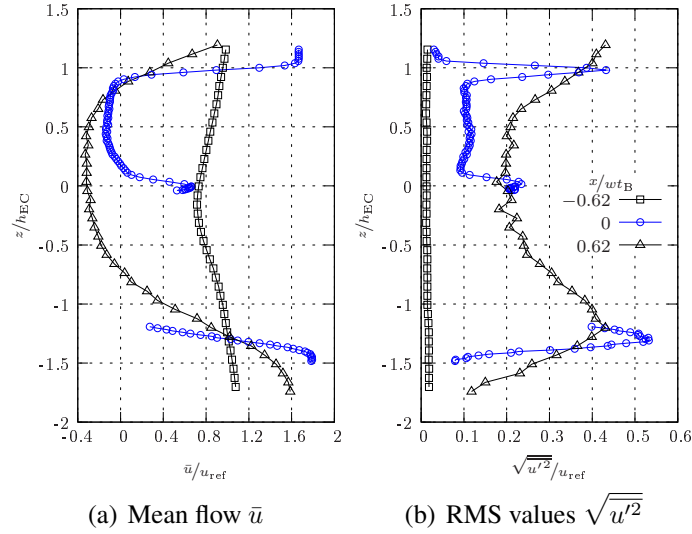


Figure 15: Profiles of axial velocity component, full bridge height, with a train present

depicts a local jet between the model underfloor and the bridge surface, probably enhanced by the strong flow blockage in the model plane.

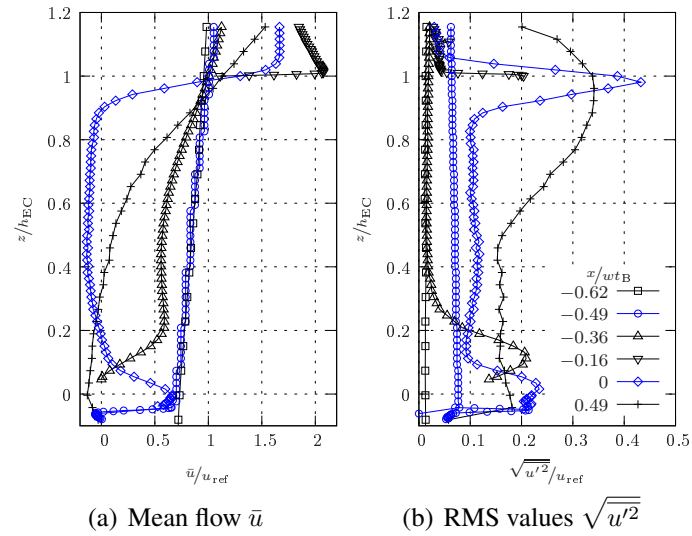


Figure 16: Profiles of axial velocity component, on top of bridge, with a train present

### 3.3 Configuration with bridge at yaw angle $30^\circ$

Fig. 17 a shows the bridge and its relative coordinate system and Fig. 17 b shows the effective flow angle resulting from the local  $\bar{u}$ - and  $\bar{v}$ -velocity components. At low  $z/h_B$ -values the flow angle is strongly deflected towards the leading edge of the bridge (positive flow angles). This is because the flow near the surface is guided parallel to the bridge, which is yawed at  $30^\circ$ .

With growing distance from the bridge the flow is deflected towards negative  $\gamma$ -angles. The change in flow direction takes place at  $z/h_B \approx 0.15$ . Apparently the flow is accelerated in  $x^*$ -direction under the influence of increasing bridge contour thickness, while it remains almost unchanged in the  $y^*$ -direction.

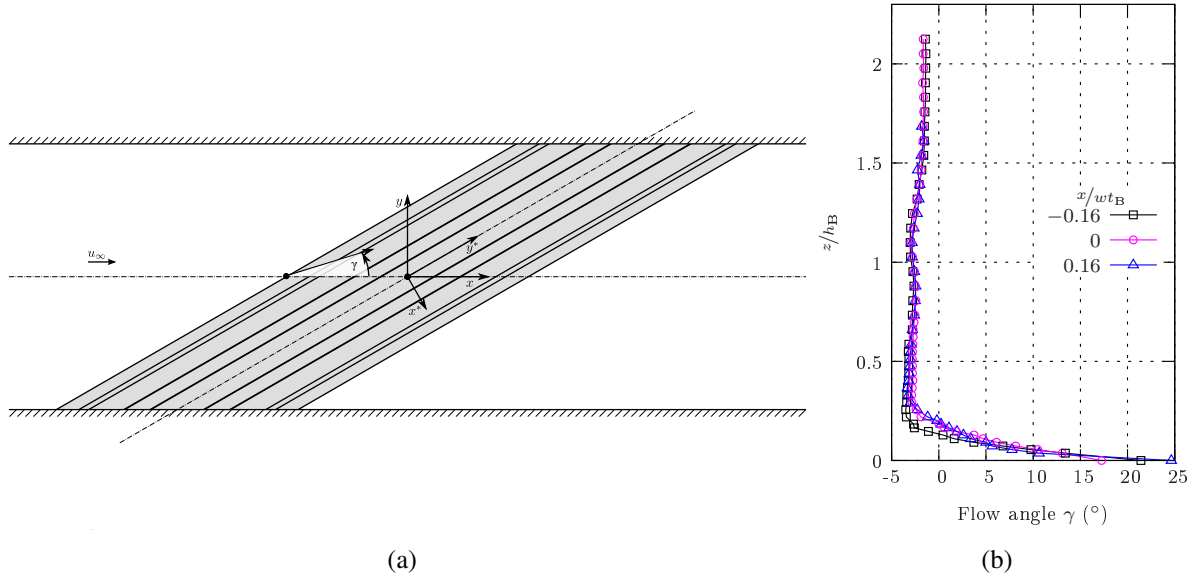


Figure 17: (a) Sketch of the bridge in the test section yawed at  $30^\circ$  with relative coordinate system, (b) Flow angle  $\gamma = \arctan \bar{v}/\bar{u}$  at the centreline of the bridge ( $x/wt_B = 0$ ) and the tracks ( $|x/wt_B| = 0.16$ ,  $y_M/wt_M \approx 0.5$ )

#### 4 Conclusions

A comprehensive wind tunnel measurement campaign was performed for different ground and bridge configurations dealing with the cross wind issue of high speed trains. The study was focused on non-intrusive LDV measurements with the application of coincidence mode which has allowed a determination of mean values as well as second order moments of the velocity components with high accuracy. The results are intended as validation data for a CFD study which could tackle the vehicle motion in a more proper physical manner than a static wind tunnel test ever could. Additional wind tunnel measurements might provide time-resolved flow quantities as well.

So, main differences of the resulting flow field for the different set-ups were highlighted. The chosen model scale of 1:15 caused a massive blockage in the test section which does not allow a straight forward comparison to other instigations with lower blockage. Nevertheless, a simple ad-hoc correction has demonstrated a good agreement to previous studies within the range of validity and has confirmed the flow over speeding assumptions about the axial velocity component. Further, the circulation around the model gains more importance for higher blockage ratios.

Moreover, some first results of not yet finished measurements for the yawed bridge flow indicate a three-dimensional flow field as the velocity profile above the bridge deck is twisted. The flow angle changes from a direction almost parallel to the bridge leading edge close to its surface to negative values in the outer boundary layer. This is probably due to two competing effects: near the bridge deck the flow is guided along the trails and further away the influence of the three-dimensional wake becomes dominant.

#### 5 ACKNOWLEDGEMENTS

The wind tunnel tests were financially supported by a grant of the Dr. Hermann & Ellen Klapproth foundation which is gratefully acknowledged.

## REFERENCES

- [1] Railtrack PLC. Resistance of railway vehicles to overturning in gales. Railway Group Standard GM/RT 2142 ISSUE 2. Safety and Standard Directorate Railtrack, London, October 2000.
- [2] DB Netz AG. Richtlinie 807.04 Bautechnik, Leit-, Signal- und Telekommunikationstechnik. Ausgewählte Maßnahmen und Anforderungen an das Gesamtsystem Fahrweg/Fahrzeug Aerodynamik/Seitenwind, Frankfurt a.M. (2006).
- [3] EC. Technical specification for interoperability relating to the "rolling stock" sub-system of the trans-european high-speed rail system. Official Journal of the European Union, 21 February 2008.
- [4] CEN. prEN 14067:2009 Railway Applications Part 6: Test procedures and requirements for cross wind assessment. CEN/TC 256, Brussels, 2009.
- [5] R.G. Gawthrope. Wind effects on ground transportation. *Journal of Wind Engineering and Industrial Aerodynamics*, 52:73–92, 1994.
- [6] M. Schober, M. Weise, A. Orellano, P. Deeg, and W. Wetzel. Wind tunnel investigation of an ICE 3 endcar on three standard ground szenarios. In *Proceedings of BBAA VI*, Milano, 2008.
- [7] H.J. Kaltenbach. On the assessment of aerodynamic coefficients on embankments & bridges. Deutsche Bahn AG, 2008.
- [8] C.J. Baker. The determination of topographical exposure factors for railway embankments. *Journal of Wind Engineering and Industrial Aerodynamics*, 21:89–99, 1985.
- [9] E. Masson and L. Hoefener. DeuFraKo project "Aerodynamics in Open Air" (AOA), WP2 cross wind issues, final report. Technical report, SNCF and Deutsche Bahn AG, 2008.
- [10] A. Kühn and P. A. Mackrodt. Windkanalmessungen der Strömungsgeschwindigkeiten hinter Windschutzzäunen auf einem Neubaustrecken-Brückenmodell. DLR, Göttingen (1988).
- [11] M. Bocciolone, F. Cheli, R. Corradi, S. Muggiasca, and G. Tomasini. Crosswind action on rail vehicles: Wind tunnel experimental analysis. *Journal of Wind Engineering and Industrial Aerodynamics*, 96:584–610, 2008.
- [12] C.J. Baker, S.J. Dalley, T. Johnson, A. Quinn, and N.G. Wright. The slipstream and wake of a high-speed train. *Proc. IMechE, Part F: J. Rail and Rapid Transit*, 215:83–99, 2001.
- [13] B. Diedrichs, M. Sima, A. Orellano, and H. Tengstrand. Crosswind stability of a high-speed train on a high embankment. *Proc. IMechE, Part F: J. Rail and Rapid Transit*, 221:205–225, 2007.
- [14] H.J. Kaltenbach, I. Alonso-Portillo, and M. Schober. A generic train-underfloor experiment for CFD validation. In *Proceedings of BBAA VI*, Milano, 2008.

# IMPORTANT GAPS IN THE SCIENCE OF CAR AERODYNAMICS

Wolf-Heinrich Hucho\*

\*Gärtnerieweg 3, D-86938 Schondorf am Ammersee  
e-mail: [huchowhh@t-online.de](mailto:huchowhh@t-online.de); [www.aerowolf.de](http://www.aerowolf.de)

**Keywords:** vehicle aerodynamics, drag

***Abstract.** Despite all the efforts to reduce the aerodynamic drag of cars, hardly any progress has been made for nearly two decades. One might even be tempted to assume that  $c_D = 0.25$  is a physical limit that cannot be bettered. However, this is not true. The “limit strategy” proposed by the present author shows how this technological stagnation can be overcome. While developing this strategy, gaps in the knowledge of vehicle aerodynamics became evident. The most important of these gaps are identified, and suggestions made for filling them.*

## 1 INTRODUCTION

Aerodynamics began to contribute to vehicle technology only when vehicle engineers stopped copying elements from flight aerodynamics and ship hydrodynamics – both slender bodies – and instead were guided by the science of fluid mechanics, especially of bluff bodies. This led to two strategies which proved effective during the aerodynamic development of vehicles: “detail optimization” and “shape optimization”<sup>1</sup>. By allowing a rational dialogue with stylists, they enabled major reductions of vehicle drag. The evolution of vehicle drag is shown in Fig. (1), and the strategies and their achievements in Tab. (1). Both detail- and shape-optimization were able to reduce drag by 100 drag counts<sup>2</sup>. However, as shown in Fig. (1), these strategies have been exhausted, with no significant reduction of production car drag values for nearly two decades. Yet much lower drag values have been realized with models of various shapes, as shown at the bottom of Fig (1).

---

<sup>1</sup> Hucho (2005)

<sup>2</sup> 100 drag counts correspond to  $\Delta c_D = 0.100$

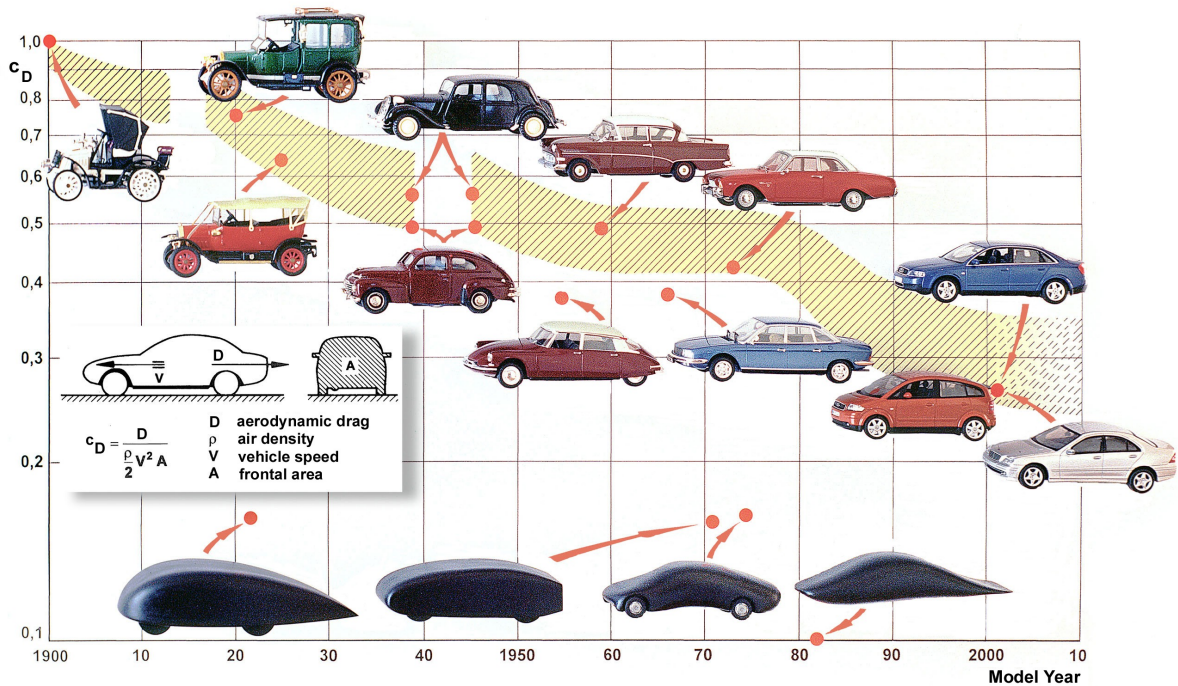


Figure 1: Development of drag coefficient  $c_D$  versus time

Strategy	achieved $\Delta c_D$	Limit $c_D$	Example
Detail optimisation (1970)	0,100	0,40	VW Golf I: $c_w$ from 0,51 to 0,41
Shape optimisation (1980)	0,100	0,30	Audi 100 III: $c_w = 0,30$
“Limit value” (200?)	0,150	0,15	?

Table 1: Three strategies for the development of car shapes

In order to overcome this stagnation, the “limit value” strategy has been proposed by the present author<sup>3</sup>. While developing this strategy, it became evident that considerable gaps in the science of vehicle aerodynamics still exist and require filling. The regions of a car that require more attention are shown in Fig. (2). They include the following:

- The underbody: Devices must be developed to improve the flow passing the wheels. Further measures must be adopted to smooth the underbody flow;
- The rear: Control of the near (and far) wake, and perhaps a rear diffuser;
- Windshield, A-pillar, and mirrors;
- Interference between the different regions, notably the front and rear parts of the car.

<sup>3</sup> Hucho (2009)

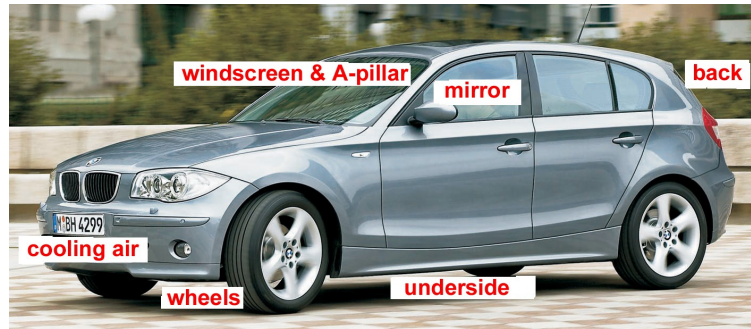


Figure 2: Regions for further improvement

## 2 DEFINITE STARTING POINTS

### 2.1 Chassis

The flow beneath the underside of a car is sketched in Fig. (3). Because of the displacement effect of the vehicle body, the flow between the underside and the road is divergent, and this effect is amplified by the cooling air flow directed to the underside. Moreover, the underbody flow is affected by the presence of the wheels.

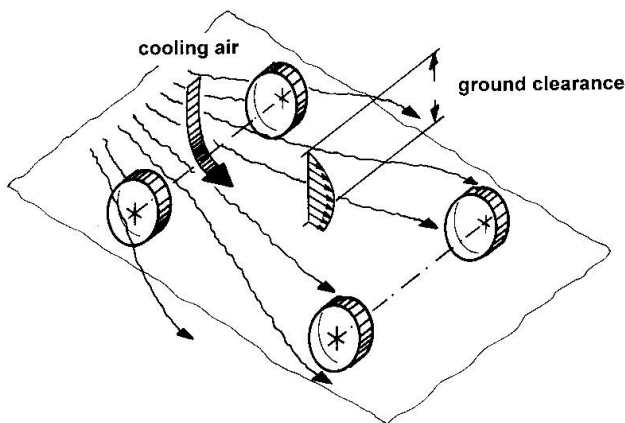


Figure 3: Flow field underneath a car

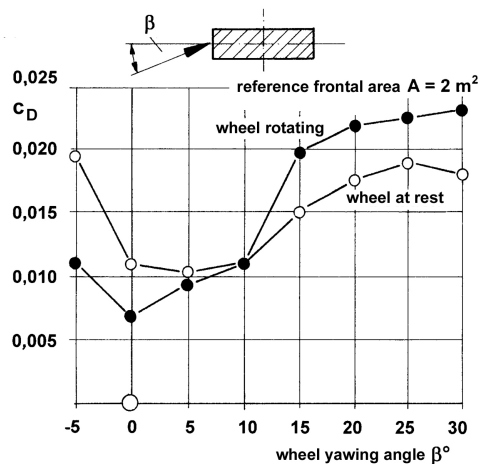


Figure 4: Drag increase of a wheel under yaw; according to Wiedemann 1996

The flow approaching the wheels is usually at a yaw angle. At the front wheels the outward yaw angle  $\beta$  seems to be larger with a smaller frontal overhang. At the rear wheels the flow may even be inward, see Aronson et al. (2000), and interfere with the flow of the underbody diffuser. Either way, the drag of a wheel is increased by the yawed flow, as can be seen in Fig.(4), and, according to Wiedemann (1996), this effect is greater when the wheel is rotating.

A device to reduce the yaw angle in front of the wheels is sketched in Fig. (5). The short frontal overhang currently favored in car design makes the design of such a device difficult. However, deformable parts are used at other points on a car, and could be applied here also. An original solution has been proposed by Wolf & Preiss (2004), see Fig. (6). The cooling air exhausts ahead of the front wheels, which should slightly reduce the local yaw angle.

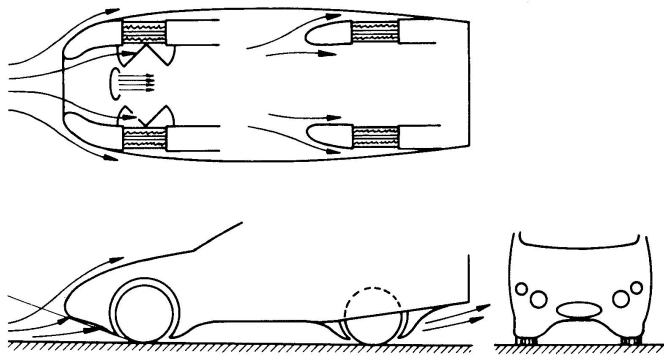


Figure 5: Author's proposition how to reduce the yaw angle in front of the wheels

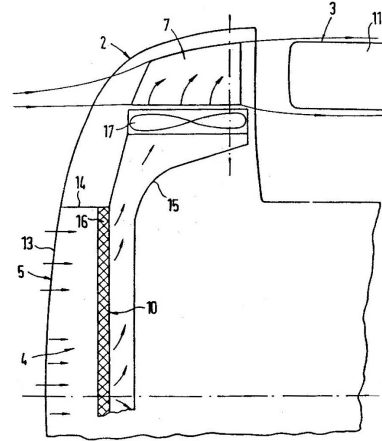


Figure 6: Directing the cooling air flow in front of a wheel, Patent drawing Porsche AG

For the underside the ideal is a smooth flat plate. Fig. (7) shows how this ideal has been approached step by step. The box in the upper right corner shows how the coefficient of friction,  $c_f$ , is converted into a drag penalty,  $\Delta c_D$ . The ratio between the “wetted” surface of the underside,  $b l$ , and the frontal area,  $A$ , is approximately 3.5. Hence according to Carr (1983), the drag penalty for the very rough undersides of the period was  $\Delta c_D \approx 0.07$ . The following assumes  $\Delta c_D = 0.08$ . By applying a front spoiler, the penalty was reduced to  $\Delta c_D = 0.06$ . With the present smooth underside, called “aero underside”,  $\Delta c_D = 0.04$  may be achieved, making a front spoiler unnecessary. How much of the remaining difference of  $\Delta c_D = 0.03$  (above the ideal  $\Delta c_D = 0.01$ ) could be recovered by closing all the remaining gaps is not known. Also it is open to question whether the design effort for the necessarily removable parts would pay off.

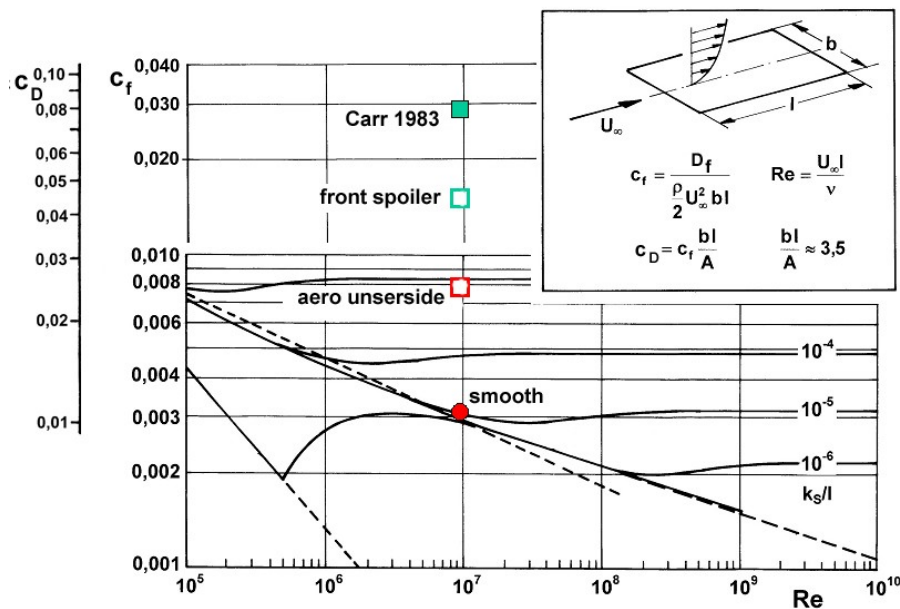


Figure 7: Under-side drag

## 2.2 The rear end

Fig. (8) shows the scope for improvement at the rear end. It refers to experiments carried out by Mair (1969). Starting with a blunt end, the drag coefficient was reduced by as much as  $\Delta c_D = 0.105$  by the various measures sketched in the figure. Of course, a long tail would not be acceptable for a present-day car. It would mean a return to early vehicle aerodynamics, to the profile developed by Klemperer (1922). The question is rather, how much could be achieved with measures that are technically feasible.

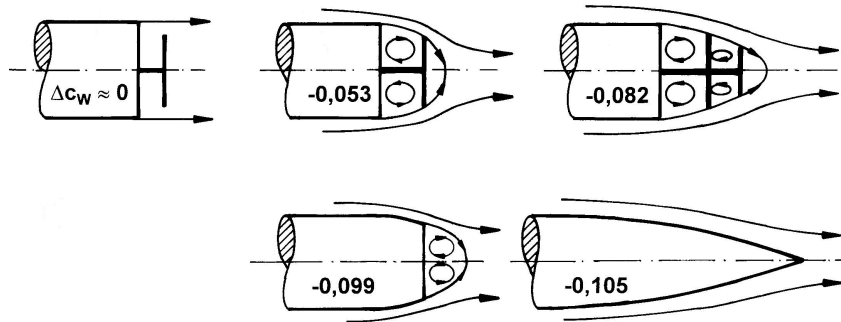


Figure 8: Base drag of a bluff body, after Mair 1969

Some well known technically feasible features are shown in Fig. (9). Their objective is to move the ring vortex, that would otherwise induce low pressure on the base, downstream, thus raising the base pressure and reducing the drag. Only variant d, the “Parapet” with inward taper, has been developed to the point where it is ready for volume application with trucks. However, despite a proven reduction in fuel consumption, it has not been adopted. Truckers don’t like it because it would be hard to use with frequent changes of trailers.

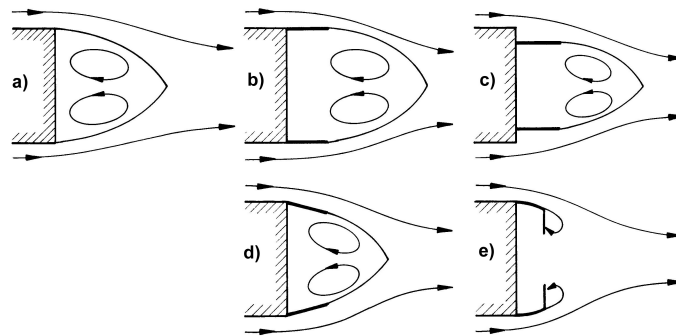


Figure 9: Various attempts to reduce base drag of a blunt-ended vehicle

Such features are perhaps more practical for buses, and more particularly coaches. These often cruise at comparatively high speed, 100 kph, over long distances. Yet they are frequently shorter than the permitted length of 15 m, so there is room for such features, and they could be removable to make parking easier.



Variant e, the “Fluid Tail” has been developed for and adapted to a square back car, a FIAT Punto, by Morelli & Di Giusto (1999). Together with a rear diffuser and using the rear wheels to pump air into the wake, the air drag was reduced by 20%.

### 2.3 Windshield, A-pillar, and mirror

In the widely-held belief that the best way to reduce air drag is to incline the windshield, this has been progressively increased. More probably, the real reason for this trend is to make the car look like a coupé. Either way, this trend is accompanied with severe drawbacks:

- the optical requirements are hard to meet;
- large windows allow easy penetration of solar heat into the interior;
- large windows are heavy - and expensive.

The obvious question is whether there are other ways to reduce the drag and so avoid the drawbacks mentioned above. Surprisingly, this has never been investigated in detail.

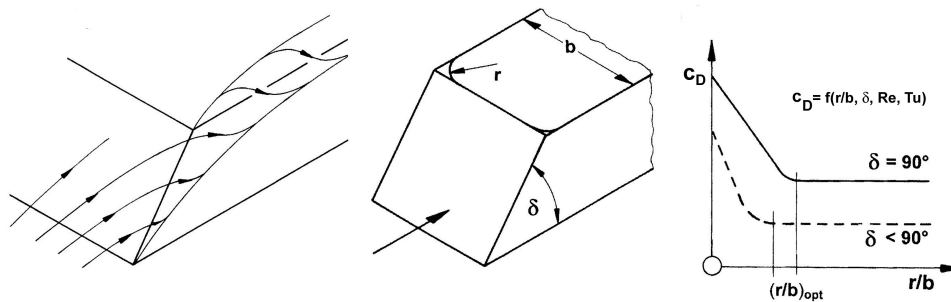


Figure 10: Generic model of windshield and A-Pillar ( $c_w = c_D$ )

The sketch in the center of Fig. (10) shows the geometry of the detail in question. In principle, only two parameters are required to describe it, and need to be investigated, the windshield angle  $\delta$  and the A-pillar radius  $r$ .

The flow pattern is sketched in Fig. (10), left side, and in Fig. (11). Current A-Pillars give

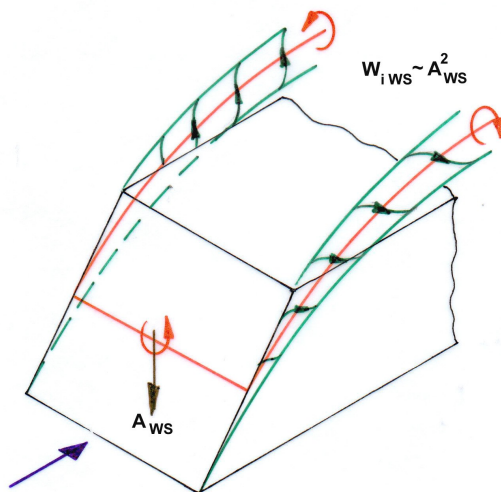


Figure 11: Horse-shoe vortex originating from the windshield ( $A = \text{lift}$ ;  $W = D$ )

rise to oblique (yawed) flows which roll up into two vortices that flow downstream over the outer parts of the roof. Together with the bound vortex on the windshield, these form a 'horse shoe' vortex, which induces a negative lift (down force) on the windshield  $A_{ws}$ . This is accompanied by a horizontal force - an induced drag,  $W_{iws}$ . Its magnitude is unknown, and consequently the graph shown on the right side of Fig. (10) is only hypothetical.

Investigating this detail would be timely. It could well turn out that a steeper but well rounded windshield is rewarded with lower drag, which would cause a problem for designers. Such shapes could be explored as numerical experiments with CFD codes.

## 2.4 Interference

Too little is known about interferences, especially those between fore- and after-bodies. Fig. (12) shows simple bodies of revolution. From the aerodynamics of bluff bodies, it is well known that the drag of such bodies can be reduced by two measures<sup>4</sup>:

- rounding the front (bow);
- tapering the rear (stern).

---

<sup>4</sup> Hucho (2002).

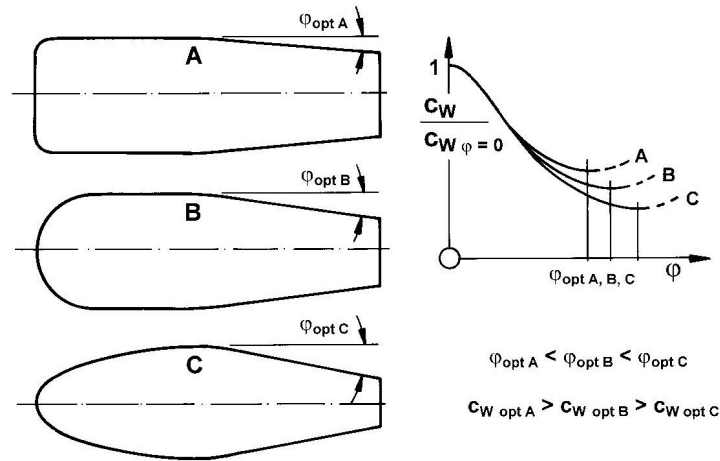


Figure 12: Interference effect between fore- and after-bodies ( $c_w = c_D$ )

Once the fore-body corners have been rounded to a given radius, case A, further increase of the radius will not reduce the drag. Hence this radius is the “optimum” for case A. However, it allows only a slight taper of the rear without separation and drag increase. If the fore-body is rounded more than this “optimum”, as in case B, and even more so in case C, the taper of the rear can be stronger, enabling a further reduction in the drag. These trends are shown in the *hypothetical* diagram at the right of the figure, for which no *quantitative* results are known. Again such shapes could be explored as numerical experiments with CFD codes.

Car body shapes with strong tapers are not currently fashionable. Instead both the front and rear tracks are often as large as possible, with the wheels positioned in the corners of a rectangular ground plan. However, older cars like the VW Type 3, Citroen DS, and NSU Ro 80 had strong tapers and drag coefficients that were low for their day. (See Fig. 1).

### 3 CONCLUSION

Vehicle aerodynamicists are today well equipped to explore even the most far-out ideas from designers. Yet no major reductions of air drag have been made for almost two decades. The “Limit value” strategy would overcome this stagnation, but requires that the gaps in the science of vehicle aerodynamics be filled. The most important of these gaps have been identified, together with suggestions for filling them.

### ACKNOWLEDGEMENT

The author owes sincerest thanks to Professor Lennart Löfdahl, and to Gordon Taylor for their valuable contributions to the paper.

### REFERENCES

- [1] Aronson, D., Brahim, S.B., Perzon, S. (2000): On the Under-body Flow of a Simplified Estate, SAE, Warrendale, PA.

- [2] Carr, G.W. (1983): Potential for Aerodynamic Drag Reduction in Car Design, *Impact of Aerodynamics on Vehicle Design.*, Vol. SP3, Ed. M.A. Dorgham, International Association for Vehicle Design, London, pp. 44 - 56.
- [3] Hucho, W.-H. (2002): *Aerodynamik der stumpfen Körper*, Vieweg Verlag, Wiesbaden.
- [4] Hucho, W.-H. (2009): Grenzwert-Strategie - Eine Halbierung des cW-Wertes scheint möglich., *ATZ*, Vol. 111, no. Januar 2009, pp. 16 - 23.
- [5] Hucho, W.-H. (Hrsg., 2005): *Aerodynamik des Automobils*, 5. Auflage, Vieweg Verlag, Wiesbaden.
- [6] Klemperer, W. (1922): Luftwiderstandsuntersuchungen an Automobil-Modellen., *Zeitschrift für Flugtechnik und Motorluftschiffahrt*, Vol. 13, pp. 201 - 206.
- [7] Mair, W.A. (1969): Reduction of Base Drag by Boat-tailed After bodies in Low Speed Flow, *Aeronautical Quarterly*, Vol. 20, pp. 307 - 320.
- [8] Morelli, A., Di Giusto, N. (1999): A New Step in Automobile Aerodynamics - Performance Improvements and Design Implications., *International Conference Vehicles and System Progress*, Ed. The Ministry of General and Professional Education, Volgograd, Russia.
- [9] Wiedemann, J. (1996): The Influence of Ground Simulation and Wheel Rotation on Aerodynamic Drag Optimisation - Potential for Reducing Fuel Consumption., *Vehicle Aerodynamics*, Vol. SP-1145, Ed. SAE, SAE, Warrendale, Pa., pp. 17 - 26.
- [10] Wolf, T., Preiss, M. (2004): Auslegung widerstandsarmer Kühlluftkonzepte am Beispiel des neuen Porsche 911 Carrera., *Fahrzeugaerodynamik*, Ed. H.d. Technik, Haus der Technik, Essen.

WHH February, 24<sup>th</sup>, 2009

## PIV INVESTIGATION OF THE FLOW FIELD UNDERNEATH A GENERIC HIGH-SPEED TRAIN CONFIGURATION

Mattias Jönsson\*, Johannes Haff\*, Hugues Richard\*, Sigfried Loose\* and Alexander Orellano†

\*Institute of Aerodynamics and Flow Technology, Department of Technical Flows (AS-TS)  
German Aerospace Center (DLR), Bunsenstrasse 10, 37073 Göttingen, Germany  
e-mail: Mattias.Joensson@dlr.de, Johannes.Haff@dlr.de, Hugues.Richard@dlr.de, Sigfried.Loose@dlr.de

† Center of Competence, Aerodynamics and Thermodynamics  
Bombardier Transportation, Am Rathenaupark, 16761 Hennigsdorf, Germany  
e-mail: Alexander.Orellano@de.transport.bombardier.com

**Keywords:** High-Speed Trains, Vehicle Aerodynamics, PIV, Euromech 509.

**Abstract.** *In this paper a 2C PIV measurement of the flow field underneath a 1:50 generic high-speed train configuration (front car, 2 coaches and tail car) and a smooth generic high-speed train configuration (the same model but without bogies and the bogie cut outs and inter car gaps filled) hauled through a water towing tank at a speed of 4 m/s is presented. The 2C PIV set-up was installed so that the vertical plane (XZ) between the ground and the train, in the centre line of the train, could be measured. The PIV system that was used could measure with an acquisition rate of 10 Hz, at this frequency 6 PIV images of the instantaneous flow field with a distance of 0.4 m from each other were made per run. The total field of view was 0.065 m x 0.025 m (WxH), to cover the entire flow field underneath the train model the position had to be shifted 8 times this was realized with the help of a trigger system. At every position 10 runs were made from which the ensemble average was calculated and reconstructed with the known shift, leading to the average flow field underneath the generic high-speed train configuration. All the presented results in this paper are from the calculated ensemble average.*

*The PIV measurement technique was applicable to measure the flow field underneath a down scaled train model in a water towing tank. The generic high-speed train configuration was compared to a full scale measurement. The same structure of the flow field was found for the flow around the head and the tail of the train. The flow field was fully developed at the beginning of the 2<sup>nd</sup> coach for both configurations. This also agrees with the full scale measurement. To achieve more realistic results in the future the simplified bogies that were used should be replaced with bogies with a higher degree of details. For the comparison between the two measured configurations a clear difference was found, the generic high-speed train configuration had a higher induced velocity underneath the train due to the protruding bogies.*

## 1 INTRODUCTION

The interest in underfloor aerodynamics of high-speed trains has increased in the last years due to the occurrence of several ballast projection incidents (flying ballast stones). Ballast projection correlated with ice/snow packing on the underbelly of the train, which later during travel falls down on the track and dislodges ballast stones, has been known since the beginning of the 1980's [1]. The measure to the snow/ice packing problem was to lower the ballast by around 4 cm beneath the sleepers [2]. In 2003 during a homologation test a ballast projection incident occurred though no winter conditions or foreign objects on the track bed were reported [3]. This was the first ballast projection incident initiated by the induced flow underneath the train. The aerodynamically loads grows quadratic with the train velocity which makes this a problem for high-speed trains. This motivated some of the operators and manufactures in the European railway industry to establish a project named AOA (Aerodynamics in Open Air) where one of the aims were to understand the mechanism of ballast projection. Within this project a full scale measurement was conducted with different types of measurement techniques installed to investigate the aerodynamically loads on the track bed [4]. Measurement techniques installed into the track bed have to be below the Top Of the Rail (TOR) due to safety reasons, hence from TOR and below the aerodynamically loads and the flow field can be measured.

To investigate the entire flow field underneath a train a PIV (Particle Image Velocimetry) measurement [5] on a 1:50 generic high-speed train configuration and a 1:50 smooth generic high-speed train (the same model but without bogies and the bogie cut outs and inter car gaps filled) in a water towing tank was carried out and described in this paper.

## 2 MEASUREMENT SETUP

### 2.1 Water Towing Tank Göttingen (WSG)

The 2C PIV measurement presented in this paper was performed in the water towing tank at DLR Göttingen. The water towing tank is an 18x1.1x1.1 m (LxWxH) big steel tank with thick glass window for optical measurements and visualizations see Fig. 1.



Figure 1: The water towing tank (left) and the generic smooth high-speed train configuration (right).

On the two upper edges of the tank rails for the moving model rig are installed. With the help of a steel cable and an electrical motor (installed outside the channel) the moving model rig can reach speeds up to 5 m/s. For this measurement a speed of 4 m/s was chosen, this corresponds to a Reynolds number of 0.24 Mio with the reference length scale of 3 m divided by the model scale (0.06 m) [6].

The 1:50 train model set (front car, 2 coaches and tail car) was attached to the moving model rig with the help of a long X-profile. Clamped onto the X-profile were 8 NACA 0030

profiles which emerged the train model into the water. The NACA profiles were chosen to minimize the influence of the flow field around the train model and were mounted on top of the roof to keep the flow field underneath the train model as undisturbed as possible. The fact that the NACA profiles might change the properties of the flow field underneath the train are not neglected but are considered as small.

For the correct ground simulation a ground plate was installed in the towing tank with a ground clearance of 0.235 m divided by the model scale (0.0047 m) that is the distance between ground and train wheel [6]. The ground plate was made out of Plexiglas plates mounted onto aluminum profiles, the ground had to be transparent for the light sheet in the 2C PIV set-up.

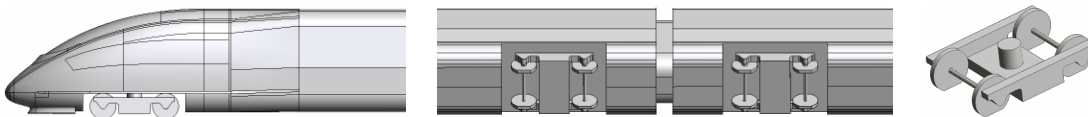


Figure 2: Shows the CAD model of the generic high-speed train configuration, head/tail (left), underbelly (middle) and the simplified bogie (right).

## 2.2 Particle Image Velocimetry Set-up and Measurement

The 2C PIV set-up that was used is shown in Fig. 3, the laser, light sheet optics and the 2 cameras are all installed outside the channel. The light sheet was so installed that the vertical plane between the ground and the train at the centre line of the train could be measured. The two cameras were installed perpendicular to the light sheet at both sides of the channel, two cameras were used to increase the measurement field or so called field of view, total field of view became 0.065x0.025 m (WxH). The 2 cameras were PCO 1600 cooled digital 14 bit CCD cameras with a resolution of 1600x1200 pixels (WxH), about 450 pixels resolved the gap between the ground and the train.

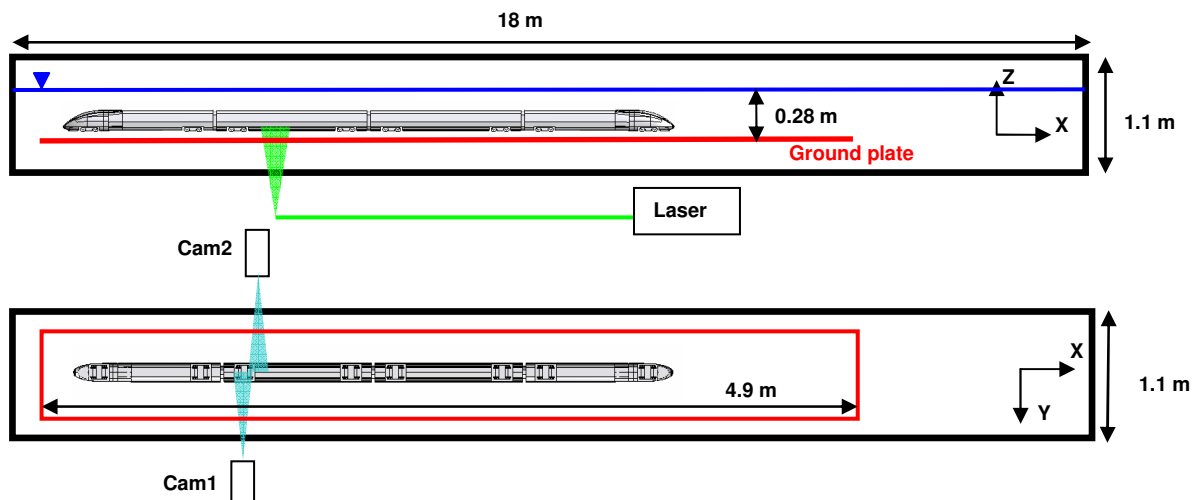


Figure 3: Sketch of the PIV set-up in the water towing tank.

The maximum acquisition rate of the PIV system was 10 Hz, with this frequency it was only possible to sample 6 PIV images with a 0.4 m distance from each other per run. To cover the entire train length (~2.1 m) the position of the train was shifted 8 times, this was done with the help of a trigger system. At every position 10 runs were made to be able to calculate

the ensemble average of the flow field, more over the post-processing of the PIV data will be explained in the next chapter.

### 3 DATA TREATMENT

#### 3.1 Evaluation of the PIV Data

The major steps in the post processing of the PIV data are listed below.

- 1) Calculate the flow field with the help of cross-correlation between the PIV images [7].
- 2) Find the shift between the runs to allocate the exact train positions.
- 3) Average the overlap between camera 1 and 2 and then shift the data into its right position for every run, thereafter the ensemble average was calculated, see Eq. 1. This was done for the flow field at every position.
- 4) Use the ensemble average flow field at every position to recreate the entire flow field underneath the train.

$$c(x_j, z_k) = \frac{1}{n} \sum_{i=1}^n c_i(x_j, z_k) \quad (1)$$

$$Cu(x, z) = \frac{U(x, z)}{U_{train}}, \quad Cw(x, z) = \frac{W(x, z)}{U_{train}} \quad (2), (3)$$

For the cross-correlation of the PIV images a multigrid interrogation (grid refinement) was used with a final interrogation window size of 24x24 pixels (0.522x0.522 mm) with an overlap of 75%. This configuration gave about 75 data points over the gap between the train and the ground.

Reference lines were painted on the side of the train to simplify the allocation of the train positions, the shift between the runs were about  $\pm 0.0024$  m. The lines enhance the accuracy of the ensemble average that was calculated for every position. When the shifts were found the PIV data from camera 1 and camera 2 were interpolated onto a slightly bigger equidistant grid ( $\Delta x = 0.00013$  m,  $\Delta z = 0.00013$  m), the bigger grid made it possible to interpolate all PIV data at one position onto the same grid independent of the magnitude of the shift, and then the overlapping data between camera 1 and camera 2 was averaged. For every position an ensemble average was calculated from the 10 runs, due to the shift between the runs, the ensemble average at the outer edges had a low sample rate and therefore a criteria was used that at least 8 samples out of 10 possible were needed to be defined as valid data. The ensemble average for every position was shifted to its right position and every overlapping region was averaged.

## 4 RESULTS

The presented results are the ensemble average of the flow field measured at the different positions and then put together to represent the entire flow field underneath the generic high-speed train configuration and the smooth generic high-speed train configuration.

### 4.1 Flow Field

In Fig. 4 the velocity field for the generic high-speed train configuration is shown in four plots, one for each part of the train set. For the upper plot where the front car is shown the effect of the head can be seen. In front of the head the water (in this case) is pushed in the same direction as the train travels, in 3D the water is pushed away from the head in all direction, this creates a reversal flow area around the head of the front car which can be seen in the plot. The reversal flow area ends shortly after the first bogie on the front car. Thereafter the flow



underneath the train is dragged in the direction of travel. The flow field underneath the train model develops with the train length until the beginning of the 2<sup>nd</sup> coach where it is fully developed. The flow field for the 2<sup>nd</sup> coach and the tail car is very similar at the beginning and until the middle of the tail car. The flow field for the second half of the tail car is influenced of the aerodynamics around the tail and that the train ends. The strong influence of the bogie-inter car gap-bogie area can also be seen, which is obviously since the underbelly is completely smooth except for these areas.

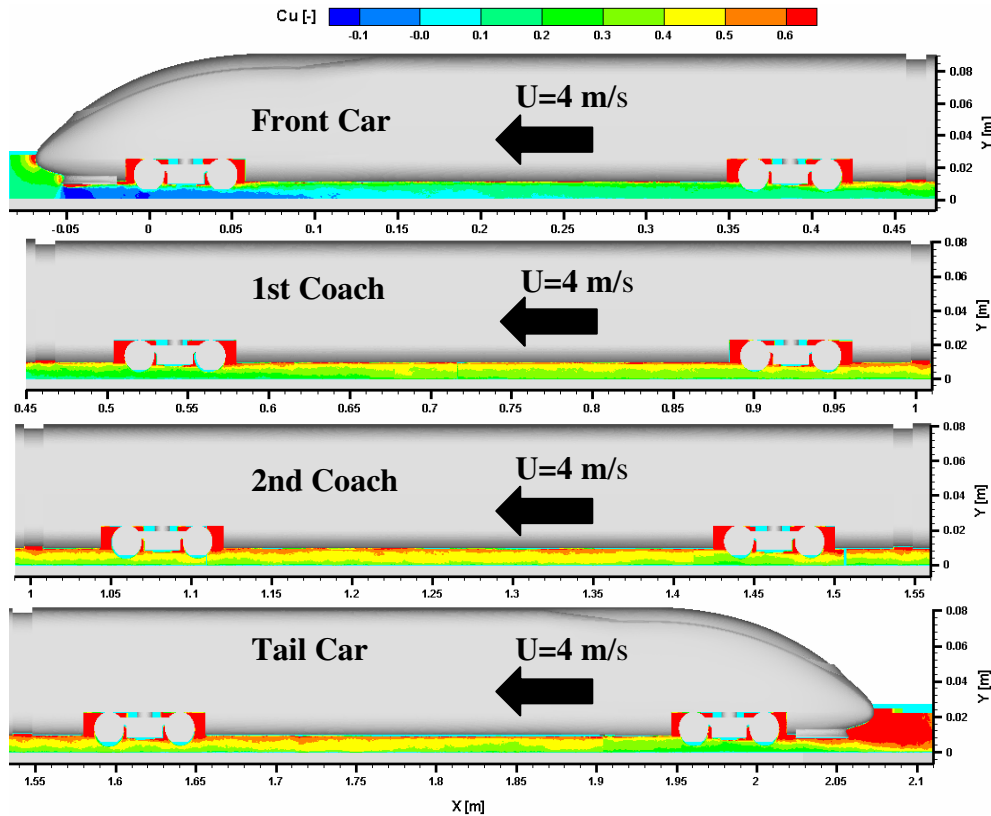


Figure 4: The Cu flow field underneath the generic high-speed train configuration.

In Fig. 5 the flow field for smooth generic high-speed train configuration is shown. At the train head the same phenomena as for the generic high-speed train configuration appears, but for this configuration the reversal flow area is more stretched out along the train length than for the generic high-speed train configuration. Also for this configuration the flow field is fully developed at the beginning of the 2<sup>nd</sup> coach. The Cu-value underneath the smooth generic high-speed configuration is smaller than for the generic high-speed train configuration, this was expected since the roughness on the underbelly was smaller. The difference between the two configurations shows the influence of the bogie-inter car gap-bogie areas. Thus it is shown that the bogie-inter car gap-bogie areas are the areas to improve to reduce the risk of ballast projection but also a topic for drag reduction of high-speed trains.

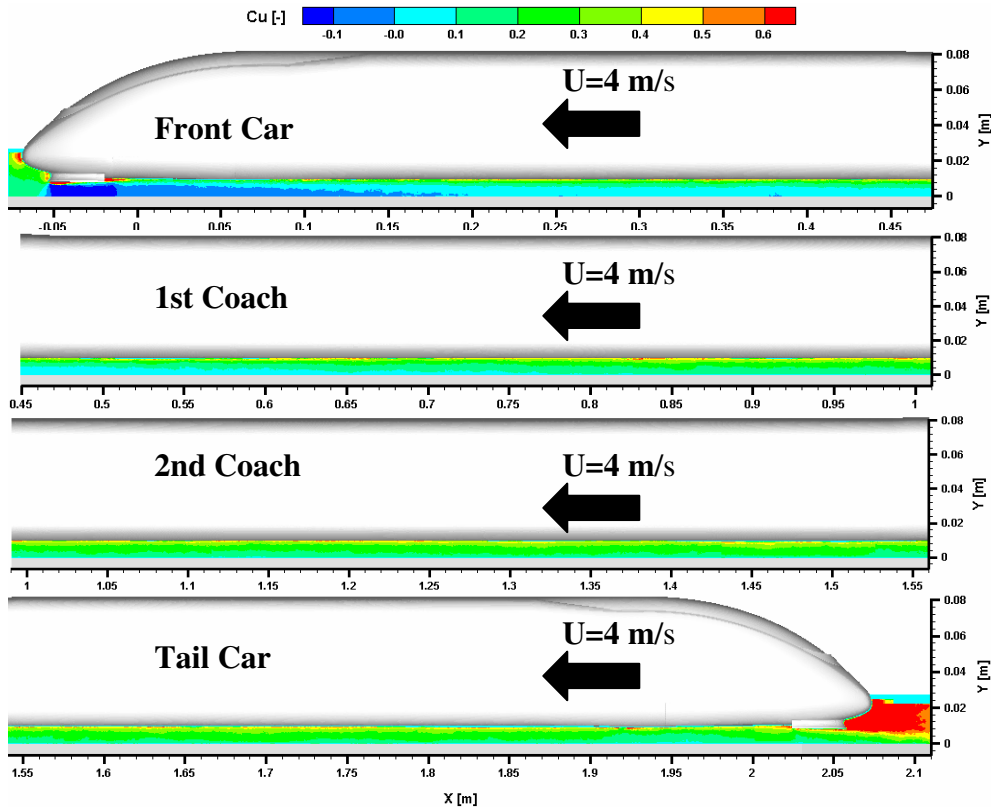


Figure 5: The Cu flow field underneath the smooth generic high-speed train configuration.

Small discrepancies between the coaches and between the two configurations might be hidden in the color scale and therefore data were extracted from the flow fields along the train length at different heights (Z-pos.) for a better comparison.

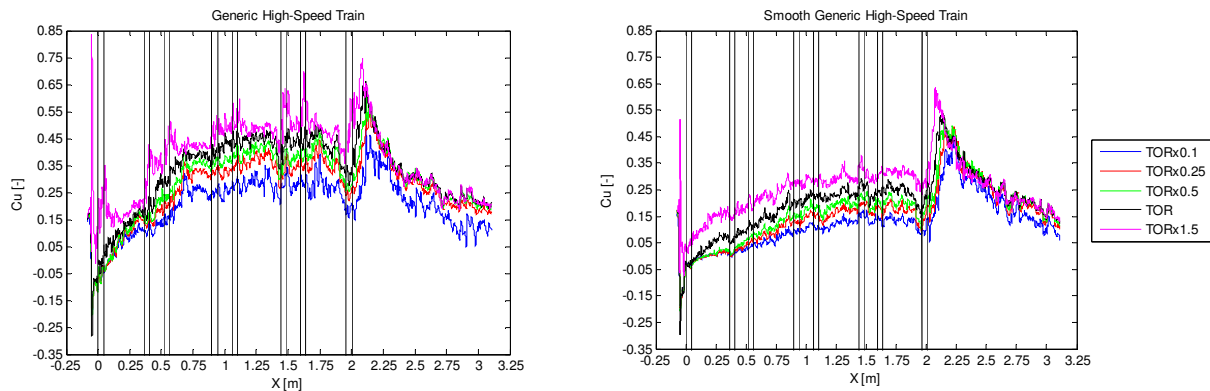


Figure 6: The Cu-value plotted against the train length for the generic high-speed train configuration (left) and the smooth generic high-speed train configuration (right) at different heights (z-pos.). The vertical black lines indicate the positions of the train axles for the generic high-speed train configuration.

The extracted data along the train length for 5 different heights are plotted in Fig. 6. For the smooth generic high-speed train configuration the trend of the curves are very similar, what separates them from each other are the magnitude of the Cu-value. The same trend was also found for the generic high-speed train configuration, except for the height 1.5xTOR (purple curve). For this height the effect of the bogies can easily be seen at every train axle where a peak in the Cu-value is found. The growth of the Cu along the train model length is pretty

constant until the beginning of the 2<sup>nd</sup> coach where the flow field is fully developed, this applies for both configurations. However the gradient for the front car and the 1<sup>st</sup> coach is higher for the generic high-speed train configuration than for the smooth generic high-speed train configuration due to the presence of the bogies.

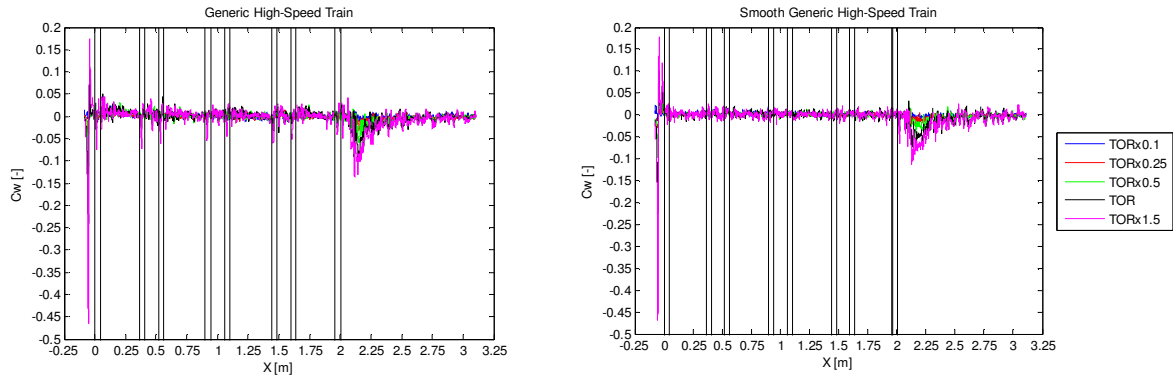


Figure 7: The  $C_w$ -value plotted against the train length for the generic high-speed train configuration (left) and the smooth generic high-speed train configuration (right) for different heights ( $z$ -pos.). The vertical black lines indicate the positions of the train axles for the generic high-speed train configuration.

In Fig. 7 the normalized vertical velocity ( $C_w$ ) for the same height as for  $C_u$  are plotted. The vertical velocity is dominant at the head and at the tail of the train for both configurations (strongest for the head). There are no protruding objects underneath the smooth generic high-speed train configuration so no vertical velocities are expected, except for the head and the tail of the train, so the vertical velocity that swings around zero along the train length is considered as noise. However for the generic high-speed train configuration protruding objects exist (bogies) vertical velocities along the train was found, especially for the height  $1.5 \times \text{TOR}$  (purple curve) which is closest to the train. The  $C_w$  peaks with a direction towards the ground found for the height  $1.5 \times \text{TOR}$  is the effect of the protruding bogie frame which is not aligned with the underbelly of the train. Also here the vertical velocity that fluctuates around zero at the middle of the coaches is considered as noise.

For the comparison between the two measured configurations the velocity data at TOR were chosen and plotted in Fig. 8.

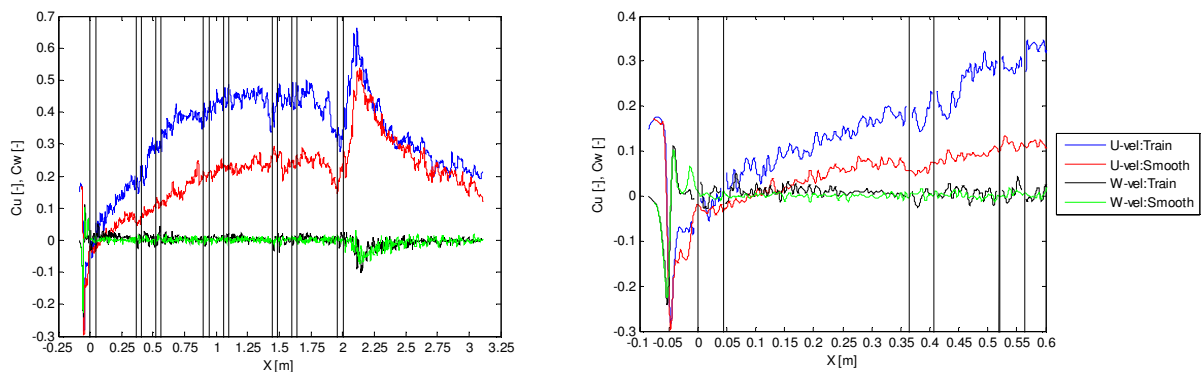


Figure 8: Comparison between the generic high-speed train configuration ( $C_u$ : blue and  $C_w$ : black) and the smooth generic high-speed configuration ( $C_u$ : red and  $C_w$ : green). The vertical black lines indicate the positions of the train axles for the generic high-speed train configuration.

In front of the train head no difference can be found between the two configurations, it is first shortly before the first bogie where the two configurations deviate from each other. After the

first bogie a clear difference for the Cu between the configurations along the entire train model length can be observed, it is first in the wake of the train model where the Cu value of both configurations comes close to each other again. However for the Cw, differences between the configurations are found around bogie areas which are no surprise since one of the configurations is totally smooth. The same tendencies were also found for the other heights as for TOR. The only difference was found for the data closer to the ground where the configurations first deviate from each other shortly after the first bogie instead of before due to the distance to the bogies.

In the two tables below the Cu average for the 2<sup>nd</sup> coach at different heights are shown and compared to each other. The average of the 2<sup>nd</sup> coach was used, instead of the entire train model length, because the flow field underneath the train model is fully developed at the beginning of the 2<sup>nd</sup> coach. For the tail car the aerodynamics around the tail and the end of the train model affects the flow field underneath the tail car. Also in [4] the front car and the first coach but also the last coach and the tail car were neglected in the calculation of the train average. For the train model set in this paper the principle in [4] could not be applied and therefore the 2<sup>nd</sup> coach was chosen.

Height	Generic High-Speed Train		Smooth Generic High-Speed Train	
	Cu [-]	Cu/Cu(TOR) [-]	Cu [-]	Cu/Cu(TOR) [-]
TOR	0.43833	1	0.23571	1
0.1xTOR	0.27901	0.63653	0.12587	0.53401
0.15xTOR	0.31723	0.72371	0.14545	0.61705
0.25xTOR	0.35306	0.80545	0.16695	0.70826
0.5xTOR	0.38994	0.88959	0.19404	0.82320
0.75xTOR	0.41397	0.94442	0.21441	0.90960
1.25xTOR	0.46315	1.05662	0.26287	1.11520
1.5xTOR	0.49494	1.12915	0.29682	1.25923

Table 1: The average Cu and the Cu normalized by the Cu(TOR) for the 2<sup>nd</sup> coach at different heights.

In Table 1 the tendency for the average Cu for the 2<sup>nd</sup> coach can easily be seen, for both configurations the Cu average grows with a decreasing distance to the train model. For the normalized Cu values (Cu/Cu(TOR)) the two measured configuration differs from each other, hence not only the magnitude of the Cu but also the gradient of Cu are different between the two configurations.

Height	Cu_train/Cu_smooth [-]
TOR	1.85960
0.1xTOR	2.21660
0.15xTOR	2.18102
0.25xTOR	2.11479
0.5xTOR	2.00957
0.75xTOR	1.93077
1.25xTOR	1.76191
1.5xTOR	1.66749

Table 2: Comparison between the two configurations of the Cu average for the 2<sup>nd</sup> coach.

A direct comparison between the two configurations was done with the Cu average for the 2<sup>nd</sup> coach, the results are shown in Table 2. As expected the generic high-speed train configuration had a higher Cu average than the smooth generic high-speed train configuration. The reason for the higher Cu averages is simply the higher roughness on the underbelly of the generic high-speed train configuration. The largest difference was found close to the ground.

## 4.2 Velocity Profiles

For a better view of the velocity distribution over the gap (ground-train) velocity profiles were extracted for both configurations. For the front car, the 2 coaches and the tail car, each 7 velocity profiles were extracted and plotted with an offset in Fig. 9 and Fig. 10. The first profile for every coach (orange line 1,8,15,22 from the left in Fig. 9 and Fig 10) has an offset of 0, the second has an offset of 1 and so on until the seventh and the last velocity profile (offset of 6). The fourth velocity profile at every coach is in the middle of the coach, the three profiles to the left and to the right are distributed with a distance of  $\Delta x=0.04$  m from each other. The regions closest to the train and the ground are chosen not to be plotted due to the reflections laser light sheet on the train model and on the ground.

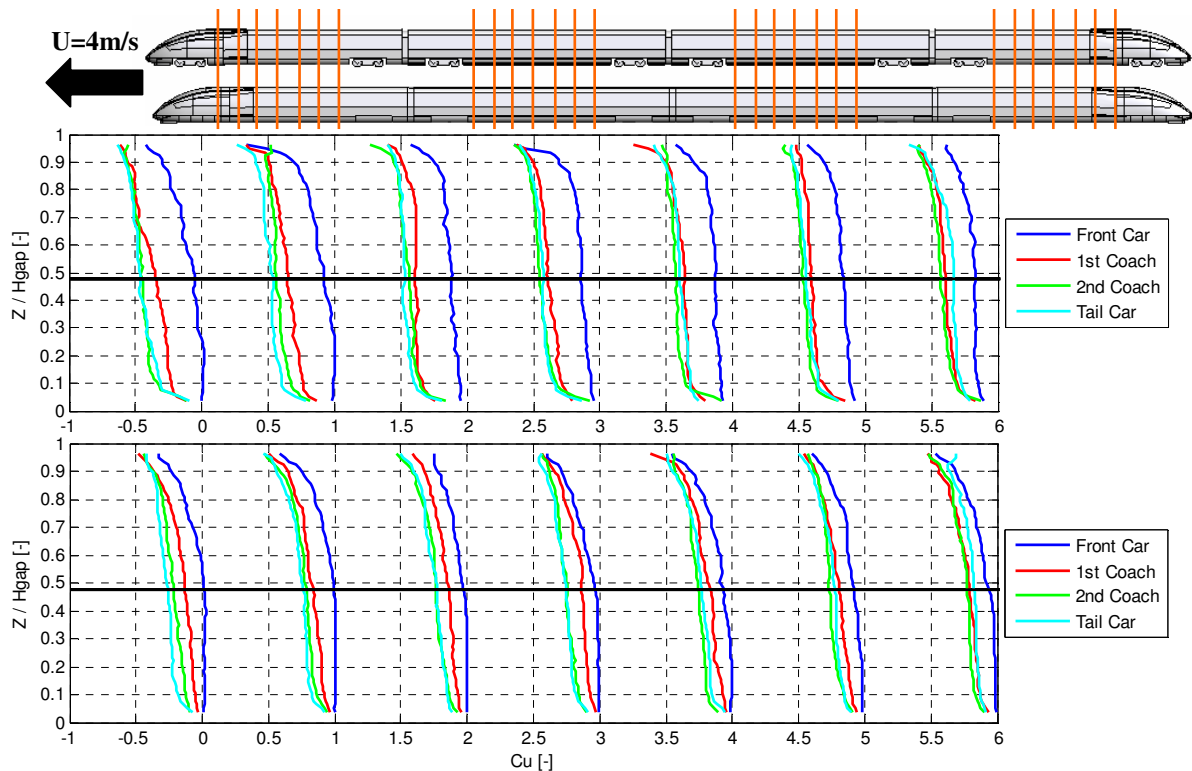


Figure 9: Comparison between the velocity profiles for the different coaches generic high-speed train configuration (upper plot) and the smooth generic high-speed train configuration (lower plot), the black solid horizontal line indicates the TOR and the orange lines on the trains above the plots shows the positions of the velocity profiles.

In Fig. 9 the velocity profiles from the front car, the 2 coaches and the tail car are plotted on top of each other for the generic high-speed train configuration (upper plot) and the smooth generic high-speed train configuration (lower plot). The velocity profiles shows the development of the flow underneath the both configurations, the flow is fully developed at the 2<sup>nd</sup> coach for both configurations since the differences between the velocity profiles for the 2<sup>nd</sup> coach (green) and the tail car (cyan) are small. Another indication that the flow is fully devel-

oped at the 2<sup>nd</sup> coach is the trend for the velocity profiles for the 1<sup>st</sup> coach (red). The profile difference between the 1<sup>st</sup> coach and the 2<sup>nd</sup> coach becomes smaller in the direction of the train model length (from left to right in Fig. 9). For the velocity profiles furthest to the right, a larger difference than before is found between the tail car (cyan) and the 2<sup>nd</sup> coach. This is probably the effects of the train model tail.

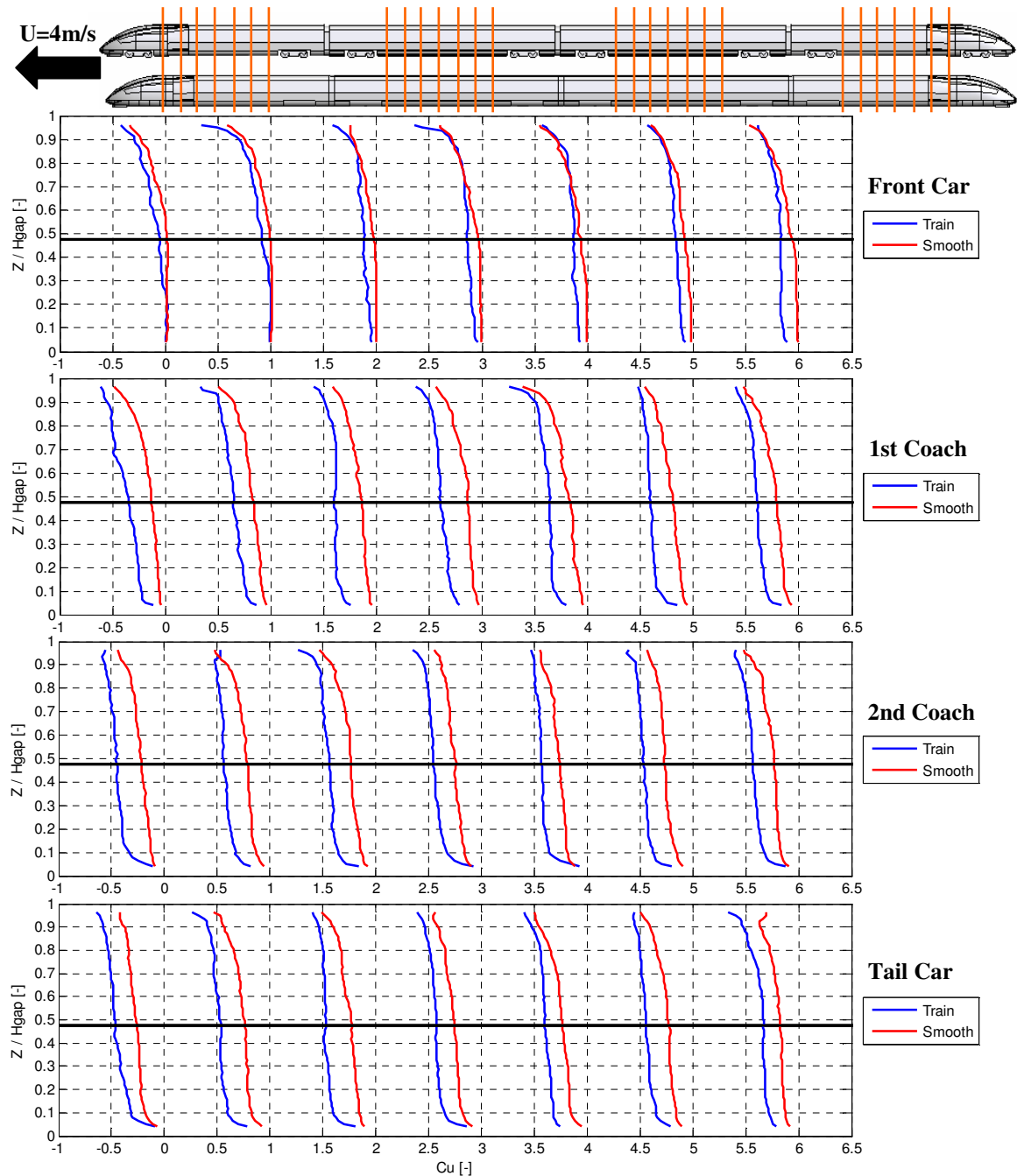


Figure 10: Comparison of the velocity profiles underneath the generic high-speed train configuration (blue) and the smooth generic high-speed train configuration (red), the black solid horizontal line indicates the TOR and the orange vertical lines on the trains above the plots shows the positions of the velocity profiles.

In Fig. 10 the velocity profiles for the two configurations are compared to each other for the front car, 1<sup>st</sup> coach, 2<sup>nd</sup> coach and the tail car. A clear difference between the two configurations can be seen for every velocity profile. It is only for the 1<sup>st</sup> and 2<sup>nd</sup> velocity profile for

the front car below  $Z/H_{gap} < 0.3$  where the profiles are hard to separate from each other. The  $C_u$  values close to the ground and the gradients are higher for the generic high-speed train configuration than for the smooth generic high-speed train configuration, hence the generic high-speed train configuration has a higher risk for ballast projection incidents. Another interesting observation is the similarities of the velocity profiles for the 1<sup>st</sup> coach, 2<sup>nd</sup> coach and the tail car between  $0.2 < Z/H_{gap} < 0.7$  where no major differences in the gradient can be seen.

### 4.3 Comparison to Full Scale Measurements

The PIV results from the water towing tank were compared to the full scale measurements on the Italian high-speed train ETR 500 [4], shown in Fig. 11. The down scaled train set had only 2 coaches except from the front car and the tail car where the ETR 500 had 12 coaches, therefore two comparisons were done one for the beginning of the ETR 500 and the other one for the end. The length scale for the PIV results in the towing tank was transformed into full scale by multiplying it by the scale factor.

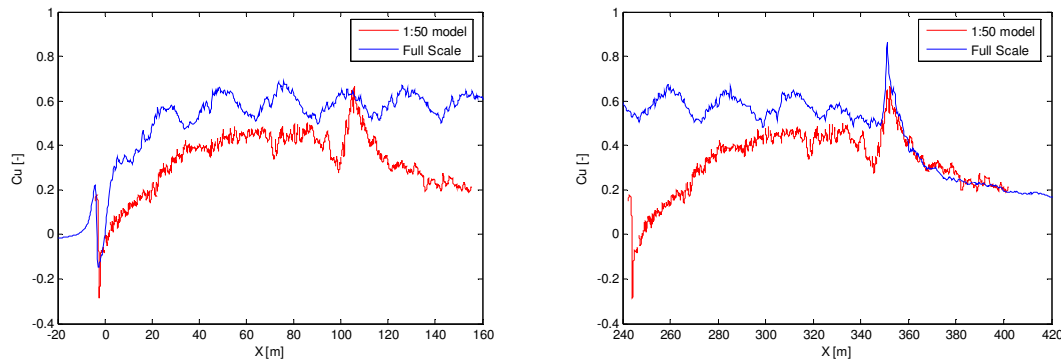


Figure 11: Comparison to full scale measurements [4].

For the generic high-speed train configuration the same structure of the flow field was found for the flow around the head and around the tail. The flow was fully developed at the beginning of the 2<sup>nd</sup> coach, which also was the case for the full scale measurement.

The down scaled train model never reached the same level of  $C_u$  as the full scale measurement. The reason for this is the simplified bogies that were used for the down scaled measurement which are completely smooth on the surface facing the ground, see Fig. 2. Hence the simplified bogies are aerodynamically better than the real bogies on a train where a lot of protruding objects exist (gear box, electrical motor, cables etc). The air can also flow into the bogie cut out and be accelerated by the train. The simplified bogies with a smooth surface shields the bogie cut out and are therefore aerodynamically better than the real ones.

Another parameter that plays an important role is the Reynolds number, also here a match could not be realized. For a full scale train with a speed of 270km/h a  $Re=15$  Mio is reached, in the down scaled measurement in the water towing tank a maximum of  $Re=0.24$  Mio was achieved.

## 5 CONCLUSIONS

- The PIV measurement technique is applicable to measure the flow field underneath a down scaled train model in a water towing tank.
- The flow field is fully developed at the beginning of the 2<sup>nd</sup> coach for both measured configurations. This also agrees with the full scale measurements.
- Underneath both configurations close to the ground the  $C_u$  is the dominant velocity, it is only at the head and at the tail where the vertical velocity ( $C_w$ ) has to be taken into account.
- A clear difference between the generic high-speed train configuration and the smooth high-speed train configuration could be found, which was expected.
- The biggest difference between the velocity profiles for the two configurations was found close to the ground. However in the middle of the gap ( $0.2 < Z/H_{gap} < 0.7$ ) for the 1<sup>st</sup> coach, 2<sup>nd</sup> coach and the tail car no major difference between the configurations could be seen, except for the magnitude of  $C_u$ .
- For the generic high-speed train configuration the same structures of the flow field was found for the flow around the head and around the tail as in the full scale measurements.
- To get more realistic data for the generic high-speed train configuration the simplified bogies should be exchanged with bogies with a higher degree of details.
- Important information can be extracted from down scaled measurements, however to extrapolate the results into full scale should be done with caution.

## REFERENCES

- [1] K. Shinojima. *Study on the Phenomena of Snow Adhering to and Dropping from Shinkansen Train, and the Countermeasures*. Quarterly Reports vol.25 No.2, p 41 – 44, 1984.
- [2] L. Karlsson. Litteraturstudier till projektet stensprut X2000. Bombardier Transportation Internal Reports. Doc. Ref. No. RES/KBM/TR-91/066, 1991.
- [3] P. Claus. AOA WP 1.2 Ballast Projection: Prestudy of Ballast Projection Incidents. 071119-AOA-WP1.2-Prestudy-V1.0, 2007.
- [4] P. Deeg, M. Jönsson, H. J. Kaltenbach, M. Schober and M. Weise. Cross-Comparison of Measurement Techniques for the determination of train induced Aerodynamic Loads on the trackbed. Proceedings of the BBAA VI, Milano, Italy, July 20-24, 2008.
- [5] H. Eckelmann. *Einführung in die Strömungsmeßtechnik*. B. G. Teubner, Stuttgart, Germany, 1997
- [6] prEN 14067-6:2006 Railway Applications – Aerodynamics – Part 6: Requirements and test procedures for cross wind assessment. 2006.
- [7] M. Raffel, C.E. Willert, S.T. Wereley and J. Kompenhans. *Particle Image Velocimetry 2nd ed.* Springer, Berlin, Germany, 2007.



## SHAPE OPTIMIZATION OF A BUS FOR CROSSWIND STABILITY

Siniša Krajnović\*, Haukur Elvar Hafsteinsson\*, Eysteinn Helgason\*

and Branislav Basara†

\*Chalmers University of Technology  
Department of Applied Mechanics, Göteborg, Sweden  
e-mail: [sinisa@chalmers.se](mailto:sinisa@chalmers.se)

†AVL List GmbH, Graz, Austria

**Keywords:** Aerodynamic shape optimization, response surface, simplex, crosswind stability.

**Abstract.** *Two numerical algorithms for optimizing the aerodynamic properties of road vehicles are presented. The first algorithm is based on a priori exploration of the design space, construction of response surfaces for the design objectives and minimizing them. This algorithm was applied in the present work to improve the crosswind stability of a bus. The second algorithm is fully automatic and starts with two initial designs that are then changed by the design algorithm during the design process. This modification of the original design is done by SIMPLEX, which is an algorithm for nonlinear optimization problems, while the resulting change of the design variables during the design process is achieved with morphing of computational grids. Only the initial results for optimization of a passenger car using this automatic algorithm are presented. Both methods are found to be promising for the optimization of the aerodynamic properties of vehicles.*

## 1 INTRODUCTION

The term *optimization of aerodynamic properties of ground vehicles* is often used when aerodynamic properties of small number vehicle shapes are explored in wind tunnels or numerical simulations. This is a very restricted definition of an *aerodynamic optimization*. In the present paper we will present two methods that are capable of finding not only a *better* aerodynamic shape but the *best aerodynamic shape*. The idea in the present work is to develop a numerical algorithm that is capable of searching the design space for the design that possesses the optimal values of the aerodynamic objectives. Systematic shape optimization of ground vehicles with the aim to improve their aerodynamic properties is very dependent on our ability to explore the design space either by numerical simulations or experiments. The present work uses numerical simulations rather than experiments to evaluate of aerodynamic objectives as the final goal is to have a completely automatic optimization procedure. An efficient way to reduce the computational effort required for exploring the design space is to use a qualitative interpolation model in the form of a response surface (RS). In this case the objective functions are evaluated in limited number of design points (called design of experiments (DOE)) that are representative for the design space. The second step of this procedure is to solve flow equations (using computational fluid dynamics (CFD)) in the DOE points and construct response surfaces for aerodynamic goal functions. Finally, the optimization is performed by minimizing or maximizing the RS function. In the present paper, we shall demonstrate this method in the optimization of the crosswind stability of a bus. In order to speed up the optimization procedure, a search algorithm can be used directly after a small number of CFD simulations without previously exploring the entire DOE and constructing RS. In the second half of the paper we use a numerical algorithm SIMPLEX to search the design space and suggest a change in the geometry. This automatic search procedure requires that the optimization procedure is capable of making new computational grids. The new computational grids are provided from the reference grid using grid morphing. The morphed grid is then sent back to the CFD solver and the loop is closed. Only a first attempt to use this promising optimization is demonstrated in the present paper.

## 2 THE BUS MODEL AND THE DESIGN VARIABLES

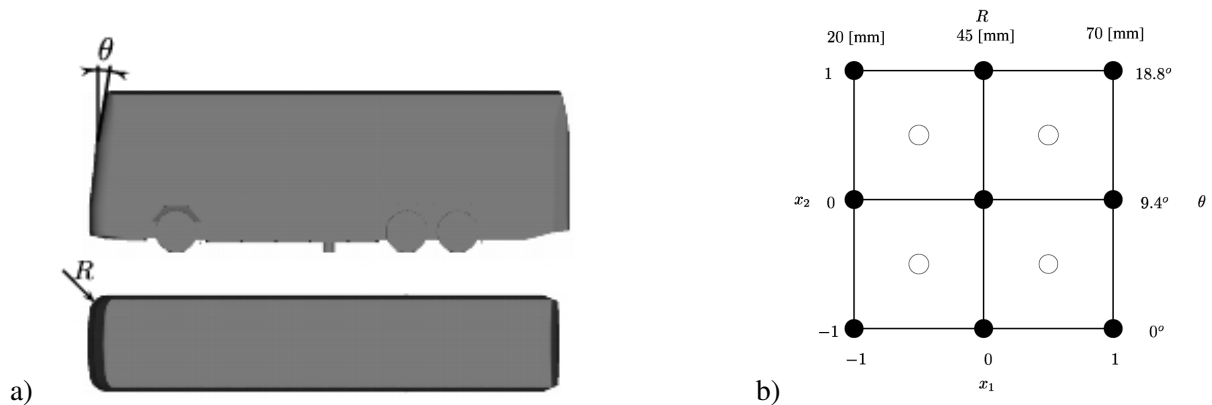


Figure 1: a) Geometry of the bus model showing design variables; angle  $\theta$  and radius  $R$ . b) Center composite design for the optimization of the bus.  $x_1$  and  $x_2$  are coded variables

The bus model used here is the one from previous work by Hemida and Krajnović (2007). It is a 1/10 scale double decked bus of type Scania K112 TL. The geometry of the original body is shown in Fig. 1a. The height and the length of the model are  $H=400$  [mm] and  $L=1190$  [mm], respectively while the width at the widest position is  $W=300$  [mm]. The model's underbody contains axles between the wheels, support for the model, beams in the spanwise and the streamwise directions (for the purpose of

simulating the roughness of the underbody) and holes between the wheelhouses.

### 3 THE REFERENCE DESIGN AND FLOW SET-UP

The computational set-up is presented in Fig. 2. The cross section of the computational tunnel is identical to that used in the experimental study by Torlund (1999). It has a circular shape with a diameter of 3.6 [m]. The inlet and the outlet are located at lengths of  $8H$  and  $21H$ , respectively, from the surface of the bus in order to minimize the influence of the domain boundaries on the flow.

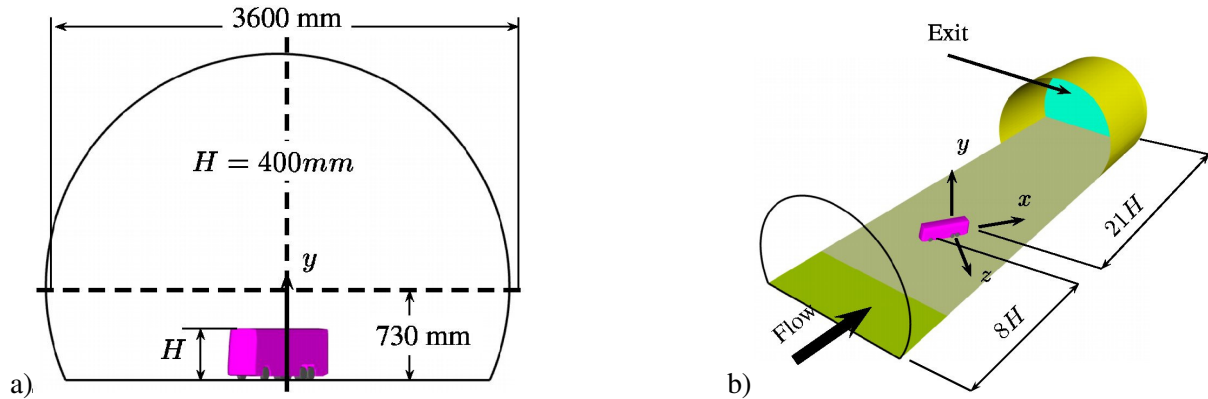


Figure 2: Computational domain showing the view from a) inlet of the tunnel and b) perspective view.

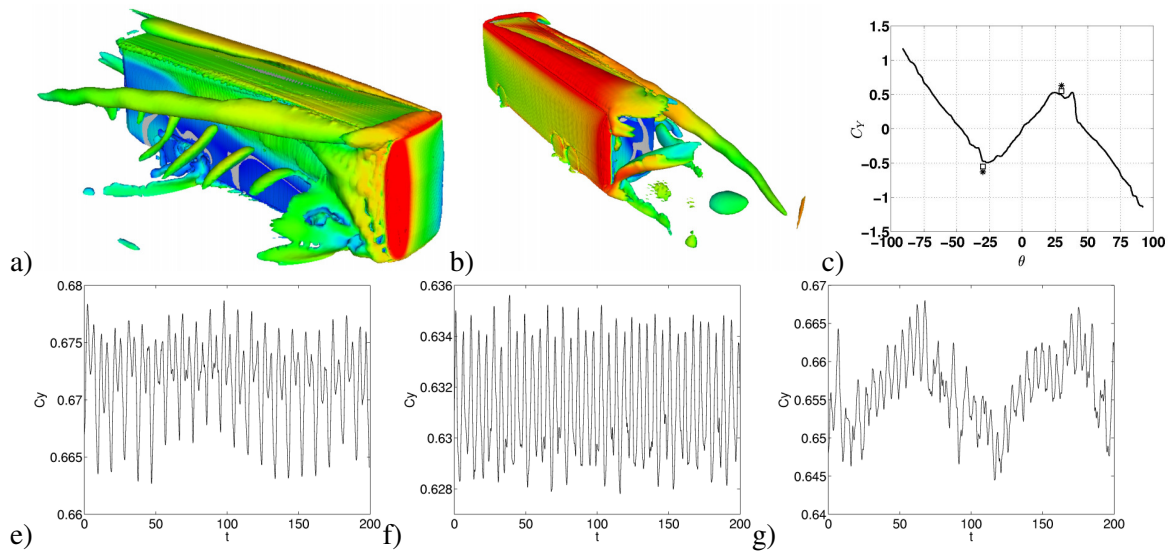


Figure 3: Instantaneous flow structures visualized using an iso-surface of second invariant of the velocity gradient  $Q$  colored with the velocity magnitude showing a) the lee side of the bus from in front of the bus and b) the wind side of the bus from behind the bus. c) Comparison of the yaw moment coefficient from experiment (solid line), previous DES (squares) from Hemida and Krajnović (2007) and present URANS using  $\zeta - f$  turbulence model (stars). e-g) Time history of the yaw moment signal for the bus with  $R=45$ [mm] and  $\theta = 0^\circ, 9.4^\circ$  and  $18.8^\circ$  in e), f) and g), respectively.

A uniform velocity profile at 57 [m/s] was applied as the inlet boundary condition. A wall approach that combines the integration up to the wall with wall functions was applied at the surface of the model, the floor and the circular wall of the tunnel. Homogeneous Neumann boundary conditions were applied at the outlet of the tunnel. The aerodynamic coefficients were obtained by normalizing the forces with density  $\rho = 1.16$  [kg/m<sup>3</sup>], free stream velocity  $U_\infty = 57$  [m/s] and the reference area  $A = 0.1$  [m<sup>2</sup>]. The same normalization was used in the previous experimental study (Torlund (1999)) and DES simulation (Hemida and Krajnović (2007)).

#### 4 NUMERICAL SIMULATIONS IN THE DESIGN POINTS

Steady Reynolds-averaged Navier-Stokes (RANS) and unsteady RANS (URANS) simulations using a  $\zeta - f$  turbulence model (called  $k - \zeta - f$  in AVL FIRE) by Hanjalić *et.al.* (2004) are used to obtain the values of the objectives at the design points. In the present paper we present only optimization results using steady RANS and only a part of the results of the URANS will be shown. The complete results using URANS will be presented in Krajnović and Basara (2009). Figure 3 a-b) shows the instantaneous flow resulting from the URANS simulation. Although the instability of the roof vortex found in DES was not predicted in our URANS, the vortex shedding process is captured. Time histories of the yawing moment coefficient are shown in Figs. 3e-g for different  $\theta$ . It is clear from these figures that both the frequency and the amplitude of the flow variables change with  $\theta$ . The yawing moment is the moment around y-axis in Fig. 2.

The commercial finite-volume code AVL FIRE v2008 (AVL AST (2008)) was used for all the simulations. The momentum equations were discretized using a bounded second-order upwind scheme (MINMOD bounded in AVL FIRE). The computational grids are made using preprocessor FAME of AVL FIRE and contain a cubic refined region around the model. Each computational grid contained approximately  $7 \times 10^6$  nodes.

The resolution, expressed in wall units, is, at the surface of the bus, approximately  $y^+ \leq 5$  for most of the computational nodes. The universal wall approach, which combines the integration up to the wall represented with the  $\zeta - f$  model with wall functions, was used for all calculations. The universal wall approach is implemented in AVL FIRE following the proposal of Popovac and Hanjalić (2007) and is known as a compound wall treatment. This approach includes the blending formula for the quantities specified at the cell next to the wall between viscous and fully turbulent values of the following variables: wall shear stress, production and dissipation of the turbulent kinetic energy. Their compound wall treatment was introduced and used in AVL FIRE under the name "Hybrid Wall Treatment" due to some simplifications of the original approach (Basara, 2006).

Simulations of all cases at the design points were run until the residuals reached an asymptotic behavior at approximately  $10^{-3}$  with residuals normalized by  $\sum_{nodes}^{all} a_p \phi_p$ , where  $a_p \phi_p$  is the left hand side in

the standard form of the finite volume equation. Another measure of convergence that was used in the present simulations is that all aerodynamic forces should stabilize. However, the  $\zeta - f$  model used in the present study tends to seek unsteady solutions when the calculation reaches low residuals. In the present work the aerodynamic forces were averaged over 200 iterations at the end of each computation in order to obtain a mean value of the forces.

#### 5 VALIDATION OF THE NUMERICAL METHOD

Before the exploration of the design space was initiated, the numerical technique chosen was validated for the reference design against the existing experimental data (Torlund (1999)) and a previous Detached Eddy Simulation (DES) by Hemida and Krajnović (2007). For example, the steady RANS us-

ing the  $\zeta - f$  model predicted  $C_D = 0.61$  and  $C_S = 3.6$  compared to the experimental values; of  $C_D^{EXP} = 0.54$  and  $C_S^{EXP} = 3.4$ . The values of  $C_D$  and  $C_S$  in the present simulation agree well with DES values from Hemida and Krajnović (2007). Another example of comparison of the result is shown in Fig. 3c for yaw moment coefficient and URANS using  $\zeta - f$  mode.

Our results confirm that the  $\zeta - f$  model used here is appropriate for the current optimization purpose. However, we are aware that only simulations in an unsteady mode are appropriate, as no steady solution exists.

## 6 EXPLORATION OF THE DESIGN SPACE

Two design variables were used in the present study: the angle of the windscreen  $\theta$  and the radius of the front vertical edges  $R$  (Fig.1a). Design constraints were set as  $0^\circ \leq \theta \leq 18.8^\circ$  and  $20 \text{ [mm]} \leq R \leq 70 \text{ [mm]}$ , which enclose the original design with  $\theta = 9.4^\circ$  and  $R = 40 \text{ [mm]}$ . These limits for the design variables were chosen to retain a shape of a bus that is easy to manufacture and does not imply large reduction of the inner space of the bus.

In the present study, center composite design (CCD) was used as a design of experiment (DOE) method. The DOE is presented in Fig. 1b. Nine designs were used for construction of the model and four design points were used for the evaluation of the accuracy of RS model. Here,  $x_1$  and  $x_2$  are design variables normalized between -1 and 1.

## 7 RESULTING FLOW FEATURES

Figure 4 shows how the near wake region behind the leeward and the base sides of the bus grows with sharper vertical front edges (i.e. lower  $R$ ) and larger angle  $\theta$ . Figure 5 shows the surface pressure and the flow structures from our URANS for the buses used in the DOE. Similar is visible from steady RANS (Krajnović *et. al.* (2008)). As shown in Krajnović *et. al.* (2008), an increase in  $R$  decreases the pressure on both the front and the leeward sides of the bus. On the other hand, increasing  $\theta$  seems to lower the pressure on the leeward and the front side of the bus. This gives a preliminary indication of the trends in aerodynamic forces. Large radius  $R$  and small angle  $\theta$  seem to be beneficial for drag while they deteriorate crosswind stability by increasing the side force.

## 8 CONSTRUCTION OF THE RESPONSE SURFACES

### 8.1 POLYNOMIAL RESPONSE SURFACE

The approximation of the true response in a polynomial RS is represented by low-order polynomials which in the present paper are quadratic. A quadratic RS model reads

$$\hat{C} = \beta_0 + \sum_{i=1}^n \beta_i x_i + \sum_{j=1}^n \sum_{i < j} \beta_{ij} x_i x_j + \sum_{i=1}^n \beta_{ii} x_i^2 \quad (1)$$

where  $n$  is the number of design variables and  $\beta_i, \beta_{ii}, \beta_{ij}$  are the regression coefficients. The regression coefficients are determined by a least square regression. The RS can be expressed in matrix notation as  $\hat{C} = \mathbf{x}^T \mathbf{b}$  where  $\mathbf{b} = (\mathbf{X}^T \mathbf{X})^{-1} \mathbf{X}^T \hat{C}$  and  $\mathbf{X}$  is the matrix containing the experimental designs.

For details about how to measure the goodness of fit and about improvement of the original polynomial model using e.g. backward elimination we refer to Krajnović *et. al.* (2008).

## 8.2 RADIAL BASIS NEURAL NETWORK RESPONSE SURFACE

Response surfaces based on Radial Basis Neural Network (RBNN) are dependent for the construction of RS dependent on training a two-layer network in DOE. As in any other neural network in RBNN, training is done by adjusting weights on the internal connections of the network through a defined training algorithm. The RBNN consists of one hidden radial basis layer and an output linear layer. The transfer function,  $a$ , of neurons in the hidden radial basis layer is given by the radial basis function

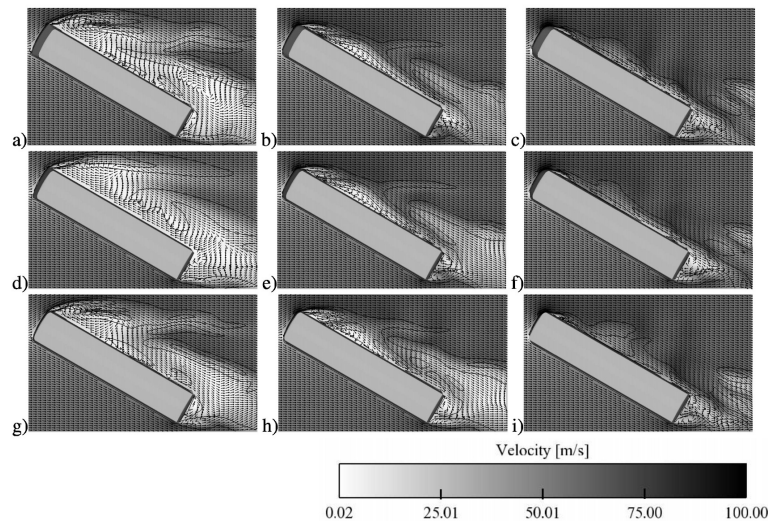


Figure 4: Velocity vectors and iso-contours of the vorticity component  $\omega_y$  for designs at the design points (black dots) of DOE presented in Fig.1b. The plane is at the mid-height of the bus.

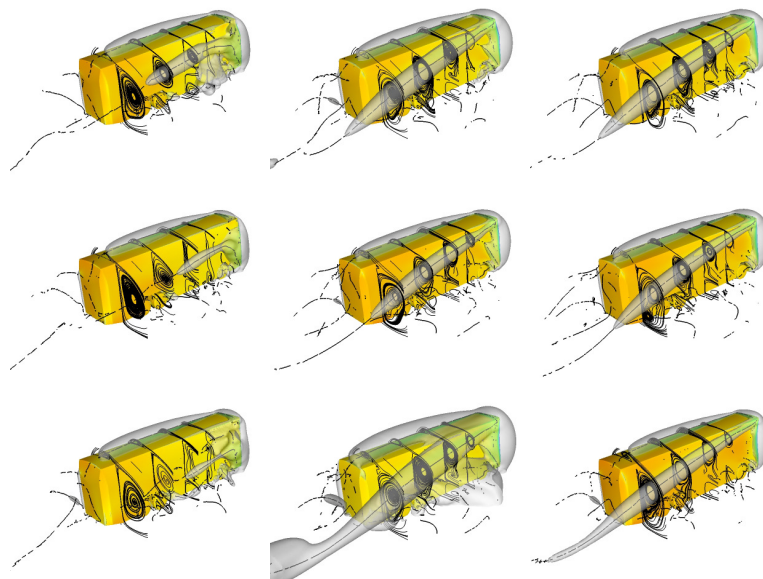


Figure 5: Surface pressure, vortex cores, and isosurface of low pressure and streamlines projected on four y-z planes along the bus for designs at the design points (black dots) of DOE presented in Fig.1b.

$a = e^{-(\|\mathbf{w}-\mathbf{x}\|b)^2}$  and in the output linear layer by the linear function  $a = \mathbf{w}^T \mathbf{x} + b$  where  $b$  is the bias,  $\mathbf{w}$  is the neuron weight vector and  $\mathbf{x}$  is the design variable vector. The RBNN in the present work is constructed with the *newrb* function in MATLAB. The *newrb* function iteratively creates a RBNN by adding neurons one by one to the hidden layer of a radial basis network until the root mean square error,  $\sigma$ , falls under a prescribed error goal. The  $\sigma$  for the test set is defined as  $\sigma = \sqrt{\sum \varepsilon_i^2 / n_i}$ , where  $\varepsilon_i$  is the error at  $i$ -th test point and  $n_i$  is the number of test points. The bias,  $b$ , for each neuron in the hidden radial basis layer is set to  $0.8326 / spread$ , where *spread* is an input constant that determines the radius of influence of each neuron.

In order to train RBNN and evaluate the accuracy of the resulting RBNN, a number of design points in the DOE are used for validation and testing while the rest are used for training. A set of nine design points (black dots in Fig. 1b) was used for the purpose of training of the RBNN, Another four points (white circles in Fig. 1b) were used as test points for measuring the predictive accuracy.

### 9 OPTIMIZATION

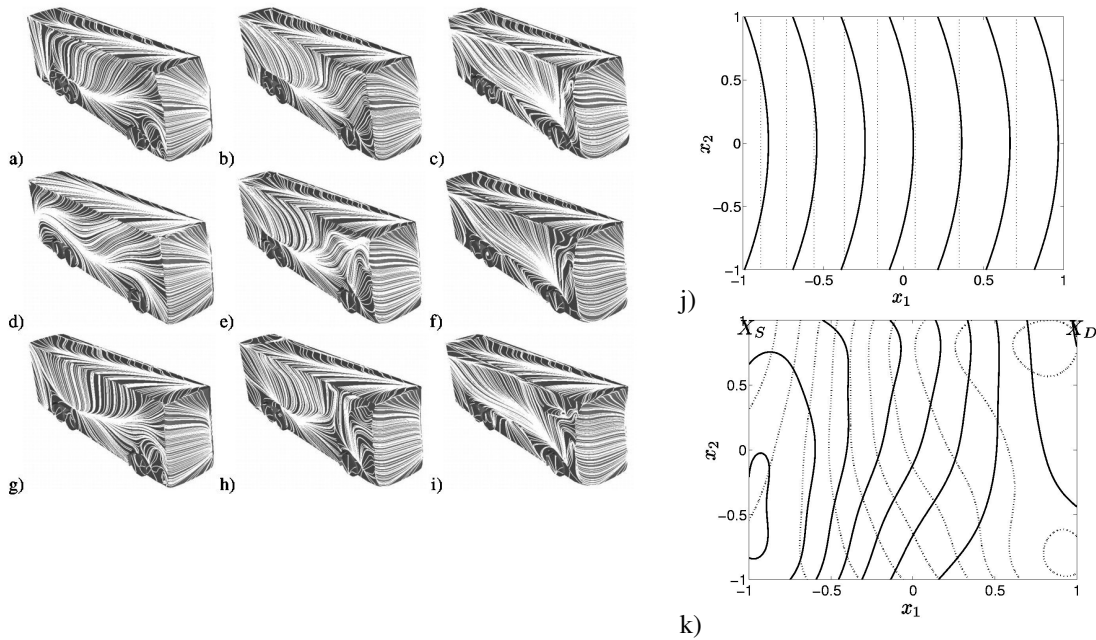


Figure 6: a-i) Particle traces on the surface of the bus for designs at the design points (black dots) of DOE; j-k) Contour plot of response surfaces for  $\hat{C}_D$  (solid line) and  $\hat{C}_S$  (dotted line). Minimal values of  $\hat{C}_D$  and  $\hat{C}_S$  are denoted with  $X_D$  and  $X_S$ , respectively. j) 2nd order polynomial functions; k) RBNN.

Contour plots of RSs of the two objective functions and for different approaches i.e. polynomial and RBNN are presented in Fig. 6j-k. Minimization of the two sets of RSs was performed using constrained nonlinear optimization in MATLAB. Figures 6j and 6k show that the RSs and their minimal values vary between the two approaches. Polynomial RS for  $C_S$  does not give a unique minimum as seen in Fig. 6j. For example there are two optimal designs for minimal drag and the side force RS is not affected by  $\theta$ . RSs based on RBNN have clear optimal values at the corners of the design space. It was found that for minimum drag and minimum side forces buses with maximum  $R$  and  $\theta$ , and minimum  $R$  and maximum  $\theta$ , respectively, are preferable (Fig. 6k). The optimal design for crosswind stability had  $C_D = 0.71$  and  $C_S = 2.72$  while the most energy efficient design (i.e. the one with the

smallest  $C_D$ ) had  $C_D = 0.4$  and  $C_S = 3.67$ . Thus, the drag was decreased by almost 50 % for the most energy efficient bus and the side force was decreased by some 24 % in the case of the design optimized for crosswind stability.

## 10 COMPARISON OF THE RESULTS WITH THE EXPERIMENTAL STUDY

Petzäll *et al.* (2008) made an experimental study of the bus model used in the present work, with the purpose of improving of the directional stability. In their study the reference bus model was modified so that the front, rear and top parts could be exchanged. The front and rear parts of the model were manufactured with both sharp corners and a radius equal to half the coach width. Three additional models were also manufactured where in one case the front had all sharp edges and in another case the front had rounded sides with a radius equal to one fourth of one coach width. In the third case, all the edges were sharp except the rounded top in the front face of the model.

Despite the differences in geometry changes between this experimental study and the present optimization strategy, the trends in shape changes were similar: the front vertical edges were made more or less rounded and the top part of the front face of the bus was made more or less curved. A study by Petzäll *et al.* (2008) used the same flow velocity as well as the wind tunnel set-up. Their results show that sharply cut-off front ends result in the smallest crosswind forces. However, it should be mentioned that the model with all sharp edges except a rounded top in the front face, i.e. similar to that with small  $R$  and large  $\theta$ , in the present study had one of the best results for crosswind stability. On the other hand, most rounded front faces (both for vertical and top edges) were best for air resistance (i.e. smallest  $C_D$ ) in agreement with the results of the present study (i.e. large  $R$  and large  $\theta$ ).

## 11 MAKING THE OPTIMIZATION ALGORITHM AUTOMATIC

Although the optimization algorithm described above was found to give good results, intervention of the user is required during the optimization process. For an optimization algorithm be integrated into production it is essential that the intervention of the user is as limited as possible and that the optimization process is closed with construction of geometry and computation grid, CFD simulations and optimization process.

An automatic shape optimization process that aims to improve the aerodynamic properties of vehicles  $C_D$  is described in the following sections. For evaluation of the method, an example of reduction of drag coefficient for a passenger car is demonstrated. Also here the AVL FIRE version 2008.2 is used for mesh generation and CFD calculations. Sculptor version 2.1.7 is used for mesh deformation. The design environment modeFRONTIER, version 4.1.0b, is used for optimization. The SIMPLEX algorithm for nonlinear optimization problems, implemented in modeFRONTIER, is used to search for an optimal solution.

### 11.1 THE SIMPLEX OPTIMIZATION ALGORITHM

SIMPLEX (ESTECO (2003)) is an algorithm for nonlinear optimization problems and does not require derivatives of the function. Hence it is more robust than an algorithm based on local gradients. In modeFrontier the original algorithm has been updated in order to take into account discrete variables and constraints.

The SIMPLEX optimization algorithm begins with initial trials. The number of initial trials is  $N+1$  where  $N$  is number of control variables. These initial trials form the first simplex, where each trial gives a vertex in the simplex. The shape of the simplex for  $N = 1$  is a line, for  $N=2$  is a triangle and for  $N = 3$  is a tetrahedron. A geometric interpretation is difficult with more variables, but the method is the same. The algorithm moves the simplex into the neighborhood of a minimizer using three operations: reflection, expansion and contraction. In the reflection movement, the node corresponding to the worst value of the objective function is reflected to the opposite face to obtain a new value. Since the direc-



tion of this movement is always away from the worst result, the reflection moves towards a favorable direction. When the reflection process gives a new minimum the simplex is expanded further as we can generally expect to decrease the function value even more. On the other hand, if the reflection process gives a new point that is worse than all of the other vertices or second worst, the simplex is contracted. Examples of these movements for a one-dimensional simplex are given in Fig.7. The algorithm stops when it cannot find improvements higher than some tolerance or when it exceeds a given maximum number of iterations

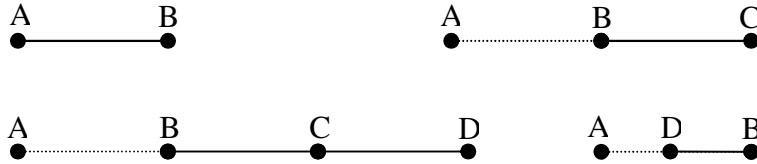


Figure 7: Top left simplex has only the two initial trials. If A is worse than B, A is reflected to the opposite site of B (top right). If point C gives a new minimum the simplex is expanded from C to point D (bottom left). If on the other hand C is worse than B the simplex is contracted (bottom right).

## 11.2 MODEL AND COMPUTATIONAL METHOD

The car model used here is called the Vrak and is a 1:1 experimental model from Volvo Car Corporation. Its geometry and computational domain are shown in Fig. 8. The height, length and width of the model are  $H=1.7$  [m],  $L=4.0$ [m] and  $W=1.6$ [m], respectively. Its cross section reference area in the x-direction is  $A = 2.08$  m<sup>2</sup>. The exterior of the model has a smooth bottom and no side mirrors. The cross section of the computational tunnel is identical to the wind tunnel at Volvo Car Corporation, Gothenburg, Sweden, where experiments have been performed on the vehicle. The dimensions of the computational tunnel are 30 [m]×9.5 [m]×9.5 [m] The inlet and outlet are located at  $x = -21$  [m] and  $x = 29$  [m] respectively in the cars coordinate system.

An uniform velocity profile, turbulence kinetic energy and dissipation rate at  $U = 10$  [m/s],  $k = 2.27 \times 10^{-3}$  [m<sup>2</sup>/s<sup>2</sup>] and  $\varepsilon = 1.54 \times 10^{-4}$  [m<sup>2</sup>/s<sup>3</sup>], respectively, are applied at the inlet. Homogeneous Neumann boundary conditions are applied at the outlet of the tunnel. Hybrid wall treatment is applied at the surface of the car and the tunnel.

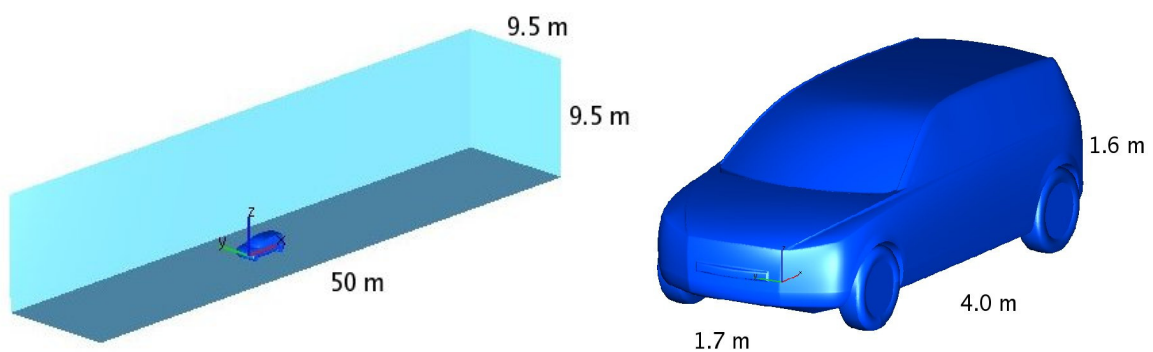


Figure 8: The computational tunnel and the car model showing its dimensions on the left and right respectively.

The Reynolds number based on the inlet velocity and height of the vehicle is  $Re = 1.06 \times 10^6$ . Steady state RANS simulations using the  $k - \varepsilon$  turbulence model are used to predict the flow around the car. A computational grid with approximately 350000 cells fills up the computational tunnel. This is of course very coarse grid which is not capable of resolving the flow but it is sufficient as the objective of

the simulation is so far only to demonstrate the optimization process. The momentum equations were discretized using a second-order upwind differencing scheme, while second-order central differences and upwind differencing schemes are used for the continuity equation and the turbulence kinetic energy equation, respectively. The simulation has converged when the normalized residuals have reached an asymptotic behavior to approximately  $10^{-3}$ . It is also checked whether the drag coefficient has stabilized. Similar like in steady RANS simulations of the bus flow above, the fully converged solutions of the RANS equation of the car flow were not obtained. When the residuals have reached a certain value, they start to oscillate, as does also the drag coefficient. Thus the flow was moving between two modes in the vortex shedding process.

Pre-processing includes mesh generation in FAME (AVL FIRE) and creation of an Arbitrary Shape Deformation (ASD) volume in Sculptor, which puts constraints on mesh deformation and defines a deformation parameter that controls the magnitude of the shape deformation. Here the rear end of the car was deformed and the changes made were relatively large. Figure 9 shows the ASD volume created in Sculptor and Figure 10 shows the deformed mesh.

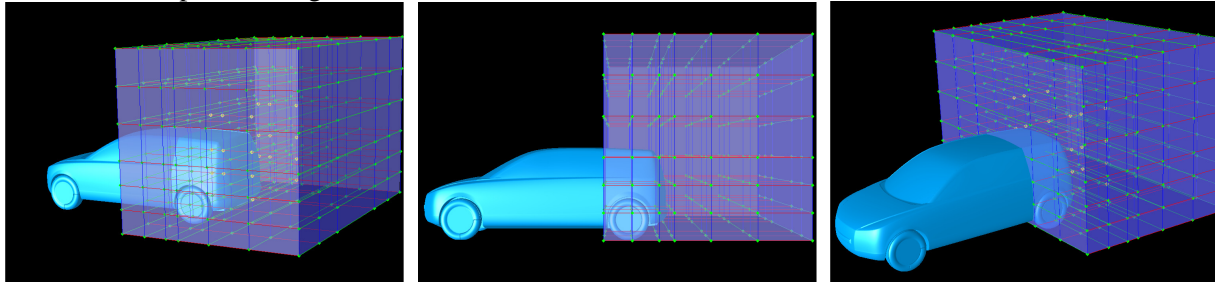


Figure 9: ASD volume is created at the rear end of the car. Inside the volume a group of points is created which control the mesh deformation.

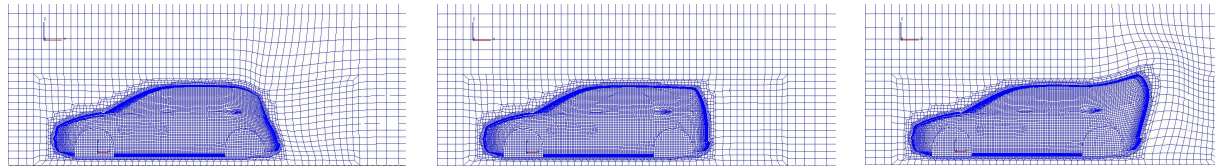


Figure 10: A cut has been made through the mesh ( $y=0$ ) in order to visualize the mesh deformation created by Sculptor. Left: Lower limit of the deformation parameter. Middle: Original mesh. Right: Upper limit of the deformation parameter.

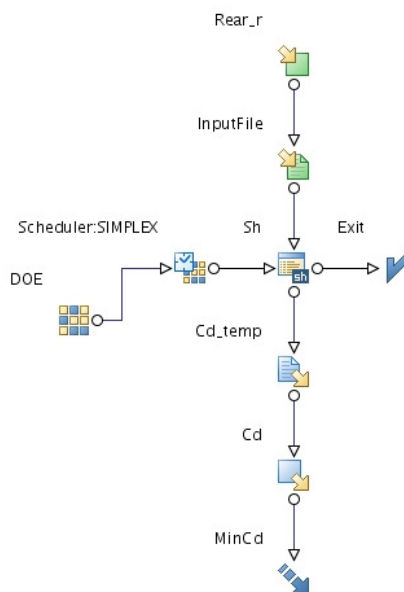


Figure 11: Workflow as it appears in modeFRONTIER.

After pre-processing the shape optimization process is made automatic by combining FIRE, Sculptor and modeFRONTIER. In this process modeFRONTIER controls an input parameter that describes the magnitude of the mesh deformation done by Sculptor. FIRE calculates the flow around the car using the newly deformed mesh and returns a value of  $C_D$  to modeFRONTIER. An optimization algorithm in modeFRONTIER, SIMPLEX, then suggests the next design by selecting the input parameter used for mesh deformation in Sculptor and closes the loop. Figure 11 shows the workflow setup as it appears in modeFRONTIER. Limits are set in **Rear\_r** for the input deformation parameter. The parameter is read in the **InputFile**. **Sh** includes a bash script that tells modeFRONTIER which program to run and in which order. **Cd\_temp** reads in the value for drag coefficient obtained from the previous simulation. The values are collected in **Cd** and it is set in **MinCd** whether the drag coefficient should be minimized or maximized. In this case, it should be minimized. The **DOE** node gives the initial values used by SIMPLEX; here the initial designs are created from the lower and upper limits defined in **Rear\_r**. The SIMPLEX optimization algo-

rithm is chosen in **Scheduler:SIMPLEX**.

### 11.3 RESULTS AND DISCUSSION

Figure 12 shows how the input morphing parameter is changed by the SIMPLEX algorithm in modeFRONTIER in order to minimize the drag coefficient. In total 13 simulations were needed before an optimal solution was reached. Note that the number of designs in Fig. 12 is 17 as the SIMPLEX algorithm returned 4 times to designs that were already used in its search. The convergence criterion for SIMPLEX was set  $10^{-3}$ , i.e. SIMPLEX has achieved an optimal solution if the changes in last two values of the drag coefficient are less than  $10^{-3}$ .

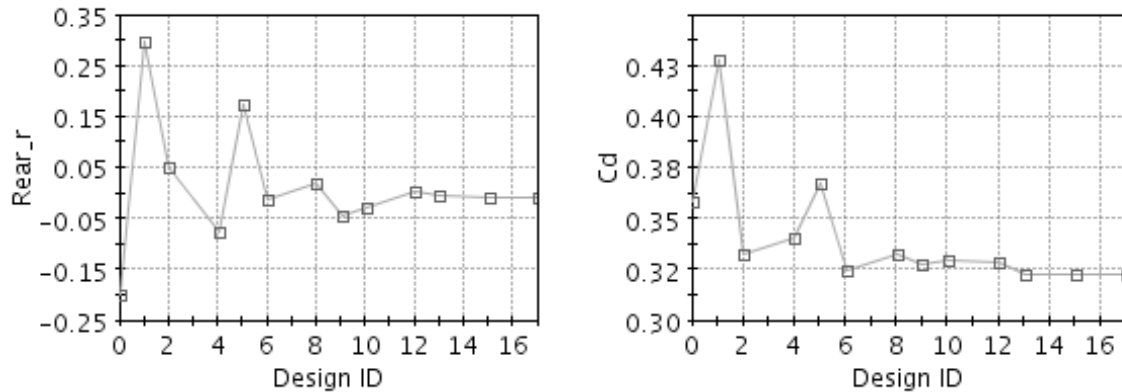


Figure 12: An input morphing parameter called **Rear\_r** vs. **Design ID** and the drag coefficient  $C_D$  vs. **Design ID** are seen on the left and right respectively. The input morphing parameter is controlled by the SIMPLEX algorithm in modeFRONTIER. Its new value is based on the history of last two results obtained for the drag coefficient,  $C_D$ .

Shape optimization is a time consuming process. The main purpose of the work was to get the automatic closed loop running. In order to reduce computer time, the total number of cells was kept at a minimum. Further work needs to be done to achieve better results. The total number of cells will be increased and a more advanced turbulence model will be used, i.e. the  $\zeta - f$  turbulence model. Also for this case the future simulations will be run unsteady, which is more appropriate with flows that have such a strong vortex shedding, and the aerodynamic forces will be averaged over a certain interval at the end of each computation in order to obtain their mean value.

## 12 FINAL WORDS

Both algorithms presented in the present paper are promising but the automatic optimization algorithm is to prefer as it removes user interventions during the design process. The deformation of the computation grid using morphing tool seems to work fine for course computation grid but it remains to investigate if the quality of the deformed grid is preserved when boundary layers are resolved. Another issue is usage of URANS where the averaging or the objective functions have to be performed between the SIMPLEX steps. It is important to explore how long time it takes before the flow has developed when the design has changed and for how long time the averaging needs to be performed. These issues are being addressed in the ongoing work by the authors.

## ACKNOWLEDGEMENTS

The work presented here was supported by the AVL List GmbH, Banverket (Swedish National Rail Administration), Volvo Car Corporation and Scania. Computer time at SNIC (Swedish National Infra-

structure for Computing) resources at the Center for Scientific Computing at Chalmers (C3SE) is gratefully acknowledged.

## REFERENCES

- [1] K. Hanjalić, M. Popovac, and M. Hadžiabdić (2004), *A robust near-wall elliptic-relaxation eddy-viscosity turbulence model for CFD*. Int. J. Heat and Fluid Flow. 25:1047 –1051.
- [2] H. Hemida and S. Krajnović (2007), *DES of the flow around a realistic bus model subjected to a side wind with 30° yaw angle*. The fifth IASME / WSEAS International Conference on FLUID MECHANICS and AERODYNAMICS, Athens, Greece, 25-27 August.
- [3] S. Krajnović (2008a), *Improvement of aerodynamic properties of high-speed trains by shape optimization and flow control*. 8th World Congress on Railway research (WCRR2008), Seoul, Korea, May 18-22.
- [4] S. Krajnović (2007), *Optimization of vortex generators for drag reduction of a high-speed train*. The Aerodynamics of Heavy Vehicles II: Trucks, Buses and Trains, Tahoe City, USA, August 26-31.
- [5] P.-Å Torlund (1999), *Experimentell undersökning av sidvindskänsligheten hos en modell av en tvåvåningsbuss i FFA:s vindtunnel LT1*. Report (in Swedish), FFA TN 2000-05.
- [6] AVL AST, (2008) *Fire Manual v2008*. AVL List GmbH, Graz.
- [7] B. Basara (2006), *An Eddy Viscosity Transport Model Based on Elliptic Relaxation Approach*, AIAA J. 44, pp. 1686-1690.
- [8] M. Popovac and K. Hanjalić (2007), *Compound Wall Treatment for RANS Computation of Complex Turbulent Flows and Heat Transfer*, Flow, Turbulence and Combustion 78, pp. 177-202.
- [9] S. Krajnović and B. Basara (2009), *IMPROVEMENT OF THE CROSSWIND STABILITY OF A BUS WITH RESPONSE SURFACES AND URANS USING  $\zeta - f$  TURBULENCE MODEL*, Second International Conference on Turbulence and Interaction - TI2009 ,31 May - 5 June , Sainte-Luce, Martinique
- [10] S. Krajnović, H. Hemida, B. Basara and J. Schneider (2008), *Optimization of the Aerodynamic Performance of Vehicles Using the  $\zeta - f$  Turbulence Model and Response Surface Models*, Robust design through simulation, Paris, France, October 16<sup>th</sup>.
- [11] J. Petzäll and P. Å. Torlund and T. Falkmer and P. Albertsson and U. Björnstlig (2008), *Aerodynamic design of high-sided coaches to reduce cross-wind sensitivity, based on wind tunnel tests*, International Journal of Crashworthiness, 13(2), pp. 185-194.
- [12] ESTECO (2003), *The SIMPLEX Method*, Technical Report 2003-005.

## FLOW FIELD AROUND AND IN A SAAB 9-3 CONVERTIBLE

Jesper Marklund\*, Håkan Danielsson<sup>†</sup>, and Lennart Löfdahl<sup>†</sup>

\*Saab Automobile AB  
46180 Trollhättan, Sweden  
e-mail: jesper.marklund@gm.com, hakan.danielsson@gm.com

<sup>†</sup> Applied mechanics department  
Chalmers University of Technology, 41296 Göteborg, Sweden  
e-mails: lennart.lofdahl@chalmers.se,

**Keywords:** Convertible, Vehicle, Aerodynamics, CFD

**Abstract.** *The aerodynamic comfort in a four seated convertible with open roof is not as good as many would like it to be. This job was initiated to look at what should be done to improve this. The car used for this study was a Saab 9-3 convertible. Most of the work was done in CFD in the commercial code Fluent.*

*The flow field in the cockpit was first of all analyzed and evaluated. The problem with convertibles is the large recirculation bubble that occurs around the passenger compartment. The rear seat passengers are located in an area of this zone with very high wind speeds compared to the front seat passengers. The flow field was analyzed by several pressure and velocity plots and a method to evaluate comfort grading was developed. The selected main variable to compare cases was the mean velocity that the passengers head is exposed to. This was found to be the most affecting parameter because it affects not only the dynamic pressure, but also the temperature discomfort. Geometry optimizations of windows, wind shield and wind blockers have been simulated and evaluated. Height and length of the side windows and a number of different wind deflectors on the wind shield, plus wind blockers inside and behind cockpit was tested. The results show that the biggest potential of improvement is the wind deflector on the windshield and some of the wind blockers.*

## 1 INTRODUCTION

The ride comfort in an open convertible is depending on several factors. The biggest discomfort normally comes from the wind comfort and the problem is extra obvious in the rear seat of a four seated car. Depending on driving speed the air velocity, velocity fluctuations and temperature can lead to strong discomfort due to air draft to head, neck and shoulders. For two seated cars the wind comfort is in general acceptable with fairly low wind speed acting on the passengers compared to a four seater. The passengers are better protected from the high speed air streams and the existing wind blockers are very effective. In four seated convertibles this is not always the case. The front seat is often acceptable to sit in, whereas the rear seat is not close to comfortable.

You can always ask the question if it is physically possible to reach a comfort level in rear seat which is considered acceptable also at main road cruising speeds. That is not removing the feeling of freedom that is so characteristic for convertibles.

Saab Automobile offers the model 9-3 as a four-seated convertible within their model program. The wind comfort in the rear seat and with the top down has been an issue discussed many times, and the wish for future convertible programs is to improve this. This job was initiated with this request and the start was to analyze the current cars and bring ideas and methods from this to the new car program. Since the comfort experience is so much depending on the wind speed that act on the passenger, it was agreed up on to work with the flow fields and velocity magnitudes. Most of the job was done in CFD but some comparing measurement and subjective comfort experience was tested in Saab Climatic wind tunnel.

## 2 AIM

The scope of this project was to look deeper into the wind comfort of the Saab 9-3 convertible. The specific goal was to find a method to analyze and identify known weaknesses, as well as presenting suggestions for improvements. The main tool for solving these tasks was CFD. Parallel wind tunnel testing was performed in full scale, in order to help getting an understanding of which parameters should be focused on and to get a confirmation of the simulated results.

## 3 COMPUTATIONAL MODEL

A description of what procedure and tools used in this work is here presented. This includes the commercial software used, as well as description of how the computational domain was created, together with the solving methodology and the result interpretation.

Ansa 12.1 was used as pre-processing tool for CAD cleanup, geometry modifications (including morphing) and surface mesh creation.

TGrid 4.0 was used for creation of triangular/tetrahedral and hexcore volume cells, as well as building of boundary layers. The files representing the computational volume were exported to Fluent as .cas files.

Fluent 6.3 CFD package as solver and post-processing of the results.

### 3.1 Computational domain

The computational part contained two different models: one in full-scale and one in 1:5 scale. The first was created from CAD data of the vehicle, then performing geometry cleanup and surface meshing. The 1:5 scale model originates from a clay model that has been laser scanned. The wind tunnel geometry was an exact representation of the wind tunnel at Chalmers University of Technology (scale model wind tunnel). For uniformity the wind tunnel

used for the full-scale model was a 5:1 scaling of the same. The result presented in this work is focusing on the full scale results.

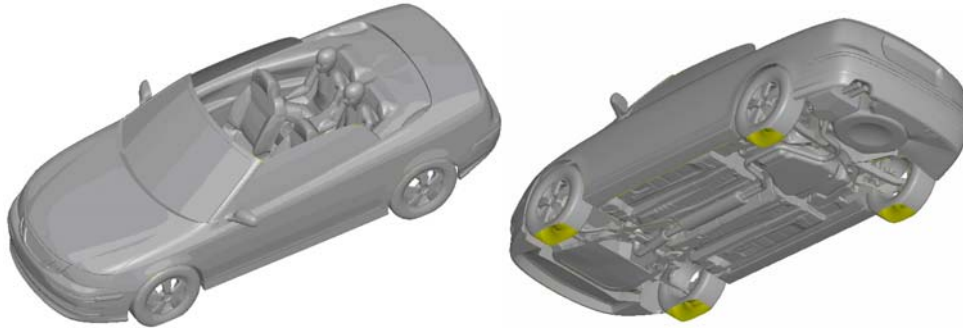


Figure 1: The geometry of the full scale model

Fig.(1) shows the surfaces of the original full-scale computational model. The upper part of the body is detailed and includes two passengers in the rear seat. Also the underbody consists of representative geometry, including spoked rims. Cooling package and engine bay flow is not included. The average parameter length is 10 mm and the frontal area is 2.058 m<sup>2</sup>.

The tunnel domain, see Fig.(2), consisted of the Chalmers wind tunnel in 5:1 scale. The total length was 60.1 m, and the maximal width and height in the contracted part were 9.00 m and 6.25 m, respectively. This meant a cross-sectional area of 52.61m<sup>2</sup>.

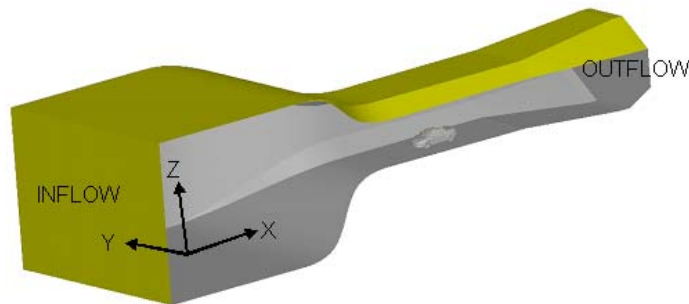


Figure 2: Tunnel domain and coordinate system used.

### 3.2 Volume mesh

The TGrid generated volume mesh consisted of 11.4 million cells for the full-scale model. As max cell length 1000 mm was specified, which corresponds to twice the maximal surface parameter length of the entire domain. Around the car max cell volume = 42875 mm<sup>3</sup> ⇔ max cell length = 35 mm. In the close wake and around the passengers max cell length = 16mm. At the front 18mm, around the mirrors 25mm and in the far wake 35mm max cell length.

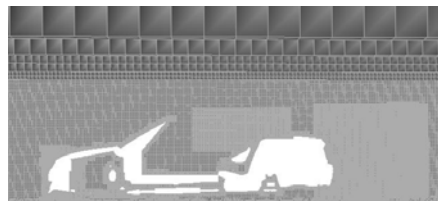


Figure 3: Overview of the volume mesh (y=0) close to the model.

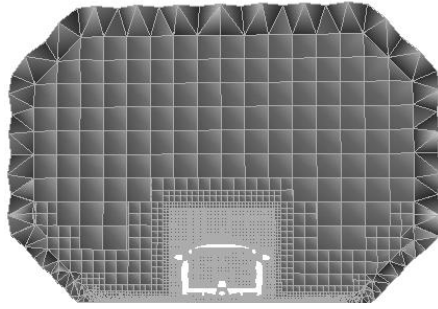


Figure 4: The volume mesh in the entire tunnel.

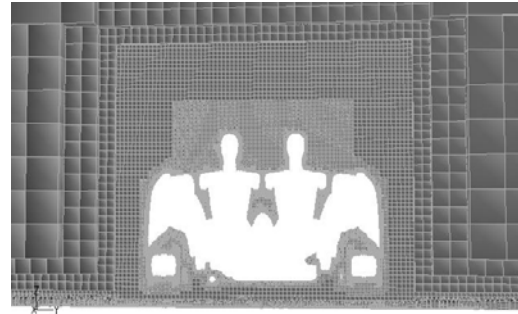


Figure 5: The volume mesh close to the model.

Overview of the mesh can be seen in Fig(3-5). Prismatic layers were used to better resolve the flow properties at near wall boundaries of the vehicle. Five layers were created with a geometrical growth rate of 20% and with a first aspect ratio of 5, which means that the height of the first layer is equal to 1/5 of the surface mesh's parameter length.

### 3.3 Solver Set-Up

As turbulence model  $k-\varepsilon$  Realizable was used. The coupled solver, with under relaxation of 0.25 for momentum and pressure, and the courant number set to 15. As near-wall treatment non equilibrium wall functions, which are sensitized to pressure gradient effects in comparison to the standard wall functions were chosen.

The inflow was set as a velocity inlet with uniform velocity profile 3.47 m/s. Due to the contraction of the tunnel before the vehicle position, this corresponds to 20 m/s in the nearby of the same. Besides, a turbulent length scale of 0.35 m and a turbulent intensity of 0.1% were set. The outflow was specified as pressure outlet, with gauge pressure = 0 and the same turbulence properties. All tunnel walls were further stated as stationary walls, just as the entire vehicle body. Air density as well as viscosity was assumed to be constant in the entire domain, and with the values  $1.205 \text{ kg/m}^3$  and  $1.805 \cdot 10^{-5} \text{ m}^2/\text{s}$ , respectively.

When using wind blockers, these were either set as walls, in order to resemble a glass window, or as a soft synthetic material. The synthetic material was modeled as a porous jump and this is only applied to a face zone. To define the pressure change, it uses a combination of Darcy's Law and an additional inertial loss term [6]. Here the parameters  $\alpha=1.5 \cdot 10^{-9} \text{ m}^2$ ,  $\Delta m=0.005 \text{ m}$  and  $C_2=0$  are used.

$$\Delta p = -\left(\frac{\mu}{\alpha} v + C_2 \frac{1}{2} \rho v^2\right) \Delta m$$

Equation 1: Pressure change in the porous jump model.

## 4 TEST MODEL DESCRIPTION

Evaluation of the wind comfort was made through flow field visualization in various ways. Also a method for wind comfort estimation, in order to see the difference between cases with small flow differences was asked for. There are many factors that influence the aerodynamic comfort like, wind speed, temperature, turbulence intensities, noise, where at the body the air hits you, and so on. After tests in the Saab climatic wind tunnel, where test people could grade aerodynamic comfort, it was decided that the overall wind speed that the passenger was exposed to was the most important. Biggest reason for that is the connection to the temperature discomfort that is experienced. Also that draft around the head and neck is considered very



unpleasant. For these reasons it was decided that an average wind speed on the head should be the foundation for the wind comfort judgment.

As a simulation method, the rear seat passengers were “cut” at the neck’s z-coordinate. The head was then widened 0.01 m to avoid too strong influence by the no-slip condition. Finally, an area weighted average of the velocity magnitude on this surface was used. In cases where a measurement of the wind comfort in the front seat was of interest, the same method was implemented, but for an introduced spherical surfaces at appropriate positions and with diameter of 0.1 m. See Fig.(6) for overview.

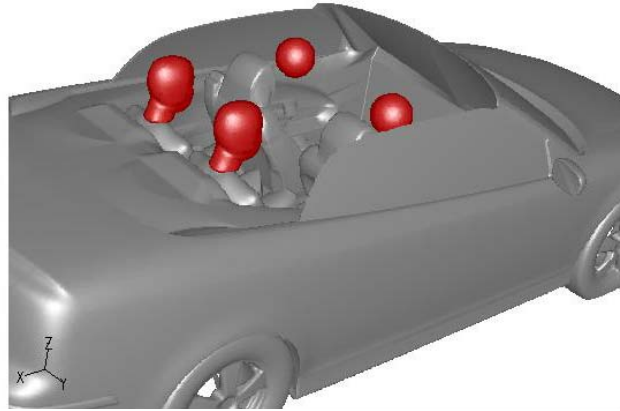


Figure 6: The surfaces (in red) over which area weighted average of the velocity magnitude was calculated

## 5 RESULTS

All the test and simulation presented here are done with a vehicle speed of 20 m/s or roughly 70km/h. First of all a description of the flow field is here included. The flow in the passenger compartment is dominated by the separation bubble as described by [4] & [5]. An estimation of the appearance of the separation bubble can be done by visualizing the surface where the total pressure is zero. See Fig(7). Below this surface the total pressure is negative, which can be interpreted as an area of pressure losses.

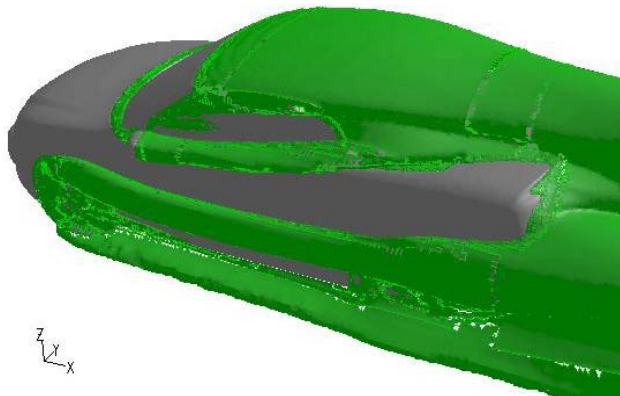


Figure 7: Surface showing the total pressure equal to zero

Deeper investigation of this dominating convertible flow feature can be carried out by looking at the flow speed and direction inside the passenger compartment. Fig(8) show the symmetry plane velocity vectors where the shear layer and a recirculation zone is visualized.

The flow is going down behind the rear passengers heads and thereafter returning in a forward going path. This also confirms work done earlier by [1].

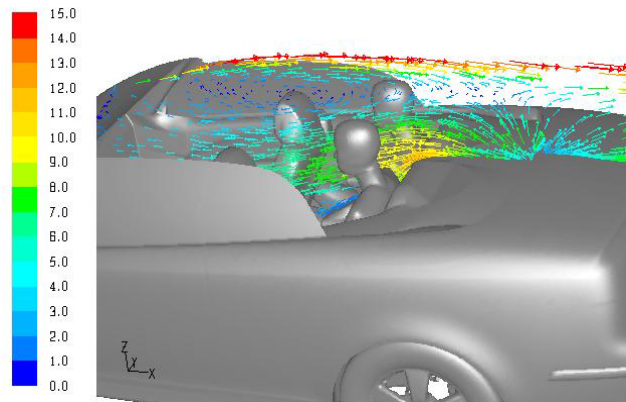


Figure 8: Vectors colored by velocity magnitude [m/s] on the symmetry plane ( $y=0$ )

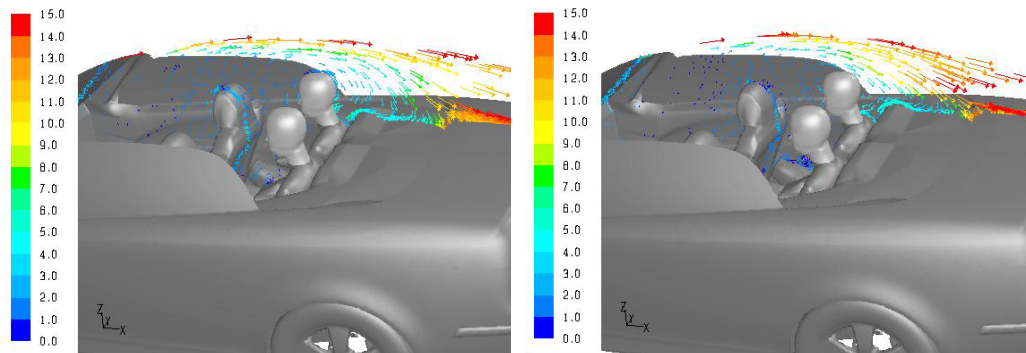


Figure 9: Vectors colored by velocity magnitude [m/s] on the surfaces  $y=0.3, 0.4$  m

The forward motion of air is clearly shown, as well as the fact that this effect is strongest in the middle and decreases towards the sides. See Fig(9). Furthermore, passengers must be of considerable length to reach the shear layer, and then experience free stream air. There should also be no doubt that air is drawn into the passenger compartment, as well as that the rear seat passengers are the ones who will suffer. This becomes even more obvious if analyzing the flow in the  $x$ - and  $z$ -planes. See Fig(10).

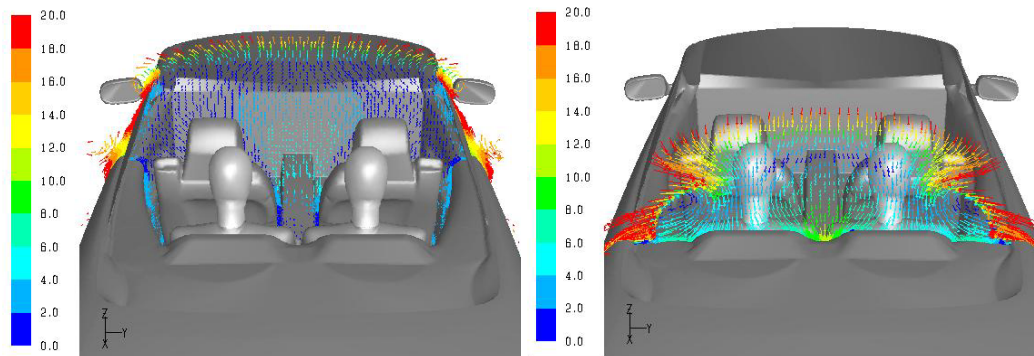


Figure 10: Vectors colored by velocity magnitude [m/s] on the surfaces  $x=3.3$  and  $4.2$  m.

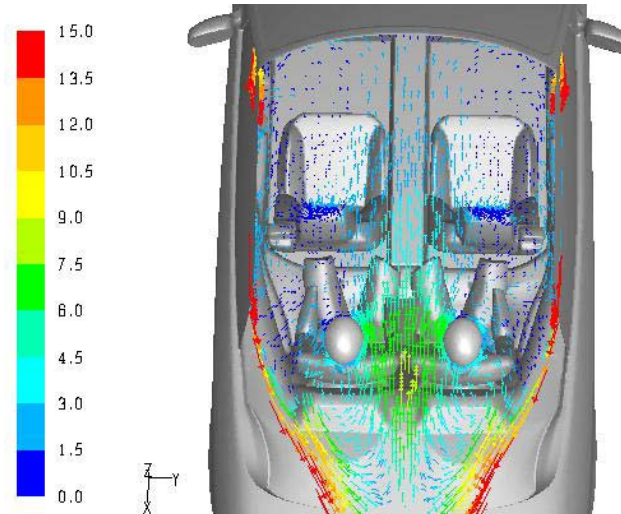


Figure 11: Vectors colored by velocity magnitude [m/s] on the surface  $z=1.2$  m

In Fig(11) the flow is visualized in  $z=1.2$ m plane and the velocity vectors show the turning around behind the passengers and the forward going jet in the center of the car. Between the front seats an air stream of 5-6m/s is going forward, splits up, slows down and come to the front passengers. The problem with inflow from the sides, and from behind can be further visualized with path lines. See Fig(12) and Fig(13).

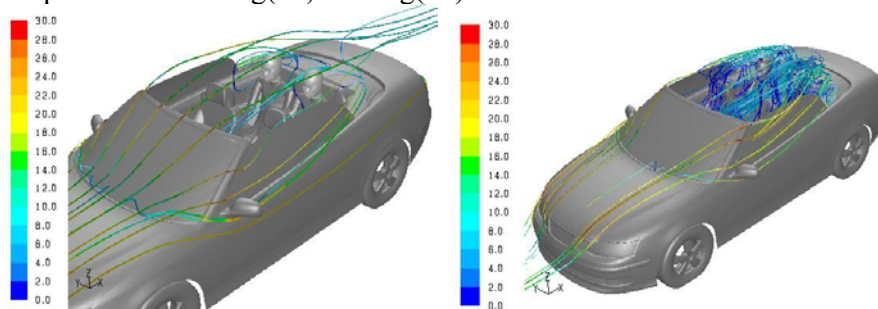


Figure 12: Pathlines colored by velocity magnitude [m/s], originating in front of the bonnet (to the left), and reversely from the passenger heads (to the right)

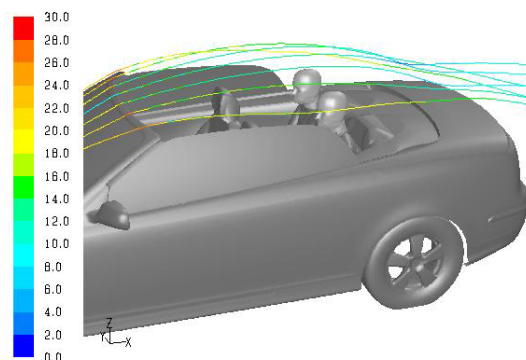


Figure 13: Pathlines colored by velocity magnitude [m/s], passing over the windshield

Fig(12) show that the direct inflow hitting the rear seat passengers is going above and at the end of the side windows. The right hand picture show the path of the air that hit the head.

After entering the cockpit, the flow pattern becomes turbulent and move around in the cockpit before coming to the head. Further, the free stream flow that passes over the windshield does not directly hit the rear seat passengers. See Fig(13).

### 5.1 Wind comfort

Concerning the selected wind comfort method, that was selected in this work, the area weighted average of the velocity magnitude around the rear seat passengers' heads was calculated to 3.08 m/s. Interesting to notice is that the calculated value is reasonably close to 2.77 m/s, which was measured in the full-scale wind tunnel test.

When it comes to the front seat, the area weighted average was 1.10 m/s. Hence, a 65% lower value compared to the rear seat. This meant a slightly bigger deviation from the result in the full-scale wind tunnel test, where the speed flow was measured to 1.53 m/s. The bigger error here originates from first of all that the front passengers head was simulated as a sphere and second that the flow in the front showed more turbulent behavior i.e. more transient effects.

Fig(14) show the velocity distribution on rear, left passenger in a color plot. Note the higher air velocity at the ear and neck on right side. This comes from the returning flow in the centerline of the car.

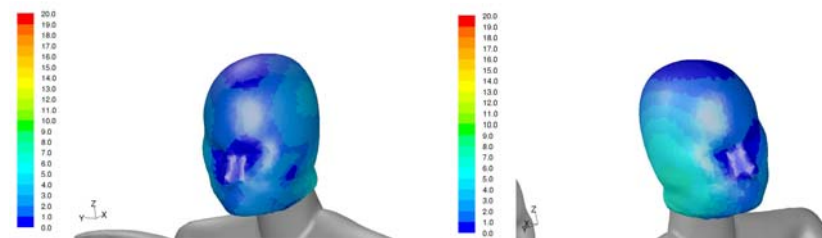


Figure 14: Velocity magnitude on left rear passenger head (left side/right side)

### 5.2 Geometry configurations

A list of configuration changes was tested to improve this air speed on the head of rear passengers. A variously angled spoiler attached and unattached at the windshield. See Fig(15). Modifications of the side window design. See Fig(16). Different wind blocker set-ups. See Fig(17,18).



Figure 15: Spoiler on the wind shield (left) and unattached spoiler (right).

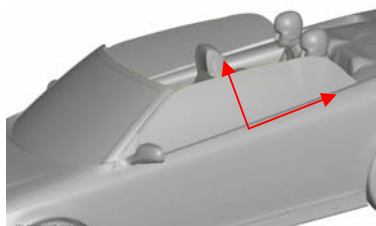


Figure 16: Modified side windows.

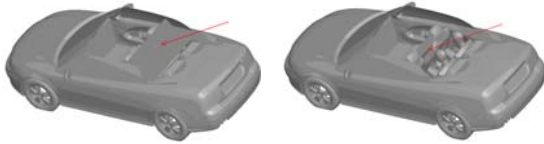


Figure 17: Wind blockers inside cockpit.

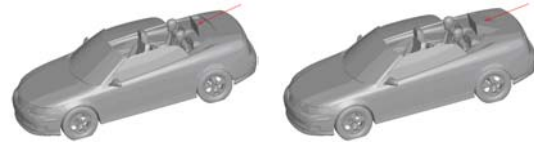


Figure 18: Wind blockers behind cockpit.

Starting with the fastened spoiler it was added as a 73 mm long curved surface at the rear end of the windshield. To change its angle parametric morphing in ANSA was used, which briefly means that the spoiler surface cells were “stretched” to preferred position while the front end was fixed. The unattached spoiler consisted of the same geometry as the fastened, but was freely moved to different positions, close to the rear end of the windshield.

Modification of the side windows may very well affect the flow in the passenger compartment, as described by [3]. Modification of the side window design was simply performed through extension of the original geometry 100 mm horizontally and 50 mm vertically, in two separate steps.

Concerning the wind blocker arrangement, four different types were used, namely two inside the passenger compartment, and two behind the rear seats. The first internal model was made to depict the existing wind blocker, available as an accessory for the Saab 9-3 convertible, see Fig(17), (left). It covers the rear seat horizontally at shoulder height, and extends vertically to the height of the imagined front seat passengers’ heads, just behind the same.

The second internal model was designed in order to still be able to use the rear seat of the vehicle, but hopefully with the same wind comfort effects for the front seat passengers. Therefore, its shape is almost like a tennis racket between the front seats.

The first arrangement behind the rear seat was simply a screening window and the second more like a triangle with extension in the vehicle’s lateral direction. See Fig(18). The width of both configurations was 501 mm (distance between head centers of the passengers), whereas the height was tested as both 250 mm and 150 mm.

## 6 RESULTS FROM GEOMETRY CONFIGURATIONS

The described geometries were simulated one by one and the idea is to change the separation bubble or change parts of the flow, in a way that will reduce the wind speed acting on the passengers.

### 6.1 Wind shield spoiler

The idea with the fastened spoiler was principally to try to control the shape of the separation bubble in a preferable way for the passengers. The hope was that the flow would stay attached a bit longer, and after that being steered so that the inflow into the low-pressure area could be decreased.

The 73 mm long spoiler was adjusted in six different angles: 0°, 10°, 15°, 20°, 30° and 40°. After having evaluated these results a 150 mm long and 15° angled spoiler was also created. Besides, this was designed to be slightly plow shaped (15 mm extra morphed height in the middle). Visualization of all set-ups follows.

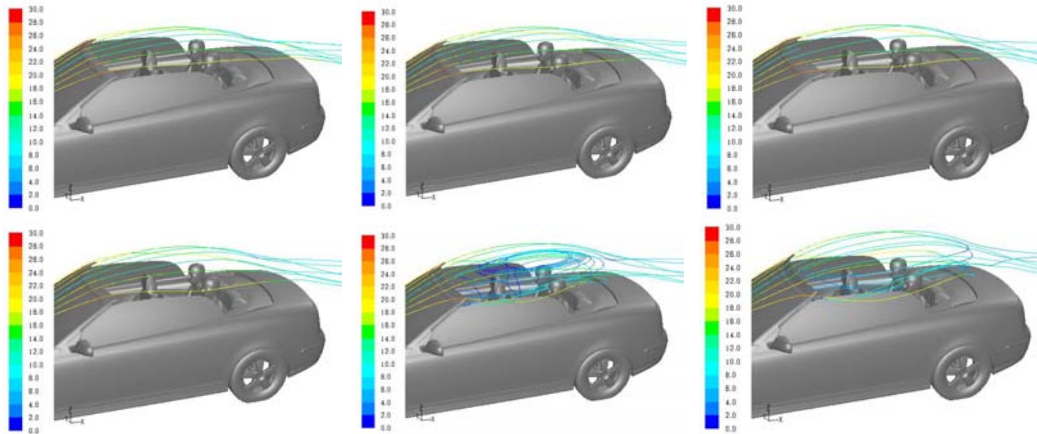


Figure 19: Path lines showing the air flow with different spoiler configuration

As the angle increases the separation bubble is first lifted, besides with a slight “plow effect” for the longer spoiler, but at 30° the flow changes dramatically. The smooth shape over the interior can no longer be preserved when the reattachment to the trunk is no more there. More air is sucked into the bubble, which means a stronger forward directed air motion inside the passenger compartment. In terms of wind comfort this is a great disadvantage.

## 6.2 Unattached wind shield spoiler

The plan with the unattached spoiler was the same as for the fastened spoiler and that is to more distinctly steer the flow after the front windshield. However, this specific approach has its ground in observed efforts to delay separation on airplane wings.

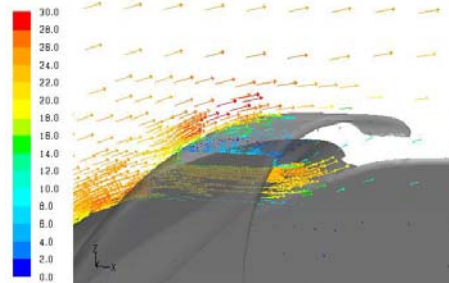


Figure 20: Velocity vectors to visualize the flow

The unattached spoiler, with the same size and shape as the fastened model, was implemented with three variables in mind. These were the distance in z- and x-direction, respectively from the windshield but also the angle of the spoiler itself. The angle was only tested as 0° or 15°, whereas the distances were varied more extensively. This means that the following set-ups, where the nomenclature is “z-distance”\_“x-distance”\_“angle”, were used: 10\_30\_0, 10\_30\_15, 10\_50\_0, 20\_30\_0 and 30\_30\_0. No particular theory acted as foundation; instead it was trial and evaluation that lead to the specific settings tested.

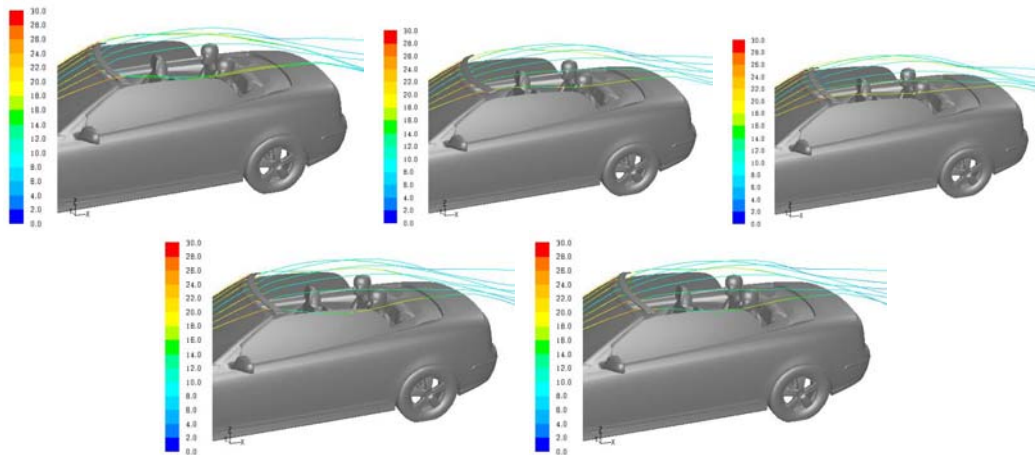


Figure 21: Pathlines colored by velocity magnitude [m/s] passing over the windshield, for the set-ups 10\_30\_0, 10\_30\_15, 10\_50\_0, 20\_30\_0 and 30\_30\_0, respectively

The main part of the flow close to the windshield passes under the spoiler, and is then again directed upwards. Thus, the shape of the separation bubble is not affected in a considerable way. It may be a bit surprising that the wind comfort seems to be rather good, when the flow is first forced downwards to the interior. But a reduced pressure gradient in the area of the shear layer is reducing the turbulent air speed in the cockpit. No insinuation that the flow would strengthen the forward directed motion in the interior could be observed.

### 6.3 Modified windows

Two design changes were carried out, where the first was to tangentially lengthen the windows 100 mm in the x-direction. The other was to, with preserved prolongation, also increase the height (in the z-direction) 50 mm tangentially.

The vector plots on the symmetry plane showed that hardly any changes have occurred, compared to the original case.

After having inspected the flow field in various ways no relevant absolute wind comfort improvements can be observed.

### 6.4 Wind blockers

The biggest reason for the wind comfort issue is air drawn into the cockpit by the low pressure inside the separation bubble. The natural solution to this then seems to be simply blocking the air with some kind of arrangement. The purpose with the existing wind blocker is to improve the comfort in the front seat and the rear seat can not be used with this installed. The wind blockers proposed here make it possible for a passenger to sit in the rear seat and the hope is that it will also improve the comfort both in front and rear seat.

For all wind blocker cases the vector plots on the symmetry plane show very clear differences, compared to the original set-up. Starting with the internal models a flow of nearly zero speed appears in the front seat. The wind speed on the head of the front passengers was reduced to about half with both these wind blockers compared to having no wind blocker. Also, in the alternative model the forward directed flow seems to be slightly weaker by the rear seat than in the original model.

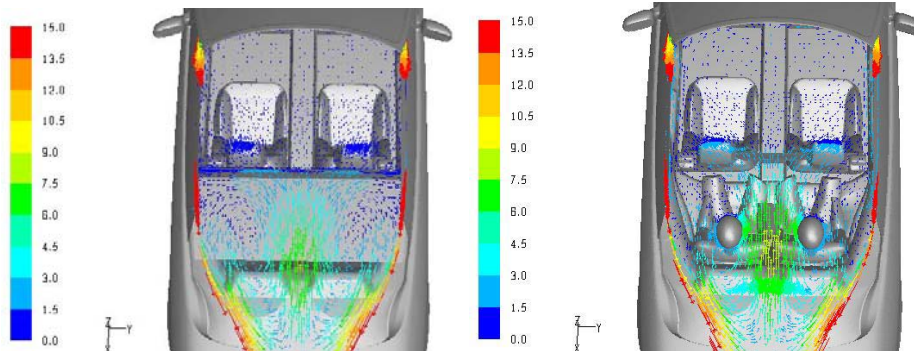


Figure 22: Vectors colored by velocity magnitude [m/s] on the surface  $z=1.2$  m, for the current internal model (left) and the alternative (right)

The screening window models on the other hand all gave surprisingly negative results. Even though the flow from behind is stopped (in very similar ways) the turning-point of the separation bubble has become stronger and more widely spread. This in turn results in a more powerful forward directed flow, most evident for the solid material model.

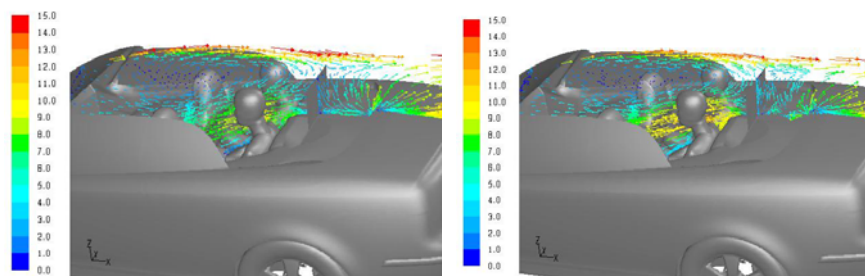


Figure 23: Vectors colored by velocity magnitude [m/s] on the symmetry plane ( $y=0$ ), for the porous screen model (left) and the solid (right)

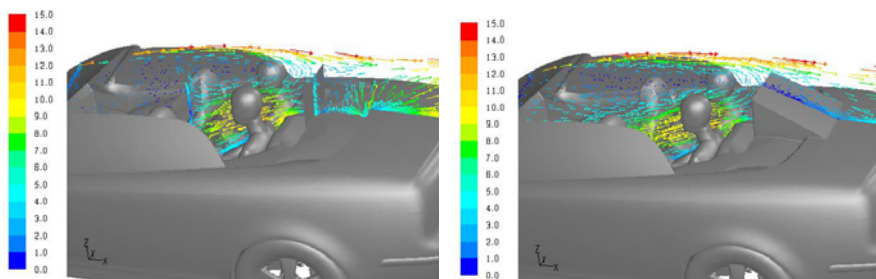


Figure 24: Vectors colored by velocity magnitude [m/s] on the symmetry plane ( $y=0$ ), for the front and rear combination (left), and the triangular model (right).

The arrangement with both internal and external wind blockers Fig(24) showed the same problem, however with a little milder forward flow effect, owing to the front blocker. It was further true that the triangular set-up made reattachment easier, but unfortunately it could neither repair the occurring damage. Lower height of the two external models on the other hand meant a lower speed of the forward directed flow, and seemed to be a compromise between stopping the flow from behind and not making the effect of the separation bubble stronger.



## 6.5 Summary of results

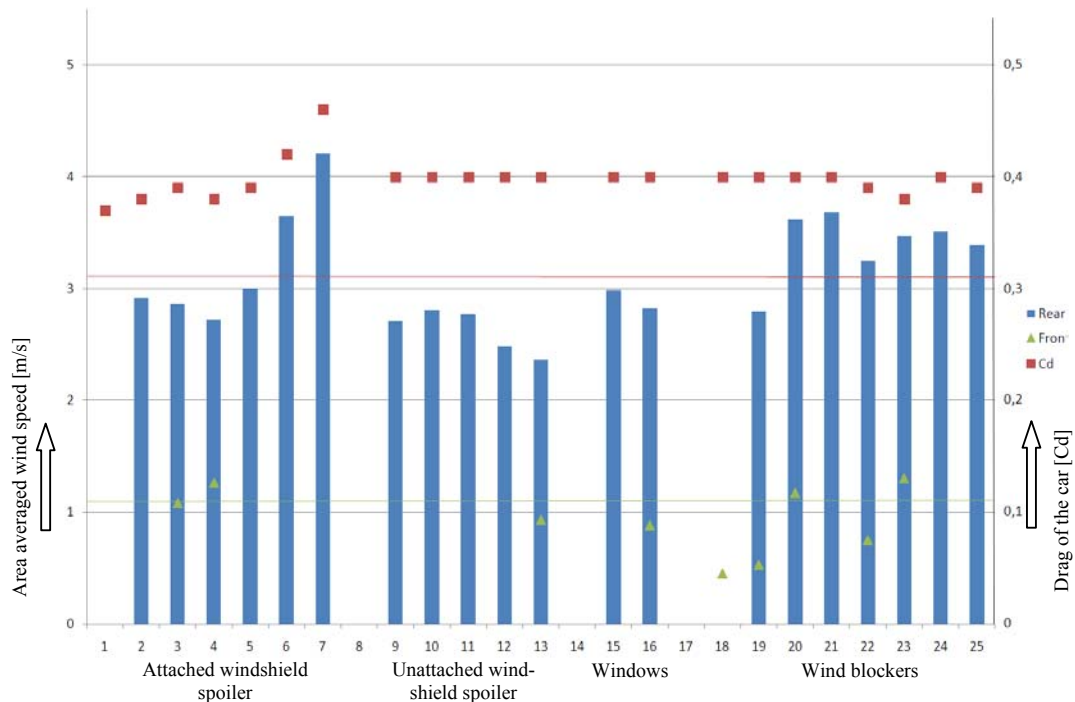


Figure 25: Result of average wind speed on passengers head

Fig(25) show a summary of the results regarding wind speed acting on the head of a passenger in the rear seat. Front seat result is marked with a green triangle and the drag is marked with a red square. The horizontal red line is the unchanged car for the rear seat, and the green line is for the front seat.

The fastened spoiler can give a small improvement when using the longer 15 degree angled spoiler that is identified by no:4 (2.9m/s). The improvement is small compared to improvement caused by the unattached spoiler that show a potential to reach 2.35(m/s) in the last configuration. The modified and enlarged side windows showed small improvement, and in principal all the wind blocker configurations made this value worse. The only wind blocker that made a small improvement was the wind blocker between the front seats (no:19).

The drag increases some with the wind shield spoilers. It also increase a significant step when the attached spoiler is angled more than 30 degrees. This indicates that the flow pattern is dramatically changed and the wake is getting bigger.

Improvement for the front seat is significant for the existing wind blocker and the wind blocker between the front seats (no:18,19).

## 7 CONCLUSIONS

This method to compare average wind speed on the passengers head in CFD is an easy to use and quick method to roughly evaluate the wind comfort of an open convertible.

For this car, the only proposed change that made any significant improvement was an unattached spoiler (with an air gap) at the wind shield.

Modification to the side windows can have some potential in improvement of the wind comfort but will probably affect the styling more than the wind comfort.

None of the wind blockers tested here made any significant improvement for the rear seat passengers comfort, but the internal models made huge improvement for the front seat passengers.

### **ACKNOWLEDGEMENTS**

This paper is based on a thesis work that was done at Saab 2007 about improving the wind comfort in a convertible, by Marcus Chistiansson. The results found here were later used as input when working with the new convertible programs. It has given a confidence in using CFD as a tool in this subject. I also want to give my thanks to everybody who participated in the tests and helped with many advises.

### **REFERENCES**

- [1] Barnard, R H. *Road Vehicle Aerodynamic Design*, Mechaero Publishing, Hertfordshire, U.K. 2001.
- [2] Panton, Ronald L. *Incompressible Flow*, John Wiley and Sons, Inc. NY, U.S.A. 1996.
- [3] Hucho, W H. *Aerodynamics of Road Vehicles*, Society of Automotive Engineers, Inc. USA, 1998.
- [4] Hucho W H. *Aerodynamik des Automobils*, Friedr. Vieweg & Sohn Verlag/GWV Fachverlage GmbH, Wiesbaden, Deutschland, 2005.
- [5] Barnard, R H (1994): *Aerodynamic Problems and Solutions in Open Cabriolet Vehicles*, Royal Aeronautic Society, Vehicle Aerodynamics Proceedings July 1994
- [6] Fluent Inc. (2006): *Fluent 6.3 User's Guide*, Fluent Inc. Lebanon

## CFD ANALYSIS OF THE UNDERFLOOR AERODYNAMICS OF A COMPLETE “TGV” HIGH SPEED TRAIN SET AT FULL SCALE

Masson Elisa\* and Allain Eliane† and Paradot Nicolas†

\* SNCF - Direction de l’Innovation et de la Recherche (Research Dpt)  
45 rue de Londres, 75 008 Paris, France  
e-mail: elisa.masson@sncf.fr

† SNCF – Centre d’Ingénierie du Matériel (Rolling Stock Dpt)  
4 allée des Gémeaux, 72 100 Le Mans, France  
e-mails: eliane.allain@sncf.fr

**Keywords:** aerodynamics, ground vehicles, high speed trains, CFD and block calculation

**Abstract:** *This paper presents CFD calculation performed on the “TGV Réseau” high speed train operated by SNCF on the French high speed network at 300 km/h. The newness of this work consists in the complete train consideration (e.g. eight trailer cars with two power cars at the extremities) at scale 1 in simple unit and double unit configuration. The methodology used is presented. The results obtained are here analyzed in term of velocity distribution around the train, velocity evolution in the underbelly region and also in term of drag coefficients. Some of them are compared to data measured in full-scale track tests.*

## 1 INTRODUCTION

With the increase of the service speed on the new high speed lines of the French network, the investigation of aerodynamic research topics is motivated by several aspects which affect system security (slipstream effect, cross wind stability, ballast projection [1]) as well as performance (drag reduction [2]). In order to study these problematics with having the more precise reference case - and for the sake of representing the most real configuration, one of the expectations at SNCF is to obtain values of velocity profiles and drag coefficients for a complete set train at scale 1 at 300 km/h.

Pressure and especially friction drag is of great importance for railway vehicles. Even if the optimisation of head and tail shape (due to bidirectional use) must be treated carefully to improve high speed train performance, attention is focused here on adjacent components like bogie or intercar gap cavities where the flow is continually disturbed by sharp edges and cross-section changes repeated along the train. These parts of the train are also considered in term of ballast projection phenomenon, as it has been demonstrated that velocity field is one of the cause of the ejection of grains on the track: the ballast grains are rolled by the flow induced under the car body by the train passage. These are two reasons why the underfloor flow field is here investigated.

Aerodynamic engineers and researchers have at their disposal three means to study flow around a vehicle: measures in line (i.e. on a real vehicle running in real circulation condition), measures in wind tunnel (i.e. for a reduced model placed in a flow induced by a fan) and calculations with a CFD (Computational Fluid Dynamics) code. All these approaches have their pros and cons and are used in function of the needs and the means of the study.

In the railway domain, many experiments have been carried out to characterize the flow around high speed rolling stock. In the case of under car body investigations, velocity profiles can be determined by Pitot tubes placed on the track between and on both sides of the rails. The velocity signal is then provided all along the train for different vertical and horizontal positions. However, for reason of operation safety, probes can not be introduced in the area between the top of the rail and the undercar body. As a consequence, these measures are limited to the very near zone to the track bed.

Figures of drag coefficients can be determined through running resistance measurements by coasting technique. This kind of measures are realized on a straightline (no gravity effect due to cant) and flat ground (no inertia effect) sample of high speed network. When the train has reached a constant speed, the motorized efforts are stopped: the only force to which the train is subjected is the running resistance. Then the method consists in the calculation of the deceleration of the train. The drag is determined by the identification of the aerodynamic C coefficient in the running resistance formula ( $RR=A+BV+CV^2$ ). These kinds of measures are very difficult to handle. Indeed, first of all it is not easy to find a straightlined and flatgrounded portion of high speed line which is long enough to achieve the complete run until the stop of the train; as a consequence, corrective coefficients have to be added. Secondly it is hard to proceed in condition without wind and several passages have to be recorded in the both operation directions. Moreover, in term of drag determination, these measures give the drag of the complete train set but do not allow to identify the contribution of each element of the train set.

For these reasons, the drag is preferably determined with wind tunnel tests. Many values of global and local drag coefficients are available on 1/7 or 1/15 train models, but due to the length of the wind tunnel section, the model is often limited to a train set constituted of three coaches. The drag of the complete train is then obtained by duplication of the drag of the

middle coach. Even if this hypothesis is realistic, it introduces some uncertainties which are added simultaneously to scale and similarity uncertainties.

An alternative between realistic configuration and operation on the one hand and measures exploitation in the other hand at disposal in railway research is CFD calculation. This approach has been considered for this study.

As the two previous means, this method presents some drawbacks. For instance, detailed calculation with a fine resolution is often limited by computational resources. However, it exists some tools to make up for these constraints. Indeed, a methodology has been developed to realize a CFD calculation on a complete train set at scale one with the actual computational resources at SNCF. This methodology is presented in the first part of the paper.

CFD simulations have been performed on the complete train set of a TGV Réseau. Then a double unit configuration has been considered: the coupling system has been modelled and the flow has been calculated around the power car and the first trailer car of the second unit. Another values than drag coefficient or velocity profiles have been treated and these calculations have allowed to qualify the flow with cartographies in different directions of the train. The results are presented in the second part of the paper.

## 2 METHODOLOGY

In this part are presented the two configurations which have been considered to be submitted under calculation in this study. According to these configurations, the necessity of the marching technique is explained and the method presented.

### 2.1 Configuration and problematic

The complete train set of the TGV Réseau in simple unit configuration is composed of height passenger cars (called R1 to R8 on Fig. 1) and two power cars at the front and rear side of the train (named respectively M1 and M2 on Fig. 1).

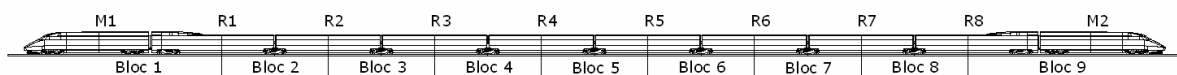


Figure 1: Scheme of the "TGV Réseau" train set in simple unit configuration

The complete train set of the TGV Réseau in multiple unit configuration is composed of two coupled simple unit configuration trains (Fig. 1bis).

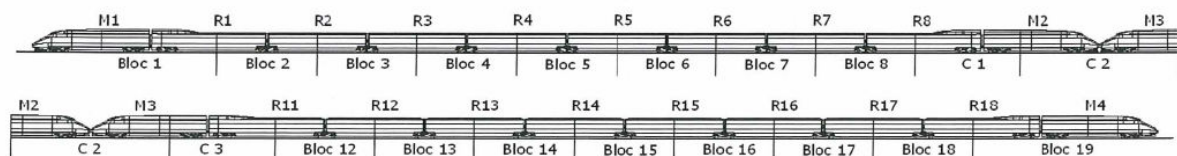


Figure 1bis: Scheme of the "TGV Réseau" train set in multiple unit configuration

The TGV Réseau presents the same characteristic feature as all trains of the "TGV" high speed train family: the two power cars have two motor bogies and each passenger car shares a trailer bogie with the previous or next passenger car, except for the two cars at the extremity of the train set which have at most their own trailer bogie.

The power pick-up is made by a pantograph located on the rear power car when the train is on circulation on high speed line; but this pantograph is not represented here as the study is focused on underfloor region. For the same reason, roof equipments are not modelled.

For sake of simplification, the infrastructure is represented only by a flatground with two rails. As it will be presented later, the effect of the ballast bed and the sleepers is represented by a roughness condition.

The investigation of underfloor flow field by simulation on the TGV Réseau in scale 1 can not be made in one set. Due to the length of the train set (about 200 m) and the detail required for the model (in particular bogie and intercar gap zones), a numerical simulation in view of an aerodynamical characterisation of the flow would need an unfeasible mesh for the available computational resources at SNCF.

A marching technique was adopted to perform the CFD computation of the undercar flow field. This kind of method recently used by industrials in external aerodynamics [7] [8] [3] [4], has been largely adopted for its flexibility: it could be executed on whatever configuration with blocks adapted to the computational resources.

## 2.2 Presentation of the methodology

The marching technique consists in splitting the computational domain along the train axial direction in order to perform sequential simulation on small parts of the train.

The first step of the methodology consists in splitting the model (i.e. the full train set with the upstream domain necessary to the boundary layer development and the downstream domain necessary for the wake) in different distinct blocks.

Each block is treated successively from upstream to downstream (in the flow direction or in other word, in the opposite direction of the train) with a cross of information from the outlet interface of a block to the inlet interface of the next block: the output of the previous simulation are used as input for the following one. In order to achieve the convergence of the physical values, several iterative cycles of “up-and-down” could be realized in the calculation process: the velocity information is propagated from upstream to downstream (i.e. from block N to block N+1) while pressure information is propagated from downstream to upstream (i.e. from inlet block N+1 to outlet block N). With the upstream and downstream boundary conditions, which are respectively velocity profile and atmospheric pressure, the propagation process must achieve the convergence of the model. However, some studies on reduced train set at reduced scale [5] have shown that this process is not necessary and a simple transfer is sufficient for convergence.

## 2.3 Presentation of the model

The model of the TGV Réseau at scale 1 has been divided in 9 blocks. The choice for splitting the train set is imposed by the characteristic feature of the TGV: bogie and intercar gap between each driving or trailing cars are very complicated regions favoured for a disturbed flow where a particular attention is required.

It has been decided to split the passenger cars in the middle. Consequently, the intermediate blocks of the model (named B2 to B8 on Fig. 1) are composed of the second half of the (n-1) car and the first half of the n car with  $n \in [2,8]$ . These blocks are fitted with a trailer bogie. In the case of the power cars, it has been decided to create a consequent block composed of the entire front (respectively rear) power car and the half of the first (respectively last) passenger car. These blocks are named B1 and B9 on Fig. 1. They are fitted with two motor bogies and the entire trailer bogie of the extreme car.

Finally, due to the construction of the blocks, the B2 to B8 blocks of the intermediate passenger cars are identical. The B9 block is the symmetric of the B1 block. This splitting solution presents the advantages of cutting the passenger cars in a zone where there is no evolution of the car body and centring the block on the trailer bogie which is a zone of flow separation and recirculation. As a consequence, the request of modularity is respected and the full train set is generated only by two modules which are represented on Fig. 2.

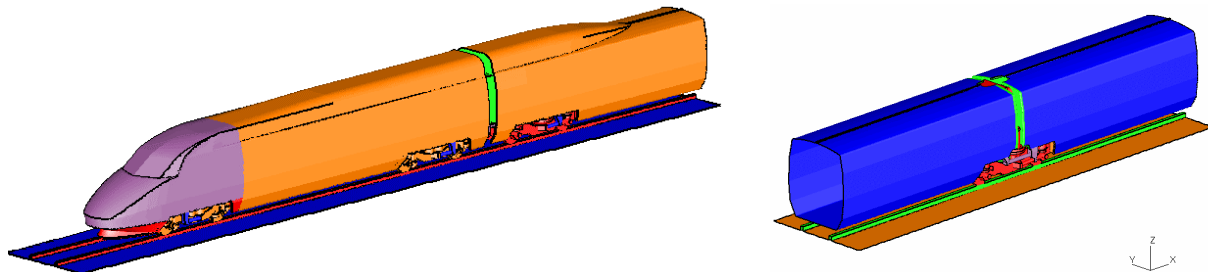


Figure 2: CAD of the blocks B1 and B9 (left) and blocks B2 to B8 (right)

For the double unit case, the same blocks have been used; only the block B9 has been modified to take into account the coupling: it has been duplicated. As the elements of this new block (two motor cars completed by the half of the last passenger car of the first train and the half of the first passenger car of the second train) can not be treated in a same model, the block has been splitted and decomposed in three blocks named C1, C2 and C3. The first block of the coupling group corresponds to the block B9 reduced of the nose of the motor car; the second block, which corresponds to the core of the coupling, is composed of the missing part of the motor car non integrated in C1 and its same but opposite part which are relied by the attach system; at least the block C3 is the symmetric of C1. These three specific blocks are presented on Fig. 3.

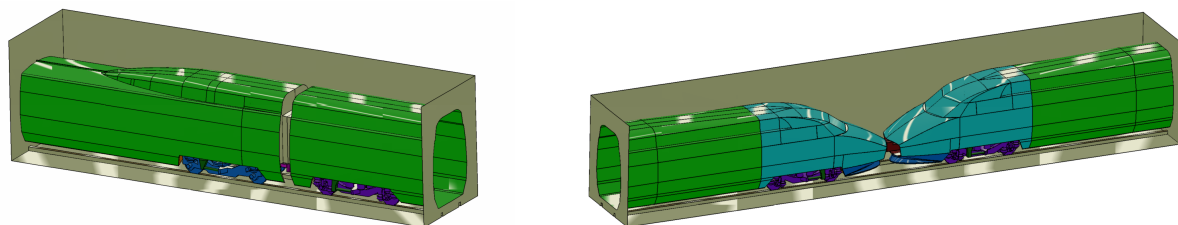


Figure 3: CAO of the blocks C1 and C3 (left) and the block C2 (right)

In order to obtain a well established velocity profile in the front of the nose of the train, an extrusion of 200 meters has been added to the block B1 in the upstream part. In the same way, an extrusion of 200 meters has been added in the downstream part of the block B9 in order to take into account the development of the wake at the rear side of the train. Moreover, for reason of calculations [8], all the blocks are extruded by a 18 meter domain to avoid an influence of the outlet boundary condition on the calculation.

## 2.4 Condition of calculation

In this part are rapidly presented the numerical conditions applied for the calculation: first of all, the mesh technique which has been adopted to represent the geometry, then the turbulence model which has been considered to model the air flow and at least the inlet and outlet conditions which have been imposed to represent the train movement.

### Mesh generation

The mesh generation procedure was performed with the CD adapco tools. The mesh is provided in three steps: generation of a subsurface at 5mm of all the surfaces of the elements of the model, generation of the mesh of the domain and finally extrusion in 3 slices of the skin of the core mesh to the surface of the elements of the model.

The undersurface is fixed surfaces of the model.

For the mesh of the domain, the “trimmed” technique has been applied, i.e. the core mesh is majoritarly composed of hexaedrical cells which are splitted when the subsurface is intersected. Then a refinement is applied for the cells near the elements in order to represent the details of the undercar geometry as well as possible (with 5mm size) and to guarantee that the mesh size is suitable for the near wall treatment (first cell size of 1.13mm) used for the different rough surfaces.

The same mesh procedure has been applied to the blocks B1 and B2 and then to the blocks C1, C2 and C3 in order to make easier the passage of the output of a block to the input of the next block. Finally the mesh of B1 is composed of 25,154,908 cells and the one of B2 of 11,890,714 cells. For the coupling zone, the mesh of the blocks C1 and C2 are respectively composed of 16,075,798 and 19,343,362 cells.

### Equation resolution

The simulation were carried out with the code Star CD in its version 3.24. The calculations have been performed with a RANS approach when system equation is closed with an eddy viscosity model of two transport equation. The k- $\epsilon$  model in its RNG form (Renormalisation Group) was used for all the simulations.

The velocity-pressure couple is provided by the SIMPLE algorithm (Semi-Implicit Method for Pressure Linked Equations) and the spatial discretisation scheme used is the second order MARS scheme (Monotone Advection and Reconstruction Scheme) specific to Star CD.

### Boundary conditions

A “pressure” condition is applied in output of each block. What should be understood is that this condition is applied at 18 meter downstream the end of the B1 to B8 blocks, as all these blocks have been extruded with a non physical domain for the numerical propagation of the boundary condition. In the case of the block B9, this condition is imposed 200 meter downstream the end of the tail of the train; by the way this last block has been extruded by a physical domain for the physical development of the wake.

An “inlet” condition is applied in input of the block B1. This condition, applied at the boundary of the domain, i.e. 200 meter upstream the nose of the train, is imposed by the velocity (83m/s), the turbulence intensity and the mixing length. For the next blocks, each boundary condition is defined from the output of the previous block. What should be understood here is not the outlet condition of the domain (i.e. the pressure condition) but the outlet condition of the block (i.e. the values of the flow field obtained at the split of the car) which are  $u$ ,  $v$ ,  $w$ ,  $k$ ,  $\epsilon$  and  $\rho$ .

The rails and the ground are defined by a “wall” condition with a stream at the same velocity as the infinite flow (83m/s). The presence of the ballast and the sleepers is represented by a roughness condition; the definition of the value of the roughness is a result of the study of the flow characteristics between the train underbody and the track obtained in the framework of the DeuFraKo AOA project [6] [7].

The wheels, the axles and the brake discs are defined with a “wall” condition and their rotation are represented by an angular velocity.



At least, a “wall” condition completed by a “slip” condition is applied to the borders of the calculation domain.

### 3 RESULTS ON THE SIMPLE UNIT CONFIGURATION

The results which are presented in this paper are analyzed in term of speed and pressure cartographies. Moreover velocity signals which could have been recorded by Pitot tubes have been plotted and compared to data measured in full-scale track tests. At least, drag coefficients have been calculated for the full train set and then decomposed for each components of the train.

#### 3.1 Velocity distribution

In this part are presented a sample of figures where the velocity magnitude  $U=(u^2+v^2+w^2)^{1/2}$  has been plotted in order to characterize the flow evolution. The flow region in the gap between the underbelly of the vehicle and the track bed poses a challenge: the Couette type flow is regularly interrupted by the passing bogies and the cross-sectional change at the intercar connections; it is characterized by flow separation and formation of vortices at sharp edges and behind bluff body geometry, and by intense secondary flow.

For instance, the right part of Fig. 4 shows the velocity magnitude in the intercar gap between the power car and the first passenger car. The left part of this figure shows the velocity magnitude in the second bogie cavity of the power car at 500mm from the ground, i.e. at about 50mm above the wheel axle. The color scale from blue to red corresponds to a repartition of the velocity magnitude from low speed to high speed.

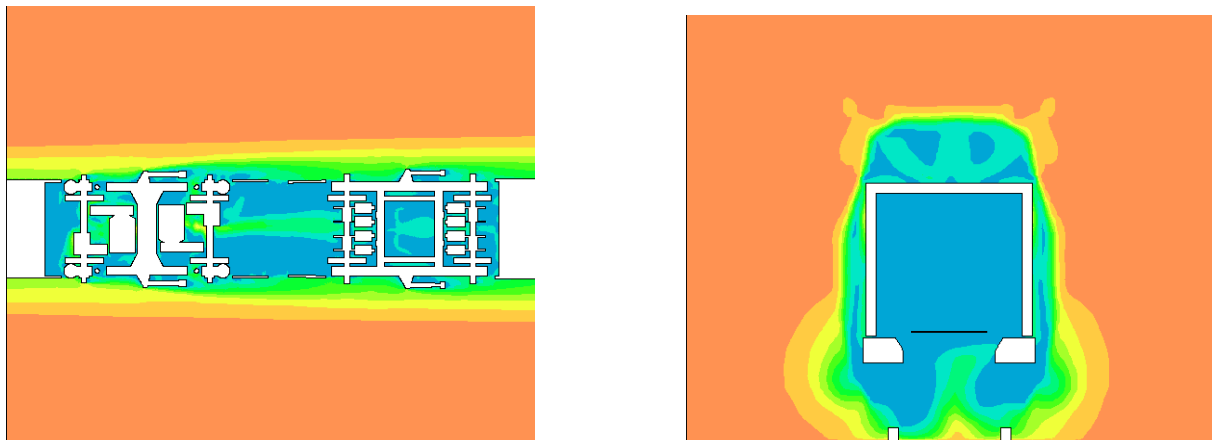


Figure 4: Velocity magnitude in the second bogie cavity of the M1 car (left) and in the intercar gap between the M1 and R1 cars (right)

It appears on Fig. 4 that the bogie cavity is a low velocity zone. This remark, which is true for all the bogie cavities (motors bogies as well as the trailer bogies) of the train set, is explained by the blockage effect due to the complexity of the geometry in this area. All the elements rising the surface, which are the suspension elements of the bogie, are an obstacle for the flow and consequently have an influence on the evolution of the boundary layer in the low part of the TGV.

This kind of view allows to display the evolution of the boundary layer along the train in the low region of the train. Indeed the transition between the light orange zone (speed range under 83m/s) and the dark orange one (speed range over 83m/s) gives an idea of its thickness.

As expected, first, this boundary layer is larger in the low part than in the upper part of the train along the wall or the roof (in a vertical point of view), and second, this boundary layer grows along the train. This evolution is more or less regular: however this zone is increased (in a horizontal point of view) when each bogie is crossed.

In order to visualize the boundary layer in the underbelly region of the train at the level of the power car and the first coach, some values of velocity have been extracted for different distance from the ground (vertical direction) and for different points under the train (longitudinal direction). Fig. 5 left shows the velocity profiles in the middle part of the track while Fig. 5 right shows this same velocity profile near the rails.

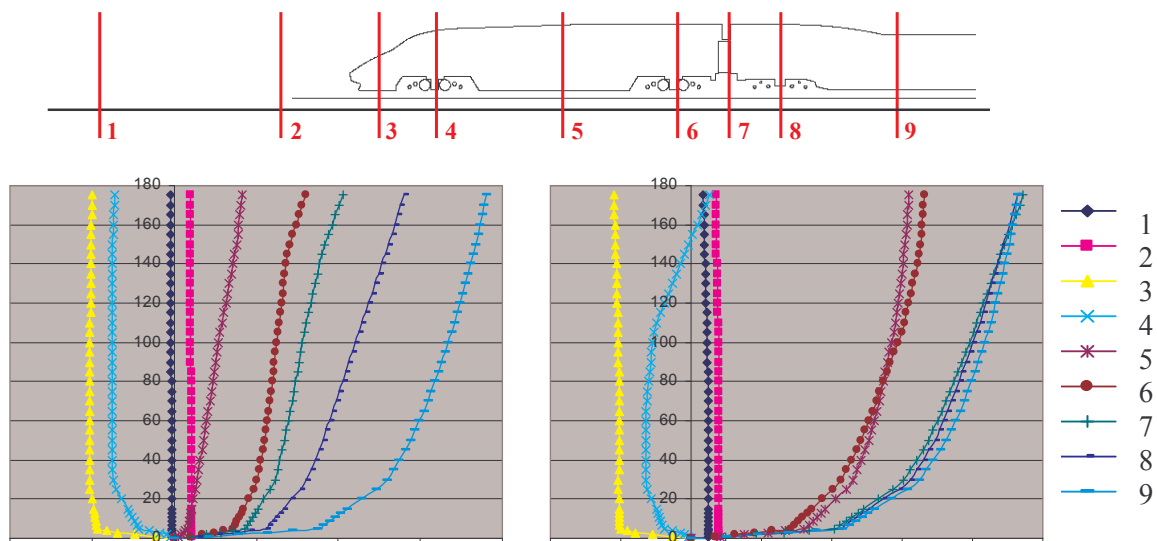


Figure 4: Evolution of the boundary layer in different positions under the M1 and R1 cars in the middle part of the track (left) and near the rail (right)

Before the passage of the motor car (dark blue #1 and pink #2 lines) the flat velocity profile which corresponds to the uniform velocity profile of the inlet condition is well observed. For the other profiles, it clearly appears that the boundary layer is fully developed at 20mm from the ground. Moreover the reversed flow under the nose of the train (yellow line #3) and in the first bogie cavity (light blue line #4) is also observed.

Fig. 6 shows the velocity magnitude for the rear motor car and behind it at 500mm from the ground, i.e. at about 50mm above the wheel axle.



Figure 6: Velocity magnitude at the rear side of the train

This view allows to visualize the end of the evolution of the boundary layer along the train which grows more and more. Moreover it allows to represent the wake of the train and to observe what can be legitimately interpreted (it could be confirmed by vorticity) as two vortices which extend from both part of the train.

### 3.2 Velocity evolution in the underbelly region

In order to quantify the critical zones of the flow in the underbelly region, the evolution of velocity under the car body has been plotted in different points of the outlines of the train.

With the help of the “sensors” objects at user disposal in Star CD, which are placed in the flow for different transversal and vertical positions, the aerodynamic signal can be plotted in the longitudinal direction as if it was measured by Pitot tubes placed on the track. As the measures recorded by the probes are unidirectional, we have used the longitudinal component  $u$  of the velocity to build the signal. Fig. 7 left presents three signals at three different height: 20mm near the ground, 75mm just under the rail and 150mm at the wheel level at a position close to the middle of the track while Fig. 7 right presents these signals at a position close to the rail inside the gauge rail.

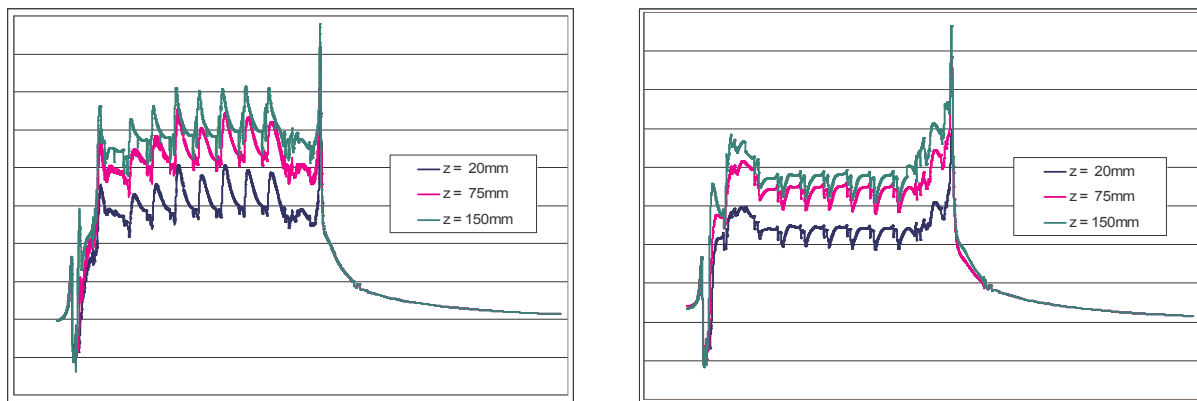


Figure 7: Evolution of the  $u$  component calculated for different “sensors” positions

Some comments can be made on these results. About a dozen of meter before the nose of the train, a quick velocity variation (about 10m/s) is recorded by the sensors, which is the effect of a surpression zone due to the air motion by the train approach. Under the stem, the velocity falls abruptly and becomes negative. This renders a strong aspiration under the nose of the TGV. Then the velocity grows rapidly, which corresponds to the flow under the body of the train. After, i.e. for the passenger coaches, it can be noticed that the periodicity of the model involves a periodicity in the signal. The passage of each bogie and intercar gap is correlated with strong perturbation of the signal characterised by a decrease of the  $u$  component of the velocity. This could be explained by the increase of the volume under the floor in which the flow can evaluate. When the train set is totally passed, an abrupt increase of the velocity is observed before a progressive return to atmospheric conditions.

These characteristic signals have been compared to signals recorded during campaign measures on the French high speed line network. The train passages recorded which have been used in this study had a speed around 300km/h (+/- 3km/h).

For the series which have been considered and compared to the results of numerical simulations, it appears that the calculated surpression zone upstream the train is less important than the measured one; on the opposite, the abrupt increase of the velocity at the tail

obtained with calculations is not represented in measures. For all the passenger cars, the calculated velocities match the measured ones.

Some compared signals are illustrated on Fig. 8. Both represent the signal near the rail at the wheel level; the left one corresponds to a Pitot tube inside the gauge while the right one corresponds to the outside track area.

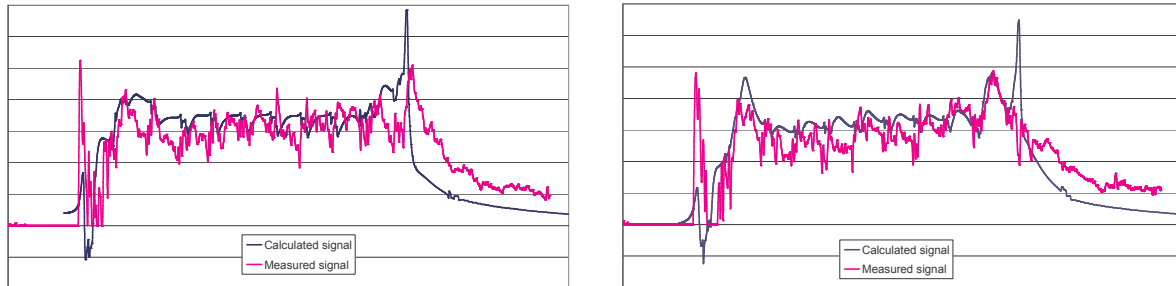


Figure 8: Evolution of the calculated (blue) and measured (pink)  $u$  component for different “sensors” positions

The decrease of the velocity in the wake is more rapid with the calculated signal than with the measured one. This could be a consequence of the extrusion of the domain which is not large enough to allow the wake development at the rear of the train.

Moreover it could be wondered what would be the effect on the signal obtained by the calculations if an atmospheric boundary layer profile had been considered instead of an uniform velocity profile. Studies in automotive domain have shown a non negligible influence of the inlet condition. Similar results could be expected in the railway domain. A new calculation could help to answer, in particular, it could allow to verify that a such correction will modify the signal in the good way, i.e. it could improve the signal calculated with Star CD and match the signal measured on the track.

### 3.3 Drag repartition

The notations used in this paragraph are the ones presented on Fig. 1.

Tab. 1 presents the contribution of the power and passenger cars in the drag coefficient of the train set. The head M1 and rear M2 power cars are composed of the body and the two motor bogies. The passenger cars are each composed of the body and twice half of the shared bogie with the previous and next passenger car, except the R1 and R8 which are fitted with the extremity trailer bogie and half of the shared bogie.

Train set	% of the total $C_x$
M1 – Head power car	21.8 %
R1 – 1st passenger car	9.4 %
R2 – 2 <sup>nd</sup> passenger car	6.7 %
R3 – 3rd passenger car	6.7 %
R4 – 4th passenger car	6.1 %
R5 – 5th passenger car	6.2 %
R6 – 6th passenger car	6.4 %
R7 – 7th passenger car	6.5 %
R8 – 8th passenger car	9.3 %
M2 – Rear power car	20.9 %
<i>Total</i>	<i>100 %</i>

Table 1: Contribution of the power and passenger cars in the drag coefficient of the train set

The front and the rear motor cars contribute respectively to 22% and 21% of the total drag. According to Tab. 2 and Tab. 3, the upstream and downstream motor bogies of the front motor car represent respectively 27% and 22% of the motor car drag coefficient while the body contributes to 50%. In the opposite, each of the two motor bogies of the rear motor car correspond to about 10% of the motor car drag coefficient (i.e. a twice less contribution) and the body represents 4/5 of the drag with a contribution of about 79%. From these figures, it can be deduced that the flow in the front side and the rear side of the train are not governed by the same phenomenon: while a great part of the drag is due to the perturbation of the flow near the bogie cavity in the nose of the train, it is due to the perturbation of the flow by the vortice structure and the wake at the tail of the train.

The contributions of the extreme passenger cars (about 10%) are more important than the other passenger cars (about 6%). There are two explanations to these figures if it is well accepted that the friction drag is influenced by the walls of the train and that the bogie cavity is inclined to increase the pressure drag. As a consequence, the first reason is that the R1 and R8 cars are a little bit longer (21m instead of 18m) than the R2 to R7 cars; the second reason is that these two extreme cars are fitted with one trailer bogie and half (the extreme one plus the half of the one shared with the R2 or R7 car) instead of one bogie (the half of the one shared with the previous and the next car).

M1 body	18.4 %	10.9 %
R1 body	9.4 %	5.6 %
R2 body	6.3 %	3.7 %
R3 body	6.3 %	3.7 %
R4 body	5.7 %	3.4 %
R5 body	6.1 %	3.6 %
R6 body	6.1 %	3.6 %
R7 body	6.3 %	3.7 %
R8 body	7.4 %	4.4 %
M2 body	28.2 %	16.7 %
<b>Total</b>	<b>100 %</b>	<b>59.1 %</b>

Table 2: Contribution of the car body in the drag coefficient of the train set (left column) and in the drag coefficient of all the bodies of the train (right column)

M1 – upstream motor bogie	14.4 %	5.9 %
M1 – downstream motor bogie	11.9 %	4.9 %
R1 – extremity trailer bogie	5.7 %	2.3 %
R1-R2 trailer bogie	7.6 %	3.1 %
R2-R3 trailer bogie	7.4 %	3.0 %
R3-R4 trailer bogie	7.1 %	2.9 %
R4-R5 trailer bogie	6.5 %	2.7 %
R5-R6 trailer bogie	6.5 %	2.7 %
R6-R7 trailer bogie	6.8 %	2.8 %
R7-R8 trailer bogie	6.8 %	2.8 %
R8 – extremity trailer bogie	8.5 %	3.5 %
M2 – upstream motor bogie	4.8 %	2.0 %
M1 – downstream motor bogie	5.9 %	2.4 %
<b>Total</b>	<b>100 %</b>	<b>40.9 %</b>

Table 3: Contribution of the motor and trailer bogies in the drag coefficient of the train set (left column) and in the drag coefficient of all the bogies (right column)

What can be extracted from all these figures in term of optimisation? The first motor bogie, which represents 27% of the drag coefficient of the motor car, contributes to 6% of the drag coefficient of the TGV Réseau. The second motor bogie contributes about 5% when each trailer bogie of the train set represents only 3%. It is clear that efforts (with fairings for instance) have to be focused on the first bogie cavity of the power car (both motor cars for reason of reversibility of the train).

However the drag coefficient of all the bogies correspond to 41% of the drag coefficient of the complete train set. This result emphasizes the role of the bogie in the drag force. Even if the bogies are shared between two cars for a TGV, the number of bogies for a 8 coaches train is sufficient to justify an improvement of the shape of the bogie cavities for the sake of the aerodynamics of the TGV.

This conclusion is emphasized by the fact it is reported that the drag of the bogies can be reduced by 20% by aggressive application of deflectors under the nose, skirts and underbelly fairings, fairings over the bogies and nonprotuding bogies.

#### 4 RESULTS ON THE DOUBLE UNIT CONFIGURATION

Now are presented the results obtained on the double unit configuration; in particular, the analysis is focused on the coupling zone.

##### 4.1 Velocity distribution

Fig. 9 left shows the velocity magnitude in the coupling zone which is located between the front motor car of the first unit and the rear motor car of the second unit in the horizontal plan at 500mm from the ground while Fig. 9 shows this velocity magnitude in a vertical plan.

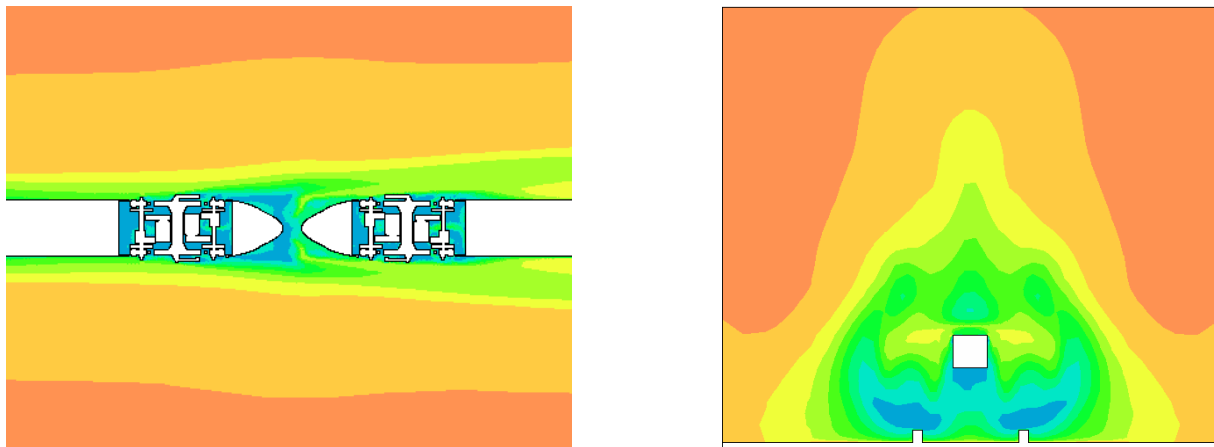


Figure 9: Velocity magnitude for the coupling zone of the trailer (left) and in the intercar gap between the power car and the first passenger car (right)

In comparison with the simple unit configuration, the flow at the rear side of the first unit train set is here modified by the presence of the second unit. In the same way, the boundary layer is already fully developed at the front side of the second unit train set.

##### 4.2 Velocity evolution in the underbelly region

Like for the simple unit configuration, the “sensors” objects have been used to plot the evolution of velocity under the car body of the train. Fig. 12 shows an example of signal build for the C1, C2 and C3 blocks. A representation of the coupling zone has been added for the

correspondence between the elements of the train and the perturbations observed for the longitudinal component of the velocity. It appears that the signal presents a high disturbed zone where the two noses of the motor cars are coupled. There is an acceleration of the flow under the stem of the rear motor car of the first unit which is followed by a velocity decrease at the coupling passage. Then, by Venturi effect due to the passage to a narrow surface, a new flow acceleration is observed under the stem of the rear motor car of the second unit.

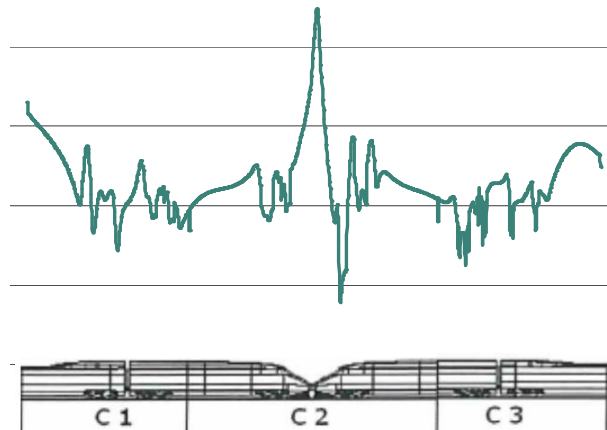


Figure 10: Evolution of the calculated  $u$  component for a "sensor" position in the coupling zone

Calculated signals are now compared to measured signals issued from the campaign on the French high speed line network. On Fig. 11 is illustrated with the pink line a sample of a record for a Pitot probe located near the rail inside the gauge at the wheel level for the passage corresponding to the coupling zone.

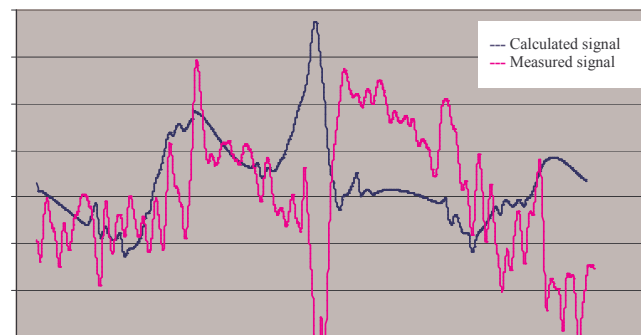


Figure 11: Evolution of the calculated (blue) and measured (pink)  $u$  component for a "sensor" position

The different signals which have been compared for different positions have all resulted in the same conclusion: the calculated signals match the measured signals very well for the zones which correspond to the C1 and C3 blocks. On the contrary, they do not match for the C2 block where the velocity peaks are in opposite direction. Some explanations can be proposed. The CAD may be too simplified: the coupling zone is totally closed and the air passage inside the coupling box is not modelled. The mesh may be not adapted and do not allow to capture the phenomenon. On an opposite point of view, the 1D Pitot tubes used for the full-scale tests may be not adapted to measure the 3D components of the flow in this complex area. Another hypothesis could be the superposition of the calculated and measured signals which could be biased by the calibration.

## 5 COMPARISON BETWEEN THE FIRST AND THE SECOND UNIT

In this part is compared the flow observed under the first coach of the second unit to the flow obtained on the first coach of the first unit train set in order to evaluate the influence of the coupling zone on the velocity field in the case of a double unit configuration.

The velocity magnitude in the bogie cavities of the first unit have been compared to the velocity magnitude for the same cavities in the second unit. The left part of Fig. 12 shows the velocity magnitude in the bogie cavity which is located between the first and the second trailers cars of the first train while the right part of Fig. 12 shows it for the second train; both are extracted at 500mm from the ground, i.e. at about 50mm above the wheel axle.

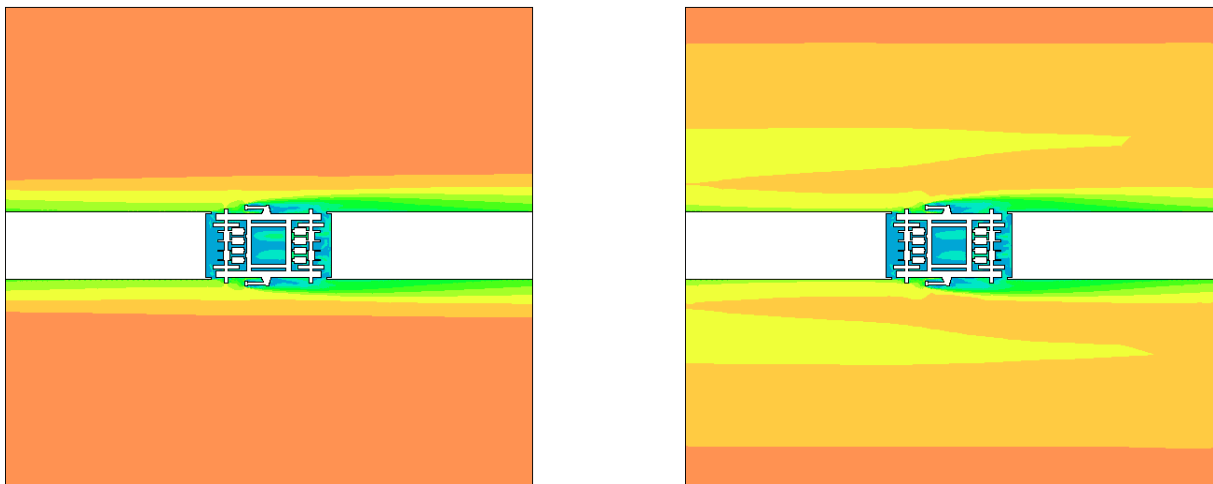


Figure 12: Velocity magnitude in the second bogie cavity of the M1 car (left) and in the intercar gap between the M1 and R1 cars (right)

As expected, the comparison is only possible in the underbelly zone between the rails as outside of this zone the boundary layer has evolved along the equivalent of a complete train set and has widened. In the underfloor zone, no difference in the flow evolution and velocity levels are observed. A thinner analyse with velocity evolution is needed to estimate the effect of the double configuration in comparison with a simple one.

For the majority of the aerodynamic signals which have been exploited and compared, it appears that the velocity component for the block B12 of the second unit is widely and superior to the velocity component obtained for the block B2 of the first unit. These differences can be explained by different phenomena. In particular, the flow which arrives on the motor car of the second unit has been accelerated by its evolution along the first unit train set and its passage of the coupling area.

In the framework of this results, in particular if attention is focused on the differences observed for the velocity magnitude at the end of the blocks 2 and 12, it is impossible to free from a complete simulation of the simple unit train set to study the flow around the second unit train: it would lead to an underestimation of the aerodynamical solicitations for the underbelly region. All the blocks which constitute the double unit configuration have to be submitted to calculation!



## 6 CONCLUSION

The study of the flow around a TGV Réseau high speed train at scale 1 has been studied by CFD calculations for a 300km/h speed operation. First a complete train set in simple unit configuration has been considered, then calculations have been performed on the power car and the first passenger cars of a multiple unit configuration.

Despite the use of a marching technique which has allowed to calculate these configurations, the computational resources have not permitted a fully detailed train to be considered. For reason of SNCF expectations in term of drag reduction or ballast projection investigations, the study has been focused on the underfloor flow between the undercar body and the track bed. Bogies and intercar gap cavities have been detailed.

The results obtained by the calculations performed with the Star CD code have allowed a better comprehension of the underfloor flow, in particular for the passage of the bogie and intercar gap cavity. The comparison of the velocity calculated between the car body and the track bed and the one measured by Pitot tubes in full-scale track tests have provided good agreement. An exploitation of the velocity profiles in all the underbelly region can be considered by calculation.

In term of drag reduction, the drag coefficients have been obtained for the complete train set but also for each coach of the train. Moreover the bogie contributions have been distinguished from the rest of the train. The effect of optimisation of the geometry of the motor and trailer bogies can be estimated for each part of the train.

At least, this study shows the drawbacks and benefits of numerical approaches available in commercial software for an engineering application. The calculation of the flow for the double unit configuration has emphasized the importance of the CAD for the representation of the phenomenon which occurs in this area. Numerical simulation as well for underfloor investigation as for nose, tail or roof parts prospectations still need improvement and should be made in the future.

## ACKNOWLEDGEMENTS

The authors would like to thank Christophe Lacroix for its contribution to this work.

## REFERENCES

- [1] A. Ido, S. Saitou, K. Nakade and S. Iikura. *Study on under-floor flow to reduce ballast flying phenomena*. Proceedings WCRR 2008, Seoul, Korea, 2008.
- [2] S. Krajnović. *Improvement of aerodynamic properties of high-speed trains by shape optimization and flow control*. Proceedings WCRR 2008, Seoul, Korea, 2008.
- [3] D. Rocchi and F. Cheli. *CFD Analysis of the under car body flow of an ETR500 train*. Proceedings BBAA VI, Milano, Italy, 2008.
- [4] M. Sima, A. Gurr and A. Orellano. *Validation of CFD for the flow under a train with 1:7 scale wind tunnel measurement*. Proceedings BBAA VI, Milano, Italy, 2008.
- [5] N. Paradot. *Étude numérique et expérimentale de la résistance à l'avancement d'un train à grande vitesse*. PhD thesis, Université de Poitiers, France, 2001.

- [6] J. García, A. Crespo, I. Alonso and G. Giménez. *Estimation of the flow characteristics between the train underbody and the ballast track*. Proceedings BBAA VI, Milano, Italy, 2008.
- [7] The DeuFraKo AOA „Aerodynamics in Open Air“ Project. WP 1 Underfloor Aerodynamics Summary Report. 2008.
- [8] The RAPIDE „Railway Aerodynamics Passing Interactions with Dynamic Effects“ Project. Executive Summary. 2001.

## DETACHED EDDY SIMULATION AND VALIDATION ON THE AERODYNAMIC TRAIN MODEL

Tomas W. Muld\*, Gunilla Efraimsson \*, Dan S. Henningson†, Astrid H. Herbst\*, and  
Alexander Orellano◇

\*Linne FLOW Centre, KTH Aeronautical and Vehicle Engineering,  
Teknikringen 8, SE-100 44 Stockholm, Sweden  
e-mails: muto02@kth.se, gef@kth.se

† Linne FLOW Centre, KTH Mechanics  
Osquars backe 18, SE-100 44 Stockholm, Sweden  
e-mail: henning@mech.kth.se

\* Aero- & Thermodynamics, Specialist Engineering  
Bombardier Transportation, Östra Ringvägen 2, SE-721 72 Västerås, Sweden  
e-mail: astrid.herbst@se.transport.bombardier.com

◇ Aero- & Thermodynamics, Specialist Engineering  
Bombardier Transportation, Hennigsdorf, Germany  
e-mail: alexander.orellano@de.transport.bombardier.com

**Keywords:** Detached Eddy Simulation, Aerodynamic Train Model, Slipstream, Validation, Vehicle Aerodynamics

**Abstract:** *We present CFD-simulations of the flow around the aerodynamic train model (ATM). The turbulence modelling technique is detached eddy-simulation (DES), where the DES model is based on the  $k-\omega$  SST RANS model. The Reynolds number for the simulation is 60.000 based on the hydraulic diameter (3m in full scale), free-stream velocity and kinematic viscosity of air. The model used is in 1:50 scale. The numerical results are compared to water tunnel experimental data on the ATM available from the German Aerospace Center (DLR). The velocity field is measured using particle image velocimetry (PIV). The numerical setup is made to match the experimental setup as close as possible. Focus of the analysis is on the flow in the wake of the train. Comparisons of the averaged velocity and the velocity fluctuations in the wake shows that the overall levels and trends are captured by the numerical simulations. However, the peak value of the velocity magnitude in the wake seems to be overestimated by the DES technique used.*

## 1 INTRODUCTION

When designing the next generation of high-speed trains it is of importance to predict the flow structures behind the train, since large velocity and pressure fluctuations in the wake affect the surroundings. This is a severe safety issue for people standing on a platform, track workers and other trains passing. Even though ground vehicles such as cars, trains or trucks have different body shapes, knowledge of the flow structures in the wake for one vehicle type will help for the understanding of the others. The large boundary layer at the rear of the train needs special consideration in train aerodynamics. The large size is an effect of the long slender body of the train.

For geometries similar to a train, two main flow patterns in the wake have been identified by Morel [1]. One flow pattern consists of a large separation bubble and the other pattern is dominated by two counter-rotating vortices.

The flow patterns also have different effects on the drag of the vehicle. For instance did Kee et. al. try to control the structures in the wake of a passenger car to reduce the drag [2]. Changing the wake was done by altering different part on the rear of the vehicle. One of their conclusions was that for one alteration the drag was reduced, but the size of the wake was increased. Even though they might not have changed the flow topology, this shows that the connection between the drag and the wake is complex.

Incidents related to slipstream in England were reviewed by the Rail Safety & Standards board in England [3]. It reports two incidents involving people and 13 involving pushchairs between 1972 and 2005 that can be connected to the slipstream phenomenon. These incidents involve people getting almost swept of their feet, pushchairs turned over or sucked under the train. Most of these are connected to freight trains. Today, as the speed of passenger trains increase, it is important to study the effects of slipstream, so that future accidents can be avoided.

Baker investigates pollutant particles and gases and how they spread in the wake [4]. The particle paths in the flow are determined by the flow field, which has to be simulated. These pollutants could be either particles from the tires or gases from the exhaust of the engine and they damage human health. Hence it is important to see how the spread around the road/rail.

For road vehicles Yang et.al. studied the effects of a truck passing a stationary car with the hood of the car open [5]. This is studied to ensure that the effect of passing truck does not cause any damage to the stationary car, such as deformation of the hood or breaking the holding mechanism. They found the force on the hood of the car to have up to five peaks. The reason for this is that the hood of the car experiences different pressure regions, with either high or low pressure. They found that some critical parameters were lateral distance between the stationary car and passing truck, the angle of the open hood and the speed of the truck. This flow case has similarities with that of a passenger standing on a train platform. Even though the distance might be different and the geometries of the passing vehicles are different, similar behavior could be expected.

In terms of computational work on high-speed trains, there are numerous articles on cross-wind stability. In [6], Large eddy simulations (LES) is used to perform calculations on a simplified train model influenced by a cross-wind. Wall functions have been used and the mesh contained 8.5 to 11.5 million cells. The results are validated against experimental data and a good agreement was found for the time-averaged pressure distribution for both the finer and the coarser grid. Also, the instantaneous values of the aerodynamic forces were studied. Analyzing these, the most dominant Strouhal number for the lift and side forces was found to be 0.1 and 0.7 respectively.

In [7] DES is used to calculate the flow around the Ahmed body. This is simplified car model, which exhibits different flow structures depending on the slant angle. The different flow structures are the same as discussed in [1]. [7] investigates the issue with grid induced separation, which could arise with DES and a badly constructed grid. The paper also investigates the difference between Reynolds-averaged Navier-Stokes (RANS) models and Detached Eddy Simulation (DES). For  $25^\circ$  slant angle, the RANS models show differences to experimental results and seem to be strongly dependent on numerical setup. The computations using DES show an improvement compared to the RANS model and is able to capture the trailing vortices in the flow.

In this paper we present CFD-simulations of the flow around the aerodynamic train model (ATM). The turbulence modelling technique is detached eddy-simulation (DES), where the DES model is based on the  $k-\omega$  SST RANS model. The numerical results are compared to water tunnel experimental data on the ATM. The velocity field is measured using particle image velocimetry (PIV). Focus of the analysis is on the flow in the wake of the train.

The paper is organized as follows. The first section contains the description of the train model and computational domain. Thereafter, the numerical and experimental setup are presented in the subsequent sections. This leads to up the section with the results of the different methods. The results are the analyzed in the next section. The paper then ends with conclusions.

## 2 THE AERODYNAMIC TRAIN MODEL

In this paper, simulations of the flow around the Aerodynamic Train Model (ATM) are analyzed. The geometry for the numerical simulation is based on an experimental setup, which consists of a stationary tank filled with water and a model of the ATM mounted on a ramp that drags the model through the water. In the numerical simulations the ATM-model is stationary and the flow is moving, which also means that the walls of the tank are moving. The ATM-model is 1:50 scale and has the dimension  $2.14\text{m} \times 0.060\text{m} \times 0.073\text{m}$ . To non-dimensionalize the results the reference length is taken as the hydraulic diameter  $d_h$  of the train. This means that with  $d_h = 3\text{m}$  for the full scale train,  $d_h = 0.06\text{m}$  for the scaled model. With the characteristic velocity as the free stream velocity  $u_\infty$  the characteristic time is  $T_{ref} = \frac{d_h}{u_\infty} = 0.0033\text{s}$ . The Reynolds number, based on the hydraulic diameter and free stream velocity is 60,000.

The computational domain is showed in Fig. 1. The  $yz$ -plane was made to correspond to the cross-section of the water tank whereas the length of the computational domain was limited due to the computational costs. Further investigations of the influence of the length of the computational domain will be done in future work.

## 3 NUMERICAL SETUP

The software used for the simulations is Star-CD 4.06 from CD-adapco. The software is a second-order finite volume solver. It has different options for turbulence modelling, (one- and two-equation models), DES and LES.

### 3.1 Grid

The computational grid used for the numerical simulation is a trim-hexa grid with 18.6 million cells. It has 5 prism layers and 6 refinement zones. When designing the grid, the resolution of the wake was prioritized, since this is the region of interest in this study. Also, it is the part of the flow field that contains most of the separated flow. The smallest cell size in the part of the wake that is closest to the train is  $0.0125d_h$ , compared to the largest cells in the free stream

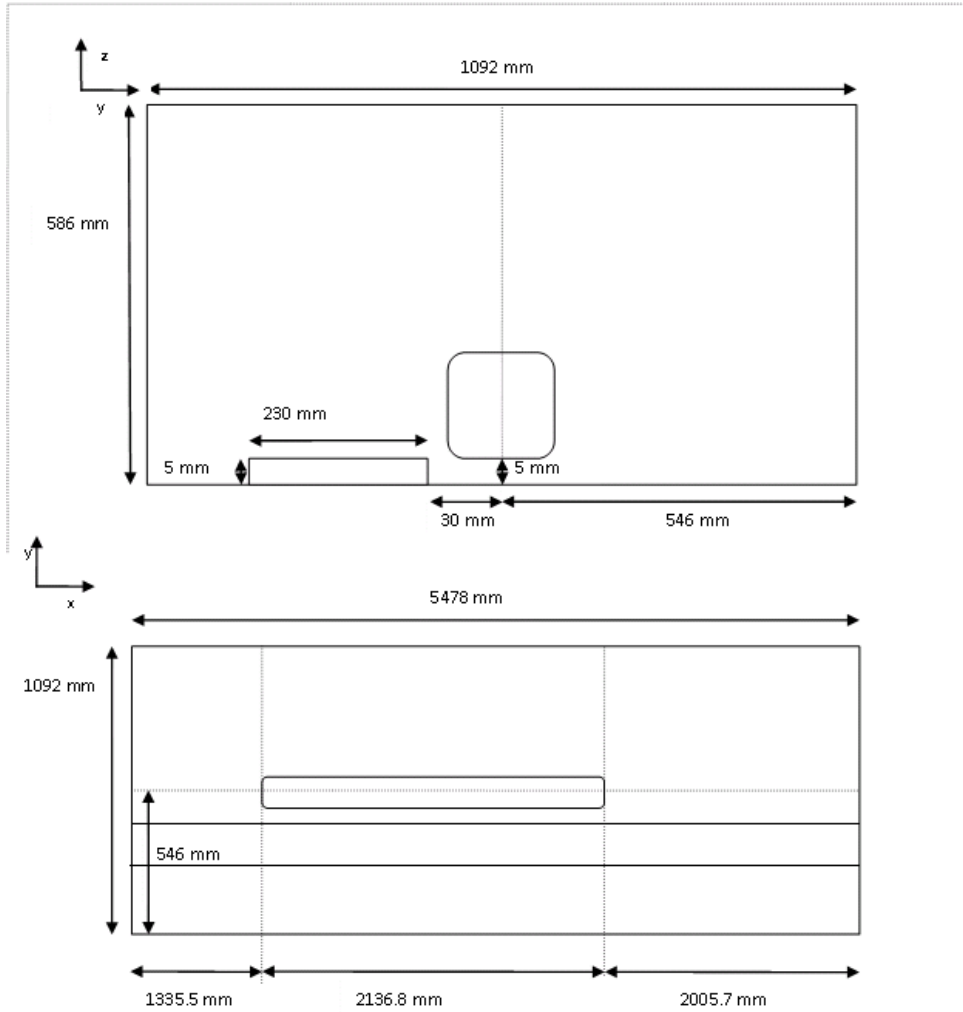


Figure 1: The computational domain

which are of size  $0.33d_h$

A schematic overview of the refinement zones are shown in Fig. 2 together with the resulting grid close to the rear of the train.

### 3.2 Turbulence model

The turbulence model used in the simulations is DES based on the  $k - \omega$  two-equation RANS model. Subsequently, we refer to this DES-model as DES- $k\omega$ . The general idea of the DES methodology is to replace a length scale in the RANS formulation to a filter length in the region of separated flow. The filter length is chosen such that the DES corresponds to a LES method in regions far from the wall and a RANS method close to the walls. The filter length  $\Delta$  of DES is

$$\Delta = \max(\Delta x, \Delta y, \Delta z). \quad (1)$$

The DES modification for the  $k - \omega$  RANS model was introduced in [8]. The length scale of the  $k - \omega$  RANS model is

$$l_{k\omega} = \frac{k^{1/2}}{C^*\omega} \quad (2)$$

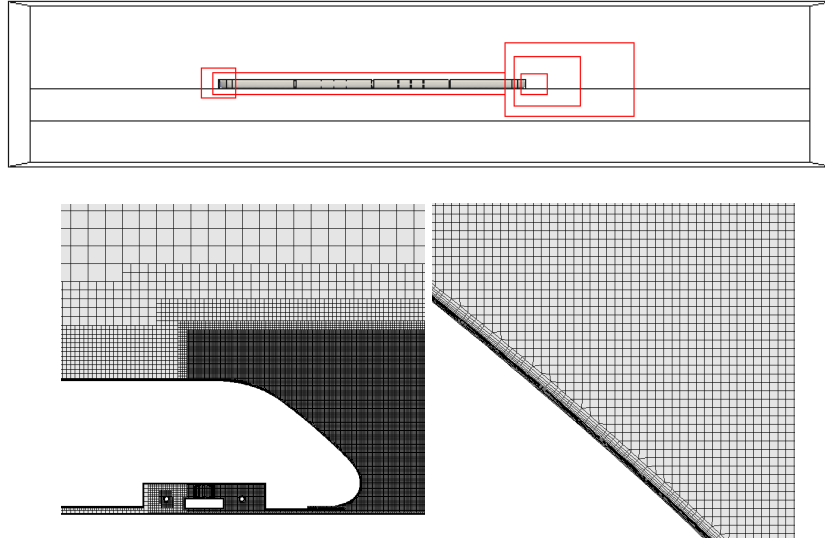


Figure 2: Grid refinement zones and grid close to the rear of the train

where  $k$  is the turbulent kinetic energy,  $\omega$  is the turbulence frequency and  $C^*$  is a constant where  $C^* \approx 0.09$ , respectively. In DES- $k\omega$  the length scale in (2) is replaced by the DES length scale  $\tilde{l}$ , where

$$\tilde{l} = \min(l_{k\omega}, C_{DES}\Delta). \quad (3)$$

When the length scale for the  $k - \omega$  model is shorter than the grid spacing, the length scale is identical to the corresponding RANS model. When the grid spacing is shorter, however, the resulting length scale is the same as in a LES.

In the  $k - \omega$  based DES model used, the modified length scale in (3) is only applied in the dissipation term in the equation for the turbulent kinetic energy. The dissipation term for  $k$  in the standard  $k - \omega$  RANS model  $D_{k\omega}^k$  is

$$D_{k\omega}^k = \frac{\rho k^{3/2}}{l_{k\omega}}. \quad (4)$$

In DES- $k\omega$  it is changed to

$$D_{DES}^k = \frac{\rho k^{3/2}}{\tilde{l}}. \quad (5)$$

### 3.3 Discretization in space and time

The numerical scheme used for discretization in space for the simulations presented in this paper is the Monotone advection and reconstruction scheme (MARS), [10]. The scheme has two steps; reconstruction and advection. The reconstruction uses a Total Variation Diminishing (TVD) scheme to compute the monotone gradients. The advection then uses the reconstructed flow properties to compute the fluxes from the advected quantities using a monotone advection scheme. This is a second order accurate scheme, with a user defined compression factor  $\gamma$ . This factor is between 0 and 1. For high values the scheme is less diffusive, but becomes computationally more demanding. The opposite hold for for low values of  $\gamma$ . In the simulations,  $\gamma$  was set to  $\gamma = 0.9$ .

For time discretization a second order implicit solver was used. The time step  $\Delta t$  of the calculation was  $\Delta t = 1.25 \cdot 10^{-2} T_{ref}$ . A smaller time step was used in the beginning for stability reasons.

### 3.4 Boundary conditions

The boundary conditions used are standard boundary conditions in Star-CD. Below, we give a short overview. For the details we refer to [10].

#### 3.4.1 Wall

There are two different wall boundary conditions used in the simulation, moving and stationary walls. A no-slip condition is set on both types, but the moving walls move with  $u_\infty$  relative to the coordinate system fixed on the train. This means that the walls corresponding to the train are stationary and the walls in the far field are moving. At the wall, a hybrid-wall model is applied. The model uses low- or high-Re models according to the  $y^+$ -values obtained at the first cell at the wall.

#### 3.4.2 Inlet

This boundary condition sets the three velocity components and two turbulent quantities at the inlet. In the present simulations, the freestream velocity  $(u_\infty, 0, 0)$  is given. Low turbulent intensity,  $5 \cdot 10^{-3}$  was assumed at the inflow boundary, since the train model was moving into a stationary fluid, and the estimated turbulent length scale is of the order of size of the train.

#### 3.4.3 Pressure outlet

At the outlet boundary the pressure is prescribed to zero gauge pressure, assuming that the outlet boundary is far enough downstream to have a uniform pressure distribution. The tangential components are put to zero and the normal components are then extrapolated from the interior of the domain.

## 4 EXPERIMENTAL SETUP

The experimental data that were used for validation was obtained from the German Aerospace Centre (DLR). In the experiments, the model train was fixed to a ramp and then dragged through a water tank. The measurements of the flow was taken with the Particle Image Velocimetry (PIV) technique. Two cameras were used with an offset towards each other, with each camera taking 80 frames per run. The velocity of the train model in the tank is 1m/s for all experiments. The measurements were taken on a horizontal plane  $z = 0.4d_h$  over the ground. The ATM-model used for the experiments had 4 cars. However, in order to mimic a longer train additional car gaps were added to the model, giving a total of 9 inter car gaps.

## 5 RESULTS

All results presented are normalized by  $u_\infty$  and  $d_h$ . The mean velocity computed in the numerical simulation is compared to the velocities measured in the experiments. In the CFD results, the mean velocity is the average over time of each discrete time step. For the experimental data the average is an ensemble average taken over different uncorrelated runs. The time average is taken over about 2000 time steps, while the ensemble is taken over 29 runs.



The reference frame is different in the numerical simulations and the experiments, i.e. the coordinate system is fixed to the train in the numerical simulations and to the ground in the experiments, respectively. Hence the velocities need to be transferred to the same reference frame. Due to the area of application, train aerodynamics, a ground fixed coordinate system has been chosen.

From the PIV measurements two-dimensional velocities in the measured plane are obtained. This means that only two velocity components of the CFD-computations are used. That is, the velocity magnitude computed is transformed according to

$$U_{exp} = \sqrt{(U_{\infty} - U_{CFD})^2 + V_{CFD}^2} \quad (6)$$

where  $U$  and  $V$  are mean values. The root-mean-square (RMS) values are also computed and compared. The  $u_{rms}$  is calculated as

$$u_{rms} = \sqrt{\langle u^2 \rangle - \langle u \rangle^2} \quad (7)$$

where  $\langle \rangle$  is the average value of the instantaneous velocity  $u$ .

First the flow fields are compared visually. In Fig. 3 the flow field from the numerical simulation and in Fig. 3 the flow field from the experimental study are shown. These are averaged quantities and is only provided to give a visual and not an absolute comparison.

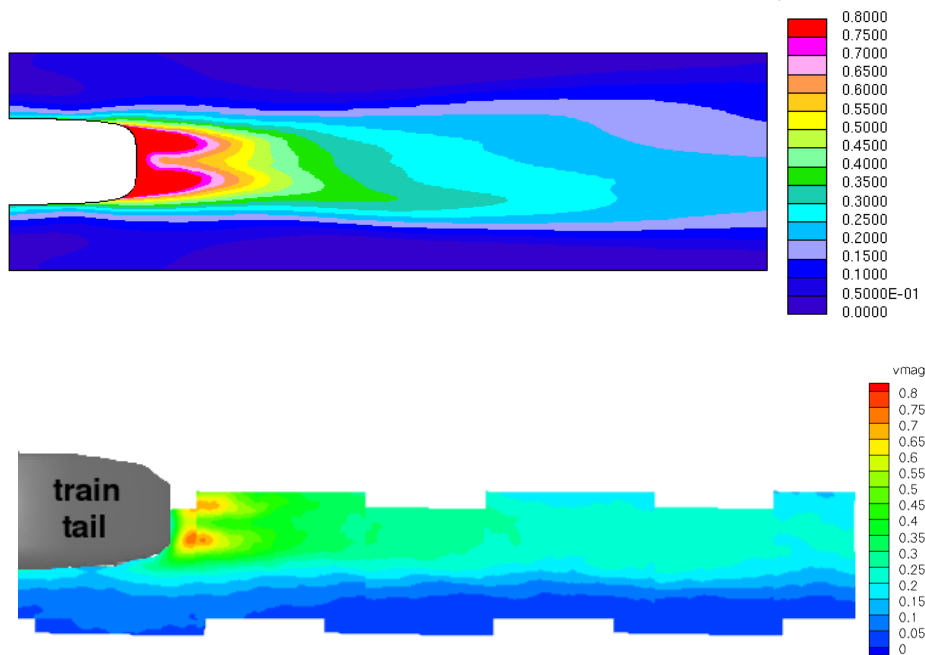


Figure 3: Velocity magnitude from numerical computations (upper figure) and from experiments (lower figure)

To illustrate the presence of vortices on the wake region, the  $Q$ -factor and pressure is plotted in Fig. 4 for the downstream positions  $x = 1.75d_h$  and  $3d_h$ . The  $Q$ -factor is defined as

$$Q = (\Omega_{ij}\Omega_{ij} - S_{ij}S_{ij}) \quad (8)$$

where  $\Omega_{ij} = \frac{1}{2}(\frac{\partial u_i}{\partial x_j} - \frac{\partial u_j}{\partial x_i})$  and  $S_{ij} = \frac{1}{2}(\frac{\partial u_i}{\partial x_j} + \frac{\partial u_j}{\partial x_i})$  are the antisymmetrical and symmetrical part of the velocity gradient, respectively. Positive and high values of  $Q$  are necessary conditions for vortex cores, see [11]. To ensure a sufficient condition, the pressure shall decrease as well. In Fig. 4 the pressure coefficient  $C_p$  is also plotted at the same downstream position.

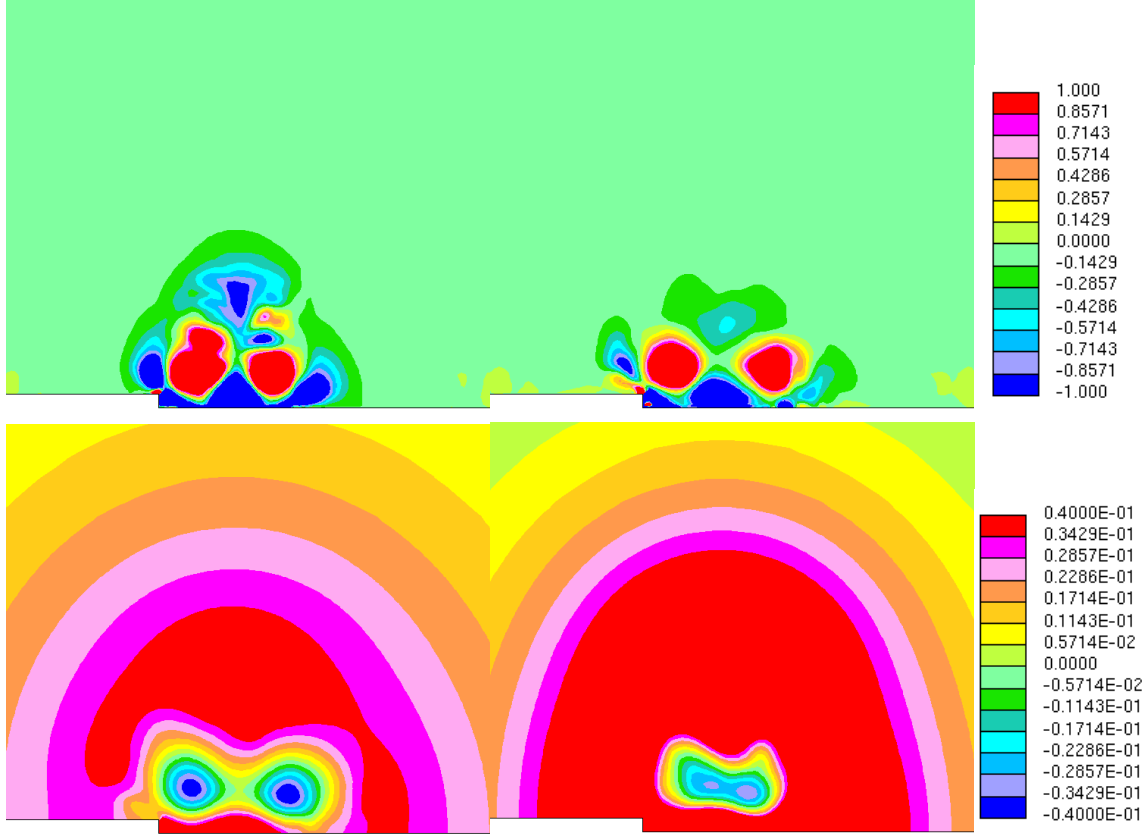


Figure 4: Normalized  $Q$ -factor and pressure coefficient for the downstream positions  $1.75d_h$  and  $x = 3.0d_h$  from the numerical computation

To be able to compare the experimental and numerical results in detail, the streamwise location has to be calibrated. The fixing of the position of the train is done manually in the post-processing of the experimental results and can therefore be inaccurate. To pursue a calibration of the exact location of the train, the mean  $u$  component and the mean velocity magnitude were used at  $y = -0.75d_h$  as shown in Fig. 5. The peak at the front of train, i.e. the head pressure pulse, was chosen as a calibration point. This calibration point was chosen since the head pressure pulse is a strong phenomenon, and can be correctly captured even in simple models. Hence, it can be assumed that this point is well described in both the experimental and numerical results, respectively.

To show the convergence of the results the streamwise velocity, the velocity magnitude, the root-mean-square value of  $u$  and the mean Reynolds stress component  $u'v'$ , respectively at the centerline of the train ( $y = 0$ ) in the wake are plotted for different times in Fig. 6 and Fig. 7. It is clear that the results are converged for the later times.

Next, the results from the numerical and experimental studies are compared in the wake of the train. Two  $xz$ - and two  $yz$ -planes have been used. First the solution along the centerline  $y = 0d_h$  and along  $y = 0.233d_h$  are plotted. The line  $y = 0.233d_h$  was chosen, since the

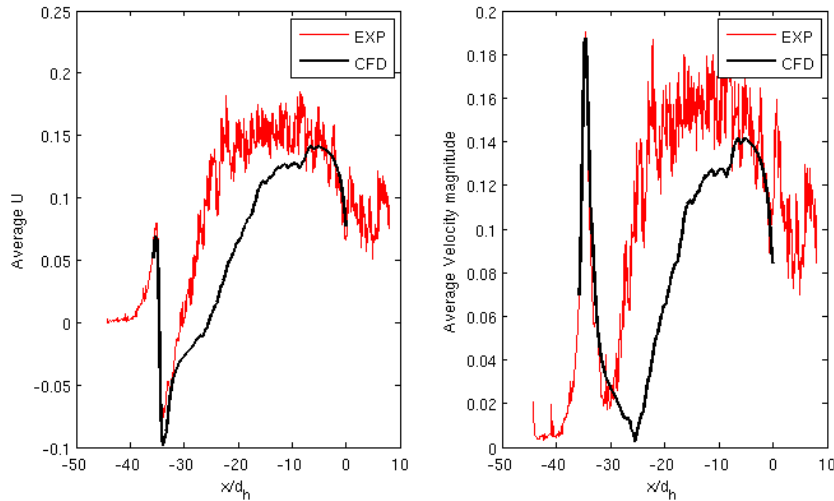


Figure 5: Average u-component of the velocity (left figure) and average velocity magnitude (right figure) as a function of  $x/d_h$  at  $y = -0.75d_h$

peak value of the velocity magnitude in the wake is located along this line. The mean velocity magnitude is shown in Fig. 8 and the  $u_{rms}$  in Fig. 9.

For the  $xz$ -planes the value  $x = 1.75d_h$ , which would correspond to the peak value of the velocity, and  $x = 3d_h$  were considered. The mean velocity magnitude is shown in Fig. 10 and the  $u_{rms}$  in Fig. 11.

## 6 ANALYSIS

From Fig. 3 it can be seen that the results are not symmetric in respect to the spanwise direction. This is an expected result since the geometry is not symmetric, due to the platform on one side of the train. This can clearly be seen in the numerical results. However, since there are only experimental results on the platform side of the train it is not possible to fully justify the asymmetry from the experimental data.

The two trailing vortices in the wake are clearly seen in Fig. 4, as the normalized  $Q$ -factor is high and the pressure is clearly lower than the ambient pressure in the vortex cores. The influence of the platform is visible and the vortex closest to the platform is lifted due to the presence of the platform.

The calibration of the location by fixing the position of the head pressure pulse can be seen in Fig. 5. The front of the train is located at  $-35d_h$  and the rear at  $0.85d_h$ . As argued in Sec. 5 the calibration of the  $x$ -location of the train was done at the head pressure pulse, that is at the front of train. However, this implies some uncertainties in the comparisons of the results in the wake of the train. For example, since the train moves in the experiments and the cameras are fixed the length of the train has to be calculated from the difference in time. This means that the velocity must be constant and known exactly. Since the comparison is sensitive to the streamwise position an error in the streamwise position affects the whole comparison.

Some of the oscillations in the experimental data are due to the overlaps between the different frames. The pictures taken from different cameras overlap so that the results can be matched. Since the pictures are taken at different times, the flow could have changed between the pictures giving a bad match. In addition, this yields two different values at the same location in space

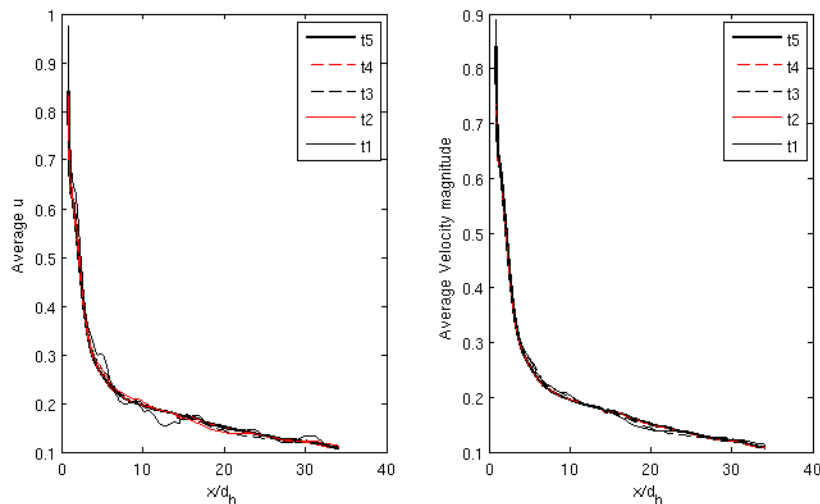


Figure 6: Average  $u$ -component of the velocity (left figure) and average velocity magnitude (right figure) as a function of  $x/d_h$  at  $y = 0d_h$ ,  $t = t_1 = 6.0 \times T_{ref}$ ,  $t_2 = 22.5 \times T_{ref}$ ,  $t_3 = 27.0 \times T_{ref}$ ,  $t_4 = 39.0 \times T_{ref}$ ,  $t_5 = 40.5 \times T_{ref}$

which causes unphysical oscillations in the plots. In general, the numerical results seem to underpredict the velocity magnitude along the train, as can be seen in Fig. 5.

In the wake the peak values of the averaged velocity magnitude do not match between the simulated and the experimental data, see Fig. 8. The experimental results seem to show that the velocity goes down towards zero and the numerical show an increase. Remembering that the results are in a ground-fixed reference frame, the  $u$ -component of the velocity should go towards the speed of the train ( $u_\infty$ ). What in Fig. 8 appears as a decrease close to the vehicle at  $y = 0.233$  is in fact an decrease followed by an increase of velocity. The decrease of the experimental data could be a problem of locating the train body in the experiments. At the train body there are no fluid particles, so the velocity can not be measured with PIV in this region. The shapes of the experimental and the numerical data are, however, in excellent agreement, although slightly shifted in the streamwise direction. The levels of the  $u_{rms}$ -values agree very well, although the shapes do not match as well as for the averaged values. Further investigations are needed before any main conclusions can be drawn about the accuracy of the turbulent quantities, although these results look promising.

As can be seen in Fig. 10 the shape of the averaged velocity in the wake is well captured by the numerical simulations. However, as in Fig. 8, the level is overpredicted. This can be due to the problem of fixating the location of the train, as mentioned above. This needs to be investigated further, since the level of the velocity magnitude is of outermost importance for slipstream investigations. The levels of the  $u_{rms}$ -values fit rather well and the shape of the curves of the numerical and experimental data agree further downstream in the wake. As above, further investigations are needed in order to draw any main conclusions of the accuracy of the turbulent quantities in the numerical simulations.

## 7 CONCLUSIONS

Numerical simulations have been performed on the aerodynamic train model. The turbulence model used is the detached eddy simulation based on the  $k - \omega$  two-equation RANS model. The

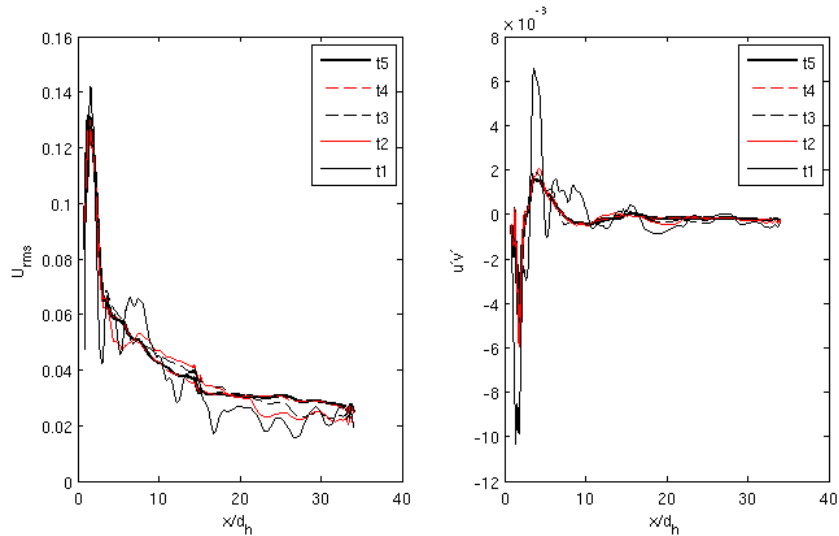


Figure 7: The  $u_{rms}$  value (left figure) and average Reynolds stress component  $u'v'$  (right figure) as a function of  $x/d_h$  at  $y = 0d_h$  for different  $t$

results are compared to results from experiments conducted in a water tank, with the exact same train model, using PIV to measure the flow.

The time-averaged values of the numerical simulation are compared in a ground-fixed coordinate system to the ensemble average of the experimental work. Because of the inability of PIV to locate the wall of the train, the streamwise position needs to be calibrated between the two methods. This is done by locating the velocity peak at the front of the train. To show that the time-average values of numerical solution has converged, the results are compared in the wake for different times.

The comparison between the two models are then performed visually by investigating the contour plot of the velocity magnitude and quantitatively by the velocity profile for two streamwise positions and two spanwise positions. The results show good agreement in terms of general trends and the length of the wake, but not in terms of peak value, where the numerical simulation give a higher peak. The numerical simulations are also investigated further by examining the  $Q$ -factor and the pressure in the wake of the train. These quantities is used to locate vortices and from the numerical simulation the two trailing vortices in the wake of the train can easily be identified.

## 8 ACKNOWLEDGEMENTS

The experimental work was performed in the framework of the collaborative research project "transient rail aerodynamics" between the German Aerospace Centre (DLR) and Bombardier. The financial and technical support of DLR is acknowledged.

The work was funded by the Swedish Rail Administration within the program Gröna Tåget. The financial support is gratefully acknowledged. The computational resources have been granted by Swedish National Infrastructure for Computing (SNIC).

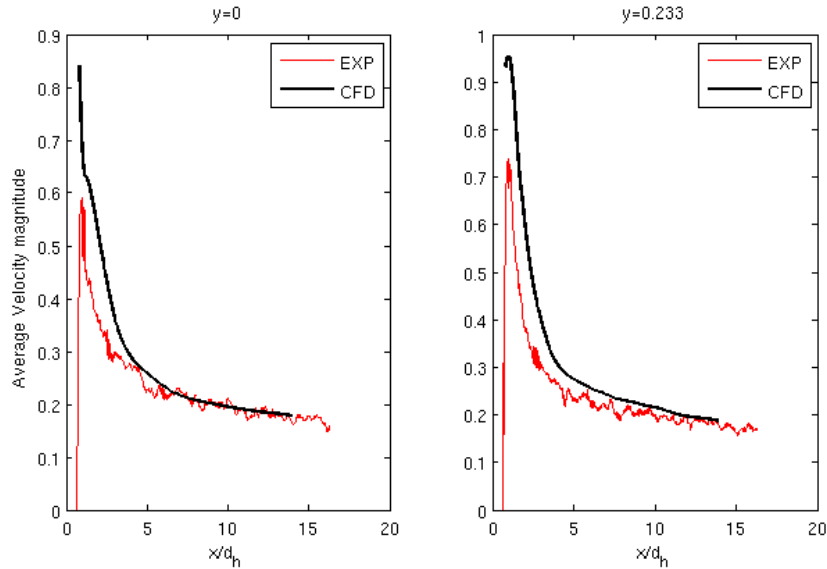


Figure 8: Comparison of mean velocity magnitude as a function of  $x/d_h$  at  $y = 0d_h$  (left figure) and  $y = 0.233d_h$  (right figure)

## REFERENCES

- [1] T. Morel. Effect of base slant on Flow on the near wake of an axisymmetric cylinder. *Aeronautical Quarterly*, 132–147, 1980
- [2] J.D. Kee, M.S. Kim and B.C. Lee. The COANDA FLOW control and Newtonian concept approach to achieving drag reduction of a passenger vehicle. *Vehicle Aerodynamics Design and Technology*. SAE Paper 2001-01-1267, 2001.
- [3] G.I. Figura-Hardy. RSSB Slipstream Safety Analysis of existing experimental data on train slipstreams including the effects on pushchairs. Rail Safety and Standards Board. 2007.
- [4] C.J. Baker. Flow and dispersion in ground vehicle wakes. *Journal of Fluids and Structures*, **15**, 1031–1060, 2001.
- [5] Z.G. Yang, J.P. Johnson, J.B. Morley, S. Unaune and S.D. Sovani. Dynamic moving mesh CFD study of semi-truck passing a stationary vehicle with hood open. *Vehicle Aerodynamics 2007*. SAE Paper 2007-01-0111, 2007.
- [6] H. Hamida, S. Krajnović and L. Davidson. Large-Eddy Simulation of the Flow Around a Simplified High Speed Train Under the Influence of a Cross-Wind. Proceedings of the 17<sup>th</sup> AIAA Computational Fluid Dynamics Conference, Toronto, Canada, June 6-9, 2005
- [7] F.R. Menter and M. Kuntz. Adaptation of Eddy-Viscosity Turbulence Models to Unsteady Separated Flow Behind Vehicles. In: R. McCallen, F. Browand and F. Ross. Symposium on the Aerodynamics of Heavy Vehicles: Trucks, Buses and Trains. Springer, New York, 2004

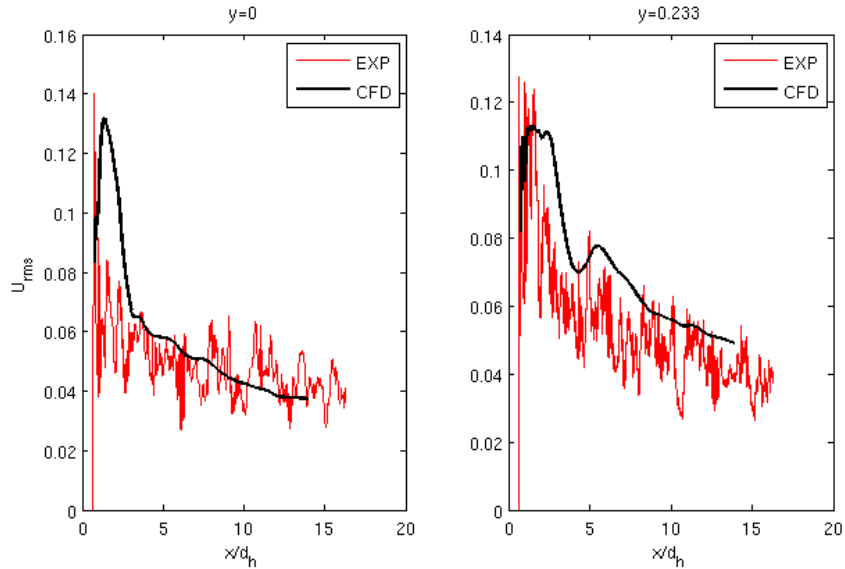


Figure 9: Comparison of  $u_{rms}$  as a function of  $x/d_h$  at  $y = 0d_h$  (left figure) and  $y = 0.233d_h$  (right figure)

- [8] A. Travin, M. Shur, M. Strelets and P.R. Spalart. Physical and numerical upgrades in the Detached-eddy simulation of complex turbulent flows. In: R. Friedrich and W. Rodi. *Advances in LES of Complex Flows*. Kluwer Academic Publishers, Netherlands, 2002.
- [9] P. Sagaut, S. Deck and M. Terracol. *Multiscale and Multisolution Approaches in Turbulence*. Imperial college press, Singapore, 2006
- [10] CD-adapco, *STAR-CD Version 4.06 Documentations*, 2008
- [11] J. Jeong and F. Hussain, *On the Identification of a Vortex* Journal of Fluid Mechanics, **285**, 69–94, 1995.

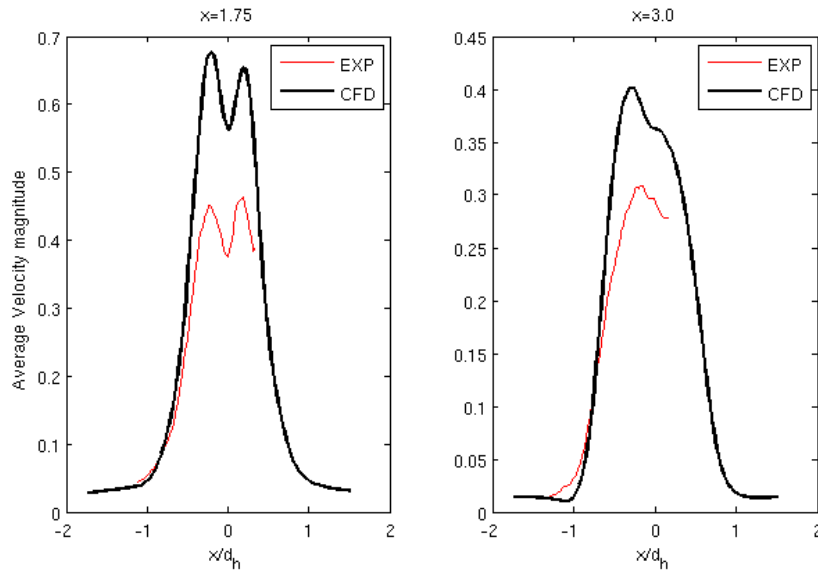


Figure 10: Comparison of mean velocity magnitude as a function of  $y/d_h$  at  $x = 1.75d_h$  (left figure) and  $x = 3.0d_h$  (right figure)

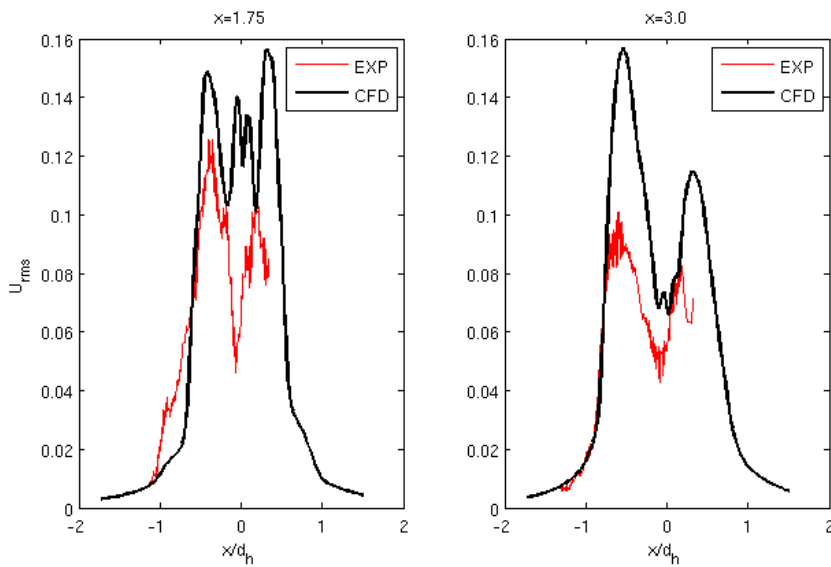


Figure 11: Comparison of  $u_{rms}$  as a function of  $y/d_h$  at  $x = 1.75d_h$  (left figure) and  $x = 3.0d_h$  (right figure)



## SINGLE- AND MULTI-OBJECTIVE AERODYNAMIC OPTIMIZATION OF A SIMPLIFIED VEHICLE TEST BODY USING EVOLUTIONARY ALGORITHMS AND ARTIFICIAL NEURAL NETWORKS

Christoph Niedermeier<sup>\*</sup>, Norbert Grün<sup>\*</sup> and Thomas Indinger<sup>†</sup>

<sup>\*</sup>Abteilung für Aerodynamik  
BMW Group, Schleißheimer Str. 424, 80788 München, Germany  
e-mails: christoph.niedermeier@mytum.de, norbert.gruen@bmw.de

<sup>†</sup>Lehrstuhl für Aerodynamik  
Technische Universität München, Boltzmannstr. 15, 85748 Garching bei München, Germany  
e-mail: thomas.indinger@tum.de

**Keywords:** Optimization, vehicle aerodynamics, evolutionary algorithms, surrogate modeling, artificial neural networks

**Abstract:** *Unlike in airfoil or turbo-engine design where stochastic optimization methods like evolutionary algorithms and auxiliary surrogate models like artificial neural networks have become a common development tool, the aerodynamic optimization of passenger vehicles is still carried out manually. That means the results of the optimization are highly depending on the knowledge and also on the preferences of the responsible engineer. In this paper common methods from aeronautics are transferred to the automotive domain. The aerodynamic properties of a simplified vehicle test body are optimized by means of evolutionary algorithms and artificial neural networks for surrogate modeling. The objective functions to be optimized are the aerodynamic properties drag, lift, and lift balance. Their evaluation is carried out by means of computational fluid dynamics, namely the commercial software package PowerFLOW with the underlying lattice Boltzmann method. In a first step the so-called covariance matrix adaptation evolution strategy (CMA-ES) - a state-of-the-art evolutionary algorithm with powerful self-adaptive capabilities - is used to minimize the drag of the test body and to prove the feasibility of the method. In a second step the multi-objective version of the CMA-ES is used to optimize all three objectives simultaneously. For evolutionary algorithms a certain population size is necessary for a reasonable application of the method. To reduce the computational cost caused by the CFD evaluations of a whole population a surrogate model like an artificial neural network can be applied. In this paper a radial basis function network is used together with the single-objective version of the CMA-ES, drastically reducing the number of exact evaluations.*

## 1 INTRODUCTION

### 1.1 Optimization in vehicle aerodynamics

In the present world with increasing ecological awareness and strict environmental legislation, the aerodynamic properties of passenger vehicles are becoming more and more important. Especially at highway speeds, drag is a main influencing factor on the fuel consumption and consequently on the carbon dioxide emissions of a car. However, lift and especially lift balance between front and rear axle may not be disregarded due to their crucial influence on the cars dynamic stability.

While wind tunnels have already been used to manually optimize the aerodynamic properties of vehicles for decades and are still a fundamental tool during the development of a new car, computational fluid dynamics (CFD) is becoming more and more important with increasing computer power. Especially in the early phase of development, numerical simulations are an advantageous tool for the evaluation of numerous different design variants. CFD hence also offers the possibility of applying numerical optimization techniques, which are a common development tool in aeronautics or turbomachinery design but which have scarcely been used in the automotive domain so far. A rather novel CFD method is the so-called lattice Boltzmann method (LBM [1]), which differs significantly from well-known finite volume methods in the underlying physical approach but which leads to comparable results in combination with some practical benefits. The most important one is that no geometry-dependent volume mesh is needed. The commercial LBM software package *PowerFLOW* was used by the present author (for details of the underlying physics see [2]), it provides the possibility of automated grid generation in the fluid domain and only needs a surface mesh of the geometry which is to be optimized.

The LBM is inherently transient which leads to noisy fitness function values of drag, lift and lift balance. Furthermore, it can be assumed that the fitness function landscapes will be multimodal and discontinuous due to abrupt changes in the flow topology when the geometry of the car is modified. For instance, stall may suddenly occur or vanish at certain points or vortices may be generated and disappear respectively. Therefore, deterministic numerical optimization methods like gradient-based methods would fail at globally optimizing the shape of the vehicle. Stochastic optimization methods are hence a reasonable choice, especially evolutionary algorithms (EA) are widely used in the aforementioned optimization of airfoils or turbomachines. Surrogate models can be additionally used to reduce the computational cost of EA, among them artificial neural networks (ANN) are quite popular. This combined approach is described in [3] for example and was also used in this work. The *Shark machine learning library* [4] is an open-source C++ library which provides a number of EA as well as surrogate models like ANN, therefore it was used as a basis to create an own workflow.

### 1.2 Geometrical parameterization of passenger cars

One reason for the rare use of numerical optimization methods in the automotive domain until now might be the suitable parameterization of a passenger vehicle. While airfoils or blades of turbomachines can adequately be described by arcs and Bezier curves, the parameterization of a car is rather vague. However, the parameterization is crucial for good optimization results and shall cope with several requirements.

On the one hand it is good to have as few parameters as possible to keep the dimensionality of the problem low and thus the amount of computational effort, because the more dimensions exist the more simulations are needed to find a good overall solution. On the other hand it

is the power of numerical optimization methods to find new and perhaps unexpected shapes. The geometry therefore should have maximized flexibility for the result to be as unaffected as possible by the user, but that tends to result in a lot of parameters. Moreover, the parameters should not influence each other so that the geometry can still be created when one parameter is set to its minimum and another one to its maximum for example. Otherwise dependent constraints would be needed which can be very complicated and again bias the outcome of the optimization. Certainly, the most important requirement is that the parameters have as much influence as possible on the flow topology, leading to a maximized influence on the fitness functions.

There are generally two possibilities of parameterizing a car, the overall and the relative approach. The overall approach means to create the whole geometry parameterized in any computer aided design (CAD) software. This is extremely complicated due to several reasons. First of all, an entire car is much more geometrically complex than an airfoil for example. It is usually built up from a multitude of different parts which all have to fit together. For instance, if you are changing the shape of the back door, you will have to change the shape of the back window as well but usually separately. Moreover, many free-form surfaces are typically included in the geometry model of a real car which cannot be parameterized at all. Parameters with the most influence on the flow topology would be such like the angle of the windshield or the back window, slant angles at the rear, the position of the greenhouse and so on. All of these are usually not directly available in a CAD model in opposition to the requirement mentioned above. For an efficient optimization, the surface mesh finally has to be created anew automatically every time the geometry is changed, this may lead to additional problems.

The relative approach means to build the geometry once and to create a surface mesh manually. Afterwards, certain deformations can be applied on the mesh. These deformations can be defined so that they are directly related to the aforementioned parameters with the most influence. One shortcoming of this approach is the necessity to define new deformations for every single design proposal, because the morphing of the mesh exclusively works with the underlying base mesh. Another one is that the optimized geometry cannot directly be used by anybody else, but the changed shape must be rebuilt with the CAD software manually.

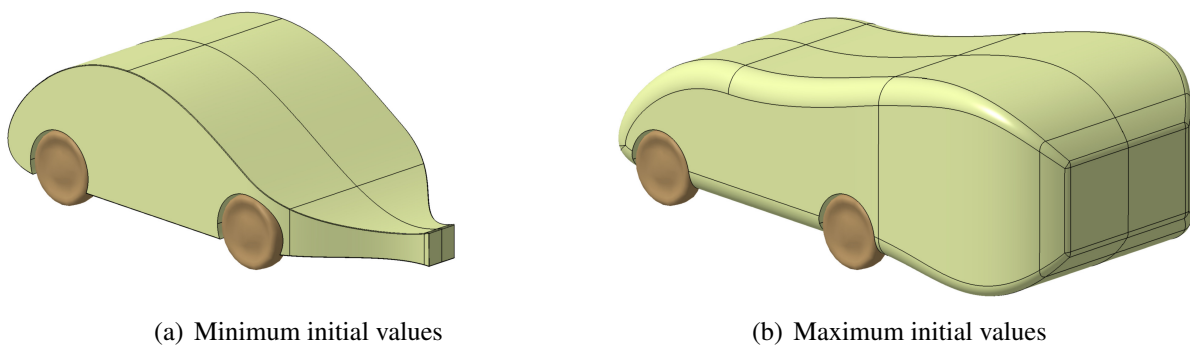


Figure 1: Exemplary variants of the test body for different parameter values

Generally, building a fully parameterized CAD model of a car for global optimization apparently is a very difficult task and in most cases the relative approach with morphing the mesh will be easier. Nevertheless, it was possible to create the simplified vehicle test body of the present work with *CATIA V5* because of its uncomplicated shape. It has eleven adjustable geometry

parameters, mainly concerning its afterbody. Length, width, and height of the rear end can be modified as well as its slant angles, the radii of its edges, and the vertical distance between its lower edge and the underbody. Additionally, the radius of the longitudinal edges can also be adjusted. All parameters are initialized between 0 and 1 for the optimizer-internal calculation, the scaling to the real values is applied when the geometry is created. Fig. 1 shows the minimum and the maximum initialization of the test body. Most of the variables may decrease below 0 and increase above 1 respectively during the optimization to be able to search for optima outside of the initialization box. Only values which would probably lead to non-feasible geometries are already discarded due to boundary conditions before the CAD software is opened. Fig. 2 shows the workflow which was used for the automated optimization of the simplified vehicle test body.

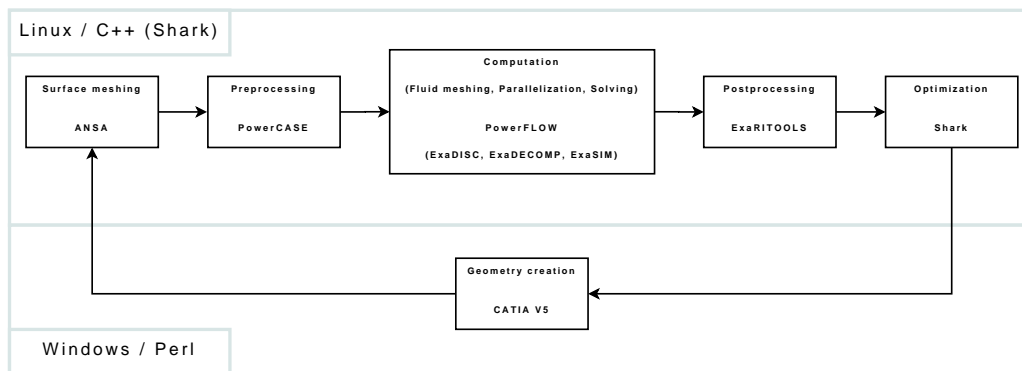


Figure 2: Workflow, C++ (the Shark library) was used for scripting with Linux, Perl was used with Windows

## 2 EVOLUTIONARY ALGORITHMS

The use of stochastic optimization methods is reasonable when dealing with noisy, multimodal and discontinuous fitness function landscapes, as mentioned above. Besides Monte Carlo methods like simulated annealing, evolutionary algorithms are the most widespread form of stochastic optimization. Based on the same natural principles, genetic algorithms (GA) and evolution strategies (ES) are the two most important kinds of EA, being developed independently from each other mainly in the USA (GA) and Germany (ES) about 40 years ago [5]. They are mimicking the process of biological evolution by means of reproduction, mutation and selection. It holds for both GA and ES that a so-called population of members - vectors of the input space together with the according output value(s), called fitness - is proceeding from one generation to another. In between, GA are emphasizing the process of reproduction, their functionality requires a coding of the input values into bitstrings. This is analogous to the human DNA. Two or more parents are selected, the parental bitstrings are then cut at a certain number of points and mixed together by crossover of the strings. This produces either two or only one offspring, if one of both is chosen at random and the other one is discarded. Then mutation is applied by flipping a certain number of bits with a given probability. Reproduction and mutation are repeated until a number of  $\lambda$  offspring has been produced. Depending on the strategy,  $\mu$  members of the new generation are selected either only from the  $\lambda$  offspring, called  $(\mu, \lambda)$ -selection, or from the whole population of parents and offspring, called  $(\mu + \lambda)$ -selection. In GA selection usually is done probabilistically, for example by assigning the individuals sectors with a size matching their fitness on a virtual roulette wheel. After the members of the new

generation are selected, reproduction starts again.

Contrary to GA, ES are real-valued optimization techniques by definition. The main operator is mutation, creating one or more offspring according to a normal distribution centered at the position of the parent individual. Then a given amount of offspring is selected deterministically according to their fitness and a new parent is created usually by intermediate recombination of the offspring. This recombination may also be weighted somehow according to the fitness of the offspring which are combined. A main feature of ES is the self-adaption of the normal distributions responsible for the mutation. In the original ES, every individual possesses an own normal distribution-defining standard deviation as strategy parameter which is mutated, recombined and selected simultaneously with the parameter values. This is very important for the ES to learn something about the fitness function landscape and to adapt the step size of the mutations. There exists a so-called evolution window [5] inside of which the optimization makes the best progress. If the step size is too small premature convergence may occur, that means the strategy might get trapped in local optima. Is it too big then random search behaviour occurs and there is no benefit from using an ES.

## 2.1 The covariance matrix adaptation evolution strategy (CMA-ES)

The original concept of ES with only the single standard deviation of a normal distribution as an own strategy parameter for each individual has some drawbacks. That is why the single standard deviation was soon replaced by more sophisticated probability distributions. Fig. 3 shows the possibility of arbitrarily adapting the normal distributions in the search space when a sufficient amount of parameters is used.

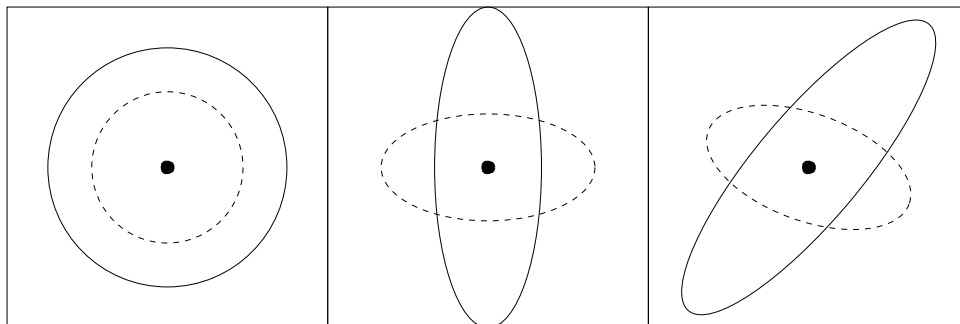


Figure 3: Lines of equal probability densities for one (left, circles),  $n$  (middle, axis-parallel ellipsoids) and  $\frac{(n^2+n)}{2}$  (right, arbitrarily oriented ellipsoids) free parameters, from [6]

The covariance matrix adaptation evolution strategy (CMA-ES) [6][7] goes even further. During the optimization process the shape of the probability distributions for mutation is stored in a covariance matrix which can be geometrically displayed as a (hyper-) ellipsoid of constant probability density. The update of the covariance matrix is completely derandomized which means that its values are not entrained into the process of mutation, recombination and selection. Instead, the so-called evolution path of the evolution steps taken up to the recent generation is used for the update of the covariance matrix, facilitating the CMA-ES to adapt to the fitness function landscape via several generations. Additionally, the global step size is decoupled from the mutation strength and weighted intermediate recombination is applied to the selected offsprings to create a new starting point for the next generation.

With  $\mathbf{x}$  as a parameter vector in the search space,  $\mathbf{m}$  as the starting point for the new genera-

tion obtained by weighted intermediate recombination of the former offspring,  $g$  numbering the generations,  $\sigma$  as the global step size,  $\mathcal{N}(0, \mathbf{C})$  as a multivariate normal distribution with zero mean and covariance matrix  $\mathbf{C}$  and  $\lambda$  as the population size the basic equation for sampling new search points reads:

$$\mathbf{x}_k^{(g+1)} \sim \mathbf{m}^{(g)} + \sigma^{(g)} \mathcal{N}(0, \mathbf{C}^{(g)}) \quad \text{for } k = 1, \dots, \lambda \quad (1)$$

For getting  $\mathbf{m}^{(g)}$ , the best  $\mu$  individuals of the current generation  $g$  are used, that means the CMA-ES is a non-elitist  $(\mu, \lambda)$ -ES. The CMA-ES also preserves all important invariance properties. Apart from the initialization, translation, rotation and reflection of the object parameter space do not have any influence on the performance of the optimization. This is an important feature because the optimization method should not be biased towards any part of the search space which might be the case if it would not be invariant against affine transformations.

The CMA-ES has shown its superiority over other evolutionary algorithms [8] and a quite small population size is sufficient for the method (according to the proposal  $\lambda = 4 + 3 \cdot \ln(n)$ , with  $n$  as the number of dimensions; in this work therefore  $n = \lambda = 11$ ). That is why it is the method of choice for the present author.

## 2.2 The multi-objective CMA-ES

Multi-objective optimization has slightly different goals than single-objective optimization. While the aim of single-objective optimization is of course to get the best possible value for the one objective which is examined, multi-objective optimization often has to deal with trade-offs between different objectives. A classical example would be to simultaneously decrease the weight of a device while increasing its stability. These are two oppositional goals so probably one has to choose which compromise of the fitness function values is the favourite one. Different ways are possible to compute such results. One way is to transfer the multi-objective problem into a single-objective one by using the method of weighted sums or the Tchebycheff method. This leads to the problem that the user has to decide before the optimization how important each objective is. Another method is the so-called Pareto approach, where each vector in the parameter space is assigned more than one fitness function value depending on the number of objectives. To decide whether an individual is better than another the concept of Pareto dominance is used. An individual of the population is Pareto dominant if all of its fitness function values are at least as good as the ones of all the other individuals and if at least one fitness function value is strictly better than the corresponding value of any other individual when compared pairwise. This might include different fitness functions for different individuals.

The concept of Pareto dominance yields the advantage of being able to choose the favourite solution with the desired compromise between the objectives from a whole set after the optimization. The multi-objective variant of the covariance matrix adaptation evolution strategy (MO-CMA-ES [9]) uses this method for its algorithm. Because all EA are dealing with populations and therefore a number of different design variants they are generally very well suited for Pareto optimization. The MO-CMA-ES works different than the CMA-ES because the single-objective variant starts from only a single point at each generation and the goal of the MO-CMA-ES is to create a diverse set of solutions. Therefore, the MO-CMA-ES works as an elitist  $(\mu+\lambda)$ -ES but with an underlying  $(1+1)$ -scheme. That means that every individual of the population produces exactly one offspring when  $\mu$  equals  $\lambda$  as used by the present author. Then all individuals are ranked and the best  $\mu$  out of the whole population of  $\mu+\lambda$  individuals are selected. The ranking is based on the Pareto approach as described above. First all dominant

individuals are assigned rank 1, then all individuals dominating the remaining population are assigned rank 2 and so on. To have a sorting criterion for individuals which share the same rank of dominance, the so-called hypervolume measure is used. This measure can be interpreted as the size of dominated space, the individuals contributing the least amount to the hypervolume are identified as the worst ones. This should maximize the diversity of the pareto front.

Because of the underlying (1+1)-scheme the cumulative step size as in the CMA-ES cannot be applied. Nevertheless, better overall performance than with any other multi-objective optimization method (like the genetical algorithm NSGA-II) is observed [9]. Therefore the MO-CMA-ES was chosen for the multi-objective optimization of the vehicle test body.

### 3 ARTIFICIAL NEURAL NETWORKS AS A SURROGATE MODEL

To reduce the computational cost of EA so-called surrogate or metamodels can be used. Their purpose generally is to distinguish good new individuals from bad ones so that only the good ones are really exactly evaluated with a CFD simulation for example. The task of a surrogate model therefore is to approximate the fitness landscape and to do any kind of inter- or extrapolation.

Among quite a few different surrogate modeling techniques like response surface modeling or Kriging, artificial neural networks are especially capable of high-dimensional interpolation [10] which means that they are well-suited for the task of this work. Generally, ANN consist of several layers of so-called neurons, highly interconnected among themselves and assigned certain activation functions and connection weights. A lot of different kinds of ANN exist, a common variant is the multilayer perceptron. It is widely used for metamodeling but another variant of ANN is even better suited for the kind of task presented here.

#### 3.1 Radial basis function networks

Radial basis function networks (RBFN) are a special kind of neural networks with three layers, namely an input, a hidden and an output layer. RBFN are fully connected and feedforward [10]. Fig. 4 shows an RBFN with a single output unit, mapping an input vector  $\mathbf{x}^{(t)}$  of dimensionality  $M$  nonlinearly to the  $N$  hidden neurons. The hidden neurons are then mapped linearly to the single output. No weights are assigned to the connections between the input and the hidden neurons but to each link from a hidden neuron to the output. Additionally, a scalar bias value might be added to the output, this possibility is not included in the figure. RBFN are especially well-suited for hypersurface approximation in a high-dimensional space what makes them predestinated as a surrogate model for EA and therefore also for the CMA-ES.

The activation functions of an RBFN assigned with the hidden neurons are radial basis functions, for example gaussian functions. Radial basis functions are functions depending on the Euclidean distance between the input neurons and the center of the hidden neuron. When using gaussian functions with variance  $v$ , the output value of the network for a dataset  $t$  is calculated as follows:

$$\zeta^{(t)} = h_0^{(t)} + \sum_{j=1}^N \Psi_j \cdot \exp \left[ -\frac{1}{2} \sum_{i=1}^M \frac{\left( x_i^{(t)} - m_j \right)^2}{v_j} \right]. \quad (2)$$

A reasonable choice for the number of hidden neurons is to set them equal to the number of training patterns [3]. This has to do with the possibility of inverting the matrix  $H$  containing the coefficients  $h_n^{(t)}$  of the hidden neurons. This is always possible when  $H$  is non-singular and

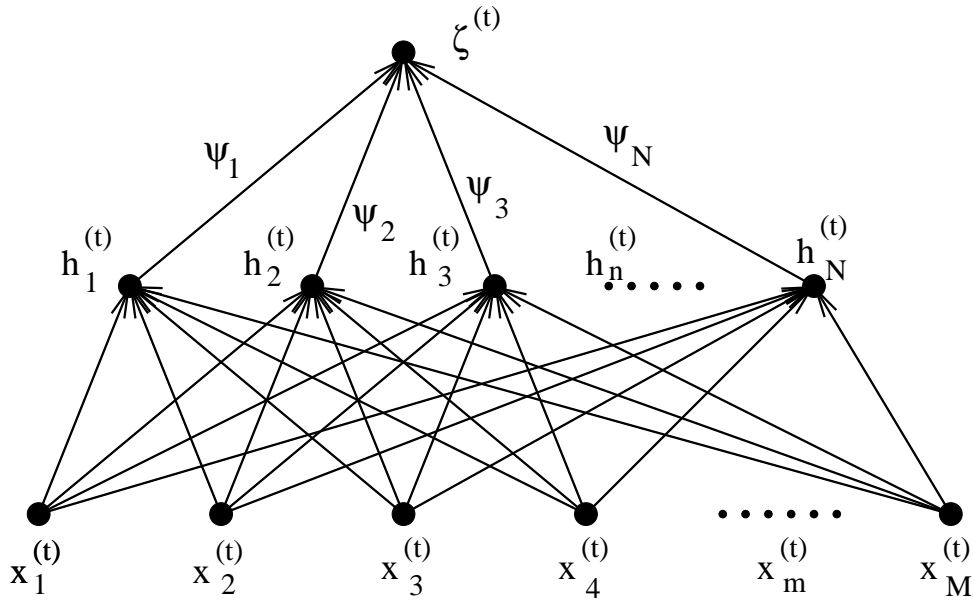


Figure 4: A radial basis function network without bias, from [11]

this is the case when gaussian functions are used (according to Michelli's theorem). An RBFN has the centers of the hidden neurons, the variances of their gaussian functions, the weights of the connections to the output and, if existent, the bias added to the output neuron as parameters. When the network is trained a mean squared error for the deviation between training patterns and the prediction of the RBFN can be used for optimization. Then the parameters can be optimized again by means of the CMA-ES to minimize the mean squared error.

### 3.2 The (MO-)CMA-ES with RBFN

To reduce the number of expensive exact CFD evaluations both the CMA-ES and the MO-CMA-ES are enhanced with an RBFN to pre-evaluate the individuals of the new generation, the concept mainly follows [3]. First a small number of generations is entirely simulated and all the individuals are stored in a database. Then local RBFN are used for every successive generation to estimate the fitness values of the individuals and only the most promising ones are evaluated via CFD and used to enlarge the database. Local RBFN mean that not the whole database is used to build the network but only a flexible, limited amount of already simulated individuals which are closest (regarding the Euclidean distance) to the new one which is to be approximated. The algorithm reads as follows (numbers according to the test case):

- Step 1: Evaluate 4 (CMA-ES) / 2 (MO-CMA-ES) generations exactly
- Step 2: For every single individual of each successive generation:
  - Step 2a: Search for the 10 nearest neighbors of the new individual in the parameter space and calculate the average distance  
Compare the distance of the next nearest neighbor to the average distance; if it is below 1.5 times the average distance incorporate the next nearest neighbor into the training set, update the average distance accordingly and repeat step 2a until the training set consists of a maximum of 20 members; if the distance is 1.5 times the average distance or above go to step 2b



- Step 2b: Create an RBFN with as many hidden neurons as individuals from the training set and optimize the centers, variances, weights and the bias with the CMA-ES to minimize the mean squared error; evaluate the network
- Step 3:
  - CMA-ES: Identify the 2 best out of the 11 offspring, simulate them via CFD and replace their estimated fitness values with the exact ones
  - MO-CMA-ES: Identify the best 4 non-dominated offspring according to the hypervolume measure; if none are non-dominated go to step 4; simulate the chosen individuals via CFD and replace their estimated fitness values with the exact ones
- Step 4:
  - CMA-ES: Create a new generation from the merged values of exact and estimated individuals, go to step 2
  - MO-CMA-ES: Create a new generation by identifying the best 20 members out of all exact individuals (maximum 24) according to the hypervolume measure, go to step 2

## 4 RESULTS

### 4.1 Single-objective optimization

The goal of the single-objective optimization was to minimize the drag. The drag force is given by the product of the drag coefficient and the effective frontal area. Often only the drag coefficient is considered, but on the one hand the drag force is the actual figure which determines the fuel consumption of a car and on the other hand it is also reasonable to use this fitness function for optimizing the test body, because it reduces the danger of futile afterbody configurations having a bigger cross-section than the front which would have been possible with the utilized parameterization.

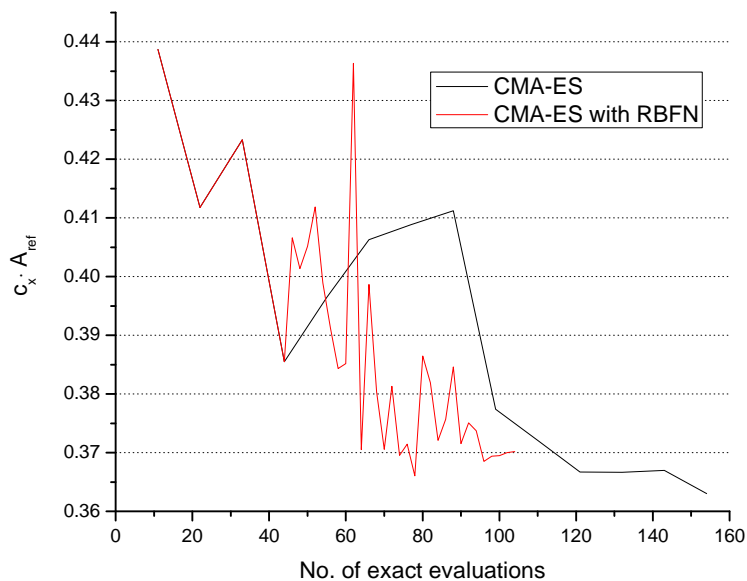


Figure 5: Results of the CMA-ES with and without additional RBFN

Fig. 5 shows that the optimization was quite successful. Within 14 generations the fitness was improved by the CMA-ES by 17.2% compared to the initial best solution. Compared to the dimensionality of the problem and the usual amount of function evaluations used with EA this is a very good result. After a learning phase of a few generations to adapt the covariance matrix the optimization passes a local minimum to find an even better one afterwards. This is a hint that using a non-elitist strategy was a good choice to prevent premature convergence in any local optimum because with an elitist strategy the best individual from generation four would have been kept and perhaps the local optimum would not have been left again. Nevertheless, the CMA-ES has not reached global convergence after 14 generations. The individuals are still quite different, especially less important parameters like the radii of the rear edges are very diverse. However, more important parameters like the radius of the longitudinal edges, the length, and the height of the rear are yet converging. Fig. 6 shows the optimum solution found within 14 generations, it obviously has a shape similar to an airfoil which was expected for the objective of drag minimization.

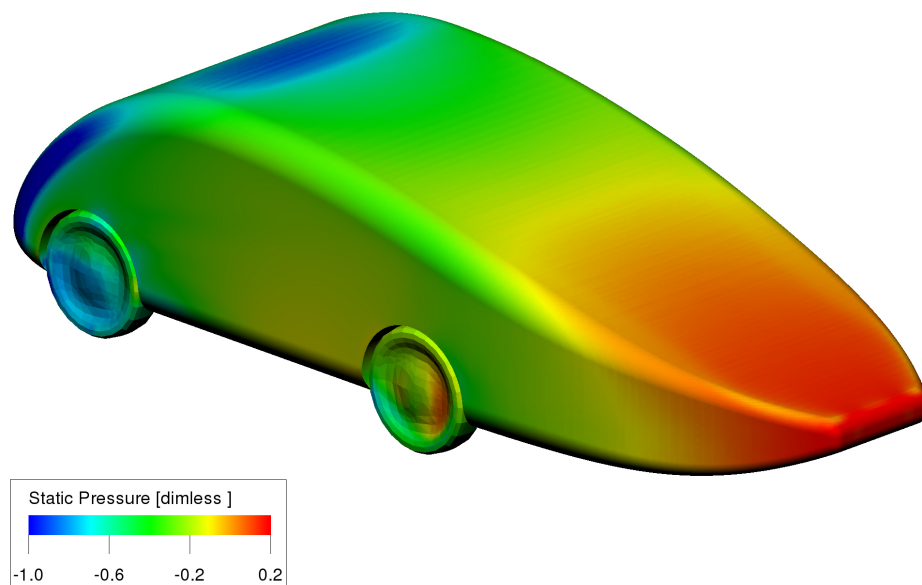


Figure 6: Static pressure distribution of the optimum solution of the CMA-ES without RBFN

Enhancing the CMA-ES with RBFN seems to be a helpful method to reduce the number of CFD simulations. Of course the optimization is fluctuating to a greater extent because it lacks exact information about the fitness function landscape compared to the CMA-ES. Also more generations are needed but the best result found after 78 CFD simulations yields an improvement of about 16.6% compared to the initial best solution. This is only a slightly worse result compared to the CMA-ES at about half of the computing cost.

## 4.2 Multi-objective optimization

The aim of the multi-objective optimization was to minimize drag, lift, and optimize the lift balance at the same time. Again not the drag coefficient but the drag force was used as fitness function. The lift balance was determined from the pitch coefficient because when it is zero, the lift coefficients at the front and rear axle are equal. Optimization of the lift balance therefore

means minimization of the absolute value of the pitch coefficient.

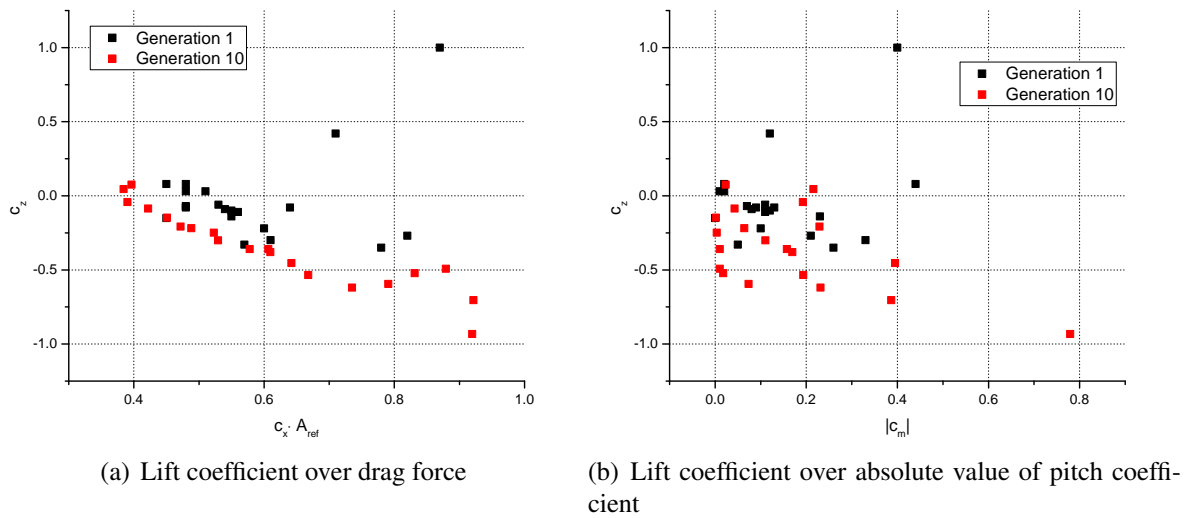


Figure 7: Results of the MO-CMA-ES after 10 generations

It becomes obvious from Fig. 7 that the MO-CMA-ES was able to create a diverse Pareto front. That means that the individuals in the set of solutions differ quite remarkably from each other. Apparently a trade-off especially between drag and lift exists, meaning that decreasing the lift increases the drag. The trade-off between lift balance and the other objectives is less apparent, there also exist individuals each with a good combination. Fig. 7(a) gives a hint that the parameterization of the test body favours variants with low lift although the CMA-ES is yet able to find good variants for low drag. Of course the MO-CMA-ES does not reach this value with the same computational effort but that is just not the aim of the multi-objective optimization. Its task is to provide a diverse set of solutions at the Pareto front and this is done well.

The multi-objective optimization enhanced with the RBFN is still in progress. The gain in the number of CFD simulations might be even bigger than with the single-objective optimization because if the RBFN does not predict any new pareto-dominant individual, no exact evaluation is carried out at all. This difference is caused by the elitist character of the MO-CMA-ES which will preserve exactly simulated individuals at the pareto front. For the CMA-ES at least one or two individuals must always be evaluated via CFD at each generation because all parents are discarded and no exact information would be available to check if the approximation is giving the correct trend and if the optimization is converging into the right direction.

## 5 CONCLUSIONS

The present work shows that evolutionary optimization is feasible for passenger vehicles if a sufficient number of simulations is available and if the problem of a sufficient parameterization of the vehicle can be solved.

The CMA-ES needs quite a few generations to clearly converge to an optimum but nevertheless any good individual found earlier might already be a feasible solution for a real-world problem. Either to be able to start an additional manual optimization from it or because the gain from the optimization is already sufficient enough.

Radial basis function networks are capable of clearly reducing the number of exact function evaluations needed for optimization although they are of course causing more fluctuations during the optimization run because of the lack of exact information about the fitness landscape.

The MO-CMA-ES is able to create a diverse set of solutions along the pareto front to choose from. Nevertheless, the use for real cars is at least questionable at present because mostly the drag draws much more attention in the development phase than the lift and the lift balance, especially with upcoming CO<sub>2</sub> taxation. Therefore it might be useful to save resources for optimizing only the drag with the CMA-ES and setting parameter boundaries in advance so that lift and lift balance may hopefully not violate any critical thresholds.

## REFERENCES

- [1] S. Chen and G.D. Doolen. Lattice Boltzmann method for fluid flows. *Annual Review of Fluid Mechanics*, 30(1):329–364, 1998.
- [2] H. Chen, C. Teixeira, and K. Molvig. Digital Physics Approach to Computational Fluid Dynamics: Some Basic Theoretical Features. *International Journal of Modern Physics C*, 8(1):675–684, 1997.
- [3] K. C. Giannakoglou. Design of optimal aerodynamic shapes using stochastic optimization methods and computational intelligence. *Progress in Aerospace Sciences*, 38(1):43–76, January 2002.
- [4] C. Igel, V. Heidrich-Meisner, and T. Glasmachers. Shark. *Journal of Machine Learning Research*, 9:993–996, June 2008.
- [5] H.-G. Beyer and H.-P. Schwefel. Evolution strategies - A comprehensive introduction. *Natural Computing: an international journal*, 1(1):3–52, May 2002.
- [6] N. Hansen and A. Ostermeier. Completely derandomized self-adaptation in evolution strategies. *Evolutionary Computation*, 9(2):159–195, 2001.
- [7] N. Hansen, S.D. Müller, and P. Koumoutsakos. Reducing the time complexity of the derandomized evolution strategy with covariance matrix adaptation (CMA-ES). *Evolutionary Computation*, 11(1):1–18, 2003.
- [8] N. Hansen and S. Kern. Evaluating the CMA evolution strategy on multimodal test functions. In X. Yao et al., editors, *Parallel Problem Solving from Nature PPSN VIII*, volume 3242 of *LNCS*, pages 282–291. Springer, 2004.
- [9] C. Igel, N. Hansen, and S. Roth. Covariance matrix adaptation for multi-objective optimization. *Evolutionary Computation*, 15(1):1–28, 2007.
- [10] S. Haykin. *Neural Networks: A Comprehensive Foundation (2nd Edition)*. Prentice Hall, 1998.
- [11] K. C. Giannakoglou. Optimization and inverse design in aeronautics: How to couple genetic algorithms with radial basis function networks. EURODAY5 2000, Innovative Tools for Scientific Computation in Aeronautical Engineering, Paris, March 2001.

## AERODYNAMIC SIMULATION OF A CAR OVERTAKING A LORRY USING EMBEDDED MESH TECHNOLOGY

Sven Perzon<sup>\*</sup>, Johan Stangvik<sup>\*</sup>, Per Österdahl<sup>\*</sup>, and Lasse Christoffersen<sup>†</sup>

<sup>\*</sup>Go Virtual Nordic AB  
Askims Verkstadsväg 5A, 436 34 Askim, Sweden  
e-mails: sven.perzon@govirtual.se, johan.stangvik@govirtual.se,  
per.osterdahl@govirtual.se

<sup>†</sup>Applied Mechanics  
Chalmers University of Technology, 412 96 Göteborg, Sweden  
e-mails: laschr@chalmers.se

**Keywords:** Vehicle, Aerodynamics, Embedded grid, Overtaking, Sudden Wind Gust

**Abstract.** *This work describes a simulation technique for the analysis of the unsteady aerodynamics behavior that occurs when a light vehicle, Volvo S60, overtakes a larger vehicle, Volvo FH truck and trailer combination, at a strong side wind. The simulation technique is based on embedded grids which make it possible to put a complete mesh of a car and its near surrounding air into a background mesh of the truck and a larger surrounding that encompass the entire mesh of the car. The car mesh is then translated inside the larger background mesh along a path and relative velocity that describes the overtaking maneuver. Forces and moments are analyzed as the overtaking takes place and the lighter and smaller car becomes more and more exposed to the side wind.*

## 1 INTRODUCTION

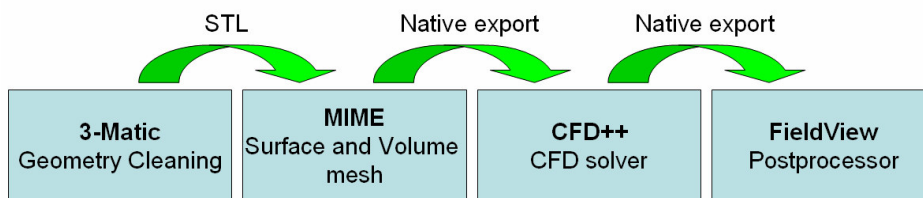
Gusts of wind has a strong influence the total vehicle aerodynamic behavior, Cooper and Watkins [1] and Watkins and Cooper [2]. Unsteady aerodynamic forces and moments acting on a vehicle are very hard to measure or estimate in a wind tunnel environment [3] and alternative methods of investigation would be desirable in order to close the gap between the wind-tunnel and track-test data.

Simulation of unsteady aerodynamics and behavior of a vehicles when exposed to a sudden wind gust has been looked into before. Yibin-He et. al. looked into using sliding mesh and an unsteady RANS for simulating a small vehicle overtaking a larger vehicle. The conclusion was that it was too compute intensive to do the real time accurate simulation and the proposal was to divide the unsteady path for a set of steady state simulations along the unsteady path and use this as an approximation. It is however likely to be the sudden change of the flow causing the boundary layers to temporarily attach much further than they would normally do in a steady state flow that is one of the major reasons for the large transients in the forces encountered at these conditions. Tsubokura et. al. used LES to analyze sudden wind gusts and modeled the gust as a bounding box inlet convective condition. This way of handling the unsteady boundary condition is easy to reproduce even though it is an idealized case. Using LES will improve simulation of turbulence in the wake region. LES is however known not to work well in the near wall region unless the mesh resolution is fine enough. Unfortunately this resolution is not plausible for most industrial simulations. Since the boundary layers are thought of as being crucial for capturing the transient behavior of this type of flow. Basara et. al. presented some tests and simulations using the  $v^2$ -f model. Again this was a quasi steady state model with a set of steady state experimental tests and simulations that were compared which is not the true road case. This work is simply a start with a demonstration of a computational technique using embedded grids that could be used for these types of simulations. The benefit is that the real on road situation can be simulated and if care is taken when doing meshes in the regular aerodynamic development process, these meshes can be reused in this type of simulation.

## 2 NUMERICAL MODEL

### 2.1 CFD Process

The following CFD process has been used for the work outlined below:



### 2.2 Meshes

The final mesh is divided in 2 parts, one for the car and its surrounding air, see Fig. 1, and one for the heavy truck trailer combination and its surrounding air. As can be seen in Fig. 2, the truck mesh is a much larger volume than the car mesh and that is because, the truck mesh

will be treated as the background mesh in this simulation.

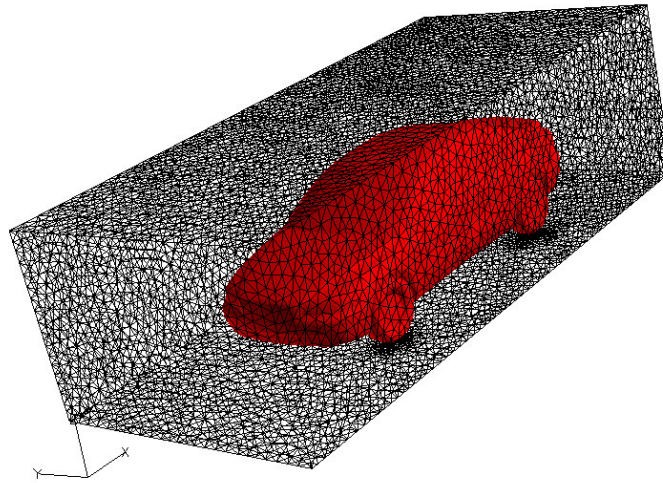


**Figure 1. Car mesh.**

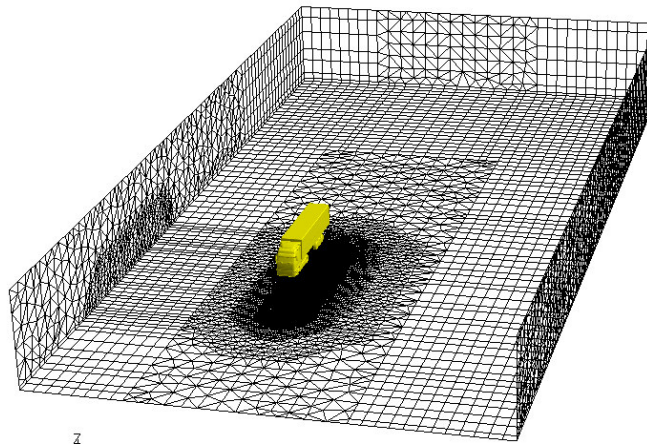


**Figure 2. Truck mesh.**

### **2.3 Embedded grid methodology**

The embedded grid technology is based on that the solver automatically takes care of two meshes and joins them together. In practice, the outer boundary of the embedded mesh, se Fig. 3, is used as a cutter of cells so that all cells in the background mesh that is completely inside the outer boundary of the embedded grid will be deleted.

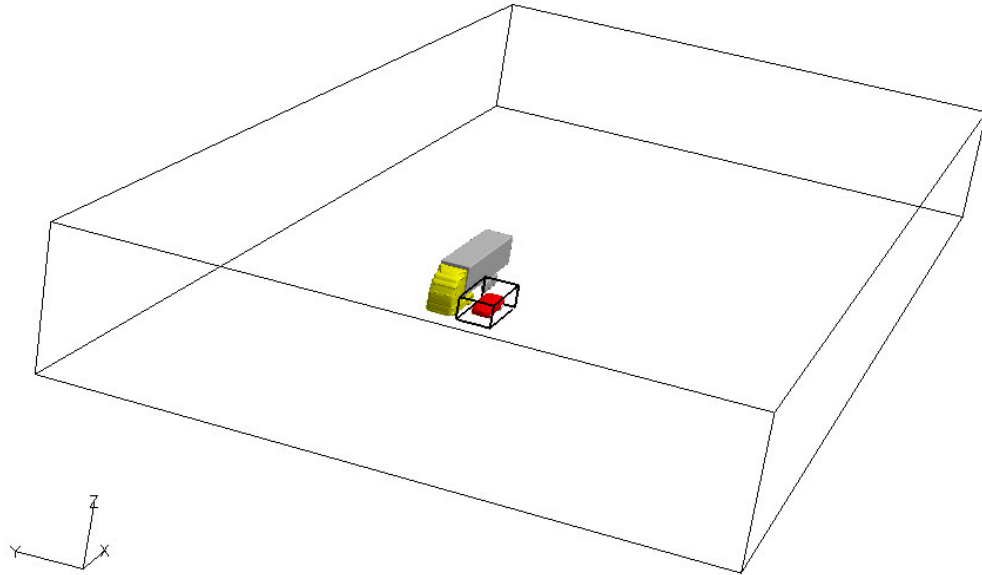


**Figure 3. Overview of the embedded mesh inside the background mesh.**

All the cells that is partially inside and partially outside this outer boundary stays in the overall grid and will be regarded as part of the overlap region. All the cells in the embedded grid that occupies any volume that is also occupied of the cells in the overlap region of the background mesh will also be part of the overlap region. The fluxes for the cells in the overlap region are then calculated based on that regardless from which mesh you are evaluating properties for a specified coordinate in the overlap region, that property will be the same. For this case, the smaller car mesh would be the embedded grid and the larger truck mesh would be the background mesh, see Fig. 3-5.

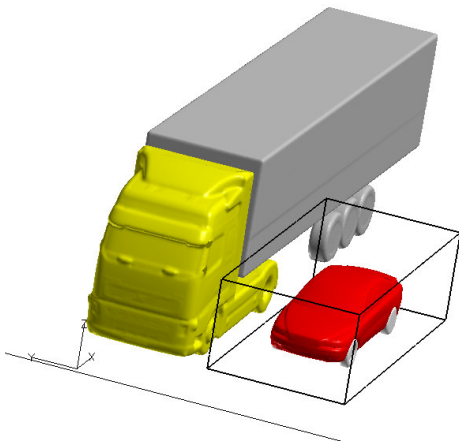


**Figure 4. Bounding box of embedded grid.**

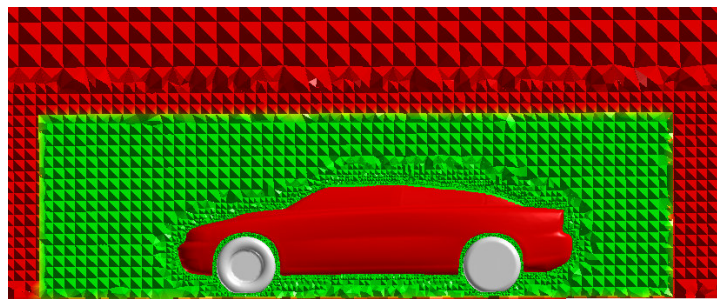


**Figure 5. Cut through an embedded grid (green) inside a background grid (red)**

## 2.4 CFD simulation

The CFD simulation was divided in 2 parts, one steady state simulation and one transient simulation. The steady state simulation was used to create an initial condition for the transient CFD simulation.



The setup of the steady state simulation was relatively straight forward with Velocity Inlet conditions imposed to the upstream 2 sides of the domain. And a pressure condition imposed to the 2 downstream sides of the domain, see Fig. 6.

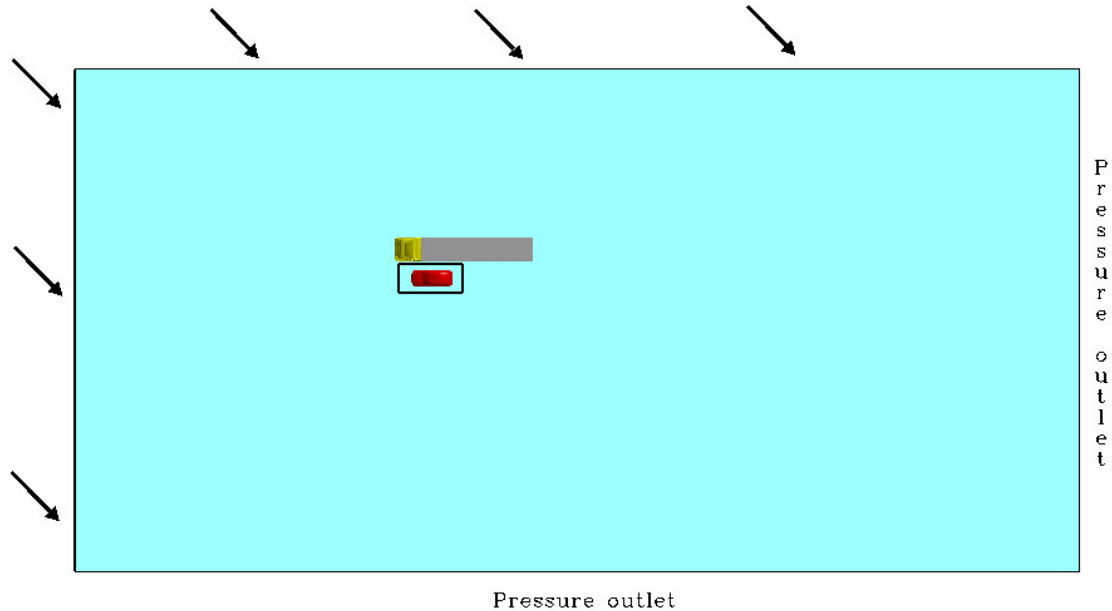


**Figure 6. Boundary condition setup for the simulation note that the black rectangle around the car and everything inside it is moving by 30km/h relative speed towards the left boundary.**

The car mesh was placed into the background mesh at its starting position and the embedded grid setting was imposed to the simulation via the GUI in CFD++. Even in the steady state simulation the velocity of the car mesh was set to the relative speed between the truck and the car, 30 km/h, even though no mesh movement is done in the steady state case. This means that the solver imposes a steady state simulation using multiple frame of references. This technology is quite often used with rotating frames like wheels and fans. In summary the truck speed was set to 90 km/h and in addition, a side wind component was evident and set to 15 m/s. The car relative speed was 30 km/h which then translates to a car speed of 120 km/h.

Having done the simulation for the steady state condition, the only condition to add for the transient simulation was to define the time step and to switch on the mesh movement for the car mesh. The CFD solver automatically strips out unwanted cells from the background mesh as well as connects the embedded region for each time step, see figure 5. The starting position is as shown in Fig. 6. Hence the simulation starts in the wake region and analyses only the sequence when the car becomes fully exposed to the side wind exiting the large truck wake.

The time step chosen was 1e-3 seconds and was selected based on a combination of what was thought of as reasonable from a physical perspective and computational cost. 15 internal iterations were done to make sure; convergence was reached in each time step. The preconditioned perfect gas compressible solver was used in CFD++ together with the Realizable k- $\epsilon$  model, Goldberg et. al. [6].

### 3 RESULTS

The results are a mix of forces and moments and some pictures with data at different time steps. In Fig. 7. the drag force of the car is presented as a function of reference coordinate center located half way between the wheels contact patches.

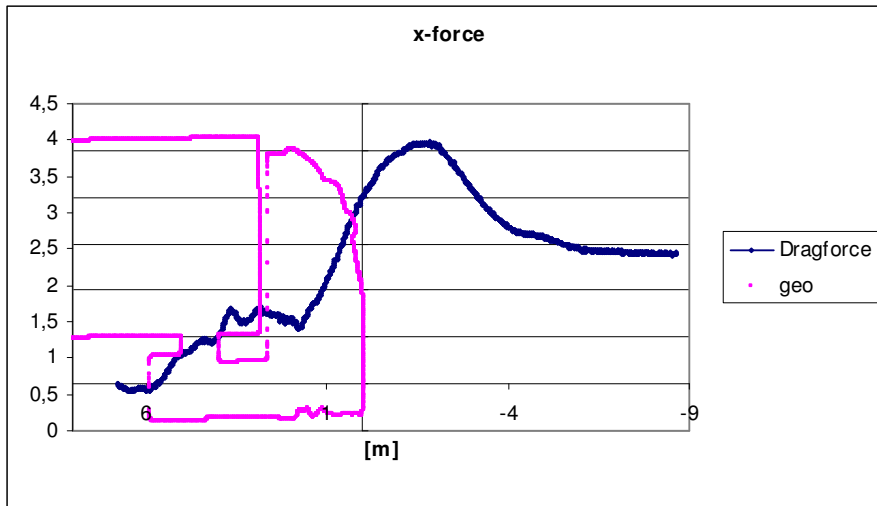


**Figure 7.** Drag force of the car scaled to fit geometry of truck body as a function of the reference point  $x$  coordinate in meters.

As can be seen the drag is very low when the car is inside the truck wake and increases drastically when the car becomes exposed to the strong side wind. It shows a peak when the car centre point is about 2 meters in front of the truck nose which corresponds to about 1.1 seconds of real time. Then drag falls off as the car fulfills the over take and fades out at a bit more than half the top value. Lift force is displayed in Fig. 8 and shows the same behavior, however the peak is located about one meter earlier at  $x = -1$  which corresponds to about 0.97 seconds real time. The side force shown in Fig 9. show a different behavior in the sense that it starts high and goes down as the car becomes exposed to the side wind. It is not shown in the picture, however the scale is from a positive side force, i.e. suction toward the truck in the wake region turning into a stronger negative side force, i.e. being pushed away from the truck when exposed to the side wind. The maximum push is again located in between  $x = -1$  to  $x = -2$ .

Moments are shown in Fig 10-12. Again, the peak occurs more or less at the same point in all graphs. It should be noted that the reference point is moving with the relative speed of the car so when evaluating these moments, this input must be part of the calculation.

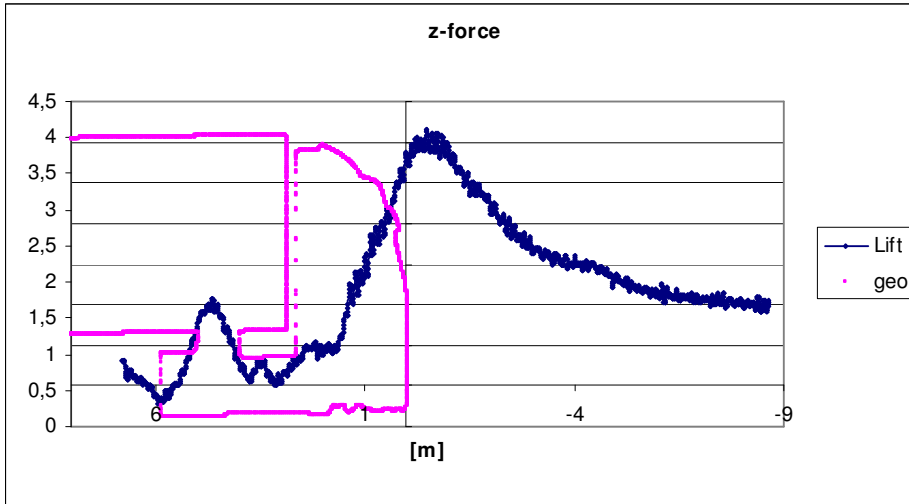


Figure 8. Lift force of the car scaled to fit geometry of the truck body as a function of the x coordinate of the reference point in meters.

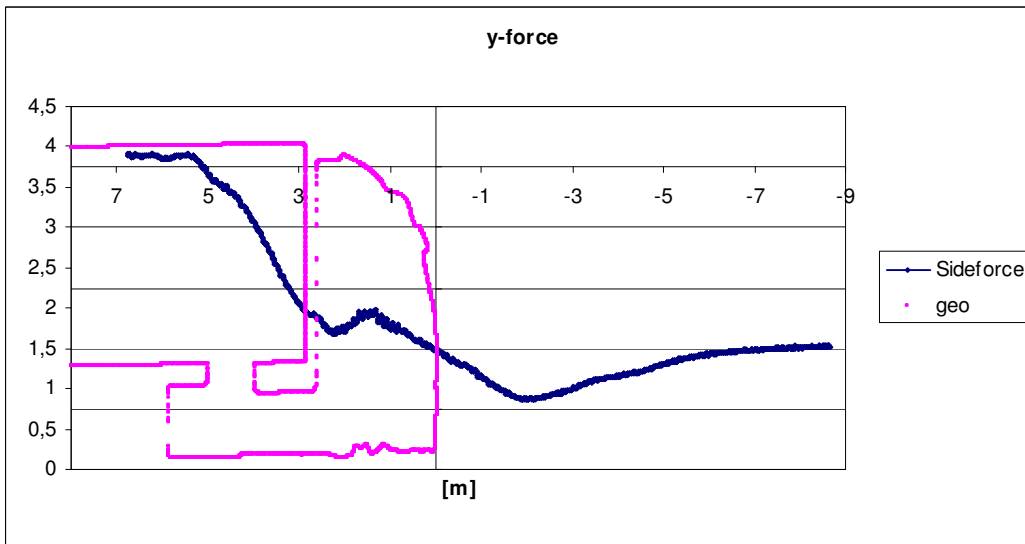


Figure 9. Side force of the car scaled to fit geometry of the truck body as a function of the x coordinate of the reference point in meters.

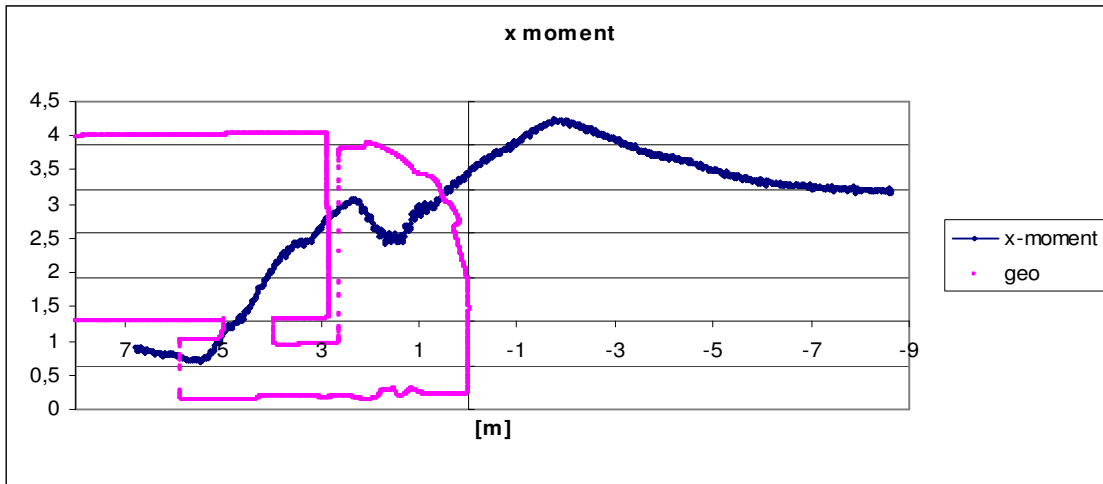


Figure 10. X-axis-moment of the car scaled to fit geometry of the truck body as a function of the x coordinate of the reference point in meters.

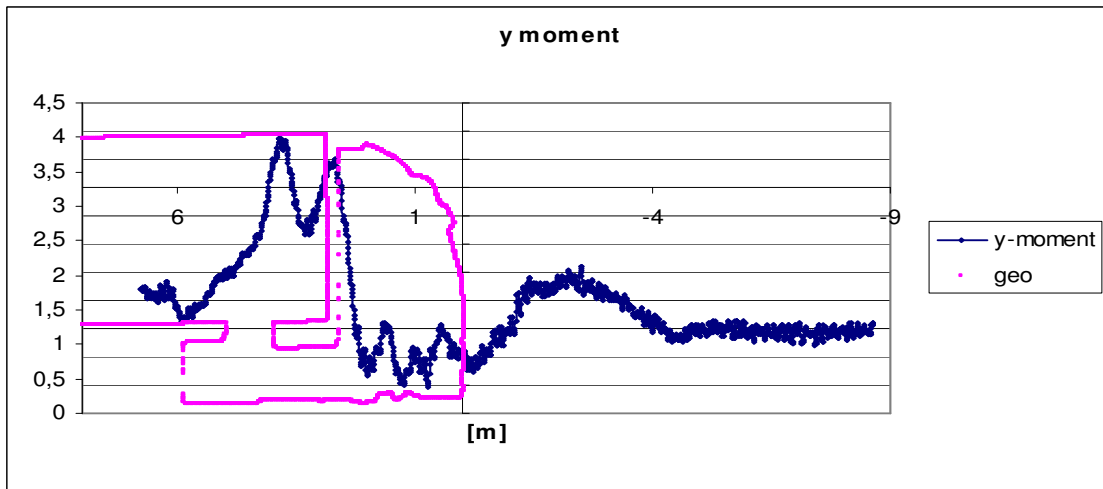


Figure 11. Y-axis-moment of the car scaled to fit geometry of the truck body as a function of the x coordinate of the reference point in meters.

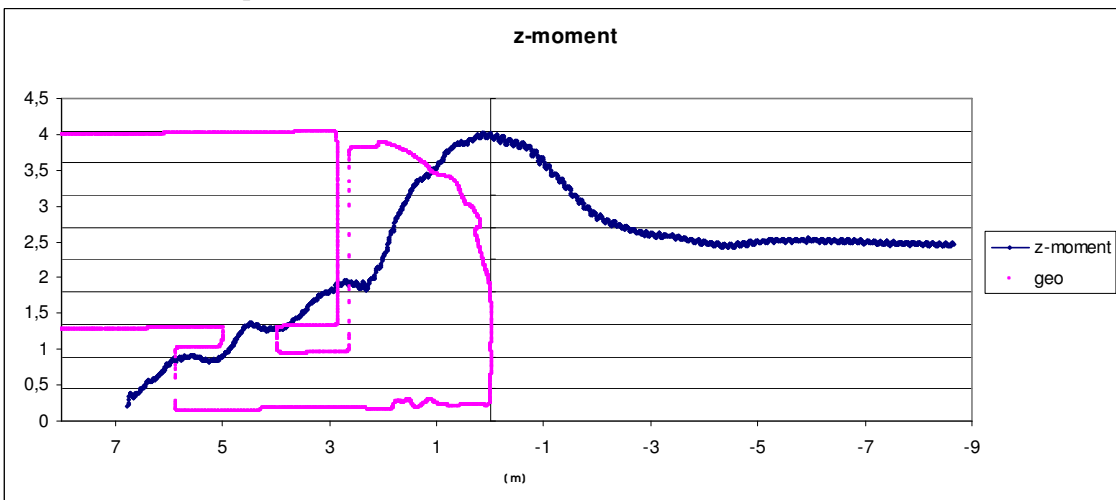
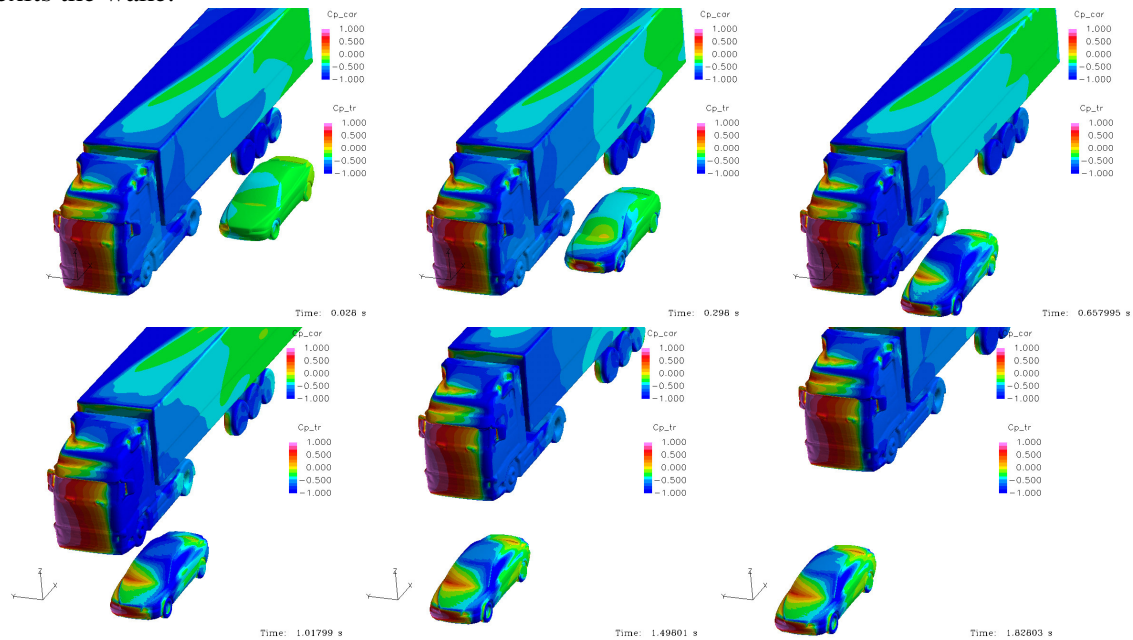


Figure 12. Z-axis-moment of the car scaled to fit geometry of the truck body as a function of the x coordinate of the reference point in meters

In Figure 13,  $C_p$  is shown for a few different time steps. It is clearly shown what a drastic aerodynamic effect the car is imposed to when exiting the wake of the truck. Inside the wake, the car is relatively neutral whereas the variation in pressure distribution is huge as the car exits the wake.



**Figure 13. Geometries colored by pressure coefficient.**

Looking at the areas where drag, lift and side force has its peak value, Fig. 14 shows these two specific times and the pressure distribution of the car somewhat zoomed in.

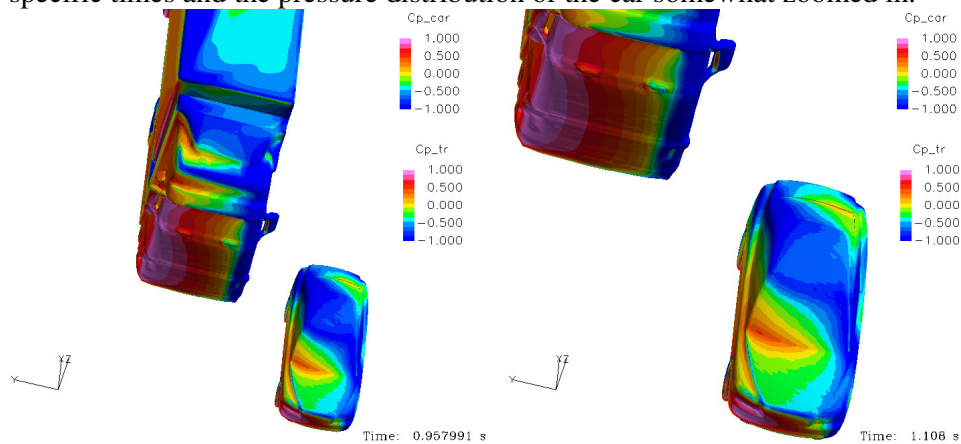


**Figure 14. Pressure distribution on the car at the time steps close to the peak of Lift (left) and Drag (right).**

The reason for the peaks being where they are is likely to be the throttle effect in the converging channel between truck and the car. In the left picture, the blockage will force the flow more in the direction over the C-pillar causing an excessive acceleration over the rear window. This will produce a large lifting area over the rear part of the roof and the rear screen. In the picture to the right, the blockage has eased off somewhat and the same type of acceleration occurs but now more around the tail of the car causing the base pressure to become lower.

## 4 CONCLUSION

A method based on embedded grids has been presented as a way to simulate the aerodynamic effect of a car overtaking a truck. In the current work standard RANS methods were used with reasonable results. It is a fact that this type of flow is extremely hard to test in any kind of controlled environment and any experiment would have poor repeatability. Hence finding a good simulation method may be the only feasible way to investigate this type of flow problem. The situation is a safety concern for all automotive car makers and as has been shown, the forces become much larger in the peak values than what a simple yaw experiment would show.

## 5 FUTURE WORK

The present work was based on RANS methodology with a simple standard realizable k-epsilon turbulence model. The method itself can be extended to using more elaborate RANS models like a full Reynolds Stress Transport model or to run LES models. The embedded grid technology is generic from a model perspective. LES becomes far too numerically intensive for this type of simulation and assuming that boundary layers play an important role for the peak values of integrated properties, a hybrid RANS/LES is likely to be the best model choice if there is enough compute power available. This is on the agenda to test in future work to improve accuracy

## ACKNOWLEDGEMENTS

Acknowledgment is directed to Volvo 3P and Volvo Car Corporation for allowing use of their geometries in the present work.

## REFERENCES

- [1] K. R. Cooper and S. Watkins. The Unsteady Wind Environment of Road Vehicles, Part One: A Review of the On-road Turbulent Wind Environment, SAE Tech Paper 2007-01-1236, 2007
- [2] S. Watkins and K. R. Cooper. The Unsteady Wind Environment of Road Vehicles, Part Two: Effects on Vehicle Development and Simulation of Turbulence. SAE Tech Paper 2007-01-1237, 2007
- [3] R. G. Dominy and A. Ryan. An Improved Wind Tunnel Configuration for the Investigation of Aerodynamic Cross Wind Gust Response”, SAE Tech Paper 1999-01-0808, 1999.
- [4] Yibin-He, Zhengqi-Gu and Zhou Wei, Numerical Simulation Analysis of Side Aerodynamic Force of Car in the Course of Passing Heavy Goods Vehicle (HGV). SAE Tech Paper 2007-01-3460, 2007
- [5] M. Tsubokura et. al. HPC-LES for the Prediction of Unsteady Aerodynamic Forces on a Vehicle in a Gusty Cross-flow Condition. SAE Tech Paper 2008-01-3001.
- [6] U. Goldberg, O. Perroomian, and S. Chakravarthy. A Wall-Distance-Free k-e Model With Enhanced Near-wall Treatment. ASME J. Fluids Engrg., volume 120, pages 457-462, September 1998.

## COMPARISON OF WIND TUNNEL TESTS RESULTS ON THE ATM TRAIN

Daniele Rocchi<sup>†</sup>, Martin Schober<sup>\*</sup>, Federico Cheli<sup>†</sup>, Alexander Orellano<sup>\*</sup> and Gisella Tomasini<sup>†</sup>

<sup>\*</sup> Centre of Competence for aerodynamics and thermodynamics Bombardier  
Am Rathenaupark, 16761 - Hennigsdorf - Germany

e-mail: [Martin.Schober@de.transport.bombardier.com](mailto:Martin.Schober@de.transport.bombardier.com), [Alexander.orellano@de.transport.bombardier.com](mailto:Alexander.orellano@de.transport.bombardier.com)

<sup>†</sup> Mechanical Department – Politecnico di Milano  
Campus Bovisa, Via La Masa 1, 20158 Milano, Italy

e-mails: [Federico.Cheli@polimi.it](mailto:Federico.Cheli@polimi.it), [Daniele.Rocchi@polimi.it](mailto:Daniele.Rocchi@polimi.it), [Gisella.Tomasini@polimi.it](mailto:Gisella.Tomasini@polimi.it)

**Keywords:** Wind tunnel, Cross Wind, Aerodynamic coefficients, Pressure distribution.

**Abstract.** *The paper presents a comparison of the results obtained by experimental campaigns, performed in different wind tunnel plants on the same train model. The comparison will be presented in terms of global forces and pressure distribution on the first vehicle of the train model. Tests have been performed on a flat ground configuration and allow to investigate the effects related to the Reynolds number on the different components of the global aerodynamic force, to the blockage ratio, and to the adoption of open or closed wind tunnel test section. The sharing of the same scaled model and the availability of detailed data regarding the pressure distribution in the different test conditions allow a good insight in the modeling of the train aerodynamics in wind tunnel.*

## 1 INTRODUCTION

One of the not yet answered questions on the assessment of the aerodynamic behavior of trains concerns the reliability of the aerodynamic coefficients measured in wind tunnel with respect to the full scale behavior. Wind tunnel tests are commonly performed in different experimental laboratories with different flow qualities, different performances, different equipments and different techniques using scaled models and scaled representation of the ground scenarios. These differences may insert uncertainties in the definition of the aerodynamic performances of trains and a deeper understanding of the physics of the flow around the vehicle should be reached to assess the importance of each single term on the experimental result. In this paper a comparison of the results obtained by three experimental campaigns, performed in the 2 test sections of the Politecnico di Milano wind tunnel (PMWT) and at the wind tunnel T103 of the Central Aerodynamic Institute TsAGI (TsAGI) on the same train model is provided. The model is a 1:10 power car and it represents a reference train built by Bombardier, called “Aerodynamic Train Model ” (ATM) for comparison purposes [1]. The model shape is similar to an ICE2 train and it shows all the interesting aerodynamic features of high speed trains. The tests have been performed using, not only the same model of the power car but also the same end car. The model allows to measure the global forces using both internal and external force balances and it is also equipped by pressure taps to measure the pressure distribution on the carbody. Tests have been performed on a flat ground configuration trying to reproduce the same boundary condition by means of splitter planes. The different characteristics of the used wind tunnel plants allows to investigate the effects related to the Reynolds number on the different components of the global aerodynamic force, to the blockage ratio, and to the adoption of open or closed wind tunnel test section. The sharing of the same scaled model and the availability of detailed data regarding the pressure distribution in the different test conditions allow a good insight in the modeling of the train aerodynamics in wind tunnel.

## 2 THE ATM TRAIN MODEL

The ATM train model is a 1:10 simplified version of an ICE2 train shape (see Figure 1a), that is used by Bombardier for research and benchmark purposes. It is made by an instrumented locomotive vehicle and by an endcar model with the same nose geometry of the leading car that is used for the boundary condition reproduction. A gap of 5mm is left between the leading car and the end car to grant that they are mechanically disconnected.

The basic dimensions of the wind tunnel model are: length=3.557m, width=0.299m and height=0.385m. The model can be equipped with bogies and with a spoiler under the train head, in the present research the model without bogies and without spoiler is considered. In this version the bogie cavities are closed by covers (Figure 1b). The model has an internal aluminum frame allowing for the connection with the supporting system in the central part.

The model is also instrumented with 91 pressure taps distributed along 8 transversal sections along the train axis (Figure 1c). The position of the instrumented sections is reported in the following table while an example of pressure taps distribution in the section is reported in Figure 1c for section 6:

Section n.	1	2	3	4	5	6	7	8
Distance from the train head [mm]	100	175	250	500	700	1500	2000	2500

Table 1: position of the instrumented sections along the train.



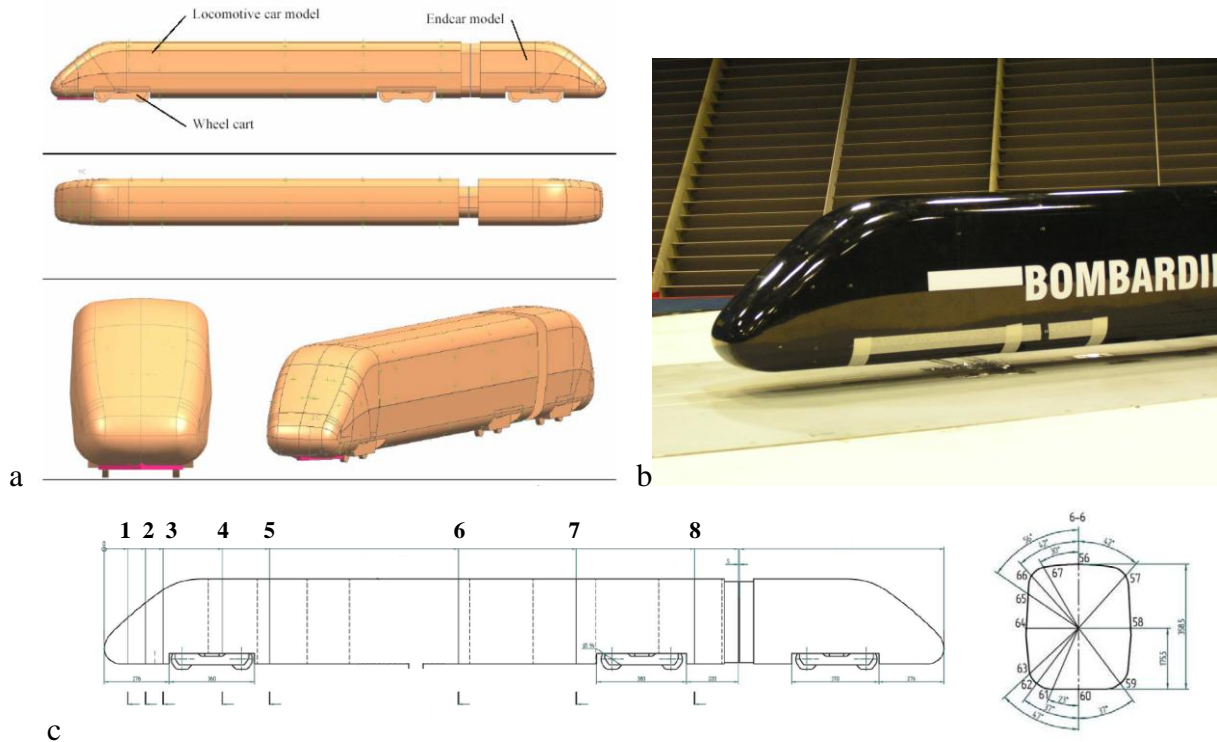


Figure 1: ATM model geometry (a); ATM model without bogies and without spoiler in the PMWT (b); position, along the train axis, of the sections instrumented with pressure taps (c)

### 3 WIND TUNNEL TESTS

The results of three wind tunnel campaigns will be compared in this papers, two of them was performed at the Politecnico di Milano Wind Tunnel (PMWT) and another one at the TsAGI T103 wind tunnel (TsAGI). Wind tunnel tests have been performed on a true flat ground scenario (flat plate without rails). A splitter plate was used in all the considered wind tunnel campaigns in order to grant similar incoming flow conditions on the model.

Aerodynamic forces were measured by external force balances while the pressure distribution was measured through pressure scanners positioned inside the train model.

#### 3.1 TsAGI wind tunnel tests

TsAGI T103 wind tunnel tests were performed in an open test section with a wind speed range between 30 and 70m/s, which corresponds to Re-numbers of  $Re_1 = 0.6 \sim 1.4 \cdot 10^6$ . Tests were performed at different yaw angles between 0 and 60 deg. The blockage ratio varies between 4% and 8% for yaw angles between  $10^\circ$  and  $30^\circ$ .

A sketch of the wind tunnel plant is reported in Figure 2a. The flat ground consists of an elliptical shaped floor which contains a turntable (Figure 2b).

The model is fixed on the turntable which can be automatically rotated during the wind tunnel measurements. Figure 2b shows the whole set up of the experiment including the ATM model and the elliptic splitter plate. An external six-component force balance was used to measure the aerodynamic forces and moments on the leading car. Data averaging was performed over 4s for each angle with a sampling frequency of 100Hz.

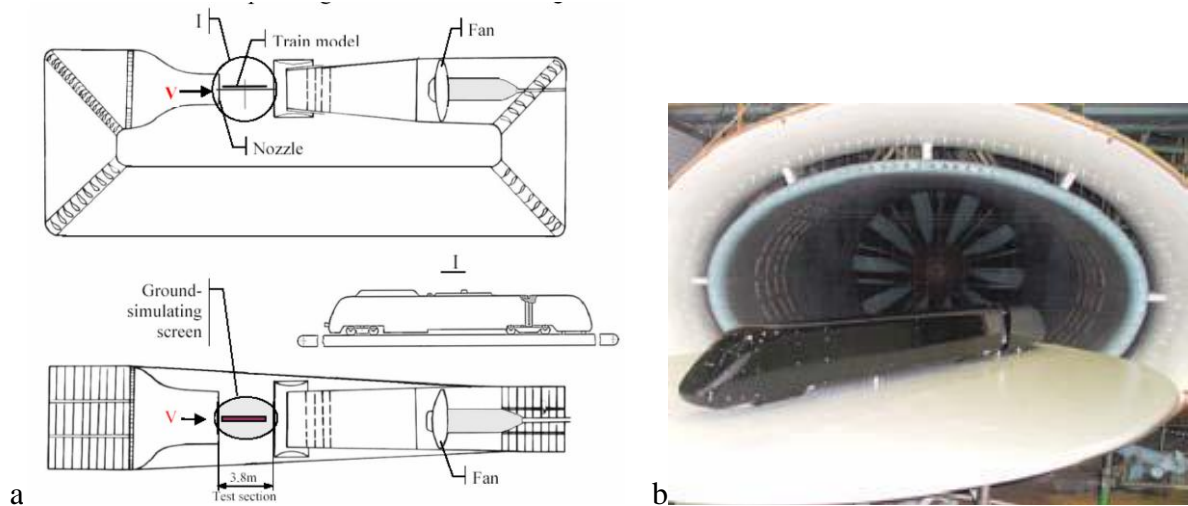


Figure 2: TsAGI wind tunnel plant scheme (a), ATM model in the TsAGI test section (b)

### 3.2 PMWT wind tunnel tests

The PMWT plant is a closed circuit wind tunnel with two test sections: a larger one (14m x 4m) where tests can be carried on with a wind speed up to 15 m/s (PMWT LS tests section) and a nominal turbulence intensity  $IT < 2\%$  and a smaller one (4m x 4m) where tests can be carried on with a wind speed up to 50 m/s (PMWT HS tests section) and a nominal turbulence intensity  $IT < 0.2\%$ . A sketch of the wind tunnel plant is reported in Figure 3.

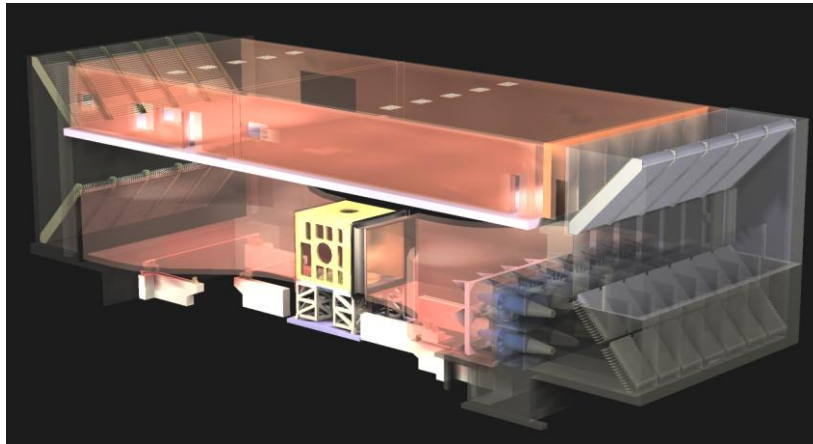


Figure 3: PMWT wind tunnel plant scheme

Tests on the ATM model were performed in both the test sections using a RUAG 6 components external force balance. Tests in the PMWT LS test section were performed in a wind speed range between 7 and 15m/s, which corresponds to Re-numbers of  $Re_1 = 1.4 \cdot 10^5 \sim 3.0 \cdot 10^5$ , with a blockage ratio that varies between 0.9% and 4.7% for the considered yaw angles between  $5^\circ$  and  $90^\circ$ . Tests in the PMWT HS test section were performed in closed arrangement at a wind speed range between 7 and 50m/s ( $Re_1 = 1.4 \cdot 10^5 \sim 1.0 \cdot 10^6$ ), with a blockage ratio that varies between 3% and 10% for the considered yaw angles between  $5^\circ$  and  $30^\circ$ .

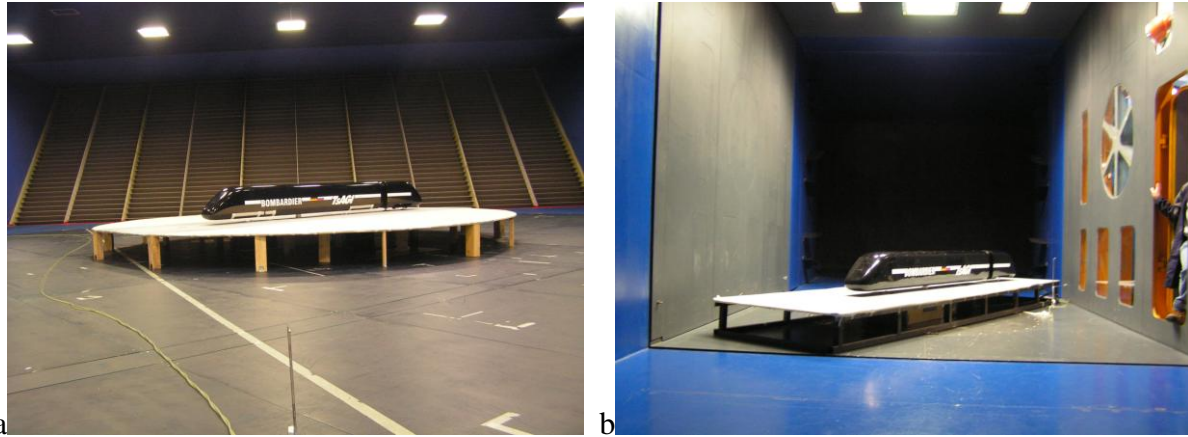


Figure 4: ATM model in the PMWT LS test section (a) and in the PMWT HS test section (b)

Pressure measurements have only been recorded at 14 m/s during the PMWT LS tests session using a PSI high frequency pressure scanner system.

#### 4 WIND TUNNEL RESULTS

The dependence of the aerodynamic coefficients on the yaw angle will be compared in the following paragraphs. Coefficients are computed according to the sign convention reported in Figure 5 and to the following formulation:

$$C_{F_i} = \frac{F_i}{\frac{1}{2}\rho U^2 S} \quad C_{M_i} = \frac{M_i}{\frac{1}{2}\rho U^2 S h} \quad C_p = \frac{\Delta p}{\frac{1}{2}\rho U^2} \quad (1)$$

where  $F_i$  ( $i = x, y, z$ ) are the aerodynamic force components in the train's reference system (Figure 5),  $M_i$  ( $i = x, y, z$ ) are the corresponding moments and  $\Delta p$  is the differential pressure measured on the generic pressure tap. In equation (1),  $\rho$  is the air density,  $U$  is wind speed,  $h$  is equal to 3m (full scale), and  $S$  is a standard reference surface which is equal to  $10\text{m}^2$  (full scale).

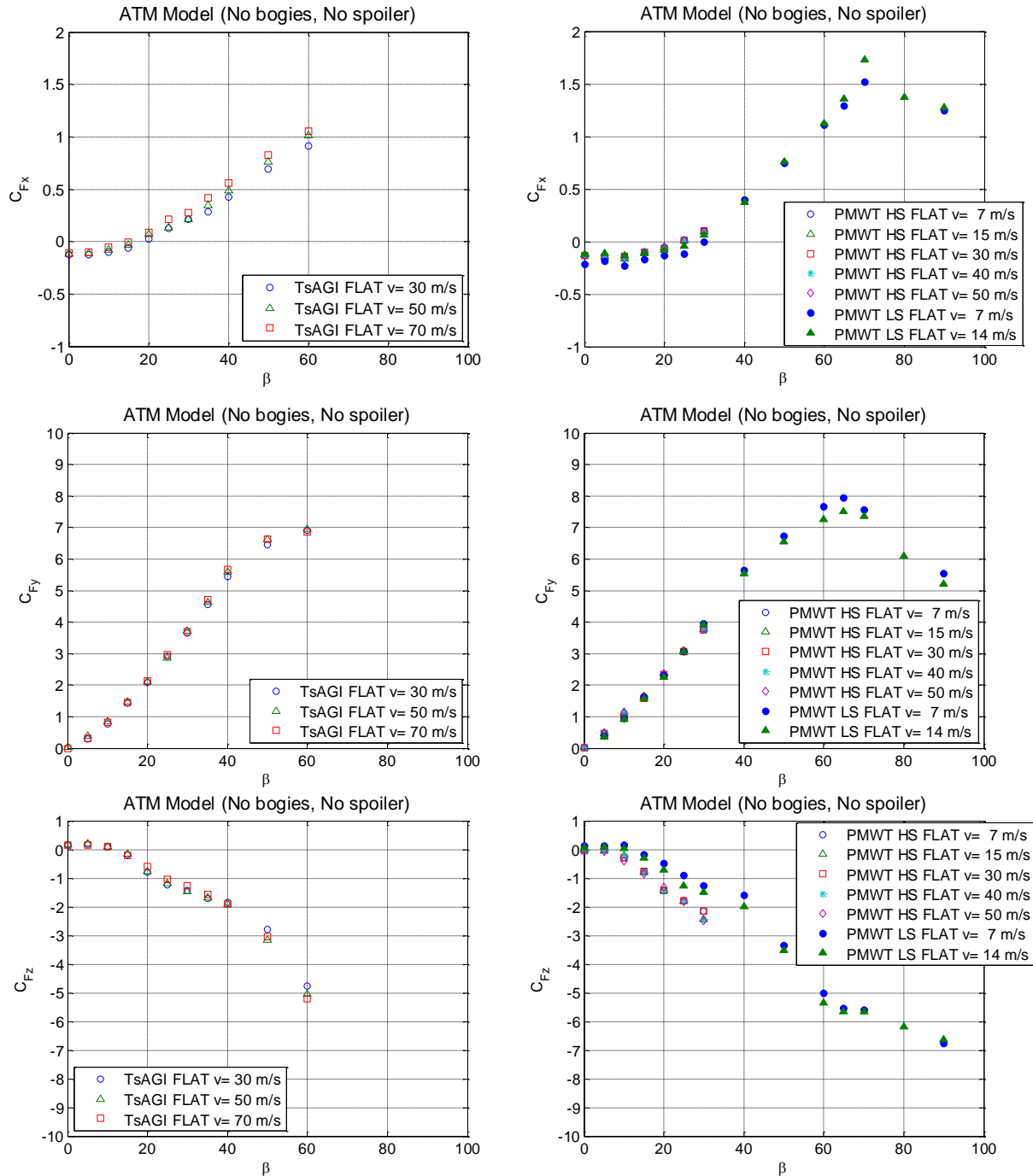


Figure 5: Aerodynamic coefficients' sign convention

### 4.1 Aerodynamic coefficients

In the following figure a comparison between the aerodynamic coefficients measured at TsAGI and PMWT is reported for different mean wind speeds and different yaw angles  $\beta$  (expressed in deg). Results obtained at PMWT in the high speed (HS) test section and in the low speed (LS) one are overlapped in the figures on the right.

Furthermore a comparison in terms of  $C_{Mx,lee}$  coefficient is reported in Figure 7.



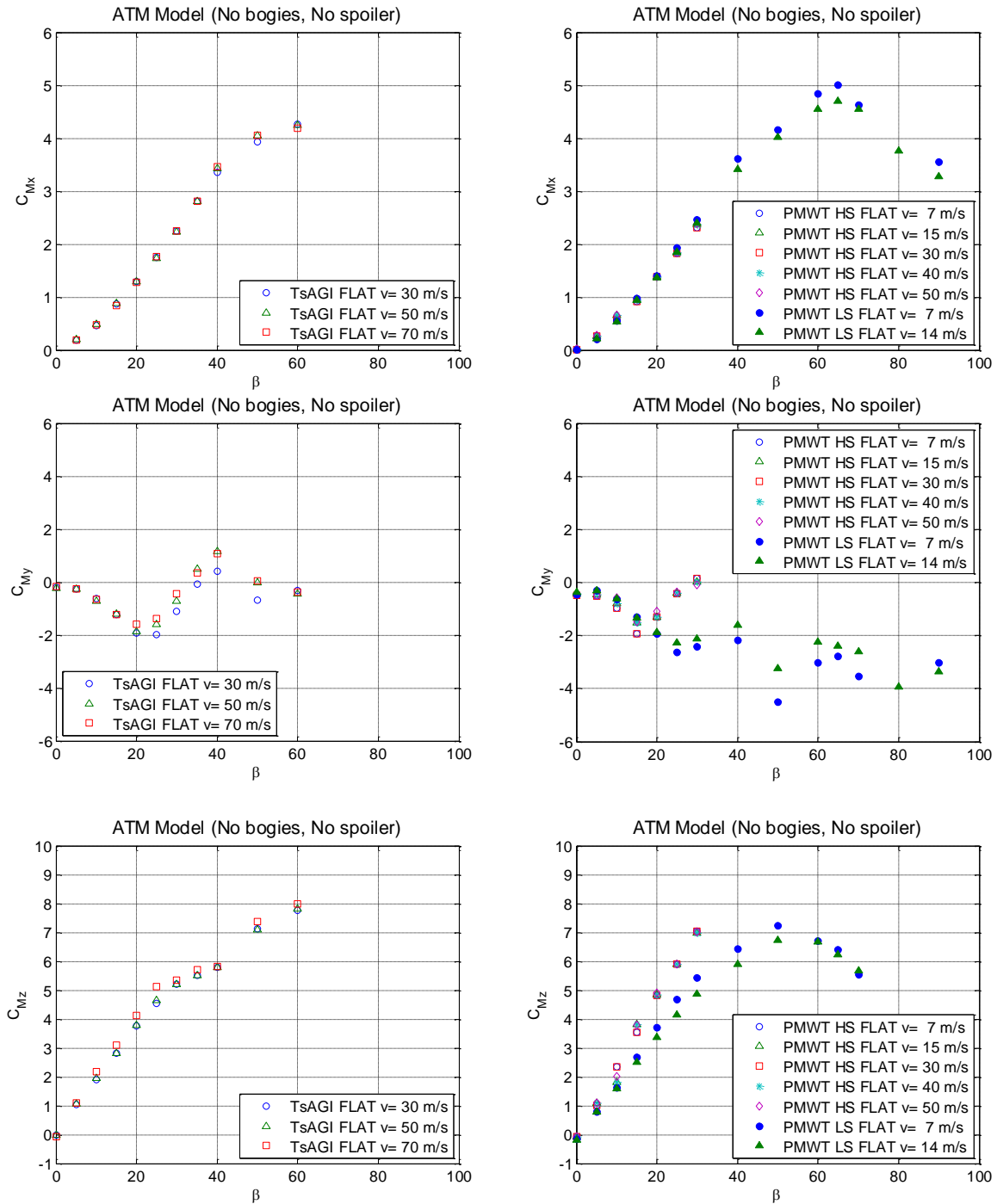


Figure 6: Aerodynamic coefficients vs yaw angle

A very good agreement is visible by the comparison of the TsAGI and the PMWT LS results for all the aerodynamic coefficients apart from  $C_{My}$ , where a similar trend is visible only up to 20 deg. For higher yaw angles, the TsAGI results show a double sign change from negative to positive  $C_{My}$  values at 35 deg and from positive to negative values at 50 deg, while PMWT LS results show the same slope changes, they never reach positive  $C_{My}$  values.

A  $C_{My}$  trend closer to the TsAGI results is highlighted by the PMWT HS data even if they seem to anticipate the minimum ( $\beta=15$  deg) and the crossing of the x-axis ( $\beta=30$  deg) to lower yaw angles.

PMWT HS results differ significantly from the PMWT LS results for the  $C_{Fz}$  and  $C_{Mz}$  coefficients where HS data overestimate the consistent values of the PMWT LS and TsAGI results.

Differences in the  $C_{Fz}$  and  $C_{My}$  coefficients indicate, for the PMWT HS data, a higher vertical lifting force positioned in the forepart of the train. It is difficult to explain this experimental evidence starting from the global force measurement, since, even if the model and the measurement system are the same, tests are performed with different turbulence intensity levels and different splitter plates. Similar considerations hold also for the  $C_{Mz}$  coefficient.

TsAGI results show a small Reynolds number dependency for the  $C_{Fx}$  coefficient that increases the slope at yaw angles higher than 20 if the wind speed is increased. The same aerodynamic coefficient seems to be not affected by Reynold number effect in the PMWT data where only the 7 m/s LS coefficient shows some differences from 0 to 30 deg.

$C_{Fy}$  and  $C_{Mx}$  coefficients don't have any Reynolds number dependency both for TsAGI and PMWT results up to 60 deg. A different maximum value is reached by the PMWT LS data, being the lower wind speed the more conservative.

Reynolds number effects are negligible also comparing the TsAGI and the PMWT HS results for the  $C_{Fz}$  and  $C_{Mz}$  coefficients even if the best agreement is shown between the TsAGI and the PMWT LS data for these coefficients.

Another discrepancy between TsAGI and PMWT LS results is present at  $\beta=60$  deg that represents the largest yaw angle tested at TsAGI due to the test section/model dimensions.  $C_{Fy}$  and  $C_{Mx}$  seem to change the slope passing from 50 to 60 deg in the TsAGI results while they continue with a different trend in the PMWT LS results. Also looking at the comparison on the  $C_{Fx}$  and  $C_{Mz}$  coefficients a difference appears at 60 deg while a very good agreement is present on the other yaw angles. This could be explained considering that, at 60 deg, the model in the TsAGI open tests section is too close to the boundaries of the flow while in the large PMWT LS test section results are less affected by the boundary conditions and wind tunnel tests may be extended up to 90 deg.

Figure 7 reports the comparison between TsAGI and PMWT data in terms of  $C_{Mx, lee}$  representing the overturning moment computed around the leeward rail axis that is a key parameter for the evaluation of the overturning effects induced by cross-wind. From the comparison it is visible the complete agreement up to 50 deg and the negligibility of the Reynolds number effects on this coefficient.

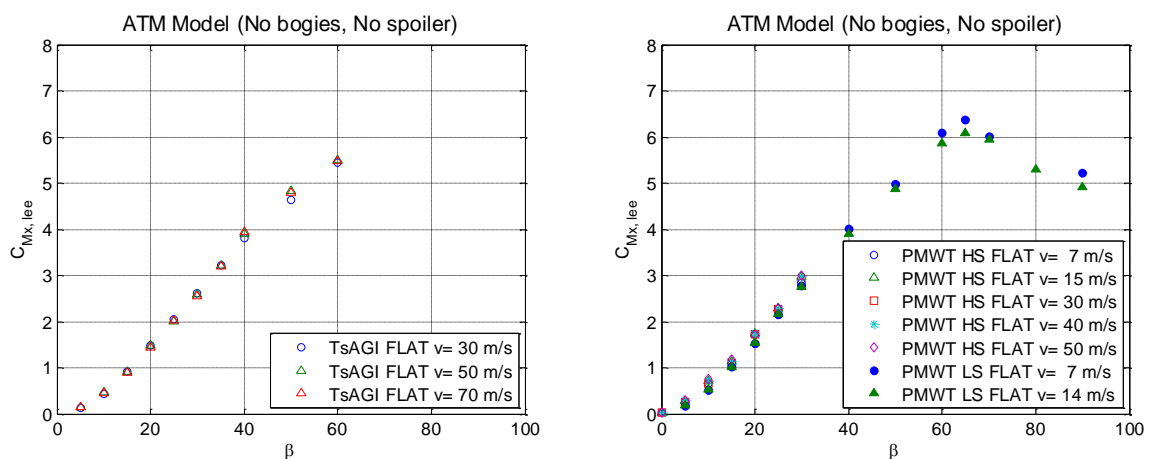


Figure 7: Comparison of  $C_{Mx, lee}$  coefficient vs yaw angle

## 4.2 Pressure distribution

The comparison of the pressure distribution on all the 8 sections measured at TsAGI and at PMWT LS is reported in Figure 8 for the yaw angle  $\beta=30$  deg in terms of pressure coefficients  $C_p$ . Arrows and points inside the section boundary represent positive values.

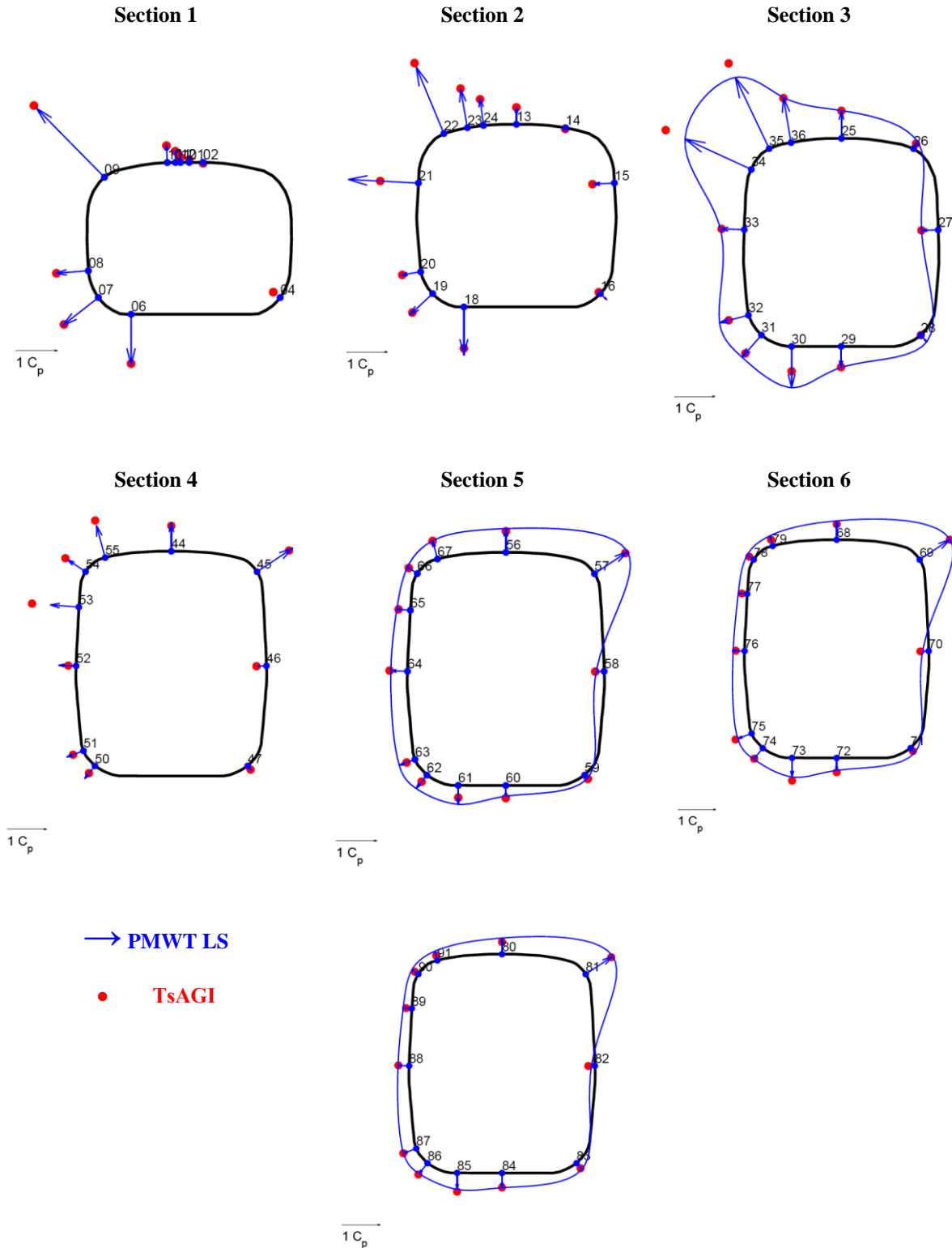


Figure 8: Pressure coefficient distribution at  $\beta=30$  deg (blue arrows: PMWT; red points: TsAGI)

A very good agreement is visible on all the 8 sections at the different pressure taps positions. TsAGI values show a slightly higher suction zone in the upper leeward part of section 3 and section 4. This difference confined in the forepart of the train model could explain the negative value of the PMWT LS  $C_{My}$  coefficient compared to the almost null value of the TsAGI being the  $C_{Fz}$  coefficients equal for both the cases.

Smaller discrepancies are visible in the lower leeward part of sections 3 and 5 where PMWT LS results present a higher suction.

Similar differences appears also in the comparison between the TsAGI results and CFD results presented in [2] and PMWT results seem to be closer to the numerical simulation data.

## 5 CONCLUSIONS

- Good agreement is reached by the comparison of wind tunnel results performed at different wind tunnel plants on the same 1:10 scaled train model.
- Results showed negligible Reynolds number effects especially for those coefficients involved in the cross wind analysis ( $C_{Fy}$  and  $C_{Mx}$ )
- Differences in the results are present in  $C_{Fz}$ ,  $C_{My}$  and  $C_{Mz}$  coefficients between PMWT HS and PMWT LS data while TsAGI (open section) and PMWT LS (large closed test section) data are in good agreement on all the coefficients apart from  $C_{My}$  for yaw angles higher than 20 deg.
- Differences between PMWT HS and PMWT LS data may be due to different wind tunnel test conditions as turbulence intensity levels and splitter plate geometry being the model and the measurement set-up the same in both the wind tunnel campaigns.
- The different  $C_{My}$  behavior, for yaw angles higher than 20 deg, between TsAGI and PMWT LS data, can be explained by analyzing the pressure distribution measured on the train model especially in the upper and lower leeward parts of the train in the forepart.

Benchmark tests and benchmark vehicles represent a good tool to compare and validate data and wind tunnel procedures that is also included in standards [3]. Among all the parameters affecting the wind tunnel results analyzed in the present work, Reynolds number seems to be not critical for cross wind analysis while other parameters as turbulence intensity and boundary layer treatment affect only some aerodynamic coefficients.

## REFERENCES

- [1] A. Orellano and M. Schober. Aerodynamic performance of a typical high-speed train. *WSEAS transactions on Fluid Mechanics*, **1**, 2006.
- [2] B. Diedrichs. Aerodynamic calculations of crosswind stability of a high-speed train using control volumes of arbitrary polyhedral shape. Proceedings of the BBAA VI, Milano, Italy, July 20-24, 2008.
- [3] prEN 14067-6. Railway Applications – Aerodynamics – Part 6: Requirements and test procedures for cross wind assessment. European standard



## REFERENCE WIND TUNNEL MEASUREMENTS ON AERODYNAMIC COEFFICIENTS OF ICE 3 END CAR

Nina Rüd<sup>\*</sup>, S. Loose<sup>†</sup>, T. Kowalski<sup>†</sup>, Arnd Rüter<sup>+</sup>, Martin Schober<sup>°</sup> and Marc Stiepel<sup>\*</sup>

<sup>\*</sup> DB Systemtechnik, VTZ 113 Aerodynamik und Klimatechnik  
Deutsche Bahn AG, Systemverbund Bahn, Völckerstraße 5, 80939 München, Germany  
e-mail: Nina.Rued@deutschebahn.com,

<sup>†</sup> Institut für Aerodynamik und Strömungstechnik Göttingen  
Deutsches Zentrum für Luft- und Raumfahrt e.V. DLR, Bunsenstraße 10, 37073 Göttingen, Germany  
e-mails: Sigfried.Loose@dlr.de, Thomas.Kowalski@dlr.de,

<sup>+</sup> Mobility Division Rolling Stock  
Siemens AG, Industry Sector, Duisburger Str. 145, 47829 Krefeld, Germany  
e-mail: Arnd.Rueter@siemens.com,

<sup>°</sup> Passengers PGR / TSSA  
Bombardier Transportation AG, Am Rathenaupark, 16761 Hennigsdorf, Germany  
e-mail: Martin.Schober@de.transport.bombardier.com,

<sup>\*</sup> Calculation & Vehicle Dynamics  
Alstom LHB GmbH, Linke-Hofmann-Busch-Straße 1, 38239 Salzgitter, Germany  
e-mail: Marc.Stiepel@transport.alstom.com

**Keywords:** Railway, Reference Measurements, ICE 3, Aerodynamic Coefficients

**Abstract.** *This article reports the results of reference wind tunnel measurements of the aerodynamic coefficients of one of the benchmark vehicles defined in the prEN 14067-6:2009, i.e. the ICE 3 end car (i) on the new single track ballast & rail (STBR) standard ground configuration and (ii) on the true flat ground configuration (TFG) as currently required by TSI HS RST and DB guideline Ril 80704. Tests were carried out at the DNW facilities (German – Dutch wind tunnels) in two different wind tunnels. Each test campaign included measurements for a range of Reynolds numbers and the two different test configurations. The compliance of both wind tunnels with the specific requirements made in prEN 14067-6 is detailed. The measured coefficients of the ICE 3 are compared and evaluated for consistency with results of different test campaigns in varying wind tunnels. Very good agreement is found and thus reproducibility of the addressed tests performed is affirmed. Due to this achievement, the test results for the ICE 3 measured on the standard configuration STBR have been introduced as reference data for aerodynamic coefficients of an ICE 3 end car to the pre-standard prEN 14067-6. PrEN 14067-6 is expected to be put in force as a European standard in 2010 and is assumed to be the basic reference for future TSIs and national regulation of cross wind safety aspects.*

## 1 INTRODUCTION

A major safety issue determined by aerodynamic aspects of railway vehicles is their operational behavior under cross wind influences. The importance of this topic for both high-speed traffic and also general rail operation has been increased in Europe in the last two decades due to the modern light-weight train concepts. For high-speed rail operation, the introduction of an “open issue” with respect to cross wind safety to the technical specification for interoperability of high-speed rolling stock (TSI HS RST) [1] acted as a trigger for increased research and engrossed knowledge on cross wind safety in European countries. The result of this development is visible in the release of several official documents on facets of cross wind safety. There are for example the DB guideline Ril 807.04 [2], the revised TSI HS RST [3] and the European pre-norm prEN 14067-6 [4]. The DB guideline, which became also mandatory for national rolling stock assessment in Germany, gives requirements for all passenger railway vehicles and railway infrastructure, while the new TSI HS RST still focuses on high-speed rolling stock. The European standard prEN 14067-6:2009, developed as a complement to the existing TSI HS RST, addresses also conventional rail and delivers (additional) methods for the evaluation of railway vehicles generally.

Cross wind characteristics of vehicles are determined by both their aerodynamic properties and their vehicle dynamics. The aerodynamic properties are evaluated in terms of aerodynamic force and moment coefficients which are used to deduce the vehicle dynamic behavior in combination with characteristic parameters such as vehicle mass, mass distribution and suspension elements. The focus of this work is on the aerodynamic share which is assessed generally by wind tunnel experiments.

## 2 SPECIFICATIONS OF PR EN 14067-6

PrEN 14067-6 [4] gives detailed description of the test procedures and requirements on carrying out wind tunnel measurements for determining the relevant aerodynamic force and moment coefficients. The basic specification of those tests is in accordance with [2] and [3] and includes the use of static models in a uniform, low turbulence onset flow. Generally tests at model scale are recommended and measurements have to be carried out for a range of angle of attack. Specific to [4] is that besides several technical requirements such as minimum Reynolds number, boundary layer thickness, instrumentation accuracies and model set-up, there is the demand of undertaking a benchmark test and showing compliance in terms of agreement between measured values and reference aerodynamic coefficients. Benchmark tests may be carried out with one of the three designated benchmark vehicles. One of those is a generic model of ICE 3 end car which is based on the ICE 3 end car without HVAC elements and with simplified bogie geometry. (In the following this benchmark vehicle will be referred to simply as “ICE 3 end car”.)

One of the major differences between the methodology as defined in prEN 14067-6:2009 and other cross wind regulations is that the prEN 14067-6:2009 defines a “single track ballast & rail” (STBR) standard ground configuration. This STBR set-up shall replace both ground configurations “true flat ground” (TFG) and “6 m standard embankment” (6EM) which currently form the basis for TSI HS RST.

## 3 WIND TUNNEL MEASUREMENTS OF ICE 3 END CAR BENCHMARK VEHICLE

Reference wind tunnel tests on the ICE 3 end car benchmark vehicle were carried out in a test campaign in 2008. The measurements were performed in accordance with requirements specified in prEN 14067-6:2009. The campaign was initiated by the German standardization

body DIN as a national contribution to support the finalization of the future European standard EN 14067-6. The campaign was executed as cooperation between 5 companies (Alstom LHB GmbH, Bombardier Transportation AG, Deutsche Bahn AG, DLR, Siemens AG) and partially funded by the Bundesministerium für Wirtschaft (German ministry of economy). The test campaign consisted of measurements in two different wind tunnels of the DNW facilities (Dutch-German wind tunnels). One of those was the DNW Kryo-Kanal Köln (DNW cryogenic wind tunnel in Cologne; also known as KKK) and the other wind tunnel used was the Hochdruckkanal Göttingen (high pressure wind tunnel in Göttingen; also known as HDG).

#### 4 KKK – CRYOGENIC WIND TUNNEL COLOGNE

The KKK wind tunnel is a closed circuit low speed tunnel. To achieve high Reynolds numbers, the gas temperature in the tunnel circuit can be lowered down to 100 K by injecting liquid nitrogen. Tunnel operation, test parameters, and the measurement and data acquisition are automatically controlled by an integrated hard- and software system. For this particular test campaign of measuring the aerodynamic coefficients of the ICE 3 end car, the wind tunnel was operated under “normal conditions”, i.e. with an operating temperature of 220 K (~ -50°C). In the following the test campaign and its set-up is detailed and checked against the specific requirements made in prEN 14067-6:2009.

##### 4.1 Block profile and turbulence level

The test section velocity distribution is shown in Figure 2. The velocity distribution in the test section was measured using 5-hole probe rake (Figure 1). The rake was equipped with 15 probes. The distance between the probes was 25 mm. For the upper part of the test section a single 5-hole probe was used.

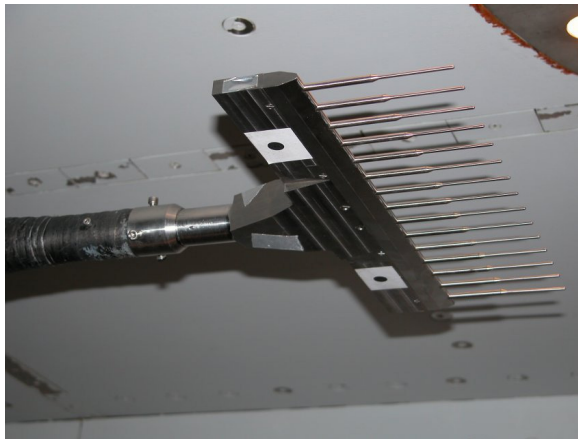


Figure 1: five holes probe rake

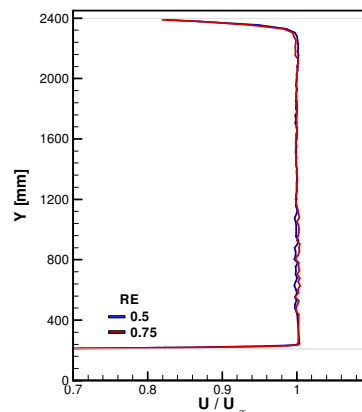


Figure 2: Measured block profile KKK

The wind tunnel turbulence level was determined in former investigations mentioned in [7]. Hot wire probes have shown that the turbulent intensity ( $Tu' = (u'^2 / U)^{0.5}$ ) in the free stream flow was between 0.05% and 0.4% depending of the Mach (from 0.1 to 0.3) and Reynolds number (from 0.5 and  $7 \cdot 10^6$ ) for temperature between 100 and 285K [7]. These measurements were performed in the center of the wind tunnel with an array of 4 hotwires and on the upper right corner of the test section using a single hotwire.

## 4.2 Model set-up

The investigated vehicle consists of a model of the ICE 3 end car next to a wake body as described in the prEN 14067-6:2009, the width of the inter car gap was 1 mm in model scale. The model scale was 1:25 and the mock-up was made of aluminum. The geometry of the ICE 3 benchmark vehicle includes all simplifications (e.g. symmetry etc.) which are described in the European pre-standard in form of a CAD file and was used as basis for modeling.

## 4.3 Instrumentation

An internal balance equipped with 9 strain gauges and 10 temperature sensors was used for all force and moment measurements. The balance was calibrated to the requirements of prEN, especially the range of loads was adapted to the expected loads for these experiments [7]. The speed in the test section was determined by using the nozzle pressure drop  $\Delta p = [p_{\text{stat}}(\text{ahead}) - p_{\text{stat}}(\text{rearward})]$ . To enable a simple blockage correction the dynamic pressure in the test section was additionally measured by a Prandtl probe positioned according to prEN 14067-6:2009.

## 4.4 Ground configuration

Two different ground configurations were investigated in the KKK test campaign. The “True Flat Ground” (TFG) as specified in TSI HS RST and in the German guideline Ril 80704 was used. Secondly the ground configuration “Single Track with Ballast and Rail” (STBR) as specified as standard ground configuration in prEN 14067-6:2009 was utilized. The former configuration serves as comparison basis as it has been applied to wind tunnel measurements of railway vehicles repeatedly and the latter configuration is investigated with the aim of providing reference values for the standard configuration. Sketches of the two configurations are shown in Fig. (3).

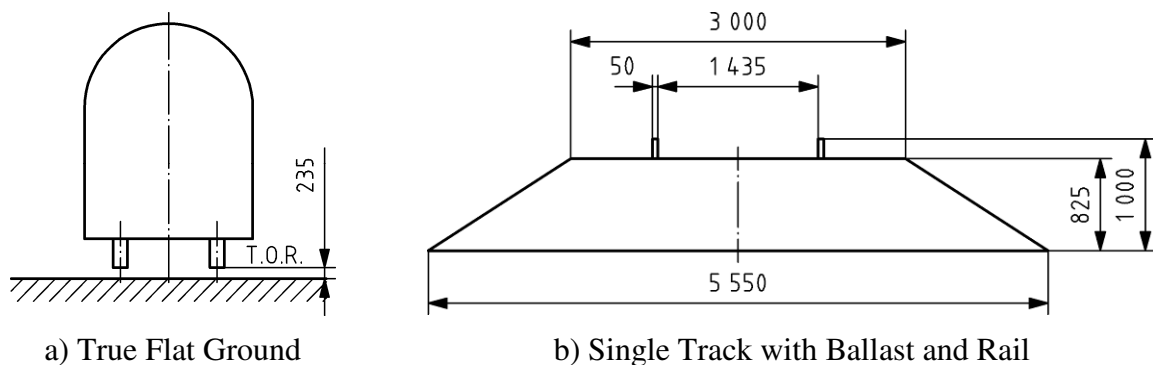


Figure 3: Wind tunnel ground configurations

## 4.5 Test program of KKK wind tunnel campaign

The test program of the measurements carried out in the KKK wind tunnel consists of investigation of both ground configurations as described above in 4.4. Both set-ups are ascertained for several Reynolds numbers. They range from  $0.5 \cdot 10^6$ ,  $0.75 \cdot 10^6$  to  $1.0 \cdot 10^6$ . The angle of attack is varied for each investigation in increments of  $5^\circ$  from  $-90^\circ$  up to  $180^\circ$ . These tests are in accordance with prEN 14067-6:2009 which requires measurements for the standard configuration STBR at a minimum Reynolds number of at least  $0.25 \cdot 10^6$ .

## 5 HDG – HIGH PRESSURE WIND TUNNEL GÖTTINGEN

The high-pressure wind tunnel of DNW (HDG) is a closed circuit low speed wind tunnel, which can be pressurized up to 100 bar. The dimensions of the test section are 0.6 m·0.6 m at a length of 1 m. For model scale of 1:100 with the maximum speed of 35 m/s and a pressure of 40 bar the achieved maximum Reynolds number was  $2.0 \cdot 10^6$ . Figure 5 shows the range of Reynolds numbers that can be obtained depending on the static pressure  $P_0$  in the wind tunnel and free stream velocity  $U_\infty$ . The flow stays incompressible over the whole range of Reynolds numbers.

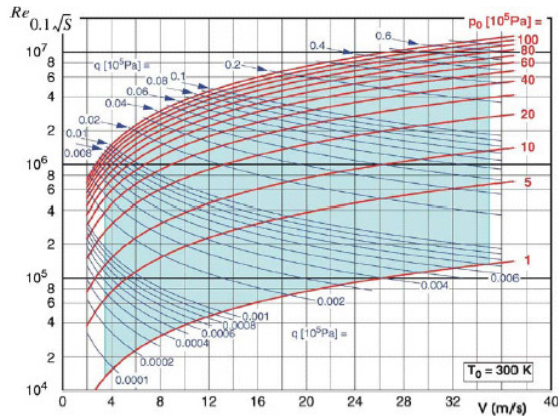


Figure 4: Reynolds number range of HDG

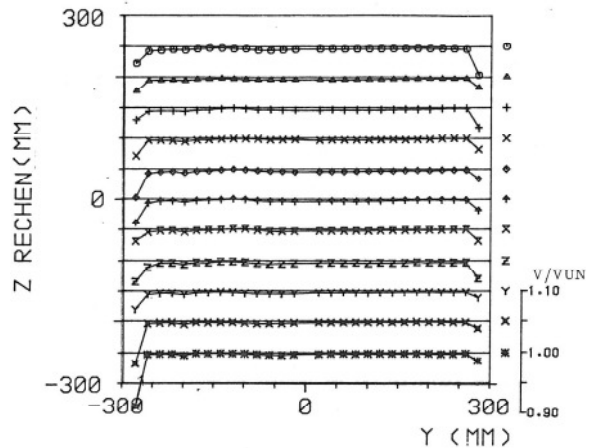


Figure 5: Block profile for HDG

### 5.1 Block profile, turbulence level

The velocity profile in the test section was measured by traversing a total pressure rake over the whole cross section at the test section center at different total pressures and velocities Figure 5. Out of the boundary layers the static pressure and velocity variation are  $|\Delta p_{\max}/q_\infty| \leq 0.013$  and  $|\Delta v_{\max}/V_\infty| \leq 0.007$ . The free stream turbulence was measured at four points of the empty test section over the whole simulation range. The measured spectra were used in the frequency range between 1 Hz and 10 kHz to determine the degrees of turbulence. The values shown below are mean values of the four locations. The turbulence increases with the Reynolds number from 0.2% to 0.7%.

### 5.2 Boundary layer

The tunnel walls boundary layer is cut-off by a splitter plate, which is mounted on the wall integrated turn table and can be designed for the individual train configuration. Especially at higher Reynolds numbers the boundary layer thickness  $\delta_{99\%}$  remains small. With the typical HDG train scale 1:100 the reference length of 3 m reduces to  $l_{\text{ref}} = 0.03$  m. Then the boundary layer thickness at  $x = 10 l_{\text{ref}}$  will be about  $\delta_{99\%}(x = 0.3 \text{ m}, \text{Re}_{0.03\text{m}} = 1 \text{ to } 3 \cdot 10^6) \approx 1.5 \text{ mm to } 0.9 \text{ mm}$ . The prEN 14067-6:2009 requires the boundary layer thickness  $\delta_{99\%} < 30\%$  of the train height, i.e. in this case less than 11 mm. This requirement is fulfilled.

### 5.3 Model set-up

The HDG model set-up was chosen analogous to the set-up employed in the KKK. The ICE 3 end car and its according wake body were modeled with the geometry given in prEN 14067-6:2009. The model scale for the HDG was 1:100 and the model was also made of alu-

minum. The modeling scale was chosen in order to realize the requested blockage ratio of less than 5%.

### 5.4 Instrumentation

The used balance is manufactured regarding to the so called “block-concept”, the strain produced by loads is recorded at 7 test positions of which each consists of four strain-gauges, arranged in a Wheatstone bridge with integrated temperature compensation. The temperature characteristics of the balance material are taken into account by the use of appropriate gauges. By setting the calibration loads according to the requirements of prEN, an optimized matrix with an even higher accuracy was achieved.

### 5.5 Ground configuration

Analogously to the set-up in the KKK (4.4), two separate ground configurations were investigated within the HDG test campaign. On the one hand the “True Flat Ground” (TFG) as specified in TSI HS RST and guideline Ril 80704 was used. On the other hand the ground configuration “Single Track with Ballast and Rail” (STBR) as specified as standard ground configuration in prEN 14067-6:2009 was utilized.

### 5.6 Test program of HDG wind tunnel campaign

The test program of the measurements carried out in the HDG wind tunnel consists of investigation of both ground configurations as described above in 5.5. Both set-ups are ascertained for several Reynolds numbers. They range from  $1.0 \cdot 10^6$ ,  $1.5 \cdot 10^6$  to  $2.0 \cdot 10^6$  and for the case of TFG additionally to  $2.25 \cdot 10^6$  and  $3.0 \cdot 10^6$ . The angle of attack is varied for each investigation in increments of  $5^\circ$  from  $-90^\circ$  up to  $90^\circ$ . These tests are in accordance with prEN 14067-6:2009 which requires measurements for the standard configuration STBR at a minimum Reynolds number of at least  $0.25 \cdot 10^6$ .

## 6 WIND TUNNEL MEASUREMENT RESULTS

### 6.1 Overview of test results of KKK wind tunnel campaign

Figure 6 and Figure 7 show exemplary the compared results for the lift coefficient  $C_z$  and for the lee rolling moment coefficient  $C_{mx}$ , for both ground configurations STBR and TFG.

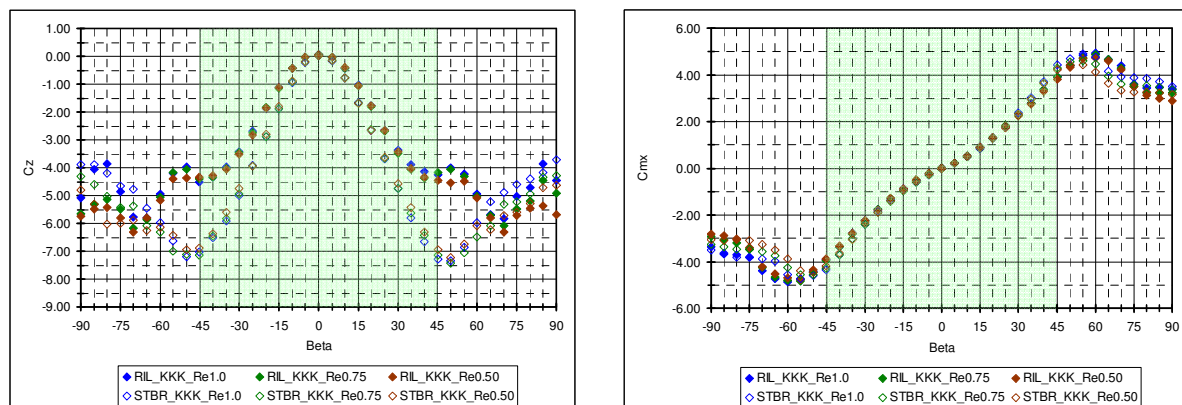


Figure 6: Comparison of measurement results in the KKK for STBR and TFG

The complete set of aerodynamic coefficients of the ICE 3 end car measured in the KKK at  $1 \cdot 10^6$  Reynolds number is detailed in chapter 8.

## 6.2 Overview of test results of HDG wind tunnel campaign

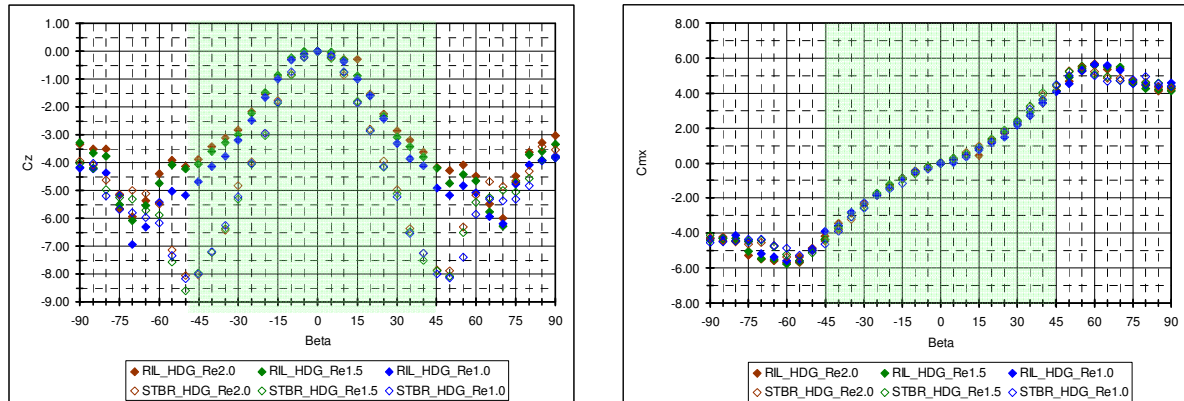


Figure 7: Comparison of measurement results in the HDG for STBR and TFG

The results show a good agreement between both facilities especially in the considered angle interval (high-lighted in green). For angles larger  $45^\circ$  one has to take into consideration that the set up and the blockage ratio in both facilities is slightly different.

The complete set of aerodynamic coefficients of the ICE 3 end car measured in the HDG at  $1 \cdot 10^6$  Reynolds number is detailed in chapter 8.

## 6.3 Reynolds number influence

All specification on wind tunnel measurement requirements rely on the test results being Reynolds number independent. In this test campaign the influence of Reynolds number was investigated in both wind tunnels for both ground configurations by repeating the measurements for at least 3 Reynolds numbers. Fig. (8) shows the lee roll moment coefficient  $c_{Mxlee}$  for the TFG configuration in the KKK and the HDG for three angles of attack. For the TFG case in the KKK, no Reynolds number effect can be observed. In the HDG, there seems to be a slight Reynolds number dependency for the TFG tests with respect to lower Reynolds numbers. The effect is diminished for Reynolds numbers larger than  $2 \cdot 10^6$  and the values for  $1 \cdot 10^6$  are almost on the same level.

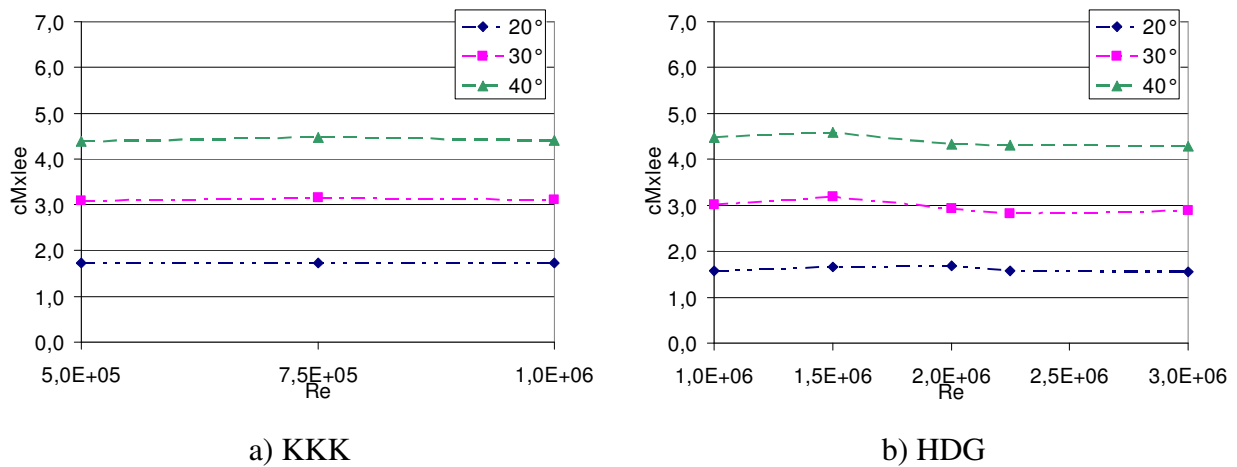


Figure 8: Influence of Reynolds number, True Flat Ground

The lee roll moment coefficient  $c_{M_{x,lee}}$  for the STBR configuration in the KKK and the HDG for three angles of attack is presented in Fig. (9). Again as for the TFG case, the measured coefficient is independent of the Reynolds number in the KKK. For the HDG the STBR configuration also shows a slight Reynolds dependency for the largest exhibited angle of attack. For the lower, more relevant angles with respect to safety calculations the effect of Reynolds number is negligible.

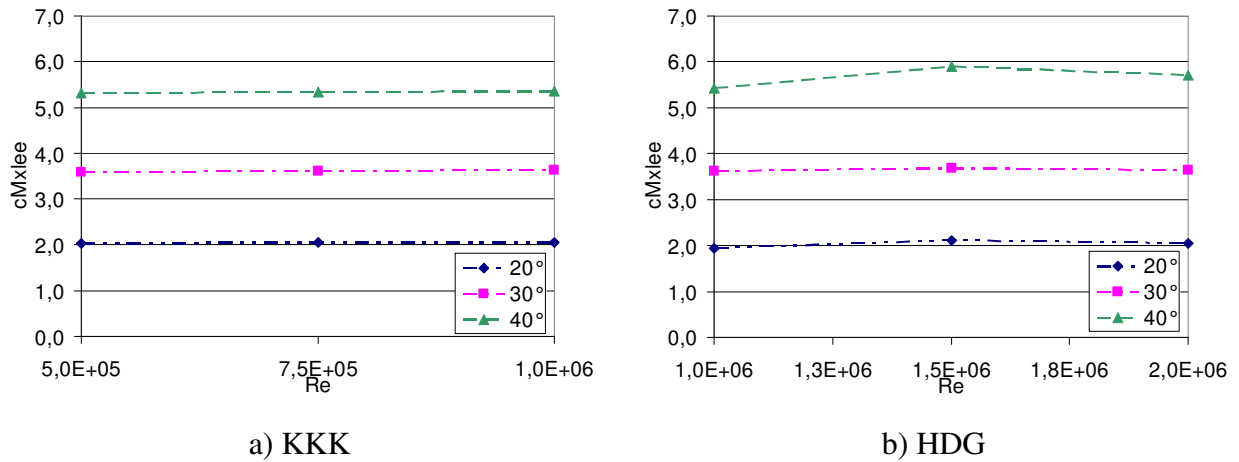


Figure 9: Influence of Reynolds number, Single Track with Ballast and Rail

#### 6.4 Comparison of test results with measurements of other campaigns

The reproducibility of the test results is to be investigated by comparing the lee roll moment coefficient measured in this campaign to that of other published data. As comparison data base, the measurement results of an ICE 3 end car in the Audi wind tunnel in Ingolstadt with scale 1:15 of 2004 [5] and those of an ICE 3 in the CSTB wind tunnel in Nantes in scale 1:7 of 2001 [6] are consulted. In both cases the tested vehicle models are not identical to those utilized here, but are generally in good agreement even though there are some differences in the geometrical simplification.

For the case of TFG, the ground configuration in all 4 wind tunnel tests was the same, as the specification for TFG has been developed early. However, for the measurements in the CSTB wind tunnel, the absence of boundary layer treatment represents a major difference in the set-up. In Fig. (10), the lee roll moment coefficient for the 4 test campaigns is presented.

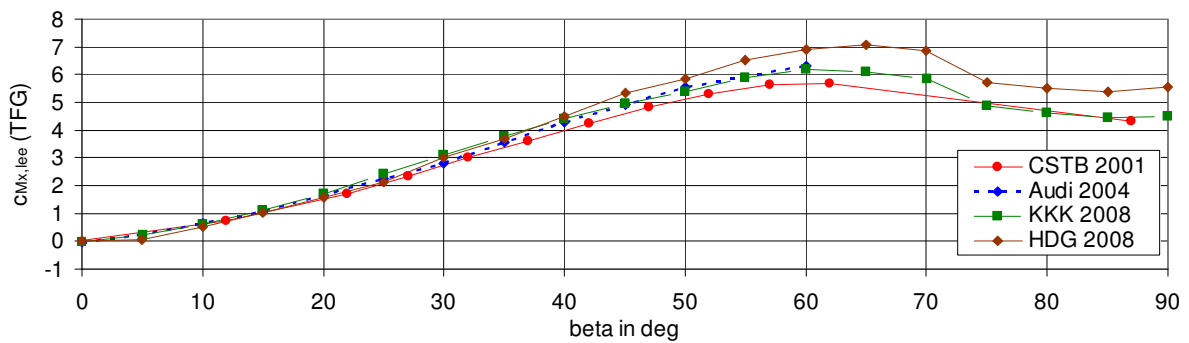


Figure 10: Comparison of lee roll moment coefficient, True Flat Ground



The values of  $c_{M_{x,lee}}$  of the measurements in the KKK and in the Audi wind tunnel are almost identical in Fig. (10). HDG results and CSTB results also show good agreement in this overview presentation. Fig. (11) presents the coefficient as relative difference with respect to the KKK measurements. This detailed presentation shows that for the relevant range of angles ( $5^\circ$  to  $45^\circ$ ), Audi and KKK values are within 10% of each other. HDG reaches for one angle of attack a slightly higher difference of 13%, while the Audi results are generally lower (up to 16%) than those of the KKK. This is expected due to the influence of the thicker boundary layer.

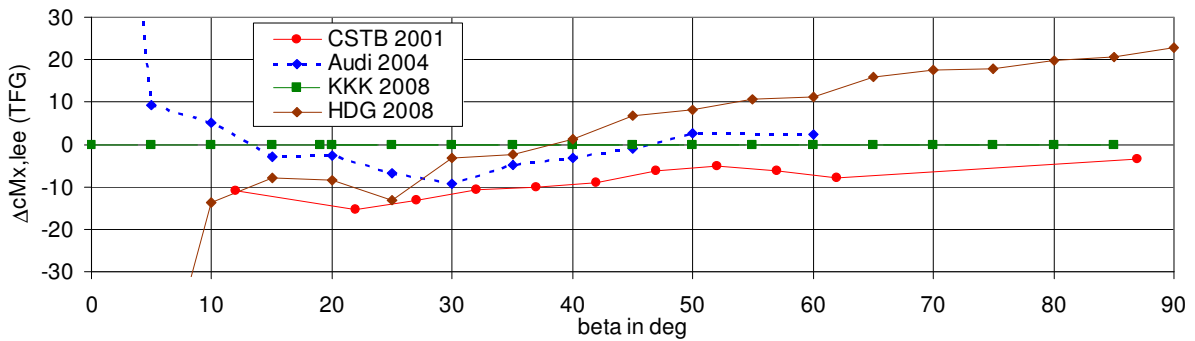


Figure 11: Comparison of lee roll moment coefficient – relative difference with respect to measurements in KKK, True Flat Ground

The same general comparison for the case of STBR is shown in the following Fig. (12). For the relevant range of angles up to  $45^\circ$  the overview shows a very good agreement between the HDG, the KKK and the Audi wind tunnel measurements. The values of the CSTB campaign are obviously lower, presumably due to the thick boundary layer plus additional differences in the ground model.

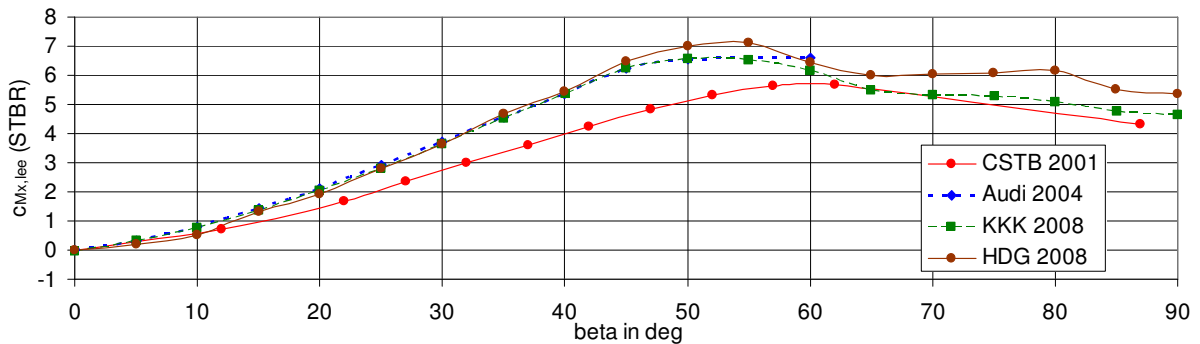


Figure 12: Comparison of lee roll moment coefficient, Single Track with Ballast and Rail

Fig. (13) shows the difference in lee roll moment coefficient with respect to the measurement results of the KKK wind tunnel. Both Audi and HDG measurements confirm very well the results of the KKK and lie within 10% difference. CSTB values are almost by 30% smaller than those measured in the KKK.

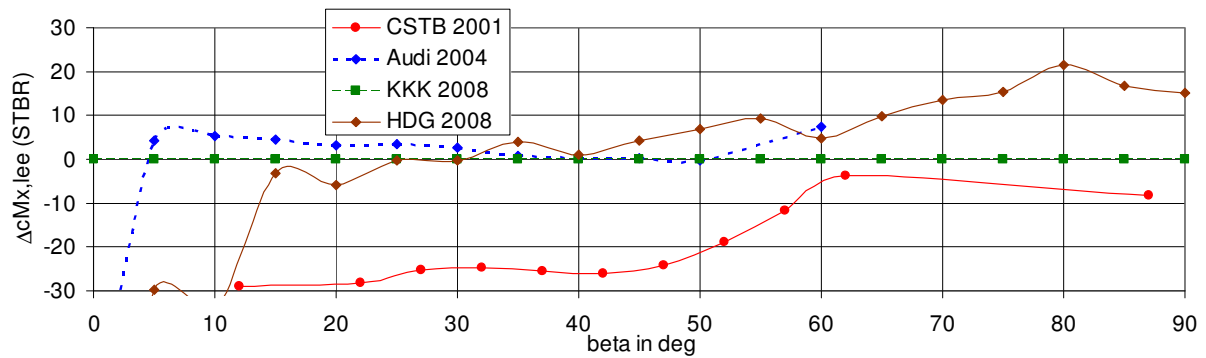


Figure 13: Comparison of lee roll moment coefficient – relative difference with respect to measurements in KKK, Single Track with Ballast and Rail

The shown comparisons lead to the conclusion that both for TFG and STBR, the measurements of the aerodynamic coefficients of the ICE 3 end car carried out in this campaign in the two wind tunnels KKK and HDG show very good agreement. They are also confirmed further by measurements in other wind tunnels with different model scales. The reproducibility of results is affirmed for both facilities and for both wind tunnel configurations.

## 7 SUMMARY AND CONCLUSIONS

Wind tunnel measurements of the ICE 3 end car benchmark vehicle were carried out in accordance with prEN 14067-6:2009 during a test campaign in 2008. The vehicle was modeled in two different scales and tested in two separate wind tunnels of the DNW facilities. The test program consisted for each wind tunnel of measurements on the two ground configurations true flat ground (TFG) and single track with ballast and rail (STBR). The measured aerodynamic coefficients of the ICE 3 end car were in good agreement for both the KKK wind tunnel and the HDG wind tunnel for a range of tests with varying Reynolds numbers for each respective test configuration. In particular the data sets for each wind tunnel measurement at Reynolds number  $10^6$  were compared to test results of other wind tunnel campaigns and the determined aerodynamic coefficients matched very well.

The good agreement of measured aerodynamic coefficients of the ICE 3 benchmark vehicle in several wind tunnels for both ground configurations affirmed the reproducibility of tests and test procedures of prEN 14067-6:2009. It was therefore deduced that the described wind tunnel measurements are valid as reference wind tunnel measurements.

The aerodynamic coefficients of the ICE 3 end car measured in the KKK wind tunnel at Reynolds number  $1 \cdot 10^6$  during the reference wind tunnel measurements were introduced to prEN 14067-6:2009 as reference values. In particular, it is a requirement of the European pre-standard that the values of the lee roll moment coefficient have to be met within a given accuracy for benchmark test carried out with the ICE 3 benchmark vehicle.

## 8 TABLES OF AERODYNAMIC COEFFICIENTS

The following four tables show the measured aerodynamic coefficients of the ICE 3 benchmark vehicle for the two sets of test configurations TFG and STBR in the two wind tunnels KKK and HDG at Reynolds number  $1 \cdot 10^6$ .

Angle of attack	C <sub>fx</sub>	C <sub>fy</sub>	C <sub>fz</sub>	C <sub>mx</sub>	C <sub>my</sub>	C <sub>mz</sub>	C <sub>mx,lee</sub>
deg	-	-	-	-	-	-	-
0	-0.169	0.007	0.060	0.006	-0.331	-0.024	-0.009
5	-0.219	0.418	-0.035	0.214	-0.496	0.936	0.222
10	-0.246	0.943	-0.428	0.500	-0.853	1.763	0.607
15	-0.277	1.563	-1.022	0.854	-1.196	2.420	1.109
20	-0.289	2.304	-1.774	1.274	-1.184	3.032	1.718
25	-0.274	3.161	-2.667	1.758	-0.451	3.613	2.425
30	-0.219	4.077	-3.380	2.261	0.951	3.954	3.106
35	-0.112	5.064	-3.881	2.792	2.293	4.056	3.763
40	0.031	6.120	-4.134	3.382	3.644	3.987	4.415
45	0.198	7.038	-4.260	3.911	3.981	4.560	4.976
50	0.369	7.912	-4.012	4.393	3.749	5.464	5.396
55	0.552	8.600	-4.214	4.829	4.066	5.957	5.882
60	0.744	8.733	-4.941	4.948	3.694	6.345	6.184
65	0.923	8.324	-5.690	4.672	3.579	6.387	6.095
70	1.060	7.926	-5.819	4.388	3.029	5.632	5.843
75	0.874	6.808	-5.037	3.613	-0.241	2.701	4.872
80	0.697	6.442	-4.724	3.433	-1.384	0.555	4.614
85	0.591	6.446	-3.860	3.485	0.954	-1.122	4.450
90	0.549	6.247	-4.462	3.390	-1.015	-2.089	4.506

Table 1: KKK TFG (Re=1 \* 10<sup>6</sup>)

Angle of attack	C <sub>fx</sub>	C <sub>fy</sub>	C <sub>fz</sub>	C <sub>mx</sub>	C <sub>my</sub>	C <sub>mz</sub>	C <sub>mx,lee</sub>
deg	-	-	-	-	-	-	-
0	-0.162	-0.026	0.037	-0.015	-0.332	-0.051	-0.024
5	-0.203	0.496	-0.151	0.264	-0.402	1.205	0.302
10	-0.232	1.072	-0.775	0.582	-0.505	2.278	0.776
15	-0.261	1.736	-1.662	0.952	-0.316	3.084	1.368
20	-0.257	2.543	-2.631	1.396	0.463	3.590	2.053
25	-0.189	3.432	-3.700	1.885	1.386	4.152	2.810
30	-0.101	4.455	-4.702	2.457	2.384	4.385	3.632
35	0.025	5.616	-5.638	3.115	3.109	4.533	4.524
40	0.200	6.806	-6.368	3.773	3.443	4.840	5.365
45	0.580	8.085	-6.979	4.480	4.099	5.460	6.225
50	0.954	8.655	-7.158	4.783	5.165	6.392	6.572
55	0.976	8.802	-6.543	4.873	5.899	5.538	6.508
60	1.041	8.511	-5.900	4.682	4.508	4.555	6.156
65	0.815	7.629	-5.270	4.157	1.756	2.276	5.474
70	0.600	7.346	-5.057	4.067	0.132	0.432	5.331
75	0.576	7.214	-5.008	4.014	-1.106	0.055	5.266
80	0.542	7.011	-4.685	3.895	-1.270	-0.754	5.066
85	0.470	6.869	-3.799	3.799	-0.201	-1.395	4.749
90	0.399	6.687	-3.794	3.695	-0.036	-2.281	4.643

Table 2: KKK STBR (Re=1 \* 10<sup>6</sup>)

Angle of attack	C <sub>fx</sub>	C <sub>fy</sub>	C <sub>fz</sub>	C <sub>mx</sub>	C <sub>my</sub>	C <sub>mz</sub>	C <sub>mx,lee</sub>
deg	-	-	-	-	-	-	-
0	-0.184	0.000	0.000	0.000	0.279	0.095	0.000
5	-0.254	0.384	-0.157	0.036	0.160	1.049	0.076
10	-0.290	0.862	-0.365	0.433	0.013	1.696	0.524
15	-0.326	1.542	-1.012	0.768	-0.437	2.681	1.021
20	-0.337	2.259	-1.591	1.177	-0.673	3.235	1.575
25	-0.338	3.110	-2.438	1.499	0.154	3.796	2.109
30	-0.318	4.212	-3.326	2.176	1.667	4.216	3.007
35	-0.231	5.332	-3.857	2.706	3.018	4.067	3.671
40	-0.121	6.204	-4.115	3.446	3.828	3.994	4.475
45	0.011	7.309	-4.904	4.092	4.444	4.306	5.318
50	0.181	8.330	-5.163	4.547	5.482	4.818	5.838
55	0.422	9.596	-4.831	5.304	7.462	5.204	6.512
60	0.609	9.761	-5.081	5.612	7.451	5.539	6.882
65	0.785	9.836	-5.943	5.571	7.073	5.769	7.057
70	1.078	9.375	-6.193	5.321	7.480	5.059	6.869
75	0.903	8.163	-4.782	4.540	4.482	2.576	5.736
80	0.589	7.542	-4.081	4.506	2.681	-0.217	5.527
85	0.467	7.393	-3.911	4.394	1.997	-1.433	5.371
90	0.379	7.358	-3.775	4.594	1.000	-2.333	5.537

Table 3: HDG TFG (Re=1 \* 10<sup>6</sup>)

Angle of attack	C <sub>fx</sub>	C <sub>fy</sub>	C <sub>fz</sub>	C <sub>mx</sub>	C <sub>my</sub>	C <sub>mz</sub>	C <sub>mx,lee</sub>
deg	-	-	-	-	-	-	-
0	-0.142	0.000	0.000	0.000	0.167	-0.192	0.000
5	-0.200	0.466	-0.163	0.172	0.116	1.187	0.212
10	-0.240	1.102	-0.753	0.320	-0.168	2.267	0.508
15	-0.245	1.759	-1.848	0.862	0.207	3.193	1.324
20	-0.247	2.561	-2.864	1.215	1.003	3.784	1.931
25	-0.243	3.556	-4.152	1.765	2.016	4.205	2.803
30	-0.193	4.723	-5.221	2.319	3.216	4.167	3.625
35	-0.072	6.008	-6.540	3.064	4.204	4.247	4.699
40	0.134	7.381	-7.265	3.610	4.550	4.683	5.426
45	0.419	8.602	-8.011	4.481	5.099	4.963	6.484
50	0.890	9.660	-8.149	4.983	7.026	5.716	7.020
55	1.016	10.450	-7.410	5.259	8.332	5.909	7.112
60	0.861	9.229	-5.869	4.980	6.404	3.551	6.447
65	0.811	8.441	-5.312	4.680	4.610	1.445	6.008
70	0.683	8.179	-5.377	4.707	3.297	0.456	6.051
75	0.594	8.127	-5.320	4.751	2.535	-0.971	6.081
80	0.472	8.052	-4.823	4.952	1.092	-2.044	6.158
85	0.424	7.424	-3.953	4.550	2.316	-1.928	5.538
90	0.264	7.399	-3.823	4.385	0.712	-2.403	5.341

Table 4: HDG STBR (Re=1 \* 10<sup>6</sup>)

## ACKNOWLEDGEMENTS

The wind tunnel tests were financially supported by a grant of the Bundesministerium für Wirtschaft (German ministry of economy) which is gratefully acknowledged.

The authors like to express their special thanks to DIN FSF for their support in terms of coordination and to the test team of DNW / DLR for running the tests.

## REFERENCES

- [1] “COMMISSION DECISION of 30 May 2002 concerning the technical specification for interoperability relating to the rolling stock subsystem of the trans-European high-speed rail system referred to in Article 6(1) of Directive 96/48/EC”, 2002/735/CE, *Official Journal of the European Union*, 212.09.2002
- [2] DB Netz AG. *Richtlinie 807.04 Bautechnik, Leit-, Signal- und Telekommunikationstechnik. Ausgewählte Maßnahmen und Anforderungen and das Gesamtsystem Fahrweg/Fahrzeug – Aerodynamik/Seitenwind*. DB Netz AG, Frankfurt a.M., 2006
- [3] “COMMISSION DECISION of 21 February 2008 concerning a technical specification for interoperability relating to the ‘rolling stock’ sub-system of the trans-European high-speed rail system”, 2008/232/CE, *Official Journal of the European Union*, 26.03.2008
- [4] prEN 14067-6:2009 Railway Applications – Part 6: Test procedures and requirements for cross wind assessment. CEN, Brussels, 2009
- [5] M. Schober, M. Weise, A. Orellano, P. Deeg, W. Wetzel. Wind Tunnel Investigation Of An ICE 3 On An Embankment. Proceedings of the BBAA VI, Milano, Italy, July 20-24, 2008
- [6] *Common DeuFraKo Research on Cross Wind Effects on High Speed Railway Operation 2001-2004*. Final Report of DeuFraKo Side Wind project. Edited by Thorsten Tielkes (Deutsche Bahn AG, DB Systemtechnik, Völckerstr. 5, D-80939 München) and Pierre-Etienne Gautier (SNCF, Direction de l’Innovation et de la Recherche, 45 Rue de Londres, F-75379 Paris), 2005
- [7] T. Kowalski, S. Loose, H. Richard. *Conformity Measurements for a Model of ICE 3 in the cryogenic wind tunnel cologne*. DLR internal report: DLR-IB 224-2009 A 27, Deutsches Zentrum für Luft- und Raumfahrttechnik DLR, Göttingen, 2009

## CROSS WIND SAFETY: OPERATION OF RAILWAY FREIGHT VEHICLES UNDER STRONG GUSTS

Nina Rüd\* and Thorsten Tielkes\*

\*VTZ 113 Aerodynamik und Klimatechnik  
Deutsche Bahn AG, Systemverbund, DB Systemtechnik, Völckerstr. 5, 80939 München, Germany  
e-mail: Nina.Rued@bahn.de, Thorsten.Tielkes@bahn.de

**Keywords:** Cross Wind, Railway, Freight Vehicle, Safety

**Abstract.** *Cross wind safety of rail operation has been a major topic for the last decades with respect to both high speed trains and also general rail traffic all over Europe. In Germany, operation of passenger railway traffic in cross wind has been regulated since the beginning of this century. However, freight vehicles have only become the focus of cross wind safety in recent years due to the introduction of modern, lightweight sliding-door wagons. In contrast, safety of cargo transport under the influence of strong winds in terms of fastening and fixation of loads has been studied a long time ago. Approaches to assess the stability of freight vehicles were developed analogue to those for vehicles of passenger traffic. These methods allow for appropriating the stability of vehicles in terms of characteristic wind curves (CWC) that show the permissible wind velocity in order to not succeed a pre-defined, still safe condition. On the basis of CWC the exposure of infrastructure to strong gusts can be evaluated and the combined safety of vehicle operation on a line can be assessed. Recent work on cross wind safety of freight vehicles focused on the advanced overall system of operational safety, i.e. the modelling of cross wind safety for the combination of vehicles and infrastructure. This document summarizes in depth the general safety assessment of railway freight vehicles operating under strong gusts.*

## 1 INTRODUCTION

Safety of railway operation under the influence of strong gusts has been a major topic for the last decades with respect to both high speed trains and also general rail traffic all over Europe. In Germany, operation of passenger railway operation in cross wind has been regulated since the beginning of this century [1]. It has been part of technical network access to the infrastructure of DB Netz AG and of both vehicle and infrastructure homologation due to setting guideline 80704 [2] in force in 2006 and the acceptance of the guideline as state of the art by the Eisenbahn-Bundesamt (EBA). Internationally, the homologation of high speed trains with respect to cross wind safety is regulated by the technical specification for interoperability of rolling stock (TSI HS RST) [3].

The focus on safe operation of railway freight vehicles is comparatively recent. In particular the introduction of modern, lightweight sliding-door wagons in the last decade, but also incidents such as the cargo train incident at Sarno, Italy in 2003 have brought attention to freight railway operation. With respect to international directives, the general issue for cross wind safety of freight wagons has been respected in terms of an open point in TSI Freight Wagon [4] and therefore relies on national regulations. In Germany, up to now there is no standard on evaluating cross wind safety of cargo vehicles and research is still ongoing, although guideline 80704 is prepared to also include specifications on cargo railway traffic. However, the related topic of safety of cargo transport under the influence of strong winds in terms of fastening and fixation of loads has been studied already in the early 1980s.

Assessment of safety of railway operation can generally be split in two main subdivisions. On the one hand there is the specific investigation of cross wind stability of vehicles and on the other hand there is the exposure of infrastructure to strong gusts. The analysis of risk in terms of combination of vehicle stability and infrastructure exposure together then delivers the overall assessment of operational safety. This report summarises research on application of these principles for evaluating cross wind safety of railway freight traffic.

## 2 CROSS WIND STABILITY OF RAILWAY FREIGHT VEHICLES

The stability of vehicles under cross wind is defined for passenger vehicles in terms of characteristic wind curves (CWC). The CWC give the permissible wind velocity a specific vehicle can withstand in order to not succeed a pre-defined, still safe condition. The calculation of CWC is determined by the aerodynamic and the vehicle dynamic characteristics of a vehicle. This principle is adopted analogously for the assessment of cross wind stability of railway freight vehicles.

### 2.1 Aerodynamics

Investigations of cross wind stability of rail freight vehicles were started at Deutsche Bahn AG (DB) in 2002 by conducting general wind tunnel tests as part of basis studies on vehicle aerodynamics. A range of freight wagons such as flat wagons with container and large sliding door wagons were investigated in terms of their cross wind sensitivity, examples are shown in Fig. (1).



Figure 1: Three examples of freight wagons investigated with respect to cross wind stability.

Tests with respect to parametrical influence of length and height and also sensitivity to test configurations were carried out. As a general conclusion it was found, that flat wagons carrying containers are relatively cross wind stable in comparison to light-weight wagons with a large side area such as the modern sliding door wagons, for example Hbbills 311 and Hbbins-tt 309.

Wind tunnel measurements and related requirements are established in both guideline 80704 [2] and in prEN14067-6:2009 [5] for passenger vehicles and locomotives. Tests are to be carried out in low turbulence wind tunnels for a reference configuration and a range of angles of attack. The reference configuration simulates the vehicle in its most cross wind sensitive train configuration in a typical infrastructure scenario. For freight wagons this configuration is equivalent to that of the investigated vehicle following an empty flat wagon.

For passenger vehicles with very high cross wind stability, wind tunnel test are not required, as a predictive equation for the lee roll moment coefficient has been provided. Analogously, the parameter studies carried out on freight wagons in wind tunnels by DB have resulted in a predictive equation for the aerodynamic coefficient of cross wind non-sensitive freight vehicles that do not require detailed wind tunnel investigation.

The research results and the requirements for rail freight vehicle aerodynamics have been introduced to the latest work of European standardisation.

## 2.2 Vehicle dynamics

There are several approaches to evaluate the vehicle dynamics behaviour under the influence of strong gusts. They vary from rather simple to very complex methods for passenger vehicles as described both in prEN14067-6 and guideline 80704. For the specific case of freight wagons, there are two methods available which have been applied for investigations and were found to be reasonable for this case. The simpler method is based on a 3 mass model which allows for the modelling of movement of centre of gravity due to uncompensated acceleration but ignores effects of unsymmetrical loads between front and aft of the vehicle. Therefore it is possible to apply this method in combination with the predictive equation for the lee roll moment coefficient. The second approach is more complex and includes these additional effects and thus requires a known full set of aerodynamic coefficients. Both methods use a quasi-static approach for modelling the wind scenario and evaluate the vehicle stability for a well-defined still-safe status. This status relates to the case of 90 % wheel unloading averaged over one bogie.

The research results for rail freight vehicle dynamics have been introduced to the latest work of European standardisation.

### 2.3 Limits / reference curves

The cross wind stability of vehicles operating for passenger traffic is evaluated by comparing the vehicle's CWC to reference curves given in TSI [3] and in the guideline 80704 [2]. A vehicle is determined to be sufficiently stable against cross wind if its CWC equals or surpasses the reference values. In [2] the requirements are defined in 5 different sets of CWC references as the vehicles are distinguished in different vehicle classes. With respect to freight railway operation this means analogously that a new class of vehicle types, i.e. freight wagons, is to be defined and that according reference CWC are to be established. The basis of this definition may be the CWC of known crosswind sensitive vehicles. Additionally, it may be acknowledged whether these vehicles have long operational experience or whether an additional margin is deemed necessary and sensible. For the definition of a reference CWC for freight vehicles, it has been decided that an extra-margin is not acceptable. The complete general process of definition of a reference curve is also determined partially by the overall limit of operational safety and by the balancing of requirements between vehicle and infrastructure aspects. Therefore an additional, generic margin on the vehicle reference curves would mean an extra burden on the infrastructure side that already exists and thus might need extra cross wind counter measures.

Recent work on this topic has identified a potential freight vehicle for delivering reference CWC. Checks for the infrastructure exposure as well as for the overall safety are based on these preliminary reference values. The assessment of freight vehicles is restricted for a range between  $80 \text{ km/h} < v_{\text{max}} \leq 160 \text{ km/h}$  in accordance with [5]. Freight wagons with higher maximum velocity are to be assessed according the rules for passenger vehicles and locomotives in [2].

## 3 CROSS WIND EXPOSURE OF INFRASTRUCTURE

The overall safety of railway vehicles under strong gusts is not only determined by the vehicle's inherit cross wind sensitivity but also by the exposure to gusts which the vehicle experiences on the infrastructure. Therefore methods are required that predict the probability of gusts along railway lines and also evaluate the risk of vehicles to be exposed to these gusts and thus the risk of overturning.

### 3.1 Infrastructure exposure

The method chosen in the German guideline 80704 for evaluating the exposure of infrastructure to strong gusts is based on a wind map approach [6]. As this method is independent of the type of vehicle investigated, this approach is also applicable for infrastructure lines that are used by freight traffic in order to determine the probability of gusts of predefined wind velocity levels.

### 3.2 CWC exceedance

The risk analysis of cross wind incidents is assessed by the parameter probability of CWC exceedance. This parameter is determined by the evaluation of probability of gust occurrence with respect to the vehicle's stability characteristic, i.e. the CWC. Therefore the probability of CWC exceedance is a risk indicating factor which relates to the still-safe vehicle condition but not to the actual overturning event. Research projects such as DeuFraKo Aerodynamics in Open Air [7] considered this risk analysis approach for both passenger and freight operation. Detailed investigations of several thousand km of railway lines for both traffic types showed that risks are correlated in terms of local points of interest with comparatively high probabili-



ties of CWC exceedance for both passenger and freight operation when using the same method for risk analysis.

## **4 SAFETY OF RAILWAY OPERATION OF FREIGHT VEHICLES**

### **4.1 Principles of Risk Assessment**

The risk assessment of railway operation under cross wind is based on the risk indicating parameter, the probability of CWC exceedance [8]. The underlying approach of risk assessment is based on the principle of “Nachweis mindestens gleicher Sicherheit” (EBO §2(1) ), i.e. verification of at least equivalent safety. This principle is related to the safety approach GAMAB (“globalement au moins aussi bon”). In this context, it is then applied in terms that existing railway operation is considered to be sufficiently safe with respect to cross wind, therefore new projects or products are justified by comparison with existing operation.

For passenger vehicles this concept is established on the evaluation of perceived collective risk and includes therefore among others the number of affected passengers, exposure time and an aversion factor. These factors can all be expressed as functions of velocity. Thus the permissible extent of still acceptable risk, i.e. the safety target, is expressed as a function of a limit value of probability of CWC exceedance and the actual vehicle velocity. The limit value of probability of CWC exceedance was determined for the most cross wind sensitive vehicle with long operational experience and therefore ensures that future projects comply with the principle of being at least as safe as existing railway operation.

For freight traffic, the individual risk outweighs the collective risk and therefore provides the basis for risk assessment. The general principles of risk modelling as used for passenger traffic are also applicable; however, the freight specific limit function for risk modelling is simpler due to reduced input parameters and velocity dependencies. This function also relies on the vehicle speed and a limit value of probability of CWC exceedance.

### **4.2 Safety target**

On the basis of a settled risk model for safety assessment, a safety target for railway freight operation under the influence of cross wind may be established. For this safety target a limit value of probability of CWC exceedance has to be fixed analogously to that for passenger traffic. The determination of this limit value can be approached by the application of several methods.

A first indication of the order of the limit value can be reached by comparing generally permissible risk rates of passenger and freight railway traffic. This kind of investigation have shown that accident rates of one to two orders of magnitude difference are easily found in praxis for several sorts of risks and thus generally higher hazard rates for freight wagons are acceptable since the consequences of an incident are much smaller than for passenger railway operation.

The approach most focused on for determining the limit value of CWC exceedance is based on finding the correct representative railway operation for verification of at least equivalent safety. This method is called “risk map” where the probabilities of CWC exceedance of operations for cross wind sensitive vehicles on highly frequented, gust exposed infrastructure is shown collectively. With this risk map it is possible to compare the local risks of both existing traffic with long operational experience and also future combinations of vehicles and lines. Therefore, it is possible to deduce the highest existing risk peaks and determining the probable limit values while checking for compliance of planned traffics.

The process of deducing a risk map for freight traffic and the applicable safety target is still ongoing. However, the relevant freight railway lines have been identified and first crosswind exposure checks have been carried out giving a first impression of the most exposed areas and a ballpark range of respective values of probability of CWC exceedance. This risk indicating parameter shows the difference between passenger and freight railway operation to be within the expected, acceptable range.

## 5 SUMMARY AND OUTLOOK

Recent work on cross wind safety of railway freight operation has made headway in the direction of assessing and regulating this safety topic. In particular, the methods for assessing freight vehicles in terms of aerodynamic and vehicle dynamic behaviour were developed, tested and settled, they were also included in the latest draft of EN 14067-6 which is expected to be published in 2009. Recent studies have shown that the infrastructure evaluation and the risk analysis itself are independent of the vehicle type and that the methods in use for passenger traffic are also applicable to freight operation. The first basis of risk assessment and the underlying principles has been tackled but there is still ongoing work in terms of setting limit values.

## ACKNOWLEDGEMENTS

The authors want to thank all members of the German cross wind forum “Arbeitskreis Seitenwind” that were involved in the recent investigations of railway freight vehicles.

## REFERENCES

- [1] Deutsche Bahn AG. *Handbuch für den Sicherheitsnachweis bei Seitenwind*. Forschungs- und Technologiezentrum München, TZF 102 Aerodynamik und Klimatechnik, München, 2001
- [2] DB Netz AG. *Richtlinie 807.04 Bautechnik, Leit-, Signal- und Telekommunikationstechnik. Ausgewählte Maßnahmen und Anforderungen an das Gesamtsystem Fahrweg/Fahrzeug – Aerodynamik/Seitenwind*. DB Netz AG, Frankfurt a.M., 2006
- [3] “COMMISSION DECISION of 21 February 2008 concerning a technical specification for interoperability relating to the ‘rolling stock’ sub-system of the trans-European high-speed rail system”, 2008/232/CE, *Official Journal of the European Union*, 26.03.2008
- [4] “COMMISSION DECISION of 28 July 2006 concerning the technical specification of interoperability relating to the subsystem ‘rolling stock —freight wagons’ of the trans-European conventional rail system”, 2006/861/EC, *Official Journal of the European Union*, 08.12.2006
- [5] prEN 14067-6:2009 Railway Applications – Part 6: Test procedures and requirements for cross wind assessment. CEN, Brussels, 2009.
- [6] J. Herb, U. Hoppmann, C. Heine, T. Tielkes. A new approach to estimate the wind speed probability distribution along a railway track based on international standards. *Journal of Wind Engineering and Industrial Aerodynamics*, **95**, 1097-1113, 2007
- [7] *DeuFraKo Project « Aerodynamics in Open Air (AOA) », WP 2 Cross Wind Issues, Final report*. Edited by E. Masson, Société Nationale des Chemins de fer français, Diréc-

tion de l'Innovation et de la Recherche, 45 Rue de Londres, F-75379 Paris; Elisa.Masson@sncf.fr), 2008.

- [8] T. Tielkes, C. Heine, M. Möller, J. Driller. *A probabilistic approach to Safeguard Cross Wind Safety of Passenger Railway Operation in Germany: The new DB Guideline Ril 80704*. Proceedings of the 8th World Congress on Railway Research (WCRR 2008), May 18-22, 2008. Seoul, Korea, 2008

## **Railway ballast flying phenomenon : from numerical computations toward risk assesment**

**Saussine Gilles<sup>\*</sup>, Masson Elisa<sup>\*</sup>, Thomas-Jean Jacques<sup>\*</sup>,**

**Paradot Nicolas<sup>†</sup>, Allain Eliane<sup>†</sup>**

**Josse Frédéric<sup>#</sup>**

<sup>\*</sup>Innovation and Reasearch Department of SNCF,  
45 rue de Londres, 75359 Paris Cedex 08, France  
e-mail: gilles.saussine@sncf.fr,

<sup>†</sup> SNCF, Rolling Stock Engineering Center,  
4 Allée des Gémeaux, 72100 Le Mans, France

<sup>#</sup> SNCF, Infrastructure Departemnt,  
6, avenue François Mitterrand, 93574 La Plaine St Denis, France

**Keywords:** flying ballast phenomenon, fiability, discrete element approach, railway ballast

***Abstract.** The phenomenon of ballast projection and the assessment of the overturning risk caused by an intense cross wind gusts are currently two subjects of risk evaluation because there is a direct impact on the safety and the reliability of commercial railway operation. The different operators which developed observing the new phenomenon to ballast projection under regular meteorological conditions identified a need to increase the knowledge about this phenomenon and the consequences on railway infrastructure and vehicle.*

*Our present work is devoted to present the application of the Stress Strength Interference Analysis approach to the ballast flying phenomenon in order to propose a methodology to evaluate the risk of ballast projection for high operation and to evaluate the degradation rate of railway infrastructure and vehicle maintenance due to this phenomenon.*

## 1 INTRODUCTION

The dropping of ice from the train into the ballast bed under winter conditions can cause ballast projection and this mechanism is known in Europe since the beginning of the 1980s with the start of railtraffic up to speeds of 200 *km/h*. Secondly foreign parts in the track-bed (e.g. cover plates) can be aerodynamically lifted during the train passage and cause single ballast stones to be moved after hitting the track-bed. The last mechanism came into focus with the start of high-speed traffic up to 350 *km/h*. Here only the aerodynamics loads on the track-bed induced by the passing train can cause the setting free of ballast stones [8,5].

Several investigations have been performed to characterize the ballast collision process, the lift under aerodynamic load and the air flow between the underbelly region of the train and the track bed. But the main difficulty is to take into account the variability of the different parameters involve into this phenomenon : track configuration, the proportion of grains on sleepers, the type of train, the speed running.

In this paper we proposed a global method for risk assesment of the ballast flying phenomenon in order to take into account :

- the properties of flow field of different type of train, by in situ measurements,
- the prediction of the number of ballast flying stones by numerical simulations,
- the risk assesment by applying the Stress Strength Interference Analysis.

We present in the first part the three-dimensional discrete element approach and fluid interaction. Then the second part present some numerical results and a relevant parameter to evaluate the ballast flying phenomenon. The last part is the application of the fiabilist approach to flying ballast phenomenon.

## 2 DISCRETE ELEMENT APPROACH

### 2.1 Numerical procedure

The simulations were carried out by means of the contact dynamics (CD) method with irregular polyhedral particles. In this section we present the properties of this numerical method and compare it to a more classical numerical approach molecular dynamics (MD).

The CD method is based on implicit time integration and nonsmooth formulation of mutual exclusion and dry friction between particles in case of contact [1,2,4]. The equation of motion for each particle are written in term of differential inclusions in which velocity jumps replace accelerations. The unilateral contact interactions and Coulomb friction law are represented as set-valued force laws according to convex analysis.

The approach is characterized by a time-stepping approximation, and in this work we use a time integrator like theta - method. The implementation of the time-stepping scheme requires that the contacts taken into account in the considered step are geometrically described: definition of contact normal and contact location.

The contact law is define by a nonsmooth relation between the normal force and the normal relative velocity, signorini conditions, and the Coulomb friction law friction force and sliding

velocity at a contact are not related together via a mono-valued function. The collision law is take into account by introduce a restitution coefficient which relate the relative velocities before and after contact. In our simulations where we consider a dense packing, we choose 0 for the normal and tangent restitution coefficient.

For a collection of particles, for each time step, the aim is to solve the core problem in order to find for each contact between particles the local relative velocities and the local reactions. This interaction problem is solve by an iterative solver called non-linear Gauss-Seidel which consist to solve a single contact problem with other contact forces treated as known and consequently updating interaction, until a certain convergence criterion is fulfilled.

At a given step of evolution, all kinematics constraints implied by enduring contacts and the possible rolling of some particles over others are *simultaneously* taken into account, together with the equations of dynamics, in order to determine all velocities and contact forces in the system. The method is thus able to deal properly with the *non local* character of the momentum transfers, resulting from the perfect rigidity of particles in contact. The CD method makes no difference between smooth evolution of a system of rigid particles during one time step and nonsmooth evolutions in time due to collisions or dry friction effects.

The MD-like methods are based on regularization schemes where impenetrability is approximated by a steep repulsive potential and Coulomb's law by a viscous- or elastic-regularized friction law, to which smooth computation methods can be applied. In this case the choice of a viscous parameter or elastic properties is not easy in particular with particles with irregular shape. This regularization implies of choice of smaller time step in order to preserve the stability of the integration scheme comparing to the CD approach. The uniqueness is not guaranteed by CD approach for perfectly rigid particles in absolute terms. However, by initializing each step of calculation with the forces calculated in the preceding step, the set of admissible solutions shrinks to fluctuations which are basically below the numerical resolution. In MD-based simulations, this "force history" is encoded by construction in the particle positions.

We used LMGC90 which is a multipurpose software developed in Montpellier, capable of modeling a collection of deformable or undeformable particles of various shapes (spherical, polyhedral, or polygonal) by different algorithms [3].

## 2.2 Numerical parameters

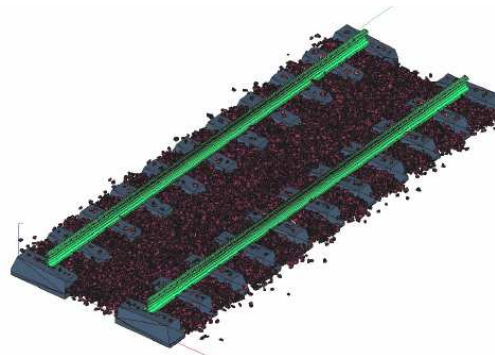


Figure 1 : Portion of track with bibloc sleepers.

The numerical simulations take into account a set of rigid grains with a polyhedral shape which come from digitalization of railway ballast grains. The considered sample presented on

figure 1 contains nearly 28000 particles which respect the ballast granulometry, 25/50 mm. The density is fixed to  $2700 \text{ kg/m}^3$ . The rail respect the geometry of rail UIC60 like sleepers are considered as rigid bodies for our computations.

The particles which represent ballast grains are initially placed on grid base the sleepers positions. The grains are deposited under gravity on rigid plan in order to obtain a ballast of 5 cm of thickness. Then some grains are deposited on the sleepers in order to analyse the worst configuration for ballast projection phenomenon.

The coefficient of friction between the particles is fixed to 1 with a restitution coefficient of 0.4.

For the numerical simulation campaign we considered that grains deposited on the sleepers are independent, i.e. there is no interaction between them. This choice has been motivated to obtain statistical results about the motion of grains depending of position, shape.

### 2.3 Fluid interaction : a low coupling approach

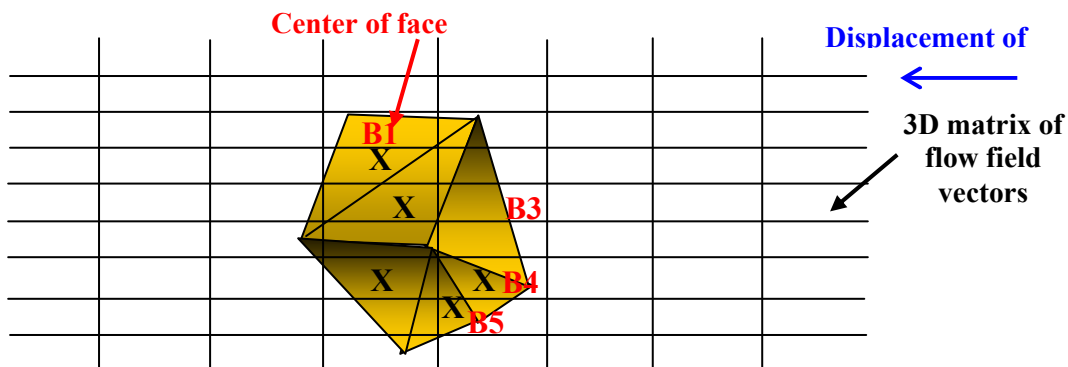


Figure 2 : General framework

The aim of coupling aerodynamic loads on track and mechanical numerical computations is to characterize the motion of ballast grains over several different aerodynamic fluid. The numerical modeling of the behaviour of a collection of rigid bodies under the action of fluid is a tricky problem.

The approach proposed is to consider the contribution of fluid as an external loading on grains, like the gravity field, then to solve the interaction problem between grains by Non Smooth Contact Dynamics approach. The aerodynamic fluid can be described as field of speed vectors represented by a three-dimensional matrix define by the space resolution corresponding to the average diameter of ballast grains for horizontal plan, 0,05 m, and 0,005 m for the vertical part.

With the aerodynamic description, the algorithm to compute the external effort exerted on a grains follows the different steps :

- for each facet of grains number  $i$  :
  - o from the coordinates of the barycenter of face, we obtain the corresponding velocity vector  $\underline{V}$  of the flow field

- the projected area  $S$  of the facet on a perpendicular plan to the velocity vector is computed,
- then the force exerted at the barycenter (eq. 1) of the face with a normal  $\underline{n}$  is computed :

$$\underline{F}_{Bi} = \left( \frac{1}{2} \times \rho \times \|V\|^2 \times S \right) \cdot -\underline{n} \quad (1)$$

- The torque of the grains considered is actualized with the effort and the momentum.

In order to represent the motion of the flow field on the track, the numerical simulation to impose a displacement of the matrix corresponding to the running speed, and for each time step, compute the effort exerted on the grains and their motion by the resolution of the interaction problem. With this approach it is possible to have a statistical analysis of ballast grains motion for different flow field.

### 3 NUMERICAL SIMULATIONS OF BALLAST FLYING

The ballast flying phenomenon has been identified as a sporadic problem which depend of the railway track configuration, the type of trains and the running conditions. The aim of the numerical computation is to investigate the motion of grains under aerodynamic field which come from CFD or measurements and to proposed a relevant parameter to describe the displacement of grains and the flow field characteristics.

#### 3.1 Flow Field description

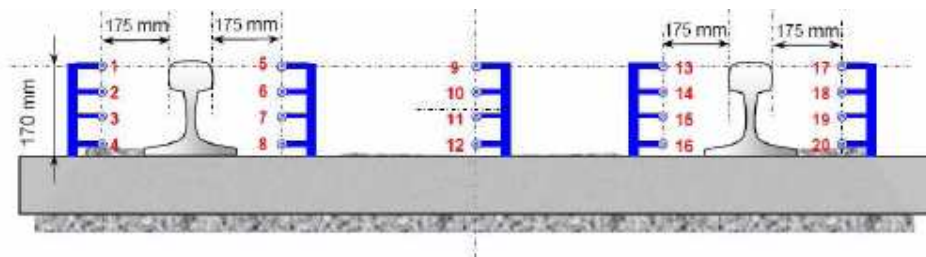


Figure 3 : Measurements setup with 20 pitot tubes.

The flow field has been constructed from in situ measurements . The measurements has been acquired from the set up presented on Fig. 3 composed of a set of 20 pitot tubes with a frame rate 2400 Hz. This setup has been implemented on the track during commercial running of trains in order to have a statistical description of flow field. These choices has been motivated from the conclusion of the report of the Deufrako project AOA. [5].

From the measurements a matrix representing the flow field has been created :

- 0,05 m againts the axis X,
- 0,05 m axis Y,
- 0,005 m on Z axis,

The interpolation between pitot 8, 12 and 16 has been considered has linear and the speed vector are equal to zero for the rail volume.



### 3.2 Validations

N° test	Speed (km/h)	Grains Wind tunnel	Grains simulations	N° test	Speed (km/h)	Grains Wind tunnel	Grains simulations
1	210	0	0	15	240	2	1
2	210	0	0	19	260	1	3
3	240	0	0	20	260	7	10
4	240	2	0	21	260	10	1
5	240	2	0	22	260	4	2
6	240	1	0	23	260	2	9
7	240	0	3	24	260	3	0
8	240	0	3	25	260	1	3
9	240	1	0	30	260	4	3
10	240	2	11	35	260	9	0

Figure 4 : Comparison between experimental test and numerical simulations [4].

The experimental setup proposed in AOA [5] represented a portion of ballast track with monoblock sleepers, with rail UIC60, and ballast grains which respect the French granularity 25/50 mm. The ballasted track is placed at 40 cm from the ground in order to avoid the effect of the boundary layer of the wind tunnel. The ballast flying phenomena is influenced by the gust effect. In order to take into account the fast rise of air speed, a special shutter system was developed, controlled by a pneumatic jack.

In order to characterize the gust, fast Pitot tubes have been used and a comparison in order to check the results has been made with hot wire anemometer (Fig. 4.5.4). We can note a strongly turbulent flow near the ballast layer and a good correlation of the gust signal for the two measurement systems. With this experimental setup a study has been carried on the influence of flow speed, position of ballast layer, and vibration of sleeper on the ballast flying phenomena. The statistical processing for each test has been done on the displacement of the grains.

From the pitot tube measurements, numerical simulations has been performed with the same track configuration and a flow field description store during the experimental tests. The results are presented on the figure 4. We can notice a good correlation for the number of ejected grains. The difference can be from the numerical model because the grain position are different between simulation and experimental setup. We have observed that after 3 or 4 gust there is no ejection.

### 3.3 Numerical simulations

The numerical simulations have been performed over 200 different cases for a ballast track configuration and 608 different shapes of grains on the 37 ballast sleepers.

From the numerical simulations we can calculate after the passage the aerodynamic matrix :

- the percentage of displaced grains,
- for grains which a displacement of 10 cm,
- the properties of the ejected grains,
- the number of grains which are ejected from the ballast bed.

From the whole simulation which have been performed, only 2 % of the total displaced grains have been considered as ejected.

### 3.4 A relevant parameter for evaluated flying ballast phenomenon

From the numerical simulations and in situ measurements, we have investigated several parameters which can describe the number of displaced grains during one train passage. The general idea is to propose a parameter which can be calculated from the characteristic of the flow field and investigated for each measurement the correlation with the percentage of grains which have been moved over 10 cm.

The relevant parameter identified is the sum of signal power for the whole of pitot tubes :

$$P_{Tot} = \frac{1}{(t_2 - t_1)} \sum_{i=1}^N \int_{t_1}^{t_2} \|V(t)\|^2 dt \quad (2)$$

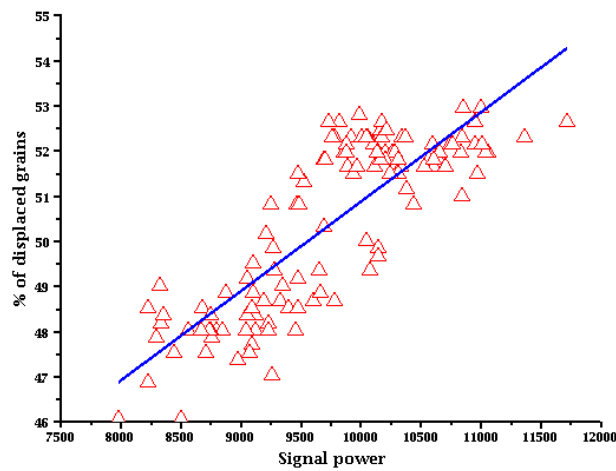


Figure 5 : relation between signal power and percentage of displaced grains.

From the numerical simulation coupling granular approach and fluid interaction, we can exhibit that a linear relation between  $P_{tot}$  (eq. 2) and the percentage of displaced grains can be a good approximation with a correlation 82 % (Fig. 5).

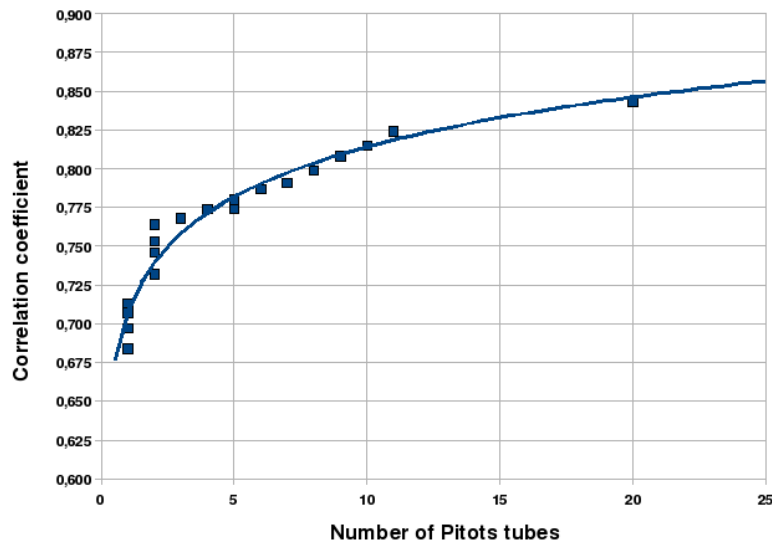


Figure 6 : Evolution of the correlation coefficient as a function of number of pitot tubes.

This correlation has been identified as a function of the number of pitot tubes (Fig. 5). But this relation is not relevant to describe the risk of ballast flying phenomenon, because for a range signal power we have an intrinsic variability which can be explained by the train properties, the track configuration.

#### 4 STRESS STRENGTH INTERFERENCE ANALYSIS FOR RISK ASSESSMENT

The risk assessment of flying ballast needs to take into account the variability of the properties of the track, the variability of the trains. From paragraph 3.4 we have identified a parameter which is relevant to evaluate the potential of a flow field to displace a quantity of grains. For a risk analysis the variability of this parameter, the signal power, has to be considered to evaluate the probability of ballast flying occurring.

In this work we proposed to apply the general approach of Stress Strength Interference Analysis on a track composed of block sleepers and grains deposited on the sleepers.

##### 4.1 Stress strength interference analysis

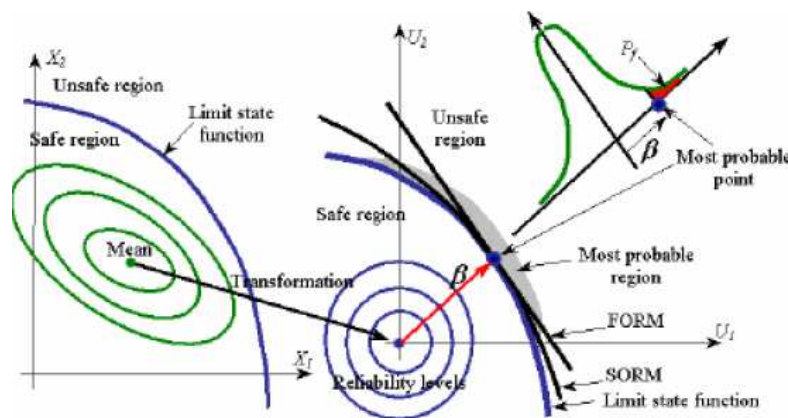


Figure 7 : Scheme of the Stress Strength Interference Analysis.

The Stress Strength Interference Analysis approach is an evaluation of the probabilistic interaction between two independent probability density function. This interference can be assumed as a failure probability for the considered problem. The general framework of the methods is summarize on the figure 6 .

The probability density function of Stress  $S_T$  and the pdf of Strength,  $S_R$  are considered as normal gaussian laws,

$$S_T \in N(\mu, \sigma), S_R \in N(\mu, \sigma) \tag{3}$$

The failure probability of these pdf can be evaluated from the following formula :

$$P_f = \int_0^{\infty} f_{S_T}(x) F_{S_R}(x) dx \tag{4}$$

with  $f_{S_T}$  the probability density function of Stress and  $F_{S_R}$  the repartition function of Strength. If we considered that the two probability density function are gaussian then we have the following analytnc formula to calculate the failure probability by considering  $Z = S_R - S_T$  :

$$\mu_z = \mu_{S_R} - \mu_{S_T}, \sigma_z = \sigma_{S_R} - \sigma_{S_T} \tag{5}$$

the standart deviation and the mean of the distribution can be write like (eq. 5) , then the probability of failure is defined as (eq. 6):

$$P_d = P(Z < 0) = P(\mu_z + U\sigma_z < 0) = P(U < \frac{\mu_{S_T} - \mu - S_R}{\sqrt{\sigma_{S_R}^2 + \sigma_{S_T}^2}}) \tag{6}$$

which can calculate by the following formula if Z is a gaussian distribution, the probability of failure with the following formula (eq. 7) :

$$P_d = \frac{1}{\sqrt{2\pi}} \int_{-\infty}^{\frac{\mu_z}{\sigma_z}} \exp(-\frac{x^2}{2}) dx \tag{7}$$

For the ballast flying phenomenon, we proposed that we characterize the Stress by the variability of the Signal Power and the Strength by the results of the numerical simulations.

#### 4.2 Definition of stress

The relevant parameter to evaluate the potential of train to generate flying ballast phenome-non has been identified as signal power of the air flow field from in situ measurements or

CFD computation. The stress apply on the one track can be define as the probability dense function of the signal power for a set of measurements. We adopt the following notation :

- SG, the general stress apply on a track by all type of trains and any range of circulation speed,
- S[type of train, velocity, track configuration], the stress apply by one type of train and defined conditions.

So the general stress is easily evaluated by calculate for each measurements, the corresponding signal power. Then we can deduce the pdf of general stress characterize by the normal distribution with parameters  $(\mu_{SG}, \sigma_{SG})$ .

### 4.3 Definition of strength

The strength can be defined as the capacity of track to limit the ballast flying phenomenon. From this consideration, we can consider the results of numerical simulation coupling aerodynamic field and discrete elements approach.

We have identified in 3.4 that the percentage of displaced grains can be linear relation with the signal power. We assume that each couple (signal power, % of displaced) follow the same linear relation, and we can deduced the probability dense function of the signal power corresponding to a maximum of displaced grains of X %.

The strength is define as the probability dense function of signal power which has a fixed percentage of displaced grains X :

$$S_{R,X\%} \in N(\mu, \sigma),,$$

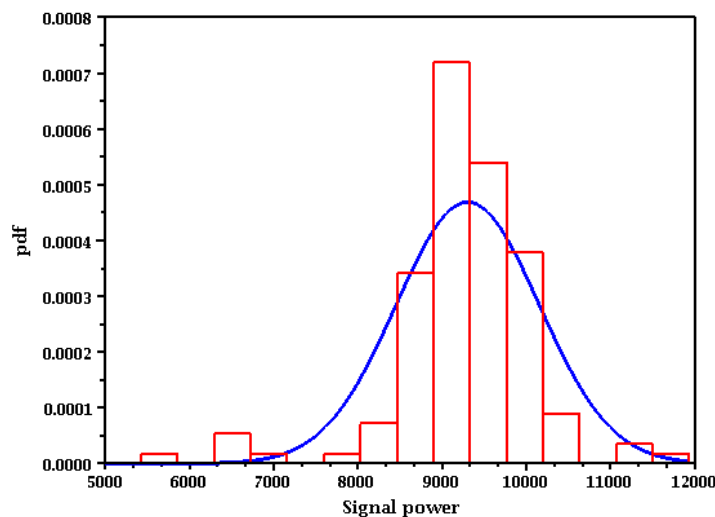


Figure 8 : Global Strength of the track for maximum of 10 % of displaced grains.

In our case from the general stress apply on a track evaluated from in situ measurements, we can deduced the Strength of the track to limit at most 10 % of displaced grains (Fig. 8).

#### 4.4 Example

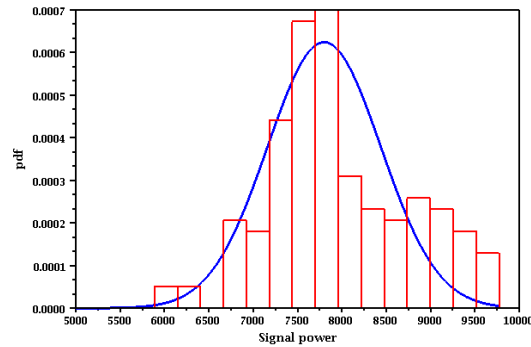


Figure 9 : Stress apply by one type of trains for 300 km/h.

On the figure 9, we present the probability dense function of Stress (Signal Power) of one type of trains for a range of speed of 300 km/h ( $\pm 2\%$ ) evaluated from 53 measurements with 11 pitot tubes.

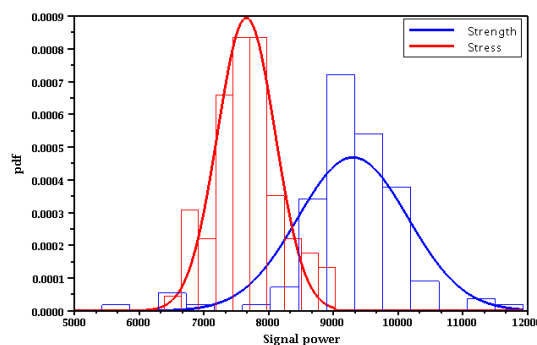


Figure 10 : Stress and Strength.

On the figure 10, we plot the Stress applied and the Strength of the track, which can be assimilate to gaussian distributions. Then we can apply the formula from the equation 7 and we found that the risk to displaced 10 % of grains more than 10 cm is about 4 %.

Then we can apply this results to the following case :

- a track composed of bibloc sleepers and ballast level at the top of the sleepers,
- 100 km of track and 1 grains every 160 m,
- for a running speed of 300 km/h,

the risk is to have 1 ejected grains every 8 running of trains over the 100 km/h considered.

## 5 CONCLUSIONS

The number of incidents is not numerous but the ballast flying phenomenon can impact the maintenance of the track and/or of the trains. From the state of the art, we have shown that this phenomenon is strongly dependent of the train type, the track, and the running speed. But it clearly a sporadic phenomenon which is difficult to predict or to analyze under real conditions.

The ballast flying phenomenon is difficult to handle because it depends of a lot of different parameters and their variability. From the whole investigations we propose a global method called Stress Strength Interference Analysis which can be applied by considering a relevant indicator to evaluate the ballast flying risk.

From the low coupling approach proposed between discrete element methods and fluid interaction we have indentified that the signal power from pitot tubes is a relevant parameter for ballast flying.

From the characterization of the variability of the signal power we can applied the Stress Strength Interference Analysis for risk assesment of ballast flying. This global approach allows to investigate the influence of track configuration, the type of trains, the speed on the ballast flying risk and to evaluated the efficiency of some solutions.

### ACKNOWLEDGEMENTS

The authors would like to acknowledge the team of LMGC90 software ([www.lmgc.univ-montp2.fr/LMGC90](http://www.lmgc.univ-montp2.fr/LMGC90)), V. Gaillot for the technical and scientific developments of the general method and the team who has performed the in situ measurements.

### REFERENCES

- [1] J.J. Moreau, "An introduction to unilateral dynamics in Novel approaches in civil engineering, *Lecture Notes in Applied and Computational Mechanics*", Frémond, M. and Maceri, F., Springer-Verlag 1-46.
- [2] J. Moreau, "Some numerical methods in multibody dynamics: application to granular materials." *European J. Mech. A Solids*, 13(4, suppl.), pp. 93-114, 1994. *Second European Solid Mechanics Conference* (Genoa, 1994).
- [3] 4 F. Dubois and M. Renouf Numerical strategies software architecture to the modelling of dynamical systems in interaction. Application to multibody dynamics, in *Multibody 2007 proceedings*, 25-28 June 2007 - Politecnico di Milano, Milano, Italy
- [4] G. Saussine, C. Cholet, P.E. Gautier, F. Dubois, C. Bohatier, J.J. Moreau, Modelling ballast behaviour under dynamic loading. Part 1: A 2D polygonal discrete element method approach, *Comput. Methods Appl. Mech. Eng.* 195 (2006) 2841 - 2859.
- [5] Hans-Jakob Kaltenbach, WP 1 Underfloor Aerodynamics Summary Report, DeuFraKo Project „Aerodynamics in Open Air“ (AOA).
- [6] J.J. Thomas, "Approche fiabiliste du dimensionnement dans l'industrie automobile.", seminar,
- [7] Jhojan Enrique Rojas Flores, Felipe Antonio Chegury Viana, Domingos Alves Rade & Valder Steffen, Jr. A procedure for structural reliability analysis based on finite element modeling, IV Congresso Nacional de Engenharia Mecânica 22 a 25 de Agosto 2006, Recife-PE.
- [8] KWON – PARK : An experimental study on the relationship between ballast-flying phenomenon and strong wind under high-speed train, Korea Railroad Research Institute, 2006,

## DYNAMICS OF FLOW IN WAKE BEHIND AHMED BODY

Václav Uruba

Fluid Dynamics Department  
Institute of Thermomechanics AS CR, v.v.i., Dolejškova 5, 182 00 Praha 8, Czech Republic  
e-mail: uruba@it.cas.cz

**Keywords:** Ahmed body, wake, dynamics, TR PIV, POD, BOD, POPs.

**Abstract.** *The flow-field in the wake of 2D Ahmed body was studied experimentally. The study is oriented on unsteady behavior of the free shear layers arising in the wake as well as on the wake itself. Both time-mean structures and typical dynamical structures in the wake are presented. The experimental data acquired using time resolved PIV method involves both temporal and spatial correlations. Special attention was paid to dynamics of flow near the separation and to evolution of the free shear layer limiting the wake. The flow-field was analyzed using the Bi-Orthogonal Decomposition method as a generalization of the Proper Orthogonal Decomposition. Then the dynamical energetic modes were identified by application of Principal Oscillation Patterns method. The provided information could be used for construction of a low-dimensional dynamic model of the flow involving physics behind the phenomenon. Such a dynamical model will be employed for improving separation control strategy based on periodical excitation of the flow.*



## 1 INTRODUCTION

The Ahmed body is a typical bluff body with separated boundary layer generating wake resulting into pressure drag. The boundary layer separation process is very important, however the separation point could be fixed on the sharp edge in the case of the Ahmed body. Knowledge of the wake dynamical structure is essential from the point of view of possible flow control. The modern control methods involve periodical process (synthetic jets, plasma actuation, etc.) modifying behavior of vortical structures in the wake (see e.g. [3]).

Our paper present detailed analysis of the flow downstream the Ahmed body from experimental data obtained by time resolved PIV method. Special attention was paid to dynamics of flow near the separation and to evolution of the free shear layer limiting the wake.

Several researchers have worked on the experiments and numerical modeling of the flow over so called Ahmed body. To develop turbulence models for complex geometry cases, a simplified car model, known as the Ahmed body, has been tested by Ahmed and his coworkers in the early 1980s – see e.g. [1]. The Ahmed body is made up of a round front part, a moveable slant plane placed in the rear of the body to study the separation phenomena at different angles, and a rectangular box, which connects the front part and the rear slant plane.

Two configurations with slant angles of 25 deg and 35 deg are considered as a test case. In the experiment perform by the Ahmed, flow velocity was taken 60 m/s, Reynolds number was 4.29 million based on the model length.

## 2 METHODS

Apparently, the phenomenon in question is substantially 3D and highly dynamical in nature in the same time. To analyse such a phenomenon, appropriate methods of analysis should be applied on experimental data. Let suppose availability of appropriate experimental data set representing both time and space correlations in the separation zone. Actually, no universal methods for such analysis are available.

### 2.1 Methods Based on POD

The Proper Orthogonal Decomposition (POD) method has applications in almost any scientific field where extended dynamical systems are involved. This fact accounts for the frequency of POD's discovery. Pearson 1901, Hotelling 1933, Kosambi 1943, Loeve 1945, Karhunen 1946, Kosambi 1943, Pougachev 1953 and Obukhov 1954 have all been credited with independent discovery of POD under one of its many titles, which include Principle Component Analysis, Karhunen-Loeve Decomposition or Expansion, Principle Factor Analysis, Hotelling Transform, and collective coordinates. Details could be found in [6].

Recently, the POD has been widely used in studies of turbulence. Historically, it was introduced in the context of turbulence by Lumley [5] as an objective definition of what was previously called big eddies and which is now widely known as coherent structures.

The POD method is optimal in sense that the series of eigenmodes converges more rapidly (in quadratic mean) than any other representation. Convergence is very fast in the flows in which large coherent structures contain a major fraction of the total kinetic energy

An advantage of the method is its objectivity and lack of bias. Given a realization of an inhomogeneous, energy-integrable velocity field, it consists of projecting the random field on a candidate structure, and selecting the structure, which maximizes the projection in quadratic mean. In other words, we are interested in the structure which is the best correlated with the random, energy-integrable field. More precisely, given an ensemble of realizations of the field, the purpose is to find the structure, which is the best, correlated with all the elements of the ensemble. Thus, a statistical measure of the magnitude of the projection, which can be given

by the mean square of its absolute value, is maximized. The calculus of variations reduces this problem of maximization to a Fredholm integral equation of the first kind whose symmetric kernel is the autocorrelation matrix. The properties of this integral equation are given by Hilbert Schmidt theory. There is denumerable set of eigenfunctions (structures). The eigenfunctions form a complete orthogonal set, which means that the random field can be reconstructed. The coefficients are uncorrelated and their mean square values are the eigenvalues themselves. The Kernel can be expanded in a uniformly and absolutely convergent series of the eigenfunctions and the turbulent kinetic energy is the sum of the eigenvalues. Thus every structure makes an independent contribution to the kinetic energy and Reynolds stress.

The method for energetic modes evaluation is based on correlation matrix  $\mathbf{R}$  analysis

$$\mathbf{R} = \langle \mathbf{u}(t) \mathbf{u}^T(t) \rangle, \quad (1)$$

where  $\mathbf{u}(t)$  is vector of velocities or velocity fluctuations. Modes are defined as the correlation matrix eigenvectors, the corresponding eigenvalues indicate energetic content.

The next step Bi-Orthogonal Decomposition (BOD) representing itself an extension of the POD. While POD analyses data in spatial domain only, the BOD performs spatiotemporal decomposition.

Aubry [2] presented the BOD as a deterministic analysis tool for complex spatiotemporal signals. First, a complete two-dimensional decomposition was performed. These decompositions were based on two-point temporal and spatial velocity correlations. A set of orthogonal spatial (“topos”) and temporal (“chronos”) eigenmodes are to be computed to allow the expansion of the velocity field.

The orthogonal decomposition is optimal in sense of a fast convergence of the expansion with a small number of terms. It should be noticed that the BOD introduces a time-space separation in the velocity field expansion. While the classic orthogonal decomposition POD is based on full two-point space-time correlations and entails space and time-dependent eigenmodes, BOD is closer to analytical and numerical studies where the velocity field is naturally expanded over products of spatial functions and temporal functions.

The decomposition methods allows studying the energy and entropy distribution in both time and space domain. In addition, truncation of the reconstruction formula neglecting high-order low energy content allows us to study dynamics of the given system using discrete methods of dynamical systems analysis in state space. Thus, the low-dimensional model of the real flow optimal from the energetic point of view is obtained. This means, that even a few lower order (that is high-energy) modes could capture principal properties of the entire system dynamics.

## 2.2 Dynamical Analysis – POPs

The Principal Oscillation Patterns (POPs) decomposition is based on modal structures based on temporal or spatial linear evolution dynamics. Each mode is characterized by a complex frequency involving information on frequency, phase and growth/decay information. On the other hand, the POPs analysis is unable to resolve standing oscillations.

The basis of the POPs analysis was formulated by Hasselmann [4] for discrete Markov processes in linearized dynamical systems driven by white noise with application in climatology. The POPs theory is a special case of more general Principal Interaction Patterns (PIPs) method for nonlinear dynamical systems.

In the POPs approach the fluctuating part of Navier-Stokes equation is modelled by Langevin equation for the linear Markov process:

$$\frac{d\mathbf{u}(t)}{dt} = \mathbf{A} \cdot \mathbf{u}(t) + \xi, \quad (2)$$

where  $\mathbf{u}(t)$  is vector of velocity fluctuations,  $\mathbf{A}$  is the deterministic feedback matrix,  $\xi$  is noise driving the system which could be interpreted as influence of smaller, unresolved scales. The equation (2) could be rewritten for time lag  $\tau$  as followed

$$\mathbf{u}(t + \tau) = \mathbf{B} \cdot \mathbf{u}(t) + \xi. \quad (3)$$

Then the POPs are the eigenfunctions of the matrix  $\mathbf{B}$ . In other words, the POPs are the empirically computed eigenmodes of the system. The Green function  $\mathbf{G}$  could be identified

$$\mathbf{G}(\tau) = \exp(\mathbf{B}\tau) = \langle \mathbf{u}(t + \tau) \mathbf{u}^T(t) \rangle \langle \mathbf{u}(t) \mathbf{u}^T(t) \rangle^{-1}. \quad (4)$$

The eigenvalues  $g_k$  of the Green function  $\mathbf{G}$  are related to eigenvalues  $\beta_k$  of the feedback matrix  $\mathbf{B}$  as follows:

$$g_k \equiv \exp(\beta_k \tau). \quad (5)$$

The real part of eigenvalues  $\beta_k$  characterizes the decay e-fold time  $\tau_e$  of the POP (more precisely its reciprocal value), this could be interpreted as the decay rate of our ability to predict development of the POP. This must be negative for stable system. The complex part gives the  $k$ -th POP's oscillation frequency.

Common eigenvectors form system of POPs. The right eigenvectors  $\mathbf{v}_{rk}$  of  $\mathbf{G}$  are computed as well as the left eigenvectors  $\mathbf{v}_{lk}$  of  $\mathbf{G}^T$ . Then the deterministic feedback matrix  $\mathbf{B}$  could be formed:

$$\mathbf{B} = \sum_k \mathbf{v}_{rk} \beta_k \mathbf{v}_{lk}^T. \quad (6)$$

Note that  $\mathbf{B}$  and  $\mathbf{G}$  are obtained solely from the time series data  $\mathbf{u}(t)$ . If the system is well described by a linear Markov process, then our estimate of  $\mathbf{B}$  will be independent of the choice of  $\tau$ . On the other hand, if nonlinear effects are important, then  $\mathbf{B}$  will vary significantly with  $\tau$ .

### 3 EXPERIMENTAL SETUP

Our model was designed as 2D placed in channel  $100 \times 250 \text{ mm}^2$ , prismatic from wall to wall (100 mm width), flow velocity 6,5 m/s, blockage was about 8 %. The model was geometrically similar to the original Ahmed body in side view, the ratio 3 : 20 meaning that length of our model was 156,6 mm. Reynolds number was by 2 orders of magnitude lower than in original Ahmed case, actual value  $\text{Re} = 5,4 \cdot 10^4$ .

The time-resolved PIV method was used for the experiments. The measuring system DANTEC consists of laser with cylindrical optics and CMOS camera. The software Dynamics Studio 2.2 was used for velocity-fields evaluation. Laser New Wave Pegasus Nd:YLF, double head, wavelength 527 nm, maximal frequency 10 kHz, a shot energy is 10 mJ for 1 kHz (corresponding power 10 W per head). Camera NanoSense MkIII, maximal resolution  $1280 \times 1024$  pixels and corresponding maximal frequency 512 double-snaps per second. For the presented measurements the camera resolution reduction  $1280 \times 512$  pixels was used with

the higher sampling frequency 1 kHz, 3272 double-snaps in sequence corresponding to 3,272 s of record for the evaluation. Other details see [7, 8]

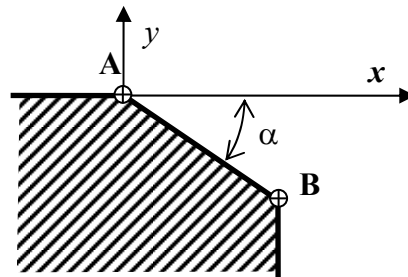


Figure 1: The Ahmed body rear part.

Origin of the coordinate system was placed to the upper corner of the ramp (point A),  $x$ -axis in the flow direction,  $y$ -axis perpendicular to the wall. Situation is depicted in Fig. (1), the corners in the body rear part are labeled as points A and B. Results for the two configurations with slant angles 25 deg and 35 deg will be presented respectively.

## 4 RESULTS

The results are shown as vector and scalar fields, the two slant angles mentioned above were being compared.

### 4.1 Mean quantities

First, only statistical mean values are evaluated covering velocity mean values and statistical moments.

The mean velocity vector fields are shown in Fig. (2), the corresponding vector lines were added on the left and mean velocity magnitude distribution is shown on the right.

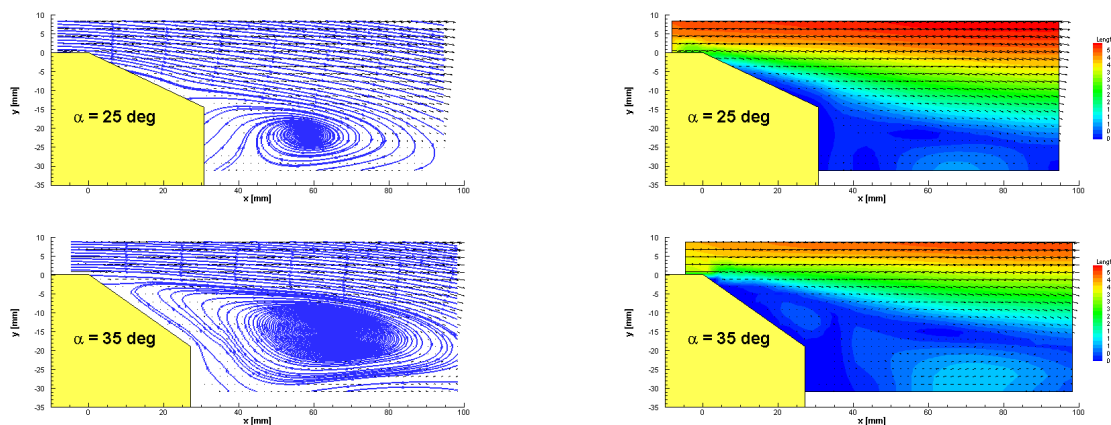


Figure 2: Mean velocity vector lines (left) and magnitude (right) distributions.

The case  $\alpha = 35$  deg exhibits much larger recirculation zone, separation of the boundary layer starts just at the upper corner A. In the  $\alpha = 25$  deg case separation occurs near the corner B forming considerably smaller recirculation zone.

In Fig. (3) comparisons of U and V mean velocity components distributions evaluated in x and y directions respectively are given. The wake is characterized by low U velocity components values and/or positive V velocity components.

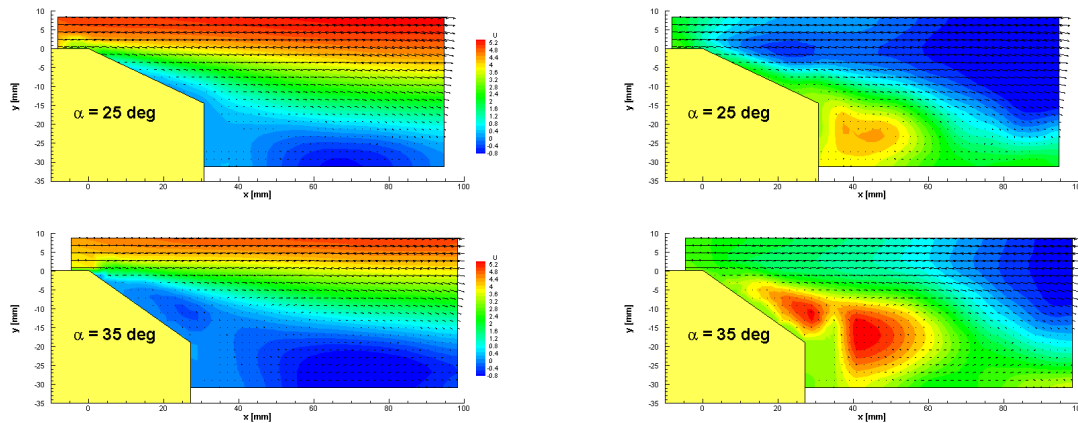


Figure 3: Mean velocity components U (left) and V (right) distributions.

In Fig. (4) comparisons of variance (left) and correlation coefficient (right) of the instantaneous velocity components distributions are given.

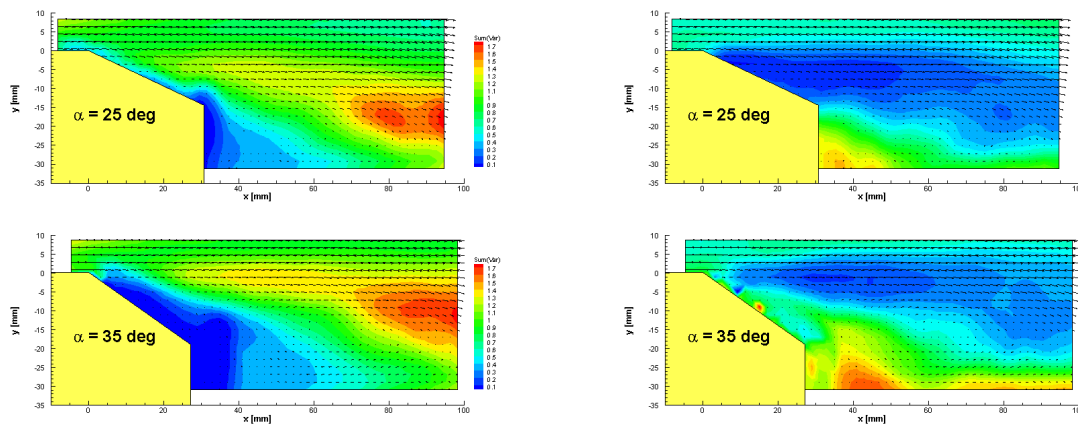


Figure 4: Variance (left) and correlation coefficient (right) distributions.

As for the velocity variance, more intensive fluctuating activity is visible in the wake near the shear layer for the 35 deg case, as could be expected. However, in this case much less activity could be seen near the surface in core of the recirculation zone. The correlation coefficient quantifies generation of Reynolds stresses and thus turbulence – maximum of turbulence generation is seen as negative correlation values. The maximum of turbulence generation is located near the free shear layer, nearly no production is in core wake. It is more pronounced for the 25 deg case.

#### 4.2 POD analysis

Mean velocity values (see above) were subtracted from all instantaneous velocity distributions. Space and time modes were evaluated from velocity fluctuations using methods described above.

Cumulative energy and absolute value of energy of individual modes are shown in Fig. (5). The cumulative

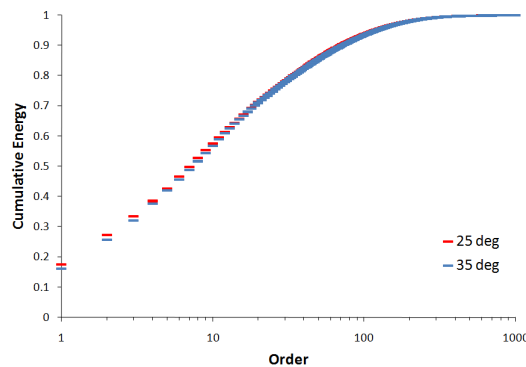


Figure 5: POD modes cumulative energy.

All chronoses could be characterized as a broad-band processes. Spectra are continuous and could be divided into two parts –low frequency part and high frequency part. Limit frequency is about 50 Hz. The higher mode order the lower energy and lower level of the low frequency part of the spectra. The high frequency parts of all spectra are nearly the same. The spectra for first 10 chronoses are shown in Fig. (6) for the 25 deg case, very similar situation was found for the 35 deg case.

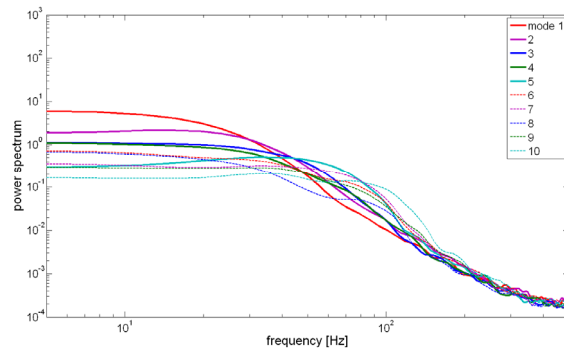
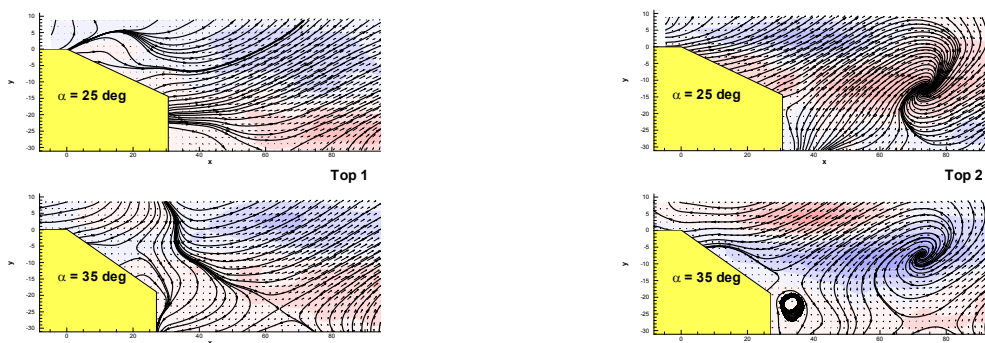


Figure 6: Spectra of first 10 chronoses.

Then a few examples of Toposes are shown in Fig. (7). Comparison of the two cases in question is presented for each mode. Coloring denotes vorticity.



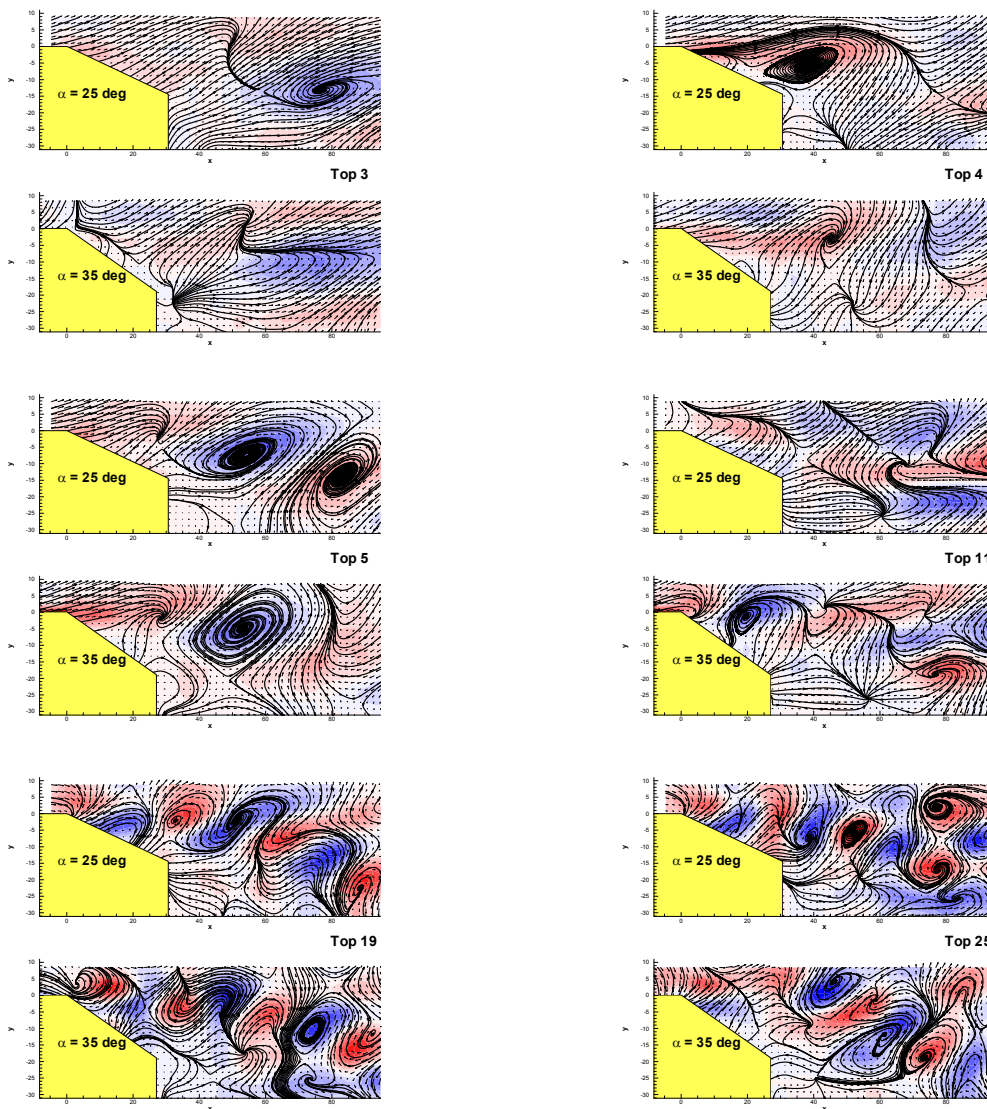


Figure 7: Toposes example.

The first toposes (Top 1) shows a saddle point in the wake for both cases, while the second toposes (Top 2) are characterized by a spiral vortex. In the toposes 4 we could see limit cycle for the 25 deg case. The higher order toposes show combinations of all above-mentioned structures. There is a general rule: the higher toposes order, the higher complexity and lower energy in the same time.

### 4.3 POPs analysis

For the POPs analysis projection on the first 25 POD modes containing approximately 75 % of total kinetic energy was used. One sample lag giving  $\tau = 1$  ms was applied in the procedure.

In Fig. (8) a few eigenvalues with the highest real part are presented. Please note that the POPs analysis gives complex conjugate eigenvalues (or real). The eigenvalues are labeled by numbers according to increasing imaginary part, i.e. increasing frequency of the mode. In literature the modes are ordered according to eigenvalue real part in descending order to present

the least stable modes first. Here the different system has been chosen to find the corresponding modes of the two cases.

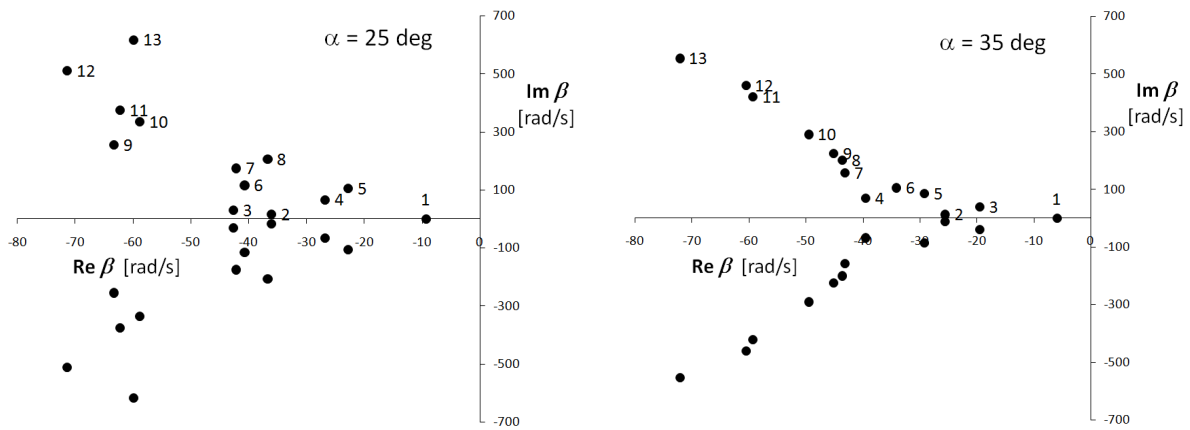


Figure 8: POPs eigenvalues.

For each eigenvalue corresponding frequency and e-fold time could be calculated as characteristic of each mode.

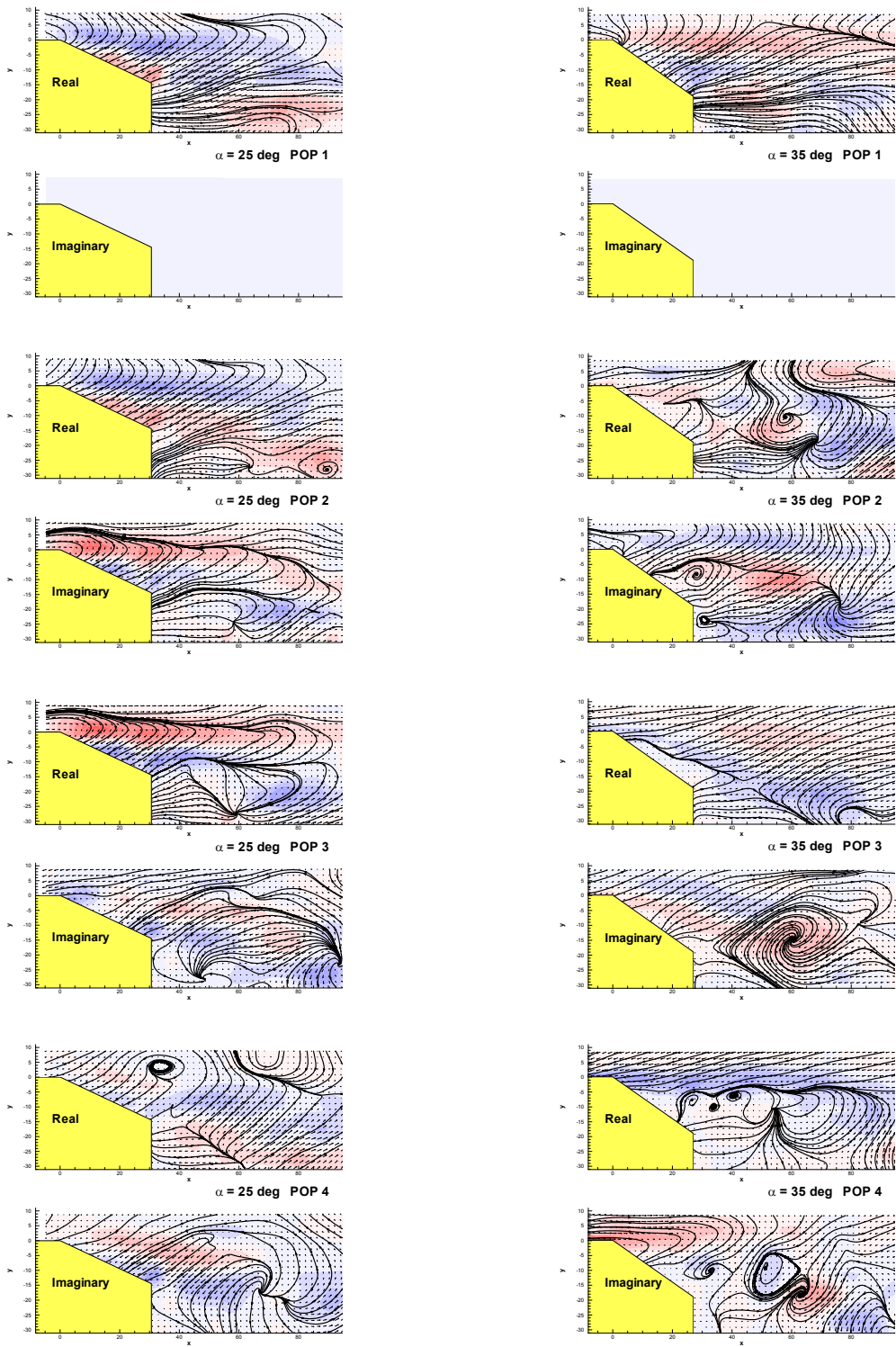
POP	$\alpha = 25$ deg		$\alpha = 35$ deg	
	$f$ [Hz]	$\tau_e$ [ms]	$f$ [Hz]	$\tau_e$ [ms]
1	0	107,53	0	169,49
2	2,56	27,70	1,97	39,06
3	4,82	23,47	6,30	51,28
4	10,55	37,31	10,93	25,31
5	16,77	43,86	13,58	34,25
6	18,40	24,57	16,71	29,33
7	27,84	23,70	24,96	23,20
8	32,87	27,25	31,91	22,94
9	40,55	15,80	35,62	22,17
10	53,36	17,01	46,20	20,20
11	59,75	16,08	66,91	16,86
12	81,25	14,01	73,29	16,53
13	98,25	16,69	88,12	13,87

Table 1: POPs frequencies and e-fold times.

The modes 1 are aperiodic characterized by frequency 0, corresponding eigenvalue is real as well as the eigenmode.

Topology of modes is given by complex eigenmodes consisting of real and imaginary parts. Examples of eigenmodes are shown in Fig. (9) for both cases in question. Modes could appear in the flow-field randomly in time. Dynamics of a given mode is characterized by its frequency, complex mode characterizes the phase shifted patterns and typical decay by factor “e” is defined by the e-fold time. The structure of individual POPs topological modes is similar to this of toposes consisting of nodes, spiral vortices, saddle points and limit cycles.





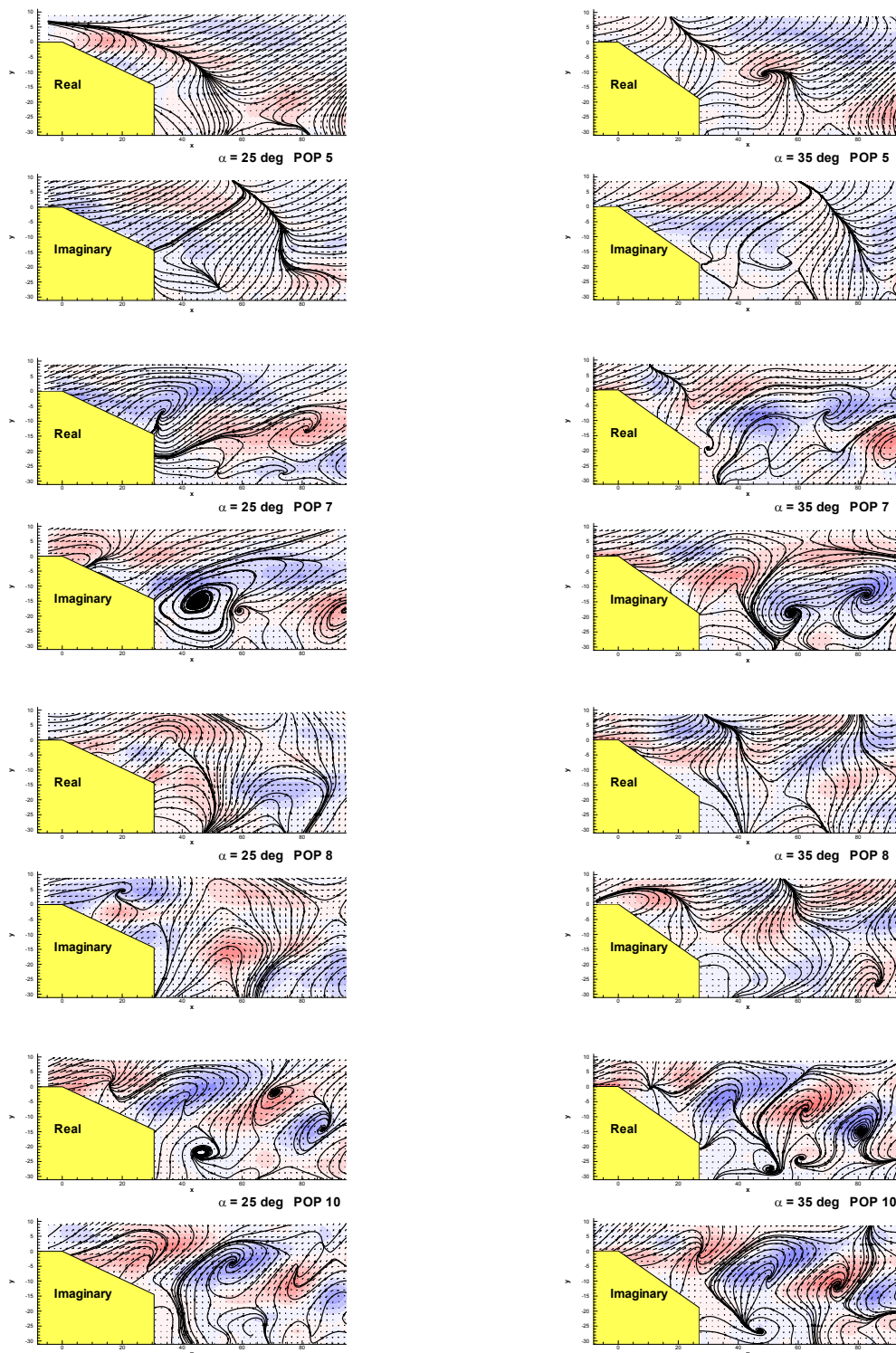


Figure 9: Example of POPs modes.

## 5 CONCLUSIONS

The upper part of the wake behind Ahmed body forming a free shear layer was studied in details. Two variants of the model with slant angles 25 deg and 35 deg were examined respectively. Angle 25 deg shows more or less attached flow, while angle 35 deg generates fully detached flow from the ramp. The presented analysis shows structures involved in dynamical behavior of the flow.

The POD and POPs methods were demonstrated as powerful tools in studying and simulation of dynamics of the wake flow-field revealing several types of structures, namely nodes, spiral vortices, saddle points and limit cycles. Promotion or suppression of some of those structures could be a good control strategy.

## ACKNOWLEDGEMENTS

This work has been supported by the Grant Agency of the Czech Republic, project No. 101/08/1112.

## REFERENCES

- [1] S.R. Ahmed. Wake Structure of typical automobile shapes. *Transactions of the ASME, Journal of Fluids Engineering*, **103**, 162-169, 1983.
- [2] N. Aubry, R. Guyonnet, R. Lima. Spatiotemporal Analysis of Complex Signals: Theory and Applications. *Journal of Statistical Physics*, **64**, 2/3, 683-739, 1991.
- [3] D. Greenblatt, I.J. Wygnanski. The control of flow separation by periodic excitation. *Progress in Aerospace Sciences*, **36**, 487-545, 2000.
- [4] K. Hasselmann. PIPs and POPs: The Reduction of Complex Dynamical Systems Using Principal Interaction and Oscillation Patterns. *Journal of Geophysical Research*, **93**, D9, 11.015-11.021, 1988.
- [5] J.L. Lumley. The structure of inhomogeneous turbulent flows. *Atm. Turb. and Radio Wave Prop.*, Yaglom and Tatarsky eds., Nauka, Moskva, 166-178, 1967.
- [6] C. Tropea, A.L. Yarin, J.F. Foss eds. *Handbook of Experimental Fluid Mechanics*. Springer, 2007.
- [7] V. Uruba, M. Matějka, Dynamics of controlled boundary layer separation on a circular cylinder. *EDRFCM 2008*, 8-11 September 2008, Ostritz - St. Marienthal.
- [8] V. Uruba. Boundary Layer Separation Dynamics. *Conference Topical Problems of Fluid Mechanics 2008*, Praha, IT AS CR, v.v.i., (Eds.: Prihoda J.; Kozel K.), 125-128.

## A PRACTICAL SCIENTIFIC APPROACH FOR AERODYNAMIC TRUCK DESIGN

Gandert Van Raemdonck\* and Michel Van Tooren†

\*Design of Aircraft and Rotorcraft, Faculty of Aerospace Engineering  
TU Delft, Kluyverweg 1, 2629HS Delft, The Netherlands  
e-mail: g.m.r.vanraemdonck@tudelft.nl

†Design of Aircraft and Rotorcraft, Faculty of Aerospace Engineering  
TU Delft, Kluyverweg 1, 2629HS Delft, The Netherlands  
e-mails: m.j.l.vantooren@tudelft.nl

**Keywords:** Aerodynamic drag, truck design, fuel economy, numerical simulation, wind tunnel experiments, road tests

**Abstract:** *The heavy duty transport sector which uses trucks to transport cargo covers a very large business area. Due to the climate change it is crucial however, to find solutions to stay sustainable in this aggressive and fast changing market. One way to address the climate change problem is to reduce the required power for road transport. Improving aerodynamic quality, i.e. reducing drag, can contribute largely to the solution to this problem.*

*With numerical analysis of a standard tractor-trailer combination a general overview of the flow around this type of vehicle has been obtained. The visualizations show a highly complex flow and large separated regions especially at the back and at the bottom of the trailer. The analysis indicates a large contribution of the underside of the trailer to the total drag of the vehicle.*

*Wind tunnel experiments in the closed circuit Low Turbulence Tunnel at the TU Delft with a 1:14 scaled truck model were performed to experimentally investigate the effect of aerodynamic aids to reduce the drag of the tractor with trailer. More than 100 different aerodynamic devices were built and tested. Covering the wheels was found to be always beneficial and a full underbody is not performing as well as the straight side skirts. Modifications to these side skirts improved the drag reductions even further up to 14% which corresponds with a drag coefficient reduction of 0.062.*

*A full-scale prototype of glass-fiber is built to execute several road tests with a tractor-trailer combination. During the operational tests, which are performed over a period of 4 weeks, an average fuel economy increase of 9% is achieved. A test day with two identical trucks (one was equipped with the aerodynamic side skirts) confirmed these results.*

## 1 INTRODUCTION

This paper presents a practical scientific approach of designing an add-on for a truck that lowers the fuel consumption significantly.

**Background.** Cargo transport by road using trucks is still one of the most efficient transport solutions within the European context. This fact manifests itself in the large amount of trucks on the road and the associated increased total volume of fuel consumed annually. The environmental concerns force the transport companies to reduce fuel consumption in an economical and sustainable way. This has renewed the interest in truck design; any reduction in truck fuel consumption can be associated with large annual fuel cost savings and emission reductions. Generally there are two ways to reduce the fuel consumption of a vehicle. One can improve the efficiency of the engine delivering power: improvements on the side of "the available power". Or one can lower the different forces acting on a truck traveling over the road: the "required power" side. The latter can be achieved by reducing the weight of the vehicle, reducing its aerodynamic drag and by reducing the friction resistance of the tires. Driving at highway speeds of 85 km/h, more than 40% of the trucks fuel consumption is caused by aerodynamic drag, [24].

**Past research.** The reduction of fuel consumption of trucks by aerodynamic means has become an accepted practice in the last decades. By installation of different add-on devices for the tractor and the trailer, on its original boxed shape. Tractor manufacturers improved the aerodynamic shape of their products while many add-ons are available to improve the aerodynamic behavior of the tractor-trailer combination. Also modifications of the general shape of the vehicle, introduced by the tractor manufacturers, improved the aerodynamic efficiency. In the past several aerodynamic devices have been developed for the front and top of the tractor, the back of the trailer and for the gap between the tractor and trailer, [1, 7, 13, 27, 28]. Also new futuristic aerodynamic designs have been presented by the European truck manufactures, [4, 5, 14, 16, 17, 21, 23]. The main focus of the manufacturers is on the development of the tractor and not particular on the trailer and the vehicle as a whole.

**Present research.** In 2005 a research program at the Delft University of Technology started to reduce the fuel consumption of heavy duty vehicles by improving the aerodynamic drag level of articulated trucks. These vehicle are used for international road transport and have a large aerodynamic drag level due to their bluff shape and high average traveling velocity.

The research has three components: (1) road testing for both requirements discovery tree and design verification, (2) numerical analysis to understand the flow and (3) wind tunnel experiments for experimental design of add-ons to lower drag. In preparation of numerical simulations and wind tunnel experiments the performance of a tractor-trailer combination is monitored during a test period of 2 months through Europe. The results, presented by Van Raemdonck [24], are used as input and as design parameters to develop an aerodynamic add-on for a trailer.

Numerical simulations of a tractor-trailer combinations are conducted to indicate the regions that cause high drag. Several aerodynamic add-ons for a trailer are designed and tested in the wind tunnel. A full-scale prototype is built to perform several road tests in order to indicate the fuel savings.

In the following sections the numerical analysis, the wind tunnel experiments and the design verification with the road tests will be discussed further. The road tests for the requirements discovery tree are discussed in Van Raemdonck [24].

## 2 NUMERICAL ANALYSIS

Numerical analysis of a generalized tractor-trailer combination with aid of Computational Fluid Dynamics is conducted to obtain insight in the flow behavior and the characteristics of the flows around a road transport vehicle.

### 2.1 Pre-processing

A surface model of a tractor-trailer combination is generated by laser scanning a full-scale tractor. A long rang scanner (accuracy of  $\pm 3$  mm) and a Konica Minolta VI-9i laser (accuracy of  $\pm 1$  mm) are used to create a surface model. The model of the standard trailer is based on technical information provided by a trailer manufacturer.

The next step is to discretize the volume around the surface model by introducing several blocks, see figure 2. The surface mesh is made of triangles that are extruded normally to create a six-layered boundary layer made of prisms ( $y^+ = 50$ , height of first cell = 1 mm, growth rate = 1.15 and total thickness = 8.8 mm, Van Raemdonck [25]). The rest of the volume around the model (length = 127.5 m, half width = 30 m; height = 30 m, Van Raemdonck [25]) is filled with tetrahedrals.

A half model is used for the simulations in order to reduce the amount of cells (total number of cells: 12.2 million, Van Raemdonck [25]) and the corresponding processing time to solve the Navier-Stokes flow equations.

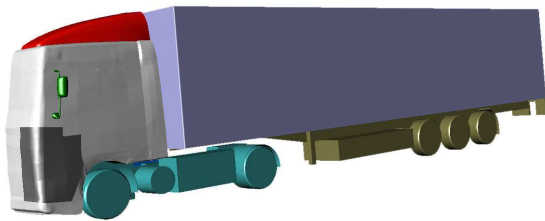


Figure 1: Surface model

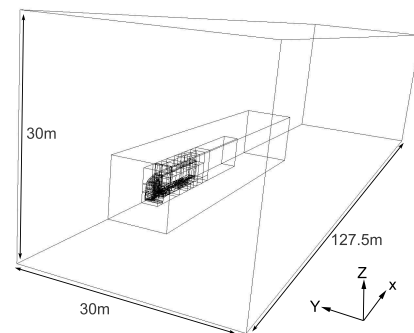


Figure 2: Control volume

### 2.2 Solver

The Navier-Stokes flow equations together with the Realizable  $k - \varepsilon$  turbulence model are solved with the commercial package Fluent. There is opted for the two-equation  $k - \varepsilon$  turbulence model and more specifically the Realizable version due to its common usage in the automobile sector, its performance with bluff bodies and its relatively low required computer power, Lanfrit [12]. As near-wall treatment for the boundary layer, the non-equilibrium wall function, is chosen. The operating pressure of 101325 Pa is defined in one of the outer corners of the computational domain.

The upstream inlet uses the velocity inlet boundary condition by setting an absolute magnitude of 25 m/s in the direction of the flow which is assumed to be uniform and has only a component in x-direction. The boundary condition for the outlet is set as pressure outlet. The actual symmetry plane as well as the other two outer planes (side and upper plane) have the symmetry boundary condition. The boundary condition of the floor is a moving wall which has a translational velocity of 25 m/s in the positive x-direction.

All the surfaces of the tractor and trailer are solid stationary walls. The wheels of the tractor and trailer have a moving wall boundary condition with the rotational velocities of  $-47.27$  rad/s and  $-44.66$  rad/s respectively. In this truck model no boundary condition is set for the radiator in order to keep the modeling of the corresponding grids and boundary layers simple.

### 2.3 Results

After twelve thousand iterations the drag and lift coefficient converged to the values of  $0.383$  and  $-0.026$  respectively. An estimation of the drag coefficient of an asymmetrical tractor-trailer combination is made by Van Raemdonck [24] on the basis of the measured power delivered by the engine. An estimated drag coefficient for the tractor-trailer combination of  $0.430$  is obtained.

Literature illustrates that already many simulations, [10, 11, 19], have been performed of a generalized model of a tractor-trailer combination. Pointer [15] executed numerical simulations for a generalized three dimensional 1:8 scaled conventional U.S. tractor-trailer combination and obtained a drag coefficient of  $0.402$  with the  $k - \varepsilon$  turbulence model. Hucho [9] illustrated that the drag coefficient of an articulated truck is between  $0.5$  and  $0.7$ .

The difference in drag coefficient has several reasons. First, the drag coefficient of  $0.430$  of the real truck is an estimated average value over a testing period of two months where the vehicle is subjected to side winds and rain. Secondly, the model for numerical calculations had several simplifications: sun visor, corner guide vanes, radiator or fans were absent and a half (symmetrical) model is used. Also a rather simple two-equation turbulence model, realizable  $k - \varepsilon$ , is used to enclose the system of flow equations.

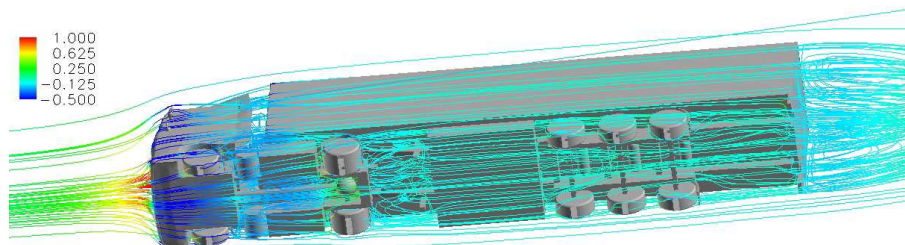


Figure 3: Streamlines at underside of model

The three dimensional streamlines around the vehicle together with the pressure coefficient are shown in figure 3. At the front surface the oncoming flow stays attached around the cabin corners and the roof deflector. The flow continues its path towards the rear of the vehicle. The recirculation zone with the two counter rotating vortices at rear is clearly visible. The streamlines at the bottom of the vehicle, especially at the underside of the trailer, have highly separated behavior. This figure indicates that two regions, the underside and the back of the trailer, have highly separated flows, which cause a lot of pressure drag.

Considering the total drag of the vehicle, the frontal area has a drag contribution of  $0.23\%$  and the back surface  $35\%$ , while from the region in between, including the underside of the vehicle, originates  $42\%$  of the total drag, Van Raemdonck [25]. The drag caused by the underside is large, it is therefore an interesting region to improve the aerodynamics towards a lower total vehicle drag.

### 3 WIND TUNNEL EXPERIMENTS

The numerical simulations provided more insight in the flow behavior around a tractor-trailer combination and the drag contributions of the several regions. The next step is to design an aerodynamic aid for the underside of the trailer in the wind tunnel that does not conflict with the European regulations for road transport vehicles.

#### 3.1 wind tunnel and model set-up

The wind tunnel experiments are executed in the Low Turbulence Tunnel at the Delft University of Technology. This closed circuit wind tunnel has an octagonal test section with a cross sectional area of  $2.07m^2$  (width = 1.8 m; height = 1.25 m) and a maximum velocity of 120 m/s. The six-component mechanical balance system measures the resulting forces acting on the truck model. Only the drag coefficient  $C_T$  of the vehicle will be discussed here.

The windtunnel does not have a moving belt to simulate the road. The major issue is that the approaching floor boundary layer is too thick. According to Cooper [2, 3] one can conclude that a fixed elevated ground board with a thinned boundary layer is sufficient for automotive and commercial vehicle applications, particularly where the underbody clearances are large and the underbodies are rough.

A 1:14 scaled truck model (TAMIYA Mercedes Benz 1838LS truck and TAMIYA container-trailer) is used. The initial truck model had sharp corners which will result in flow separation at the front and therefore would make any aerodynamic improvement ineffective. A new cover, see figure 4, with properly chosen round-off edges, based on consideration given in Hoerner [8] and Cooper [2], is made which prevents flow separation at the front cabin corners and initiates a turbulent boundary layer before it reaches the back edges of the tractor. The model is not equipped with a fan system and is mounted up-side-down due to the location of the balance system.

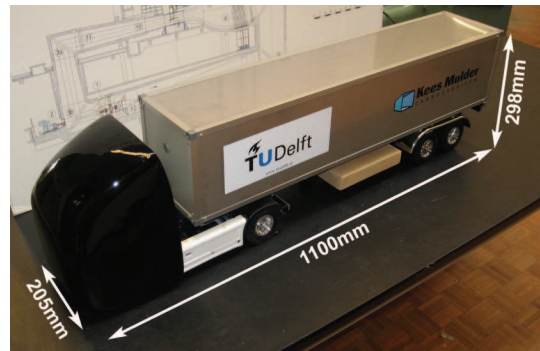


Figure 4: Wind tunnel model dimensions

The Reynolds number for a full scale truck, based on the square root of the frontal area of  $A = 10.34m^2$  and a driving velocity of 25 m/s, becomes  $5.4 \times 10^6$ . The scaled wind tunnel model has a Reynolds number (with a tunnel speed of 60 m/s) of  $0.98 \times 10^6$  which is high enough for bluff bodies, SAE J1252 [20]. After testing a Reynolds number range, no Reynolds effects are deducted, Van Raemdonck [25]. Also no wind tunnel corrections methods are applied on the dynamic pressure.

#### 3.2 Results

During the experimental measurements more than 100 different aerodynamic devices are built and tested on different vehicle configurations. Only a short selection is being discussed here. A more profound overview of the results can be found in Van Raemdonck [25] and [26]. All the drag coefficients  $C_T$  in longitudinal direction of the vehicle with the different aerodynamic devices are compared with the standard tractor-trailer combination ( $C_T = 0.443$  at zero yaw angle, figure 5). The results are showing a drag difference in terms of percentage. Removing the mud flaps gives a general drag decrease of 5% over the whole range of yaw angles, [26].



Blocking the underbody flow by mounting a vertical plate between the lower-end of the trailer and floor has disastrous effects on the drag of the vehicle, [26]: the underbody flow is crucial for the drag built up of a truck.

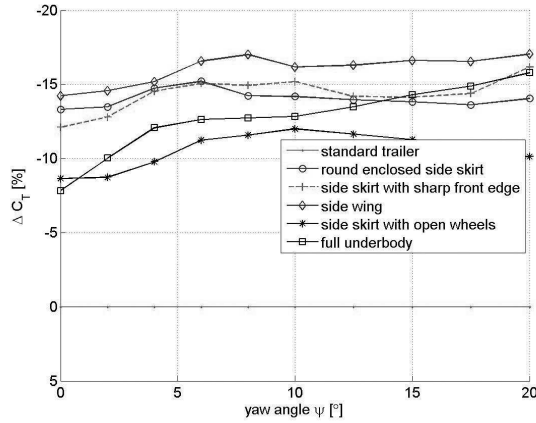


Figure 5: Drag reduction results

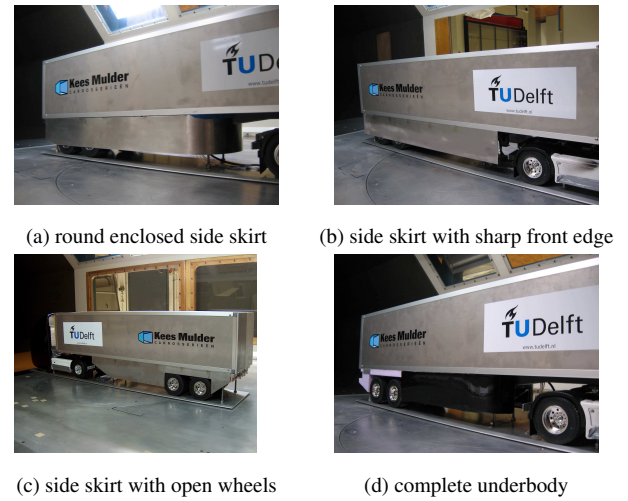


Figure 6: Aerodynamic add-ons

The most basic straight side skirt with covered wheels, figure 6(b), reduces the drag coefficient  $C_T$  with 12% ( $\Delta C_T = -0.049$ ) at a yaw angle of zero degrees and stays almost the same with increasing yaw angle, figure 5. Existing side skirts often have the front and rear edge cut off for esthetic purposes and aerodynamic reasons. The results [26] show that a steep cut back-edge reduces the drag coefficient even further.

The different configurations for the straight side skirt have covered wheels, while real trucks often have open wheels. Nowadays side skirts with uncovered wheels, see figure 6(c), perform aerodynamically much worse, figure 5. Uncovered wheels introduce significant drag that results in a lower drag reduction: 4% at zero yaw angle, or an increase of  $C_T$  with 0.018.

Another aerodynamic aid is the round enclosed side skirt, figure 6(a), which encapsulates the pallet box and the support legs in a round curve and covering the wheels towards the back of the trailer. The reduction in aerodynamic drag is 12.5% or  $\Delta C_T = -0.055$  at zero degree yaw angle and a maximum of 14.5% ( $\Delta C_T = -0.064$ ) at  $6^\circ$  as plotted in figure 5. If the bottom of round front side skirt and the back-end is closed, the drag measurements [26] indicate that the drag reduction is less than the solution with the open bottom.

A side skirt with the hollow front, instead of the more spherical round front side skirt is another modification. This hollow front lies parallel with the turning radius of the tractor. This solution has, at a zero degree yaw angle, a larger benefit in drag coefficient [26], but it is not that efficient as the round front side skirt when the yaw angle increases.

At larger yaw angles the flow can not pass the sharp vertical edge at front of the standard side skirt without immediate separation. Rounding-off the sharp edges should give a drag benefit. Several rounding configurations are applied. The configuration with the rounding at the outside performed worst [26] over the range of yaw angles: the flow has to overcome an extra obstacle. With the rounding at both the in- and outside a slight improvement in drag benefit at the higher yaw angles is noticeable, [26]. The best result of the three configurations is obtained with the side skirt with the rounding at the inside. At a yaw angle of zero degrees this solution produces 11% less drag in comparison to the base configuration instead of 7% for the other two, [26].

The applied rounding, a half circle, is not an ideal aerodynamic shape in this case. Therefore an airfoil profile is placed at the front inside. With the optimized profile a drag reduction of 14% or  $\Delta C_T = -0.061$  at zero degree yaw angle and a maximum of 16% ( $\Delta C_T = -0.069$ ) at a yaw angle of  $8^\circ$  is obtained figure 5. This drag reduction of 14% can be translated in a fuel economy reduction of 7%, Rose [18].

Another type of aerodynamic add-on is the so-called underbody. The measured drag benefit of the complete underbody, figure 6(d), is plot in figure 5: it generates at zero yaw angle 7% less drag ( $\Delta C_T = -0.030$ ) and 12% or  $\Delta C_T = -0.052$  at  $6^\circ$  yaw angle.

A second version of the underbody has covered wheels to show its influence on the drag coefficient  $C_T$ . Again better results are achieved [26] with the wheels covered: a decrease of 3% ( $\Delta C_T = -0.013$ ) of the drag coefficient with respect to the similar configuration with the open wheels.

## 4 ROAD TESTS

The results of the wind tunnel experiments with the side skirts with the profile, called side wings, were so promising that a full scale prototype is built and tested on the public road. For all three road tests a Scania R340 tractor with a standard 2-axle trailer is used. The aerodynamic aid is mounted on the underside of the trailer. An elaborated test report of the road test can be found at [6].

### 4.1 Prototype

The full scale prototype of the side wings is made from glass fibre reinforced polyester, see figure 7. For the three dimensional airfoil a positive foam mould is used together with vacuum injection moulding. The prototype is mounted with the state-of-the-art techniques at the underside of the trailer. The outside of the panels are smoothed and painted white as can be seen figure 8.

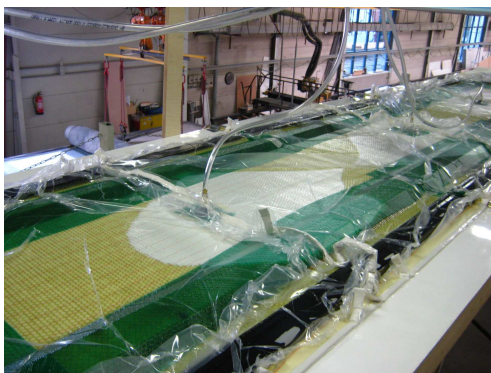


Figure 7: Manufacture of the prototype



Figure 8: The side wing mounted on a trailer

## 4.2 Test 01: proof of concept test

The goal of the first road test was to measure the fuel consumption on a straight public road (3 Merenweg, Vijfhuizen, The Netherlands) in order to define the aerodynamic impact on the fuel economy. A special fuel tank with load sensors, developed by Squarell Technology [22], is installed on the existing tank of the tractor. The measured values are corrected according to the inclination angle of the tank and to the fuel temperature. In addition, a data acquisition system is connected through CANbus to the board computer of the tractor.

The trailer was not carrying any load during the test. The course length was 7.5 km and had clear surroundings together with excellent pavement. The truck driver accelerated to 85 km/h and decelerated, each time at the same spots. This velocity in between was maintained constant using the cruise control.

Two different trailer configurations are tested in Test 01: (1) the standard trailer without aerodynamic aid and (2) the trailer equipped with the side wing. During the testing day the weather circumstances were measured and recorded. No rain fall is noticed during the day. Comparing the conditions of configuration 1 in the morning and 2 in the afternoon, large differences are observed in both the wind direction and the wind velocity. The wind velocity increased from 4.0 m/s to 6.8 m/s and the wind direction changed from South to South-South-East.

The trailer equipped with the aerodynamic side wings, realized a fuel economy improvement of 4.8% (tail wind) and 15.7% (head wind) with respect to the standard trailer without the side skirts. Although the weather changed in negative sense the performances of the side wings are very good. Even with an increased cross wind the reduction of the aerodynamic forces is higher.

## 4.3 Test 02: operational test

Test 02 is executed in two periods of two weeks of driving with and without the side wing during operational conditions. The goal of this test is to define an averaged fuel consumption reduction over a period of 4 weeks and to discover how the aerodynamic add-on will fit into daily practical issues. The tractor is not equipped with the special fuel tank because of the low capacity of only 30 litres. The data acquisition system is connected to the board computer to measure the fuel flow rate, vehicle velocity, power and several other parameters, Van Raemdonck [25].

The first two weeks the trailer is equipped with the aerodynamic aid. After this testing period the side wings are dismounted, and the vehicle drove once again two weeks. The whole four weeks the combination did one particular ride each day, namely Eindhoven-Luik-Eindhoven. The truck driver was the same and the vehicle transported cargo during these 4 weeks. This period had an average wind velocity of 5.4 m/s with a South-West direction.

The results show again a fuel economy increase above the 5%, even an average of 9% is achieved during this operational tests of 4 weeks. The positive feedback of the drivers about the side wings used during operational daily tasks was even more important for the final design of the product.

#### 4.4 Test 03: comparison test

The goal of this third and last test is to quantify the aerodynamic impact of the side wings on the fuel consumption using two identical vehicles. The construction year and the type of both tractors and trailers are the same. The reason to perform a test with two identical vehicles is to switch very fast and easily between trailers (one trailer is equipped with the aerodynamic add-on, the other is not) in order to neutralize changing weather conditions. Both trailers were not transporting any cargo. The condition of the tires of both vehicle combinations was similar. The test location was a trajectory between two cloverleafs at the South of Arnhem. The trajectory was approximately 26 km long and consisted out of good smooth pavement and clear surroundings.

Both vehicles drove the trajectory two times. When the drivers crossed fixed points on the trajectory, they activated cruise-control on 85 km/h at the first fixed point and started braking at the second. A consistent comparison between the different configurations for each tractor could be made by neutralizing the influence of the driver behavior. During the day the wind velocity stayed very low (average wind velocity of 2.8 m/s) and the wind direction South did not change. Both tractors were equipped with a data acquisition system to measure the fuel rate.

A fuel economy increase of 6.38% and 7.5% for both tractors is measured. Although the type and the construction year of both tractors are the same, this difference of 1.12% can be found in the fact that the first tractor had double the mileage of the second. In Test 01 higher fuel economy figures, even up to 15%, are measured compared to this test. The reason for this difference is explained by the lower average wind speed in Test 03.

## 5 CONCLUSIONS

This research proved that with a practical approach a large drag reduction and a corresponding fuel economy increase can be achieved by improving the aerodynamic drag of trucks. Extensive monitoring of truck performance data delivered input for the design conditions of the aerodynamic aid. The numerical simulations provided insight in the flow behavior and in the drag contributions of several regions. The underside of the trailer was responsible for more than 40% of the total drag of the vehicle combination. This region is also characterized with highly separated flows.

Based on the numerical simulations it was decided to design an aerodynamic add-on for the trailer in the wind tunnel. In total more than 100 different configurations were tested. The configurations with the straight side skirts and the optimized profile, named the side wing, generated the highest drag reduction: up to 14% at zero yaw angle.

The side wings proved to have an aerodynamic impact on the fuel economy of a tractor-trailer combination. Through several tests a reduction of the fuel consumption between 5% up to 15% was measured. The operational test indicated an average reduction of 9%. The difference between the tests can be related to the difference in weather conditions. Test 03 is performed on a day with nearly wind still, while Test 02 is executed over 4 weeks in February and March with changing weather conditions.

## 6 ACKNOWLEDGMENTS

The building of the prototype and the execution of the road tests were only possible and successful due to close cooperation with PART, Platform for Aerodynamic Road Transport ([www.part20.eu](http://www.part20.eu)). PART is a consortium of a public-private partnership that initiates aerodynamic projects to improve the fuel efficiency of trucks. The spin-off company Ephicas, [www.ephicas.eu](http://www.ephicas.eu), is further developing the side wings into a commercial product to introduce this aerodynamic add-on in the international transport market.



Figure 9: Group photo of road tests

## REFERENCES

- [1] Browand, F., McCallen, R. and Ross, J., *Aerodynamics of Heavy Duty Vehicles II: Trucks, Busses and Trains*. Springer, 2008.
- [2] Cooper, K., *Bluff-Body Aerodynamics as Applied to Vehicles*. Journal of Wind Engineering and Industrial Aerodynamics. Vol. 49, 1993, pp.1-21.
- [3] Cooper, K., *The Wind Tunnel Testing of Heavy Duty Trucks to Reduce Fuel Consumption*. SAE Paper 821285, 1982.
- [4] *DAF Extreme Future Concept*. <http://www.daf.com>
- [5] Durelli, E., *Iveco Transport Concept*. <http://www.iveco.com>
- [6] *Road Testing of the Aerodynamic Prototype of the Ephicas Side Wing*. [http://www.ephicas.eu/wordpress/wp-content/uploads/test\\_report\\_ephicas\\_sidewing.pdf](http://www.ephicas.eu/wordpress/wp-content/uploads/test_report_ephicas_sidewing.pdf)
- [7] Freight Best Practice, *Aerodynamics of Efficient Road Transport*. Department for Transport, United Kingdom, 2003.
- [8] Hoerner, S., *Fluid-Dynamic Drag*. Hoerner Fluid Dynamics, Vancouver, 1965.
- [9] Hucho, W.-H., *Aerodynamic of Road Vehicles, Fourth Edition*. Society of Automotive Engineers, 1998.
- [10] Krajnovic S. and Davidson L., *Large-Eddy Simulation of the Flow around a Ground Vehicle Body*. SAE Paper, 2001-01-0702, 2001.
- [11] Krajnovic S. and Davidson L., *Large-Eddy Simulation of the Flow around Simplified Car Model*. SAE Paper, 2004-01-0227, 2004.
- [12] Lanfrit, M., *Best Practice Guidelines for Handling Automotive External Aerodynamics with FLUENT*. Version 1.2, <http://www.fluentusers.com>, 2005.
- [13] McCallen, R., Browand, F. and Ross, J., *Aerodynamics of Heavy Duty Vehicles: Trucks, Busses and Trains*. Springer, 2004.
- [14] *Mercedes EXT92*. <http://www.mercedes-benz.com>
- [15] Pointer W.D., *Evaluation of Commercial CFD Code Capabilities for Prediction of Heavy Duty Drag Coefficients*. AIAA Paper 2004-2254, June 2004.
- [16] *Renault Radiance*, <http://www.renault-trucks.com>
- [17] *Volvo Trucks*, <http://www.volvo.com/trucks>
- [18] Rose, M.J., *Commercial Vehicle Fuel Economy - The Correlation Between Aerodynamic Drag and Fuel Consumption of a Typical Truck*. Journal of Wind Engineering and Industrial Aerodynamics, Vol.9:89-100, 1981.

- [19] Roy C.J., brown j.C., DeChant L.J. and Barone M.F., *Unsteady Turbulent Flow Simulations of the Base of a Generic Tractor/Trailer*. AIAA Journal, 2004-2255, 2004.
- [20] Society of Automotive Engineers, *SAE Wind Tunnel Test Procedure for Truck and Buses*. SAE J1252, 1981.
- [21] *Scania Concept Truck for 2010*. <http://www.scania.com>
- [22] *Squarell Technology*. <http://www.squarell.com>
- [23] Schaller, K. V., *Transport Efficiency - the Vehicle*. MAN IAA Advance Press conference, presentatie, 2008.
- [24] Van Raemdonck, G.M.R., *Data Acquisition System of a Tractor-Trailer Combination to Register Aerodynamic Performances*. Aerodynamic of Heavy Duty Vehicles II: Trucks, Busses and Trains, Springer, 2008.
- [25] Van Raemdonck, G.M.R., *Design of an Aerodynamic Aid for a Tractor-Trailer Combination*. Master's thesis, Delft University of Technology, Faculty of Aerospace Engineering, 2006.
- [26] Van Raemdonck, G.M.R., *Design of an Aerodynamic Aid for the Underbody of a Trailer within a Tractor-Trailer Combination*. Bluff Body Aerodynamics and Application Conference, Milan, Italy, 2008.
- [27] Wood, R., *Impact of Advanced Aerodynamic Technology on Transportation Energy Consumption*. SAE Paper 2004-01-1306, 2004.
- [28] Wood, R. and Bauer, S., *Simple and Low-Cost Aerodynamic Drag Reduction Devices*. SAE Paper 2003-01-337, 2003.

# Flow control over simplified 3D bluff-bodies and road vehicles

J.-L. Aider<sup>1,2,\*</sup>, J.J. Lasserre<sup>1</sup>, J.F. Beaudoin<sup>1,2</sup>, V. Herbert<sup>1</sup>, J.E. Wesfreid<sup>2</sup>

<sup>1</sup> Aerodynamics Research Team

Direction de la Recherche et de l'Innovation Automobile  
PSA Peugeot-Citroën, 2, route de Gisy, 78943Vélizy-Villacoublay, France

<sup>2</sup> Laboratoire Physique et Mécanique des Milieux Hétérogènes (PMMH)

CNRS UMR 7636; ESPCI; Paris6; Paris7,

ESPCI, 10, rue Vauquelin, 75231 Paris cedex 05, France

\*aider@pmmh.espci.fr

In this paper, we present a short review of our recent work on flow control applied to automotive aerodynamics. Various experimental studies were carried out on different 3D bluff-bodies, from classic or modified Ahmed bluff-body (Figure 1-a) to concept-cars (Citroën C-SportLounge as shown on Figure 1-b) or real road vehicles (Citroën C4).

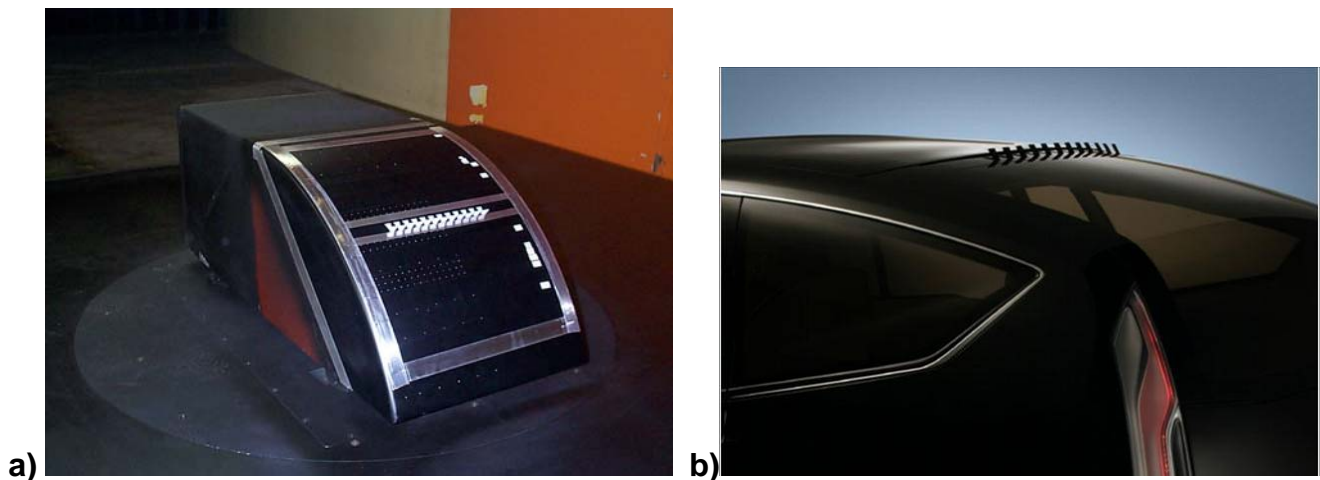


**Figure 1.** Pictures showing an active Vortex Generators device integrated in two different 3D bluff-bodies. The flow control device is integrated in a modified Ahmed body with a rear rounded slant (a) and also in the rear of the roof of the Citroën concept-car C-SportLounge (b).

Many different control devices were tested on these bluff-bodies or vehicles. One example is illustrated on Figure 1-a) where one can see a modified Ahmed body (rounded rear slant instead of the classic flat rear panel [1]) equipped with a motorized vortex generators device. A detailed parametric study showed that one can obtain large drag and lift reduction with the proper parameters [2]. It was also shown that the near-wake structure could be completely modified for large drag gains or losses. The same kind of “active” vortex generators device was also tested and successfully applied on road vehicles like C-SportLounge (Citroën concept-car) as shown on Figure 1-b) or the common Citroën C4. Another system has been studied and validated: a set of motorized flaps integrated along the different junctions around the rear of a classic Ahmed body with 30° rear flat panel. Thanks to a detailed parametric study, one could also find very favorable configurations leading to large drag and lift reductions [3]. All these examples of control strategies, including, for the first time, the applications to road vehicles, will be illustrated in the paper.

## References

- [1] Ahmed SR, Ramm R, Faltin G (1984) Some salient features of the time-averaged ground vehicle wake. SAE Paper, pp 1-30, 840300.
- [2] J. L. Aider, J. F. Beaudoin, J. E. Wesfreid (2008) *Reduction of the drag and lift of a 3D bluff body using vortex generators*, submitted to Exp. in Fluids.
- [3] J. L. Aider, J. F. Beaudoin (2008) Reduction of the drag and lift of a 3D bluff body using flaps, Exp. in Fluids, 44 (4), 491-501.

# **The effect of unsteady crosswind forces on train dynamic behaviour**

**Chris Baker**

**University of Birmingham**

Whilst not common, a number of incidents of trains overturning in high winds have been reported from around the world over the last few decades. A great deal of work has been carried out in recent years to determine the risk of such accidents occurring and to develop suitable alleviation methods – in the UK for the Advanced Passenger train in the late 1970's, and more recently to investigate the crosswind stability of the Class 390 Pendolino train. A number of pan-European projects have also studied the problem - TRANSAERO , RAPIDE, DEUFRAKO and AOA, and considerable progress has recently been made in the development of European standards and TSI documentation in this field. Work is also underway out in Japan and Korea. Train overturning is not however the only problem caused by high crosswinds. For example the train body can be deflected sideways on its suspension system that can, in extreme circumstances, result in the infringement of the kinematic envelope, or can cause the pantograph (the electrical current collection system) to deflect such that it loses contact with the overhead transmission wire - the so-called pantograph dewirement problem..

To make proper assessments of these effects, it has come to be realised that the static overturning calculations used in earlier investigations are not wholly adequate, and that some account has to be taken of the train dynamic systems, and some simulation of the unsteady nature of wind gusts is also required. Currently a number of alternative recommendations are made concerning how such calculations are carried out – from the use of relatively simple linearised models, through the use of a typical, average, gust profile (the so called “Chinese” hat profile”) in multi-body simulations, to the use of simulated wind fields on full dynamic models of vehicles.

It is the purpose of this presentation to address some of the fundamental issues associated with work of this sort. It describes in some detail how the fluctuating crosswind force and moment time histories on trains can be specified and calculated and then goes on to describe the use of these time histories in a train dynamic model to investigate the combined effects of these forces on wheel rail forces and train displacements with track roughness, cant, twist, track defects etc. The outline of the calculation procedure is as follows.

- The specification of the wind field seen by a train moving along a track, through the development of a relatively simple computational method.
- The specification of the aerodynamic admittances and weighting function on which the calculation method is based, through an analysis of wind tunnel experimental results.
- The transformation of the admittances and weighting functions that were obtained from static wind tunnel experiments into a form suitable for the application to moving vehicles in the full scale situation.
- The calculation of the aerodynamic forces through the convolution of the velocity time histories with the weighting functions, and the application of these forces to the practical issues outlined above.

The presentation will give full details of each of the above steps and present details of how the aerodynamic forces develop in a number of idealised cases (step wind input, exponential gust, spatial and temporal sinusoidal wind fields), which give a physical insight into the nature of the simulation. It will also illustrate the procedure with the application to the pantograph dewirement problem outlined above.



## **Further development and application of the SaOB actuator array for manipulation of large vehicle Aerodynamics**

**Isaac Dayan, Ilan Fono and Avi Seifert**  
(Seifert@eng.tau.ac.il)

**School of Mechanical Engineering, Faculty of Engineering**  
**Tel Aviv University, Ramat Aviv 69978 ISRAEL**

Aerodynamic design of large vehicle aerodynamics is often constrained by functionality considerations. Known examples are aft-end of truck trailers and small radius of curvature of double deck trains (in cross section view). The above constraints lead to increased aerodynamic drag of trucks and reduced stability of trains to cross-winds. The common feature of these two seemingly different problems is the boundary layer separation and the associated low pressure region at the lee-side of the relative (to the) vehicle wind. Active flow control or active boundary layer control (BLC) is a known practice from the times of Prandtl. Upon discovering the boundary layer and its failure (i.e., separation), Prandtl also suggested a remedy, flow control. By energizing or removing the boundary layer, its separation can be delayed or even eliminated. Prandtl even suggested the use of steady suction for BLC. For several decades now, active BLC has also been studied at Tel Aviv University. The approach was to utilize flow instability to enhance the effectiveness of forced oscillations and the resulting spanwise as well as streamwise vortices as mixing enhancers [1]. More recently (Arwatz et al, 2008) it was suggested to combine steady suction and pulsed blowing in close proximity for active BLC. The device, called *Suction and Oscillatory Blowing* (SaOB) actuator, is capable of generating the two control mechanisms using one miniature device with no moving parts. An array of 15 valves was used by Sperber et al (in Seifert et al, 2008) to reduce the drag of a circular cylinder and by Seifert et al (2008) to reduce the drag of 2D and 3D truck models, using an “add on”, small scale device attached to the lee-side of the truck.

The current study is aimed at modeling, controlling and testing the importance of valve array synchronization. Theoretical and experimental work is on-going to allow synchronized operation of a large valve array with no moving parts. Once satisfactory results will be reached, the importance of valve array synchronization on the attainable drag reduction using a given energetic input will be evaluated.

The conference paper will review the recent activities from a fundamental point of view (valve array development) and from the applicable side (obtainable drag reductions) considering the energetic cost, with the aim of net saving in fuel consumption as well as increased stability to side winds.

### References

1. Seifert, A., Darabi, A. and Wagnanski, I., 1996, “Delay of Airfoil Stall by Periodic Excitation”, *J. of Aircraft*. Vol. 33, No. 4, pp. 691-699.
2. Arwatz, G., Fono, I. and Seifert, A., "Suction and Oscillatory Blowing Actuator", *AIAA J.*, V. 40, N. 5, pp. 1007-1017, May 2008.
3. Seifert et al, “Heavy trucks drag reduction by active flow control”, *AIAA paper* 2008-0743, Jan 2008.

## **Determination of aerodynamic coefficients of the TGV Duplex in wind tunnel for flat ground configurations**

Rémi Grégoire<sup>1</sup>, Nicolas Paradot<sup>2</sup> and Jean-Paul Bouchet<sup>3</sup>

<sup>1</sup>Alstom Transport, Aytré Unit, Avenue du Commandant Lysiack - 17001 La Rochelle, France

<sup>2</sup>Société Nationale des Chemins de fer Français (SNCF), Rolling Stock Engineering Centre,  
4 Allée des Gémeaux 72100 Le Mans, France

<sup>3</sup>Centre Scientifique et Technique du Bâtiment (CSTB), 11 rue Henri Picherit, 44323 Nantes, France

The cross-winds sensitivity of a high-speed train is given by the maximum lateral wind this train can withstand before a characteristic limit for wheel unloading is exceeded. From the collection of these maximum wind values for all considered yaw angle configurations are deduced the Characteristic Wind Curves (CWCs) of the rolling stock, through Multi Body Simulations, as defined by the Technical Specifications for Interoperability (TSI) of High-Speed Rolling Stock. The comparison between the obtained CWC and a set of Reference CWCs (RCWCs) allows the assessment of the cross wind stability of the train being considered. The reference curves were deduced from the aerodynamic coefficients established for three reference trains: the ICE3, the TGV Duplex and the ETR500.

Currently the TSI define the reference curves for both a flat ground and a 6m reference embankment configuration. The flat ground configuration does not incorporate a representation of the ballast bed and rails, unlike the embankment configuration, and mainly for reasons of reproducibility in wind tunnel. The representation of a single track with ballast and rails was recently integrated as for the flat ground configuration in the current draft of the European norm EN 14067-6, dealing with cross wind stability. It seemed therefore necessary to identify the aerodynamic load for this configuration, and to assess the difference between the TSI and newly proposed CEN flat ground configurations.

This paper aims at presenting the aerodynamic properties of one of the cross wind reference vehicles, namely the TGV Duplex, recently measured in wind tunnel for both flat ground configurations with and without ballast and rails.

First the results show the qualification of test procedure at scale 1/15<sup>th</sup> at CSTB large wind tunnel, regarding experimental TSI requirements (Reynolds number independency, boundary layer thickness, ...). An agreement is found between with reference data measured at DNW wind tunnel for the TSI flat ground configuration and the ones obtained here.

Then the measurements for single track with ballast and rails are presented, giving the estimation of the increase of the rolling moment (main parameter for overturning phenomenon) compared to the previous configuration.

The resulting database may be used as reference data for validation of wind tunnel assessment of future rolling stock aerodynamics.

---

# COMPARISON OF THE FLOW FIELD AND AERODYNAMIC PERFORMANCE OF DIFFERENT REGIONAL TRAINS EXPOSED TO CROSS WINDS BY MEANS OF CFD AND WIND TUNNEL EXPERIMENTS

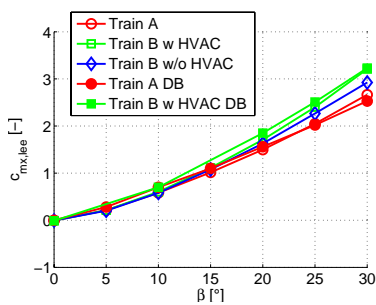
Henning Kroll<sup>\*</sup>, M. Schober<sup>†</sup>, C. N. Nayeri<sup>°</sup>, C. O. Paschereit<sup>°</sup>

<sup>\*</sup>Institut für Luft- und Raumfahrt, Technische Universität Berlin  
email: henning.kroll@ilr.tu-berlin.de

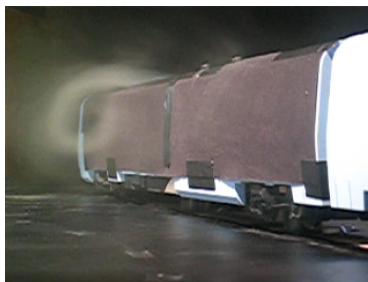
<sup>†</sup>Center of Competence Aerodynamics & Thermodynamics, Bombardier Transportation

<sup>°</sup>Hermann-Föttinger-Institut, Technische Universität Berlin

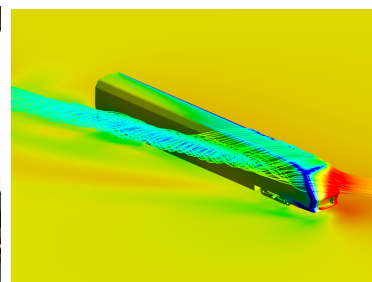
**Abstract.** *The focal point of this study is the comparison of two differently designed regional train models (train A and B), composed of the leading vehicle and a dummy on two different ground formations. The comparison between the vehicles is made with regards to the aerodynamic performance related to crosswind stability represented by the aerodynamic loads, which are quantified by experimental and numerical means. The flow of air past the two simplified 1:15 scaled regional train geometries, has been simulated numerically by solving the steady three-dimensional RANS equations, in addition to an experimental investigation performed in a wind tunnel, wherein fairly similar train geometries and same  $Re$  are used. Special attention is paid to the comparison of the numerical results and the experimental data. Figure (a) shows the experimentally obtained moment coefficient about the leeward rail  $c_{m_x,lee}$ , representing the most relevant parameter for over turning, as a function of yawing angle. A comparison with previous wind tunnel experiments carried out by DB shows a consistent trend. Starting with relatively small differences in  $c_{m_x,lee}$  for small yaw angles, train A performs significantly better as the yaw angle increases. The differences increase with increasing yaw angle up to 20% for  $\beta = 30^\circ$ . By experimental means the HVAC on train B's roof-top was found to have a major impact on the observed differences in the crucial loads between the trains. The side force and the roll moments respectively displayed definite lower values if the HVAC was removed, whereas the lift force was almost unaffected. Removing the HVAC compensated about 50% of the differences in the roll moment coefficients  $c_{m_x}$  and  $c_{m_x,lee}$  for larger yaw angles as  $30^\circ$ . These relative differences between the trains were confirmed in the simulations, and a fairly nice agreement with the experimental data could be achieved. Figures (b) and (c) show the lee-vortex visualized with smoke in the experiments, and illustrated by 3D-streamlines in the simulations. The lee-vortex to a large degree effects the magnitude of the roll moment by its strength and its distance to the train and the ground.*



(a)



(b)



(c)

## TOWING TANK EXPERIMENTS FOR HEAVY VEHICLE AERODYNAMICS

**Christian Navid Nayeri, Jakob Marquard, Andreas Fischer and  
Christian Oliver Paschereit**

Hermann-Föttinger Institut (ISTA)  
TU-Berlin, Müller-Breslau Str.8, 10623 Berlin, Germany  
e-mail: [christian.nayeri@tu-berlin.de](mailto:christian.nayeri@tu-berlin.de)

**Keywords:** heavy vehicle, aerodynamics, drag, moving ground

### Abstract

In ongoing studies on drag reducing devices for heavy vehicles, wind tunnel experiments have been carried out at the Hermann-Föttinger Institute of the TU-Berlin. As the wind tunnel is not equipped with a moving belt or a suction system to remove the boundary layer of the wind tunnel floor, the experiments do not include the simulation of a moving ground (road). Therefore, the use of a towing tank which is also available at the TU-Berlin was considered and realized. The towing tank has a length of 250 m and a depth of up to 4.5 m. The maximal carriage speed is 12 m/s. In order to gain experience with the towing tank preliminary experiments with a bluff body were carried out. The body is a box with the dimensions 1.35x0.2x0.3 m (LxWxH) and corresponds to a simplified European trailer at a scale of 1:10. The box was equipped with an internal force transducer to measure  $f_x$ . The maximum towing speed used was 4 m/s leading to a Reynolds number of  $Re \approx 5 \cdot 10^5$ . To estimate the influence of the water surface on the drag experiments were carried out at different depths. It was found out that below a depth of 1m the drag changes only marginally. As a next step comparative measurements in the wind tunnel and the towing tank were carried out with the box. Besides measurements with just the box also experiments with so called baseflaps as drag reducing devices were performed. After these studies, were the ground effect was not of interest yet, experiments were carried out with the model positioned near the floor of the wind tunnel. In the case of the towing tank an installation representing the road surface was submerged in the water (see figure). The results compared acceptable for such preliminary experiments. However, the towing tank set-up needs some more optimization regarding the attachment of the model to the carriage, the internal force transducer and the length of the "road". These optimizations are currently in progress.



# Aerodynamic analysis of high-speed trains by CFD simulations based on Lattice Boltzmann and Finite Volume Method

Yiwei Wang and Yiran An

With the increase of speed, aerodynamic problems of trains are emerging. Analysis of high-speed trains' aerodynamic performance in China has been carried out by different CFD methodologies. All results under different working conditions are in good agreement with actual situations.

Lattice Boltzmann Method (LBM) is adopted to simulate the aerodynamic performance of trains running in open air, in tunnel and under strong crosswind respectively. Non-simplified train model was used and the number of space grids reached tens of millions. Results show that CRH2's aerodynamic performance is good when running in open air (see Figure 1), but deteriorates severely when running in tunnel (see Figure 2) and under strong crosswind (see Figure 3), which provide a technological basis for the design of high-speed trains.

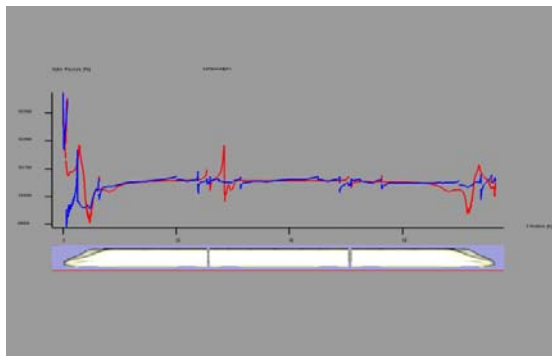


Figure 1 Surface pressure distribution on the train axis

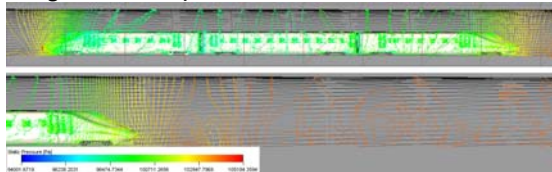


Figure 2 Pressure contours on train and tunnel's surfaces

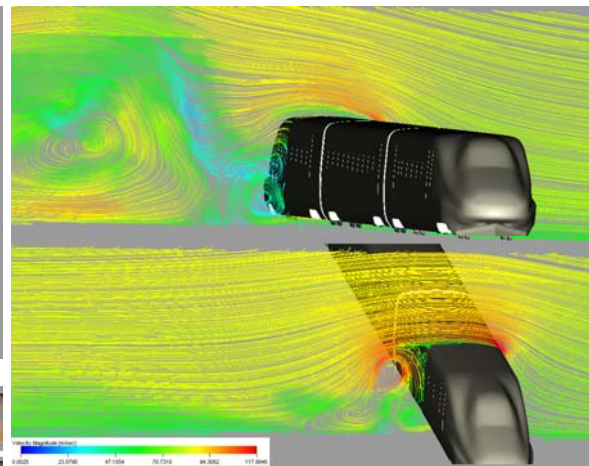


Figure 3 Flow pattern of the train running under strong crosswind

The pressure wave induced by different trains passing by each other (see Figure 4) has been obtained by using the commercial Finite Volume Method (FVM) software Fluent with dynamic mesh approach. Results indicate that complicated aerodynamic loads act on train bodies and deserve much attention.

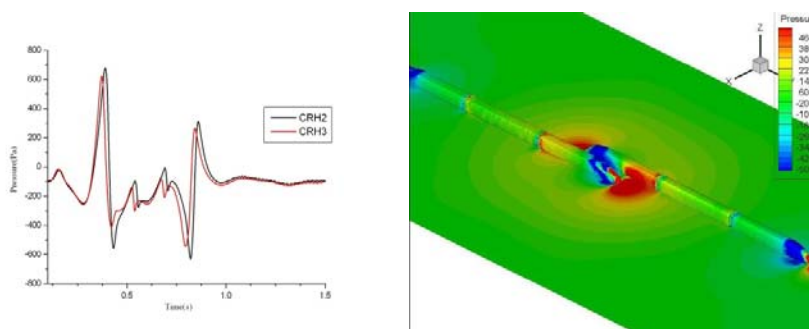


Figure 4 Contrast of pressure waves on two different trains passing by each other

# EUROMECH Colloquium 509 "Vehicle Aerodynamics"

## List of Participants

Aider, Jean-Luc	Laboratoire PMMH ESPCI, 10, rue Vauquelin, 75231 Paris, France <a href="mailto:aider@pmmh.espci.fr">aider@pmmh.espci.fr</a>
André, José Maria C.S.	Instituto Superior Tecnico, Technical University of Lisbon Av. Rovisco Pais 1, 1049-001 Lisboa, Portugal <a href="mailto:jmandre@hidro1.ist.utl.pt">jmandre@hidro1.ist.utl.pt</a>
Baker, Chris	University of Birmingham, Edgbaston, Birmingham B15 ZTT, UK <a href="mailto:c.j.baker@bham.ac.uk">c.j.baker@bham.ac.uk</a>
Berasarte, Aitor	CAF, J.M. Iturrioz, 26, 20200 Beasain, Spain <a href="mailto:aberasarte@caf.net">aberasarte@caf.net</a>
Bouchet, Jean-Paul	CSTB, Etablissement de Nantes, 11 Rue Henri Picherit, BP 82341, 44323 Nantes Cedex 3, France <a href="mailto:jean-paul.bouchet@cstb.fr">jean-paul.bouchet@cstb.fr</a>
Bruse, Martin	German-Dutch Wind Tunnels – DNW, Bunsenstr. 10, 37073 Göttingen <a href="mailto:martin.bruse@dnw.aero">martin.bruse@dnw.aero</a>
Carranini, Antonio	Deutsches Zentrum für Luft- und Raumfahrt, P.O. Box 1116, 82230 Wessling, Germany <a href="mailto:antonio.carranini@dlr.de">antonio.carranini@dlr.de</a>
Cortey, Edgar	CFD-Numerics – Fluid Flow Optimisation, 33, quai Arloing – CS 10306, 69337 Lyon Cedex 09, France <a href="mailto:edgar.cortey@cfd-numerics.com">edgar.cortey@cfd-numerics.com</a>
Diedrichs, Ben	Royal Institute of Technology (KTH), Aeronautical and Vehicle Engineering: Division of Rail Vehicles, Teknikringen 8, 100 44 Stockholm, Sweden <a href="mailto:Ben.Diedrichs@se.transport.bombardier.com">Ben.Diedrichs@se.transport.bombardier.com</a>
Duriez, Thomas	Laboratoire PMMH ESPCI, 10, rue Vauquelin, 75231 Paris, France <a href="mailto:thomas.duriez@espci.org">thomas.duriez@espci.org</a>

Eichinger, Sandor	Institut für Strömungsmechanik und Technische Akustik, Technische Universität Berlin, Müller-Breslau-Str. 8, 10623 Berlin, Germany <a href="mailto:sandor.eichinger@cf-d.tu-berlin.de">sandor.eichinger@cf-d.tu-berlin.de</a>
Eng, Matthias	Technische Universität Berlin, Müller-Breslau-Str. 8, 10623 Berlin, Germany <a href="mailto:eng.matthias@gmail.com">eng.matthias@gmail.com</a>
Fischer, Oliver	Forschungsinstitut für Kraftfahrwesen und Fahrzeugmotoren Stuttgart, Pfaffenwaldring 12, 70569 Stuttgart, Germany <a href="mailto:oliver.fischer@fkfs.de">oliver.fischer@fkfs.de</a>
Garcia, Javier	Universidad Politécnica de Madrid, Dpto. Ing. Energetica y Fluidmecánica, C/ Jose Gutierrez Abascal, 2, 28006 Madrid, Spain <a href="mailto:garcia@etsii.upm.es">garcia@etsii.upm.es</a>
Grégoire, Rémi	Core Competence Network Leader, Aerodynamics ALSTOM Transport, Etablissement d'Aytré-La Rochelle, Avenue du Commandant Lysiack, B.P. 359, 17001 La Rochelle Cedex, France <a href="mailto:remi.gregoire@transport.alstom.com">remi.gregoire@transport.alstom.com</a>
Haff, Johannes	Deutsches Zentrum für Luft- und Raumfahrt, Bunsenstr. 10, 37073 Göttingen, Germany <a href="mailto:johannes.haff@dlr.de">johannes.haff@dlr.de</a>
Herbst, Astrid	Bombardier Transportation, Östra Ringvägen 2B, 721 73 Västerås, Sweden <a href="mailto:astrid.herbst@se.transport.bombardier.com">astrid.herbst@se.transport.bombardier.com</a>
Hoefener, Lars	Deutsche Bahn AG, Systemtechnik, Völckerstr. 5, 80939 München, Germany <a href="mailto:lars.hoefener@deutschebahn.com">lars.hoefener@deutschebahn.com</a>
Hucho, Wolf-Heinrich	Gärtnerieweg 3, 86938 Schondorf am Ammersee, Germany <a href="mailto:HuchoWHH@t-online.de">HuchoWHH@t-online.de</a>
Jönsson, Mattias	Deutsches Zentrum für Luft- und Raumfahrt, Bunsenstr. 10, 37073 Göttingen, Germany <a href="mailto:matthias.joensson@dlr.de">matthias.joensson@dlr.de</a>
Johnson, Terry	Rail Safety & Standards Board, 160 Euston Rd. London NW1 2DX, UK <a href="mailto:terry.johnson@deltarail.com">terry.johnson@deltarail.com</a>

Kopp, Stephan	MAN Nutzfahrzeuge AG, Dachauer Str. 667, 80995 München, Germany <a href="mailto:stephan.kopp@man.eu">stephan.kopp@man.eu</a>
Kowalski, Thomas	Deutsches Zentrum für Luft- und Raumfahrt, Bunsenstr. 10, 37073 Göttingen, Germany <a href="mailto:thomas.kowalski@dlr.de">thomas.kowalski@dlr.de</a>
Krajnović, Siniša	Chalmers University of Technology, Department of Applied Mechanics, 412 96 Gothenburg, Sweden <a href="mailto:sinisa@chalmers.se">sinisa@chalmers.se</a>
Kroll, Henning	Institut für Luft- und Raumfahrt, TU Berlin, Marchstr. 12, Sekr. F2, 10587 Berlin, Germany <a href="mailto:henning.kroll@ilr.tu-berlin.de">henning.kroll@ilr.tu-berlin.de</a>
Löfdahl, Lennart	Chalmers University of Technology, Department of Thermo- and Fluid Dynamics, 412 96 Göteborg, Sweden <a href="mailto:lennart.lofdahl@chalmers.se">lennart.lofdahl@chalmers.se</a>
Marklund, Jesper	Chalmers University of Technology, Department of Applied Mechanics, 412 96 Gothenburg, Sweden <a href="mailto:ture@chalmers.se">ture@chalmers.se</a>
Masson, Elisa	SNCF, Direction de l'Innovation et de la Recherche, 45 rue de Londres, 75908 Paris, France <a href="mailto:elisa.masson@sncf.fr">elisa.masson@sncf.fr</a>
Meskine, Mohammed	EXA, Les Collines de l'Arche, 76 Route de la Demi-Lune, 92057 Paris la Défense Cedex, France <a href="mailto:mmeskine@exa.com">mmeskine@exa.com</a>
Muld, Thomas	Royal Institute of Technology (KTH) Teknikringen 8, 100 44 Stockholm, Sweden <a href="mailto:muto02@kth.se">muto02@kth.se</a>
Naumann, Rolf	FH Bielefeld, University of Applied Sciences, Am Stadtholz 24, 33609 Bielefeld, Germany <a href="mailto:rolf.naumann@fh-bielefeld.de">rolf.naumann@fh-bielefeld.de</a>
Nayeri, Christian Navid	Hermann-Föttinger-Institut (ISTA), Technische Universität Berlin, Müller-Breslau-Str. 8, 10623 Berlin, Germany <a href="mailto:christian.nayeri@tu-berlin.de">christian.nayeri@tu-berlin.de</a>
Niedermeier, Christoph	BMW Group, Bergstr. 5, 85395 Attenkirchen, Germany <a href="mailto:christoph.niedermeier@mytum.de">christoph.niedermeier@mytum.de</a>



Niesner, Reinhold	Volkswagen AG, PF 1737, 38436 Wolfsburg, Germany <a href="mailto:reinhold-niesner@volkswagen.de">reinhold-niesner@volkswagen.de</a>
Orellano, Alexander	Bombardier Transportation, Am Rathenaupark, 16761 Henningsdorf, Germany <a href="mailto:alexander.orellano@de.transport.bombardier.com">alexander.orellano@de.transport.bombardier.com</a>
Paradot, Nicolas	SNCF – CIM, 4 Allee des Gemeaux, 72100 Le Mans, France <a href="mailto:nicolas.paradot@sncf.fr">nicolas.paradot@sncf.fr</a>
Paschereit, Christian Oliver	Hermann-Föttinger-Institut (ISTA), Technische Universität Berlin, Müller-Breslau-Str. 8, 10623 Berlin, Germany <a href="mailto:oliver.paschereit@tu-berlin.de">oliver.paschereit@tu-berlin.de</a>
Perzon, Sven	Go Virtual Nordic AB, Askims Verkstadsväg 5A, 436 34 Askim, Sweden <a href="mailto:sven.perzon@govirtual.se">sven.perzon@govirtual.se</a>
Preissler, Martin	MAN Nutzfahrzeuge AG, Dachauer Str. 667, 80996 München, Germany <a href="mailto:martin-gerald.preissler@man.eu">martin-gerald.preissler@man.eu</a>
Raemdonck van, Gandert	TU Delft, Kluyverweg 1, 2629 HS Delft, The Netherlands <a href="mailto:g.m.r.vanraemdonck@tudelft.nl">g.m.r.vanraemdonck@tudelft.nl</a>
Ripamonti, Francesco	Mechanical Department – Politecnico Milano, Via la Masa 1, 20158 Milano, Italy <a href="mailto:francesco.ripamonti@polimi.it">francesco.ripamonti@polimi.it</a>
Rocchi, Daniele	Mechanical Department – Politecnico Milano, Via la Masa 1, 20158 Milano, Italy <a href="mailto:daniele.rocchi@polimi.it">daniele.rocchi@polimi.it</a>
Rüd, Nina	Deutsche Bahn AG, Völckerstr. 5, 80939 München, Germany <a href="mailto:nina.rued@bahn.de">nina.rued@bahn.de</a>
Saussine, Gilles	SNCF, Transportation and Research Department, 45 rue de Londres, 75908 Paris, France <a href="mailto:gilles.saussine@sncf.fr">gilles.saussine@sncf.fr</a>
Schober, Martin	Bombardier Transportation, Am Rathenaupark, 16761 Henningsdorf, Germany <a href="mailto:martin.schober@de.transport.bombardier.com">martin.schober@de.transport.bombardier.com</a>

Schwarze, Rüdiger TU Bergakademie Freiberg,  
Institute of Mechanics and Fluid Dynamics,  
Lampadiusstr. 4, 09599 Freiberg, Germany  
[Ruediger.Schwarze@imfd.tu-freiberg.de](mailto:Ruediger.Schwarze@imfd.tu-freiberg.de)

Seifert, Avraham Tel Aviv University, Ramat Aviv, 69978, Israel  
[seifert@eng.tau.ac.il](mailto:seifert@eng.tau.ac.il)

Stiepel, Marc ALSTOM LHB GmbH – Berechnung und Laufdynamik  
Linke-Hofmann-Busch-Str. 1, 38239 Salzgitter, Germany  
[marc.stiepel@transport.alstom.com](mailto:marc.stiepel@transport.alstom.com)

Tielkes, Thorsten Deutsche Bahn AG, Völckerstr. 5, 80939 München, Germany  
[thorsten.tielkes@deutschebahn.com](mailto:thorsten.tielkes@deutschebahn.com)

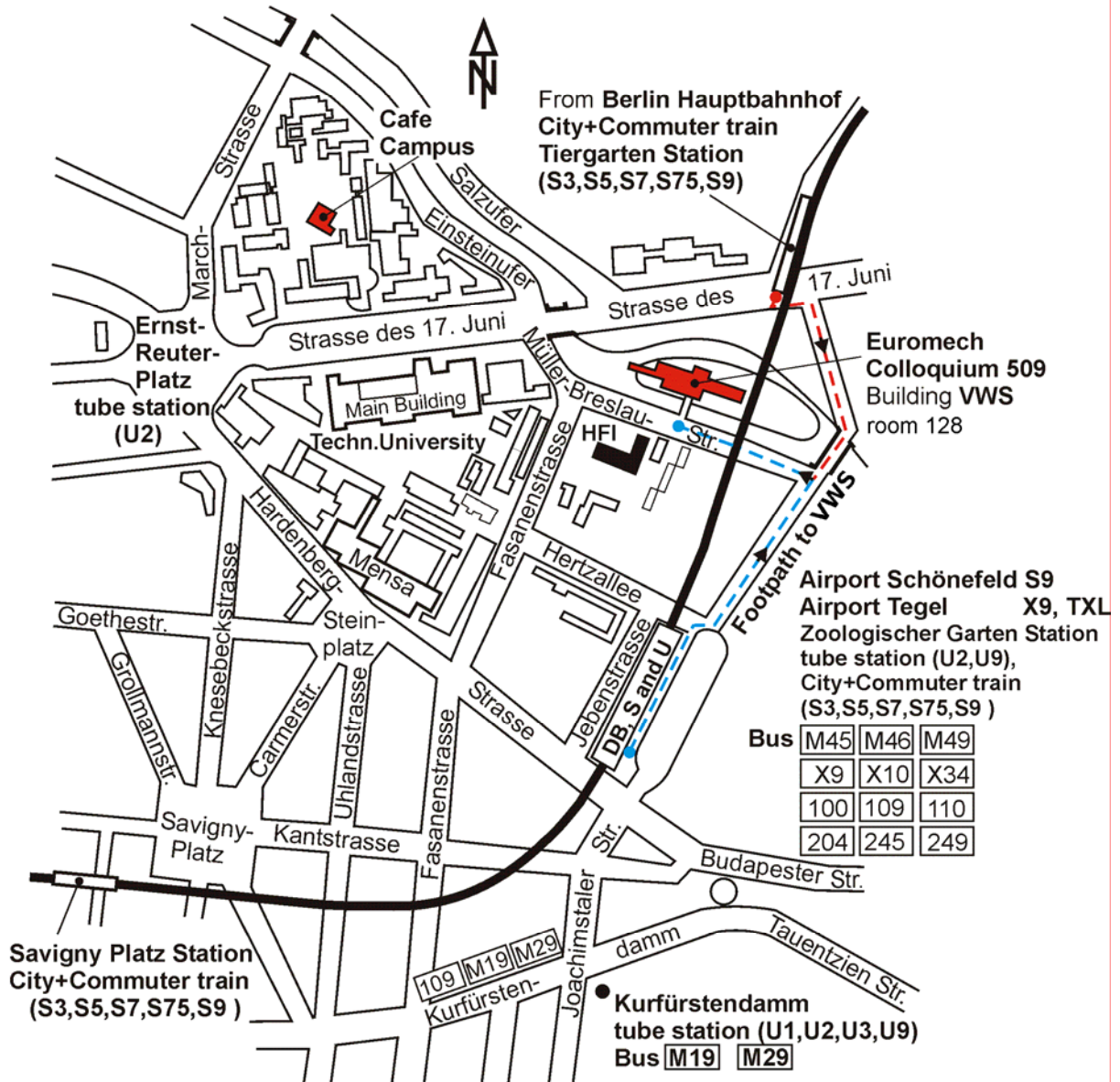
Tomasini, Gisella Mechanical Department – Politecnico Milano, Via la Masa 1,  
20158 Milano, Italy  
[gisella.tomasini@polimi.it](mailto:gisella.tomasini@polimi.it)

Traore, Achmed ALSTOM LHB GmbH – Berechnung und Laufdynamik  
Linke-Hofmann-Busch-Str. 1, 38239 Salzgitter, Germany  
[achmed.traore@transport.alstom.com](mailto:achmed.traore@transport.alstom.com)

Uruba, Václav Institute of Thermomechanics, Dolejškova 5, Praha 8,  
Czech Republic  
[uruba@it.cas.cz](mailto:uruba@it.cas.cz)

Wassen, Erik Institut für Strömungsmechanik und Technische Akustik,  
Technische Universität Berlin, Müller-Breslau-Str. 8,  
10623 Berlin, Germany  
[erik.wassen@cf.tu-berlin.de](mailto:erik.wassen@cf.tu-berlin.de)

## Institut für Strömungsmechanik und Technische Akustik



Follow the broken line from the train and bus station **Zoologischer Garten** or **Tiergarten** as shown on the map, above until the restaurant "Schleusenkrug" and then turn under the bridge into the Müller-Breslau-Strasse.

Adresse: Institut für Strömungsmechanik und Technische Akustik  
Technische Universität Berlin  
Müller-Breslau-Strasse 8  
10623 Berlin-Charlottenburg  
phone: 030/31423359